MEDYNA 2017

2nd Euro-Mediterranean Conference on Structural Dynamics and Vibroacoustics

25-27 Apr 2017 Sevilla (Spain)
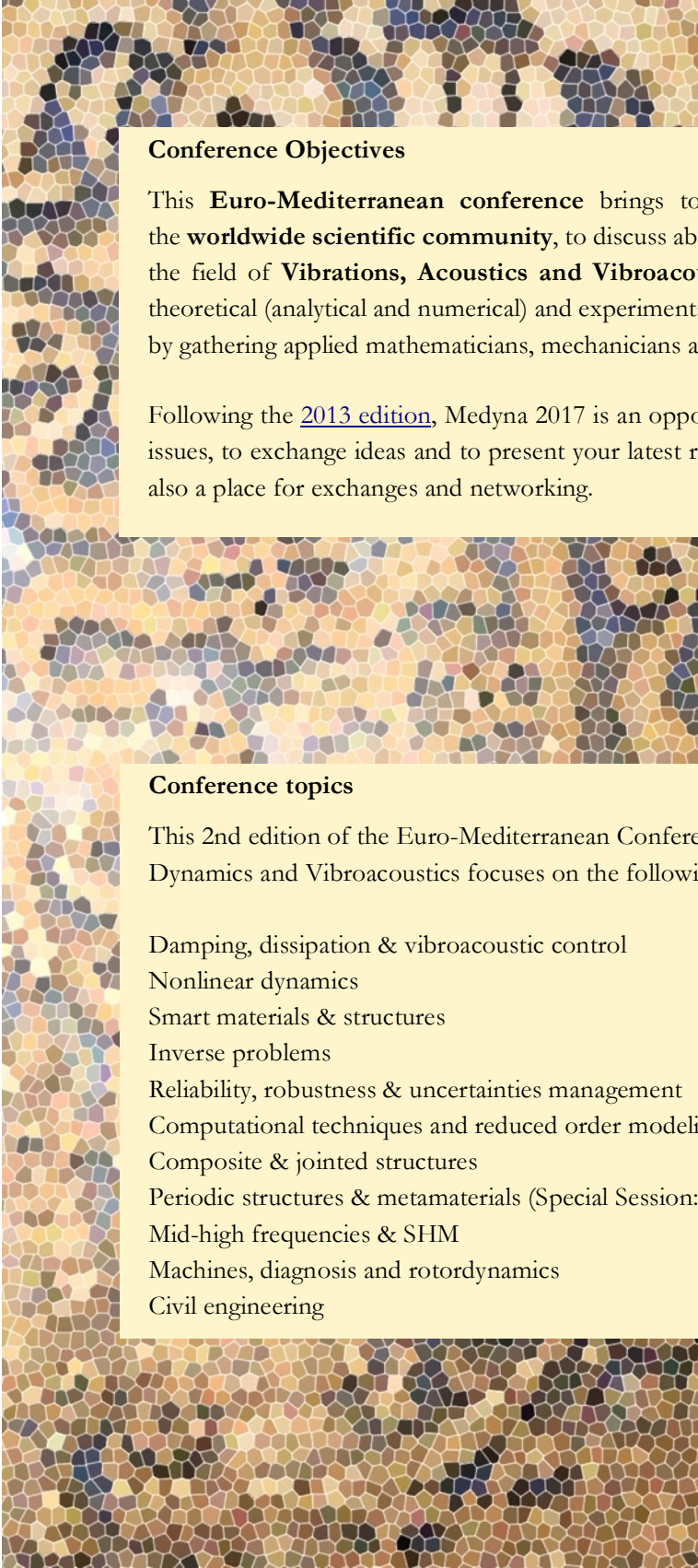
Supported by

AMVA — Association Marocaine de Vibration et Acoustique

AFM — ASSOCIATION FRANÇAISE DE MECANIQUE

SFA

ATAVI

SEA

Hosted by

Escuela Técnica Superior de
INGENIERÍA DE SEVILLA

Book of Proceedings

Conference Objectives

This **Euro-Mediterranean conference** brings together researchers from the **worldwide scientific community**, to discuss about the major advances in the field of **Vibrations, Acoustics and Vibroacoustics**. It addresses both theoretical (analytical and numerical) and experimental methods in these topics by gathering applied mathematicians, mechanicians and acousticians.

Following the 2013 edition, Medyna 2017 is an opportunity to discuss current issues, to exchange ideas and to present your latest researches in this area, but also a place for exchanges and networking.

Conference topics

This 2nd edition of the Euro-Mediterranean Conference on Structural Dynamics and Vibroacoustics focuses on the following topics :

Damping, dissipation & vibroacoustic control
Nonlinear dynamics
Smart materials & structures
Inverse problems
Reliability, robustness & uncertainties management
Computational techniques and reduced order modeling
Composite & jointed structures
Periodic structures & metamaterials (Special Session: ITN EJD VIPER)
Mid-high frequencies & SHM
Machines, diagnosis and rotordynamics
Civil engineering

MEDYNA
2017

Scientific Committee

Adnan Akay

Makrem Arfaoui

Pierre Argoul

José Roberto de França Arruda

Noureddine Atalla

Mohamed Belhaq

Mabrouk Ben Tahar

Rhali Benamar

Hachmi Ben Dhia

Noureddine Bouhaddi

Claude Boutin

Jérôme Buffe

Kenneth A. Cunefare

Sergio Da Rosa

Arnaud Deraemaeker

Wim Desmet

Jean-François Deü

Régis Dufour

Peter Eberhard

Emmanuel Foltête

François Gautier

Jean-Claude Golinval

Mohamed Haddar

Lotfi Hammami

Jan Holnicki

Mohamed Ichchou

Eric Jacquelin

Daniel Juvé

Chafik Karra

Alexandre Kawano

Gaetan Kerschen

Faouzi Lakrad

Robin Langley

Alain Le Bot

Hervé Lissek

Brian Mace

Jarir Mahfoud

Anders Nilsson

Goran Pavic

Joel Perret-Liaudet

Carles Pézerat

Domingos Alves Rade

Pedro Ribeiro

Massimo Ruzzene

Rubens Sampaio

Fabrizio Scarpa

Fusheng Sui

Jing Tian

Bernard Troclet

Jun Yang

Abdelmalek Zine

MEDYNA
2017

The 2nd edition of **MEDYNA** brought together **96 attendants** in Sevilla from **12 countries** (Belgium, Brazil, Canada, France, Germany, Italy, Morocco, Spain, Switzerland, Tunisia, Turkey, United Kingdom).

The **Best Student Communication Award** was delivered to **Thibaut GRAS** for the paper untitled "Wave finite elements - finite elements coupling to compute the dynamic response of an heterogeneous railway track" by Thibaut Gras, Mohamed-Ali Hamdi, Mabrouk Bentahar, Samir Assaf.
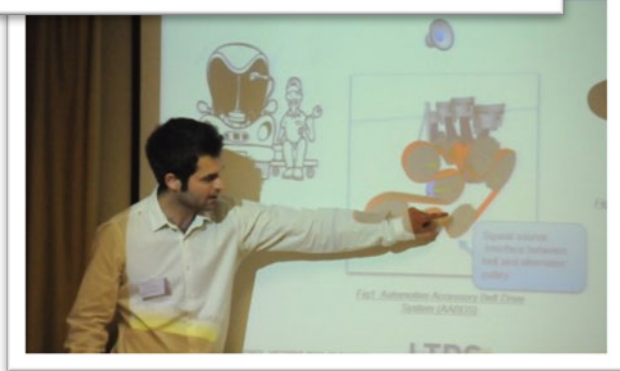
The Conference Board

Morvan Ouisse (FEMTO-ST, France)	General Chair
Olivier Bareille (LTDS – ECL, France)	General Co-Chair
Faouzi Lakrad (Morocco)	Regional Co-Chair - Morocco
Tahar Fakhakh (ENIS, Tunisia)	Regional Co-Chair - Tunisia
Jaime Domínguez Abascal (U. Sevilla, Spain)	Regional Co-Chair - Spain
Nicolas Peyret (SUPMECA, FR)	Organizing Committee Co-Chair

Organizing Committee

Pedro Galvin, Juana Mayo, Mario Solís, Daniel García Vallejo	Local committee
Zsoka Bori, Christine Froidevaux, Isabelle Navarro, Hélène Schoch, Christelle Tisserand	Registrations, administrative support
Jean-François Deü	Best communication award organization
Olivier Bareille, Morvan Ouisse	Web site & Program
Adrien Pelat	Reviewing
Simon Chesné, Kerem Ege	Proceedings Edition

MEDYNA
2017

Keynote lecture

Sondipon Adhikari - Swansea University (UK) - Homogenisation and dynamics of randomly irregular metamaterial

Abstract: Metamaterials based on hexagonal periodic cells (honeycombs) have gained considerable attention in recent years. This can be an advanced material due to its capability of meeting high performance requirements in various critically desirable application-specific parameters. These structural assemblies not only make an efficient use of material, but are also characterized by interesting dynamic and wave propagation properties. A semi-analytical formulation has been developed for wave propagation in irregular honeycombs. Spatial structural irregularity of hexagonal lattices has been considered. There are few scientific literatures available concerning analysis of wave propagation in regular honeycombs. However, due to inevitable uncertainties associated with manufacturing and service conditions, honeycomb lattices may not be always perfectly regular. The effect of spatially random structural irregularity in wave velocities of such irregular honeycombs will be discussed. The nature of so called 'pass band' and 'stop bands' due to irregularities will be explained.

Prof Adhikari is the chair of Aerospace Engineering in the College of Engineering of Swansea University. Currently he is a Wolfson Research Merit Award holder from the Royal Society. He received his PhD in 2001 from the University of Cambridge (in Trinity College). He was an Engineering and Physical Science Research Council (EPSRC) Advanced Research Fellow and winner of the Philip Leverhulme Prize (2007). He was a lecturer at the Bristol University and a Junior Research Fellow in Fitzwilliam College, Cambridge. He was a visiting Professor at the Carleton University, The University of Paris East and a visiting scientist at the Los Alamos National Laboratory. From 2015 he has been a Distinguished Visiting Professor at the University of Johannesburg.

His research areas are multidisciplinary in nature and include uncertainty quantification in dynamic systems, computational nanomechanics (nanotubes, graphene, nano-bio sensors), dynamics of complex systems, inverse problems for linear and non-linear dynamics and vibration energy harvesting. He has obtained more than £1.5M of competitive research funding as principal investigator, published four books, 251 international journal papers and over 150 conference papers in these areas. His works have been widely cited (over 7000 citations and a H-index of 45 in Google scholar) in the scientific community.

Professor Adhikari is in the editorial board of 17 international journals, research grant reviewer of 15 funding councils and served in over 40 Scientific and Technical Committees. He is an associate Fellow of American Institute of Aeronautics and Astronautics (AIAA) and a member of AIAA Non-Deterministic Approaches Technical committee (NDA-TC).

MEDYNA 2017

Mohamed Belhaq - University Hassan II of Casablanca (MA) - On the stability loss of limit cycle oscillations near strong resonances: synchronization and heteroclinic bifurcation

Abstract: In self-excited nonlinear oscillators subjected to harmonicforcing, frequency-locking can occur near strong resonances. This phenomenon results from synchronization between the frequency of theforcing and the frequency of the limit cycle oscillation leading to frequency-locked motions for which the response of the system follows the forcing frequency.

In the case of 1:4 resonance, which is considered as one of the unsolved problem in nonlinear dynamics the limit cycle loses its stability at the synchronization via heteroclinic bifurcation. Usually, the transition between quasi-periodic and synchronized motions occurs via heteroclinic connections at two different frequencies causing hysteresis and bistability. Therefore, analytical approximation of heteroclinic bifurcations near the 1:4 resonance is of great importance since they determine the locations at which the frequency-locked motion takes place.

The existence of heteroclinic orbits in ordinary differential equations corresponds to the existence of coherent structures such as solitons and fronts in certain partial differential equations. For instance, they form the profiles of traveling wave solutions in reaction–diffusion problems and spatially localized post-buckling states in static dynamics. Also, heteroclinic orbits correspond to the onset of various types of synchronization in certain problems in physics and biology. Therefore, one of the challenging problems is the analytical capture of the heteroclinic bifurcations location near the strong resonances. To the best of our knowledge, rigorous analytical expressions of heteroclinic bifurcation near these resonances have not been obtained, only numerical methods have been performed. In this talk, recent analytical methods to capture approximation of such heteroclinic bifurcations in the problem of stability loss of limit cycle oscillations near the 1:4 resonance will be presented. The problem of 1:3 resonance will be also discussed.

* Joint work with W. Qin, K.W. Chung and A. Fahsi

Mohamed Belhaq is Professor of Mechanics at University Hassan II-Casablanca. He received his Ph.D. at the University Paul Sabatier, France. He has been a visiting professor and lecturer at FU Berlin, University of Sevilla, University of L'Aquila, EC Lyon, INSA Lyon, UC Madrid, Military University of Warsaw, University of Munich, Cornell University, Virginia Tech University, Perdue University, Indiana State University and University of Jordan. Belhaq received two Fulbright Scholarships for conducting research at Cornell University and at Virginia Tech University and has been DAAD scholar at FU Berlin. He is in the editorial board of several international journals and serves as an Associate Editor to the Journal of Vibration and Control. Belhaq is a member of the International Research Center for Mathematics & Mechanics of Complex Systems (M&MoCS). He edited two books, published 124 papers in leading journals of mechanics and nonlinear dynamics, and he contributed in many international conferences.

José Luis Escalona - University of Sevilla (SP) - Multibody modeling and simulation of the dynamics of railroad vehicles and tracks

Abstract: Computational analysis of the dynamics of railroad vehicles is becoming an essential tool for this industry. Vehicle designers, rolling stock manufactures and railroad administrations benefit from the special modeling tools provided by the different railroad multibody softwares that are present in the market. Railroad dynamics is nowadays a sub-field of multibody dynamics that is characterized by the use of special algorithms for the treatment of the track geometry and the wheel-rail interaction.

This presentation shows the theoretical foundations of these algorithms. Railroad vehicles have been traditionally designed using linearized equations that uncouple the longitudinal, lateral and vertical dynamics. Linear models can be used to find a first approximation of the response of the vehicle to the track geometric irregularities, the lateral stability or the curving behavior. Linear models are based on the kinematics of the conical wheels, linear creep wheel-rail forces and the vehicle is considered as a collection of rigid bodies connected by springs and dashpots.

On the other hand, multibody models of the railroad vehicles and track take into account the complex wheel-rail contact geometry and their normal and tangential interaction forces. The railroad vehicle bodies are assumed to be connected by kinematic joints and the can be considered as deformable. These modeling capabilities provide a more detailed insight into the vehicle dynamics at the expense of much longer computational analysis. However, special techniques like the use of trajectory coordinates or contact lookup tables alleviate this problem without significant reduction in accuracy. This presentation shows the modelling keys for the real-time simulation of railway vehicles using multibody dynamics that can be used in on–board applications.

José L. Escalona is professor of Mechanical Engineering at the University of Seville, Spain. His research fields are Flexible Multibody Dynamics and Railway Dynamics. He received his degree in Mechanical Engineering and Ph.D. at the University of Seville. He has been Fulbright scholar at the University of Illinois at Chicago, research scholar at the University of Stuttgart and visiting professor at Lappeenranta University of Technology. He is associate editor of the ASME Journal of Computational and Nonlinear Dynamics, member of the scientific board of the International Journal of Railway Technology, Secretary of the IFToMM Committee for Multibody Dynamics and member of the ASME Committee for Multibody and Nonlinear Dynamics. Escalona has published 36 journal papers and over 60 conference papers. Escalona is also founder of the spin-off company "virtualmech".

Special forum session

"In honour of Prof. Mohamed Ali Hamdi" (UTC / FR)

organized by Noureddine Attala (GAUS / CA)

This forum session will be the opportunity for the conference attendes to acknowledge Professor Hamdi's contributions in the field of vibroacoustics. Some researchers who have close association with Prof. Hamdi, past and present collaborators, will participate to this forum, including:

  - **Noureddine Atalla** (GAUS / CA) - Introduction

  - **Claude Lesueur** (video only) (ISAT / FR)

  - **Mohamed Ali Hamdi** (UTC / FR)

  - **Jean-Michel Ville** (UTC / FR)

  - **Christian Glandier** (Daimler-Benz AG / DE)

  - **Marc Anciant** (ESI Group / FR)

  - **Thibaut Gras** (UTC / FR)

  - **Gérard Borello** (InterAC / FR)

  - **Bernard Troclet** (Airbus Safran Launchers / FR)

  - **Bryce Gardner** (ESI Group / FR)

Mohamed-Ali Hamdi is Professor at the University of Technology of Compiegne (UTC, France) since 1978. Doctor Es-sciences (1982), Doctor Engineer (1978) and Mechanical Engineer of "Ecole Nationale Supérieure des Arts et Métiers (Angers 71-74, Paris 1975)".

Known as worldwide expert in computational vibro-acoustics. He developed numerical methods based on Boundary and Finite Element Methods (BEM-FEM) for solving noise & vibration problems encountered in aerospace, aeronautic and ground transportation industries. He supervise 27 PhD's and published over 100 scientific papers.

He founded in 1986 STRACO (STRuctural ACOustics), a Technology Transfer company spin-off of his research team at UTC, specialized in development of Vibro-Acoustic (VA) Computer Aided Engineering (CAE) Software tools (RAYON® BEM-FEM Solvers) dedicated to modeling and solving of Noise, Vibration and Harshness (NVH) problems. STRACO has been acquired early 2001 by ESI Group, a top 5 worldwide software editor leader, specialized in virtual prototyping and virtual manufacturing. Since 2001 Professor Hamdi is acting as Scientific Director of the Vibro-Acostic Software Branch of ESI Group.

He has been awarded by the "National Order of Merit" in Education and Sciences in 1996 and by the Award Technology Transfer University-Industry of the French Acoustic Society in 2008.

MEDYNA 2017

08:45 - 09:00	Opening Ceremony - Conference chairs	**Sala de Grados**
09:00 - 09:40	Keynote Lecture Chair : Olivier Bareille	
09:00 - 09:40	On the stability loss of limit cycle oscillations near strong resonances: synchronization and heteroclinic bifurcation - *Mohammed Belhaq, Université de Casablanca, Faculty of Sciences, Casablanca, MAROC*	

09:40 - 10:20	Coffee break

Sala de grados

10:20 - 12:40	Computational techniques & Reduced Order Modeling Chair : Jean-François Deü
10:20 - 10:40	› A fixed point algorithm and model reduction in jointed structures simulation - *Nicolas Peyret, Gael Chevallier, Anthony Meurdefroid*
10:40 - 11:00	› Vibroacoustic control of double-panel structures using viscoelastic and piezoelectric materials - a finite element reduced order modeling - *Walid Larbi, Jean-François Deü, Roger Ohayon*
11:00 - 11:20	› Simulation of rack-pinion gears in steering systems using elastic multibody models - *Christian Pfister, Jens Pfister, Peter Eberhard*
11:20 - 11:40	› Time domain finite element analysis of structures with fractional viscoelastic damping using time-diffusive scheme - *Lucie Rouleau, Jean-François Deü, Denis Matignon*
11:40 - 12:00	i› Extension of the variational theory of complex rays for heterogeneous media - *Herve Riou, Hao Li, Pierre Ladevèze*
12:00 - 12:20	› A spectral boundary element approach to represent scattered waves in unbounded acoustic regions - *F.J. Cruz-Muñoz, Antonio Romero Ordóñez, P. Galvín, A. Tadeu*

Sala de Juntas

10:20 - 12:40	Periodic structures and metamaterials (Special Session: ITN EJD VIPER) Chair : Mohamed Ichchou
10:20 - 10:35	› Aerodynamic Loading of Periodic Structures - *Fabrizio Errico, Mohamed Ichchou, Olivier Bareille, Sergio De Rosa, Francesco Franco*
10:35 - 11:00	› First literature review for the analysis of quasi-periodicity variability effects and modeling strategies - *Safiullah Timorian, Sergio De Rosa, Franco Francesco, Morvan Ouisse, Noureddine Bouhaddi*
11:00 - 11:15	› Kirigami inspired natural fibre cellular structures for future vibroacoustics applications - *Simone Del Broccolo, Marc-Antoine Campana, Rita Palumbo, Yousef Dobah, Fabrizio Scarpa, Morvan Ouisse, Mohamed Ichchou*
11:15 - 11:30	› A literature review for the analysis of viboracoustic properties of periodic inclusions in porous materials - *Dario Magliacano, Morvan Ouisse, R. Chaléat, Abdelkrim Khelif, Sergio De Rosa, Francesco Franco*
11:30 - 11:45	› Multi-layer core topology systems - *Nassardin Guenfoud, Mohamed Ichchou, Olivier Bareille, Wim Desmet, Bert Pluymers*
11:45 - 12:00	› Industrial application of periodic structures to aircraft/launchers - *Giovanni Tufano, Mohamed Ichchou, Olivier Bareille, Abdel-Malek Zine, Wim Desmet, Bert Pluymers*
12:00 - 12:15	› A literature review for the analysis of structured and unstructured uncertainty effects on vibroacoustic - *Ravi Pratap Singh, Sergio De Rosa, Francesco Franco, Mohamed Ichchou, Olivier Bareille*
12:15 - 12:35	› Continuous description for the dynamic behaviour of 1d framed structures - *Xiangkun Sun, Changwei Zhou, Mohamed Ichchou, Abdelmalek Zine, Jean-Pierre Lainé, Stéphane Hans, Claude Boutin*

12:20 - 13:40	

13:40 - 15:40 — Nonlinear dynamics
Chair : Mohamed Belhaq

13:40 - 14:00	› Dynamical regimes for a time-correlated randomly excited bouncing ball model - *Joel Perret-Liaudet, Chaima Zouabi, Julien Scheibert*
14:00 - 14:20	› Vertical dynamics of two sliding rough surfaces : comparison between numerical and analytical approaches to describe the excitation source - *Nicolas Ponthus, Julien scheibert, Joel Perret-Liaudet*
14:20 - 14:40	› On the Wet Belt Squeal: Characterization of the Mechanical Vibration and Influence of the Mechanical Properties of the Belt on Friction-Induced Instabilities - *Simon Gatignol, Thierry Desmassougne, Alain Le Bot*
14:40 - 15:00	› Analysis of large amplitude oscillations of simply supported beams through the use of the Nonlinear Normal Modes (NNM) method - *Daniel García-Vallejo, Jaime Domínguez, Javier González Carbajal*
15:00 - 15:20	› Analysis of nonlinear and non-smooth dynamics of a self-oscillating series resonant inverter - *Enrique Ponce, Abdelali El Aroudi, Luis Benadero*
15:20 - 15:40	› Geometrically non-linear vibrations of beams carrying a point mass and restrained by translational and rotational springs at the ends - *Adri Ahmed*

Sala de Grados

13:40 - 15:40 — Smart materials & structures for vibroacoustics
Chair : Simon Chesné & Hervé Lissek

13:40 - 14:00	› Energy harvesting in a nonlinear harvester under modulated delay amplitude - *Zakaria Ghouli, Mustapha Hamdi, Faouzi Lakrad, Mohamed Belhaq*
14:00 - 14:20	› Design and experimental validation of an active acoustic liner for aircraft engine noise reduction - *Gaël Matten, Morvan Ouisse, Manuel Collet, Sami Karkar, Hervé Lissek, Romain Boulandet, Marc Versaevel*
14:20 - 14:40	› Shunted Piezoelectric Trap Device to Enhance Energy Harvesting - *Fabien Maugan, Kaijun Yi, Mélodie Monteil, Simon Chesne, Manuel Collet*
14:40 - 15:00	› Vibration reduction of composite plates with shunted piezopatches: analytical modeling and numerical validation - *Amirreza Aghakhani, Murat Gozum, Ipek Basdogan*
15:00 - 15:20	› Phase compensator for hyperstable hybrid mass damper - *Simon Chesne, Christophe Collette*
15:20 - 15:40	› Structural health monitoring of a smart composite structure with a Time-of-Flight method - *Xianlong Chen, Yann Meyer, Rémy Lachat, Morvan Ouisse*

Sala de Juntas

15:40 - 16:20 — Coffee break

16:20 - 17:40 — Nonlinear dynamics
Chair : Mohamed Belhaq

16:20 - 16:40	› Modal interactions in a two-nanomechanical-resonator array - *Clément Grenat, Sébastien Baguet, Régis Dufour, Claude-Henri Lamarque*
16:40 - 17:00	, › Geometrically nonlinear of orthotropic plates using semi-analytical method - *Hanane Bhar, Omar Baho, Rhali Benamar, Bilal Harras*
17:00 - 17:20	› An effective formulation and a physical discrete model for geometrically nonlinear transverse vibrations of a symmetrically laminated composite beam - *Abdellatif Rahmouni, Rhali Benamar*
17:20 - 17:40	› Geometric nonlinearties effect on cable linear vibrations - *Achref Mansour, Giuseppe Rega, Othman Ben Mekki, Sami Montassar*

Sala de Grados

16:20 - 17:00 — Smart materials & structures for vibroacoustics
Chair : Simon Chesné & Hervé Lissek

16:20 - 16:40	› Bayesian Control of a Helicopter Main Gearbox Semi-active Suspension System - Experiments on a quarter-suspension prototype - *Jonathan Rodriguez, François Malburet*
16:40 - 17:00	› Design of active multiple-degrees-of-freedom electroacoustic resonators for use as broadband sound absorbers - *Hervé Lissek, Etienne Rivet, Sami Karkar, Romain Boulandet*

Sala de Juntas

20:30 - 22:00 — Welcome Reception

Wednesday , April 26th - morning

Sala de Grados

08:30 - 09:10 — Keynote Lecture
Chair : Daniel García Vallejo

08:30 - 09:10 Multibody modeling and simulation of the dynamics of railroad vehicles and tracks - *José Luis Escalona, Universidad de Sevilla*

Sala de Grados

09:10 - 10:50 — Mid-High Frequencies & SHM
Chair : Alain Le Bot

09:10 - 09:30 › Vibro-acoustic energy flow on a car floor structure using dynamical energy analysis - *Timo Hartmann, Gregor Tanner, Gang Xie*

09:30 - 09:50 › High-frequency structure- and air-borne sound transmission for a tractor model using dynamical energy analysis- *Gregor Tanner, Timo Hartmann, Satoshi Morita*

09:50 - 10:10 › Simulation of finite-sized dynamic systems using wave transmission method - *Gerard Borello*

10:10 - 10:30 › Uncertainty quantification in mid-frequency range simulations using the statistical modal energy distribution analysis - *Emeline Sadoulet-Reboul, Kendra Van Buren, Morvan Ouisse, Scott Cogan, Laurent Maxit*

10:30 - 10:50 › Statistical energy analysis, assumptions and validity - *Alain Le Bot, Nicolas Totaro, Thibault Lafont*

Sala de Juntas

09:10 - 10:50 — Machines, diagnosis & Rotordynamics
Chair : Jarir Mahfoud & Patrick Keogh

09:10 - 09:30 › External disturbance rejection for compressors on active magnetic bearings - *Angelo Bonfitto, Andrea Tonoli, Nicola Amati*

09:30 - 09:50 › On the use of flexibly-mounted, internal-stator magnetic bearings for vibration control of a flexible rotor- *Christopher Lusty, Patrick Keogh*

09:50 - 10:10 › The induced by meshing stiffness variation dynamics of planetary gears using an iterative spectral method - *Joel Perret-Liaudet, Huiyang Xu, Jessica Neufond, Emmanuel Rigaud*

10:10 - 10:30 › Stability of rotating machine supported by active magnetic bearings during base motion - *Jarir Mahfoud, Clément Jarroux, Régis Dufour, Franck Legrand, Benjamin Defoy, Thomas Alban*

10:30 - 10:50 › The dynamics, stability and control of rotor touchdown in active magnetic bearing systems - *Patrick Keogh, Chris Lusty*

10:50 - 11:20 Coffee break

Sala de Grados

11:20 - 12:40 — Mid-High Frequencies & SHM
Chair : Alain Le Bot

11:20 - 11:40 › Wave conversion process in lightweight structures: diffusion through defects in the transition bandwidth - *Christophe Droz, Philip Becht, Bert Pluymers, Wim Desmet*

11:40 - 12:00 › A lagrangian based damage indicator for use on complex structures - *Yi Hui, Hian Lee Kwa, Olivier Bareille, Mohamed Ichchou*

12:00 - 12:20 › MUSIC algorithm for vibro-acoustic defect detection - *Philip Becht, Elke Deckers, Claus Claeys, Bert Pluymers, Wim Desmet*

12:20 - 12:40 › A discrete model for vibration of cracked beams resting partially elastic foundations - *Rhali Benamar, Ahmed Khnaijar*

Sala de Juntas

11:20 - 12:40 — Inverse problems in vibroacoustics
Chair : Nabil Gmati & Antonio González

11:20 - 11:40 › Numerical model to simulate the forward and reverse sound transmision mechanism in hearing - *Antonio Gonzalez-Herrera, Javier Camacho, Jose Garcia-Manrique*

11:40 - 12:00 › Timpanic membrane prestrain evaluation based on the dynamic response - *Antonio Gonzalez-Herrera, Luis Caminos*

12:00 - 12:20 › Identification of structural forces from acoustic measurement using the inverse simplified energy method - *Mohamed Amine Ben Souf, Ahmed Samet, Olivier Bareille, Tahar Fakhfakh, Mohamed Ichchou, Mohamed Haddar*

12:20 - 12:40 › Inverse characterization of sandwich structures using single-shot wave speed measurements - *Christophe Droz, Olivier Bareille, Mohamed Ichchou*

12:40 - 14:00 Lunch

14:00 - 16:00 Special forum session In honour of Prof. Mohamed Ali Hamdi
Chair : Noureddine Atalla

14:00 - 14:10 › Introduction - *Noureddine Attala, Department of Mechanical Engineering, Université de Sherbrooke*

14:10 - 14:20 › Video message for Prof. Mohamed Ali Hamdi - *Claude Lesueur, Département de Recherche en Ingénierie des Véhicules pour l'Environnement*

14:20 - 15:00 › Symmetric variational coupling of Boundary and Finite Element Methods for solving Vibro-Acoustic problems - *Mohamed-Ali Hamdi, Laboratoire Roberval UMR 7337*

15:00 - 15:20 › Engine sources Identification using an Inverse BEM technique - *Christian Glandier, T. Vogt, J. Morkholt, Abderrazak Omrani, Mohamed-Ali Hamdi - Daimler-Benz AG*

15:20 - 15:40 › The development of RAYON-PEM solver - Academic & Industrial Milestones - *Marc Anciant, Lassen Mebarek - ESI-Group*

15:40 - 16:00 › Aero-acoustic experimental identification of feedback mechanisms due to HVAC components - J*ean-Michel Ville, Université de Technologie de Compiègne*

16:00 - 16:30 Coffee break

16:30 - 18:10 Special forum session In honour of Prof. Mohamed Ali Hamdi
Chair : Noureddine Atalla

16:30 - 16:50 › Lessons Learned from ARIANE 4 and ARIANE 5 Vibroacoustics Analysis - *Bernard Troclet, AIRBUS Defence & Space*

16:50 - 17:10 › Prediction of acoustic and shock responses of spacecrafts over broadband frequency range - *Gerard Borello, InterAC*

17:10 - 17:30 › Diffuse field loading of space structures - modeling and test - *Bryce Gardner, ESI US R&D*

17:30 - 17:50 › Wave finite elements - finite elements coupling to compute the dynamic response of an heteroheneous railway track - *Thibaut GRAS, Institut de Recherche Technologique Railenium*

17:50 - 18:10 › Application of the Partition of Unity Finite Element Method to exterior acoustics problems - *Jean-Daniel Chazot, Laboratoire Roberval UMR 7337*

20:30 - 23:00 Gala Dinner

Sala de Grados

Sala de Grados

Sala de Grados

09:00 - 09:40	Keynote Lecture Chair : Morvan Ouisse
09:00 - 09:40	› Homogenisation and dynamics of randomly irregular metamaterial - *Sondipon Adhikari, swansea university*

Sala de Junta

09:40 - 10:40	Damping, dissipation and vibroacoustic control including rubber-like materials Chair : Makrem Arfaoui, Adnane Boukamel, Ramzi Othman & Abdelmalek Zine
09:40 - 10:00	› Predictive capabilities of four finite strain viscoelastic models under seperability assumption - *Nidhal Jridi, Arfaoui Makrem, Hamdi Adel, Olivier Bareille, Mohamed Ichchou, Jalel Ben Abdallah*
10:00 - 10:20	› Nonfactorizable viscoelastic behavior: modeling and identification - *Adel Tayeb, Abdelmalek Zine, Makrem Arfaoui, Mohamed Ichchou, Adel Hamdi, Jalel Ben Abdallah*
10:20 - 10:40	› Study on the lifecycle of rubber suspension elements for optimised maintenance and safe dynamic behaviour - *Andrés Malo Estepa, Adnane Boukamel, Thierry Tison, Franck Massa*

Sala de Grados

09:40 - 10:40	Periodic structures and metamaterials (Special Session: ITN EJD VIPER) Chair : Fabrizio Scarpa
09:40 - 10:00	› Analytical and numerical local sensitivity analysis of periodic spring-mass chains - *Leandro Rodrigues Cunha, Morvan Ouisse, Domingos Alves Rade*
10:00 - 10:20	› Study of the first Bragg band gap features of Euler contrasted periodic beams - *Adrien Pelat, Thomas Gallot, François Gautier*
10:20 - 10:40	› Hybrid wave based-finite element unit cell model to predict reflection, transmission and absorption coefficients of periodic material systems - *Lucas Van Belle, Elke Deckers, Stijn Jonckheere, Claus Claeys, Wim Desmet*

10:40 - 11:20	Coffee break

Sala de Junta

11:20 - 12:40	Reliability, robustness & uncertainties management Chair : Domingos Alves Rade & Noureddine Bouhaddi
11:20 - 11:40	› Stochastic acoustic control of internal sound using TMD - *Elyes Mrabet, , Mohamed Ichchou, Noureddine Bouhaddi*
11:40 - 12:00	› Global sensitivity analysis on sandwich panel's acoustic characteristics with correlated inputs - *Wenqi Chai, Zakaria Zergoune, Abdelmalek Zine, Mohamed Ichchou*
12:00 - 12:20	› Stochastic analysis of near-periodic coupled pendulums chain - *Noureddine Bouhaddi, Khaoula Chikhaoui, Noureddine Bouhaddi, Najib Kacem, Mohamed Ichchou*
12:20 - 12:40	› Robust aeroelastic optimization of towsteered composite panels - *Domingos Rade, Thiago Guimarães*

Sala de Grados

11:20 - 12:40	Periodic structures and metamaterials (Special Session: ITN EJD VIPER) Chair : Mohamed Ichchou
11:20 - 11:40	› Spatial spectra of the eigenmodes of ribbed plates projected on dispersion branches - *Xavier Boutillon, Gautier Lefebvre, Marcel Filoche*
11:40 - 12:00	› Chiral Lattice Hinge Metamaterial for multi-broadband vibroacoustics - *Fabrizio Scarpa, Wenjiao Zhang, Dayi Zhang, Robin Neville, Lifeng Wang, Roderic Lakes*
12:00 - 12:20	› Design and experimental validation of a hierarchical auxetic rectangular perforated metamaterial - *Kevin Billon, Fabrizio Scarpa, Morvan Ouisse, Emeline Sadoulet-Reboul, Manuel Collet, Gaël Chevallier*
12:20 - 12:40	› Structural-acoustic optimization of 2-D Gradient Auxetic Sandwich Panels - *Mohammad Sadegh Mazloomi, Mostafa Ranjbar, Luca Boldrin, Fabrizio Scarpa, Neriman Ozada*

Sala de Grados

12:40 - 13:00	Best Student Paper Award & Closing Ceremony - Conference Chairs

Table of contents

Session
Periodic structures and metamaterials (special session: ITN EJD VIPER)
Chair : Mohamed Ichchou & Fabrizio Scarpa

NONFACTORIZABLE VISCOELASTIC BEHAVIOR: MODELING AND IDENTIFICATION

A. Tayeb[1,2] ,A. Zine[3] ,M. Arfaoui[1], M. Ichchou[2*], A. Hamdi[1] and J. Benabdallah[1]

[1] LR-11-ES19 Laboratoire de Mcanique Appliquée et Ingénierie
Université de Tunis El Manar, École Nationale dIngnieurs de Tunis
Tunis 1002, Tunisie
Email: teyebadel@yahoo.fr, makremarfaoui@yahoo.fr, ahamdi.tn@gmail.com and
jalel.benabdallah@enit.rnu.tn

[2]Laboratoire de tribologie et dynamique des systèmes
'Ecole Centrale de Lyon, Ecully 69130, France
Email: mohamed.ichchou@ec-lyon.fr

[3]Université de Lyon, Institut Camille Jordan, CNRSUMR5208, Département de
Mathématiques et Informatique
'Ecole Centrale de Lyon, Ecully 69130, France
Email: abdel-malek.zine@ec-lyon.fr

ABSTRACT

A three dimensional viscoelastic model at finite strain representing nonfactorizable behaviour of rubber like materials is proposed. The model is based upon the internal state variables approach within the framework of rational thermodynamics such that the second principle of thermodynamics is satisfied. Motivated by experimental and rheological results, the nonfactorizable aspect of the behavior was introduced via strain dependent relaxation times which leads to a reduced time with a strain shift function. The identification of the models parameters and its capacity to predict the nonfactorizable behaviour of rubber like materials with the multi-integral viscoelastic model of Pipkin is addressed.

1   INTRODUCTION

It is well known that rubber-like materials exhibit nonlinear viscoelastic behavior over a wide range of strain and strain rates confronted in several engineering applications such as civil engineering, automotive and aerospace industries. Further, the time dependent properties of these materials, such as shear relaxation modulus and creep compliance, are, in general, functions of the history of the strain or the stress [1]. Therefore, in a wide range of strain a linear viscoelasticity theory is no longer applicable for such material. Hence, new constitutive equations are required to fully depict the behavior of rubber-like. In this work we shall develop a nonlinear model at finite strain for nonfactorizable viscoelastic materials within the framework of rational thermodynamics and the approach of internal state variables, see [2], [3] and [4] taking into account the dependence of the time dependent functions upon the state of the strain. The identification of several functions in the model to the multi-integral model of Pipkin [5] is performed with Matlab software. This paper is organized as follows: in section 2 the mechanical framework and the model are recalled. In section 3 a brief review of the model by [5] is presented and the results of the identification are highlighted.

2   MECHANICAL FRAMEWORK AND CONSTITUTIVE EQUATIONS

Consider a viscoelastic material with reference placement Ω_0 in the reference configuration C_0. It occupies at the time t the placement Ω in the deformed configuration C_t. Let φ denote a macroscopic motion between the two configurations, which maps any point X in the reference configuration C_0 to the point x in the deformed configuration. Let $F(X,t) = \partial x / \partial X$ be the deformation gradient tensor. Likewise, let $J = \det(F)$ be the jacobian of the deformation gradient tensor. From the deformation gradient $F(X,t)$, the right and left Cauchy-Green strain tensors $C = F^t F$ and $B = FF^t$ are obtained. The formulation of the constitutive equations in the nonlinear range of behavior is based upon the decomposition of the deformation gradient tensor $F(X,t)$ into volumetric and isochoric parts such that:

$$\bar{F} = J^{-1/3}F \qquad \text{where } \det\left(\bar{F}\right) = 1 \tag{1}$$

in which $\bar{F}$ is the isochoric part of the deformation gradient tensor, the right and left Cauchy-Green strain tensors associated with it reads:

$$\bar{C} = \bar{F}^t \bar{F} = J^{-2/3}C, \ \ \bar{B} = \bar{F}\bar{F}^t = J^{-2/3}B \tag{2}$$

The free energy density according to [2] is expressed as follows:

$$\Psi\left(\bar{C}, Q\right) = U^0\left(J\right) + \bar{\Psi}^0\left(\bar{C}\right) - \frac{1}{2}Q : \bar{C} + \Psi_I\left(Q\right) \tag{3}$$

in which Q is a second order tensor internal variable akin to the second Piola-Kirchhoff stress tensor, its evolution law is expressed as follow:

$$\frac{\partial Q}{\partial \xi} + \frac{1}{\tau}Q = \frac{\gamma}{\tau}DEV\left[2\frac{\partial \Psi^0\left(\bar{C}\right)}{\partial \bar{C}}\right] \quad \text{with } \xi\left(t\right) = \int_0^t \frac{dt'}{a\left(\bar{C}\right)} \tag{4}$$

in which $DEV\left(\bullet\right) = \left(\bullet\right) - \frac{1}{3}\left[C : \left(\bullet\right)\right]C^{-1}$ denotes the deviator operator in the reference configuration. γ and τ are the viscoelastic parameter and the relaxation time of the Prony series respectively, in relation 4 ξ denotes the reduced time which is an increasing function of real time t and $a(\bar{C})$ is a positive function of the left Cauchy-Green strain tensor called a strain-shift

---

2

function. Application of the Clausius-Duhem inequality and the resolution of the evolution equation 4 along with the form of the free energy density of equation 3 lead to the expression of the second Piola-Kirchhoff stress tensor.

$$S = J^{-2/3} \int_0^\xi G\left(\xi - \xi'\right) \frac{\partial}{\partial \xi'} DEV \left(2\frac{\partial \Psi^0\left(\bar{C}\right)}{\partial \bar{C}}\right) d\xi' + JpC^{-1} \tag{5}$$

3 IDENTIFICATION OF THE PIPKIN MODEL

3.1 Pipkin isotropic model

Pipkin [5] proposed a third order development of the tensorial response function Q for an isotropic incompressible material. The principle of material indifference requires that the Cauchy stress tensor takes the following form:

$$\sigma = RQR^t + pI \tag{6}$$

R is the rotation tensor obtained from the polar decomposition of the transformation gradient tensor F and p is the indeterminate parameter due to incompressibility. The third functional development of Q reads

$$Q\left(t\right) = \int_0^t r_1\left(t - t'\right)\dot{E}\left(t'\right) dt' + \int_0^t \int_0^t r_2(t - t', t - t'')\dot{E}\left(t'\right)\dot{E}\left(t''\right) dt'\, dt'' + \\ \int_0^t \int_0^t \int_0^t r_3\left(t - t', t - t'', t - t'''\right) tr\left[\dot{E}\left(t'\right)\dot{E}\left(t''\right)\right]\dot{E}\left(t'''\right) dt'dt''dt''' + \\ \int_0^t \int_0^t \int_0^t r_4\left(t - t', t - t'', t - t'''\right)\dot{E}\left(t'\right)\dot{E}\left(t''\right)\dot{E}\left(t'''\right) dt'dt''dt''' \tag{7}$$

$r_i\, i = 1...4$ are the relaxation kernels expressed by a decaying exponential functions and $\dot{E}\left(t\right)$ is the time derivative of the Green-Lagrange deformation tensor $E = 1/2\left(C - I\right)$.

3.2 Identification of the model's functions

The free energy density Ψ^0, the viscoelastic kernel $G(\xi)$ and the reduced time $\xi(t)$ of relation 5 are identified separately. To this end data in pure shear and simple extension were generated following relations 6 and 7. Equilibrium tests of simple extension and pure shear are used in the identification of Ψ^0, relaxation tests with small level of strain in pure shear are used in the identification of $G(\xi)$ and monotonic tests of simple extension are used in the identification of $\xi(t)$ and then the whole identification procedure is validated by predicting the response of the model to a monotonic test of pure shear. Each identification procedure turns out to a least square minimization problem. The results of this identification are plotted in figure 1 in terms of the hyperelastic response and in figure 2 in terms of the reduced time function and the predicted response of the model in pure shear for two different strain rates: $\dot{\varepsilon} = 100\%$ and $\dot{\varepsilon} = 200\%$.

4 CONCLUDING REMARKS

A nonlinear viscoelastic model at finite strain to describe nonfactorizable behavior of rubber like materials has been proposed. The model is formulated using the decomposition of the deformation gradient tensor which makes it applicable to both compressible and incompressible materials. The identification of the model's functions to the multi-integral isotropic model of Pipkin [5] is highlighted and a significant potential of the model to track the response of this model is obtained.
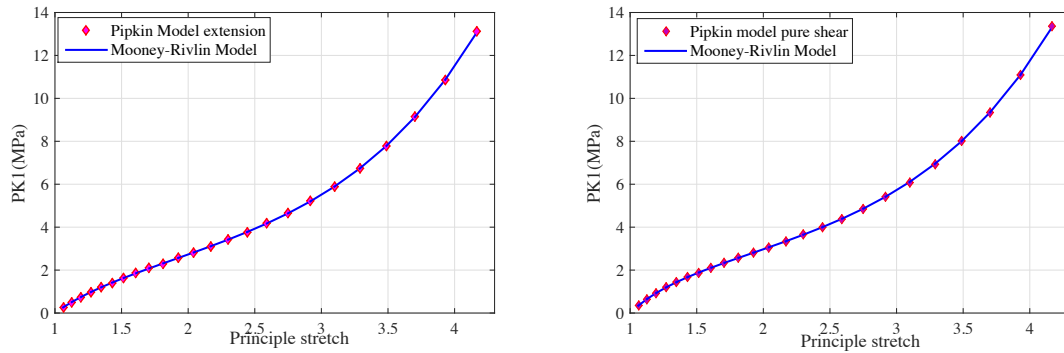
(a) Piola-Kirchhoff stress versus principle stretch for simple extension

(b) Piola-Kirchhoff stress versus principle stretch for pure shear

Figure 1. Equilibrium response for the Pipkin model and the Mooney-Rivlin model [6]
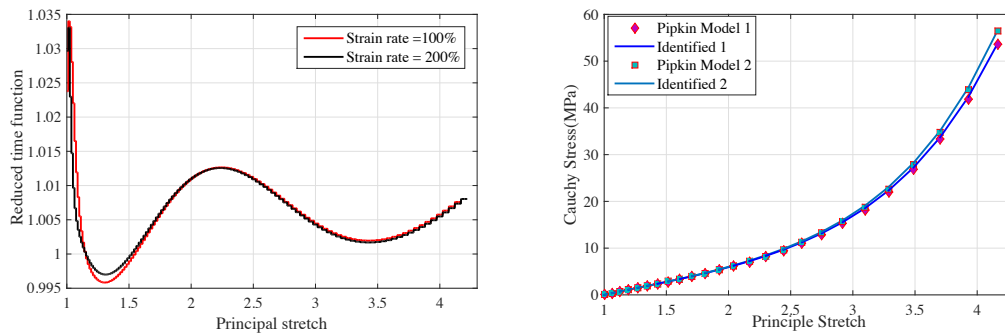
(a) Reduced time function $a(\bar{C})$ versus principle stretch for two strain rates

(b) Cauchy stress in simple shear versus principle stretch for two strain rates

Figure 2. Identification results: Reduced time function and Cauchy stress

REFERENCES

[1] R. A. Schapery. An engineering theory of nonlinear viscoelasticity with applications. *International Journal of Solids and Structures*, 2(3):407–425, July 1966.

[2] R. A. Simo. On a fully three-dimensional finite-strain viscoelastic damage model: Formulation and computational aspects. *Computer Methods in Applied Mechanics and Engineering*, 60:153–173, 1987.

[3] G. Holzapfel and R. A. Simo. A new viscoelastic constitutive model for continuous media at finite thermomechanical changes. *International Journal of Solids and Structures*, 33:3019–3034, 1996.

[4] S. Reese and S. Govindjee. A theory of viscoelasticity and numerical applications. *International Journal of Solids and Structures*, 35:3455–3482, 1998.

[5] A. C. Pipkin. Small finite deformations of viscoelastic solids. *Reviews of Modern Physics*, 36(4):1034–1041, 1964.

[6] R.S. Rivlin. Large elastic deformations of isotropic materials. iv. further developments of the general theory. *Philosophical Transactions of the Royal Society of London A: Mathematical, Physical and Engineering Sciences*, 241(835):379–397, 1948.

4

PREDICTIVE CAPABILITIES OF FOUR FINITE STRAIN VISCOELASTIC MODELS UNDER SEPERABILITY ASSUMPTION

Nidhal JRIDI[1,2*] , Makrem ARFAOUI[1], Adel HAMDI[1], Olivier BAREILLE[2], Mohamed ICHCHOU[2] and Jalel BEN ABDALLAH[1]

[1]Université de Tunis El Manar, Ecole Nationale d'Ingénieurs de Tunis, Laboratoire de Mécanique Appliquée et Ingénierie LR-11-ES19 (LRMAI), BP 37 Le Belvedere 1002 Tunis, Tunisie
email: jridinidhal@gmail.com

[2]Ecole Centrale de Lyon, Laboratoire de Tribologie et Dynamique des Systèmes (LTDS) CNRS UMR 5513, 36 Avenue Guy de Collongues, 69130 Ecully, France

ABSTRACT

The predictive capabilities of some integral-based finite strain viscoelastic models under the time-strain seperability assumption have been investigated through experimental data for monotonic, relaxation and dynamic shear loads, in time and frequency domains. This survey is instigated by experimental observations on three vulcanized rubber material intended for an engineering damping application. Models under consideration are Christensen, Fosdick & Yu, a variant of BKZ model and the Simo model. In the time domain, for each test case and for each model, the nominal stress is hence compared to experimental data, and the predictive capabilities are then examined with respect to three polynomial forms hyperelastic potentials. In the frequency domain, the predictive capabilities have been analysed with respect to the frequency and predeformation effects.

1   INTRODUCTION

Elastomeric compounds are widely used in industry for their mechanical properties particularly their damping capabilities e.g tires, shock-absorbing bushes, construction industry, aerospace applications... To design industrial compounds efficiently, it is of major importance to be able to predict the impact of the nonlinearity effects on the products, and estimating the damping capability is a primary feature to be considered in many engineering applications. While many contributions investigated either the purely elastic phenomena for elastomers at large deformations [1] or the viscoelastic phenomenon [2], the attention is here focused on the hysteritic time dependent part of the response.

The objective of the current work is the analysis of the predictive capabilities of some heridi-tary integral-based constitutive models in time and frequency domains, under the separability assumption [3][4]. From an historically point of view, the constitutive theory of finite linear viscoelasticity [5] have been of a major contribution and is founded on an extension of the Boltzmann superposition principle to finite strain. The stress quantity is decomposed to an equilibrium part corresponding to the stress response at highly slow rate, and an overstress quantity expressed as an heriditary integral including a measure of material's memory through relaxation functions. Based on experimental observations, the time-strain separability or factorability assumption [4] is frequently introduced in the formulation of finite strain viscoelasticity constitutive models and afford a large theoretical simplicity.

2   MODELS UNDER CONSIDERATION

In the present work, some of major contributions finite strain viscoelastic models involving heriditary integral have been considered under the seperability assumption, chosen so as to not require a special identification procedure. All parameters have been identified using Abaqus Evaluate Module. The models under consideration are: Christensen [6], Fosdick & Yu [7], a variant of BKZ [8] and Simo Model [9]:

$$\boldsymbol{\sigma}^{Ch} = -p\mathbf{I} + 2\mathbf{B}\frac{\partial W}{\partial \mathbf{B}} + \mathbf{F}\,G_0\int_0^t g_1(t-s)\frac{\partial \mathbf{E}(\mathbf{s})}{\partial s}ds\mathbf{F}^T \tag{1a}$$

$$\boldsymbol{\sigma}^{FY} = -p\mathbf{I} + 2\mathbf{B}\frac{\partial W}{\partial \mathbf{B}} + G_0\int_0^t g_1(t-s)\frac{\partial \mathbf{E}_t(s)}{\partial s}ds \tag{1b}$$

$$\boldsymbol{\sigma}^{BKZ} = -p\mathbf{I} + 2\mathbf{B}\frac{\partial W}{\partial \mathbf{B}} - 2\,\mathbf{F}\,G_0\int_0^t g_1(t-s)\frac{\partial \mathbf{C}^{-1}}{\partial s}ds\,\mathbf{F}^T \tag{1c}$$

$$\boldsymbol{\sigma}^{Si} = -p\mathbf{I} + 2\mathbf{B}\frac{\partial W}{\partial \mathbf{B}}\frac{1}{g_\infty}+$$
$$dev\left[\int_0^t \frac{\partial g_1(s)}{\partial s}\mathbf{F}_t^{-1}(t-s)\frac{2}{g_\infty}\mathbf{B}(t-s)\frac{\partial W}{\partial \mathbf{B}}\mathbf{F}_t^{-T}(t-s)\,ds\right] \tag{1d}$$

where $\mathbf{F} = \frac{\partial \mathbf{x}}{\partial \mathbf{X}}$ is the deformation gradient. The right and left Cauchy-Green strain tensor are consecutively $\mathbf{C} = \mathbf{F}^T\mathbf{F}$ and $\mathbf{B} = \mathbf{F}\mathbf{F}^T$. The Green-Saint-Venant strain tensor is $\mathbf{E} = \frac{1}{2}(\mathbf{C}-\mathbf{I})$. the hyperelastic free energy potential $W = W(I_1, I_2)$ and I_1 and I_2 stands for the isotropic scalar-valued invariants of $\mathbf{C}$. $g_1(t)$ is the dimensionless relaxation kernel defined as a Prony series and commonly taken as: $g_1(t) = \sum_{i=1}^N g_i(e^{\frac{-t}{\tau_i}})$ with g_i and τ_i are material's parameters. $g_i > 0$, $g_\infty = 1 - \sum_{i=1}^N g_i$. G_0 is the instantaneous linear shear modulus.

2

3   ON THE CAPABILITY TO PREDICT TIME-DEPENDENT EXPERIMENTS

3.1   Monotonic tests

The available experimental data are for an uniaxial tension test and a simple shear test, with different strain-rates. Considering purely hyperelastic response, we make use of the equilibrium strain-stress curves for the identification of the hyperelastic potential. Herein, we made the choice on the polynomial hyperelasic form and its particular cases NeoHookean and Mooney-Rivlin. Considering viscoelastic phenomena, we identified the prony series through normalized shear relaxation data.

The response of monotonic tension/shear nominal stress for bromobutyl BIIR material are reported in Fig.1 . The considered models present the capability to take into account a strain rate effect, with higher stain rates leading to a higher stress at same deformation level. Considering a Neo-Hookean or a Mooney-Rivlin hyperelastic potential, the predicted data are seen to be non accurate, and all the models could not predict the second inflection point. Considering the 2nd Order Polynomial hyperelastic potential, we observed that the Christensen model (1a) is seen to highly over-estimate the nominal stress level for high strains, not to exceed 100% of deformation. Fosdick & Yu model (1b) is seen to underestimate the stress level for the three materials, and has the lowest stress level through all models. Nevertheless, the predicted level is seen to be acceptable. Meanwhile, both BKZ (1c) and Simo (1d) models were able to give a better approximation of the stress level. The prediction is quite good and the predicted stress is in a good range.
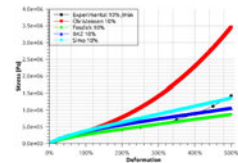
(a) NeoHoohean 10 % min^{-1}
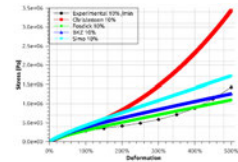
(b) Mooney Rivlin 10 % min^{-1}
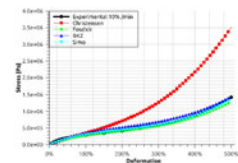
(c) 2nd Ord. poly 10 % min^{-1}
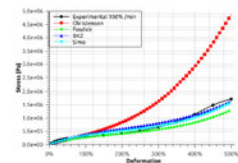
(d) 2nd Ord. poly 100 % min^{-1}

Figure 1: BIIR monotonic tension

3.2   Relaxation tests

The evaluation of the prony series is available in the abaqus evaluation module for normalized shear stress relaxation experiments. The deformation taken into account for shear relaxation tests is less than 50% of deformation. For a very long relaxation time i.e $t \rightarrow \infty$, the relaxation equilibrium expression:

$$\sigma_{12}^{Poly\,Equil} = 2\left(C_{10} + 2C_{20}\gamma_0^2 + C_{11}\gamma_0^2 + C_{01} + 2C_{02}\gamma_0^2 + C_{11}\gamma_0^2\right)\gamma_0 \qquad (2)$$

Comparison of models response is graphically shown in Fig. 2. We observed that the Neo-Hookean hyperelastic potential, as well as Mooney-Rivlin, the models are seen to not well predict the relaxation test data. The 2nd order Polynomial hyperelastic model offers the best prediction for the long-term relaxation stress response and the measured error is of an acceptable level. The major difference between models is seen for the hysteritic part. The Simo model is seen to offer a good fidelity to approximate low times stress. Christensen and Fosdick & Yu models underestimate the hysteritic stress level while the BKZ model is observed to highly overestimate the instantaneous relaxation stress.

4   ON THE CAPABILITY TO PREDICT FREQUENCY-DEPENDENT EXPERIMENTS

The determination of the complex shear modulus was introduced by [6] and is a Fourrier transform of the governing equations defined for a kinematically small perturbation about a predeformed state. Since the available experimental data in the frequency domain are limited to

(a) NeoHookean   (b) Mooney-Rivlin   (c) 2nd Order Polynomial
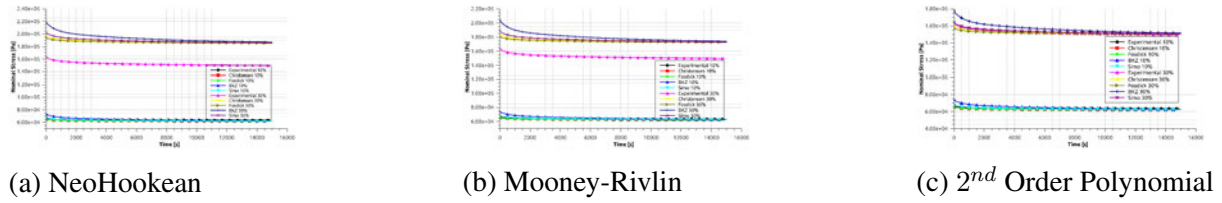
Figure 2: Relaxation response with different hyperelastic model: Material NR

30%, and the procedure is linearized for high order strains, a Mooney-Rivlin potential leads to sufficient results. Therefore, we used the following state of loading:

$$\gamma(s) = 0 \quad s < 0 \quad ; \quad \gamma(s) = \gamma_0 \quad 0 \leqslant s \leqslant t_0 \quad ; \quad \gamma(s) = \gamma_0 + \gamma_a e^{(i\omega t)} \quad t_0 \leqslant s \leqslant t \quad (3)$$

We assume that $|\gamma_a| << 1$ and that a steady-state solution is obtained. The dynamic stress has the form:

$$\sigma^*(\omega) = G^*(\omega, \gamma_0)\gamma(\omega) \quad ; \quad G^*(\omega, \gamma_0) = G_s(\omega, \gamma_0) + iG_l(\omega, \gamma_0) \quad (4)$$

where $G_s = \Re\left[G^*(\omega, \gamma_0)\right]$ and $G_l = \Im\left[G^*(\omega, \gamma_0)\right]$ are the shear storage and loss modulus.

As shows Fig 3, following observations have been made for the shear storage modulus: Simo model have shown an excellent approximation of the dynamic shear storage modulus with respect to frequency and predeformationw while Christensen model underestimates the shear modulus at 10% of deformations and overestimate the properties at higher predeformation: this model was not able to predict the softening of the material occuring with increasing predeformation level. Fosdick and Yu model's response underestimates the materials response and the BKZ model's response is not in an acceptable range. Interested in the shear loss factor, the frequency dependence of the compared models is pronounced, and all models are seen to offer a good approximation of this factor. The Simo model slightly underestimate the response, and the maximum deviation is of about 10%. One can observe that although the BKZ model could not predict the storage modulus, is have shown the ability to well approximate the damping of the materials.

(a) shear storage, (b) shear storage, 10% predeformation 30% predeformation

(c) loss factor, 10% (d) loss factor, 30% predeformation   predeformation
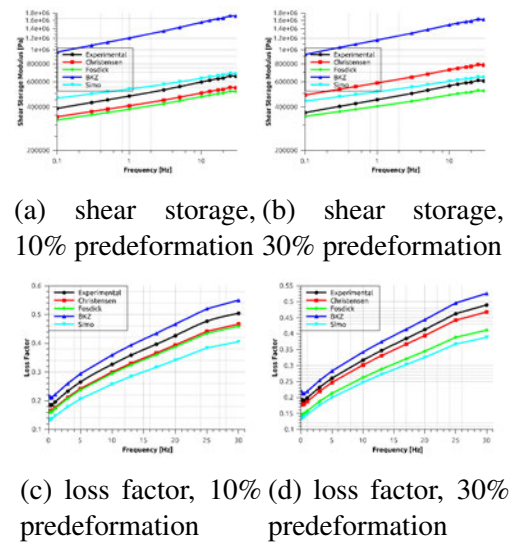
Figure 3: NR/BIIR dynamic properties at different predeformation levels

REFERENCES

[1] Raymond W Ogden. *Non-linear elastic deformations.* Courier Corporation, 1997.

[2] F J Lockett. Creep and stress-relaxation experiments for non-linear materials. *International Journal of Engineering Science*, 3(1):59–75, 1965.

[3] SD Hong, RF Fedors, F Schwarzl, J Moacanin, and RF Landel. Analysis of the tensile stress-strain behavior of elastomers at constant strain rates. i. criteria for separability of the time and strain effects. *Polymer Engineering & Science*, 21(11):688–695, 1981.

[4] J L Sullivan. Viscoelastic properties of a gum vulcanizate at large static deformations. *Journal of Applied Polymer Science*, 28(6):1993–2003, 1983.

[5] Bernard D Coleman and Walter Noll. Foundations of linear viscoelasticity. *Reviews of modern physics*, 33(2):239, 1961.

[6] R M Christensen. A nonlinear theory of viscoelasticity for application to elastomers. *Journal of Applied Mechanics*, 47(4):762–768, 1980.

[7] Roger Fosdick and Jang-Horng Yu. Thermodynamics, stability and non-linear oscillations of viscoelastic solidsII. History type solids. *International journal of non-linear mechanics*, 33(1):165–188, 1998.

[8] J. C. Petiteau, E. Verron, R. Othman, H. Le Sourne, J. F. Sigrist, and G. Barras. Large strain rate-dependent response of elastomers at different strain rates: Convolution integral vs. internal variable formulations. *Mechanics of Time-Dependent Materials*, 17(3):349–367, 2013.

[9] J C Simo. On a fully three-dimensional finite-strain viscoelastic damage model: formulation and computational aspects. *Computer methods in applied mechanics and engineering*, 60(2):153–173, 1987.

4

STUDY OF THE LIFECYCLE OF RUBBER SUSPENSION ELEMENTS FOR OPTIMISED MAINTENANCE AND SAFE DYNAMIC BEHAVIOUR

A. Malo Estepa[1], A. Boukamel[1], T. Tison[2], F. Massa[2]

[1]IRT RAILENIUM
Technopôle Transalley, 180 rue Joseph-Louis Lagrange, 59308 Valenciennes CEDEX, FRANCE
Email: andres.malo-estepa@railenium.eu, adnane.boukamel@railenium.eu

[2]Laboratoire d'automatique et de mécanique industrielles et humaines (LAMIH)
CNRS : UMR8201, Université de Valenciennes et du Hainaut-Cambrésis
LE MONT HOUY 59313 VALENCIENNES CEDEX 9 - France

ABSTRACT

Transport industry and, more specifically, railway industry, is confronted with a permanent need of improvement of its products. The competitiveness of rolling stock does not come only from low-cost production, but also from well-calculated lifecycle costs. Nowadays, many contracts for railway operators include not only trains, but also maintenance services throughout its lifetime, which may reach 30% of global costs. Hence, deep knowledge about the system's ageing is a strong asset to assess a good performance, both on quality of service and financial costs.

Rubber parts are widely used on railway technology because of their material properties, providing both mechanical stiffness and, to a certain extent, additional damping and vibration filtering. Contrary to metallic parts, whose mechanical characteristics remain relatively stable, rubber's properties can change throughout a lifecycle, due to service loads and environmental influence. Such changes might have an impact on the system's behaviour and lead to undesirable scenarii. For a given bogie model, we search to estimate the stiffness variation on some rubber parts, which are deemed relevant for safe operation.

1   SUMMARY

The works on our project are carried out with a partnership with a rolling stock manufacturer. The article will explain briefly the current safety norms and constraints which apply to rolling stock. The link between safety assessment and mechanical characteristics will be addressed, outlining the need of thorough knowledge on the evolution of rubber's mechanical characteristics. Evolution mechanisms will be described, as well as a strategy to study the impact of these changes on the pieces' global characteristics. Finally, a recall on maintenance objectives will be outlined.

2   SAFETY ASSESSMENT ON RAILWAY ROLLING STOCK

Railway industry has to meet several safety norms to obtain the homologation of its products, allowing the exploitation of rolling stock on one or more networks. Compliance is assessed according to each country's or operator's legal frame, but a common basis is set up by UIC (French initials for "International Railway Union") and EN European norms.

Accordingly to UIC 518 and its European transposition EN 14363, we carry out simulation tests on derailment aptitude, roll coefficient of the vehicle and safety assessment for dynamic behaviour. We use the MBS calculation software SIMPACK. Each test demands to meet several performance indexes, whose value depends on the mechanical characteristics of the system and which are limited by the norms stated above [2, 3]; among this indexes one can find:

- ratio of lateral and vertical loads over a wheel, Y/Q [a-dimensional], lower than 1.2 ;
- wheel lift, Δz [mm], lower than 5 mm;
- roll coefficient of the carbody, S_R [a-dimensional], depends on the train (e.g. trains with a pantograph must be below 0.21);
- shift forces over an axle, ΣY [kN], given by the Prud'homme formula;
- acceleration levels in both vertical and lateral directions in several positions, $\ddot{y}$ and $\ddot{z}$ [m/s^2].

3   RUBBER SUSPENSION ELEMENTS

The use of composed rubber parts on train suspensions began on the 1960's and 1970's. The main interest on this parts is that they can handle loads as good as a metallic part would do, with the additional advantage of an inherent damping behaviour. This parts play a key role on providing both structural strength on the system, as well as filtering properties for vibration purposes. Their structure can be very different, depending on the desired role: first examples came as stacked layers of rubber and steel, evolving to more complex forms like stacked-layer chevrons or conical rubber-metal springs [1] (e.g. Figure 1, 1^{ary} springs on Renfe CIVIA).

Figure 1. Renfe CIVIA bogie featuring primary rubber elements [4].

The bogie which we have chosen has several metallic-rubber parts. The knowledge from our partner states that rubber elements might increase their stiffness up to 30% during their lifecycle.

Thus, we have performed several simulations varying the characteristics of this elements, from +5% to +30% homogeneously over a whole train. The obtained results show that an increase of stiffness has an influence on the vehicle's derailment aptitude, leading to higher values on the Y/Q ratio (see Graphic 1). Hence, we can state an upper boundary on the element's stiffness to prevent the risk of non-compliance with safety norms.
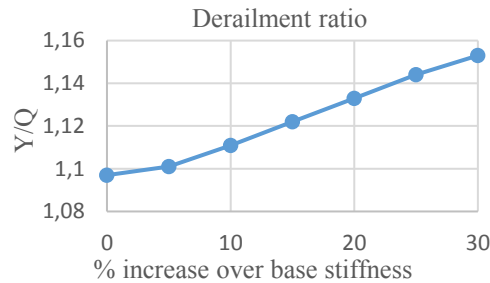
Graphic 1. Evolution of the derailment coefficient depending on the increase of stiffness.

4   EVOLUTION ON MECHANICAL CHARACTERISTICS

It is well-known that rubber is subjected to several phenomena which can affect its properties throughout time. In the case of railway applications, we can expect either an increase or a decrease of stiffness, which may come from faulty manufacturing or from changes within the rubber itself. Inherent changes might come from two sources: degradation due to mechanical loadings and chemical degradation due to environmental aspects (UV radiation, thermal cycles (-20°C, +55°C), humidity, grease, etc.). Thus, we propose a reference dissipative model permitting the description of the stiffness changes on new parts, under mechanical loads.

4.1 Experimental observations: Payne and Fletcher-Gent Effects

Elastomeric parts subjected to cyclical loading might experience several effects depending on the amplitude of the loads and on their material history. Although our suspension elements are NR based, their behaviour can be compared to that of another dissipative elastomer: silicone reinforced with silica particles. Tests performed on standard ISO 37 H2 samples have shown two phenomena, the effects Payne and Fletcher-Gent, which are most important to model the dissipative behaviour.

- the Payne Effect is characterised as a softening of the material under increasing strain amplitude. This phenomenon is temperature-dependant; the material shows a loss of dissipative capacity and a lesser loss of stiffness due to strain amplitude at higher temperatures (see Graphics 2a and 2b). The rate of fillers within the material makes this effect more evident.
- the Fletcher-Gent Effect is a strain-rate-dependent effect, which shows the softening of the material and the increase of its dissipative capacity under higher strain rates. Temperature has an influence as well on the dissipative capacity of the material and on its stiffness, which is lower at higher temperatures (see Graphics 3a and 3b).
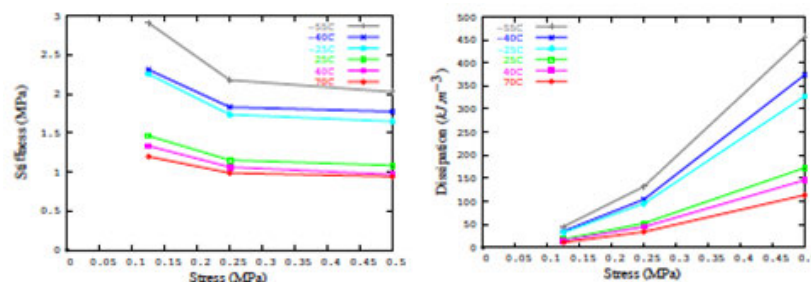
Graphics 2. Payne Effect. Left (a) decrease on stiffness; right (b) dissipative behaviour [5].
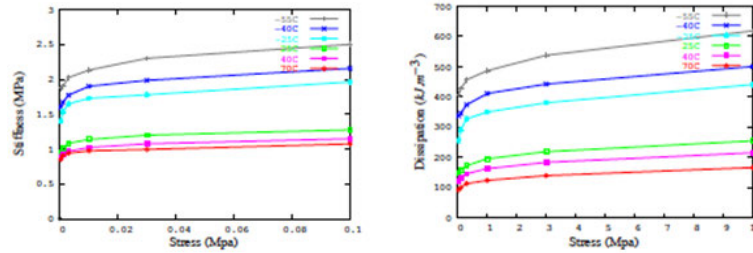
Graphics 3. Fletcher-Gent Effect. Left (a) increase on stiffness; right (b) dissipative behaviour [5].

4.2 Building an elasto-dissipative phenomenological model

A proper modelization of the suspension elements requires a model which can account for non-linearity due to large strains, dissipative behaviour due to viscosity coupled with hyperelastic behaviour, plus a dynamic response over a wide range of frequencies, (in particular the Fletcher-Gent effect) and the softening due to increasing strain amplitude (Payne Effect). The model that we propose is based on the thermodynamics of irreversible processes. Instead of choosing a discrete n-branch model with each branch matching a relaxation time, we propose a statistical approach using a continuous model with two branches, as shown on figure 3a.
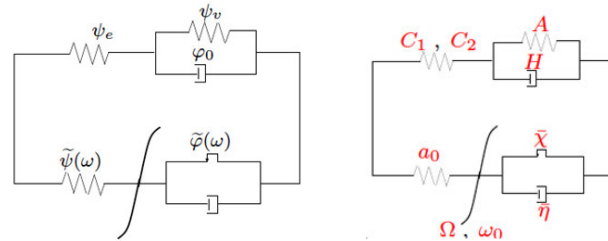
Figure 3. Left (a), statistical model; right (b) model parameters to identify.

The upper Poynting-Thomson branch accounts for the hyper-viscoelastic behaviour, with the free energy function $\psi_e + \psi_v$ and the pseudo-potential of dissipation φ_0. The lower Bingham branch matches the hyper-visco-plastic characteristics of the material, with its own functions $\tilde{\psi}$ and $\tilde{\varphi}$ biased by a weighing function which depends on a random variable ω. The chosen potentials are a Gent-Thomas or Neo-Hookean models for the hyperelastic branches; a quadratic form for the pseudo-potential of viscous dissipation; a perfectly plastic pseudo-potential for the slider element; and a Gaussian form for the distribution function combined with simple variations of Bingham characteristics according to the random variable ω. The model has 8 parameters to be identified.

4.3 Identification of the model's parameters

The identification of these parameters is done through several successive steps. The hyperelastic parameters and the plasticity yield are pre-identified with quasi-static tests. Then, viscoelastic parameters are identified through multi-level relaxation tests. Last, several cyclic tests are performed at different strain rates, allowing the identification of the statistical parameters and the correction of the viscoelastic parameters determined before.
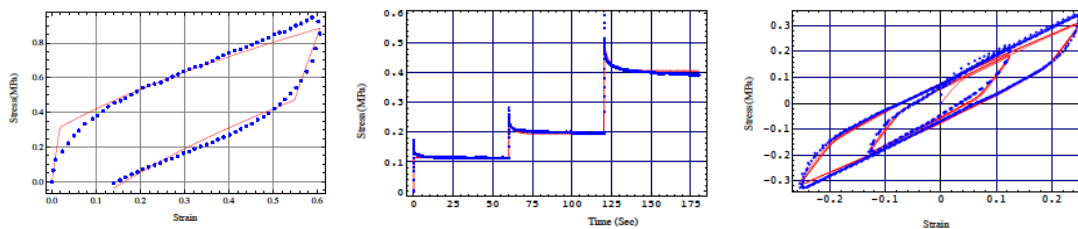
Graphics 3. Left (a), pre-identification under quasi-static loading; middle (b) estimation of viscoelastic parameters; right (c) correction of the parameters with cyclic tests [6].

Using the identified model, one can perform several simulations of the material's behaviour and verify the fitness of the model with respect to the dynamic effects observed on the material. As shown on Graphics 4a and 4b, the model shows the decrease of stiffness with increasing strain amplitude which is characteristic of the Payne Effect, as well as the stiffening with increasing frequency, due to the Fletcher-Gent Effect.
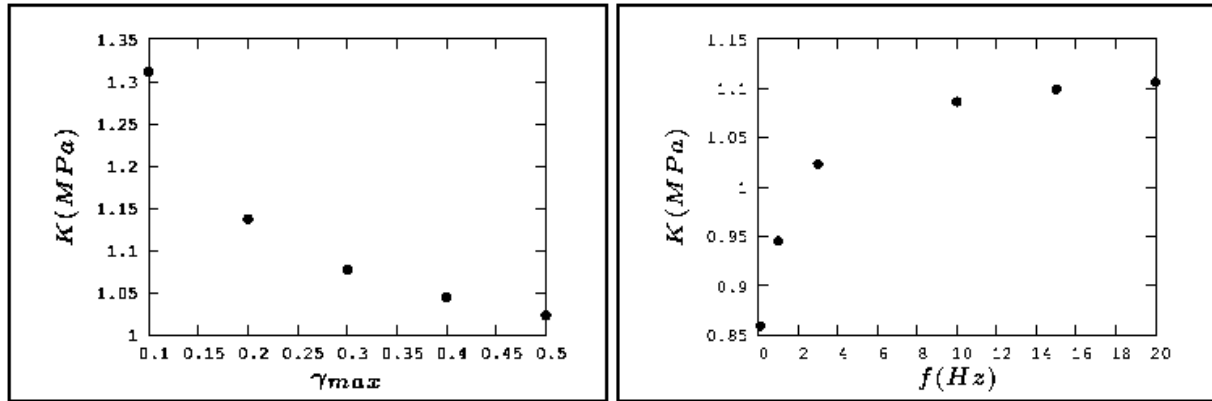
Graphics 4. Left (a) Payne Effect; right (b) Fletcher-Gent Effect [6].

5 CONCLUSION

Maintenance optimisation depends, among others, on the suspension element's lifecycle. Building a precise model of the material's behaviour can allow to predict its evolution along its lifecycle. This knowledge is necessary to build calculation tools with a certain accuracy, which can provide some predictive assessment to complete the empirical expertise on lifecycle behaviour of rubber parts. Coupling the expected stiffness evolution of rubber parts with the operation boundaries of the system may show that overhaul delays can be extended accordingly with safety norms.

REFERENCES

[1]   S. Iwnicki. *Handbook of Railway Vehicle Dynamics*. CRC Press, Boca Raton FL, US, 2006.

[2]   UIC Code 518, Testing and approval of railway vehicles from the point of view of their dynamic behaviour – Safety – Track fatigue – Running behaviour. Printed by UIC, Paris, 2009.

[3]   EN 14363, Railway applications – Testing for the acceptance of running characteristics of railway vehicles – Testing on running behaviour and stationary tests. CEN Brussels, 2005.

[4]   Jtcurses. http://www.ferropedia.es/mediawiki/index.php/Archivo:Bogie_-_Civia.jpg, last checked the 02/02/2017.

[5]   J.-M. Martinez, A. Boukamel, S. Méo, S. Lejeunes, Statistical approach for a hyper-viscoplastic model for filled rubber: experimental characterization and numerical modeling. European Journal of Mechanics - A/Solids (2011) 30, 6 :1028-1039

[6]   J. Grandcoin, A. Boukamel, S. Lejeunes, A micro-mechanically based continuum damage model for fatigue life prediction of filled rubbers, International Journal of Solids and Structures, (2014),51, 6 :1274-1286

DYNAMICAL REGIMES FOR A TIME-CORRELATED RANDOMLY EXCITED BOUNCING BALL MODEL

J. Perret-Liaudet[1], C. Zouabi[2] and J. Scheibert[1]

[1]Laboratoire de Tribologie et Dynamique des Systèmes, UMR 5513
École centrale de Lyon, member of the Université de Lyon, F69134 Écully, FRANCE
Email: joel.perret-liaudet@ec-lyon.fr, julien.scheibert@ec-lyon.fr

[2]CESI - Lyon, 19 Avenue Guy de Collongue - F69130 Écully, FRANCE
Email: czouabi@cesi.fr

ABSTRACT

The popular bouncing ball model, which consists in a ball submitted to the gravitational field and bouncing vertically on a vibrating plate with inelastic impacts, is under study in this paper. Contrary of most of studies witch assume a harmonic vertical motion of the plate, one considers random excitations of the ball induced by the plate motion. More precisely, we consider the dynamic behaviour of a revisited stochastic version of the bouncing ball model, by introducing the table displacement as a continuous time Gaussian random process with tunable correlation time. The memory effect of the excitation is then analysed, by investigating the dynamic behaviour through numerous numerical simulations. One shows that the dynamic behaviour is not only governed by the restitution coefficient at impacts and the dimensionless excitation amplitude level, but also by the correlation time of the excitation process. One highlights the relevant parameter that distinguishes the well-differentiated dynamic regimes. Quickly says, this dimensionless parameter depends for the essential from the bandwidth of the excitation signal.

1   INTRODUCTION

The popular bouncing ball (BB) model, which consists in a ball submitted to the gravitational field and bouncing vertically on a vibrating plate with inelastic impacts, has been widely studied in the last decades. This is due to both its simplicity and the amazing richness of its dynamics, from harmonic to chaotic, through subharmonic and quasi-periodic responses. It is now one of the paradigms for nonlinear dynamics and chaos (see, *e.g.* [1, 2] for BB in textbooks). Most of the studies achieved to date consider harmonic vertical motion of the plate. On the contrary, few of them include random vibrations of the plate, in spite of its undeniable relevance. Moreover, the excitation induced by the plate motion at successive bounces is generally assumed to be a discrete Markovian memoryless process. However, the real plate motions are always characterized by a finite auto-correlation time t_{corr} below which the signal keeps memory of its previous values. The Markovian assumption of independent successive impacts corresponds to the fact that the ballistic flight time of the ball between two successive bounces is much larger than t_{corr}. This is the case with the so-called Chirikov conditions [3]. Conversely, for two bounces separated by a short flight time, the two relevant plate velocities can be strongly correlated. Thus, in regimes in which short flight times are dominant, the standard Markovian approach is expected to fail to capture the BB model dynamics.

In this context, the main purpose of this study is to characterize the BB model dynamics with stochastic excitation, when memory effects cannot be neglected.

2   THE REVISITED BOUNCING BALL MODEL

Consider the popular BB model (see Figure 1) consisting on a point-like ball of finite mass bouncing vertically under the action of gravity, g, on an infinitely massive vibrating plate, the originality of our model is to introduce, for the vibrating plate, a correlated stochastic motion, $h(t)$, with tunable correlation time, t_{corr}. To this end, $h(t)$ is obtained from an uncorrelated Gaussian white noise $\psi(t)$, filtered by a second-order filter as

$$\ddot{h} + 2\zeta\Omega\dot{h} + \Omega^2 h = \psi(t) \tag{1}$$

with Ω being the center frequency of the filter and ζ its damping coefficient. Note that ζ is related to the frequency contents of the signal because the bandwidth of its power spectrum density (PSD), $S_{hh}(\omega)$ is equal to $2\zeta\Omega$. The autocorrelation function $< h(t)h(t+\tau) >$ of h is equal to $\sigma_h^2 \exp(-\zeta\Omega|\tau|) f(\tau)$ with f a periodic function and σ_h the standard deviation of h, so the correlation time can be defined as $t_{corr} = 1/\zeta\Omega$. To avoid infinite energy in the acceleration signal the displacement is further filtered by a first-order low-pass filter with a cutoff frequency higher than Ω. Typical simulated PSDs are shown in Figure 2 for the two cases, narrow and broadband.
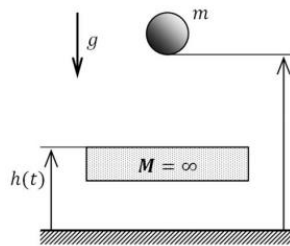
Figure 1. Sketch of the bouncing ball (BB) model.
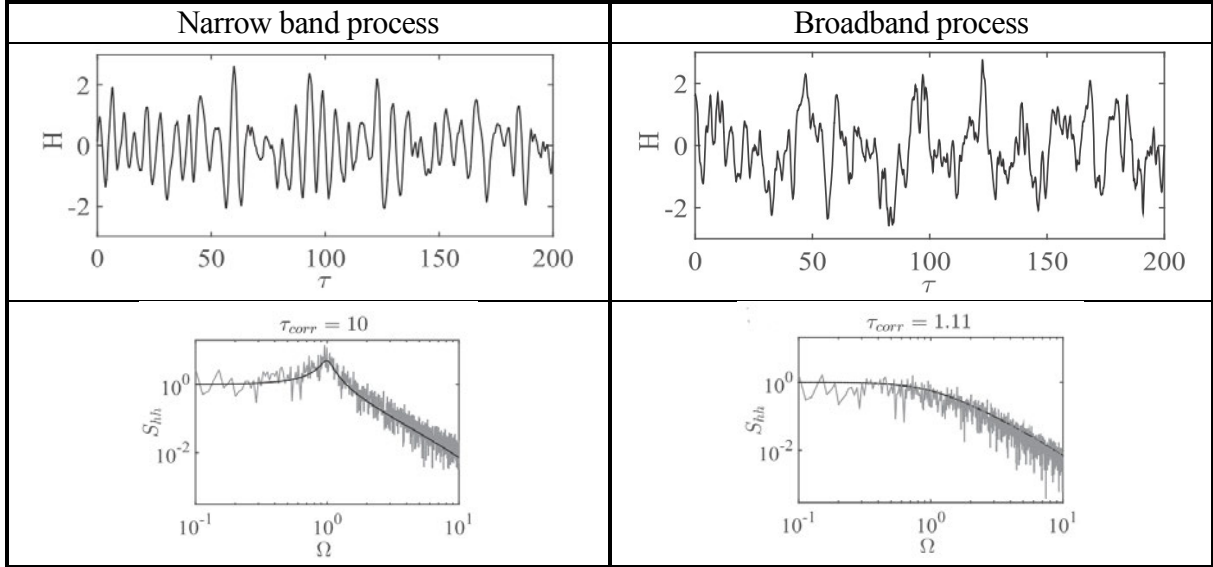
Figure 2. Typical realizations of the dimensionless plate time-displacement and its power spectral densities (PSD): narrow and broadband cases.

Now, for any generated excitation signal, we then solve the bouncing ball problem by calculating the values of the post impact velocity, v_n, and instant, t_n, of the all-successive impacts. In practice, we solve the following equations:

$$t_{n+1} = t_n + \theta_n \tag{2}$$

$$v_{n+1} = -e(v_n - g\theta_n) + (1 + e)w_{n+1} \tag{3}$$

with e the restitution coefficient introduced to take into account the partially inelastic impact characteristic, w_n the plate velocity at impact, and θ_n the flight time obtained from the following equation:

$$-\frac{1}{2}g\theta_n^2 + v_n\theta_n + h_n - h_{n+1} = 0 \tag{4}$$

In fact, Equations (2) and (3) define the classical Poincaré map for the BB model. A dimensional analysis shows that the system is governed only by three dimensionless parameters, i.e. the restitution coefficient e, the reduced plate acceleration defined by $\Lambda = \sigma_w^2/g\sigma_h$ and the dimensionless correlation time $\tau_{corr} = \Omega t_{corr}$. On this basis, we have performed simulations for a large number of values of this triplet [4].

3   RESULTS

Typical probability density functions (pdf) of the dimensionless take-off velocity $V_n = v_n/\sigma_w$ are shown in Figure 3. Wood and Byrne have studied the case of a completely uncorrelated Markovian excitation [5], and their results (velocity quoted V_{WB}) are used as a reference to highlight the differences brought by our improved model which includes the correlation in the excitation. As we can see, memory effects become negligible when individual flight times are larger than the correlation time. This case is favoured for large excitations Λ and/or short correlation time τ_{corr}.
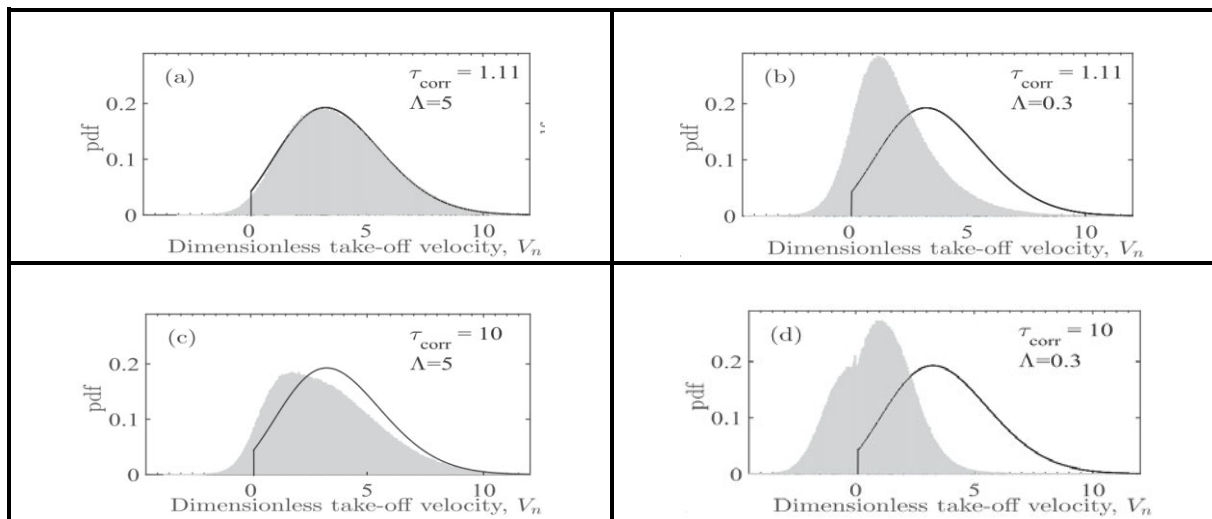
Figure 3. Typical pdf of the dimensionless take-off velocity for selected Λ and τ_{corr}, with the example of $e = 0.8$. Solid lines correspond to the Wood and Byrne results.

A detailed analysis [6] shows that the relevant parameter consists on the ratio of the Markovian mean flight time of the ball and the mean time between successive peaks in the plate motion. This dimensionless parameter depends on the bandwidth of the excitation signal. When the parameter is large, the Markovian approach is appropriate; but for low levels, memory effects become not negligible leading to a significant decrease of jump durations; and finally at smallest values of the ratio, chattering occurs.

ACKNOWLEDGMENT

REFERENCES

[1]   N. Tufillaro, and T. Abbot, and J. Reilly. *An experimental approach to nonlinear dynamics and chaos*. Addison-Wesley, Redwood City, 1992.

[2]   J. Guckenheimer, and P. Holmes. *Nonlinear oscillations, dynamical systems, and bifurcations of vector fields*. Springer-Verlag, New-York, 1993.

[3]   B. Chirikov. A universal instability of many-dimensional oscillator systems. *Physics reports*. 52(5):263-379, 1979.

[4]   C. Zouabi. *Dynamique d'un contact glissant rugueux-rugueux sous faible charge: experiences et modélisation*. Thèse de doctorat, École centrale de Lyon, 2016.

[5]   L. Wood, and K. Byrne. Analysis of a random repeated impact process. *J. Sound and Vibration*. 78: 329-345, 1981.

[6]   C. Zouabi, J. Scheibert, and J. Perret-Liaudet. Memory in random bouncing ball dynamics. *EPL*. 115(50006) 5p., 2016.

MODAL INTERACTIONS IN A
TWO-NANOMECHANICAL-RESONATOR ARRAY

C. GRENAT[1], S. BAGUET[1], R. DUFOUR[1] and C-H. LAMARQUE [2]

[1] Univ Lyon, INSA-Lyon, CNRS UMR5259, LaMCoS, F-69621, France
Email: clement.grenat@insa-lyon.fr, sebastien.baguet@insa-lyon.fr, regis.dufour@insa-lyon.fr

[2]Univ Lyon, ENTPE, CNRS UMR5513, LTDS , F-69518, France
Email: claude.lamarque@entpe.fr

ABSTRACT

Most studies on nanomechanical resonators in the literature are concerned with a single resonator. In this work, an array of two nanomechanical resonators is analyzed. A quasi-analytic approach with averaging method is used to compare the beams responses with and without electrostatic coupling terms. The results show modal interactions between the two beams due to the electrostatic coupling. It is shown that the qualitative behavior of the coupled resonators can be infered from the response curves of the uncoupled resonators. In particular, additional loops occur due to the algebraic structure of the coupled system. The contribution lies in the deduction of the beam array responses curve by using multiple uncoupled responses of the single-beam resonators.

1   INTRODUCTION

Arrays of MEMS or NEMS present complex dynamical behaviors due to electric, magnetic and mechanic nonlinear couplings. Lifshitz and Cross [1] studied the responses of n electrical and mechanical coupled oscillators with parametric resonance in the low nonlinear limit by using a perturbation method. Gutschmidt and Goettlieb worked on arrays with electrical coupling. They focused on the n-beam dynamic behaviour in the region of internal one-to-one, parametric and several internal three-to-one resonances corresponding to low, medium and large DC voltages [2]. Kacem et al. developed a single beam model to investigate the sensitivity of the resonance with respect to the electrostatic forcing. Their researches were carried out using averaging method validated by HBM+ANM [3]. In this paper, an array of $n = 2$ identical clamped-clamped beams is also considered but coupled only by an electrostatic force in order to study the modal interactions between the two beams due to the electrostatic coupling.

2   ARRAY OF TWO NANOMECHANICAL RESONATORS

A 2-moving-beam array is considered, as sketched in Figure 1. The two beams located at the ends of the array are fixed and serve only as electrostatic actuator. All 4 beams are identical. l, b, h, I, g are the dimensions of the beams, i.e., length, width, height, moment of inertia, gap between two adjacent beams. E, ρ be the Young's modulus and the material density. Each
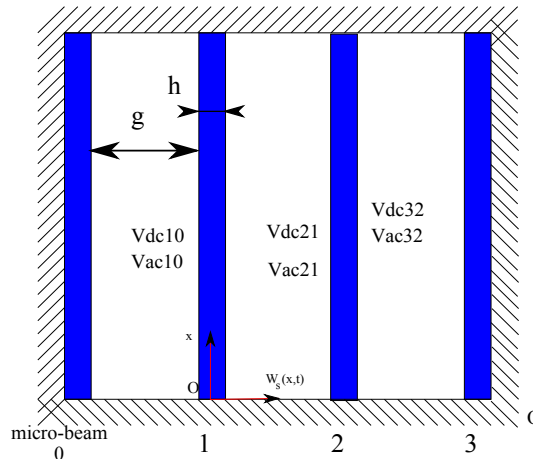
Figure 1: Array of two clamped-clamped M/NEMS beams.

beam is an electrostatic actuator for its adjacent beams. $V_{s,s+1} = V_{dcs,s+1} + V_{acs,s+1}\cos(\Omega t)$ is the voltage applied between the successive beams s and $s + 1$ with V_{dc}, V_{ac} the continuous and alternative voltages. The equation of the beam s in bending is as follows [2].

$$EI\frac{\partial^4 \tilde{w}_s(\tilde{x},\tilde{t})}{\partial \tilde{x}^4} + \rho bh\frac{\partial^2 \tilde{w}_s(\tilde{x},\tilde{t})}{\partial \tilde{t}^2} - \Big[\tilde{N} + \frac{Ebh}{2l}\int_0^l \big(\frac{\partial \tilde{w}_s(\tilde{x},\tilde{t})}{\partial \tilde{x}}\big)^2 \, \mathrm{d}\tilde{x}\Big]\frac{\partial^2 \tilde{w}_s(\tilde{x},\tilde{t})}{\partial \tilde{x}^2}$$

$$= \frac{\epsilon_0 b C_n}{2}\left[\frac{V_{s,s+1}^2}{\big(g + \tilde{w}_{s+1} - \tilde{w}_s\big)^2} - \frac{V_{s-1,s}^2}{\big(g + \tilde{w}_s - \tilde{w}_{s-1}\big)^2}\right] \quad (1)$$

with $s = 1, 2$. Let ϵ_0, C_n be the dielectric constant and fringing the coefficient respectively. $\tilde{N}$ represents the lineic load along the x-axis. The beams 1 and 2 are clamped-clamped.

2

3   AVERAGING METHOD

The responses of the beams are more complicated than those of a single beam resonator. A quasi-analytic solution obtained by the averaging method can be used to explain why the electrostatic coupling generates additional loops onto the responses. First, the beam lateral deflection is expanded on its fundamental mode only:

$$w_1(x,t) = \phi_1(x)a_{11}(t), \qquad w_2(x,t) = \phi_1(x)a_{21}(t) \tag{2}$$

First-order Taylor series are then used to simplify the analytic calculation:

$$\frac{1}{(1 + w_{s+1} - w_s)^2} \simeq 1 - 2(w_{s+1} - w_s), \qquad \frac{1}{(1 + w_s - w_{s-1})^2} \simeq 1 - 2(w_s - w_{s-1}) \tag{3}$$

Since the resonators of the 2-beam array have the same boundary conditions, their eigenmodes are identical. Therefore, a Galerkin method is used to eliminate the spatial dependence from the equation of motion (1). Then using the averaging method and considering the solutions $a_{11}(t), a_{21}(t)$ in following forms

$$a_{11} = A_{11}(t)\cos(\Omega t) + B_{11}(t)\sin(\Omega t), \tag{4}$$

$$a_{21} = A_{21}(t)\cos(\Omega t) + B_{21}(t)\sin(\Omega t), \tag{5}$$

yield

$$\Omega\dot{A}_{11} = \quad -B_{11}\omega_1\epsilon\sigma_1 - \frac{1}{2}cA_{11}\Omega + \frac{3}{8}\beta_{11}A_{11}^2B_{11} + \frac{3}{8}\beta_{11}B_{11}^3$$

$$+\frac{1}{8}\beta_{13}B_{11} + \frac{1}{2}\delta_{11}B_{21} + \frac{1}{8}\delta_{13}B_{21} \tag{6}$$

$$\Omega\dot{B}_{11} = \quad \frac{1}{2}cB_{11}\Omega + \frac{3}{8}\beta_{11}A_{11}^3 + \frac{3}{8}\beta_{13}A_{11} + \frac{1}{2}\gamma_{12} + \frac{3}{8}\beta_{11}A_{11}B_{11}^2$$

$$-A_{11}\omega_1\epsilon\sigma_1 + \frac{1}{2}\delta_{11}A_{21} + \frac{3}{8}\delta_{13}A_{21} \tag{7}$$

$$\Omega\dot{A}_{21} = \quad -B_{21}\omega_2\epsilon\sigma_2 - \frac{1}{2}cA_{21}\Omega + \frac{3}{8}\beta_{21}A_{21}^2B_{21} + \frac{3}{8}\beta_{21}B_{21}^3$$

$$+\frac{1}{8}\beta_{23}B_{21} + \frac{1}{2}\delta_{21}B_{11} + \frac{1}{8}\delta_{23}B_{11} \tag{8}$$

$$\Omega\dot{B}_{21} = \quad \frac{1}{2}cB_{21}\Omega + \frac{3}{8}\beta_{21}A_{21}^3 + \frac{3}{8}\beta_{23}A_{21} + \frac{1}{2}\gamma_{22} + \frac{3}{8}\beta_{21}A_{21}B_{21}^2$$

$$-A_{21}\omega_2\epsilon\sigma_2 + \frac{1}{2}\delta_{21}A_{11} + \frac{3}{8}\delta_{23}A_{11} \tag{9}$$

where the coefficients β_{ij}, γ_{ij}, δ_{ij} depend on the beam characteristics and on the applied voltages. They are not detailed here for the sake of conciseness. In Equations (6)-(9), the coupling terms $(\frac{1}{2}\delta_{11} + \frac{1}{8}\delta_{13})B_{21}$ and $(\frac{1}{2}\delta_{11} + \frac{1}{8}\delta_{13})A_{21}$ represent the influence of the second beam on the first beam and the coupling terms $(\frac{1}{2}\delta_{21} + \frac{1}{8}\delta_{23})B_{11}$, $(\frac{1}{2}\delta_{21} + \frac{3}{8}\delta_{23})A_{11}$ the influence of the first beam on the second beam. When $\dot{A}_{11} = \dot{B}_{11} = \dot{A}_{21} = \dot{B}_{21} = 0$ the steady-state motions appear. The corresponding nonlinear algebraic system is solved by an adapted numerical method, the obtained approximated solution is in agreement with a reference solution obtained by HBM+ANM [3] not shown here.

   In order to analyze the influence of the coupling terms, Equations (6)-(9) with and without coupling terms are examined. The response curves with (red curves) and without (blue curves) coupling terms are plotted in Figure 2. Without these coupling terms Equations (6)-(7)

3
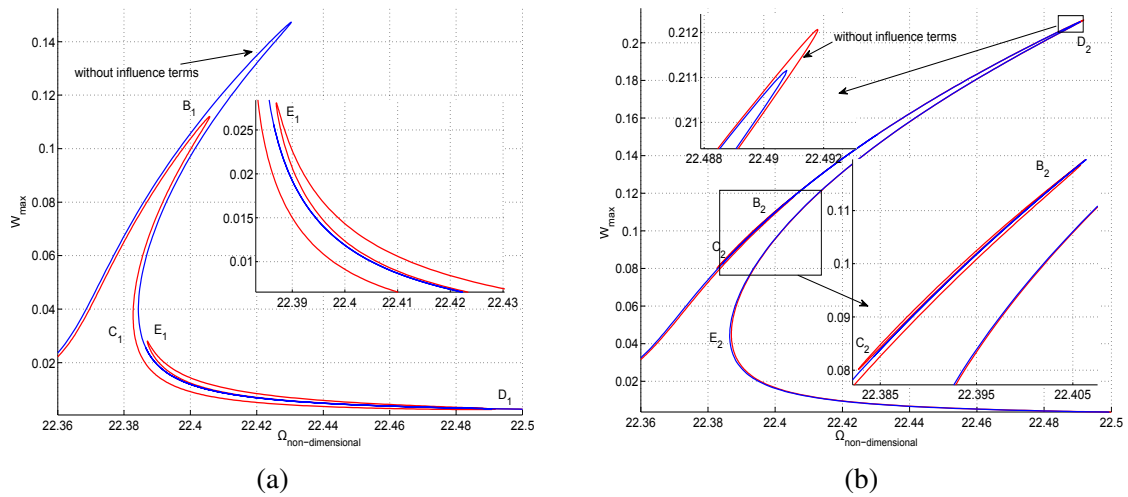
Figure 2: Design 1 without added mass, Response by neglecting the coupling terms (blue), complete response (red). (a): first-beam response, (b): second-beam response.

and (8)-(9) form two independent systems of equations. Therefore, the responses of the two beams, (blue response curves in Figure 2) are similar to two single-beam responses.

With coupling terms Equations (6)-(9) are dependent and share the same bifurcation points and stability. When a bifurcation point is present on a response curve, the same bifurcation point will also be present at the same frequency on the other beam response. Therefore, the limit points originated from the responses without coupling terms will be present on all the other beam responses with coupling terms. This leads to the appearance of additional limit points on the response curves. In Figure 2, the limit points B_1 and C_1 on the first beam response generate at the same frequencies the loop $B_2 - C_2$ on the second-beam response. In the same way, D_2 and E_2 on the second-beam response produce the loop $D_1 - E_1$ on the first-beam response.

4   CONCLUSION

A quasi-analytic analysis with the averaging method of a two-nanomechanical-resonator array has been carried out. The existence of modal interactions between the two beams due to the electrostatic coupling has been enlightened. The appearance of additional loops onto response curves has been explained. The form of the response curves of an electrostatic coupled beam array can be anticipated using the uncoupled single-beam-resonator responses. This research represents an increment towards the comprehension and modeling of resonator arrays for application in mass sensing.

REFERENCES

[1] R. Lifshitz and M. C. Cross. *Nonlinear Dynamics of Nanomechanical and Micromechanical Resonators*, pages 1–52. Wiley-VCH Verlag GmbH & Co. KGaA, 2009.

[2] S. Gutschmidt and O. Gottlieb. Nonlinear dynamic behavior of a microbeam array subject to parametric actuation at low, medium and large dc-voltages. *Nonlinear Dynamics*, 67(1):1–36, 2012.

[3] N. Kacem, S. Baguet, S. Hentz, and R. Dufour. Computational and quasi-analytical models for non-linear vibrations of resonant mems and nems sensors. *International Journal of Non-Linear Mechanics*, 46(3):532–542, 2011.

4

ON THE WET BELT SQUEAL : CHARACTERIZATION OF THE MECHANICAL VIBRATION AND INFLUENCE OF THE MECHANICAL PROPERTIES OF THE BELT ON FRICTION-INDUCED INSTABILITIES

S. GATIGNOL[1,2*] , T. DEMASSOUGNE[2] and A. LE BOT[1]

[1]Laboratoire de Tribologie et de Dynamique des Systemes (LTDS)
Ecole Centrale de Lyon, Ecully, FRANCE
Email: simon.gatignol@doctorant.ec-lyon.fr, alain.le-bot@ec-lyon.fr
[2]HUTCHINSON SNC
Joue-les-Tours, FRANCE

ABSTRACT

Under wet conditions, V-ribbed belts of the Automotive Accessory Belt Drive System might emit a typical squeal noise. A test rig consisting of a static v-ribbed belt in contact with a pulley lubricated with water allow to replicate the phenomenon. Measurements of the belt vibrations suggest that whereas the pulley plays a minor role, the belt vibrations can be directly linked to the squeal emission and it is shown that a single tooth - or single "v"- is sufficient to generate squeal. The source of these vibrations is often considered to be friction-induced vibrations. However, the friction behaviour of the belts is shown unsufficient to explain the outbreak of squeal and the mechanical properties also influence the domain of instability. A characterization of the mechanical properties of the belt has been carried out using DMA experiments and leads to a better understanding of the relation between the different belt structures and their aptitude to generate noise.

1   INDUSTRIAL AND SCIENTIFIC CONTEXT

During the last decades, the global noise emission of vehicles has decreased from 82 to 74 dB. This let emerge parasite noises such as brake or wiper blade squeal. A typical squeal noise can also be emitted by v-ribbed belts in the Automotive Accessory Belt Drive System. Previous studies has allowed the suppression of noise in the case of a dry belt however a solution is still needed in the presence of humidity. The squeal noise that appears on motors between the v-ribbed belt and the alternator pulley has been replicated on a specific test rig presented in section 2. The link between the noise and the mechanical vibrations of both the pulley and the belt is then established in section 3 before the role of friction-induced instabilities features in the occurence of the belt squeal are briefly recalled in section 4. As a more precise understanding is needed, the influence of the mechanical properties of the belt is investigated in section 5.

2   EXPERIMENTAL SETUP
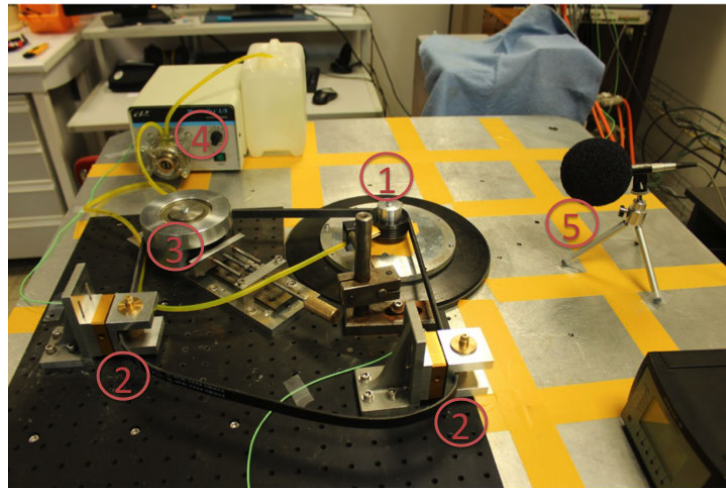
Figure 1: Experimental Setup consisting of: a *pulley* and a *v-ribbed belt* (1) clamped in *2 tension sensors* (2), plus a tensionner(3), a microphon (5) and a peristaltic pump (4)

The test rig used in the following studies is presented in Figure 1. The contact between the v-ribbed belt and the pulley is replicated. The specificity is that the belt remains static so that sliding exist all along the wrap - or contact - angle which is not the case on motors. The rotation of the pulley is controlled so that the sliding velocity is known. The lubrification of the contact is regulated with a peristaltic pump. Sensors measure the evolution of the tensions in both slack and tight free spans. A minimum tension is maintained in slack span thanks to a belt tensioner. The coefficient of friction is computed from the measurement of the tensions using Euler's formula. Measurements of the vibrations of the belt have been carried out with both accelerometers and laser vibrometers. The sound is recorded with a microphon 30 centimeters far from the pulley. Experiments consist in progressively increasing the rotational velocity with a constant supply in water - about 1 mL/s. The belt initial tensions and the ramp of velocity are modified and v-ribbed belts with different coatings are used. The rotational velocity can be stationnary or with a sinusoidal form in order to replicate the phenomenon of acyclism.

2

3   MECHANICAL VIBRATION AT THE ORIGIN OF THE BELT SQUEAL

Role of the Pulley   It is assumed that the contact between the belt and the pulley is necessary for the squeal noise to occur. However, the tests described in section 2 have been carried out with different forms of pulley - plain or empty - without any change on the acoustic signature of the squeal noise. Moreover, the modes of vibrations of the pulley have been investigated using an impact hammer and no likeness has been observed between the natural modes of the pulley and the fundamental mode of the squeal noise.

Role of the Belt   Laser vibrometers have been used to investigate the link between the squeal noise and the vibrations of the belt. A time frequency analysis of the belt velocity or vibrations show that the squeal appear at the same time that strong belt vibrations occur. Moreover, the spectral signature is the same for the belt vibrations and the squeal noise. Therefore, a link between the belt vibrations and the squeal noise exist. Another experiment consist to reach the range of parameters - sliding velocity, tension in free spans, and water supply - at which a stationary noise exist and then to clamp the belt with fingers at proximity of the contact with the pulley. The immediate disappearance of the squeal confirm that the mechanical vibrations of the belt play a key role in the generation of the squeal noise. Similar experiments with the pulley doesn't have any effect.

So the mode of vibrations of the belt has been studied more in detail. On one side, the data of the vibrometers has been completed with measurements using 3D accelerometers detecting belt vibrations in the 3 directions. On another side, belt samples with only one rib have been tested and a squeal noise with the same acoustical signature has been observed as previously. These results highlight that the mode of vibrations of the belts that cause the appearance of the squeal noise doesn't involve the whole structure of the belt but only each tooth separately as mentionned by Dalgarno et al. [1]. However it is difficult to conclude on the excited mode as several directions vibrates.

Therefore, the vibrations of the belt are necessary for the squeal to occur. The conditions that let appear the mechanical vibrations of the belt has been studied The role of friction-induced instabilities is summed up in the next section.

4   FRICTION-INDUCED INSTABILITIES AT THE ORIGIN OF BELT SQUEAL

Friction-induced instability features have been widely used to explain belt squeal both for dry and wet belt. Sheng [2] has highlighted the role of the transition in a mixed lubrication regime and the related negative slope of the friction versus sliding velocity curve as the main feature for the noise to be triggered.

However, recent results show that the correspondance between the level of slope and the appearance of noise is not obvious [3]. The consideration of low velocity sliding highlights that the squeal appears after the strong decrease in friction coefficient, as it can be observed on Figure 2. Moreover the transition from static to dynamic friction - for example the stick-slip motion - is also unsufficient to explain the appearance of squeal [3].

Thus the separated consideration of the friction behaviour is not enough to understand the generation of the instability, a finer understanding of the mechanical properties of the belt is also required.

5   INFLUENCE OF THE BELT MECHANICAL PROPERTIES

The main mechanical properties of the belt are the stiffness of cords in its tension member (back of the belt) and both the stiffness and the damping properties of its teeth. Belts with
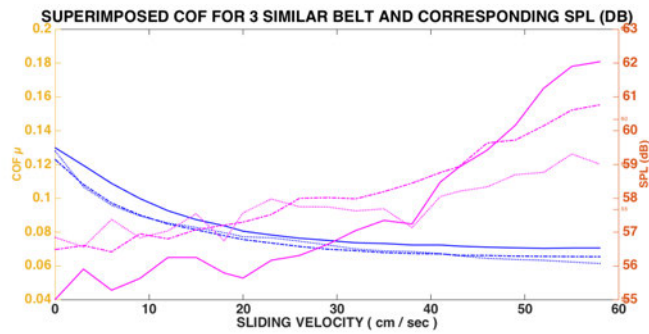
Figure 2: Coefficient of Friction (COF - blue line) and Sound Pressure Level (SPL magenta line) with respect to the sliding velocity for 3 similar belts

modified cords and teeth has been tested as describes in section 2. The results show that the domain where the instability and the noise occur strongly depends on both cords and teeth properties.

That is why the cords stiffness have been measured by traction tests whereas Dynamic Mechanical Analysis (DMA) has been used for the tooth properties. The applicabilty of the Time Temperature Superposition have been checked and the resulting mastercurves show the evolution of the belt tooth properties on a large range of frequencies , as observed on Figure 3. The different belt teeths were distinguishable as a function of their coatings and belt mixtures. Further investigations consist to link the quantitative values reached thanks to the DMA
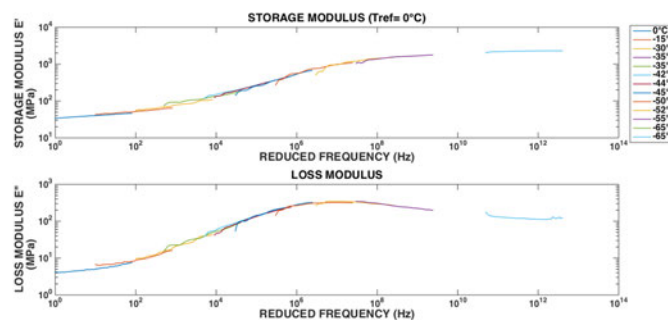
Figure 3. Mastercurves for the storage (top) and the loss (bottom) modulus

experiments with the outbreak of the squeal phenomenon.

REFERENCES

[1] J.E. Connell ,R.A.L. Rorrer. Friction-induced vibration in V-ribbed belt applications. *Proceedings of the ASME conference*, DE-Vol.49(), 75-85, 1992.

[2] G. Sheng et al..Wet belt friction-induced dynamic instability and noise in Automotive Accessory Belt Drive Systems, *Int. J. Vehicle Noise and Vibration*, 2(3), 249-265, 2006.

[3] S. Gatignol, T. Demassougne and A. Le Bot. Detection of friction-induced instabilities at the origin of the squeal of wet poly-V belts, *Proceedings of the conference InterNoise2016*, 7349-7359, 2016.

4

VERTICAL DYNAMICS OF TWO SLIDING ROUGH SURFACES: COMPARISON BETWEEN NUMERICAL AND ANALYTICAL APPROACHES TO DESCRIBE THE EXCITATION SOURCE

N. Ponthus[1] , J.Scheibert[1], J.Perret-Liaudet[1], A.Malthe-Sorrensen[2], K.Thøgersen[2] and J.Trømborg[2]

[1]Laboratoire de Tribologie et Dynamique des Systèmes UMR 5513
Ecole Centrale de Lyon, 36 avenue Guy de Collongue, Ecully, FRANCE
Email: nicolas.ponthus@doctorant.ec-lyon.fr, julien.scheibert@ec-lyon.fr,
joel.perret-liaudet@ec-lyon.fr

[2]University of Oslo
P.O. Box 1072 Blindern, 0316 Oslo , Norway

ABSTRACT

The vibration induced by the roughness of two surfaces sliding one upon each other is the excitation source for a so-called roughness noise. This source is a stochastic process, the spectral and statistic properties of which have to be described. Often the topographic properties of the surfaces are known. However, those properties are not related in a simple way to the excitation. The latter is determined by the statistics of the highest asperities of each surface. The aim of this study is to explore this relationship between topography and vibration. To achieve this goal, numerical and analytical methods have been implemented

1 INTRODUCTION

When two rough surfaces are sliding one upon each other under weak load, the strains of the asperities are low and a macroscopic vertical vibration of the two solids appears. This vibration can be the source of jumps [1, 2] and is also a value of interest for the calculation of dispersive forces [3]. However this vibration can not be directly associated to the combination of the two surface topographies. Indeed only the highest asperities of each surface are in contact. The aim of this study is to characterize this geometrical filtering. To address this issue, the statistical properties of the contact of the highest asperities have to be understood. Analytical methods for extremal events exist and are commonly used in finance, dimensioning and quantification of risks [4]. To adapt such methods to our problem, a simplified system is studied considering the relative distance between two surfaces touching in only one contact point and sliding one upon each other. Let us call the upper one the slider which is considered square. An analytical calculation is done and compared to a numerical simulation of the problem. These simulation enable conclusions about the spectral properties of this vibration.

2 ANALYTICAL METHOD

Searching the first contact point between two surfaces is equivalent to find the maximum of a process that has the properties of the sum of the two surfaces. This problem of maxima has been widely studied. To apply those calculations to our case, a discrete way to describe surfaces with independent variables has been used. A surface is described through the height probability density function (pdf) and a power spectral density function (PSD). To convert this continuous representation to a convenient discrete description of the surfaces let us define the correlation length λ of the surface. If two points of the surface are further than λ, they are completely uncorrelated. If L is the side length of the slider, we can thus define a number of points that are independent and represent the surface, with $N = \frac{L^2}{\lambda^2}$. We assume that those N points have the same pdf p as the sum of the surfaces. Introducing the associated cumulative density function (cdf) $\mathcal{P}$ and following [4], the pdf g of the height of the maximum z is:

$$g(z) = Np(z)\mathcal{P}(z)^{N-1} \tag{1}$$

The two surfaces sliding one upon each other can be considered as a sequence of draws of a maximum. The vertical vibration statistics should then follow the law given in equation 1. Examples for various N are given in the figure 1 considering p Gaussian.

3 NUMERICAL METHOD

To compare to the results given by the analytical method presented above, the first contact point problem is now studied numerically. Realistic rough surfaces are generated numerically from typical PSD (rectangular shaped and fractal) with a Gaussian height distribution. The topography of a slider and a track, 5 times longer than the slider, are generated. A typical example of the topographies is shown on the figure 2. The slider is placed on one side of the track and move along it with a discretization step equal to the surface discretization. No rocking motion is taken into account. Let x be the horizontal offset from the initial position. The first contact point when approaching the two surfaces is searched for each discretization point. All height differences between the two median planes are collected giving the first contact point profile $h(x)$. A typical histogram of h is given in figure 3. Spectral properties can also be deduced from the numerous simulations.

2
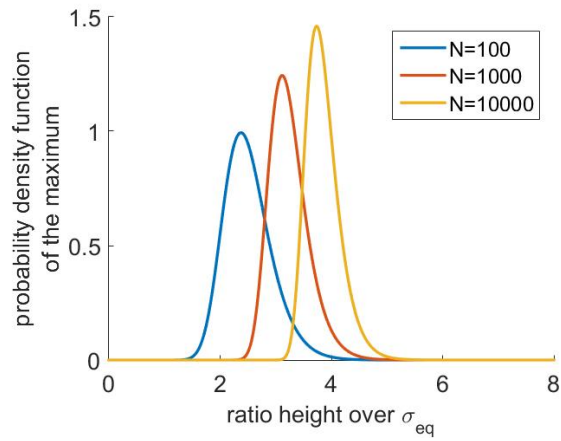
Figure 1: pdf of the maximum for various N. The height is normalized by σ_{eq}, the standard deviation of the sum of the surfaces
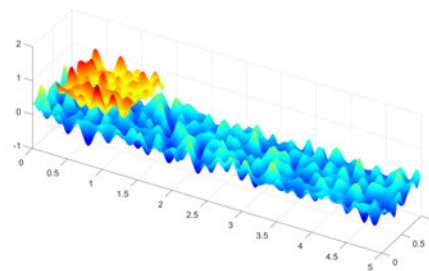
Figure 2: typical example of the topographies used to obtain the first contact point profile (arbitrary scale)
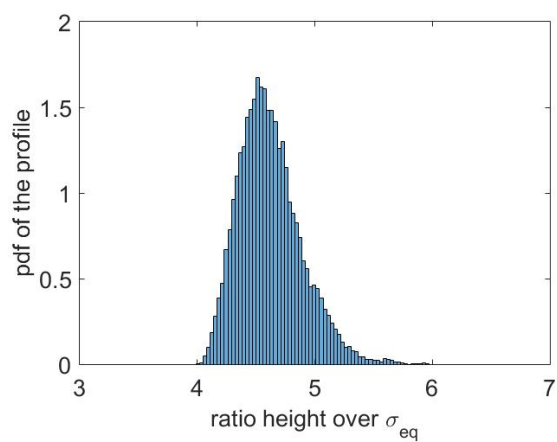
Figure 3. histogram of the numerical first contact point profile

3

4   COMPARISON AND CONCLUSION

The shapes of the pdf plotted in figures 1 and 3 are relatively similar. Numerous numerical results have been compared to an analytical model exhibiting a good agreement between the numerical and analytical results. Simulations have also brought spectral description of those signals. This work enables then a complete description of the vibration due to the roughness of two surfaces. It can then be used as an excitation source for dynamical models such as the bouncing ball [5].

REFERENCES

[1] Viet Dang, Joel Perret-Liaudet, Julien Scheibert, and Alain Le Bot. Direct numerical simulation of the dynamics of sliding rough surfaces. *Computational Mechanics*, 52(5):1169–1183, November 2013.

[2] C. Zouabi. *Dynamique d'un contact glissant rugueux-rugueux sous faible charge: experience et modelisation*. PhD thesis, Ecole Centrale de Lyon, 2016.

[3] P. J. van Zwol, V. B. Svetovoy, and G. Palasantzas. Distance upon contact: Determination from roughness profile. *Physical Review B*, 80(23):235401, December 2009.

[4] Didier Sornette. *Critical Phenomena in Natural Sciences*. Springer Series in Synergetics. Springer-Verlag, Berlin/Heidelberg, 2006.

[5] C. Zouabi, J. Scheibert, and J. Perret-Liaudet. Memory in random bouncing ball dynamics. *EPL (Europhysics Letters)*, 115(5):50006, October 2016.

AN EFFECTIVE FORMULATION AND A PHYSICAL DISCRETE MODEL FOR GEOMETRICALLY NONLINEAR TRANSVERSE VIBRATIONS OF A SYMMETRICALLY LAMINATED COMPOSITE BEAM

A. Rahmouni[1,2], R. Benamar[1]

[1] Equipe d'Etudes et Recherches en Simulation, Instrumentation et Mesures (EERSIM)
Mohammed V University in Rabat - Ecole Mohammadia des Ingénieurs, Avenue Ibn Sina, Agdal, Rabat, Morocco
rhali.benamar@gmail.com

[2] Laboratoire de Mécanique Productique et Génie Industriel (LMPGI) Université Hassan II
Ain Chock in Casablanca, Ecole Supérieure de Technologie, KM 7 Route El Jadida, B.P 8012
Oasis, Casablanca, Morocco
abd.rahmouni@gmail.com

ABSTRACT

The problem of geometrically nonlinear free vibration of symmetrically laminated composite clamped beams (SLCCB) is described by an N-dof discrete model of an equivalent isotropic beam, with effective bending and axial stiffness parameters. The model is made of (N +1) bars, connected by N masses placed at the bar ends, connected by rotational springs, presenting the beam flexural rigidity. The large transverse displacements of the bar ends induce a variation in their lengths giving rise to axial forces causing the nonlinear effect and modeled by longitudinal springs. The nonlinear vibration problem, defined in terms of the mass tensor m_{ij}, the linear rigidity tensor k_{ij} and the nonlinearity tensor b_{ijk}, is reduced, via application of Hamilton's principle, to a nonlinear algebraic system solved using an explicit method for calculating the (SLCCB) fundamental nonlinear mode and associated amplitude dependent frequency parameters. The numerical results are found to be in a good agreement with previously published results, based on a semi analytical composite beam continuous theory. The discrete system for the (SLCCB), developed and validated here, can be used in further applications to investigate nonlinear vibrations of non-uniform composite beams, with irregularities in the mass or in the stiffness distributions.

1   INTRODUCTION

In a series of previous works, it has been shown, both theoretically and experimentally, that beams constrained at both ends exhibit significant geometrical nonlinear behaviour at large vibration amplitudes, due to the axial strains induced by the large displacements. It has been shown also that composite structures exhibit a more accentuated nonlinear behaviour than those made of classical materials [1]. Symmetrically laminated clamped composite beams (SLCCB) are used in the design of many engineering structures such as aircrafts, space vehicles, and defence industries. Very often, they are subjected to high excitation levels in severe work environments inducing large vibration amplitudes. It is important in such situations, for obvious security and comfort reasons, that analytical and numerical tools are available, which enable designers to analyze and estimate accurately how far the structural dynamic characteristics deviate from those predicted by linear theory. In [2], the nonlinear homogeneous beam bending vibrations have been investigated using an N dof discrete system made of (N +1) bars, connected by N masses placed at the bar ends, connected by (N+2) rotational springs, presenting the beam flexural rigidity (see figure 1). The large transverse displacements of the ends of the bars, modelled by longitudinal springs (see figure 2), induce a variation in their lengths giving rise to axial forces causing geometrical nonlinearity. The analogy between the characteristics of the classical continuous beam model and those of the present discrete model was developed. The nonlinear vibration problem, defined in terms of the mass tensor m_{ij}, the linear rigidity tensor k_{ij} and the nonlinearity tensor b_{ijkl}, was reduced, via application of Hamilton's principle, to a nonlinear algebraic system solved using the so-called first formulation developed in [3]. The main advantage of nonlinear physical discrete models is their ability to be used quite easily to analyze the nonlinear behaviour of beams with irregularities in the geometry, mass or stiffness distributions. It was then interesting to examine the extension of the discrete model to inhomogeneous beams, such as the (SLCCB) examined in the present work. The approach adopted is based on the combination of a homogenization procedure [4, 5] with the N dof discrete model [2] to obtain an equivalent homogeneous beam with effective bending and axial stiffness parameters.
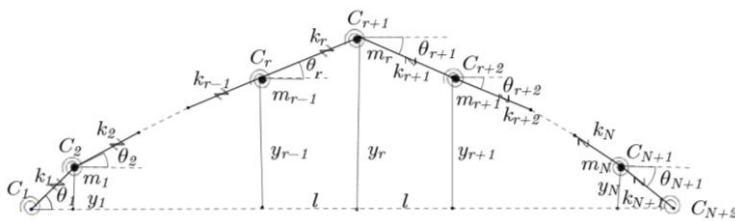
Figure1: The N dof discrete model of the (SLCCB)
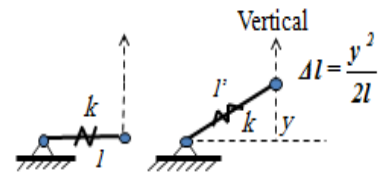
Figure 2: Nonlinear effect due to the Pythagorean Theorem

2   DISCRETE FORMULATION AND NUMERICAL RESULTS

The (SLCCB) studied in [4], [5] and [6] and examined in this work (Figure 3) has the following geometrical and mechanical characteristics: h = 0,001; b = 0,01; L = 0,25m; E_1=155 GPa, E_2=21,1GPa, ρ=1560 Kg/m3, υ_{12} = 0,248). The intermediate parameters and Lay-up allowing calculation of the equivalent isotropic beam parameters, i.e. $(ES)_{eff} = bA_{11}$ and

$(EI)_{eff} = b(D_{11} + (B_{11}^2/A_{11}))$, which are the effective axial and bending stiffness respectively, for the four composite beams considered in the present paper are given in Figure 3.

	A_{11}	B_{11}	D_{11}	$(ES)_{eff}$	$(EI)_{eff}$
Unidirectional	155749200	0	12.979	1557492	0.1298
(0/90/90)s	59997696	0	9.4336	599977	0.0943
(90/90/0)s	59945424	0	1.4564	599454	0.0145
Cross-ply	12120000	0	1.0100	121200	0.0101
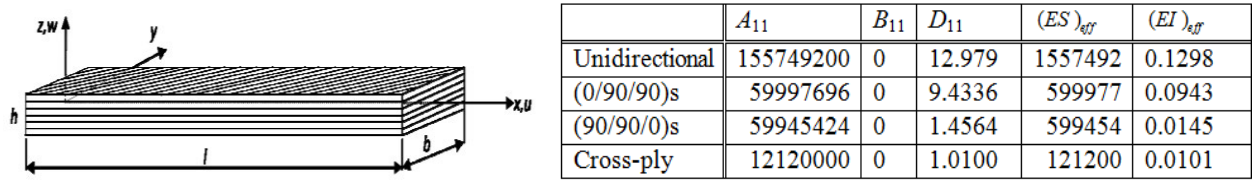
Figure 3: Laminated beam notation and characteristics

Consider the N dof discrete system developed in [1] for an isotropic beam. The nonlinear differential equations governing the system nonlinear dynamics is written in the displacement basis (DB) in a matrix form as follows:

$$[K]\{A\} - \omega^2[M]\{A\} + [B(A)]\{A\} = \{0\} \tag{1}$$

A discretization procedure, similar to that developed in [1], is applied to the equivalent isotropic beam using the parameters $(ES)_{eff}$ and $(EI)_{eff}$ calculated as functions of the composite beam stiffness coefficients A_{11}, B_{11} and D_{11} by: $(ES)_{eff} = bA_{11}$; $(EI)_{eff} = b(D_{11} + (B_{11}^2/A_{11}))$ [4, 5].The effective parameters are inserted in the rigidity matrix $[K]$ and the nonlinear rigidity tensor $[B(A)]$ presenting the discrete system through the rotational and longitudinal spring stiffness defined by: $C = \dfrac{(EI)_{eff}}{l}$ and $k = \dfrac{(ES)_{eff}}{l}$. It should be noted that the calculations, based on the so-called first formulation presented in [3], are performed in the modal basis (MB), in order to yield good estimates of the (SLCCB) amplitude dependent nonlinear frequencies using the single mode approach (SMA), giving: $(\omega_{disc}^{nl})^2 = \dfrac{\overline{k_{11}}}{m_{11}} + \dfrac{3}{2}\dfrac{\overline{b_{1111}}}{m_{11}}a_1^2$. For validation purposes, the numerical results, based on equation (1), for (SLCCB) vibration amplitudes up to 1.5 times the beam thickness are presented in Figure 4 for four composite beams and compared to those of references [5], [6] showing a satisfactory agreement. For higher amplitudes, the so-called second formulation developed in [3], which is known to have a wider range of validity, may be used as an alternative to the iterative method for solving the nonlinear amplitude equation.
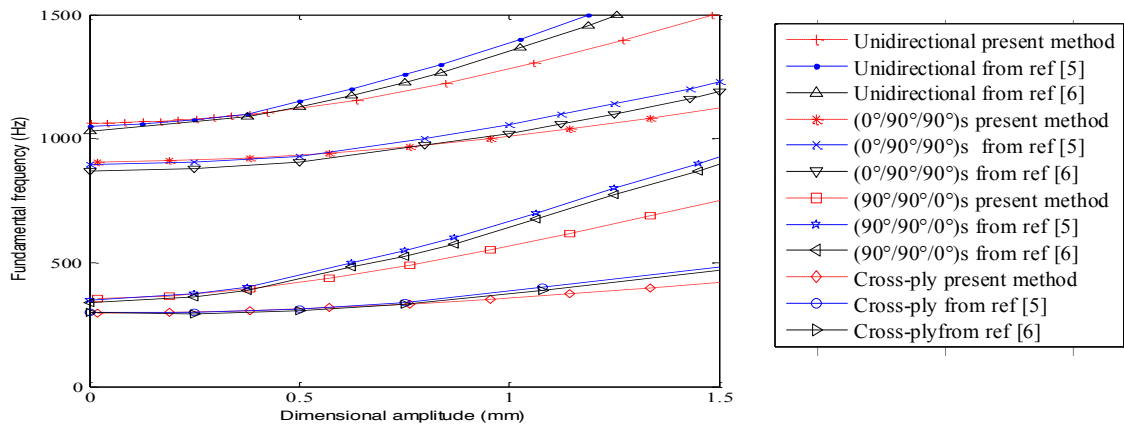
Figure 4: Comparison of the nonlinear frequencies obtained for different (SLCCB) lay-up by the present discrete model with previously published results

3

3 Conclusion

The problem of geometrically nonlinear vibrations of (SLCCB) is described by an *N*-dof discrete model of an equivalent isotropic beam, with effective bending and axial stiffness parameters. The model is made of (*N* +1) bars, connected by *N* masses placed at the bar ends, connected by rotational springs, presenting the beam flexural rigidity. The large transverse displacements of the bar ends induce a variation in their lengths giving rise to axial forces causing the nonlinear effect and modelled by longitudinal springs. The nonlinear vibration problem, defined in terms of the mass tensor m_{ij}, the linear rigidity tensor k_{ij} and the nonlinearity tensor b_{ijkl}, is reduced, via application of Hamilton's principle, to a nonlinear algebraic system solved using an explicit method for calculating the (SLCCB) fundamental nonlinear mode and associated amplitude dependent frequencies. The numerical results are found to be in a good agreement with previously published results, based on a semi analytical composite beam continuous theory. As has been done with isotropic beams in [4, 5 and 6], the discrete system for the (SLCCB), developed and validated here, may be used in further applications to investigate nonlinear vibrations of non-uniform composite beams, carrying point masses, or beams with irregularities in the mass [7] or in the stiffness distributions.

REFERENCES

[1]   R. Benamar, Nonlinear dynamic behaviour of fully clamped Beams and rectangular isotropic and laminated plates, Ph.D. Thesis, University of Southampton (1990).

[2]   A. Rahmouni, Z. Beidouri and R. Benamar (2013) A discrete model for geometrically nonlinear transverse free constrained vibrations of beams with various end conditions. Journal of Sound and Vibration 332(20): 5115-5134. doi: 10.1016/j.jsv.2013.04.011.

[3]   M.E. Kadiri, R. Benamar and R.G. White (2002) Improvement of the semi-analytical method for determining the geometrically nonlinear response of thin straight structures, part I: application to clamped–clamped and simply supported–clamped beams, Journal of Sound and Vibration 249 (2) 263–305.

[4]   K. Elbikri, E. Merrimi and R. Benamar (2012) Applied Mechanics and Materials Vols 105-107 (2012) pp 1681-1684 Online: 2011-09-27 © (2012) Trans Tech Publications, Switzerland doi:10.4028/www.scientific.net/AMM.105-107.1681

[5]   R.K. Jagadish Babu Gunda, Gupta, G. Gundabathula Rao, and Venkateswara Rao: Post-buckling and Large Amplitude Free Vibration Analysis of Composite Beams: Simple Intuitive Formulation Composite Structures; J. Inst. Eng. India Ser Vol. 93 (2015), C DOI 0.1007/s40032-015-0204-y.

[6]   Jagadish Babu Gunda, Gupta R.K., Ranga Janardhan G., and Venkateswara Rao:
Large amplitude vibration analysis of composite beams: Simple closed-form solutions
Composite, Structures Vol. 93 (2011), p. 870–879.

[7]   A. Rahmouni and R. Benamar (2016) Examining nonlinear transverse vibrations of clamped beams carrying N concentrated masses at various locations using discrete Model. International Journal of Computational Engineering Research 06: 2250-3005.

ANALYSIS OF LARGE AMPLITUDE OSCILLATIONS OF SIMPLY SUPPORTED BEAMS THROUGH THE USE OF THE NONLINEAR NORMAL MODES (NNM) METHOD

J.G. Carbajal, J. Domínguez and D. García-Vallejo

[1]Departamento de Ingeniería Mecánica y Fabricación
Escuela Técnica Superior de Ingeniería, Universidad de Sevilla
C/. Camino de los Descubrimientos S/N, 41092 Seville, SPAIN
Email: jgonzalezcarbajal@gmail.com

ABSTRACT

Simply supported beams are usually classified into two groups, depending on whether longitudinal displacements are restrained or not. This work goes deeper into the fact that the nonlinear behavior of the beam is significantly different in these two cases: one in which axial motion is allowed at one end but restricted at the other; and another in which there is no restriction to axial displacements at both ends. The analytical treatment of the problem leads to a relation between nonlinear frequency and amplitude for the different modes of vibration of the beam. A well-known commercial finite element software is used to validate the results of the analytical models. Nonlinear normal mode (NNM) shapes may be represented as a combination of several linear ones. The results of this investigation show that the contribution of linear modes other than the first one to each nonlinear one is significant. Different simulations are conducted with the aim to provide recommendations for the need of including such modes.

1   INTRODUCTION

The dynamic behaviour of linear elastic beams under hypothesis of small strains and small displacements is well-known. However, in numerous applications, deflections are large enough to make the assumption of small displacements no more suitable. In these cases, the equilibrium needs to be imposed on the deformed configuration of the structure, what makes the system nonlinear.

Although nonlinear vibrations of beams have been widely studied, available results are sometimes unclear and often contradictory [1[5]. For this reason, the present article intends to get some insight into the physical phenomenon and quantify the effect of the mentioned nonlinearities on the dynamics of simply supported beams with moderately large displacements.

Simply supported beams are usually classified into two groups, depending on whether longitudinal displacements are restrained or not. This article deals with both groups separately. It will be shown that the nonlinear behaviour of the beam is strongly different in these two cases: one in which axial motion is allowed at one end (unsymmetrical case) and restricted at the other and another one where there is no restriction to axial displacements (symmetrical case).

The analytical treatment of the simply supported axially unrestrained beam problem leads to a relation between nonlinear frequency and amplitude for the different modes of vibration of the beam. Some finite element simulations are carried out in order to validate the results, which are also compared to those obtained by other authors.

Later, the axially restrained case, where both ends of the beam are immovable, is also briefly studied. The aim of this part is to cast light on the question about whether nonlinearities other than midline stretching should or not be included in the model. Once again, different results can be found in the literature in this regard [1[5, [6, [7].

The analytical treatment in this work uses the concept of Nonlinear Normal Modes (NNMs) introduced by Rosenberg in the 60s [8], which has experienced a great development since 1990 due to the works of Pierre, Shaw, Vakakis, etc. [9, [10]. In short, for an unforced conservative system, a NNM can be defined as a family of periodic motions which occur onto a 2D invariant manifold in the phase space of the system. This manifold passes through a stable equilibrium point and, at that point, is tangent to one of the Linear Normal Modes (LNMs) of the linearized system. Then, NNMs are a natural generalization of LNMs, suitable to Nonlinear Systems. For a detailed exposition on NNMs, the reader is referred to [11].

2   SIMPLY SUPPORTED BEAM WITH UNRESTRAINED AXIAL DISPLACEMENTS

The procedure followed by Nayfeh in [6 [12] for obtaining the NNMs of continuous systems has been used in this investigation. **Fig. 1** show Frequency-Amplitude curves for the first NNMs and the configurations of axially unrestrained simply supported beams. Obviously, we are not taking into account the rigid body mode present in the symmetrical case.

In both figures, the blue curve corresponds to an analytical model, while the blue circles correspond to Finite Element results. We have used commercial program Abaqus®, discretizing the beam in 16 elements with cubic interpolation. The initial conditions for these Finite Element simulations have been chosen to correspond to one particular NNM. For the first NNM, we have also included some results from the literature.
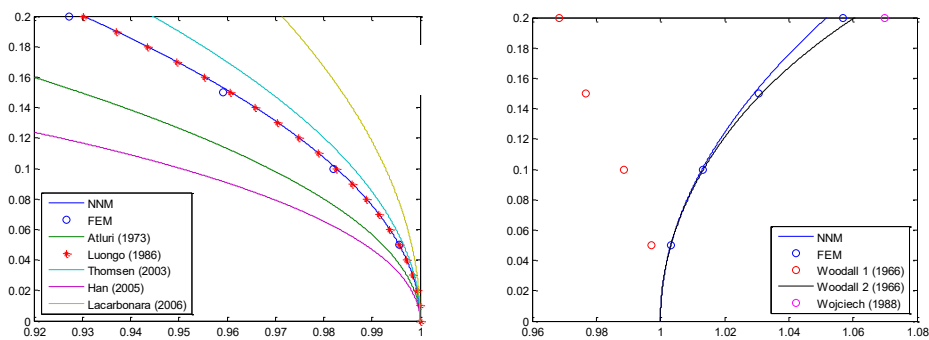
Fig. 1 frequency vs amplitude curves for the first NNM: unsymmetrical case (left) symmetrical case (right)

Fig. 2 shows in blue the deformed shapes for the first NNMs, including the contributions of the first 5 linear modes. Rigid body motion in the symmetrical case has been avoided.
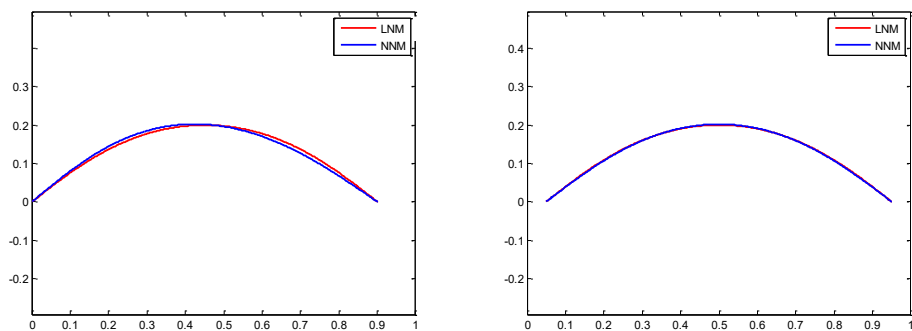
Fig. 2 Deformed shape corresponding to the first NNM: Unsymmetrical case (left) and Symmetrical case (right)

The main issue about a nonlinear frequency-amplitude curve (usually called *Backbone Curve*) is whether it shows hardening or softening behavior. It can be observed that, for the first mode, the unsymmetrical beam softens, while the symmetrical one hardens. The first immediate consequence is that, when dealing with a simply supported beam, it is not enough to specify whether axial motion is restrained or not since, even within the axially unrestrained group there exist different kinds of behavior.

3   CONCLUSIONS

It is found that, in the axially unrestrained case, two kinds on nonlinearities influence the motion of the beam. One is of geometric nature, while the other is due to longitudinal inertia. For the simply supported beam they produce, respectively, hardening and softening, but this may be different for other boundary conditions.

Two different configurations of axially unrestrained simply supported beams have been considered, one having a fixed end and other with both ends free in the longitudinal direction. They have been shown to exhibit different behaviours, suggesting that the usual distinction between axially restrained and unrestrained simply supported beams [5] is not enough for characterizing their dynamics. For the first NNM, the beam undergoes hardening in the symmetrical case and softening in the unsymmetrical case.

The reasonably good accordance between analytical and Finite Element results (with axially extensible elements) indicates that the assumption of inextensible middle line, used for the axially unrestrained case, is pertinent –at least for the first two NNMs–.

4   REFERENCES

[1]   A. Luongo, G. Rega, F. Vestroni (1986) *On Nonlinear Dynamics of Planar Shear Indeformable Beams*, Journal of Applied Mechanics, **53**, 619-624.

[2]   S. Atluri (1973) *Nolinear Vibrations of a Hinged Beam Including Nonlinear Inertia Effects*, Journal of Applied Mechanics, **40**, 121-126.

[3]   J. J. Thomsen (2003) *Vibrations and Stability*, Springer Verlag, Berlin, Heidelberg, New York.

[4]   Qiang Han, Xiangfeng Zheng (2005) *Chaotic Response of a Large Deflection Beam and Effect of the Second Order Mode*, European Journal of Mechanics A/ Solids, **24**, 944-956.

[5]   W. Lacarbonara, H. Yabuno (2006) *Refined Models of Elastic Beams Undergoing Large In-plane Motions: Theory and Experiment*, Int. J. Solids and Structures, **43**, 5066-5084

[6]   A. H. Nayfeh, S. A. Nayfeh (1994) *On Nonlinear Modes of Continuous Systems*, Journal of Vibration and Acoustics, **116**, 129-136.

[7]   E. Mettler (1962) *Handbook of Engineering Mechanics*, McGraw-Hill, New York.

[8]   R. M. Rosenberg (1962) *The Normal Modes of Nonlinear N-Degree-of-freedom Systems*, Journal of Applied Mechanics, **29**, 7-14.

[9]   A. F. Vakakis (1990) *Analysis and Identification of Linear and Nonlinear Normal Modes in Vibrating Systems*, PhD disertation, California Institute of Technology, California (USA).

[10]   S. W. Shaw, C. Pierre (1991) *Nonlinear Normal Modes and Invariant Manifolds*, Journal of Sound and Vibration, **150**, 17.

[11]   G. Kerschen, M. Peeters, J. C. Golinval, A. F. Vakakis (2009) *Nonlinear Normal Modes, Part I: A Useful Framework for the Structural Dynamicist*, Mechanical Systems and Signal Processing, **23**, 170-194.

[12]   A. H. Nayfeh, C. Chin, S. A. Nayfeh (1995) *Nonlinear Normal Modes of a Cantilever Beam*, Journal of Vibration and Acoustics, **117**, 477-481.

GEOMETRICALLY NON-LINEAR VIBRATIONS OF BEAMS CARRYING A POINT MASS AND RESTRAINED BY TRANSLATIONAL AND ROTATIONAL SPRINGS AT THE ENDS.

A. Adri[1*], R. Benamar[2]

[1]Laboratoire de Mécanique Productique & Génie Industriel (LMPGI)
Hassan II University in Casablanca, Casablanca, MOROCCO
Email: ahmedadri@gmail.com

Laboratoire des Études et Recherches en Simulation et Instrumentation
Mohammed V University in Rabat, MOROCCO
Email: benamar@emi.ac.ma

ABSTRACT

The non-linear vibrations of a beam carrying a point mass at an arbitrary location and restrained by translational and rotational springs at the two ends are investigated analytically and a parametric study is performed, allowing examination of all possible combinations of classical restrained end conditions, including elastic restraints. The dynamic equation was written at two intervals of the beam span with appropriate end and continuity conditions. After the necessary algebraic transformations, the generalised transcendental frequency equation was solved iteratively using the Newton Raphson method. Once the corresponding program implemented, investigations have been made of the changes in the beam frequencies and mode shapes for many values of the mass, mass location and spring stiffness. Numerical results and plots have been given here of the beam frequencies and first mode shape corresponding to various situations. The effect of geometrical non-linearity has then been investigated using a semi analytical method based on Hamilton's principle and spectral analysis leading to solution of a non-linear amplitude equation. A single mode approach, performed in the modal basis, has been adopted in order to obtain, for various configurations of the beam examined, the backbone curves giving the amplitude dependent nonlinear frequencies.

1   INTRODUCTION

The operation of machines (machine tools, automotive, robot manipulators and others) introduces dynamic constraints on the various components of the engine and the supporting elements. To ensure correct operation, reduce the induced noise, and increase the machine fatigue life, it is essential to determine the natural frequencies of the system, in both the linear and non-linear regimes. Many such situations may be modeled by a beam carrying one or many masses, restrained at its ends by flexible rotational and translational springs [1-2]. This makes it possible to study different types of restrained end conditions, such as simply supported or clamped, depending on the values assigned to the spring stiffness. The vibrations of restrained beams supporting point masses have been partially examined before [1-3] but all of the studies available are restricted to the linear case. The present paper is based on a systematic parametric study allowing easy choice of the position of the mass to be added in order to adapt the linear frequencies and avoid possible resonances. In the second part, the effect of geometrical nonlinearity on the system "beam + added mass" amplitude dependent nonlinear frequencies is investigated. A single mode approach is adopted, combining the semi analytical method for nonlinear structural vibrations developed previously [4] and the linear modes calculated in the first part, and allowing various backbone curves to be drawn, corresponding to various values of the spring stiffness and added mass.
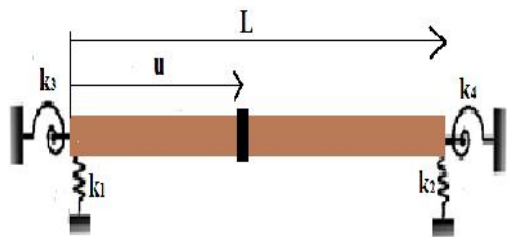
Figure. 1. The restrained beam with a point mass. Beam characteristics (L, S, ρ, E, I)

η	$K_3=10\ k_4=10$		$K_3=100\ k_4=100$		$K_3=10\ k_4=100$	
	M=0,5	M=1	M=0,5	M=1	M=0,5	M=1
0	4,15566	4,15566	4,64132	4,64132	4,39001	4,39001
0,1	4,10204	4,04572	4,61416	4,58502	4,31999	4,24643
0,2	3,89071	3,66687	4,40167	4,17988	4,06073	3,79719
0,3	3,64396	3,32802	4,07685	3,72112	3,78953	3,44078
0,4	3,48471	3,13988	3,85720	3,46419	3,63523	3,26359
0,5	3,43214	3,08101	3,78481	3,38463	3,60750	3,23319

Table1: eigenvalues of the "beam mass" for different values of the rotational stiffness, mass and mass locations

2   VIBRATION OF A RESTRAINED BEAM CARRYING A POINT MASS

Consider the beam shown in Figure1, with a point mass m, restrained at the ends by translational and rotational springs.   The beam transverse displacement is $W(x,t)=w(x)\sin(\omega t)$ The problem under consideration is governed by the following differential equation:

$$\frac{d^4 w}{dx^4} - \beta^4 w = 0 \quad \text{with} \quad \beta^4 = \frac{\rho S}{EI}\omega^2 \tag{1}$$

The function w is defined in piecewise by: $w_1(\eta)$ and $w_2(\eta)$ in $]0,\xi[$ and $]\xi,1[$ respectively, with

$\eta = \frac{x}{L}; \xi = \frac{u}{L}$. The general solution for transverse vibration in the first and second span, can be written as:

$$w_1(\eta) = a_1\cosh(\beta_i L\eta) + b_1\sinh(\beta_i L\eta) + c_1\cos(\beta_i L\eta) + d_1\sin(\beta_i L\eta) \tag{2}$$

$$w_2(\eta) = a_2\cosh(\beta_i L(\eta-\xi)) + b_2\sinh(\beta_i L(\eta-\xi)) + c_2\cos(\beta_i L(\eta-\xi)) + d_2\sin(\beta_i L(\eta-\xi)) \tag{3}$$

In which $\beta_i = \sqrt[4]{\frac{\rho S\omega_i^2}{EI}}$ for i= 1, 2, ... are the mode shape parameters of the beam with an added point mass. The constants a_j, b_j, c_j, d_j are determined by the continuity and end conditions:

At the ends:
$$\left.\frac{d^3 w_{1i}(\eta)}{d\eta^3}\right|_{\eta=0} = -k_1 w_{1i}(\eta)\big|_{\eta=0} \ ; \ \left.\frac{d^2 w_{1i}(\eta)}{d\eta^2}\right|_{\eta=0} = k_3\left.\frac{dw_{1i}(\eta)}{d\eta}\right|_{\eta=0} \tag{4}$$

2

Continuity conditions:
$$\left.\frac{d^3 w_{(n+1)i}(\eta)}{d\eta^3}\right|_{\eta=1} = k_2 w_{(n+1)i}(\eta)\Big|_{\eta=1} \quad ; \quad \left.\frac{d^2 w_{(n+1)i}(\eta)}{d\eta^2}\right|_{\eta=1} = -k_4 \left.\frac{dw_{(n+1)i}(\eta)}{d\eta}\right|_{\eta=1} \tag{5}$$

$$w_{2i}(\eta)\Big|_{\eta=\xi} = w_{1i}(\eta)\Big|_{\eta=\xi} \quad ; \quad \left.\frac{dw_{2i}}{d\eta}\right|_{\eta=\xi} = \left.\frac{dw_{1i}}{d\eta}\right|_{\eta=\xi} \quad ; \quad \left.\frac{d^2 w_{2i}}{d\eta^2}\right|_{\eta=\xi} = \left.\frac{d^2 w_{1i}}{d\eta^2}\right|_{\eta=\xi} \tag{6}$$

$$\left.\frac{d^3 w_{2i}}{d\eta^3}\right|_{\eta=\xi} = \left.\frac{d^3 w_{1i}}{d\eta^3}\right|_{\eta=\xi} + M(\beta_i L)^4 w_{1i}(\eta)\Big|_{\eta=\xi} \qquad \text{Where } M = \frac{m}{\rho SL} \tag{7}$$

Equations 4 to 7 give a linear system with eight equations and eight unknowns whose determinant must vanish, leading via application of a Newton–Raphson algorithm, to the vibrating beam frequencies and mode shapes. The corresponding numerical results are summarised in Table1.

3   APPLICATION: A UNIFORM RESTRAINED BEAM WITH ONE POINT MASS

The effect of the added mass location on the beam first frequency, with its associated mode and curvatures, is shown in Figure 2 for various values of the rotational stiffness for $M = 0.5$. located at u=L/2. These results are summarised in Table 1.
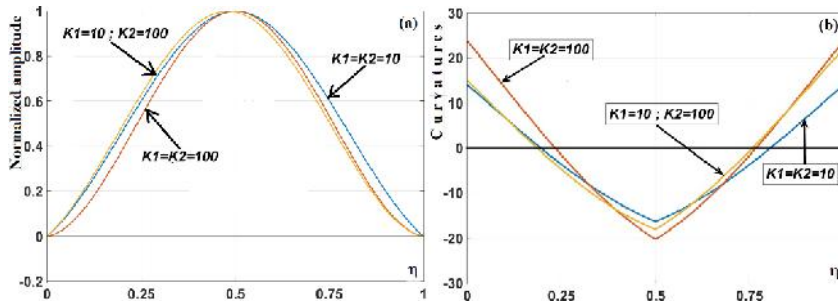
Figure. 2 (a) First mode and (b) Curvatures for $M = 0.5$, u=0.5 and various values of k

4   GEOMETRICALLY NONLINEAR VIBRATION OF A RESTRAINED BEAM CARRYING A CONCENTRATED MASS.

At large vibration amplitudes, the beam shown in Figure1 kinetic energy T, linear strain energy V_{lin} and nonlinear strain energy V_{Nlin} induced by large deflections can be expressed as [4]:

$$T = \frac{1}{2}\rho S \int_0^L \left(\frac{\partial w(x,t)}{\partial t}\right)^2 dx + \frac{1}{2}m\left(\frac{\partial w(x_j,t)}{\partial t}\right)^2 ; V_{Lin} = \frac{1}{2}EI\int_0^L \left(\frac{\partial^2 w(x,t)}{\partial x^2}\right)^2 dx ; V_{Nlin} = \frac{1}{8}\frac{ES}{L}\left[\int_0^L \left(\frac{\partial w(x,t)}{\partial x}\right)^2 dx\right]^2 \tag{8}$$

Expanding $w(x,t)$ as a series of basic spatial functions: $w(x,t) = q_i(t)w_i(x) = a_i w_i \sin(\omega t)$ and applying Hamilton's principle and integrating the time functions over a period of vibration, the system dynamics is governed by [1]:

$$2[K]\{A\} + 3\big[B(\{A\})\big]\{A\} = 2\omega^2 [M]\{A\} \tag{9}$$

in which {A} is the column vector of the basic function coefficients, and [K] and [M] are the rigidity and mass matrices, and $\big[B(\{A\})\big]$ is the nonlinear geometrical rigidity. Equation 9 is the Rayleigh-Ritz formulation of the nonlinear problem, to be solved numerically, or explicitly. From equation 9, the frequency ω may be obtained by pre multiplying the two hand sides of the equation by $\{A\}^T$, which gives:

$$\omega^2 = \frac{\{A\}^T[K]\{A\} + \frac{3}{2}\{A\}^T\big[B(\{A\})\big]\{A\}}{\{A\}^T[M]\{A\}}, \quad \text{(a)} \quad ; \quad \omega^2 = \frac{k}{m} + \frac{3}{2}a^2\frac{b}{m}, \quad \text{(b)} \tag{10}$$

3

The single mode approach, consists of neglecting all the basic functions except a single ''resonant'' mode. Thus, it reduces equation 10(a) to 10(b), in which $[K]=k_{11}$, $[M]=m_{11}$, $[B(\{A\})]=b_{1111}$. Figure 3(a) shows the backbone curves corresponding to various values of the mass, mass location and rotational spring stiffness. Figure 3(b) shows the curvatures associated to the first nonlinear mode.
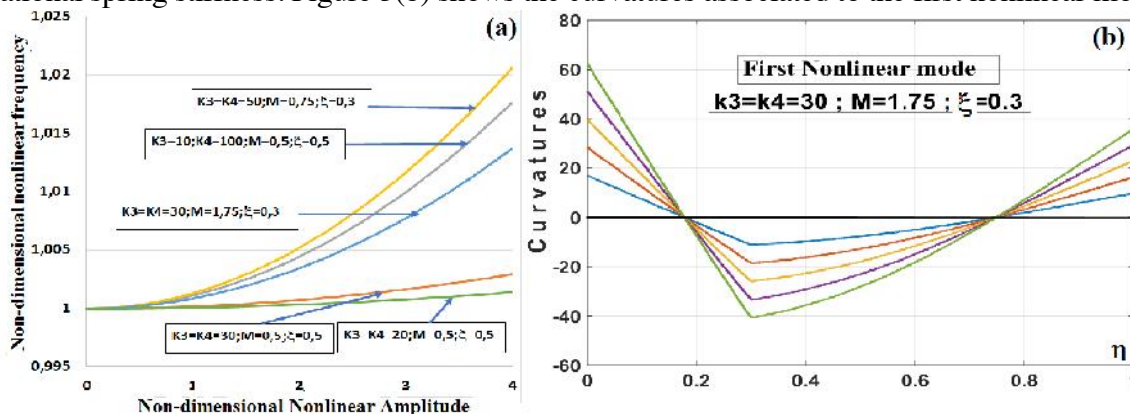
Figure 3 (a)Backbone curves for various values of the mass, mass location and rotational stiffness; (b) curvatures associated to the first nonlinear mode

5   CONCLUSION

The non-linear vibrations of a beam carrying a point mass at an arbitrary location and supported by translational and rotational springs at the two ends have been investigated analytically and a parametric study was performed, allowing examination of many combinations of classical end conditions, including elastic restraints. The dynamic equation was written at two intervals of the beam span with appropriate end and continuity conditions. After the necessary algebraic transformations, the generalised transcendental frequency equation was solved iteratively using the Newton Raphson method. Numerical results and plots have been given of the beam frequencies and first mode shape corresponding to various situations. The effect of geometrical non-linearity has then been investigated using a semi analytical method based on Hamilton's principle and spectral analysis leading to solution of a non-linear amplitude equation. A single mode approach, performed in the modal basis, has been adopted in order to obtain, for various configurations of the beam examined, the backbone curves giving the amplitude dependent nonlinear frequencies.

REFERENCES
[1]   Adri A, Beidouri Z, El kadiri M, Benamar R. Geometrically Nonlinear Free Vibration of a Beam Carrying Concentrated Masses International. Journal of Engineering Research & Technology (IJERT) ISSN: 2278-0181 Vol. 5 Issue 01, January-2016
[2]   Santiago Maiz et al, Transverse vibration of Bernoulli–Euler beams carrying point masses and taking into account their rotatory inertia: Exact solution, Journal of Sound and Vibration 303 (2007) 895–908
[3]   A. H. REGISTER, a note on the vibrations of generally restrained end-loaded beams, Journal of Sound and Vibration (1994) 172(4), 561-571
[4]   Azrar R. L , Benamar R. , White R.G.. 1999. "A semi-analytical approach to the non-linear dynamic response problem of S-S and C-C beams at the large   vibration amplitudes part1: General theory and application to the single mode approach to free and forced vibration analysis". Journal of Sound and Vibration 224 (2), 183-207
 [5]   EL Kadiri M., Benamar R. and White.R.G. 2002. "Improvement of the semi-analytical method, based on Hamilton's principle and spectral analysis, for determination of the geometrically nonlinear free response of thin straight structures. Part I: Application to C-C and SS-C beams". Journal Sound and Vibration (2002) 249(2), pp 263-305.

GEOMETRICALLY NONLINEAR OF ORTHOTROPIC PLATES USING SEMI-ANALYTICAL METHOD

H. Bhar[1], O. Baho[2], R. Benamar[1], and B. Harras[2]

[1]Laboratoire d'Etudes et de Recherches en Simulation, Instrumentation et Mesure
Ecole Mohammadia d'Ingénieurs, Université Mohammed V,
BP 765 Agdal, Rabat, Morocco
Email: bhar.hanane@gmail.com, rbenamar@emi.ac.ma

[2]Laboratoire de Génie mécanique
FST de Fès, Route d'Immouzer, BP 2202 Fès, Morocco
Email: bharras@gmail.com, omar.uinv@gmail.com

ABSTRACT

The present paper concerns the nonlinear dynamic behaviour of orthotropic rectangular plate under boundary conditions (C-C-C-SS) and (C-C-SS-SS). The main objective is to find semi analytical solutions for the first non-linear mode shapes and the associated non-linear frequencies of the composite plates at large vibration amplitudes. The basic formulation of nonlinear free vibrations has been developed based on the classical plate theory (CPT) and the nonlinear strain-displacement relation. The nonlinear governing equations are derived from Hamilton's principle and the Von Kármán geometrical non-linearity assumptions. Assuming the out-of-plane displacement as a double trigonometric function, the in-plane displacement components are found by solving the nonlinear algebraic equations of motion expressed in terms of displacements. The improved version of the Newton-Raphson method and the semi-analytical model developed by El Kadiri et al. for fully clamped rectangular plates, has been adapted to the above cases.

1   INTRODUCTION

Laminated composite plates are frequently used in various engineering applications in the aerospace, mechanical, marine, and automotive industries because of their advantages such as high stiffness-to-weight and strength-to-weight ratios. In the case where these structures are subjected to dynamic loads may induce large amplitude vibrations and, thus, the structure may exhibit significant nonlinear behaviour that must be studied for the efficient design of such structures.

Numerous methods have been developed to perform geometrically nonlinear analysis of plates. Benamar et al [1] presented a theoretical formulation of the plate vibration problem at large displacement amplitudes. Han and Petyt [2], Ribeiro and Petyt [3] have been presented dealing with the geometrically non-linear dynamic behaviour of symmetrically laminated plates by using the hierarchical finite element method (HFEM). Harras and Benamar [4] investigated theoretical and experimental of the non-linear behaviour of various fully clamped rectangular composite panels at large vibration amplitudes. El Kadiri et all [5, 6] presented a semi-analytical method, based on Hamilton's principle and spectral analysis, for the determination of the geometrically non-linear free response of thin straight structures. Several review articles on orthtropic plates have been reported in the literature by various researchers, such as Leissa [7], Reddy [8], and Noor et al. [9].

In the present paper the method developed by El Kadiri et al. is extended to the geometrically nonlinear analysis of orthotropic plate with two boundary conditions (C-C-C-SS) and (C-C-SS-SS). This boundary conditions are widely used in aerospace structures. On the other hand, this study will contribute to generalize and extend the model to different conditions.

2   THEORY

Consider the transverse vibration of C-C-SS-SS rectangular plate which is clamped on two edges, and simply supported in the other edges. This plate is shown in figure 1.
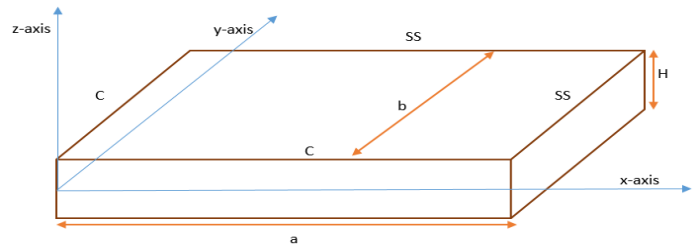
Figure 1. Plate notation

For the classical plate laminated theory, the strain-displacement relationship for large deflections:

$$\begin{bmatrix} \varepsilon_x \\ \varepsilon_{y_y} \\ \gamma_{xy} \end{bmatrix} = \begin{bmatrix} \dfrac{\partial U}{\partial x} \\ \dfrac{\partial V}{\partial y} \\ \dfrac{\partial U}{\partial x} + \dfrac{\partial V}{\partial y} \end{bmatrix} + \begin{bmatrix} -\dfrac{\partial^2 W}{\partial x^2} \\ -\dfrac{\partial^2 W}{\partial y^2} \\ -2\dfrac{\partial^2 W}{\partial x \partial y} \end{bmatrix} + \begin{bmatrix} \dfrac{1}{2}\left(\dfrac{\partial W}{\partial x}\right)^2 \\ \dfrac{1}{2}\left(\dfrac{\partial W}{\partial y}\right)^2 \\ \dfrac{\partial W}{\partial x}\dfrac{\partial W}{\partial y} \end{bmatrix} \equiv \{\varepsilon\} = \{\varepsilon^0\} + z\{\kappa\} + \{\lambda^0\} \qquad (1)$$

where $\{\varepsilon^0\}$ and $z\{\kappa\}$ are the membrane and the flexural strain tensors, respectively, and U, V, W are the middle surface displacement components in the x, y and z directions respectively.

The free vibrations of the structure are governed by Hamilton's principle which is symbolically written as

$$\delta \int_0^{2\pi} (V - T)dt = 0 \qquad (2)$$

In which δ indicates the variation of the integral. V and T are respectively the total strain energy and the kinetic energy, where $V = V_a + V_b$. Replacing T and V in this equation by their expressions given above, integrating the time functions, and calculating the derivatives with respect to the a_i, leads to the following set of non-linear algebraic equations:

2

$$3a_i a_j a_k b^*_{ijkl} + 2a_j k^*_{ir} - 2a_i \omega^{*2} m^*_{ir} = 0, \quad i = 1, ..., n. \tag{3}$$

$$m_{ij} = \rho H^5 ab \, m^*_{ij} , k_{ij} = \frac{aH^5 E}{b^3} k^*_{ij} , b_{ijkl} = \frac{aH^5 E}{b^3} b^*_{ijkl} \tag{4}$$

a, b: length, width of the plate; E: Young's modulus; H: plate thickness; a_k: contributions corresponding to the kth basic functions; ρ: mass density per unit volume of the plate.

ω, and ω* are the frequency and non-dimensional frequency parameters respectively.

k^*_{ij}, m^*_{ij} and b^*_{ijkl}: General term of the non-dimensional rigidity tensor, mass tensor and non-linearity tensor respectively.

2.1 Explicit procedure

In modal functions basis for the first mode (MFB):

$$w^*(x^*, y^*) = \sum_{i=1}^{n} a_i \Phi^*_i(x^*, y^*) = \{A\}^T \{\Phi^*\} \tag{5}$$

with $\{\Phi^*\}^T = [\Phi^*_1 \ \Phi^*_2 ... \Phi^*_n]$ and $\{A\}^T = [a_1 \ \epsilon_2 ... \epsilon_n]$

$$\epsilon_r = \frac{3a_1 b^*_{r111}}{2((k^*_{11} + a_1^2 b^*_{1111}) \frac{m^*_{rr}}{m_{11}} - k^*_{rr})} \quad (r = 2, 3 ... 16) \tag{6}$$

$$w^*_{nl1}(x^*, y^*, a_1) = a_1 \Phi^*_1(x^*, y^*) + \epsilon_2 \Phi^*_1(x^*, y^*) + \cdots + \epsilon_{16} \Phi^*_{16}(x^*, y^*) \tag{7}$$

The chosen basic functions $P^*_i(x)$ were the linear clamped-simply supported beam functions and $Q^*_i(x)$ were linear clamped-clamped beam.

➤ Clamped-Simply supported beam

$$P^*_i(x) = ch\,(l_i x^*) - \cos(l_i x^*) - (sh\,(l_i x^*) - \sin\,(l_i x^*))\left(\frac{(ch\,(l_i) - \cos\,(l_i)}{sh\,(l_i) - \sin\,l_i}\right) \tag{8}$$

➤ Clamped-Clamped beam

$$Q^*_i(x) = \frac{ch\left(\frac{v_i x}{a}\right) - \cos(\frac{v_i x}{a})}{ch\,(v_i) - \cos\,(v_i)} - \frac{sh\left(\frac{v_i x}{a}\right) - \sin\,(\frac{v_i x}{a})}{sh\,(v_i) - \sin\,(v_i)} \tag{9}$$

3   RESULTS OF NON-LINEAR ANALYSIS

The geometrical and material properties are defined in Table 1.

Geometric properties	Material properties
Orientation of principale axes :[90,45,-45,0]$_{sym}$ a=485.7mm ; b=322.9 mm ; h=1 mm	Ex=120.5 GPa; Ey=9.63GPa; Gxy=3.58 GPa; v_{xy}=0.32; $\rho = 1540 \ kg/m^3$

Table 1. Geometric and material properties of thin plate
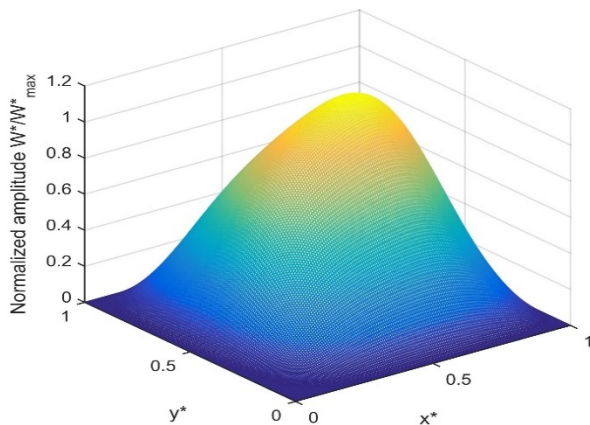
Figure 1. First non-linear mode rectangular C-C-SS-SS plate α=b/a=2/3, w*(x*,y*).
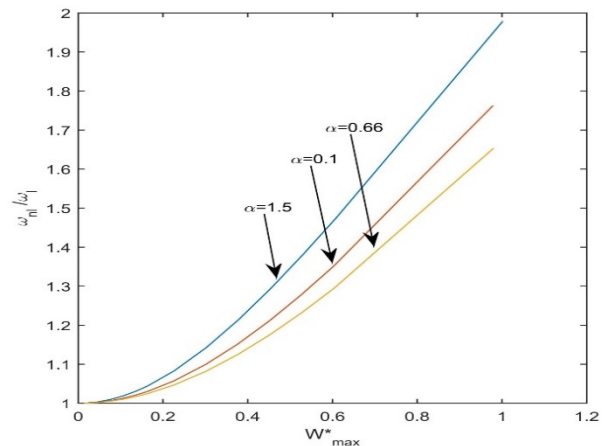
Figure 2. Comparison of the change frequency of the first mode for: $\alpha = 1,5 ; \alpha = 1; \alpha = 1,5.$

3
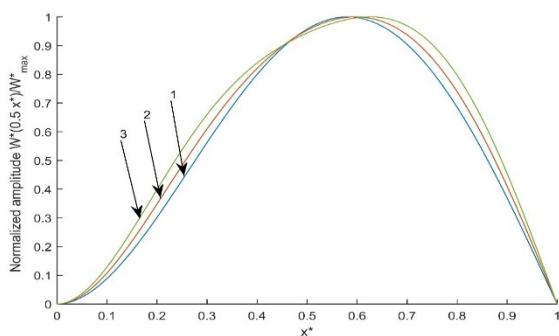
Figure 3. Normalised first non-linear mode rectangular C-C-SS-SS plate α=1,5, x*=0,5. Curve 1, lowest amplitude ; curve 3, highest amplitude.
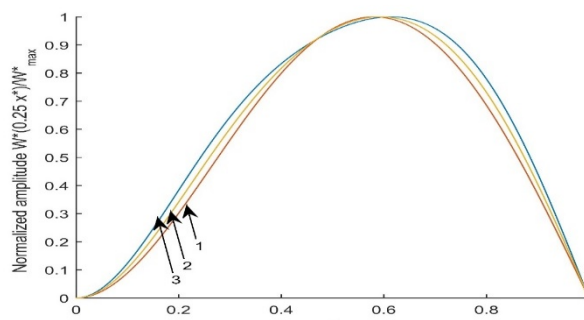
Figure 4. Normalised first non-linear mode rectangular C-C-SS-SS plate α=1,5, x* =0,25. Curve 1, lowest amplitude ; curve 3, highest amplitude.

Comparison of the non-linear frequency and linear frequency of the C-C-SS-SS rectangular plate, for various plate aspect ratios (α =a/b), where a_1 represent the amplitude of vibration (Table 2).

α =a/b	0.4	0.66	1	1.5
ω_l^*	79.420	86.249	102.37	143.73
$\omega_{nl}^*(a_1 = 0,01)$	79.4366	86.268	102.40	143.79
$\omega_{nl}^*(a_1 = 0,25)$	88.988	97.063	117.93	174.59

Table 2. Comparison of non-dimensional frequency parameters

4   CONCLUSION

o   The first non-linear mode of C-C-S-S and the explicit analytical expressions for the higher mode contribution coefficients to the first non-linear mode shape have been obtained.
o   Numerical results obtained from the application of C-C-SS-SS rectangular plate with different values of aspect ratio $\boldsymbol{\alpha}$ have been given.
o   The validity of the current approach will be compared later those of finite element methods (FEM),

5   REFERENCES

[1]   R. Benamar, R. White, and M. Bennouna, "The effects of large vibration amplitudes on the fundamental mode shape of a fully clamped, symmetrically laminated, rectangular plate," in *Structural Dynamics: Recent Advances*, 1991, pp. 749-760.
[2]   W. Han and M. Petyt, "Linear vibration analysis of laminated rectangular plates using the hierarchical finite element method—I. Free vibration analysis," *Computers & structures,* vol. 61, pp. 705-712, 1996.
[3]   P. Ribeiro and M. Petyt, "Multi-modal geometrical non-linear free vibration of fully clamped composite laminated plates," *Journal of sound and vibration,* vol. 225, pp. 127-152, 1999.
[4]   B. Harras, R. Benamar, and R. White, "Investigation of non-linear free vibrations of fully clamped symmetrically laminated carbon-fibre-reinforced PEEK (AS4/APC2) rectangular composite panels," *Composites science and technology,* vol. 62, pp. 719-727, 2002.
[5]   M. El Kadiri and R. Benamar, "Improvement of the semi-analytical method, based on Hamilton's principle and spectral analysis, for determination of the geometrically non-linear response of thin straight structures. Part III: steady state periodic forced response of rectangular plates," *Journal of Sound and Vibration,* vol. 264, pp. 1-35, 2003.
[6]   M. El Kadiri, R. Benamar, and R. White, "Improvement of the semi-analytical method, for determining the geometrically non-linear response of thin straight structures. Part I: application to clamped–clamped and simply supported–clamped beams," *Journal of sound and vibration,* vol. 249, pp. 263-305, 2002.
[7]   A. W. Leissa, "The free vibration of rectangular plates," *Journal of Sound and vibration,* vol. 31, pp. 257-293, 1973.
[8]   J. Reddy, "On refined computational models of composite laminates," *International Journal for numerical methods in engineering,* vol. 27, pp. 361-382, 1989.
[9]   A. Noor and W. Burton, "Refinement of higher-order laminated plate theories," *ASME Appl. Mech. Rev,* vol. 42, pp. 1-13, 1989.

4

GEOMETRIC NONLINEARITIES EFFECT ON CABLE LINEAR VIBRATIONS

Achref Mansour[1], Othman Ben Mekki[1], Sami Montassar[1] and Giuseppe Rega [2]

[1] Ecole Nationale d'Ingénieurs de Tunis, LGC, BP 37, Le Belvédère, 1002
Université de Tunis El Manar, Tunis, Tunisia
Email: achref.mansour@enit.rnu.tn

[2] Dipartimento di Ingegneria Strutturale e Geotecnica
Universita di Roma La Sapienza, Via A. Gramsci 53, 00197 Roma, Italy
Email: giuseppe.rega@uniroma1.it

ABSTRACT

The present work investigates the free undamped vibrations of arbitrarily sagged cables according to the catenary theory. Defining the dynamic equilibrium configuration around the catenary static profile, an exact solution of the free linear transverse vibrations is developed analytically. The effectiveness of the established model is shown by means of comparisons between with results determined by classic formulations in case of horizontal and inclined shallow/non-shallow cables.

1 INTRODUCTION

The dynamic motion of cables is mainly studied with respect to both parabolic and the catenary static profiles. Based on the first works of Irvine [1] dedicated to the free linear oscillations of suspended cables, several research were developed according to the parabolic approach. Nevertheless, the necessity to account the catenary effect has been demonstrated for different types of cables with important sag as those used in suspended bridges or as transmission lines. Accordingly, the catenary model has been adopted in some recent papers: while an analytical solution specific to the transversal motion was proposed by Lacarbonara et al. [2] by considering the exact nonlinear static profile of horizontal non-shallow cables, Zhou et al. [3] has solved the in-plane dynamic problem specific to taut inclined cables by introducing the cubic approximation of the catenary geometry. In the light of previous models, the present work provides accurate analytical solution based on the elastic catenary theory and related to the free linear vibrations of both horizontal and inclined cables.

2 ANALYTICAL SOLUTION TO THE CABLE DYNAMIC PROBLEM

A suspended cable between two fixed supports A and B displayed in Figure 1 is characterized by a specific weight γ_c, a non deformable cross-section denoted by A_c and a linearly elastic material defined by a Young elastic modulus E_c. A local Cartesian coordinate system (x, y, z) is attached to the cable's chord having an angle α with respect to l defining the horizontal projection of the chord cable length L.
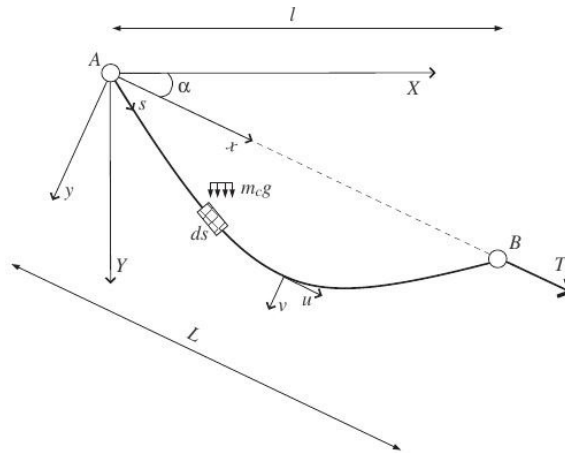
Figure 1. Static equilibrium configuration of a suspended cable

Under the action of its total weight, the strained static profile is determined expressed as follows:

$$
\begin{cases}
\dfrac{y(x,\tau)}{L} = \dfrac{\cosh\left(C_1\left(\tau\right)\right) - \cosh\left(C_1\left(\tau\right) - \tau\frac{x}{L}\right)}{\tau} \quad ; \quad \tau = \dfrac{m_c g L}{T} \\[2ex]
C(\tau) = \dfrac{\tau e^\tau}{e^\tau - 1}\tan\alpha \quad ; \quad C_1(\tau) = \ln\left(C + \sqrt{C^2 + e^\tau}\right)
\end{cases}
\tag{1}
$$

Considering the static equilibrium configuration defined by the catenary profile given previously and taking into account the assumptions related to the linear vibration theory, the cable dynamic motion reduces to the transversal component characterized by dimensionless frequencies Ω_k

obtained as roots of the following transcendental equation:

$$\tan \Omega_k \left[\frac{(\Omega_k^2 + \tau^2)^2}{\lambda_c^2} - \frac{I}{\tau L} (\Omega_k^2 + \tau^2) - \rho_4 \tau \right] + 2\rho_3 \tau \sin \Omega_k - \rho_1 \Omega_k + \frac{\rho_2}{\cos \Omega_k} \Omega_k = 0 \quad (2)$$

with:

$$\begin{cases} I = \dfrac{L}{2} + \dfrac{L}{4\tau} \ ; \ \ \rho_1 = \cosh^2 C_1 + \cosh^2 (C_1 - \tau) \ ; \ \ \rho_2 = \cosh C_1 \cosh (C_1 - \tau) \\[3mm] \rho_3 = \cosh C_1 \sinh (C_1 - \tau) \ ; \ \ \rho_4 = \dfrac{\sinh (2 (C_1 - \tau)) + \sinh (2C_1)}{2} \ ; \ \ \lambda^2 = \dfrac{\tau^2}{\eta \chi} \end{cases} \quad (3)$$

where λ is the Irvine parameter depending on the dimensionless thrust $\eta = T/E_c A_c$ and the cable's curvature χ tending to unity in case of horizontal cables according to Irvine formulation [1] based on parabolic approach. However, accurate expression of the curvature term is obtained according to the actual formulation for both horizontal and inclined arbitrarily sagged cables:

$$\chi = \frac{\sinh \left(\frac{3\tau}{2} \right) \cosh \left(3 \left(C_1 - \frac{\tau}{2} \right) \right) + 9 \sinh \left(\frac{\tau}{2} \right) \cosh \left(C_1 - \frac{\tau}{2} \right)}{6\tau} \quad (4)$$

It must be noted that equation (4) reduces to the formula proposed by Lacarbonara et al. [2] for horizontal non-shallow cables given by:

$$\chi = \frac{9 \sinh \left(\frac{\tau}{2} \right) + \sinh \left(\frac{3\tau}{2} \right)}{6\tau} \quad (5)$$

3   MODEL VALIDATION

	τ	Irvine's	Enhanced Irvine's	Present	Exact
	1.5	8.95	8.79	8.48	8.44
Error(%)		6.04	4.15	0.47	
	2.5	8.95	8.66	7.85	7.63
Error(%)		17.30	13.50	2.88	

Table 1: Lowest symmetric frequencies of horizontal cables with $\lambda = 10\pi$ obtained with Irvine theory, enhanced Irvine theory, and present model, and relative errors (%) with respect to the exact (non-condensed) model.

In order to show the accuracy of the proposed solution, an investigation is performed regarding the evaluation of dimensionless frequencies obtained according to the actual formulation from one side and using models found in th literatue. The results related to the comparison held on non-shallow horizontal profiles and taut inclined cables are respectively reported in Table 1 and illustrated by Figure 2. As it may be remarked from Table 1, the error made by the general catenary-based model is by far smaller than those inherent to proposed solutions by Irvine [1] and Lacaronara et.[2]. In fact, the difference between present results and exact ones ranges

3

from 0.47% to 2.88%, with an expected increase for the looser cable, where the effect of the longitudinal dynamics (herein neglected) becomes more important; however, it increases more for both the enhanced (from 4.15% to 13.5%) and the original Irvine theory (6.04% to 17.30%). On the other side, the validity of the present model is demonstrated by the the Figure 2 specific to the case of taut inclined cables. As a matter of fact, the absolute relative error with respect to the frequencies found by the Galerkin (resp. Zhou) varies from 0.03% (resp. 0.07%) to 1.202% (resp. 1.47%) for an inclination $\alpha = 10^{\circ}$ and ranges from 0.05% (resp. 0.048%) to 0.79% (resp. 0.95%) when $\alpha = 60^{\circ}$. It must be noted that the results obtained analytically remain acceptable since the absolute relative error with respect to Zhou's results - which are nearly concident with the "exact" ones - does not exceed about 1.5%: such small error is likely due to the factor of the weight component parallel to the cable chord accounted in Zhou's model and neglected in the present formulation.
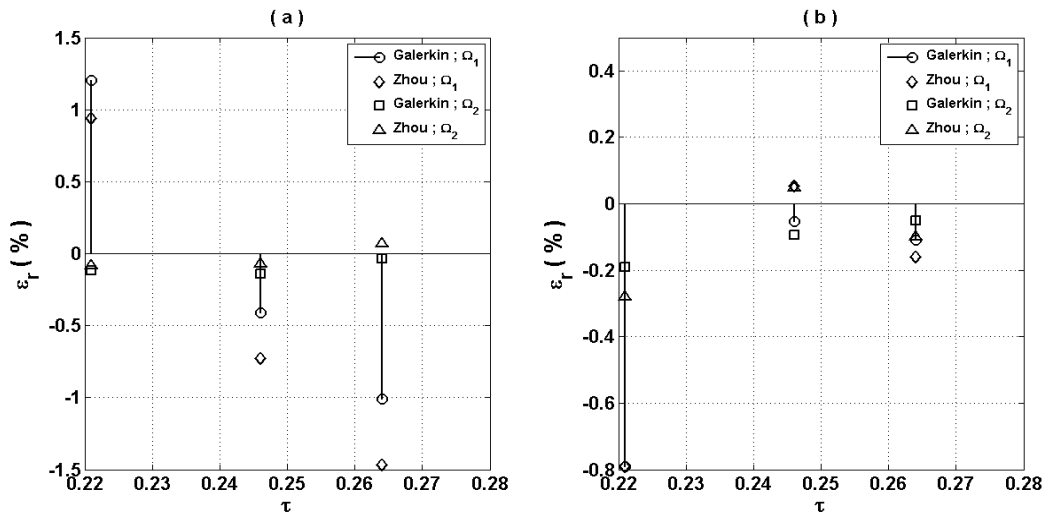
Figure 2: Relative errors $\epsilon_r(\%)$ related to the 1st and 2nd dimensionless frequencies $\Omega_{1,2}$ with respect to results obtained by both Galerkin and Zhou's methods and presented in [3] for inclined cables with: (a) $\alpha = 10^{\circ}$; (b) $\alpha = 60^{\circ}$

4   CONCLUSION

A general catenary-based model is developed analytically for the transverse linear free undamped vibrations of shallow/non shallow arbitrarily inclined cables. The exactitude of the proposed solution is exhibited by a maximum absolute relative errors $|\epsilon_r| = 2.88\%$ and $|\epsilon_r| \simeq 1.5\%$ calculated with respect to the exact results respectively for non-shallow horizontal cables ($\tau = 2.5$) and taut inclined cables.

REFERENCES

[1] H. M. Irvine. *Cable structures*. The MIT Press, 1981.

[2] W. Lacarbonara, A. Paolone, and F. Vestroni. Elastodynamics of nonshallow suspended cables: linear modal properties. *Journal of Vibration and Acoustics*, 129(4):425–433, 2007.

[3] X. Zhou, S. Yan, and F. Chu. In-plane free vibrations of an inclined taut cable. *Journal of Vibration and Acoustics*, 133(3):031001, 2011.

4

ANALYSIS OF NONLINEAR AND NON-SMOOTH DYNAMICS OF A SELF-OSCILLATING SERIES RESONANT INVERTER

L. Benadero [1] , E. Ponce[2] and A. El Aroudi[3*]

[1]Departament de Física,
Universitat Politècnica de Catalunya, Barcelona, Spain,
email: luis@fa.upc.edu
[2]Departamento de Matemática Aplicada,
Escuela Técnica Superior de Ingeniería, Sevilla, Spain,
email: eponcem@us.es
[3]Departament d'Enginyeria Electrònica, Elèctrica i Automàtica,
Universitat Rovira i Virgili, Tarragona, Spain,
email: abdelali.elaroudi@urv.cat

ABSTRACT

In this paper, the dynamics of a dc-ac resonant self-oscillating LC series inverter is analyzed from the point of view of piecewise smooth dynamical systems. Our system is defined by two symmetric configurations and its bifurcation analysis can be given in a one dimensional parameter space, thus finding a non smooth transition between two strongly different dynamics. The oscillating regime, which is the one useful for applications and involves a repetitive switching action between those configurations, is given whenever their open loop equilibrium is a focus. Otherwise, the only attractors are equilibrium points of node type whose stable manifolds preclude the appearance of oscillations.
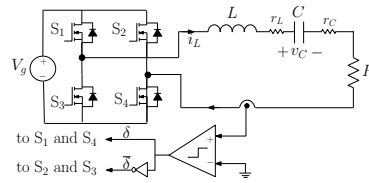
Figure 1. Schematic diagram of the LC series resonant inverter.

1   INTRODUCTION

In this paper we deal with an analysis of the LC series resonant inverter, similar to the one developed in [1] for its LC parallel counterpart. We put in evidence some relevant differences between these two implementations from the point of view of dynamics and bifurcations, which are mainly related to the location of the equilibria regarding the switching manifold. The rest of this paper is organized as follows. Section 2 presents the mathematical switched model of the system and its normalization, thus resulting in a unique bifurcation parameter. In section 3, we find that the transition from spiral to node of the open loop equilibrium further implies a non smooth global bifurcation, thus inhibiting the desired oscillatory mode. Finally, concluding remarks are drawn in the last section.

2   SYSTEM DESCRIPTION AND MATHEMATICAL MODELING

Figure 1 shows the circuit diagram of the system considered in this study that is an LC series resonant inverter [2]. he switches S_1 and S_4 are ON when $i_L > 0$ ($\delta = 1$), and they are turned OFF when $i_L < 0$ ($\delta = 0$). The switches S_2 and S_3 are driven in a complementary way to S_1 and S_4. Let v_C be the voltage of the output capacitor, i_L the inductor current and $\mathbf{z} = (v_C, i_L)^\mathsf{T}$ the vector state. Let also u be the variable determined by the control in the form $u = 2\delta - 1$, that is $u = 1$ if $i_L > 0$ and $u = -1$ if $i_L < 0$. Let us define τ and $\mathbf{x} = (x_1, x_2)^\mathsf{T}$ as follows:

$$\tau = \omega_0 t, \quad x_1 = \frac{v_C}{V_g}, \quad x_2 = \frac{i_L Z_0}{V_g}.$$

The dynamical model of the system is as follows:

$$\dot{\mathbf{x}} = \mathbf{A}\mathbf{x} + \mathbf{B}u, \tag{1}$$
$$h(\mathbf{x}) = \mathbf{C}^\mathsf{T}\mathbf{x}, \tag{2}$$

where the matrix $\mathbf{A}$ and the vector $\mathbf{B}$ are redefined as

$$\mathbf{A} = \begin{pmatrix} 0 & 1 \\ -1 & -\dfrac{1}{Q} \end{pmatrix}, \quad \mathbf{B} = \begin{pmatrix} 0 \\ 1 \end{pmatrix}.$$

Note that above parameters are the natural frequency ω_0, the characteristic impedance Z_0 and the quality factor Q of the LCR resonant series circuit, which are given by the expressions

$$\omega_0 = \sqrt{\frac{1}{LC}}, \quad Z_0 = \sqrt{\frac{L}{C}}, \quad Q = \frac{Z_0}{R_S},$$

where $R_S = R + r_C + r_L$ is the equivalent series resistance of the circuit. Note also that the open loop system (1), in which the switch variable u remains constant, either $u = 1$ or $u = -1$, has as unique attractor the equilibrium point $\overline{\mathbf{x}} = (u, 0)^\mathsf{T}$. The eigenvalues of the matrix $\mathbf{A}$ are

$$p^\pm = -\frac{1}{2Q} \pm \sqrt{\frac{1}{4Q^2} - 1},$$

2

and it can be deduced, due the physical restriction $Q > 0$, which implies eigenvalues with negative real part, that the open loop equilibrium is always stable. However, there is a minor transition at $Q = 1/2$, because the eigenvalues change from real to complex values. If $Q > 1/2$, the two eigenvalues are complex conjugated, so that the equilibrium is surrounded by spiraling trajectories. Otherwise, if $Q \leq 1/2$, the equilibrium is a node, and so the orbits tend to the stable manifold corresponding to the eigenvector associated to the highest or to the lowest eigenvalue considering forward or backward time evolution respectively. Unlike in the linear system, we will prove that in our piecewise smooth system (1)-(2), a non trivial non smooth bifurcation is produced at the same value $Q = 1/2$.

3 PIECEWISE SMOOTH ANALYSIS

3.1 The switching manifold and the sliding subset

Recall that from (2), the switching manifold is defined here as $\Sigma = \{\mathbf{x} : x_2 = 0\}$. According to the Filippov theory, sliding dynamics can occur in a subset Σ_S of the switching manifold Σ, if the vector fields $\mathbf{F}^+$ and $\mathbf{F}^-$ satisfy the condition

$$\Sigma_S = \left\{ \mathbf{x} \in \Sigma : (\nabla h(\mathbf{x}) \cdot \mathbf{F}^+(\mathbf{x})) \, (\nabla h(\mathbf{x}) \cdot \mathbf{F}^-(\mathbf{x})) < 0 \right\}, \tag{3}$$

in which $\nabla(\cdot)$ is the gradient operator. This means that in a sliding region, the vector field points inwards or outwards at both sides of Σ_S. Conversely, in the points not belonging to Σ_S, the vector field crosses Σ. Roughly speaking, three different cases of switching dynamics can exist, one of them corresponding to simple crossing associated to Carathéodory solutions. The other two cases are the attracting and the rejecting sliding motions. In our case, the field $\mathbf{F}^+$ and $\mathbf{F}^-$ points outwards Σ_S, so the sliding is repelling and it is defined in the subset

$$\Sigma_S = \left\{ \mathbf{x} : -1 < x_1 < 1, x_2 = 0 \right\}.$$

3.2 The non oscillatory dynamics

We deal first with the non oscillatory dynamics. Actually, this a malfunction of the inverter in real applications, which occurs under the over damping condition, that is in the parameter domain $0 < Q \leq 1/2$. This case is illustrated in Fig. 2 using $Q = 0.4$, where some ad hoc trajectories have been depicted. If $0 < Q \leq 1/2$, the eigenvalues of the matrix $\mathbf{A}$ are real and negative, and so the dynamics evolving around each equilibrium cannot cross their corresponding stable manifolds. The consequence of this fact is that for any arbitrary trajectory, at most only one switching can be produced and therefore, the oscillating regimen cannot be attained. The boundary of attraction between the twin equilibrium points, which is also depicted in Fig. 2 using red color, is made up of three pieces: the sliding subset Σ_S and the part of stable manifold corresponding to the lowest (more negative) eigenvalue in the valid side of the state plane for each equilibrium.

3.3 The self oscillating dynamics

In the following, we consider the quality factor restricted to the range $Q > 1/2$. Then, system (1)-(2) has an oscillatory dynamics, which is the one useful for inverter applications. Notice that for the linear case (1), with either $u = 1$ or $u = -1$, we have naturally a focus dynamics converging to an equilibrium, so that the self sustained oscillation is only enabled by the switching action introduced in (2). To prove this, let us choose an initial point located in the upper half plane. The dynamical integration forces the trajectory to cross Σ at a point $(y_1 > 1, y_2 = 0)$,
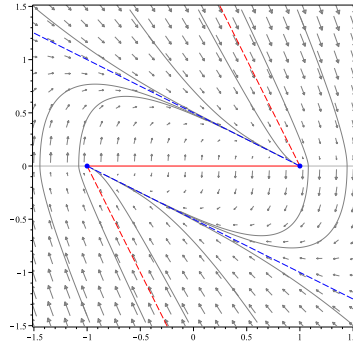
Figure 2: Boundaries of the attraction basin of the twin equilibria (blue points) for the system (1)-(2) with $Q = 0.4 < 1/2$, defined by the rejecting sliding segment and the eigenvectors corresponding to the lowest eigenvalue (red lines). A scheme of the piecewise smooth vector field and some illustrative trajectories have been also plotted. Notice that they tend to the stable manifold corresponding to the highest eigenvalue (blue lines).
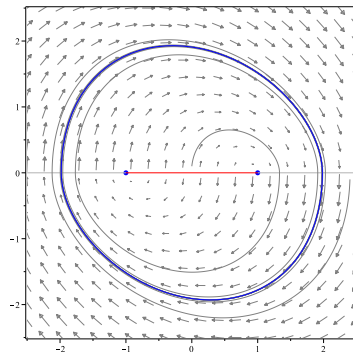
Figure 3: Oscillatory dynamics for system (1)-(2) with $Q = 1.5 > 1/2$, thus converging to a limit cycle, depicted in blue color, which is defined by two half cycles connected each other.

because it evolves clockwise around the right side equilibrium $\overline{\mathbf{x}}^+ = (1, 0)$. Then, the trajectory enters the lower half plane, so evolving clockwise around the left side equilibrium $\overline{\mathbf{x}}^- = (-1, 0)$ to reach and cross Σ again at a point $(y_1 < -1, y_2 = 0)$. This process is repeated indefinitely, thus converging the trajectory to a finite limit cycle, that is the oscillatory dynamics, due to the dissipative character of the system. To get an expression of the stable limit cycle, it turns out more convenient to introduce the bifurcation parameter γ as the quotient between the real and the imaginary parts of the focus eigenvalue p^+ that is

$$p^+ = -\frac{1}{2Q} + i\sqrt{1 - \frac{1}{4Q^2}} = \sigma + i\omega_r = \sigma\left(1 + \frac{i}{\gamma}\right),$$

in which

$$\gamma = \frac{\sigma}{\omega_r} = -\frac{1}{2Q\sqrt{1 - 1/(4Q^2)}} = -\frac{1}{\sqrt{4Q^2 - 1}} < 0.$$

Fig. 4 shows the evolution of the parameter γ in terms of the quality factor Q. Notice that ω_r is the ratio between the free running frequency ω and the natural frequency ω_0 in the real system, that is $\omega = \omega_r\omega_0$. Thus, if we take the new time and variables

$$\theta = \omega_r\tau, \quad y_1 = x_1, \quad y_2 = \omega_r x_2,$$

4
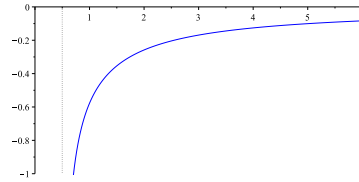
Figure 4. The plot of the focus parameter γ versus the quality factor Q.

(a) Y_1 versus γ

(b) Y_1 versus Q
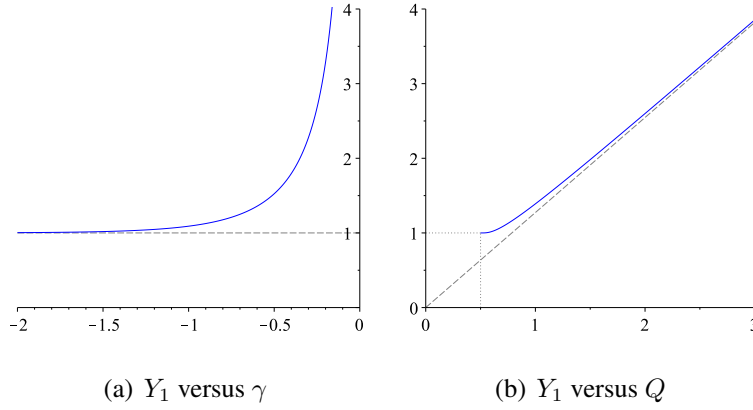
Figure 5: Amplitude of the limit cycle versus γ and Q. The gray dashed lines are the asymptotes to which the amplitude tends for high absolute values of the corresponding parameter.

and take into account that $\omega_r^{-2} = \gamma^2 + 1$, we obtain from (1)-(2) the normalized system

$$\frac{d\mathbf{y}}{d\theta} = \begin{pmatrix} 0 & \gamma^2 + 1 \\ -1 & 2\gamma \end{pmatrix} \mathbf{y} + \begin{pmatrix} 0 \\ 1 \end{pmatrix} u, \tag{4}$$

$$h(\mathbf{y}) = \mathbf{C}^\mathsf{T} \mathbf{y}, \tag{5}$$

in which $\mathbf{y} = (y_1, y_2)$. Accordingly, the switching manifold is redefined as $\Sigma = \{\mathbf{y} : y_2 = 0\}$. Taking into account the symmetry of the vector field with respect to the origin, we focus our attention only to the half-plane $y_2 \geq 0$, where $u = 1$ with the focus located at point $(1, 0)$. Thus, solving equation (4) with $u = 1$, we get

$$\begin{pmatrix} y_1(\theta) - 1 \\ y_2(\theta) \end{pmatrix} = \mathbf{\Phi}(\theta) \begin{pmatrix} y_1(0) - 1 \\ y_2(0) \end{pmatrix}, \tag{6}$$

where $\mathbf{\Phi}(\theta)$ is an evolution operator given by

$$\mathbf{\Phi}(\theta) = \mathrm{e}^{\gamma\theta} \begin{pmatrix} \cos\theta - \gamma\sin\theta & (\gamma^2 + 1)\sin\theta \\ -\sin\theta & \cos\theta + \gamma\sin\theta \end{pmatrix}. \tag{7}$$

Since we are dealing with orbits for $y_2 \geq 0$ starting at Σ and returning to Σ at time θ_1 after surrounding the focus, we can write $y_2(0) = y_2(\theta_1) = 0$ in (6) thus resulting $\theta_1 = \pi$. This simple solution reflects the fact that any orbit running from Σ to Σ surrounding the focus, will last exactly half time of the cycle because both focus are at Σ itself. Imposing also the symmetry condition $y_1(\theta_1) = -y_1(0)$, we obtain after some algebra an expression for the amplitude of the limit cycle, as the crossing point of the limit cycle at Σ, namely

$$Y_1 = y_1(\theta_1) = \coth\left(-\frac{\gamma\pi}{2}\right).$$

5

(a) $Q = 5$ $(\gamma = -0.3535)$ (b) $\gamma = -1$ $(Q = 0.7071)$
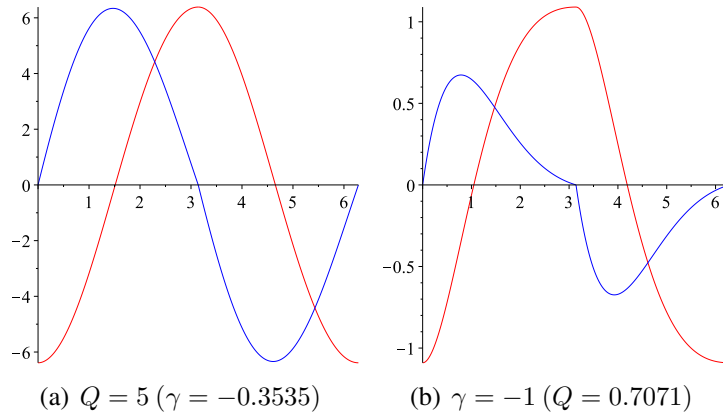
Figure 6. Waveforms of $y_1(\theta)$ in red and of $y_2(\theta)$ in blue, for the limit cycle.

In Fig. 5, the value of the normalized variable y_1 at the switching condition, called here Y_1, is represented in front of the two parameters γ and Q. It is worth noting that if the quality factor is high enough, the expression $Y_1 \approx 4Q/\pi$ is a reasonable approximation for the amplitude of the steady oscillation. Also, if γ is made negative enough, Y_1 converges to its lowest value $Y_1 = 1$. Both asymptotic behaviors can be seen in the same diagrams. In Fig. 6, the normalized values (y_1, y_2) for one cycle of the steady state oscillation have been represented for two different parameters $Q = 5$ $(\gamma = -0.3535)$ and $\gamma = -1$ $(Q = 0.7071)$. Focusing on applications, let us define a new variable y_R to account for the relative load voltage. Thus, recalling that $y_2 = \omega_r i_L Z_0 / V_g$ and considering the voltage divider relation $\alpha = R/R_S$ between the load R and the series equivalent R_S we deduce that

$$y_R = \frac{i_L R}{V_g} = \frac{\alpha y_2}{\omega_r Q}, \tag{8}$$

and for one of the two symmetrical half cycles in the steady state we deduce from (6)-(7) the expression $y_2(\theta) = (1 + Y_1)e^{\gamma\theta}\sin\theta$, and then $y_R(\theta) = Y_R(\gamma)g(\gamma, \theta)$ follows, in which the constant Y_R is a sort of amplitude and g takes care of the dependence on time. These terms are

$$Y_R = -2\alpha\gamma\left(1 - \coth\left(\frac{\gamma\pi}{2}\right)\right), \quad g(\gamma, \theta) = e^{\gamma\theta}\sin\theta.$$

ACKNOWLEDGMENTS

REFERENCES

[1] E. Ponce, L. Benadero, A. El Aroudi and L. Martínez-Salamero, "Sliding Bifurcations in Resonant Inverters," *International Multi-Conference on Systems, Signals and Devices,* accepted, SSD'2017.

[2] R. Erickson and D. Maksimovic, *Fundamentals of Power Electronics*, 2nd ed. Springer, 2001.

6

ENERGY HARVESTING IN A NONLINEAR HARVESTER UNDER MODULATED DELAY AMPLITUDE

Zakaria Ghouli[1], Mustapha Hamdi[2], Faouzi Lakrad[1] and Mohamed Belhaq[1]

[1]Faculty of Sciences Ain Chock, University Hassan II-Casablanca, Morocco
Email: ghoulizakaria@gmail.com, lakrad@hotmail.com, mbelhaq@yahoo.fr

[2]FST-Al Hoceima
University Mohammed I Oujda, Al-Hoceima, Morocco
Email: hamustapha2000@yahoo.fr

ABSTRACT

We explore periodic and quasi-periodic (QP) vibration-based energy harvesting (EH) in a delayed nonlinear oscillator in which time delay feedback is inherently present in the system. The EH system consists in a delayed Duffing-van der Pol oscillator coupled to an electric circuit through an electromechanical coupling mechanism. We assume that the delay amplitude is modulated around a mean value with a certain frequency, and we consider the case of delay parametric resonance for which the frequency of the modulation is near twice the natural frequency of the oscillator. Application of the double-step perturbation method enables the approximation of the amplitude of the QP vibrations which is used to extract power from the harvester device. Results show that for small values of unmodulated delay amplitude, only the periodic vibration can be used to extract energy, while for larger values of unmodulated delay amplitude the periodic solution turns to unstable and only QP vibration can be used to extract energy with better performance. Numerical simulation is conducted to support the analytical predictions.

1   INTRODUCTION AND MODEL DESCRIPTION

In EH systems, the limitation of the linear attachment has been overcome by considering non-linear stiffness in the mechanical part of the harvester. In this case the EH capability is improved [1, 2]. However, the EH performance provided by nonlinear attachments can suffer from instabilities and jump phenomena near the boundaries of the stable branch of the frequency response. To circumvent such instabilities, the idea of using QP vibrations is proposed to extract energy from delayed self-excited harvester systems [3]. The concept of using delayed feedback vibration absorber has also been used to enhance EH capability [4]. The purpose of the present work is to study the EH performance in a Duffing-van der Pol-type harvester device in which time delay is inherently present in the operating system, as in milling and turning operations [5]. The energy harvesting system consists then in a delayed Duffing-van der Pol oscillator coupled to an electric circuit through an electromechanical coupling mechanism; see Fig. 1.
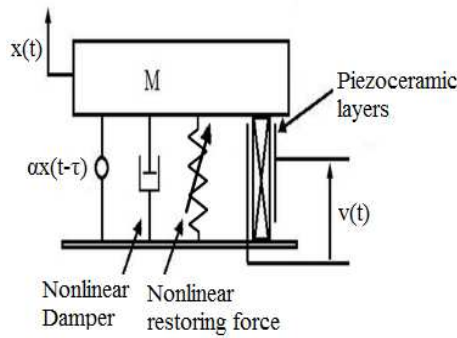
Figure 1. Schematic description of the EH system

The governing equation for the harvester system can be written in the dimensionless form as

$$\ddot{x}(t) + \delta\dot{x}(t) + \lambda\dot{x}(t)x(t)^2 + \omega_0^2 x(t) + \gamma x(t)^3 - \chi v(t) = \alpha x(t - \tau) \tag{1}$$

$$\dot{v}(t) + \beta v(t) + \kappa\dot{x}(t) = 0 \tag{2}$$

where $x(t)$ is the relative displacement of the rigid mass M, $v(t)$ is the voltage across the load resistance, δ and λ are the mechanical damping ratio, γ is the stiffness parameter, χ is the piezoelectric coupling term in the mechanical attachment, κ is the piezoelectric coupling term in the electrical circuit, β is the reciprocal of the time constant of the electrical circuit, α and τ are, respectively, the feedback gain and time delay. In this study we assume that the delay amplitude α is modulated around a mean value such that:

$$\alpha = \alpha_1 + \alpha_2\cos(\omega t) \tag{3}$$

where α_1 is the unmodulated delay amplitude and α_2, ω are, respectively, the amplitude and the frequency of the modulation. Note that the case where the nonlinear stiffness is absent ($\gamma = 0$) has been explored in [3] and the case of linear damper and unmodulated time delay was studied in [6].

2   MAIN RESULTS

We investigate the response of the system near the delay parametric resonance for which the frequency of the delay modulation is near twice the natural frequency of the oscillator. Appli-

2

cation of the double-step perturbation method [7] enables the approximation of the amplitude of the QP vibrations which is used to extract power from the harvester device.
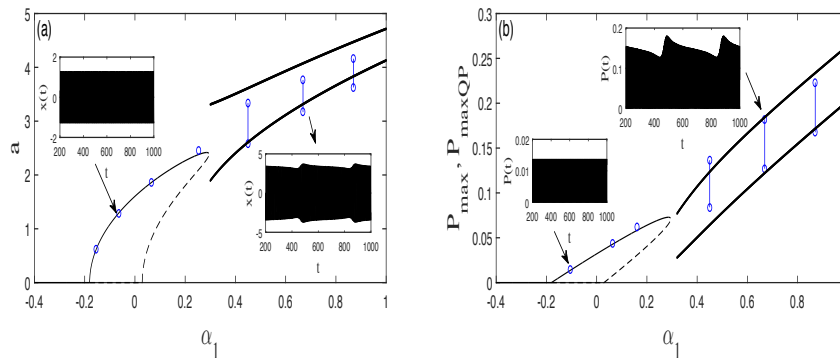
Figure 2: Vibration (a) and powers (b) amplitudes vs α_1 for $\alpha_2 = 0.25$, $\omega = 2$, $\chi = 0.05$, $\beta = 0.05$, $\lambda = 0.2$, $\delta = -0.1$, $\gamma = 0.05$, $\kappa = 0.5$, $\omega_0 = 1$ and $\tau = 5.2$. Analytical prediction (solid lines for stable and dashed line for unstable) and numerical simulation (circles).

In Fig. 2 is shown the variation of the amplitude of the periodic and the QP responses as well as the maximum output power amplitudes (P_{max}, P_{maxQP}) versus the unmodulated delay amplitude α_1 and for $\alpha_2 = 0.25$. The boxes inset in the figures show time histories of the amplitudes (Fig. 2a) and the power responses (Fig. 2b). It can be seen that for a small values of delay amplitude α_1, only the periodic vibration-based EH can be extracted. On the other hand, for relatively increasing value of α_1, the stable periodic solution disappear via saddle-node bifurcation, while energy can be extracted from QP vibration with better performance comparing with the periodic output power.

REFERENCES

[1] Mann, B.P. Sims, N.D.: Energy harvesting from the nonlinear oscillations of magnetic levitation. J. Sound Vib. **319**, 515-530 (2009)

[2] Erturk, A., Inman, D.J.: Broadband piezoelectric power generation on high-energy orbits of the bistable Duffing oscillator with electromechanical coupling. J. Sound Vib. **330**, 2339-2353 (2011)

[3] Belhaq, M., Hamdi, M.: Energy harversting from quasi-periodic vibrations. Nonlinear Dyn. DOI 10.1007/s11071-016-2668-6 (2016)

[4] Kammer, A.S. Olgac, N.: Delayed-feedback vibration absorbers to enhance energy harvesting. J. Sound Vib. **363**, 54-67 (2016)

[5] Kalmar-Nagy, T., Stepan, G., Moon, F.C.: Subcritical Hopf Bifurcation in the Delay Equation Model for Machine Tool Vibrations, Nonlinear Dyn. **26**, 121-142 (2001)

[6] Ghouli, Z., Hamdi, M., Lakrad, F., Belhaq, M.: Energy harvesting in a delayed and excited Duffing harvester device. MATEC Web of Conferences **83**. EDP Sciences. DOI 10.1051/matecconf/20168302001 (2016)

[7] Belhaq, M., Houssni, M.: Quasi-periodic oscillations, chaos and suppression of chaos in a nonlinear oscillator driven by parametric and external excitations. Nonlinear Dyn. **18**, 1-24 (1999)

3

Structural health monitoring of a smart composite structure with a Time-of-Flight method

Xianlong CHEN[1,3], Yann MEYER[1,a], Rémy LACHAT[2] & Morvan OUISSE[3]

[1]Univ. Bourgogne Franche-Comté, UTBM, Belfort, FRANCE
Email: xianlong.chen@utbm.fr, yann.meyer@utbm.fr

[2]ICB UMR 6303, CNRS Univ. Bourgogne Franche-Comté, UTBM, Belfort, FRANCE
Email: remy.lachat@utbm.fr

[3]Univ. Bourgogne Franche-Comté, FEMTO-ST Institute, CNRS/UFC/ENSMM/UTBM,
Besançon, FRANCE
Email: morvan.ouisse@femto-st.fr

ABSTRACT

Smart composite structures with a fully distributed set of integrated piezoelectric transducers are used to demonstrate the feasibility of embedded Structural health monitoring (SHM). Indeed, the piezo ceramics elements have been directly integrated into the heart of the composite during the manufacturing process. Then, a Time-of-Flight method has been applied. This technique is based on the duration measurements of a wave propagation with a simple and low cost experimental setup. Integrated piezoelectric transducers are used for monitoring the behavior of the structure.
In this research, special plates (with a piezo ceramics disk on each corner), made of glass fibre composite, are manufactured. Different kinds of damages are simulated on these plates, including holes with different diameters. Then a Time-of-Flight method is used for the SHM of these plates. Finally, the preliminary test results obtained on one plate are compared and discussed.

Keywords: Composite structure, Smart material, Piezoelectric transducers Integration, Health monitoring, Time-of-Flight method, Lamb wave.

1   INTRODUCTION

Structural health monitoring (SHM) is a technology which combines advanced sensor technologies with intelligent algorithms to interrogate the 'health' condition of structures in real time or whenever necessary. SHM has been defined in the literature as the "acquisition, validation and analysis of technical data to facilitate life-cycle management decisions" [1]. The potential benefits of SHM technology include improvement of reliability and safety, enhancement of performance and operation, and reduction of lifecycle cost.

Several techniques have been investigated for detecting damage in composite materials. However, Lamb wave based methods have recently re-emerged as a reliable way to detect and potentially locate damages [2-5]. These techniques have been implemented in several ways in the literature, including the use of separate actuators and sensors to monitor transmitted waves and/or reflected waves, and multipurpose patches which both actuate and sense. Each of these techniques offer their own advantages and drawbacks in detecting certain types of damage with various levels of complexity.

This paper is focused on the structural health monitoring (SHM) of plates made of a glass fibre composite, by using a Time-of-Flight method. As lamb wave techniques provide more information about damage presence and severity than other tested methods (for instance, frequency response techniques), and provide the possibility of determining damage location due to their local response nature, this technique is selected. The paper is organized as follow. Section 2 shows the experimental setup and the experiment procedure. In Section 3, the results as well as the comparison of these results are presented and discussed. Then the concluding remarks are given.

2   EXPERIMENTAL PROCEDURE

The idea is to manufacture test plates, then simulate different damages on this plate and interrogate the 'health' condition of the structure with a Time-of-Flight method. When the signal travels from the piezo-ceramics actuator through the region where there is a change in material properties. Consequently, some changes are observed in the response signals from the piezo-ceramics sensor.
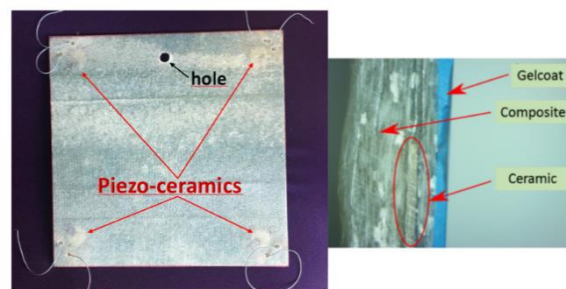
Figure 1. Samples to be tested - the Poisson's plates

The plates are instrumented with four piezo-ceramics, which are positioned at each corner of the plates, as shown in Figure 1. The characteristics of these transducers are given in [6]. The plates tested are 298 mm side and 2 mm thick with a gelcoat of 0.2 mm. The plates are manufactured in the Belfort-Montbéliard University of Technology (UTBM), France. These are laminated composites, composed of 6 layers of glass fibres and a polyester resin matrix. The technique of infusion is used as manufacturing method. The fibre volume ratio is about 35 to 40%. At the end, one layer of gelcoat is present on the top surface of the plates. The piezoelectric elements are placed between the first and the second layer. The layer of gelcoat is set as the reference for numbering of

the layers. Then, to simulate strong and calibrated damages, holes with different diameters are drilled in the plates as shows in Figure 1. The main idea is to evaluate the potentiality of a ToF technique with a clear damage. The selected diameters are 4.5mm, 6mm, 8mm, 10mm, 12mm and 13mm, the holes were drilled in the same plate by increasing diameters and the measurement were done between two machinings.

The Time-of-Flight method exploits the ultrasonic wave propagation properties and, particularly, Lamb waves propagation properties [8]. Such waves have the particularity to spread over long distances in the composite [9]. To generate and capture the wave trains, the piezoelectric transducers integrated in the composite are used. The transducers have a resonant frequency for the radial mode measured in air around 100 kHz [6]. Once incorporated into the composite by backing effect, the central frequency of this radial mode decreases up to 64 kHz in the analysed plates. Then the frequency-thickness product (f.h) is around 0.15 MHz.mm. The phase velocity and the group velocity of the symmetric mode S_0 are then equivalent. So, it is possible to measure the S_0 group velocity and use the formulas of extraction of the materials parameters developed for the phase velocity [8].

After a set of optimisation tests, a short number of sinusoidal bursts (1 to 3 cycles) are chosen as the excitation signals. The experimental setup to generate and measure the wave trains is similar to the setup described in [7]. A function generator (Keithley, 3390) is used to generate excitation signals via a miniature power amplifier (PiezoDrive, PDM200B). The signals are then captured via a digital oscilloscope (Pico Technology, PS 4424).

3   RESULTS & DISCUSSION

For the experiments, the sinusoidal bursts signals travel through the structure between two piezo-ceramics actuator and sensor. A hole is drilled in the middle of this path (see Figure 1). The response signals obtained for the plate with different hole diameters are shown in Figure 2.
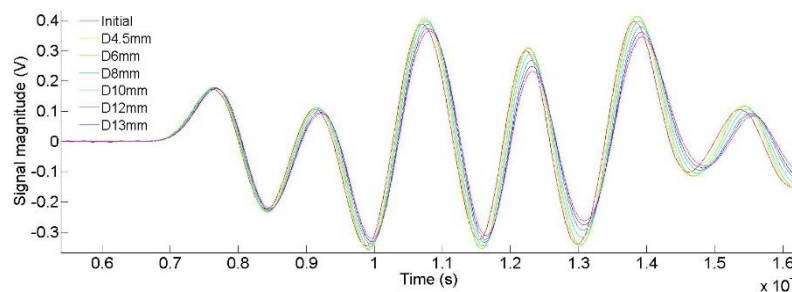
Figure 2. Response signals for the plate with a hole of different diameters

The time-of-flight from the actuator to the sensor has been recorded for each situation. At the same time, a Fast Fourier transform has been applied to deal with the data. The results are shown in Figure 3. To analyse the influence of the hole diameter on the FFT, we have selected an analysis frequency of 64 kHz, at which the FFT amplitude is maximum.

In Figure 3, the tendencies shown are quite clear for the Time-of-Flight vs hole diameter or the FFT amplitude at 64 kHz vs hole diameter. As it shows in the curve of FFT amplitude vs hole diameter, the vibration energy has a strong relationship with the damage index [10]. The bigger damage is, the weaker vibration energy will be, so the lower FFT amplitude will be.

These results give a quite good reference for the future investigations. Along this way, it is possible to use a Time-of-Flight method in Structural Health Monitoring.

3
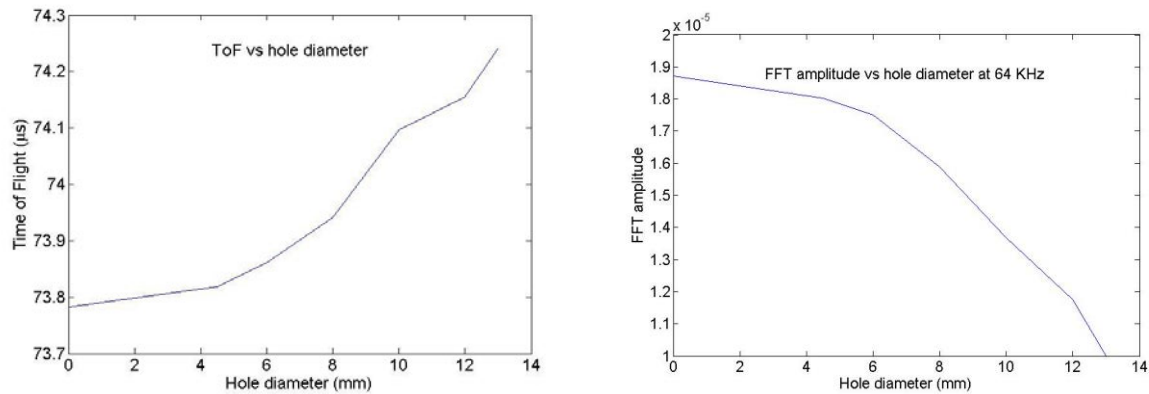
Figure 3. Tendency for different hole diameters

ACKNOWLEDGEMENT

REFERENCES

[1]   Hall S.R. "The Effective Management and Use of Structural Health Data." *Proceedings of the 2nd International Workshop on Structural Health Monitoring*, 265-275, 1999.

[2]   Bar-Cohen Y. "NDE of Fiber Reinforced Composite Materials—A Review." *Materials Evaluation*, 44, 446-454, 1986.

[3]   Chang F.K. "Structural Health Monitoring: A Summary Report." *Proceedings of the 2nd International Workshop on Structural Health Monitoring*, Stanford, CA, September 8-10, 1999.

[4]   Giurgiutiu V., Jingjing B. and W. Zhao "Active Sensor Wave Propagation Health Monitoring of Bean and Plate Structures." *Proceedings of the SPIE International Symposium on Smart Structures and Material*, 2001.

[5]   Kessler S.S., Spearing S.M. & Soutis C. Damage detection in composite materials using Lamb wave methods. *Smart Materials and Structures*, 11(2), 269, 2002.

[6]   Meyer Y. and Lachat R. Vibration characterization procedure of piezoelectric ceramic parameters. In *Proc.4eme Colloque francophone d'Analyse Vibratoire Expérimentale (AVE 14),* Blois, France, 2014.

[7]   Chen X.L., Lachat R., Salmon S., Ouisse M. and Meyer Y. Complex Composite Structures with Integrated Piezoelectric Transducers. *International Journal of Computational Methods and Experimental Measurements*, 5(2), 125-134, 2017.

[8]   Tucker B.J. Ultrasonic plate waves in wood-based composite panels. *PhD thesis, Washington State University,* 2001.

[9]   Monnier T. Ondes de Lamb dans les milieux stratifiés: application à la surveillance in situ et en temps réel de l'endommagement de structures composites. *PhD thesis, INSA de Lyon,* 2001.

[10]   Ihn J.B. & Chang F.K. Pitch-catch active sensing methods in structural health monitoring for aircraft structures. *Structural Health Monitoring,* 7(1), 5-19, 2008.

4

BAYESIAN CONTROL OF A HELICOPTER MAIN GEARBOX SEMI-ACTIVE SUSPENSION SYSTEM - EXPERIMENTS ON A QUARTER-SUSPENSION PROTOTYPE

J. Rodriguez[1*] , F. Malburet[2]

[1]ENSAM / Airbus Helicopters
ENSAM - LSIS Aix en Provence, FRANCE
Email: jonathan.rodriguez@ensam.eu , francois.malburet@ensam.eu

ABSTRACT

This short paper considers the control of a helicopter gearbox semi-active suspension. As the future generation of helicopters will include variable engine RPM during flight, it is interesting to consider implementing control on their suspension systems in order to always optimally filter the main disturbance frequency. Here, a semi-active suspension based on the DAVI principle is developed, simulated and tested with its control algorithm based on Bayesian optimization. This control method based on the Bayes theorem is a trial/error algorithm allows to significantly reduce the number of evaluations of the real objective function for a given set of parameters θ. Thus the system is capable to fastly determine its own optimal set of parameters to maximize the objective function. The objective is to prove experimentally the ability of the Bayesian optimization to lead the learning behavior of a semi-active resonant suspension.
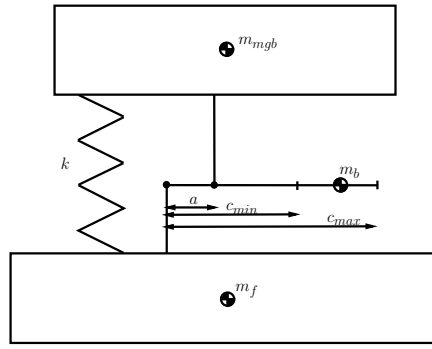
Figure 1: semi active DAVI principle adapted to helicopter, m_{mgb}: main gearbox and rotor, m_f: fuselage, m_b: flapping mass.

1 INTRODUCTION

Fuselage vibrations are a major problem in the design of helicopters. This paper will focus on the development of a new active hybrid vibration absorber which reduces the effects of the cyclic loads ($n\Omega$ harmonics) on the helicopter structure due to the main rotor.

2 THE SEMI-ACTIVE DAVI

In 1976, Flannelly [1] presents an anti-resonant vibration absorber called DAVI which uses a rigid arm carrying a flapping mass. The inertia of the bobweight mass generates an anti-resonance at the characteristical frequency ω_c depending on some parameters : dynamic amplification, overall stiffness and flapping mass. Airbus Helicopters company developed during the 1990's the SARIB$^{©}$ suspension, a DAVI suspension integrated in the helicopter between the MGB and the structure tuned to be as close as possible to the $b\Omega$ frequency (b number of blades and Ω the rotor speed).

With the arrival of variable engine RPM during flight, it is relevant to integrate some actuation in a DAVI system in order to be able "track" the $b\Omega$ frequency and adapt the steady state parameters of the suspension to the varying frequency of the disturbing input force. One can control the DAVI dynamic amplification ratio by modifying the position of the bobweight mass on its flapping arm as in figure 1 where m_f represents the helicopter structure, m_b is the flapping mass, m_{mgb} the main gearbox and rotor and k is the overall suspension stiffness. The dynamic amplification ratio λ is defined as c/a and has a direct influence on the anti-resonance frequency ω_c :

$$\omega_c^2 = \frac{k}{-\lambda(\lambda - 1)m_b} \tag{1}$$

Figure 2 shows the transmissibility H of the DAVI suspension for different values of λ. It is clearly visible that a suitable control of the variable c (position of the flapping mass) can modify in flight the anti-resonance frequency.

3 THE BAYESIAN OPTIMIZATION

The Bayesian optimization [2] [3] is used for computing the maximum of expensive cost functions. It is applicable when the estimation of the objective function for a particular case of x_i is costly and possibly noisy. The ability of the algorithm to significantly reduce the number of function evaluations before reaching the optimum value is due to the incorporation of the

2
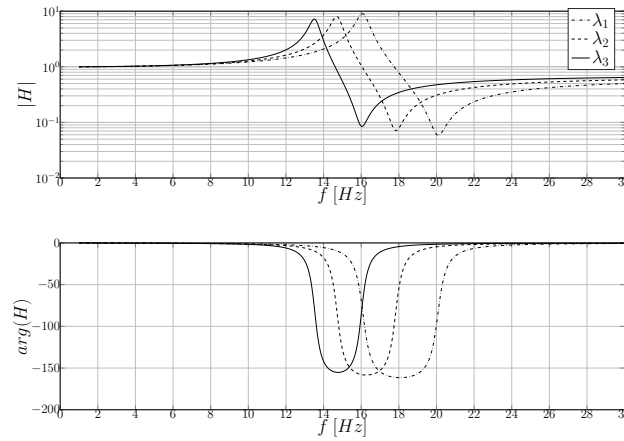
Figure 2: Transmissibility $H(f)$ of the DAVI suspension for different values of λ.

prior belief. This prior knowledge is used to determine the new input vector x_i which will be evaluated by making a trade off between exploitation (use of prior data) and exploration of the search space. At each cost function evaluation, the algorithm computes an estimation of the function $f(x)$ for the complete search space Π ($x \in \Pi$).

From the prior knowledge of the cost function is computed the posterior distribution which represents the updated beliefs about $f(x)$. Then, the Bayesian optimization uses an acquisition function to determine the next input vector x_{i+1} and measure the process response $f(x_{i+1})$.

The objective here is to adapt the dynamic amplification ratio λ i.e. the position c of the bobweight mass on the flapping arm for every solicitation frequency $\omega_0 \in [\omega_c(c_{max}); \omega_c(c_{min})]$. The input parameter x represents here the position c of the bobweight mass and the cost function $f(x)$ is mostly characterized by the acceleration level of the fuselage.

The strong assumption of the Bayesian optimization is that it is possible to consider the function $f(x)$ as a GP (Gaussian Process). For every input vector x, the GP will return the mean m and the covariance k of a normal distribution over the possible values of $f(x)$ as it follows :

$$f(x) \sim GP(m(x), k(x, x')) \qquad (2)$$

In the Bayesian method, the choice of the covariance function is very important as it determines the smoothness properties of the estimation of $f(x)$. This smoothness is generally controlled by one or more hyperparameters θ. A wide variety of covariance functions has been investigated in litterature, as in [4] we propose to use the Matern 5/2 kernel. To determine the hyperparameters of this statistical model, the ARD (Automatic Relevance Determination) method has been applied. The table 1 summarizes the main steps of the Bayesian optimization with Auto Relevance Determination method described just before.

Bayesian optimization of $f(x)$	
While	*optimize* do
1	Prior knowledge available $\mathcal{D}_{1:i} = \{\mathbf{x}_{1:i}, \mathbf{f}_{1:i}\}$
2	Auto Relevance Determination of $\theta_{opt}(i)$ using gradient method
3	Computation of μ and σ^2
4	Computation of the acquisition function $EI(x)$ on the search space Π
5	Maximization of $EI(x)$ and so determination of x_{i+1}
6	Evaluation $f(x_{i+1})$
7	$i = i + 1$ and go to step 1

Table 1: Overview of the Bayesian optimization with ARD.

3
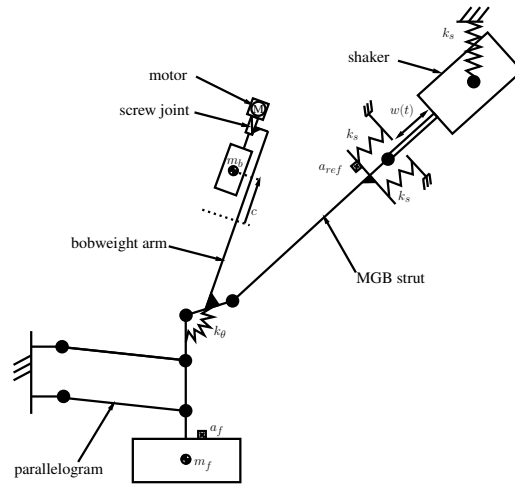
Figure 3: Test setup scheme.

4   EXPERIMENTS

As explained previously, the system we control here with the Bayesian optimization is the semi-active SARIB$^\copyright$ from Airbus Helicopters. The test setup represents an isolated MGB strut linked to a semi-active DAVI bobweight arm. The figure 3 represents a diagram of the test bench (no pictures allowed due to Airbus confidentiality policy), one can notice that the flapper arm is linked by a fitting to a mass m_f representing the helicopter structure. In order to keep all movements in a plane, a mechanical parallelogram is added to the experimental set-up.

Three different learning sequences have been used to teach the program. We define a learning sequence as the order of appearance of every frequency ω within the antiresonance bandwidth of the semi-active DAVI $[\omega_c(c_{max}); \omega_c(c_{min})]$.
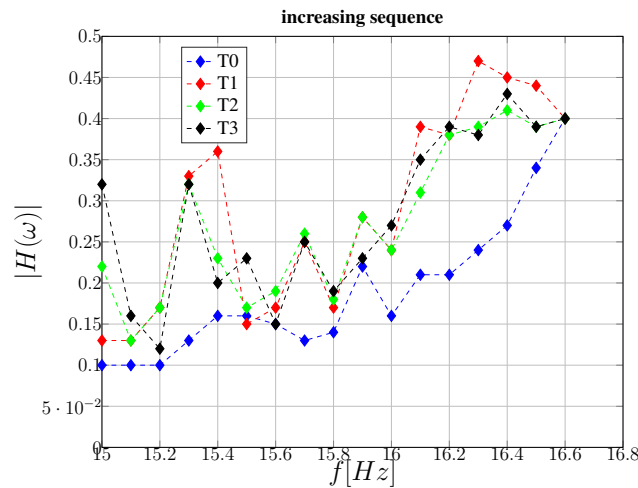
Figure 4: Increasing sequence - suspension transmissibility.

The real optimal positions $c_{ref}(\omega) \; \forall \omega \in \Pi$ are also computed to set a reference vector $d0$. As a result (see 4 and 5), the Bayesian optimization always finds a solution acceptable for the mass position giving a transmissibility around 0.45 for the worst results and 0.1 for the best ones. In addition to the Bayesian optimization, it has been added a learning method to keep in a database the "good" positions tested for each frequency. The objective is to reduce the number of iterations necessary to the algorithm to find the optimal position.

4
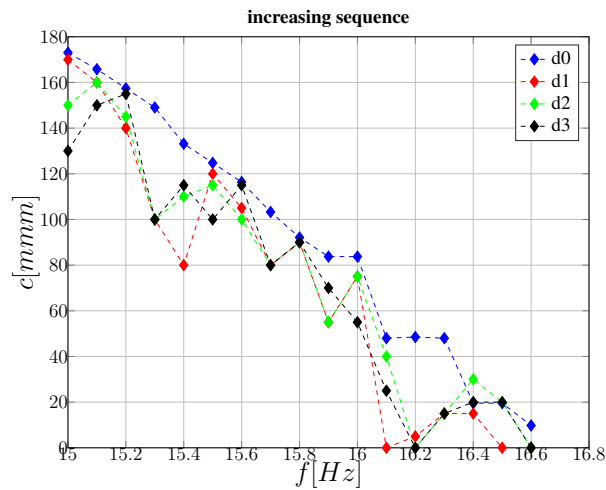
Figure 5: Increasing sequence - mass position.

5   CONCLUSION AND PROSPECTS

The main difficulties encountered during the development of the control algorithm were to deal with the resonant behavior of the DAVI. Controlling a dynamic system near its anti-resonance or resonance frequency implies fast and unstable phase changes which makes harder having a clean and fine tuning. The fact that this optimization technique is based on a stochastic, not deterministic model which is updated using prior knowledge on every measurement made, presents a strong advantage in comparison to other semi-active control methods. There is no need of a complex mathematical model of the system or prior identification.

Good results were achieved in terms of vibration isolation : a suspension transmissibility going from 0.1 to 0.41 and no absurd final mass position c were observed in spite of the system noise. The learning sequence order demonstrated to have a limited impact on the final results.

As a conclusion, control adaptivity, learning methods and auto-tuning of control parameters even without particular mathematical model of the system or prior asumptions are the current keys for the future evolutions of the dynamics control field.

REFERENCES

[1] W.G. FLANNELLY. The dynamic anti-resonant vibration isolator. *AHS*, 1976.

[2] Vlad M. Cora Eric Brochu and Nando de Freitas. A tutorial on bayesian optimization of expensive cost functions, with application to active user modeling and hierarchical reinforcement learning. 2010.

[3] Jan Peters Marc Peter Deisenroth Roberto Calandra, Andr Seyfarth. Bayesian optimization for learning gaits under uncertainty : An experimental comparison on a dynamic bipedal walker. *Annals of Mathematics and Artificial Intelligence*, 2013.

[4] Ryan P. Adams Jasper Snoek, Hugo Larochelle. Practical bayesian optimization of machine learning algorithms. *Advances in Neural Information Processing Systems, 2951-2959*, 2012.

5

Vibration reduction of composite plates with shunted piezo-patches: Analytical modeling and numerical validation

A. Aghakhani, M.M. Gozum, and I. Basdogan

Vibration and Acoustics Laboratory (VAL),
Koc University, Istanbul, TURKEY
Email: aaghakhani@ku.edu.tr, mgozum@ku.edu.tr, ibasdogan@ku.edu.tr

ABSTRACT

Laminated composite plates are frequently used in various aerospace, automotive and space applications. In such applications, undesired vibrations can be reduced by using active and passive vibration control methods. Integrating piezo-patches into such plates is an alternative way to damp the structural vibrations. However, accurate models are required to predict the dynamics of such plates when the piezo is attached to the host structure. In this paper, analytical modeling of composite plates with two surface-bonded piezo-patches in parallel shunted to a resistive load is presented using Rayleigh-Ritz method. The analytical model accounts for mass and stiffness contribution of piezo-patches as well as two-way electromechanical coupling effect. Furthermore, electromechanical frequency response functions obtained by the developed analytical model are validated by finite-element analysis in ANSYS. Finally, the performance of the shunt damping method on the composite structure for a range of resistive loads is demonstrated by the reduction in the displacement frequency response functions.

1   INTRODUCTION

Thin composite plates are of interest in many engineering applications, for their superior mechanical characteristics such as high stiffness-to-weight ratio and low density. However, in harsh environments, they are exposed to severe vibrations which result in reduced structural life and eventually mechanical failure [1]. Piezoelectric patches integrated into such flexible structures can be utilized to passively damp the vibrations through shunting the piezo-patch electrodes with an electrical circuit [2,3]. Few analytical models have been proposed in the literature for vibration analysis of thin plates with surface-bonded piezo-patches [4,5]. In the reported works, only piezoelectric coupling effect is included in the analytical modeling, whereas mass and stiffness contribution of piezo-patches are ignored due to the low volumetric ratio of piezo-patches with respect to the isotropic plate (made of Aluminium). This assumption, however, does not remain valid for lightweight composite plates. Therefore, in this study, the effect of piezoelectric shunt damping on the composite plates is investigated through analytical modeling that accounts for mass and stiffness properties of the piezoelectric material and two-way electromechanical coupling. Moreover, the analytical model results and vibration reduction of the host structure using the piezo patches is validated by finite-element simulations in ANSYS.

2   ANALYTICAL MODELING

In this section, equations of motions for a composite plate with two surface-bonded piezo-patches are presented. Figure 1 shows the schematics of the electromechanical system where a pair of piezo-patches are connected in parallel to a resistive load.
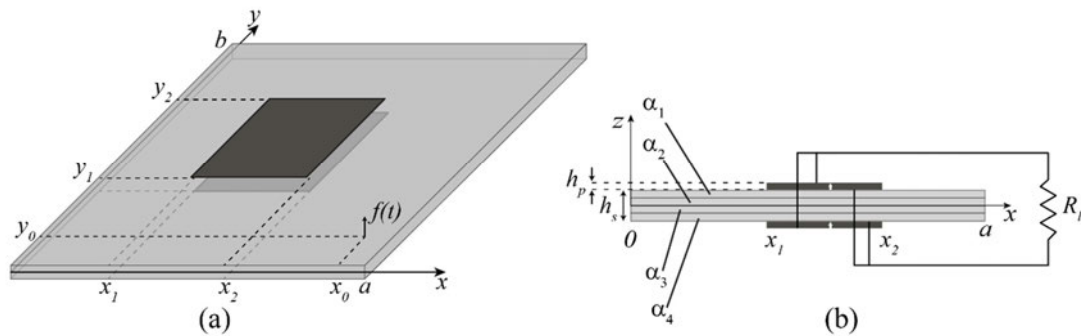
Figure 1. (a) schematics of a composite plate with two surface-bonded piezo-patches, (b) cross-section view of the laminated composite (with four ply angles α_1, α_2, α_3, α_4) where piezo-patches are shunted in parallel to a resistive load.

Applying Hamilton's principle and using Rayleigh-Ritz method for modal analysis procedure [6], we obtain the following electromechanical equations for the two structurally integrated piezo-patches connected in parallel to a resistive load in the modal coordinates:

$$\frac{\mathrm{d}^2\eta_{mn}(t)}{\mathrm{d}t^2} + 2\zeta_{mn}\omega_{mn}\frac{\mathrm{d}\eta_{mn}(t)}{\mathrm{d}t} + \omega_{mn}^2\eta_{mn}(t) - v(t)\sum_{k=1}^{2}(\widetilde{\theta}_{mn})_k = f_{mn}(t) \tag{1}$$

$$\sum_{k=1}^{2}\sum_{n=1}^{\infty}\sum_{m=1}^{\infty}(\widetilde{\theta}_{mn})_k\frac{\mathrm{d}\eta_{mn}(t)}{\mathrm{d}t} + \frac{\mathrm{d}v(t)}{\mathrm{d}t}\sum_{k=1}^{2}(C_{\mathrm{p}})_k + \frac{v(t)}{R_l} = 0 \tag{2}$$

2

where $\eta_{mn}(t)$ and $v(t)$ are the mechanical modal coordinate and voltage over across the resistive load. Here, $(C_p)_k$ is the equivalent capacitance for the kth patch and given by $(C_p)_k = (\bar{\varepsilon}_{33}^S)_k (A_p)_k / (h_p)_k$ (where $\bar{\varepsilon}_{33}^S$, A_p, and h_p are the dielectric permittivity, the piezo-patch area and thickness in z-direction, respectively). The Modal forcing input and the electromechanical coupling term can be expressed as:

$$f_{mn}(t) = f(t)U_{mn}W_{mn}(x_0, y_0) \tag{3}$$

$$(\widetilde{\theta}_{mn})_k = (\frac{h_p + h_s}{2})(\bar{e}_{31})_k \int\limits_{y_1}^{y_2} \int\limits_{x_1}^{x_2} U_{mn}\left[\frac{\partial^2 W_{mn}(x, y)}{\partial x^2} + \frac{\partial^2 W_{mn}(x, y)}{\partial y^2}\right]dxdy \tag{4}$$

here, $\bar{e}_{31}$ is the effective piezoelectric constant, and $U_{mn}W_{mn}(x, y)$ are the assumed modes where $m = 1, 2, ..., M$, $n = 1, 2, ..., N$ (M, N indicate the number of modes).

It should be noted that mass and stiffness effect of piezoelectric patches are included in the modal analysis procedure using the following indicator function $P(x, y)$, which determines the area on the plate that is covered by the piezo-patch as

$$P(x, y) = [H(x - x_1) - H(x - x_2)] \times [H(y - y_1) - H(y - y_2)] \tag{5}$$

where H denotes the Heaviside unit-step function.

For the electromechanical frequency response functions (FRFs), one can substitute the harmonic forms of $f(t) = F_0 e^{j\omega t}$, $\eta_{mn}(t) = H_{mn}e^{j\omega t}$, and $v(t) = Ve^{j\omega t}$ at steady-state into Equations (1) and (2), and obtain the displacement output to force input FRF as follows:

$$\beta(x, y, \omega) = \frac{w(x, y, t)}{F_0 e^{j\omega t}}, \quad w(x, y, t) = \sum_{m=1}^{M}\sum_{n=1}^{N} U_{mn}W_{mn}(x, y)\eta_{mn}(t) \tag{6}$$

3   RESULTS AND DISCUSSIONS

Figure 2 shows the electromechanical frequency responses (voltage and displacement outputs per unit force input) of the coupled system for validation of the proposed analytical model.
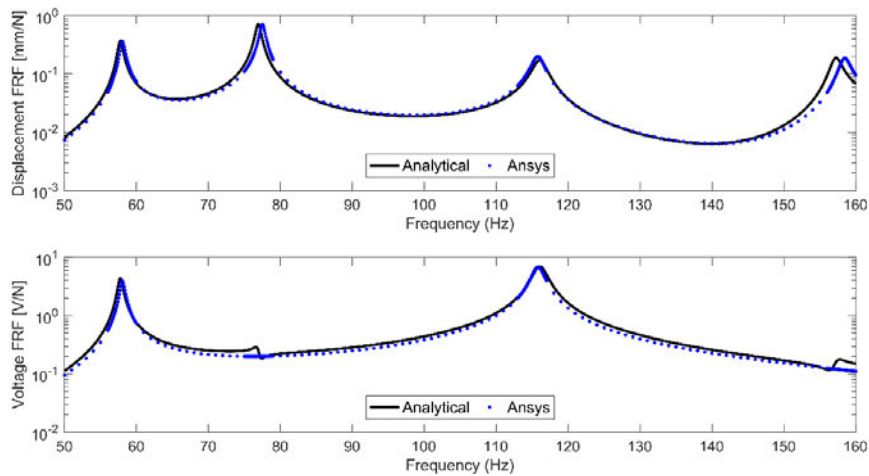
Figure 2. Comparison of Analytical voltage and displacement FRF with the corresponding ANSYS simulations.

3

As it can be observed from the graph, the analytical solution based on Rayleigh-Ritz method agrees well with the ANSYS simulation results. The electrical resistive load value is taken as 1 kΩ in the presented FRFs. The vibration response shown in Figure 2 is measured at the center of the top-left quarter of the plate. The voltage FRF shows a cancellation for the second and fourth modes since the piezo-patches are located in the center of the plate. These charge cancellations can be explained by the in-phase and out-phase strain distribution that occurs in the area of the plate covered by the patches. This result show that, one should carefully choose the location of the patches for effectively reducing the vibrations at the target frequency such that no electrical cancellation occurs.

4   CONCLUSION

An analytical modeling of a laminated composite plate with surface bonded piezoelectric patches, in bimorph configuration, using Rayleigh-Ritz method was presented. Analytical solutions for electromechanical FRFs were validated against ANSYS simulation results. The analytical model accounts for mass and stiffness effect of piezo-patches on the composite plate along with two-way electromechanical coupling effect. It was shown that using the analytical model, one can correctly predict the vibration response of the plate in presence of shunted piezo-patches. Furthermore, an optimum resistance value can be obtained for maximum reduction of vibration level at a target excitation frequency.

REFERENCES

[1]   Fleming A J and Moheimani S O R 2003 Adaptive piezoelectric shunt damping *Smart Mater. Struct.* **12** 36–48

[2]   Saravanos D A 1999 Damped Vibration of Composite Plates With Passive Piezoelectric-Resistor Elements *J. Sound Vib.* **221** 867–85

[3]   Hagood N W and von Flotow A 1991 Damping of structural vibrations with piezoelectric materials and passive electrical networks *J. Sound Vib.* **146** 243–68

[4]   Bayik B, Aghakhani A, Basdogan I and Erturk A 2016 Equivalent circuit modeling of a piezo-patch energy harvester on a thin plate with AC – DC conversion *Smart Mater. Struct.* **25** 55015

[5]   Aridogan U, Basdogan I and Erturk A 2014 Multiple patch-based broadband piezoelectric energy harvesting on plate-based structures *J. Intell. Mater. Syst. Struct.* **25** 1664–80

[6]   Yoon H, Youn B D and Kim H S 2016 Kirchhoff plate theory-based electromechanically-coupled analytical model considering inertia and stiffness effects of a surface-bonded piezoelectric patch *Smart Mater. Struct.* **25** 25017

4

PHASE COMPENSATOR FOR HYPERSTABLE HYBRID MASS DAMPER

S. Chesné[1*] and C. Collette[2]

[1]LaMCoS
Université de Lyon, CNRS INSA-Lyon, LaMCoS UMR5259, F-69621, Villeurbanne, FRANCE
Email: simon.chesne@insa-lyon.fr

[2]BEAMS department,
Université Libre de Bruxelles, 50, F.D. Roosevelt av., 1050 Brussels BELGIUM
Email: ccollette@ulb.ac.be

ABSTRACT

In this paper, we propose and validate a simple control law, dedicated to hybrid mass dampers in order to improve stability and performance. A particular phase compensator is added to the original velocity feedback to correct the dynamics of the actuator face to the one of the controlled structure. The resulting system is hyperstable theoritically. The main interest of this kind of devices is its fail-safe property which is essential for aerospace applications. Theoritical analysis and experimentation illustrate this hybrid control device and its performances.

1   INTRODUCTION

Usually, when inertial actuators are used to actively control structures, the resonance frequency of the actuator is much lower than the fundamental resonance frequency of the controlled structures. The resulting device is called Active Mass Damper (AMD) and many control strategies have been developed [1, 6, 9]. Some approaches consider the problem of the tuning and the possible vinicity of the actuator resonance frequency to the one of the main structure. A compensator in the feedback loop [4, 8] is introduced to activelty soften the actuator. But the pole-zero cancellation principle on which they are based presents some known dangers. Another class of dampers called Hybrid Mass Damper (HMD), or Hybrid Vibration Absorber (HVA) have recently appeared, trying to combine passive [5] and active vibration control. The objectives are: (i) to increase the performance, (ii) reduce the consumption on the considered bandwidth and (iii) to ensure a fail-safe behavior [2, 7] .

In this contribution, we propose a simple control law previously theoritically introduced in [3]. We show that it improves the performance of classical hybrid dampers based on decentralized velocity feedback techniques. Actually, a compensator is introduced in the control loop to correct the phase of the actuator in order to become stable at the considered frequency. The resulting system is hyperstable [3] and fail-safe.

2   THE α-HYBRID MASS DAMPER

The section briefly presents the basic principles of the α-Hybrid Mass Damper. More details can found in [3].
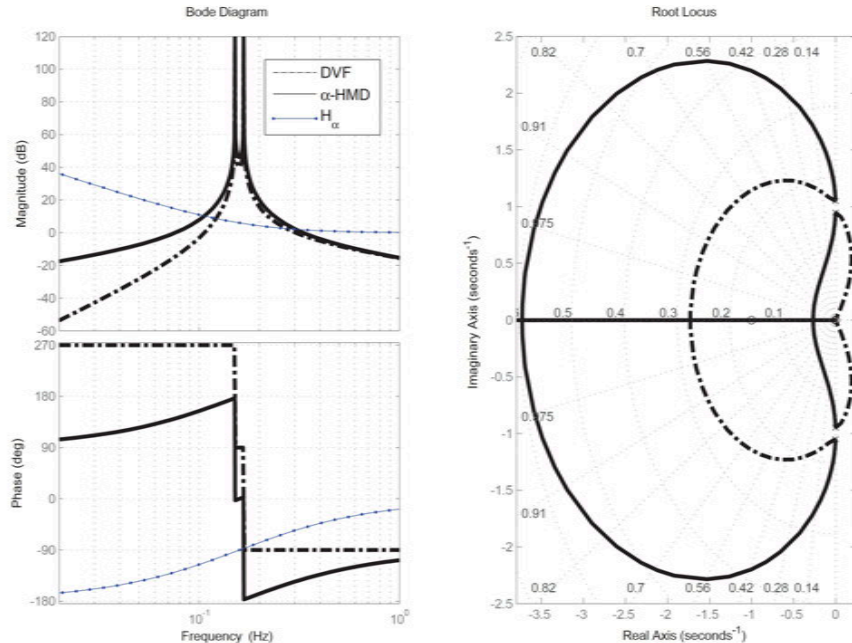
Figure 1: (a) Bode and (b)root locus plots of sensor-actuator open loop transfer function for Direct Velocity Feedback (black dashed line) and for α controller using $\alpha = \omega_0$ (continuous black line). Transfer function $H_\alpha(s)$ in blue dotted line.

Consider a system with a resonant frequency of $\omega_0 = \sqrt{k_1/m_1} = 1 \ rad.s^{-1}$ without damping. To this system, a classical dynamic vibration absorber is associated (mass ratio $\mu = 1\%$). Usually, AMD are used with Direct Velocity Feedback (DVF) law. A control law proportional to the measured velocity of the main structure is generated to drive the actuator.

2

The open loop transfer function and the root locus are plotted in fig 1 (black dashed lines). By analyzing the stability margins, we see that the system is stable only at very low feedback gain. One sees also on the root locus that the lower frequency pole goes immediately in the right half plane, leading to instability. The closed loop system will always be marginally stable. This is mainly due to the absence of zero between the pole of the TMD and the pole of the structure.

A simple alternative to recover stability is to adequately place a pair of zeros at the right frequency. The controller is still a velocity feedback, however, a filter named α-controller is added in the control loop [3]:

$$H_\alpha(s) = g\frac{(s+\alpha)^2}{s^2} \tag{1}$$

The phase has been modified below the first resonant frequency (see its transfer function in fig 1 (a), blue dotted line). The parameter α is tuned to make the controller hyperstable. In this study, its value is $\alpha = \omega_0$. The rootlocus of the α-HMD is plotted in fig 1(b) (black continuous line). We can see that the whole root locus plot is in the left half plane, meaning an unconditional stability of the feedback system (infinite gain margin). More analysis and details can be founded in [3].
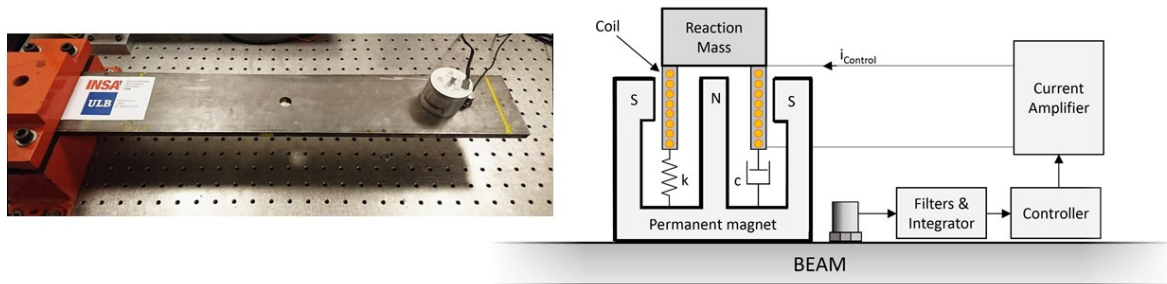
Figure 2: Picture of the experimental set-up used to test the proposed controller and the schematic of the control device

3   EXPERIMENTAL SET-UP

The structure and the control device are shown in Figure 2 The targeted mode is the first bending mode of the beam. The control device is Micromega products initially designed for purely active control (ADD-5N). Its reaction mass is 160gr, its frequency is around 21Hz and its damping of $\xi = 11.9\%$. The main structure used for the validation is a cantilever steel beam (Length: $58cm$, width: $10cm$, thickness: $1cm$). An accelerometer is fixed nearby the actuator to feed the controller.

4   PERFORMANCES AND CONCLUSIONS

Figure 3 show the effects of the proposed HMD in term of FRF and integrated RMS value. The first one shows the damping introduced by the control on the targeted mode and the second graphic shows its wide range effect. Indeed contrary to passive TMD, more than one mode is damped. Note that the damping on the first mode without any control is 0.24%; with the passive device it is around 9% due to the high mass ratio, and with the α-controller it reaches more than 16% for both resulting peaks.

3
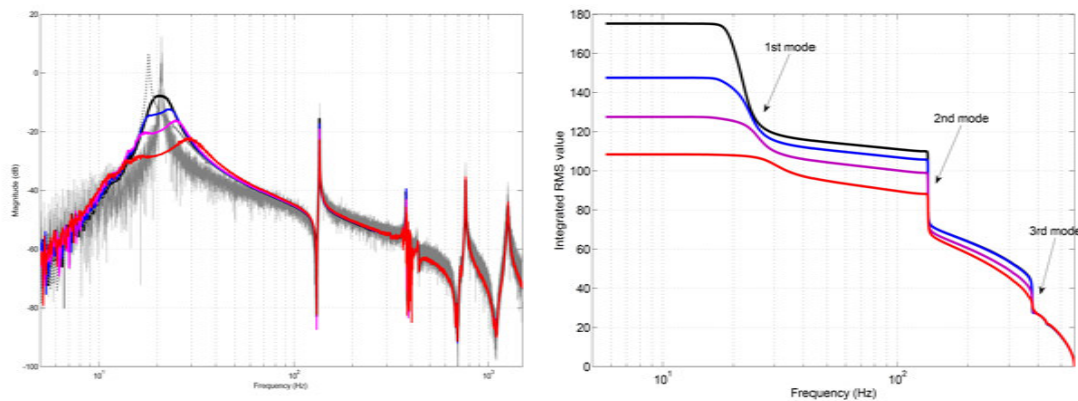
Figure 3: (a) Frequency response functions and (b) Integrated RMS value $[0-500]Hz$, without control (grey), with passive TMD (black), with DVF (grey dotted line) and with α-controller using various gain ($g = 1$ in blue, $g = 3$ in purple, $g = 9$ in red).

These figures validate the proposed robust hybrid mass damper. It combines two features: an unconditional stability, and a fail-safe characteristic by modifying the classical DVF law on a TMD.

REFERENCES

[1] Burgos O, Hizon J and Sison L (2004) *Comparison of classical and fuzzy control in active mass damping of a flexible structure using acceleration feedback, in: TENCON, 2004 IEEE Region 10 Conference*, Vol. D, pp. 645–648 Vol.4.

[2] Cheung Y, Wong W and Cheng L (2012)*Design optimization of a damped hybrid vibration absorber*, Journal of Sound and Vibration 331 (4) (2012) 750 – 766.

[3] Collette C and Chesne S (2016) *Robust Hybrid Mass Damper*, Journal of Sound and Vibration, Vol. 375, pp. 19–27.

[4] Elliott S.J and Rohlfing J (2012) *Multifunctional design of inertially-actuated velocity feedback*, Journal of Aoustical Society of America, Vol. 131(2), pp. 1150–1157.

[5] DenHartog J (1956) *Mechanical Vibrations*, 4th Ed., Mc Graw-Hill, New York.

[6] Preumont A and Seto K (2008) *Active control of Structures*, John Wiley and sons, West Sussex, United Kingdom.

[7] Rodriguez J, Cranga P, Chesne S and Gaudiller L (2016) *Hybrid active suspension system of a helicopter main gearbox*, Journal of Vibration and Control, july 2016, pp. 1–19.

[8] Rohlfing J, Elliott S.J and Gardonio P (2012) *Feedback compensator for control units with proof-mass electrodynamic actuators*, Journal of Sound and Vibration, Vol. 331, pp. 3437–3450.

[9] Tso M, Yuan J and Wong W (2013) *Design and experimental study of a hybrid vibration absorber for global vibration control*, Engineering Structures 56, 1058 – 1069.

4

SHUNTED PIEZOELECTRIC TRAP DEVICE TO ENHANCE ENERGY HARVESTING

F. K. Maugan[1], K. Yi[2], M. Monteil[1], S. Chesné[1] and M. Collet[2]

[1]LaMCoS
Université de Lyon, CNRS INSA-Lyon, LaMCoS UMR5259, F69621 Villeurbanne
Email: fabien.maugan@insa-lyon.fr, simon.chesne@insa-lyon.fr

[2]LTDS
UMR 5513, Ecole Centrale de Lyon, 36 avenue Guy de Collongue, 69130 Ecully
Email: yikaijun88@gmail.com, manuel.collet@ec-lyon.fr

ABSTRACT

Innovative technologies aim at reducing structural masses using composite materials. These new light structures are, however, very sensitive to vibrations. Originals disciplinarian fields such as metacomposites or structronics show up from this context in order to explore new vibratory stabilities and its applications in acoustical attenuations, health monitoring, or energy harvesting in order to give robustness and autonomy to subsystems. This paper focuses on an academic structure where a piezoelectric transducer frame works as a trap device. The latter concentrate the energy from vibrations to a place where an SSHI (Synchronized Switch Harvesting in Inductor) type harvesting device is located. After a presentation of the structure, and the conversion-extraction device, its capability to improve the harvested energy are verified in comparison with a purely passive structure.

1   INTRODUCTION

In a context of new materials and architectures, fields as structronics or metacomposites aim at explore new vibrating stabilities for various applications such as energy harvesting. A standard harvesting system is hereby applied to a multimodal structure in coupling with a trap device. The methodologies and models have previously been tested and validated on a monomodal structure and are in accordance with the theory.

All the results are presented in the case of the weak coupling of the structure, in other words, in a constant displacement case. That means the electronic parts of the system don't affect the dynamics of the structural components.

2   DESIGN OF TRAP DEVICE COMPOSED OF SHUNTED PIEZOELECTRIC CELLS

The global geometry of the studied system and the piezoelectric trap device principle are hereby detailed.

2.1 Structure of interest

The figure 1 displays the structure of interest which consists in a 2.5m long cantilever beam. The two 0.6m long trap devices are composed of gradually varying parameters [1, 2] designed to trap the vibration energy in the 0.4m long trap zone of the structure where a harvesting device is placed. The background beam and the trap zone are made of aluminum.
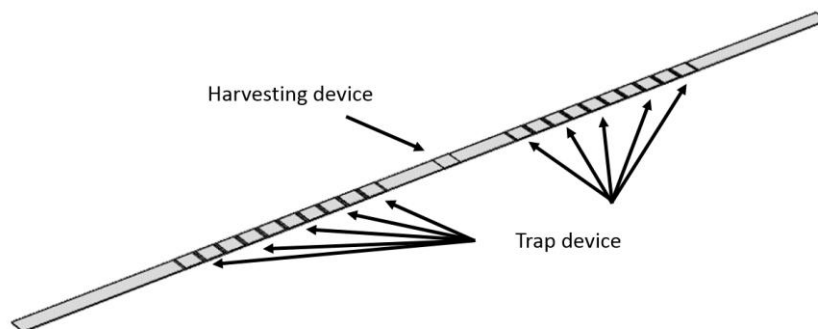
Figure 1. System geometry.

2.2 Shunted piezoelectric cells network for trap device

Above mentioned trap device can be achieved in different ways, designing geometry parameters or combinations of several ones. Here, the chosen approach is to modify the Young modulus. This parameter has to be continuous in order to avoid reflections in wave's propagation [2]. In figure 2, the black solid lines show this decreasing in Young modulus from the outside to the inside edges of the trap devices.

Due to the difficulty to make a continuously varying parameter all along the two trap devices, each one is divided into ten cells with identical geometrical properties. For each one, the target Yong modulus portion of curve is discretized (red crosses on figure 2) and materially made

using a piezoelectric patch. Each one of these patches is shunted in order to realize negative capacitances able to modify the system dynamics [3].
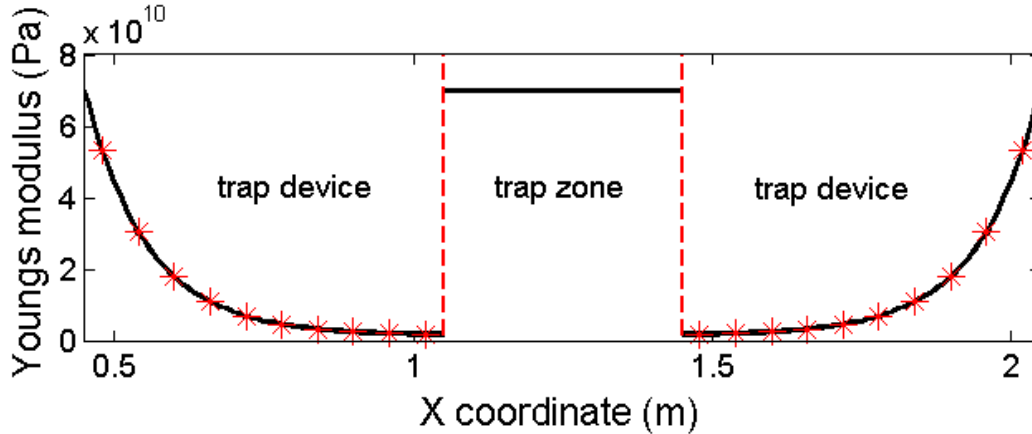
Figure 2. Trap device design.

3 ENERGY HARVESTING DEVICE

As a first step, a very classical harvesting system is used [4]. It is composed of a diode bridge, a smoothening capacitor C_R, the piezoelectrical capacitance C_0 and a resistor R. The whole device is connected to a piezoelectric element placed at the centre of the trap zone. The time constant $\tau = RC_R = 10s$ in order to guaranty that the output tension V_s reaches its steady state in an honest amount of time.
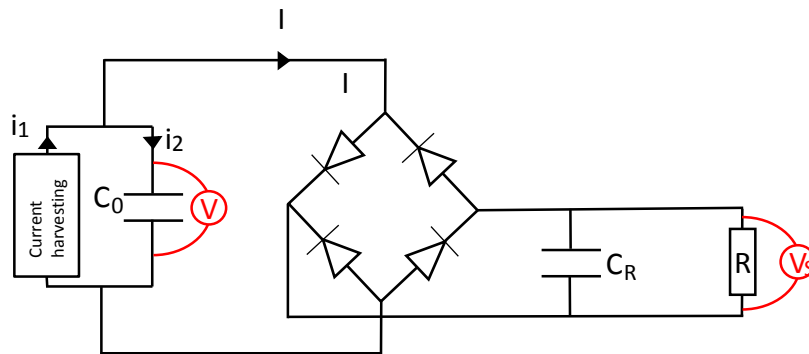
Figure 3. Energy harvesting device.

The tuning of the above electronic device to the natural frequency of interest of the structure implies each time a modification of the R value. C_R has also to be changed for τ to remain a constant. These parameters finally allow computing the performance criteria; the output tension V_s and the harvested power P_{stand}:

$$V_s = \frac{R\Phi^T\alpha}{C_0R\omega_0 + \dfrac{\pi}{2}}\omega_0 q_m \qquad\qquad P_{stand} = \frac{V_s^2}{R} \tag{1}$$

With the modal matrix Φ, the coupling coefficient α and for the generalized coordinate q_m and a working angular frequency ω_0.

4   PERFORMANCES

The studied system is multimodal with 20 modes but the presented work will focus on the 17th flexure mode at 151.46Hz of the structure which presents good coupling with the harvesting and trap devices. The excitation is made on the free end of the beam. Figure 4 gives the resulting performances. V_s and P_{stand} are displayed for both activated (red) and deactivated (blue) trap devices, in the case of weak coupling.
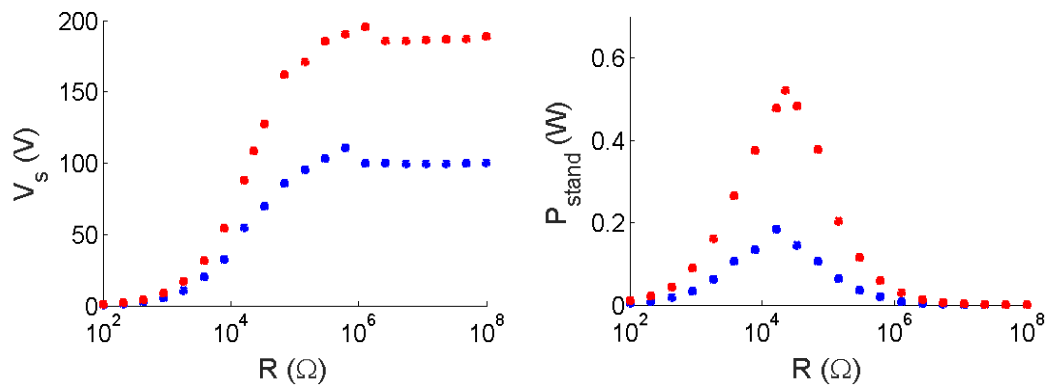
Figure 4. Vs and P.

The topology of the obtained curves fits with the ones from the literature [4]. The harvesting improvement due to the trap device activation can clearly be seen and reaches 0.52W for a 2.26e4Ω resistor. That corresponds to 2.84 times the results obtained without trap.

5   CONCLUDING REMARKS

The improvement in adding a trap device to concentrate the mechanical energy in a place of the structure where the harvester is placed has been demonstrated on an academic multimodal system. Even if only weak coupling has been taken into account, results from strong coupling present some computation issues that will be addressed in further communications.

REFERENCES

[1]   C. Vermula, A. N. Norris, G. D. Cody. Attenuation of waves in plate and bars using a graded impedance interface at edges. *Journal of sound and vibration*. 1996, 196(1): 107-127.

[2]   V. V. Krylov, F. Tilman. Acoustic 'black hole' for flexural waves as effective vibration dampers. *Journal of sound and vibration*. 2004, 274(3): 605-619.

[3]   S. Livet, M. Collet, M. Berthillier, and al. Structural multi-modal damping by optimizing shunted piezoelectric transducers. *European Journal of Computation Mechanics*. 2011, 20(1-4) 73-102

[4]   M. Lallart, *Amélioration de la conversion électroactive de matériaux piézoélectriques et pyroélectriques pour le contrôle vibratoire et la récupération d'énergie*. Phd thesis, 2cole doctorale : Electronique, Electrotechnique et Automatique de Lyon, 2008.

DESIGN OF ACTIVE MULTIPLE-DEGREES-OF-FREEDOM ELECTROACOUSTIC RESONATORS FOR USE AS BROADBAND SOUND ABSORBERS

H. Lissek[1] , E. Rivet[1], S. Karkar[2], R. Boulandet[1]

[1]Laboratoire de Traitement des Signaux LTS2
Ecole Polytechnique Fédérale de Lausanne, Lausanne, SWITZERLAND Email:
herve.lissek@epfl.ch, etienne.ribvet@epfl.ch, romain.boulandet@epfl.ch

[2]Laboratoire de Tribologie et Dynamique des Systèmes LTDS
Ecole Centrale Lyon, Lyon, FRANCE Email: sami.karakr@iec-lyon.fr

ABSTRACT

We present a novel control method achieving stable multiple-degrees-of-freedom electroacoustic resonators. Such broadband absorbers, composed of a feedback-controlled electrodynamic loudspeaker, have many practical applications to real-world acoustic engineering problems, such as low-frequency industrial noise reduction in the range of [20 - 200 Hz]. The proposed control architecture combines a conventional microphone-based feedback control loop and a current-driven direct acoustic impedance control scheme, proven to perform optimally in recently reported acoustic impedance synthesis methods. This paper presents a methodology for designing the transfer function to be implemented in the controller, after specifying a target multiple-degree-of-freedom acoustic resonator impedance. Numerical simulations presents the expected acoustic performances, confirmed by experimental assessments in an impedance tube.

1 INTRODUCTION

Low-frequency noise is present everywhere in the environment, emanating either from transportation facilities or industrial equipments. However, soundproofing is hardly achievable below 200 Hz with conventional passive acoustic materials such as porous layers or Helmholtz resonators [1]. Therefore, active control techniques have been investigated in the last decades to identify novel soundproofing concepts capable of targeting this unaffordable frequency range. The concept of "electroacoustic absorber" [2] encompasses loudspeaker system, namely a loudspeaker in a dedicated cabinet, the electrical terminals of which can be loaded either by passive components (RLC resonators [3]), or active ones (feedback control based on pressure and/or velocity sensing). It has especially given rise to the more general concept of "electroacoustic resonator" [4], that may present multiple-degrees-of-freedom (MDOF) characteristics. In the following, we consider the situation where the loudspeaker is fed back with a current driven by a given filtered version of the sound pressure on its diaphragm [5].

2 ACHIEVING MDOF ELECTROACOUSTIC RESONATORS

2.1 Model of the electroacoustic resonator

The transducer used in the following is an electrodynamic loudspeaker, that can be assimilated to a single-degree-of-freedom oscillator (suspended diaphragm) mechanically driven by a voice coil within a permanent and almost constant magnetic field. Figure 1 (left) highlights the mechanical part assimilated to a simple mass - spring - losses resonator, with mass M_{ms}, spring compliance C_{mc}, and mechanical resistance R_{ms}. It is assumed that all forces acting on the transducer, especially those resulting from the total pressure p_t, are small enough so that the displacements remain proportional to applied forces.
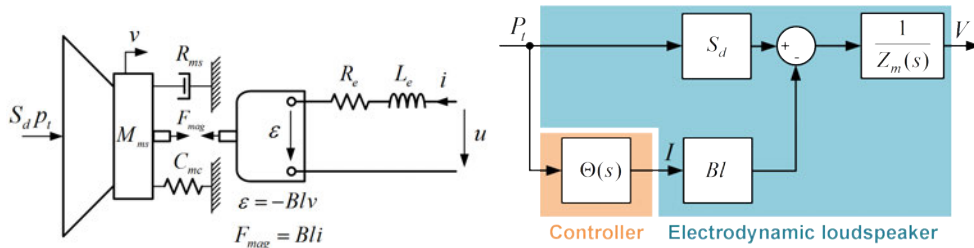
Figure 1: Left:Schematic representation of the closed-box electrodynamic loudspeaker; right:Block diagram of the electroacoustic resonator.

If we denote S_d the effective piston area and Bl the force factor of the moving-coil transducer, the equation of motion of the loudspeaker membrane (Newton's second law) and the mesh law can be written in the Laplace domain ($s = j2\pi f$, where f is the frequency):

$$S_d P_t(s) = Z_m(s)V(s) + Bl\, I(s) \tag{1}$$

where $V(s)$ represents the membrane velocity, $P_t(s)$ represents the total sound pressure at the membrane surface, combination of the incident and reflected waves, and $I(s)$ is the current flowing through the voice coil. Here $Z_m(s) = sM_{ms} + R_{ms} + 1/(sC_{mc})$ is the mechanical impedance of the closed-box loudspeaker. We can also define the acoustic impedance $Z_s(s)$ presented by the diaphragm of the loudspeaker, considered as an electroacoustic resonator, as:

$$Z_s(s) = \frac{P_t(s)}{V(s)}. \tag{2}$$

2.2 Acoustic impedance control scheme

In the present concept, the loudspeaker is electrically fed with a current-driven amplifier, through a controller providing a filtered version of pressure P_t at the diaphragm through transfer function $\Theta(s)$, as illustrated on Figure 1 (right). Then, to assign a prescribed acoustic impedance Z_{st} at the electroacoustic resonator, the transfer function can be easily derived from Equation1:

$$\Theta(s) = \frac{I(s)}{P_t(s)} = \frac{S_d Z_{st}(s) - Z_m(s)}{Bl\, Z_{st}(s)}. \tag{3}$$

With this setup, the closed-form expression of the achieved acoustic impedance at the electroacoustic resonator is given by:

$$Z_s(s) = \frac{P_t(s)}{V(s)} = \frac{Z_m(s)}{S_d - Bl\Theta(s)}. \tag{4}$$

2.3 Assigning a prescribed MDOF impedance

The MDOF resonator acoustic impedance considered here consists in the parallel arrangement of n one-degree-of-freedom acoustic resonators as:

$$Z_{st}(s) = \frac{1}{\sum_{k=1}^{n} j\omega \frac{M_{ms}}{\nu_{2k-1}S_d} + R_{st,k} + \frac{1}{j\omega}\frac{1}{S_d\nu_{2k}C_{mc}}} \tag{5}$$

where $R_{st,k}$ represents target acoustic resistances, and ν_i are real coefficients.

3 SIMULATION AND EXPERIMENTAL ASSESSMENT

The electrodynamic loudspeaker is a Peerless SDS-P830657, in a closed cabinet of volume $V_b = 10$ dm^3 (see Table 1). The various control parameters (C0, C2 and C3) are given in Table 2. The theoretical acoustic impedance achieved with each control configuration is processed according to Equations 3-5, and compared to experimental results measured in an impedance tube, as illustrated on Figure 2. The experimental results are in a good agreement with the analytical model, and show the significant extension of the resonator bandwidth when coupled with the proposed MDOF control architecture.

Parameter	Notation	Value	Unit
Effective piston area	S_d	151	cm^2
Moving mass	M_{ms}	12.9	g
Mechanical resistance	R_{ms}	1.23	N.s.m^1
Mechanical compliance	C_{mc}	260.79	μm.N^1
Force factor	Bl	5.98	N.A^1

Table 1. Peerless SDS-P830657 Thiele-Small parameters.

4 CONCLUDING REMARKS

The present concept aims at achieving MDOF resonators out of a conventional loudspeaker and a simple control law. The control architecture allows broadening the resonator bandwidth compared to the passive resonator (configuration $C0$). It is also possible to assign different values of acoustic resistance $R_{st,k}$ at prescribed frequencies $f_k = \frac{\nu_{2k-1}}{\nu_{2k}}\frac{1}{2\pi\sqrt{M_{ms}C_{mc}}}$, which is

3

Table 2. Control parameter values of one (C0), two (C2), and three (C3) DOF resonators.

	ν_1	R_{st_1}	ν_2	ν_3	R_{st_3}	ν_4	ν_5	R_{st_5}	ν_6
	(-)	(Pa·s·m^{-1})	(-)	(-)	(Pa·s·m^{-1})	(-)	(-)	(Pa·s·m^{-1})	(-)
C0	1.00	R_{ms}/S_d	1.00	-	-	-	-	-	-
C2	2.16	67.01	2.36	4.09	55.24	22.64	-	-	-
C3	1.86	85.99	2.86	1.32	54.81	1.11	3.07	57.32	21.03
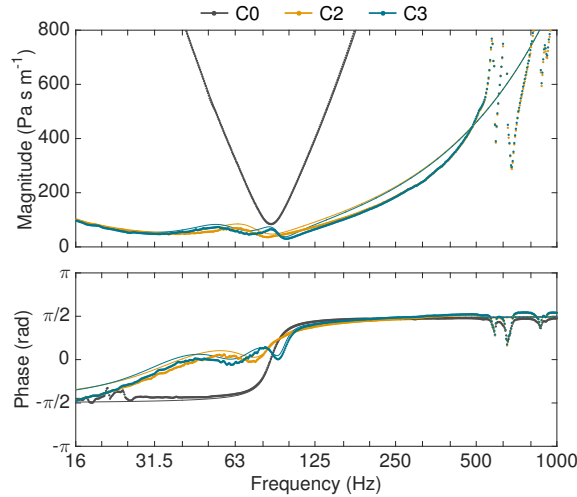
Figure 2: Bode plot of the specific acoustic impedance of the electroacoustic absorber computed (solid lines) and measured (dotted lines) in cases C0, C2, and C3.

useful in the context of room modes damping [6]. This concept is readily applicable to low-frequency noise reduction

REFERENCES

[1] T. J. Cox and P. D'Antonio. *Acoustic absorbers and diffusers: Theory, design and application*. Taylor and Francis, 2nd edition, 2009.

[2] H. Lissek, R. Boulandet, and R. Fleury. Electroacoustic absorbers: Bridging the gap between shunt loudspeakers and active sound absorption. *J. Acous. Soc. of Am.*, 129(5):2968, 2011.

[3] H. Lissek, R. Boulandet, and Etienne Rivet. Optimization of electric shunt resonant circuits for electroacoustic absorbers. In *Acoustics 2012*, Nantes, France, April 23-27, 2012.

[4] R. Boulandet and H. Lissek. Toward broadband electroacoustic resonators through optimized feedback control strategies. *J. Sound and Vibration*, 333(20):4810 – 4825, 2014.

[5] E. Rivet, S. Karkar, and H. Lissek. Broadband low-frequency electroacoustic absorbers through hybrid sensor-/shunt-based impedance control. *IEEE Transactions on Control Systems Technology*, 25(1):63–72, Jan 2017.

[6] E. Rivet, S. Karkar, H. Lissek, T. Thorsen, and V. Adam. Experimental assessment of low-frequency electroacoustic absorbers for modal equalization in actual listening rooms. In *Audio Engineering Society Convention 140*, May 2016.

DESIGN AND EXPERIMENTAL VALIDATION OF AN ACTIVE ACOUSTIC LINER FOR AIRCRAFT ENGINE NOISE REDUCTION

G. MATTEN[1], M. OUISSE[1], M. COLLET[2], S. KARKAR[2], H. LISSEK[3], R. BOULANDET[3], M. VERSAEVEL[4]

[1]Univ. Bourgogne Franche-Comté
FEMTO-ST Institute
CNRS/UFC/ENSMM/UTBM
Department of Applied Mechanics
25000 Besançon, FRANCE
Email: gael.matten@femto-st.fr, morvan.ouisse@femto-st.fr

[2]Ecole Centrale de Lyon
36 av Guy de Collongue, 69131 Lyon, FRANCE
Email: manuel.collet@ec-lyon.fr, sami.karkar@ec-lyon.fr

[3]EPFL STI IEL LTS2
Station 11, 1015 Lausanne, SWITZERLAND
Email: herve.lissek@epfl.ch, romain.boulandet@epfl.ch

[4]SAFRAN Nacelles
Route du Pont 8 - BP91
LH089 - A22
76700 Gonfreville l'Orcher, FRANCE
Email: marc.versaevel@safran-nacelles.com

ABSTRACT

The use of acoustic liners in aviation industry is a quite common solution for reducing the engines acoustic emissions. Although the current solutions based on single or multilayer liners are efficient and compact for the mid and high frequencies, noise mitigation in the low frequencies would require large volumes, making the integration in the nacelle difficult. Moreover, the passive liners are tuned to attenuate fixed frequencies and are optimized for specific flights regimes. An active electroacoustic skin based on a distribution of loudspeaker and microphones is presented here. The acoustic impedance is controlled by an embedded electronic system and can be changed in real time. Compared to a conventional passive liner, it is shown that the resonance frequency of the active skin can be adjusted to better match the flight phase and that the performance is better at low frequency. An experimental campaign in a wind tunnel has been performed and is presented here.

1   INTRODUCTION

The reduction of noise pollution due to civil aviation has become a major challenge for aircraft manufacturers. The use of passive liners inside aircraft nacelles is commonly used to attenuate the acoustic emissions of aircrafts but the efficiency is not broadband and the attenuation in low frequencies is poor. Moreover, the optimum acoustic impedance of the liner evolves according to the flight phase. Active noise control strategies have already shown their effectiveness [1, 2]. The solution proposed here lies in the use of an active coating for acoustic impedance control. A prototype of this system is presented hereinafter.

2   ACOUSTIC IMPEDANCE CONTROL

The active skin presented here is made of an arrangement of unit cells used to synthesize a target acoustic impedance. A unit cell is the assembly of a speaker (actuator), four microphones (sensors) and an electronic control stage. The strategy consists in estimating the pressure at the center of the cell by averaging the signal of the four microphones and to act on the velocity field by the action of the membrane of the speaker.

The equation of control has been established in [3] and is based on the Thiele/Small speaker model [4]:

$$H_{loc}(p) = \frac{S_d}{Bl} \left(1 - \frac{M_{ms}p^2 + R_{ms}p + \frac{1}{C_{ms}}}{\mu_1 M_{ms}p^2 + S_d R_{at}p + \frac{\mu_2}{C_{ms}}} \right) \tag{1}$$

With :

- p : Laplace variable;

- S_d : Effective piston area;

- Bl : Electromechanical conversion factor ;

- M_{ms} : Mass of the mobile assembly;

- R_{ms} : Mechanical resistance;

- C_{ms} : Compliance of membrane suspensions;

- R_{at} : Target acoustic resistance of the mobile assembly;

- $\mu_1, \mu_2 \in [0; 1]$: Control parameters.

This control law is used to alter the dynamics of the electrodynamic actuator and would ideally synthesize a purely resistive acoustic impedance when $\mu_1 = \mu_2 = 0$. For stability considerations, these parameters can never be null, which would be equivalent to cancel the mass and the compliance of the loudspeaker. However μ_1 controls the apparent mass of the speaker and μ_2 its compliance.

3   EXPERIMENTAL DEVELOPMENTS

3.1   Prototype of active skin

The prototype is made of thirty 50x50mm cells. Each cell is the assembly of a speaker and each corner is equipped with a microphone (see figure 1). The current through the speaker is

2

controlled by a Howland current source [5]. A micro-controller computes the equation driving the dynamic of the electric current in the speaker reel depending on the average measured pressure. The output current is updated at a rate of 50kHz. The computations are performed locally but all the cells are connected to an interface card through a serial bus. Thus the parameters of all the cells can be changed and local features (RMS pressure and RMS current) are accessible from a computer.
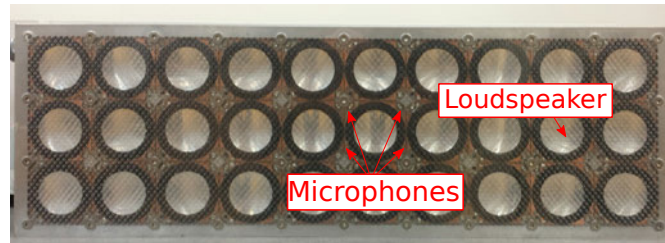
Figure 1: Picture of the active skin prototype comprising 30 loudspeakers and 120 microphones.

3.2 Power consumption

With the control off, the active skin has a power of 12.5W, including 0.2W per micro-controller. The electronics is able to feed each speaker with a current of 0.25A *i.e.* a power of 1.25W. The maximum electric power is then 50W. In practice, with a controlled noise of 110dB RMS, only 5mA are required per speaker so the overall power is 20W for 30 cells.

3.3 Wind tunnel

The active skin prototype has been wall mounted in the wind tunnel FDF of the Netherlands Aerospace Centre (NLR). The test bench is shown in figure 2. The difference of acoustic intensity between the upstream and the downstream reverberant rooms gives the IL (*insertion loss*). The IL evaluates the acoustic energy absorbed by the active skin. The acoustic source is placed in the upstream room (downstream configuration) or in the downstream room (upstream configuration). Tests have been run with air flow up to Mach 0.15. The flow noise has saturated the microphones for flows faster that Mach 0.15. The figure 3 shows the results with flow in downstream and upstream configuration and the results without flow for a target resistance of $\frac{\rho c}{2}$. Mitigations up to 16 dB have been measured. The resonance frequency of the speaker is denoted f_0. The flow does not affect significantly the efficiency.
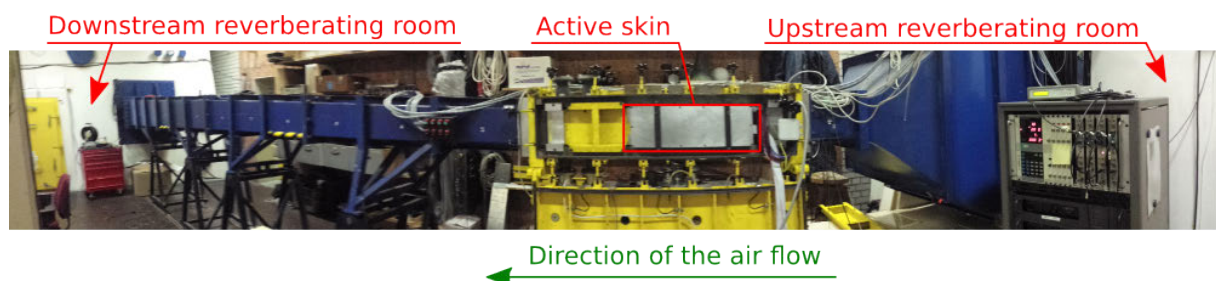
Figure 2. Experimental validation in a wind tunnel (NLR,the Netherlands).

3
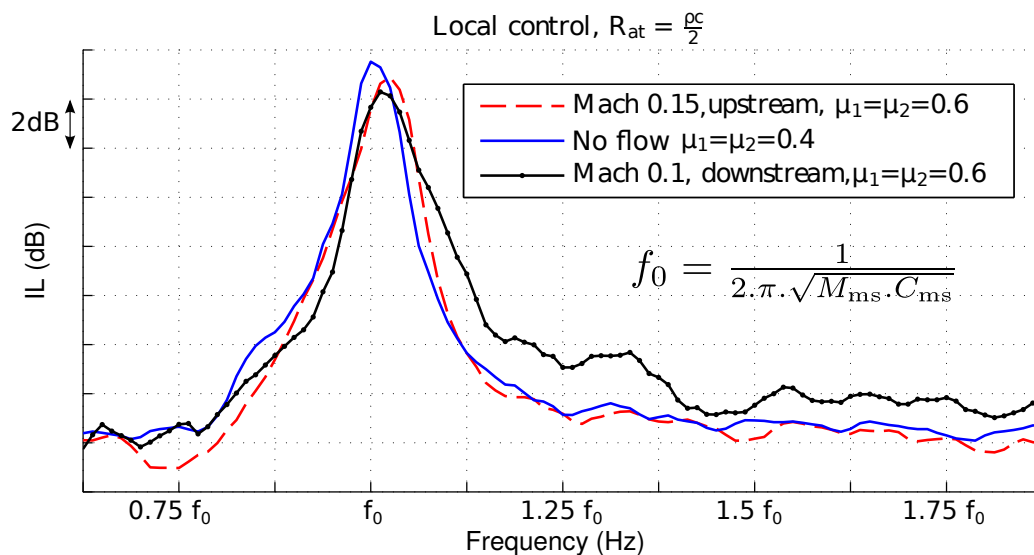
Figure 3. Insertion Loss for a target resistance $R_{\mathrm{at}} = \frac{\rho c}{2}$ with and without flow.

4 CONCLUSION AND PERSPECTIVES

The prototype presented here is an active skin able to synthesize specified acoustic impedances. It aims at replacing passive liners in aircraft nacelles and has been tested in a wind tunnel with airflow up to Mach 0.15. *Insertion Loss* up to 16 dB have been measured. The acoustic impedance of the skin is re-programmable in real time so adaptive strategies can be implemented to best match the phases of flight.

5 ACKNOWLEDGEMENTS

REFERENCES

[1] Manuel Collet, Petr David, and Marc Berthillier. Active acoustical impedance using distributed electrodynamical transducers. *The Journal of the Acoustical Society of America*, 125(2):882–94, feb 2009.

[2] Hervé Lissek, Romain Boulandet, and Romain Fleury. Electroacoustic absorbers: bridging the gap between shunt loudspeakers and active sound absorption. *The Journal of the Acoustical Society of America*, 129(5):2968–78, may 2011.

[3] Etienne Rivet, Sami Karkar, and Herve Lissek. Broadband Low-Frequency Electroacoustic Absorbers Through Hybrid Sensor-/Shunt-Based Impedance Control. *IEEE Transactions on Control Systems Technology*, 25(1):63–72, jan 2017.

[4] Richard H Small. Closed-Box Loudspeaker Systems-Part 1: Analysis. *J. Audio Eng. Soc*, 20(10):798–808, 1972.

[5] Alexander S Ross, G J Saulnier, J C Newell, and D Isaacson. Current source design for electrical impedance tomography. *Physiological measurement*, 24(2):509–516, may 2003.

INVERSE CHARACTERIZATION OF SANDWICH STRUCTURES USING SINGLE-SHOT WAVE SPEED MEASUREMENTS

Christophe Droz[1*] , Olivier Bareille[1] and Mohamed Ichchou[1]

[1]Tribology and System Dynamics Laboratory (LTDS)
Ecole Centrale de Lyon, Ecully, FRANCE
Email: Christophe.Droz@ec-lyon.fr, Olivier.Bareille@ec-lyon.fr,
Mohamed.Ichchou@ec-lyon.fr

ABSTRACT

We propose an innovative method for the local inverse characterization of sandwich panels using a simple experimental procedure based on single shot pulse measurements. The method exploits a typical wave conversion phenomenon called bending-to-shear transition, producing a local energy velocity maximum within the transition bandwidth. Analytic expressions are derived for the first wave transition and used to retrieve skin's tensile modulus and equivalent honeycomb core's shear modulus from the transition frequency and the maximal group velocity. A simple iterative procedure is described to identify the transition frequency by comparison of the time delays between the pulse source and single measurement point. The group velocity can then be advantageously estimated using First Phase Arrival (FPA) times. A carbon fiber-reinforced sandwich panel with Nomex honeycomb core is considered for case study. The proposed method exhibits considerably reduced measuring and post-processing times, while experimental results are in good agreement with static measurements and the results from the Inhomogeneous Wave Correlation (IWC) method.

1   INTRODUCTION

Modelling sandwich structures in vibroacoustic environments is a challenging task due to the difficulty to perform accurate models of composite structures in the medium frequency range. Although the literature is abundant on mechanical characteristics of sandwich panels, the material properties of a sandwich structure can change significantly depending on the manufacturing process, or the panel location considered. It is therefore crucial to perform a thorough characterization, rather than rely on material values reported in literature. Besides, the values obtained using static measurements can result in considerable discrepancies in the vibroacoustic range. In a context of increasing need for reliable and cost-effective characterization techniques, a number of developments were made for sandwich structures. One can cite the work of Karakoc and Freund [1] on the experimental determination of the compliance matrix of Nomex structures, or the identification technique proposed by Matter et al. [2] for evaluating the elastic and damping properties of sandwich laminates with soft cores from modal analyses.In composites, several studies have been conducted on the use of high-frequency waves to retrieve elastic constants from energy velocity measurements [3] with remarkable accuracy. However, the rapid development of the so-called "meta-structures", involving stiffened or locally resonant components distributed along periodic patterns yields considerable challenges in terms of dispersion analyses, hence for the use of these high-frequency techniques. Model-based inverse identification of the equivalent material properties in medium frequencies was also investigated. The Inhomogeneous Wave Correlation (IWC) method was developed for the identification of the dispersion curves. Material estimation is based on the wavenumber measurement technique developed by McDaniels and Shepard [4]. These methods however require to measure and post-process the entire displacement field to extract the *k-space*, leading to expensive and time-consuming characterizations. This paper presents a wave-based characterization technique for sandwich panels in the medium frequencies based on single-shot measurements [5], where complex scattering effects can be avoided. It combines the advantage of involving a simple experimental set-up with the need for local or in-situ characterizations procedures.

2   TRANSITION ANALYSIS: THEORY AND SIMULATIONS

Consider the propagation of flexural waves in a symmetric sandwich plate along the in-plane direction θ, where k is the directional wavenumber $k_\theta = f(\mu, S_\theta, D_\theta)$. Assuming the rotation inertia is negligible compared with the shear effects and the bending stiffness per unit width of the skins are small in comparison with the one of the plate, the dispersion relation becomes:

$$k^2 = \frac{\mu}{2S}\left(\omega^2 + \omega\sqrt{\omega^2 + \frac{4S^2}{\mu D}}\right) \tag{1}$$

where $S = h_c G_c \left(1 + \frac{h_s}{h_c}\right)^2$ and $D \simeq E_s h_s \left(\frac{h_c^2}{2} + h_c h_s + \frac{2h_s^2}{3}\right)$ are the transverse shear rigidity and bending stiffness of the plate, μ is the mass per unit area, while h_s h_c G_c and E_s denote the skin's and core's thickness, shear coefficient and Young modulus, respectively. The group velocity reaches a local maximum when $\frac{\partial c_g}{\partial \omega} = 0$ admits a solution, resulting in the following equation:

$$\frac{\omega^2\Omega - \Omega^3 + 2\omega_0^2\omega}{\left(\omega^2\Omega + \Omega^3 + 2\omega_0\omega^2 + 2\omega^3\right)\sqrt{\frac{\mu}{2S}(\omega\Omega + \omega^2)}} = 0 \tag{2}$$

2

The solution $\omega_T = \dfrac{2S}{\sqrt{3\mu D}}$ provides a definition of the so-called transition frequency. Note that

the maximal velocity, $c_{max} = \dfrac{4}{3}\sqrt{\dfrac{2S}{3\mu}}$ is independent of the bending stiffness D of the plate.

Material	Thickness	Density (kg.m^{-1})	Young modulus (GPa)	Shear modulus (MPa)
Skin	0.3 mm	1451	$E_s = 81$	$G_s = 2780$
Core	25 mm	53	$E_c = 5.23$	$G_c = 50$

Table 1: Dimensions and material characteristics of the sandwich beam. Note that the core is described as an homogeneous medium. The beam's width is $l_y = 10$ mm and the damping is not considered in this model.

A numerical case-study is considered for the sandwich waveguide described in Table 1. The group velocity is estimated using tone burst signals of amplitude $U_0 = 1\,\mu$m involving n_0 cycles at the frequency f_0 with Hanning window defined for $t \leq \dfrac{n_0}{f_0}$ by: $U_0 \sin\left(\dfrac{\pi f_0 t}{n_0}\right)\sin(2\pi f_0 t)$

$$u(t) = U_0 \sin\left(\frac{\pi f_0 t}{n_0}\right)\sin(2\pi f_0 t) \tag{3}$$

Noteworthy, the velocities shown in Figure 1 are in very good agreement with analytical results. The accuracy is good, considering the frequency spectrum bandwidth of the excitation signals. Using the proposed wave speed measurements results in a 2.1% overestimation of the shear S coefficient. The transition is observed at 1.8 kHz at the velocity $c_{max} = 831.6$ m.s^{-1}. This yields:

$$E_{\text{trans}} = 81.16\,\text{GPa} \quad \text{and} \quad G_{\text{trans}} = 50.04\,\text{MPa} \tag{4}$$

which is is very good agreement with the exact material parameters shown in Table 1.
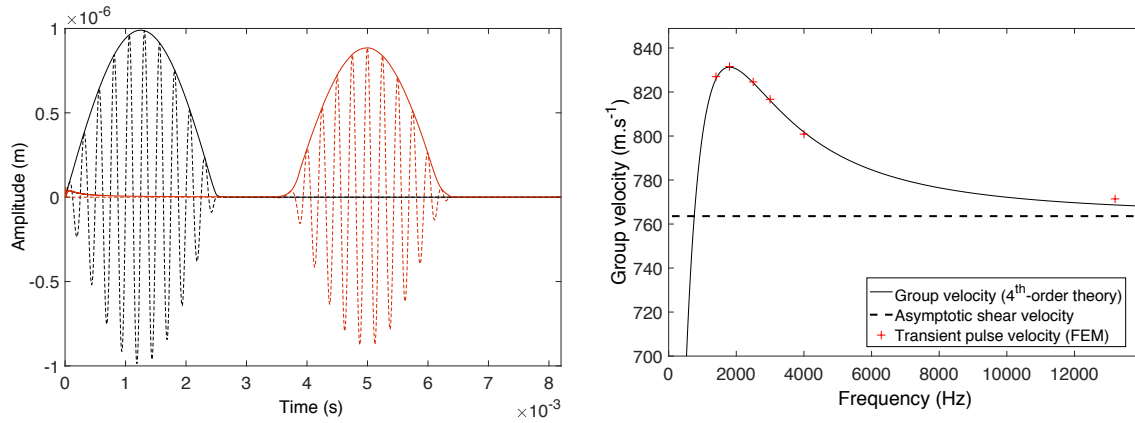
Figure 1: (a) Transient FEM simulation of a short monochromatic wave pulse, pulsation is 4000 Hz, propagation is considered along 3 m. (b) Dispersion curves of the sandwich waveguide: comparison with FEM simulations using group velocity measurements.

3   EXPERIMENTAL RESULTS

This method based on transition and maximum velocity measurements is tested on a 60 cm × 288 cm sandwich panel made of a 10 mm-thick Nomex honeycomb core involving a 3.2 mm cell size, while propagation is considered in the W-direction. The core is surrounded by 0.6 mm-thick Hexforce skins with multi-axial carbon-reinforced fibres mixed with SR1700 epoxy resin.

3

The density of the skins is $\rho_s = 1451\,\text{kg.m}^{-3}$ and the core's density is measured using the overall panel's weight $\rho_c = 99\,\text{kg.m}^{-3}$ (manufacturer: $96\,\text{kg.m}^{-3}$). The experimental set-up consists in a shaker producing wave pulses and a measurement point located at 1 m from the excitation. Results from the Inhomogeneous Wave Correlation (IWC) method and the proposed characterisation strategy are compared in Table 2 with the manufacturer's data based on static measurements on a different sample. It shows a very good accuracy compared with other wave-based method, considering that the proposed method only involves two measurement points.

Parameter	IWC method (67 points)	Manufacturer (static)	**Proposed method (2 points, ToF)**
E (GPa)	62	70	**69.8**
G (MPa)	37.8	[30 − 38]	**36.5**

Table 2: Comparison of the estimated parameters obtained by two wave-based methods and manufacturer's values.

4 CONCLUDING REMARKS

To summarize, the paper presents a definition for the transition phenomenon using the existence of a local energy velocity maxima within the wave transition bandwidth and an in-situ procedure for measuring effective mechanical parameters of sandwich plates in the vibroacoustic range, described in Figure 2.
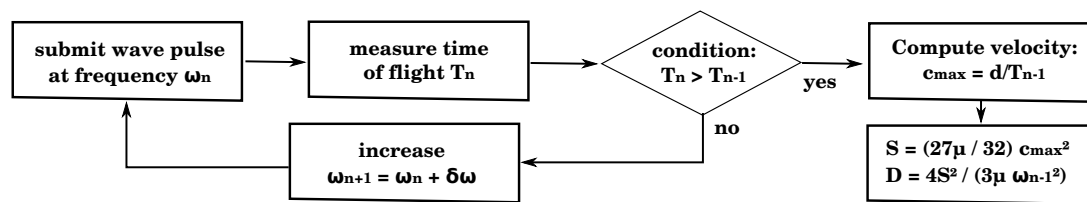
Figure 2. Experimental procedure summarized as a flow diagram.

REFERENCES

[1] A. Karakoç and J. Freund. Experimental studies on mechanical properties of cellular structures using nomex honeycomb cores. *Comp. Struct.*, 94(6):2017–2024, 2012.

[2] M. Matter, T. Gmür, J. Cugnoni, and A. Schorderet. Identification of the elastic and damping properties in sandwich structures with a low core-to-skin stiffness ratio. *Compos. Struct.*, 93(2):331–341, 2011.

[3] T-T Wu and Y-H Liu. On the measurement of anisotropic elastic constants of fiber-reinforced composite plate using ultrasonic bulk wave and laser generated lamb wave. *Ultrasonics*, 37(6):405–412, 1999.

[4] J.G. McDaniel and W.S. Shepard Jr. Estimation of structural wave numbers from spatially sparse response measurements. *J. Acous. Soc. Am.*, 108(4):1674–1682, 2000.

[5] C. Droz, O. Bareille, and M. Ichchou. A new procedure for the determination of structural characteristics of sandwich plates in medium frequencies. *Composites Part B: Engineering (2017)*, doi:10.1016/j.compositesb.2016.12.023.

NUMERICAL MODEL TO SIMULATE THE FORWARD AND REVERSE SOUND TRANSMISION MECHANISM IN HEARING

J. Camacho[1], J. Garcia-Manrique[1] and A. Gonzalez-Herrera[1*]

[1]Department of Civil Engineering, Materials and Fabrication
University of Malaga, Malaga, SPAIN
Email: javepz@gmail.com, josegmo@uma.es, agh@uma.es

ABSTRACT

The human hearing system captures acoustic waves in air that are transmitted to the cochlea where are converted in nerve signal. Meanwhile, at the cochlea, some sensory cell are active provoking sound transmission in the reverse direction. These called otoacoustic emissions are measured in the ear canal as diagnostic method. Forward and reverse transmission mechanisms are complex being a matter of research. Its study presents great difficulty, either by experimental or numerical methods.

A simplified experiment has been designed to evaluate both mechanisms. It consists of a system with the basic elements (air, tympanic membrane and ossicular chain).The present paper presents results corresponding to a previous numerical study. Methodology is described, it is based in previous work. Main results are shown in terms of modal analysis and sound pressure fields.

Comparing with the behavior of a membrane , the presence of the umbo adds stiffness and mass to the system. Results prove that the effect of the mass is more significant, increasing the number of modes present in the range of frequency of interest. Comparing forward and reverse mechanisms, the main difference is on the side of the stimuli, similar to the opposite side.

1   INTRODUCTION

The human hearing system is a complex mechanical system intended to capture acoustic waves in air and transmit them to the cochlea responsible for the transduction in a nerve signal. In its basic behaviour sound is collected by the pinna (ear) and conducted through the ear canal to the tympanic membrane (TM). The TM transforms the acoustic waves in mechanic vibrations which are transmitted through the ossicular chain to the oval windows on the cochlea. There, an acoustic wave is propagated in the fluid displacing the basilar membrane where sensory cells are placed (hair cells). These cells produce the nerve signal. This is the forward transmission mechanism.
Part of these cells (outer hair cells) present motility capabilities. This active mechanism enhances the sensitivity of the transduction and produces sound inside the cochlea (otoacoustic emissions, OAEs). This wave is transmitted to the ear canal. This is the reverse transmission mechanism. OAEs can be measured at the ear canal and is the base for different diagnostic techniques.
Forward and reverse transmission mechanisms are not symmetric and both are matter of research currently. Its study, either by experimental or numerical methods [1,2,3], presents great difficulty due to the complexity of the system and the coupling of different phenomena. So a simplified experiment has been designed to evaluate both mechanisms. It consists of a system where the basic element are present (air, TM and ossicular chain) and can be controlled. In the present paper, results corresponding to a previous study based on a Finite Element model are shown.

2   EXPERIMENT DESCRIPTION

An scheme of the experiment is displayed on Fig 1. It is based in previous works where a membrane was subject to a sound stimuli and its response measured by different methods [4,5]. The membrane is supported by a baffle that blocks sound to the opposite side.
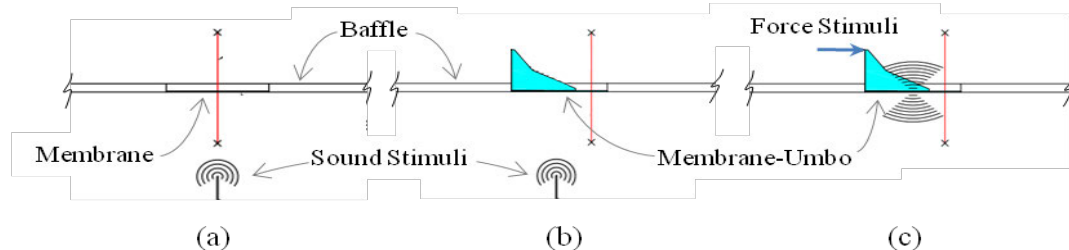
Figure 1. Experiment setup.

An additional piece is added to the membrane. It represents the part of the malleus bone in contact with the TM (umbo). This is a simplified way to represent the effect of the ossicular chain. With this system, forward and reverse mechanism can be modelled. When the system is subject to sound stimuli, displacement can be obtained at the tip of the umbo (Forward transmission, Fig 1b). Alternatively, a force or displacement can be applied at the tip and membrane motion and sound pressure can be measured (Reverse transmission, Fig 1c).
Dimensions resemble the human system. Diameter is 1 cm and thickness 100 um. The umbo extend to 2/3 of the diameter. The umbo high is 0.5 cm and the thickness 0.3 mm. Stimuli is applied at a distance of 1 cm from the membrane. The mechanical properties of the material are: density 1200 Kg/m^3, Poisson´s ratio 0.35 and Young´s modulus 2 GPa.

3   NUMERICAL METHODOLOGY

A brief description of the methodology will be made. It follows previous works and details can be consulted in references [4,5]. The FE model is shown in Fig 2 with a detail of the membrane-

2

umbo model in Fig 2b. It is composed by three parts, a rigid solid (baffle and sound source), an elastic body (membrane-umbo system) and the fluid surrounding. The solid domain is considered as a rigid body and is represented by the correspondent motion constraint (as rigid surfaces).
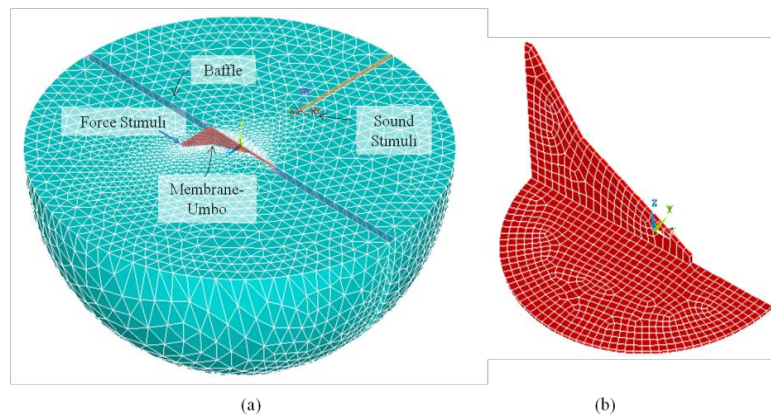
Figure 2. Finite Element Model.

The others two domains conform the numerical model, the elastic domain corresponding to the membrane-umbo system and the fluid domain represents the surrounding air. A coupled fluid-structure interaction problem is implemented in their contact areas. The fluid is bounded by an sphere to represent open field condition. Its surface is meshed with an element which represents a fluid domain that extends to infinity. The speaker is modeled as a rigid cylinder with dimensions similar to the real one. Symmetry is applied and only half problem is modeled. The fluid is meshed with acoustic elements and the membrane with eight nodes solid element.

The influence of other modeling parameter (mesh size, element formulation, sphere size...) has been analyzed and carefully selected. Especial care is paid to the mesh size, selected according to previous studies [5]. An harmonic analysis has been done for a range of frequencies from 0 to 20 kHz. Additional modal analysis has been done to obtain modal shapes and frequencies.

4   MODAL ANALYSIS

Modal analysis provides a first sight on the response of the system. Mode shapes are displayed on Fig 3 and frequencies in Table 1. The membrane follows the classic pattern. Membrane-umbo modes show more irregularity. Unless the first frequency is similar (aprox 2.5 kHz), the other modes tend to be lower with more modes present in the range of frequency of study. This means that the stiffness increase is cancelled by the mass added.
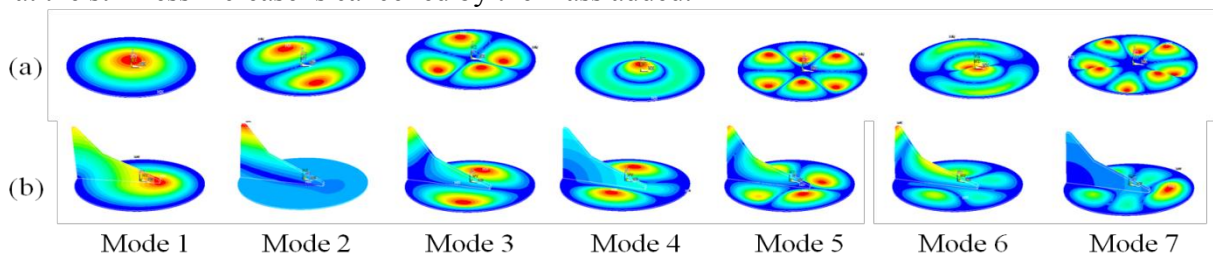
Figure 3. Modal shapes. Membrane (a) and Membrane-Umbo (b)

mode	1	2	3	4	5	6	7	8	9	10
Membrane	2.56	5.33	8.78	10.1	12.8	15.4	17.5	21.5	22.7	28.2
Membrane-Umbo	2.4	2.9	6.3	8.1	10	10.7	13.1	14.4	16.7	17.2

Table 1. Modal Frequencies (kHz).

3

5   RESULTS

Many variables can be obtained (velocity, sound pressure). Sound pressure fields are one of the most relevant. On Fig. 4, sound pressure is plotted along lines normal to the membrane (shown in Fig 1) with a double spatial and frequency domain. Spatial z axis corresponds to the distance to the membrane, placed at z=0, negative values are closer to the stimuli. The different behaviour are easily visualized. Comparing (a) and (b), the presence of the umbo is manifest with a higher complexity in the response due to the higher number of modes present in the range of frequency of interest. Comparing forward (b) and reverse (c) behaviour, it can be observed how the response is symmetric in the reverse case, and very similar to that obtained in (b) for the sound transmitted to the opposite side of the stimuli.
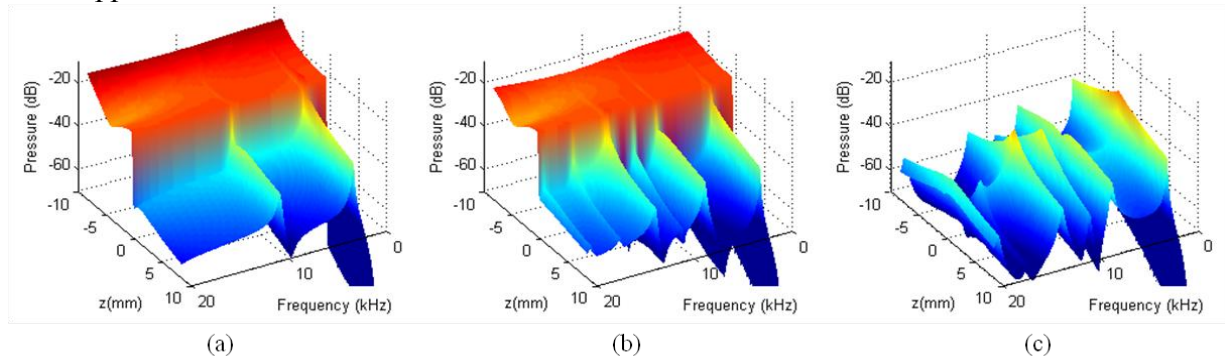
Figure 4. Sound pressure. Membrane (a), Membrane-Umbo forward (b) and reverse (c)

6   CONCLUDING REMARKS

A simplified numerical model to simulate the forward and reverse sound transmission mechanism has been build. This model will be used to adjust proper dimensions to facilitate the experiment. The presence of the umbo adds stiffness and mass to the system. Results prove that the effect of the mass is more significant, increasing the number of modes present in the range of frequency of interest. Comparing forward and reverse mechanisms the main difference is in the response on the side of the membrane where the stimuli is present.

REFERENCES

[1]   W. Dong, E.S. Olson, Middle ear forward and reverse transmission in gerbil. *Journal of Neurophysiology* 95(5), 2951-2961, 2006

[2]   J.T. Cheng, E. Harrington, R. Horwitz, C. Furlong, J.J. Rosowski, *Progress in Auditory Biomechanics, 11th International Mechanics of Hearing Workshop, AIP*. 1403:521-527, 2011

[3]   C. Stieger, J.J. Rosowski, H.H. Nakajima, Comparison of forward (ear-canal) and reverse (round-window) sound stimulation of the cochlea. *Hearing Research*. 301:105-114, 2013

[4]   A. Gonzalez-Herrera, J.T. Cheng, J.J. Rosowski, Analysis of the influence of the speaker position on the study of the dynamic behavior of a membrane combining holography technique and finite element models. *22nd Int. Cong. on Sound and Vibration (IIAV)*, Florence, Italy, 2015

[5]   A. Gonzalez-Herrera, E.S. Olson, A study of sound transmission in an abstract middle ear using physical and finite element models. *J. Acoust. Soc. Am*. 138(5): 2972–2985, 2015

TIMPANIC MEMBRANE PRESTRAIN EVALUATION BASED ON THE DYNAMIC REPSONSE

L. Caminos[1] and A. Gonzalez-Herrera[2*]

[1]Department of Mechanical Engineering
University of Tachira, VENEZUELA
Email: lcaminos@unet.edu.ve

[2]Department of Civil Engineering, Materials and Fabrication
University of Malaga, Malaga, SPAIN
Email: agh@uma.es

ABSTRACT

Sound transmission in human hearing is easy to understand at low frequencies but at higher frequencies the tympanic membrane (TM) presents complex vibration patterns. They have been studied experimentally with holography and numerically with Finite Element models. These models need proper material properties to be valid. Particularly, the Young's Modulus of the TM is a key parameter. A broad range of values has been obtained depending on the methodology used (20 to 300 MPa). Controversy exists about its correct value. Passive prestrain can be argued as a cause of differences. It is present on dynamic tests but not in static tests.
 In this paper, modal analysis is used to check the potential effect of prestrain as the cause of the higher stiffness observed. As direct model update is difficult due to the complexity of the system a methodology based on comparison of modal shapes with experimental patterns observed with holography will be applied to identify prestrain level.
Different FE models are employed to obtain modal values. Prestrain provides similar shapes but frequencies proportional to the prestrain (stiffness). Comparing with experimental patterns at high frequencies a prestrain value can be identify coherent with the properties commonly accepted (E=32 MPa).

1   INTRODUCTION

At low frequencies, sound transmission in human hearing is easy to understand. The Tympanic Membrane (TM) captures acoustic waves and by means of a piston-like motion transfers air sound pressure waves into the cochlea. However, at higher frequencies the TM motion is not so simple, appearing complex vibration patterns. These patterns have been studied experimentally with techniques as holography. Rosowski et al. [1] established a qualitative description based on the pattern observed and related with the range of frequency where they were present. They considered a simple pattern when only one maximum displacement zone was observed (below 2 kHz), complex pattern when more than one maximum appeared (2 to 8 kHz) and ordered pattern when a high number of maximum spread along the membrane (above 8 kHz).

The other alternative of study is numerical simulation. Finite Element (FE) models have been used as a tool to study the behaviour of the system [2,3]. Nevertheless, uncertainties regarding the material properties limit the conclusions. This is particularly significant in the case of the study of the TM. Many experimental works have been devoted to the determination of the Young's Modulus of the TM. Most of the results obtained are in the range 20 to 40 MPa, being the more accepted value 32 MPa. Some are based on tension tests on small samples and other use different indentation techniques. Fay et al. [4] suggested that these values could be underestimated; the main difference in their methodology was that it was based on the dynamic response of the TM. By using composite laminate theory and correlating experimental dynamic wave length patterns they suggested values from 100 to 300 MPa.

There exists controversy about the correct values for this parameter. One of the reasons of this higher stiffness value could be found on the potential effect of prestrain on the membrane. It would be present on dynamic tests but not in static tests. Passive prestrain has been named by several authors but no quantitative estimation has been made.

In the present paper, modal analysis is used to check the potential effect of prestrain on the dynamic response of the TM. Direct model update is difficult due to the complexity of the system [2,3] and the experiment itself [1,5]. So a methodology based on comparison of modal shapes with experimental patterns observed with holography will be applied to identify prestrain level.
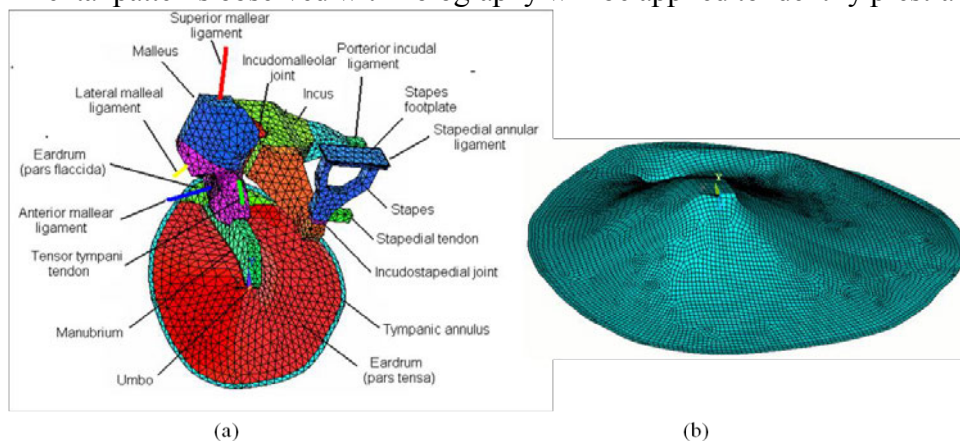
Figure 1. Finite Element Models. TOS model (a) and simplified model (b).

2   NUMERICAL METHODOLOGY

Two different FE models will be shown. The first one includes all the element of the middle ear, it will be referred as the Tympanic-Ossicular System (TOS) model (Fig 1a). The second one, only include the TM and the approximate effect of the manubrium (Fig 1b).

The TOS FE model was built with a geometric model of the different components, they were meshed and additional components and boundary condition added. The anatomic measures and functional properties were based on published data [2,3]. TM Young Modulus is 32 MPa.

Regarding the simplified model (Fig. 1b), most of the component has been removed. The connection with the manubrium is modelled with shell elements but the mechanical properties represent the inertia and stiffness of the ossicular chain. These equivalent properties has been obtained comparing with the TOS model. A key difference is that the membrane has been meshed with a higher number of elements to increase the accuracy at high frequency.

3   MODAL ANALYSIS

A modal analysis of the TOS was made as reference. Some selected mode shape has been drawn in Fig. 2a. Different types of modes are present, some reflect a TM vibration pattern and the classic piston-like motion (modes 11 and 13). Modes 14 and 25 correspond to the transition to complex pattern and mode 29 represent the ordered pattern. The results of the modal analysis of the simplified model are on Fig. 2b. It can be seen the equivalence between both system at certain modes (with different numbering). Mode 7 is the first complex patterns. Modes 11 represents the transition to ordered pattern. Finally, mode 50 correspond clearly to the ordered pattern. The small element size used in this model to mesh the TM captures these modes accurately. At this frequency range, the absence of the ossicular chain has a low influence, so for the purpose of the present study this simplified model is acceptable.

(a)

| Mode 3: | Mode 11: | Mode 13: | Mode 14: | Mode 25: | Mode 29: |
| 330.8 Hz | 880.5 Hz | 1073.3 Hz | 1552.7 Hz | 2343.3 Hz | 2683.1 Hz |

(b)

| Mode 1: | Mode 2: | Mode 3: | Mode 7: | Mode 11: | Mode 50: |
| 870.2 Hz | 1263.5 Hz | 1555.3 Hz | 2457.4 Hz | 3008 Hz | 6336.3 Hz |
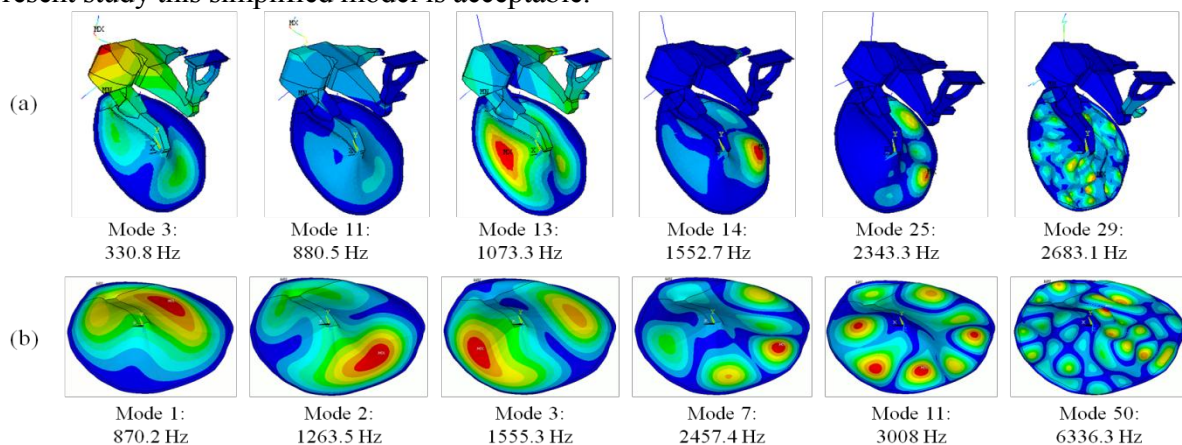
Figure 2. Modal shapes. TOS (a) and simplified model (b)

4   RESULTS

The simplified model has been used to evaluate the influence of passive prestrain in the membrane. It is an aspect of the system with direct influence on the natural frequencies. An homogeneous isotropic strain has been considered for the whole membrane, ranging from 0.1% to 1% ($\varepsilon_{11} = \varepsilon_{22} = 0.001\text{-}0.01$, in the plane of the TM and $\varepsilon_{33} = -2\varepsilon_{11}$). Modal analysis has been repeated for different values of prestrain. Modal shapes are similar but frequencies increase proportionally to the prestrain level. Natural frequencies are plotted in Fig. 3 in terms of the mode number. We can see how the reference values (E = 32 MPa, black triangle, no prestrain) for the simplified model are coincident with the complete system (TOS, white circle).

Observing these results at lower frequencies is difficult to establish clear differences. But, if we focuses on the higher modes, some distinctions can be done comparing with the experimental observation. Considering mode 50 as a reference, this type of pattern has been detected in human at frequencies above 8 kHz [1], in the case without prestrain, this pattern appears at 6 kHz that

3

could be considered very low and erroneous. Following this, the case pst = 0.3% could be considered more realistic. This observation cannot be considered a closed result as the increase of the elastic modulus has the same effect. A different combination of elastic modulus and prestrain provides similar responses. However, it point out to the dynamic analysis as a tool to clarify these effect instead of static tests. Modal shapes comparison is a limited first step procedure that must be followed by the direct numerical-experimental comparison of the response of the system including the fluid interaction. Although some methodological aspect must be solved first [5].
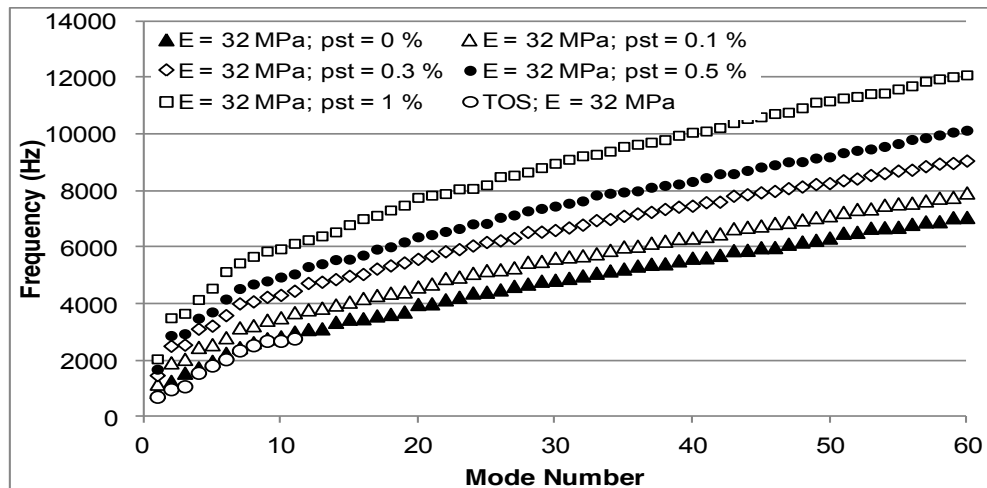
Figure 3. Tympanic Membrane modal frequencies with different prestrain (pst) level

5   CONCLUDING REMARKS

Supported on experimental observation with holography techniques, prestrain has been evaluated on the TM. It causes an stiffness increase difficult to distinguish from the effect of the elastic modulus of the material. This could be the reason for the lack of agreement of its estimation. Comparing modal shapes with experimental patterns, the appearances of complex patterns at higher frequencies can be used to check a valid value for the properties assigned to the model. Modal shapes comparison can be considered an starting step to be followed by direct numerical-experimental comparison of the response of the system.

REFERENCES

[1]   J.J.Rosowski, J.T.Cheng, M.E.Ravicz, N.Hulli, M.Hernandez, E.Harrington, C.Furlong, Computer-assisted time-averaged holograms of the motion of the surface of the mammalian tympanic membrane with sound stimuli of 0.4–25 kHz. *Hearing Research* 253:83-96, 2009

[2]   A. Garcia-Gonzalez, C. Castro-Egler, A. Gonzalez-Herrera, Analysis of the mechano-acoustic influence of the tympanic cavity in the auditory system. *BioMed Eng.OnLine* 15:33, 2016

[3]   L. Caminos, M. Torres, A. Gonzalez–Herrera, Dynamic behavior of the human tympanic membrane using a viscoelastic model. *22 Int. C. Sound and Vibration (IIAV)*, Florence, 2015

[4]   Fay, J., Puria, S., Decraemer, W.F., Steele, C.,. Three approaches for estimating the elastic modulus of the tympanic membrane. *Journal of Biomechanics* 38:1807-1815, 2005

[5]   A. Gonzalez-Herrera, J.T. Cheng, J.J. Rosowski, Analysis of the influence of the speaker position on the study of the dynamic behavior of a membrane combining holography technique and finite element models. *22nd Int. Cong. on Sound and Vibration (IIAV)*, Florence, Italy, 2015

4

IDENTIFICATION OF STRUCTURAL FORCES FROM ACOUSTIC MEASUREMENT USING THE INVERSE SIMPLIFIED ENERGY METHOD

A. Samet[1,2] , M. A. Ben Souf[1,2*] , O. Bareille[2] , T. Fakhfakh[1] , M. N. Ichchou[2] , M. Haddar[1]

[1]Laboratoire de Mécanique, Modélisation et Productique
École Nationale d'Ingénieurs de Sfax, Tunisie
Email: samet.ahmed14@hotmail.com, bensouf.mohamedamine@gmail.com,
tahar.fakhfakh@gmail.com, mohamed.haddar@enis.rnu.tn

[2]Laboratoire de tribologie et dynamique des systémes
École Centrale Lyon, 36 Avenue Guy de Collongue, F-69134 Ecully Cedex, France
Email: olivier.bareille@ec-lyon.fr, Mohamed.Ichchou@ec-lyon.fr

ABSTRACT

The identification of structural forces acting on plate coupled with an acoustic cavity from an acoustic measurement is presented in this paper. An energy-based method called simplified energy method (MES) has been presented to predict the radiation of the plate coupled with an acoustic cavity at high frequency range. This paper proposes to use this energy approach to solve inverse structural problems to identify the structural sources thanks to the inverse formulation of the method (IMES). Example concerning different acoustic measurement points are presented to validate the proposed method.

1   INTRODUCTION

The identification of structural forces acting on structures from operating measurements is an important topic that has been treated by several researchers. Nevertheless, direct measurements of sources are not feasible to quantify the position of the exciting forces. As a result, an inverse process for estimating the exciting sources is often employed to solve the problem. In the range of medium and high frequencies numerical methods as the finite element method (FEM) and the boundary element method (BEM) present limits when the frequency is increased. For that, the energy methods based on energy quantities are often used. Among these methods the simplified energy method (MES). The direct theory formulation has been applied in various domains including beam [1], membrane and plates [2] and acoustic applications [3]. An inverse energy flow method (IMES) has been developed for acoustical application [4] and plate [5], and for a complex structure modeled with a set of assembled plates [6]. The main novelty of this paper is to develop this inverse method in order to detect the structural force applied in plate coupled with an acoustic cavity through a measurement data of the acoustic energy field.

2   DIRECT MES FORMULATION

The simplified energy method is a vibro-acoustic method developed for the purpose to predict the energy density distribution for structural acoustic problem in high frequency ranges. This method is based on a description of two local energy quantities: the energy density W is defined as a sum of the kinetic and potential energy densities and the energy vector $\vec{I}$ which is the energy flow inside systems. The energy W_s on the structure is defined as the sum of the primary source ρ_s (direct field) coming from the excitation point S, and the fictitious sources σ_s coming from the boundary P of structure as shown in Figure 1.
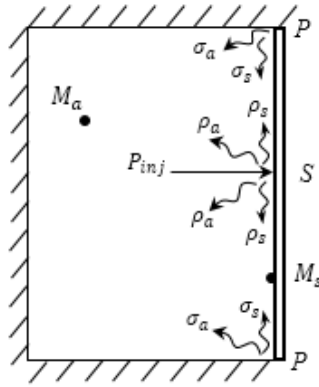
Figure 1. System decomposition.

$$W_s(M_s) = \int_{\Omega_s} \varrho_s(S) G_s(S, M_s) dS + \int_{\partial\Omega_s} \sigma_s(P) \overrightarrow{u}_{SM_s} . \overrightarrow{n}_P G_s(P, M_s) dP \qquad (1)$$

The acoustical energy W_a radiated from the structure is located at the excitation points S and structure boundaries P. In addition, according to the assumption that propagative waves are uncorrelated, the acoustical energy W_a at any point M_a inside the cavity is the sum of energy radiated from the excitation sources W_a^{exci} and energy radiated from the structure extremity W_a^{edge}:

$$W_a(M_a) = W_a^{exci}(M_a) + W_a^{edge}(M_a) \qquad (2)$$

2

where

$$W_a^{exci}(M_a) = \int_{\Omega_s} \varrho_a(S, \overrightarrow{u}_{SM_a}) G_a(S, M_a) dS, \tag{3}$$

and

$$W_a^{edge}(M_a) = \int_{\Omega_s} \sigma_a(P, \overrightarrow{u}_{PM_a}) G_a(P, M_a) dP. \tag{4}$$

3   INVERSE MES FORMULATION

This section focuses on developing an inverse MES formulation for a plate coupled with an acoustic cavity, by applying a discrete format of the acoustic energy equation. The IMES formulation aims to invert the matrix formulation of Equation. (2). The structural force applied in plate can then be estimated and localized from an acoustic measurement. It is expressed as follows:

$$P^{struc} = S_a^+ . W_a \tag{5}$$

where $+$ is the pseudo inverse, $W_a = W_a^{exci} + W_a^{edge}$ and $S_a = S_a^{exci} + S_a^{edge}$. Matrix S_a can be well-conditioned, but is often ill-conditioned, which will disturb the results. In the next parts, we studied the matrix S_a inversion influence on the numerical results.

4   NUMERICAL RESULTS

This section deals with numerical tests of different cases in order to validate the presented formulation. The presented system is a structure which consists of a plate (ρ_s = 7800 kg/m^3, ν
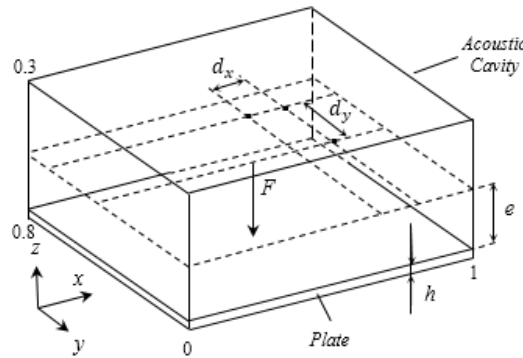
Figure 2. Boundary conditions.

= 0.3, E = 210.10^9 Pa) coupled with an acoustic cavity (ρ_a = 1.3 kg/m^3 , c_a = 340 m/s). The structure is a rectangular plate, their lengths are L = 1 m, l = 0.8 m and thickness h = 3.10^3 m, clamped on their extremity and damped with coefficient η_s = 1 %. The acoustic cavity is undamped and with dimensions (L = 1 m, l = 0.8 m, H = 0.3 m) as shown in Figure 2. The plate is excited with an input power P_{in} = 1.551 W/m^2, at point S given by (0.45 m, 0.45 m, 0). The numerical simulation methodology presented in Figure 2 consists of implementing the inverse energy flow approach IMES when using a set of density energy prediction based in the finite element method FEM modelled using the finite element software COMSOL multiphysics (FEM/IMES simulation). This example deals with the influence of acoustic measurements in the detection and quantification of the vibration source. A new numerical methodology to identify the loads acting on the structure using FE method was presented in this example. A more realistic test case was then considered. The first step consists in subdividing a plane

3
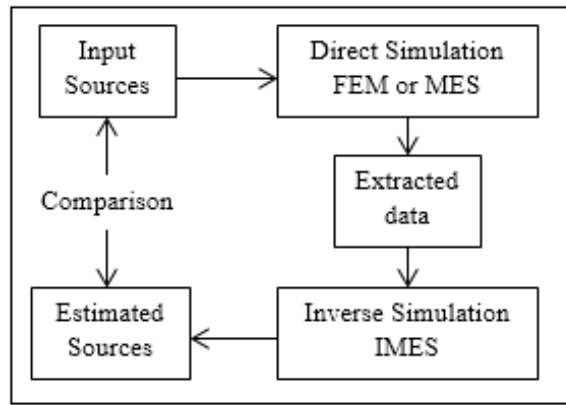
Figure 3. Flow chart of numerical methodology.

parallel to the plate with a distance $e = 0.05$ m, into nine areas, and placing a microphone in the middle of each area. In fact, the $n_{M_a} = 9$ acoustic measurement were distributed as shown in Figure 4.

(a)   (b)
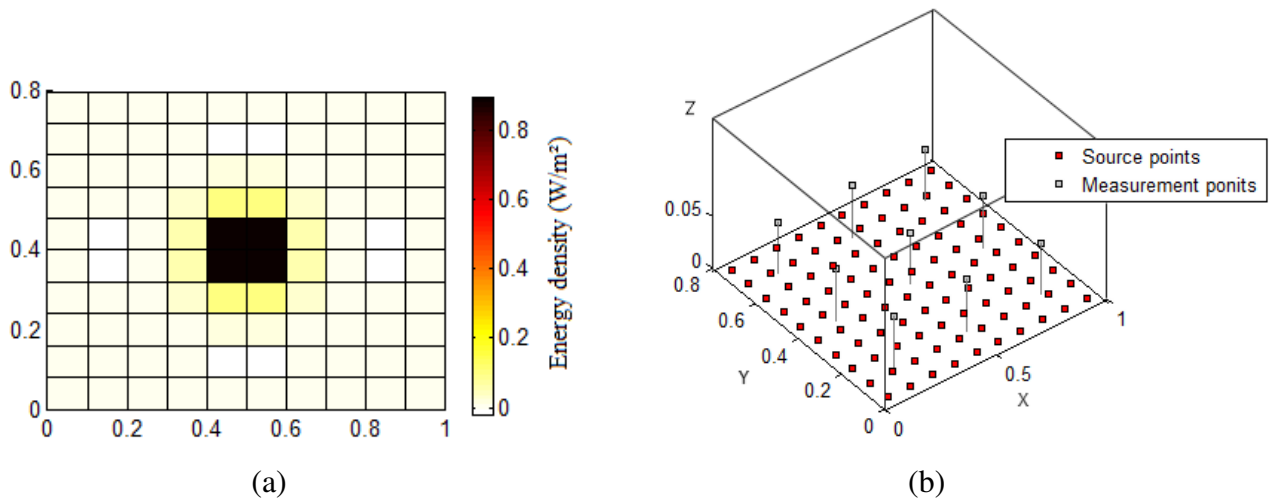
Figure 4. FEM/IMES Simulation for $d_x = 0.33$ m and $d_y = 0.26$ m

.

A color map of the estimated power repartition in plate was drown in Figure 4. From a first view, the highest value of power was estimated with a value equal to 0.8949 W/m^2. The next step consists in distributing the same number of microphone near the highest power surfaces with an equal distance $d_x = d_y = 0.09$ m as shown in Figure 5. As seen in this figure, a good input power prediction is observed. The results show that the amount of source information increases as the measurement point is so close from the source. Therefore, it is preferable that the distances between source and nearest measurement points are as short as possible. Moreover, it seems that choosing a good disposition of acoustic measurement is quite important to estimate the input force. Finally, this section confirmed that the present method tends to estimate the input force in the structure for a few number of acoustic measurements, and can be applied for industrial problems, such as aeronautics and automotive industry.

4

(a)   (b)
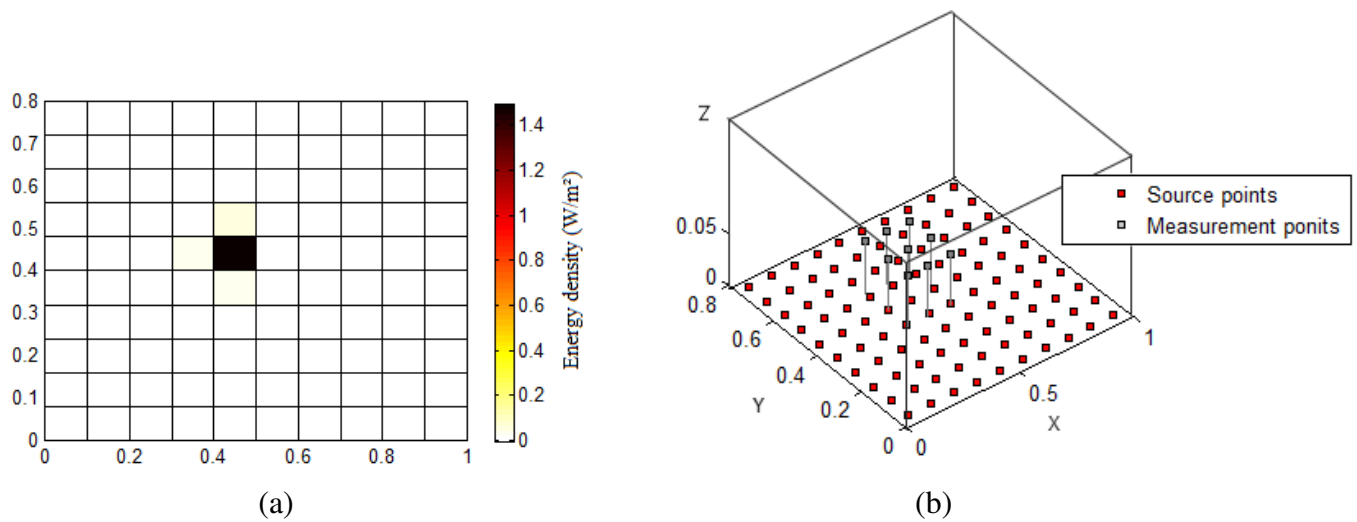
Figure 5. FEM/IMES Simulation for $d_x = d_y = 0.09$ m.

5   CONCLUSION

In this paper, numerical results are presented in order to localize the vibration source from acoustic measurement. The new IMES formulation based predictive tool has been first developed. Several test cases involving different measurement points and external forces were considered. The inverse solutions were compared to results given by the direct MES and FEM simulations. The obtained results confirm that the proposed approach exactly estimates the excitation force with a low density of measurement points.

REFERENCES

[1] M.N. Ichchou, A. Le bot, and L. Jezequel. A transient local energy approach as an alternative to transient sea: wave and telegraph equations. *Journal of Sound and Vibration*, 246(5):829–840, 2001.

[2] M.N. Ichchou and L. Jezequel. Letter to the editor: comments on simple models of the energy flow in vibrating membranes and on simple models of the energetics of transversely vibrating plates. *Journal of Sound and Vibration*, 195(4):679–685, 1996.

[3] S. Besset, M.N. Ichchou, and L. Jezequel. A coupled bem and energy flow method for mid-high frequency internal acoustic. *Journal of Computational Acoustic*, 18(1):69–85, 2010.

[4] M.A. Chachoub, S.Basset, and M. N. Ichchou. Identification of acoustic sources through an inverse energy method. *Inverse Problems in Science and Engineering*, 19:903–919, 2011.

[5] M.A. Chachoub, S.Basset, and M. N. Ichchou. Structural sources identification through an inverse mid-high frequency energy method. *Mechanical Systems and Signal Processing*, 25:2948–2961, 2011.

[6] A. Samet, M.A. Ben Souf, O. Bareille, M.N. Ichchou, T. Fakhfakh, and M. Haddar. Vibration sources identification in coupled thin plates through an inverse energy method. *Applied Acoustics*, 2017.

Stochastic acoustic control of internal sound using TMD

Elyes Mrabet[1], Mohamed Ichchou[2] and Noureddine Bouhaddi[3]

[1] Laboratoire de Mécanique, Modélisation et Productique, Ecole Nationale d'Ingénieurs de Sfax, Route Soukra Km 3.5 B.P 1173-3038, Sfax, Tunisie
Email : elyes.mrabet@isetkr.rnu.tn
[2] LTDS UMR5513 Ecole Centrale de Lyon, Université de Lyon, Ecully, France
Email: mohamed.ichchou@ec-lyon.fr
[3] FEMTO-ST Institute, UMR 6174, Department of Applied Mechanics, University of Franche-Comte, UBFC, 24 rue de l'Epitaphe F-25000 Besançon, France
Email: noureddine.bouhaddi@femto-st.fr

ABSTRACT

The present work is intended to introduce a stochastic acoustic optimization of Tuned Mass Damper (TMD) parameters used to control the internal sound induced by random vibrations of a flexible structure coupled to a cavity filled with air. Assuming linear behavior of the entire vibro-acoustic system, the modal interaction approach can be used and the control, made in the low frequency range, can be performed considering the root mean square acoustic pressure (RMSAP) as the objective function to be minimized. Indeed, in presence of random excitation applied to the flexible structure, the acoustic pressure measured at a given location into the cavity can be characterized by its RMSAP. A spectral analysis has been made over different bandwidth values and the RMSAP is evaluated. Depending on the bandwidth parameter, used to evaluate the objective function, two kind of control has been defined: (1) the broadband control, corresponding to small values of the bandwidth parameter, and (2) the narrowband control corresponding to large values of the bandwidth parameter. The numerical investigations showed that for the coupled mode dominated by an in-vacuo structural mode, a broadband control allows obtaining satisfactory performance and the TMD has been acting as a dissipative device. In the opposite, for the coupled mode dominated by a rigid-walled cavity mode, a narrowband control is more efficient and the TMD has been acting as a highly reactive device.

1   INTRODUCTION

The potentialities of the TMD device in structural vibration mitigation [1] as well as in the internal sound control are recognized. The performance of such device strongly depends on its parameters and in the present work a new stochastic optimization strategy based on an acoustic criterion is presented. The strategy consists to find the optimum TMD parameters as well as the optimum location, minimizing the RMSAP measured at a given location into the cavity. The numerical investigations showed that the proposed strategy can deal with the two kind of coupled modes (i.e. those are dominated by the structure and those dominated by the cavity [2]).

2   GOVERNING EQUATIONS, THE OPTIMIZATION STRATEGY
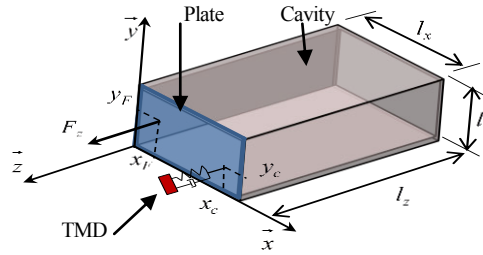
Figure 1. The TMD device attached to a flexible plate coupled to a cavity

Figure 1 shows a TMD with mass m_T, a natural frequency $\omega_T = \sqrt{k_T/m_T}$ and a damping ratio $\xi_T = c_T/2m_T\omega_T$, attached to a flexible plate (with a thickness h) coupled to a cavity, which is in turn, filled with air. The stationary zero mean white noise excitation F_z is applied at $\mathbf{r}_F = (x_F, y_F)^T$ whereas the TMD is attached at $\mathbf{r}_c = (x_c, y_c)^T$. The dimensions of the system are as shown in Figure 1. Let Ns and Na be the number of modes considered in the analysis for the structure and the cavity; by assuming linear behaviour and light proportional damping in the structure and the cavity [2, 3], the modal interaction approach [2] can be used and the governing equations can be written in modal coordinates as follows:

$$\mathbf{M\ddot{q}} + \mathbf{D\dot{q}} + \mathbf{Kq} = \mathbf{\Phi}^T F_z \tag{1}$$

where $\mathbf{q} = \left(\mathbf{w}^T, \mathbf{p}^T, z_T\right)^T$, $\mathbf{w}$ and $\mathbf{p}$ are the ($Ns\times1$) and the ($Na\times1$) vectors of the modal participation factor, respectively; z_T is the displacement of the TMD; $\mathbf{\Phi} = \left(\mathbf{\varphi}_F \quad \mathbf{\psi}_0 \quad 0\right)$, $\mathbf{\varphi}_F$ is the ($Ns\times1$) vector of the plate mode shapes computed at force location (x_F, y_F) and $\mathbf{\psi}_0$ is a ($Na\times1$) vector of

zeros; $\mathbf{M} = \begin{bmatrix} \mathbf{\Lambda}_m & \mathbf{0} & \mathbf{0} \\ S\mathbf{C}_{nm} & \dfrac{1}{\rho_0 c_0^2}\mathbf{\Lambda}_n & \mathbf{0} \\ \mathbf{0} & \mathbf{0} & m_T \end{bmatrix}$, $\mathbf{\Lambda}_m = \begin{bmatrix} \ddots & & \\ & \Lambda_m & \\ & & \ddots \end{bmatrix}$, $\mathbf{\Lambda}_n = \begin{bmatrix} \ddots & & \\ & \Lambda_n & \\ & & \ddots \end{bmatrix}$;

$\mathbf{D} = \begin{bmatrix} \mathbf{D}_m + c_T\mathbf{\varphi}_c^T\mathbf{\varphi}_c & \mathbf{0} & -c_T\mathbf{\varphi}_c^T \\ \mathbf{0} & \mathbf{D}_n & \mathbf{0} \\ -c_T\mathbf{\varphi}_c & \mathbf{0} & c_T \end{bmatrix}$, $\mathbf{D}_m = \begin{bmatrix} \ddots & & \\ & 2\xi_m\omega_m\Lambda_m & \\ & & \ddots \end{bmatrix}$ $\mathbf{D}_n = \dfrac{1}{\rho_0 c_0^2}\begin{bmatrix} \ddots & & \\ & 2\xi_n\omega_n\Lambda_n & \\ & & \ddots \end{bmatrix}$; ρ_0

is the density of air, c_0 is the celerity of sound in air , Λ_m and Λ_n are the structural modal mass and the modal volumes of the cavity, respectively; $S = l_x \times l_y$; $\mathbf{\varphi}_c$ is the ($1\times Ns$) vector of the plate mode shapes calculated at TMD location (x_c, y_c) and ξ_m, ξ_n are the damping ratios of the

plate and the cavity, for a given modes *"m"* and *"n"*, respectively; $\mathbf{C}_{nm}$ is the coupling matrix [3];

$$\mathbf{K} = \begin{bmatrix} \mathbf{K}_m + k_T \boldsymbol{\varphi}_c^{\mathrm{T}} \boldsymbol{\varphi}_c & -S\mathbf{C}_{nm}^{\mathrm{T}} & -k_T \boldsymbol{\varphi}_c^{\mathrm{T}} \\ \mathbf{0} & \mathbf{K}_n & \mathbf{0} \\ -k_T \boldsymbol{\varphi}_c & \mathbf{0} & k_T \end{bmatrix}, \quad \mathbf{K}_m = \begin{bmatrix} \ddots & & \\ & \omega_m^2 \Lambda_m & \\ & & \ddots \end{bmatrix}, \quad \mathbf{K}_n = \frac{1}{\rho_0 c_0^2} \begin{bmatrix} \ddots & & \\ & \omega_n^2 \Lambda_n & \\ & & \ddots \end{bmatrix}. \text{ It}$$

can be noted that readers can refer to [2, 3] for further details about the model. Let $\widetilde{\mathbf{q}}(\omega)$, $\widetilde{\mathbf{w}}(\omega)$, $\widetilde{\mathbf{p}}(\omega)$, $\widetilde{z}_T(\omega)$ and $\widetilde{F}_z$ be the finite Fourier transform of $\mathbf{q}$, $\mathbf{w}$, z_T and F_z respectively. The Fourier transform of both sides of Equation (1) yields to $\widetilde{\mathbf{q}} = \left(-\omega^2 \mathbf{M} + j\omega \mathbf{D} + \mathbf{K}\right)^{-1} \boldsymbol{\Phi}^{\mathrm{T}} \widetilde{F}_z$. The modal acoustic pressure $\widetilde{\mathbf{p}}(\omega)$ is given by $\widetilde{\mathbf{p}}(\omega) = \mathbf{Y}\boldsymbol{\Phi}^{\mathrm{T}} \widetilde{F}_z$, where $\mathbf{Y}$ is the $Na \times (Ns + Na + 1)$ sub-matrix extracted from the matrix $\left(-\omega^2 \mathbf{M} + j\omega \mathbf{D} + \mathbf{K}\right)^{-1}$ by taking the Na rows corresponding to the modal acoustic pressure $\widetilde{\mathbf{p}}(\omega)$. The power spectral density (PSD) of the acoustic pressure at a given location $\mathbf{r}_a$ into the cavity and for a force location $\mathbf{r}_F$ can be expressed as follows $S_{\widetilde{p}\widetilde{p}}(\mathbf{r}_a, \mathbf{r}_F, \omega) = |H(\omega, \mathbf{r}_a, \mathbf{r}_F)|^2 S_{FF}$, where S_{FF} is the constant PSD of the white noise force applied to the plate and $H(\omega, \mathbf{r}_a, \mathbf{r}_F) = \boldsymbol{\psi}(\mathbf{r}_a)\mathbf{Y}(\omega)\boldsymbol{\Phi}^{\mathrm{T}}(\mathbf{r}_F)$; $\boldsymbol{\psi}(\mathbf{r}_a)$ is the $(1 \times Na)$ vector of the acoustic mode shape calculated at location $\mathbf{r}_a$ (microphone location). Once the acoustic PSD response is obtained, the stochastic acoustic optimization strategy based on the RMSAP can be formulated as follows:

$$\text{Find } \mathbf{d} = (\omega_T, \xi_T, \mathbf{r}_c)^{\mathrm{T}} \text{ to minimize } \text{RMSAP} = \sigma_p(\mathbf{r}_a, \mathbf{r}_F, \mathbf{d}) = \sqrt{\int_{\omega_1}^{\omega_2} S_{\widetilde{p}\widetilde{p}}(\mathbf{r}_a, \mathbf{r}_F, \mathbf{d}, \omega) d\omega} \tag{2}$$

The evaluation of the objective function depends on the bandwidth $\Delta f = [\omega_1, \omega_2]$ therefore two kind of control have been defined: (1) the narrowband control, corresponding to small bandwidth parameter, and (2) the broadband control, corresponding to large bandwidth parameter. The performance of the TMD device will depend on this parameter.

3   NUMERICAL STUDY

The numerical values of the vibro-acoustic system are taken, $l_x = 0.5\text{m}$, $l_y = 0.3\text{m}$, $l_z = 1.1\text{m}$, $h = 3\text{mm}$; the plate has a Young's modulus $E = 70 \times 10^9 \text{ Pa}$, a density $\rho_s = 2700 \text{ kg.m}^{-3}$ and a Poisson's ratio $\upsilon = 0.3$; $\rho_0 = 1.21 \text{ Kg.m}^{-3}$, $c_0 = 344 \text{ m.s}^{-1}$, $Ns = 21$ and $Na = 102$. The mass of the TMD is taken 2% of the total mass of the plate; $S_{FF} = 0.1 \text{ N}^2 \times \text{Hz}^{-1}$, $\mathbf{r}_a = (0.35, 0.1, -0.875)^{\mathrm{T}}$ and $\mathbf{r}_F = (0.05, 0.05)^{\mathrm{T}}$. The frequency range of interest is taken [0, 220 Hz] where it has been observed two resonant coupled modes corresponding to $\varpi_1 = 108.59\text{Hz}$ and $\varpi_2 = 159.52\text{Hz}$. The first mode is dominated by the *in-vacuo* structural mode (1,1) whereas the second is dominated by the *rigid-walled* cavity mode (0,0,1).

Table 1 shows the optimum TMD parameters and their corresponding optimum locations for different bandwidth parameters Δf for the both resonant modes of interest. The inspection of the optimum damping ratios in Table 1 demonstrate that for the mode dominated by the *in-vacuo* structural mode (ϖ_1), the TMD device acts as a dissipative device whereas it acts as a highly reactive device when the mode dominated by the rigid-walled cavity mode (ϖ_2), is controlled. The obtained optimum TMD locations are always in the vicinity of the anti-node point of the *in-vacuo* structural mode (1,1). This result is predictable because both coupled modes (ϖ_1 and ϖ_2) involve the same *in-vacuo* structural mode (1,1).

In Figure 2 the PSD responses, for different Δf are presented when the two modes are separately controlled.

Targeted frequency	Δf (Hz)	ξ_T^* (%)	f_T^* (Hz)	x_c^* (m)	y_c^* (m)	σ_p^* (Pa)
$\varpi_1 = 108.59$Hz	2	0.010	110.897	0.240	0.149	0.003
	20	1.160	110.694	0.243	0.149	0.123
	40	13.45	110.919	0.253	0.151	0.328
$\varpi_2 = 159.52$Hz	2	0.693	155.554	0.192	0.147	0.008
	20	0.010	175.472	0.261	0.156	0. 125
	40	0.010	184.877	0.275	0.156	0.210

Table 1. Optimum TMD parameters for different bandwidth control.

The inspection of Figure 2 (a) shows that a reduction of 27.5 dB can be reached when a broadband control ($\Delta f = 40$Hz), of the targeted frequency ϖ_1, is achieved. A narrowband control produces two others peaks and the performance of the TMD device is less desirable. In Figure 2 (b), it's shown that a narrowband control ($\Delta f = 2$Hz) allows good performance of the TMD where a reduction of 20.6 dB is reached.
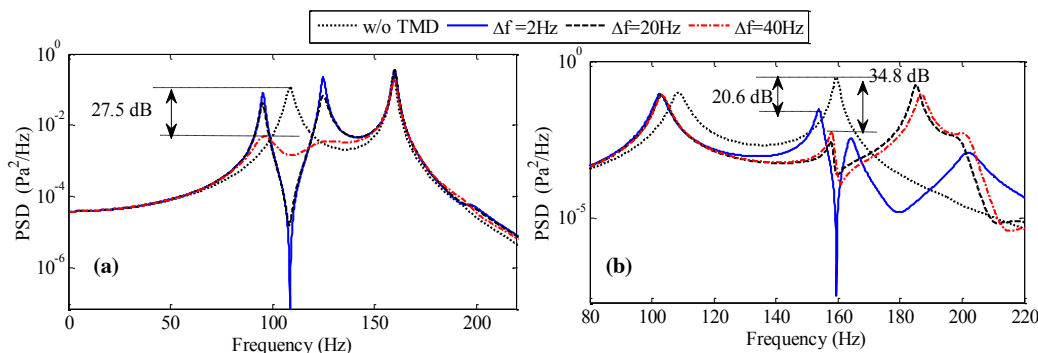
Figure 2. PSDs responses for different bandwidth parameters; (a): $\varpi_1 = 108.59$Hz, (b): $\varpi_2 = 159.52$Hz

4   CONCLUSIONS

In the present work a stochastic acoustic optimization strategy of TMD parameters is presented in order to control, in the low frequency range, the internal sound induced by stochastic vibrations of a flexible structure. The obtained results showed that for the coupled modes dominated by the *in-vacuo* structural mode, a broadband control is suitable to obtain satisfactory performance of the TMD, which has been acting as a dissipative device. In the opposite, for the mode controlled by the rigid-walled cavity mode, a narrowband control is more efficient in the internal sound control, where the TMD acted as a highly reactive device.

REFERENCES

[1]   P. Gardonio and M. Zilletti. Integrated tuned vibration absorbers: A theoretical study. *The Journal of the Acoustical Society of America*. 134: 3631-3644, 2013.

[2]   F. Fahy and P. Gardonio. *Sound and Structural Vibration (Second Edition)*. ed Oxford: Academic Press, Oxford, 2007.

[3]   C. Q. Howard and B. S. Cazzolato. *Acoustic Analyses Using Matlab and Ansys*. CRC Press, New York, 2014.

STOCHASTIC ANALYSIS OF NEAR-PERIODIC COUPLED PENDULUMS CHAIN

K. Chikhaoui[1], N. Bouhaddi[1], N. Kacem[1] and M. Ichchou[2]

[1] Univ. Bourgogne Franche-Comté, FEMTO-ST Institute, CNRS/UFC/ENSMM/UTBM,
Department of Applied Mechanics, 25000 Besançon, France
[2] LTDS, UMR 5513, Ecole Centrale de Lyon, Ecully, France
Email: khaoula.chikhaoui@femto-st.fr, noureddine.bouhaddi@femto-st.fr,
najib.kacem@femto-st.fr, mohamed.ichchou@ec-lyon.fr

ABSTRACT

It is known that, when the mechanical coupling between the components is weak, small imperfections in a periodic structure can induce vibration localization. Stochastic analysis of near-periodic coupled pendulums chain is discussed in this paper. Perfect periodicity of the system is disturbed by varying randomly the length of one of the pendulums which is considered as an uncertain parameter. Its randomness is modeled in a probabilistic framework by a random variable according to a given range of dispersion level. Stochastic effects on vibration localization in mistuned four coupled pendulums chain is investigated through statistical evaluations. To do so, the propagation of uncertainties is performed using the Latin Hypercube Sampling method.

1   INTRODUCTION

Mistuning, or disorder, resulting from material defects, structural damage, manufacturing defaults, etc., breaks the perfect arrangement of periodic structures and alters significantly their dynamic behavior. The structure then becomes nearly periodic or called mistuned and vibration localization could occur under certain circumstances [1]. Zhu et al. [2] studied localization in randomly disordered coupled beams and proved that the wave propagation and localization can be altered by properly adjusting the structural parameters. Recently, Malaji et al. [3] investigated the effect of mistuning on vibration localization in two coupled pendulums chain. The main purpose of the present study is to investigate the stochastic effects of uncertain mistuning on vibration localization in a coupled pendulums chain.

2   MODEL

The scheme of N coupled pendulums chain is illustrated in figure 1. The pendulums have same mass m, torsional stiffness k_r and proportional damping constant c and are weakly coupled by translational springs k_t. An external base excitation x_g is applied to the system.
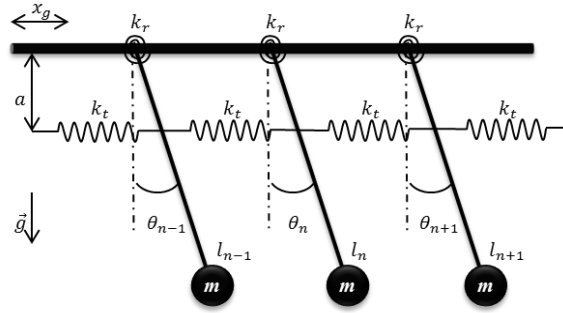
Figure 1. Periodic coupled pendulums chain.

The equation of motion of the nth pendulum is written as follows:

$$ml_n^2\ddot{\theta}_n + cl_n^2\dot{\theta}_n + k_r\theta_n + k_t a^2\left(2\theta_n - \theta_{n-1} - \theta_{n+1}\right) = -ml_n\ddot{x}_g \tag{1}$$

To disturb the periodicity of the system, one pendulum is assumed to have slightly different length from the others. This mistuning is quantified by a length ratio α_n between the nth pendulum length and the nominal length.

For simplification, dimensionless variables are defined as follows:

$$\theta_n = \Theta_n e^{j\omega t}; x_g = X_g e^{j\omega t}; \alpha_n = \frac{l_n}{l}; \omega_0 = \sqrt{\frac{k_r}{ml^2}}; \eta = \frac{c}{m\omega_0}; \beta = \frac{k_t a^2}{k_r}; f = \frac{X_g}{l}; \Omega = \frac{\omega}{\omega_0} \tag{2}$$

where η is the damping factor, β the coupling factor and $j^2 = -1$. Eqs. (1) and (2) lead to:

$$\left(-\alpha_n^2\Omega^2 + j\alpha_n^2\eta\Omega + 1\right)\theta_n + \beta\left(2\theta_n - \theta_{n-1} - \theta_{n+1}\right) = \alpha_n\Omega^2 f \quad n = 1...N \tag{3}$$

This system of equations is solved for each angular frequency of excitation Ω.

3   NUMERICAL RESULTS

Let's consider a chain of four weakly coupled pendulums with $\eta = 0.01$, $\beta = 0.005$, $f = 1$.

If the pendulum chain is perfectly periodic, the dimensionless eigenfrequencies are $\Omega_1=1.001$, $\Omega_2=1.003$, $\Omega_3=1.007$, $\Omega_4=1.009$ and conformity occurs between the amplitude pairs (Θ_1, Θ_4) and (Θ_2, Θ_3) reflecting the symmetry of the chain. This symmetry is broken when $\alpha_2 = 1.01$ ($\alpha_1 = \alpha_3 = \alpha_4 = 1$), as shown in figure 2.a. The dimensionless eigenfrequencies become $\Omega_1=0.994$, $\Omega_2=1.003$, $\Omega_3=1.006$, $\Omega_4=1.008$ and an amplitude mistuning occurs. The amplitude of the 2nd pendulum response is the highest with $\Theta_{2max}= 128.18$.
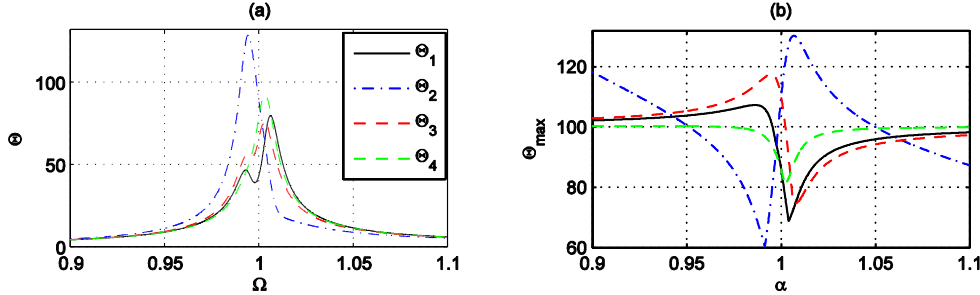
Figure 2. a. Dimensionless amplitudes for $\alpha_2 = 1.01$, b. Variation of maximal dimensionless amplitudes due to variation of α_2 from 0.9 to 1.1.

Small variation of α_2 from 0.9 to 1.1 causes significant variation of maximal amplitudes as shown in Figure 2.b. The difference $\Delta\Theta_{max}$ between higher maximal amplitude and lower one is highest at $\alpha_2 = 1.005$ ($\Delta\Theta_{max} = 59.09$) between Θ_{2max} and Θ_{1max}. The symmetry between Θ_2 and Θ_3 is more disturbed than the symmetry between Θ_1 and Θ_4.

For more realistic representation of imperfection, we suppose that α_2 is an uncertain parameter which varies according to:

$$\alpha_2 = \alpha_0\left(1+\delta\xi\right) \tag{4}$$

where ξ is a Gaussian random variable, $\alpha_0 = 1$ and δ is the dispersion value.

The Latin Hypercube Sampling method is used with 1000 samples. The analysis of the trends in the output data (eigenfrequencies and amplitudes) is achieved by statistical evaluations: envelope (extreme statistics), dispersion (standard deviation / mean), skewness γ (distribution asymmetry) and kurtosis κ (heaviness of tail of the distribution).
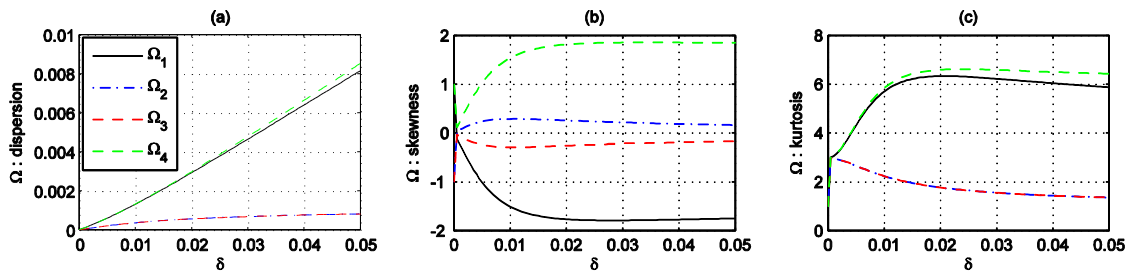
Figure 3. a. Dispersion, b. skewness and c. kurtosis of the stochastic dimensionless eigenfrequencies for $0 \leq \delta \leq 0.05$.

Figure 3 shows that the variation of Ω_1 and Ω_4 is much more important than the variation of Ω_2 and Ω_3. This is illustrated through increasing dispersions (Figure 3.a). Ω_2 and Ω_3 distributions are

3

fairly symmetrical (-0.5 < γ < -0.5, Figure 3.b). Nevertheless, Ω_1 and Ω_4 are highly skewed with asymmetrical distributions (γ < -1 or γ > 1) which are heavier than those of Ω_2 and Ω_3 (higher kurtosis values for Ω_1 and Ω_4, Figure 3.c).

The evolution of maximal amplitude with respect to δ is illustrated in figure 4. Higher dispersion is obtained for Θ_{2max} as shown in Figure 4.a. Smaller and nearly similar dispersions are obtained for Θ_{1max} and Θ_{3max} since 1st and 3rd pendulums are coupled to the disturbed one. Smallest dispersion is obtained for Θ_{4max} since the 4th pendulum is not directly coupled to the 2nd one. Maximal vibration localization is achieved for δ_m = 2.45% (Θ_{2max}=130.30) and remains constant up to δ = 5%. At δ = 3.3%, dispersion of Θ_2 reaches it maximum (24.44%) and decreases beyond. Up to δ = 3.3%, the Θ_{3max} distribution has heaviest (highest κ, Figure 4.c) long tail to the left (γ < 0, Figure 4.b), meaning that Θ_{3max} has the most tendency to decrease.
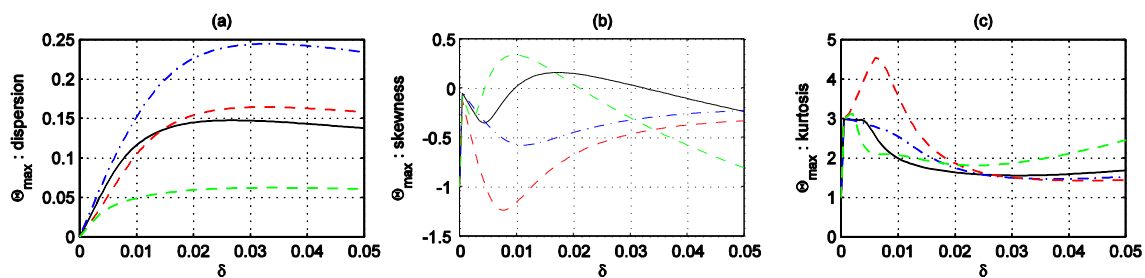
Figure 4. a. Dispersion, b. skewness and c. kurtosis of the stochastic maximal dimensionless amplitudes for $0 \leq \delta \leq 0.05$.

4   CONCLUDING REMARKS

Stochastic analysis of uncertain mistuning effects on vibration localization in near-periodic coupled pendulums chain was performed in this paper. Vibration localization reaches its maximum for a given dispersion level. Future work will consist in generalizing the proposed concept to Mdof near-periodic structures in order to extract the benefits of random imperfections in term of vibration localization. This denotes an interesting challenge for energy harvesting in presence of uncertainty, meriting particular attention.

ACKNOWLEDGMENT

REFERENCES

[1]   C. Pierre. Weak and strong vibration localization in disordered structures: a statistical investigation. *Journal of Sound and Vibration*. 139(l):111-132, 1990.

[2]   H-p. Zhu, L. Ding and T. Yin. Wave Propagation and Localization in a Randomly Disordered Periodic Piezoelectric Axial-Bending Coupled Beam. *Advances in Structural Engineering*. 16(9):1513-1522, 2013.

[3]   P.V. Malaji and S.F. Ali. Energy Harvesting from Near Periodic Structures. *Vibration Engineering and Technology of Machinery*. 2:411-420, 2015.

GLOBAL SENSITIVITY ANALYSIS ON SANDWICH PANEL'S ACOUSTIC CHARACTERISTICS WITH CORRELATED INPUTS

W. Chai[1] , Z. Zergoune[1] , A. Zine[2] and M. Ichchou[1*]

[1]Laboratoire de Tribologie et Dynamique des Systmes
Ecole Centrale de Lyon, Ecully, FRANCE
Email: chinachaiwq@gmail.com, zergoune.uni@gmail.com, mohamed.ichchou@ec-lyon.fr
[2]Institut Camille Jordan
Ecole Centrale de Lyon, Ecully, FRANCE
Email: abdel-malek.zine@ec-lyon.fr

ABSTRACT

In this paper, a piece of sandwich composite material's mechanical parameters have been investigated to reveal the influence of its sound transmission properties using some Global Sensitivity Analysis (GSA) methods. Particularly, the correlation among these variables, which is caused by the core layer's meso-structure designs, is taken into consideration. For this purpose, some advanced Fourier Amplitude Sensitivity Test (FAST) algorithms are applied on the classic Mead's analytical sound transmission model. The test results show that the correlation and the variation of meso-structures both can greatly change the influence of these mechanical parameters on the characteristic sound transmission properties, the transmisson loss, for example. The statistics obtained in this research indicate that, in the industrial production process, the importance of some variables's uncertainty control should be re-evaluated when taking into consideration their distribution dependence caused by different meso-structures.

1   INTRODUCTION

In about recent 30 years, very fast development has been observed in the engineering research and industrial applications of sandwich composite panels. These panels have great advantage in their stiffness-to-mass ratio, leading to wide application in aeronautic and civil engineering, which raises the importance of evaluating and improving their sound proof capacity. Produced in high quantity and applied in various strict conditions, their quality control practices become more important than ever in the design and production phase. There are some researches that have been published with the implementation of some Global Sensitivity Analysis (GSA) methods, such as the one of Christen et al. [1]. But with the fast development of sandwich panels' meso-structures[2], the correlation effects can no longer be ignored.

2   SOUND TRANSMISSION IN SANDWICH COMPOSITE MATERIALS

Considering a piece of material's sound proof capacity, the transmission loss is a direct indicator of energy attenuation for a sound wave propagating through the material with a certain angle. For an analytical estimation, we prefer to use the classical Mead's model[3] with some corrections and simplifications by Clarkson and Ranky [4] . Under several assumptions and approximations, the vibration equation can be represented in this form:

$$D_f\nabla^6 w - g'(D_f + D)\nabla^4 w + m\omega^2\nabla^2 w - mg'\omega^2 w = \nabla^2 p - g'p, \qquad (1)$$

then the structural impedance can be developed like this:

$$Z(\omega) = \frac{(1 + \mathrm{i}\eta)D_f k^6 + (1 + \mathrm{i}\eta)g(D_f + D)k^4 - m\omega^2 k^2 - m\omega^2 g(1 - \nu^2)}{\mathrm{i}\omega(k^2 + g)}. \qquad (2)$$

The TL can then be simply calculated with Z obtained for a certain acoustic angular frequency ω. In Equation (2), supposing that the geometric parameters are all pre-determined and k defined as the wavenumber, the other variables can be related to 5 basic mechanical parameters: E the faceplate Young's modulus, G_{xz} the core shear modulus in y-axis, G_{yz} the core shear modulus in x-axis, m the structural area density and η the structural damping factor. Among them, E and mostly contributes to D and D_f the structural and faceplate stiffness while G_{xz}, G_{yz} and η mainly contribute on g the core shear stiffness factor.

3   MESO-STRUCTURE AND ITS MECHANICAL PROPERTIES

The meso-structure is a general conception for the porous design of sandwich panel's core layer, among which the honeycomb structure is the most often seen, as presented in Figure 1.
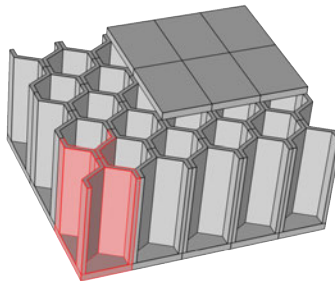

Figure 1. Sandwich panel with double vertical thickness honeycomb meso-structure

Limited to analytical models, only a small part of regular meso-structures can have simple expressions, including the double vertical thickness honeycomb structure, whose accurate

2

analytical model is recently given by Malek and Gibson [5]. With this, we can evaluate the approximate homogenized structural parameters G_{xz}, G_{yz} and m with some given geometric values.

So, as G_{xz}, G_{yz} and m are all outputs of the meso-structural model, some correlations may exist among them while E and η are preset to be independent. And here is the correlation matrix obtained for this honeycomb structure:

$$
\begin{array}{c}
\\
eta \\
G_{xz} \\
G_{yz} \\
m \\
\eta
\end{array}
\begin{array}{ccccc}
E & G_{xz} & G_{yz} & m & \eta \\
\left[\begin{array}{ccccc}
1 & -0.00 & -0.00 & 0.01 & -0.00 \\
-0.00 & 1 & 0.68 & 0.51 & 0.02 \\
-0.00 & 0.68 & 1 & 0.61 & 0.01 \\
0.01 & 0.51 & 0.61 & 1 & 0.01 \\
-0.00 & 0.02 & 0.01 & 0.01 & 1
\end{array}\right]
\end{array}, \tag{3}
$$

which indicates that the three variables are very positively correlated, especially for the two shear modulus.

4   GLOBAL SENSITIVITY ANALYSIS WITH CORRELATED VARIABLES

In the domain of GSA, ANOVA (ANalysis Of VAriance) is one of the most mentioned system of SA algorithms. It's established on a high dimension expansion of the output's variance, supposing the model $Y = f(x_1, x_2, ..., x_n)$, it could be uniquely decomposed into this form:

$$
V(Y) = \sum_i V_i(x_i) + \sum_i \sum_{j>i} V_{ij}(x_i, x_j) + \sum_i \sum_{j>i} \sum_{l>j} V_{ijl}(...) + ... + V_{123...n}(x_1, ..., x_n). \tag{4}
$$

Therefore, the definition of the first order sensitivity index is $S_i = V_{X_i}(E_{X_{\sim i}}(Y|X_i))/V(Y)$, where $X_{\sim i}$ means all the inputs except X_i. The index S_i represents the ratio of variance of the output Y explained by the input X_i. Higher the value is, more important the uncertainty control is for this variable.

In this research, the sensitivity analysis methods applied belong to Fourier Amplitude Sensitivity Test (FAST) series, which have great advantage in calculation efficiency of first order sensitivity indices. Its classical version the FAST was realized by Saltelli and Bolado [6], but this one can not take variables's correlation properties into consideration. So two advanced algorithm with correlation are applied for comparison purpose, including the FASTC (proposed by Xu and Gertner [7]) and the FAST-orig (proposed by author).

5   TEST RESULTS

As shown in Figure 2, three SA algorithms are applied on the Mead's sound transmission model with correlated variables generated by the double vertical thickness honeycomb meso-structure for the frequency band from 100 to 10000Hz. Regarding the general form of these SI curves, some basic acoustic knowledge can be verified: the dominant role of m the mass per area at low frequency, and the importance of shear effect for mid-high frequency sound wave isolation.

Comparing the SA results obtained by FAST methods with (FAST-orig, FASTC) and without (FAST) correlation design, some interesting phenomena can be observed. With strong positive correlation among G_{xz}, G_{yz} and m, m becomes also significantly important at high frequency while G_{xz} and G_{yz} are no longer negligible at low frequency. Stroked by their increase of SI, η's importance is greatly compressed but no obvious change can be observed for SI(E). It's interesting to mention that though the mean value of G_{xz} and G_{yz} have huge difference because of the double vertical thickness, their SI curves have almost the same form with or without correlation.
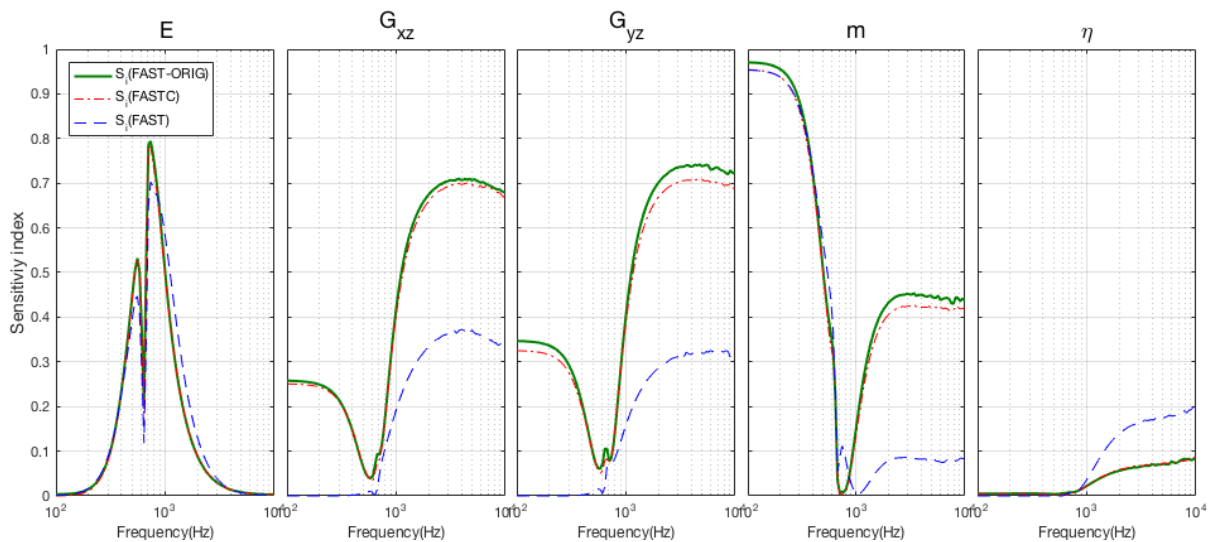
Figure 2. SI curves for the 5 mechanical parameters on the transmisson loss

6   CONCLUSION

In this research, some interesting features are observed when GSA methods are applied on an acoustic sandwich panel model with correlated mechanical parameters. As the correlation properties are generated by the sandwich core layer's meso-structures, it might be very interesting if various meso-structures can be tested. Also, for the sake of calculation efficiency, analytical models are chosen to be evaluated in GSA progress, some more convincible results could be obtained if finite element simulation or even experimental data can be directly taken into application.

REFERENCES

[1] J-L. Christen, M. Ichchou, B. Troclet, and M. Ouisse. Global sensitivity analysis of acoustic transmission models. *Journal of Sound and Vibration*, 368:1–9, 2014.

[2] Q. Zhang, X. Yang, P. Li, G. Huang, S. Feng, C. Shen, B. Han, X. Zhang, F. Jin, F. Xu, and T. Lu. Bioinspired engineering of honeycomb structure - Using nature to inspire human innovation. *Progress in Materials Science*, 74:332–400, 2015.

[3] D. J. Mead and S. Markus. The forced vibration of a three-layer, damped sandwich beam with arbitrary boundary conditions. *Journal of Sound and Vibration*, 10:163–175, 1969.

[4] B. L. Clarkson and M. F. Ranky. Modal density of honeycomb plates. *Sound And Vibration*, 91:103–118, 1983.

[5] S. Malek and L. Gibson. Effective elastic properties of periodic hexagonal honeycombs. *Mechanics of Materials*, 91(P1):226–240, 2015.

[6] A. Saltelli and R. Bolado. An alternative way to compute fourier amplitude sensitivity test (fast). *Computational Statistics & Data Analysis*, 26(4):445–460, 1998.

[7] C. Xu and G. Z. Gertner. A general first-order global sensitivity analysis method. *Reliability Engineering & System Safety*, 93(7):1060–1071, 2008.

4

ROBUST AEROELASTIC OPTIMIZATION OF TOW-STEERED COMPOSITE PANELS

T. A. M. Guimarães[1], D. A. Rade[2]

[1]Federal University of Uberlândia, School of Mechanical Engineering, Uberlândia, MG, BRAZIL, E-mail: thiagoamg@ufu.br

[2]Technological Institute of Aeronautics, Division of Mechanical Engineering, São José dos Campos, SP, BRAZIL, E-mail: rade@ita.br

ABSTRACT

Due to recent advances in automated manufacturing technology, the so-called tow-steered laminates, in which the fibers in the layers are deposited following arbitrary curvilinear paths, have become viable. A number of previous studies have demonstrated that tow-steered laminates can exhibit improved structural performance in terms of bending, buckling, vibration and aeroelastic behavior, as compared to traditional unidirectional laminates. The classical design strategy to cope with aeroelastic stability criteria, known as aeroelastic tailoring, consists essentially in stacking unidirectional fiber plies of different orientations. The application of aeroelastic tailoring to two-steered laminates potentially opens new possibilities of performance improvement, since the fiber trajectories can be dealt with as additional design variables. On the other hand, the performance of composite structures is strongly influenced by manufacturing imperfections, which, in this study are regarded as uncertainties. The present paper is devoted to the numerical study of the influence of uncertainties affecting the fiber trajectories on the aeroelastic stability of tow-steered composite panels, including: stochastic sensitivity analysis, aiming at evaluating the impact of uncertainties on the flutter instability boundaries, and stochastic robust optimization, intended for minimizing this impact on the optimized aeroelastic behavior. The Classical Lamination Theory is adopted to model the layered composite plates, duly adapted to account for curvilinear fiber trajectories on each layer. The aeroelastic model is based on the Ritz method, with the aerodynamic forces modeled according to the supersonic piston theory. The flutter stability boundaries for designs obtained by using deterministic and stochastic optimization of a tow-steered plate are compared., confirming improvements in terms of robustness against perturbations in the fiber trajectories.

1   INTRODUCTION

Panel flutter is an instability condition caused by the interaction of inertial, elastic and aerodynamic forces generated by the interaction of elastic plate-like or shell-like structures with surrounding supersonic airflows [1].

Recent achievements in automation have been leading to the continuous improvement of manufacturing processes of composite materials. In particular, Automated Fiber Placement (AFP) process currently enables to manufacture the so-called Variable Stiffness Panels (VSP), which are characterized by non-uniform fiber distribution over the plies. A particular type of VSP are tow-steered plates (TSP), in which the fibers are deposited following curvilinear paths. As compared to traditional unidirectional composite laminates, TSP can potentially be designed more effectively to comply with static, buckling, vibration and aeroelastic requirements [2]. On the other hand, the performance of TSPs is strongly influenced by manufacturing imperfections, which can be considered random uncertainties [2]. In the present paper, the influence of uncertainties affecting the fiber trajectories on the aeroelastic stability of tow-steered composite panels is numerically appraised, including stochastic sensitivity analysis and stochastic robust optimization.

2   AEROELASTIC MODEL OF TOW-STEERED COMPOSITE PLATES

The i-th ply of a rectangular TSP of dimensions $s \times c$ is depicted in Fig. 1, in which θ indicates the fiber angle, assumed to vary according to:

$$\theta_i(x) = \overline{\theta}_i + \frac{\theta_s - \theta_0}{s} x + \theta_0 \qquad (1)$$

where $\overline{\theta}_i$ is the orientation angle of the ply and θ_0, θ_s are, respectively, the fiber angles at $x = 0$ and $x = s$. In Fig. 1, U indicates the airflow velocity.
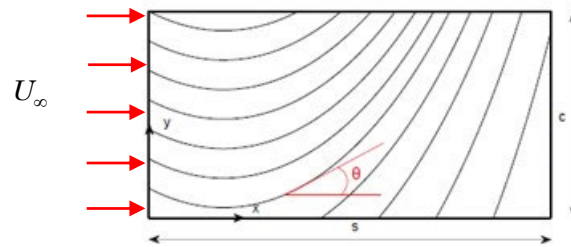
Fig. 1. Illustration of a typical ply of a tow-steered laminate.

Assuming that the laminate is sufficiently thin, it is modeled according to the Classical Lamination Theory (CLT), and the transverse displacements $w(x, y, t)$ are assumed to be constant through the plate thickness. Moreover, each ply is assumed to be in plane strain state, and other hypotheses of Kirchhoff's plate theory are adopted. Neglecting in-plane loads, the relations between moments $\tilde{\boldsymbol{M}} = \begin{bmatrix} M_x & M_y & M_{xy} \end{bmatrix}^T$ and curvatures $\tilde{\boldsymbol{\kappa}} = \begin{bmatrix} \kappa_x & \kappa_y & \kappa_{xy} \end{bmatrix}^T$ for the laminate are expressed as [3]:

$$\tilde{\boldsymbol{M}} = \boldsymbol{D}(\theta_1, \theta_2, ...) \tilde{\boldsymbol{\kappa}} \qquad (2)$$

It can be shown that matrix $\boldsymbol{D}$ can be expressed in terms of a set of *lamination parameters*, defined as follows (h is the thickness of the laminate) [3].

$$\{W_1, W_2, W_3, W_4\} = \frac{12}{h^3} \int_{-h/2}^{-h/2} z^2 \{cos(2\theta), sin(2\theta), cos(4\theta), sin(4\theta)\} dz \tag{3}$$

As for the aerodynamic loads, the pressure is modeled as follows, according to the method proposed by Ashley [4], known as first order piston theory (ρ is the fluid density and M_∞ is the Mach number):

$$\Delta P = \lambda \frac{\partial w}{\partial x} = \frac{\rho_\infty U_\infty^2}{\sqrt{M_\infty^2 - 1}} \frac{\partial w}{\partial x} \tag{4}$$

According to the Assumed-Modes approach, the transverse displacement field is approximated as a linear combination of trial functions, as follows:

$$w(x,y) = \sum_{i=1}^{m} \sum_{j=1}^{n} r_i \phi_i(x) \cdot s_j \varphi_j(y) = \sum_{k=1}^{N} q_k \eta_k(x,y) = \boldsymbol{N}(x,y)\boldsymbol{q} \tag{5}$$

After formulating the strain and kinetic energies and applying Lagrange's Equations, the equations of motion are found in the form of set of linear second-order ordinary differential equations, to which the following eigenvalue problem is associated:

$$\left(\lambda \boldsymbol{K}_a + \boldsymbol{K} - \mu \boldsymbol{M} \right) \boldsymbol{q} = \boldsymbol{0}, \tag{6}$$

Stability analysis is performed by inspecting the eigenvalues μ for increasing values of the parameter λ, associated to the flow speed.

3   SENSITIVITY ANALYSIS AND ROBUST OPTIMIZATION

The sensitivity index of the response y with respect to a random parameter p_i is defined as ($E(.)$ and $\sigma^2(.)$ denote the expected value and variance, respectively):

$$S_i = \frac{\sigma^2 \left[E\left(y | p_i \right) \right]}{\sigma^2 \left[E(y) \right]}, \tag{7}$$

In evaluating (7), Polynomial Chaos Expansion (PCE) is used based on the use of Hermite polynomials for the expansion of Gaussian random variables.

The multi-objective robust optimization problem is defined as follows:

$$\begin{aligned} \text{Minimize: } J_1(\boldsymbol{p}) &= -E\left(U_{flutter}\right) \\ J_2(\boldsymbol{p}) &= \sigma^2\left(U_{flutter}\right) , \\ \text{Subjected to } \boldsymbol{p}_{min} &\leq \boldsymbol{p} \leq \boldsymbol{p}_{max} \end{aligned} \tag{8}$$

where $\boldsymbol{p}$ is the vector of design parameters.

The construction of Pareto front for non-dominated optimal solutions is carried-out by using a multi-criteria version of Differential Evolution (DE) optimization method.

The deterministic optimization is defined when the objective function is simply $J(\boldsymbol{p}) = -U_{flutter}$.

4   NUMERICAL RESULTS

A composite rectangular simply supported plate with s=400 mm, c=300 mm, consisting of eight graphite/epoxy plies of uniform thickness t=0.19 mm. The mechanical properties of the plies are: $E_1 = 129.50$ GPa, $E_2 = 9.37$ GPa, $G_{12} = 5.24$ GPa, $\mu_{12} = 0.38$, $\rho = 0.38$. As a baseline configuration one adopts a unidirectional (unsteered) laminate with stacking sequence $\begin{bmatrix} 0 & 45 & -45 & 90 \end{bmatrix}_s$. For this configuration, the evolution of the natural frequencies as function of parameter λ is depicted in Figure 2; the coalescent of two of those frequencies indicates the onset of instability (flutter) at λ=2.05×10^5.

For the tow-steered configuration, for which the stacking sequence of the baseline plate was also adopted, the sensitivity analysis for parameters $\left(\theta_0, \theta_s, E_1, E_2, G_{12}, \mu_{12}, \rho \right)$ leads to the results presented in Figure 3. From these results, parameters $\left(\theta_0, \theta_s \right)$ were chosen as optimization design variables. Table 2 enables to compare the results of deterministic and robust optimizations.
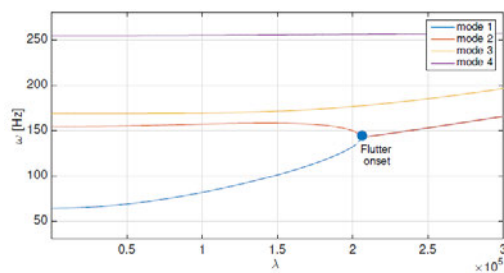
Figure 2. Evolution of the natural frequencies for the baseline configuration.
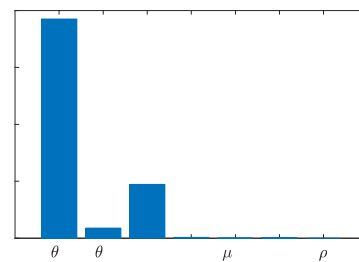
Figure 3. Sensitivity index for the two-steered composite plate.

	Deterministic sol.	Robust sol.
θ_0, θ_s **(deg.)**	−17.72, 5.12	−21.90, 3.22
J	2.17×10^5	-
J_1, J_2	-	2.14×10^5, 3.58×10^3

Table 2. Deterministic and robust optimization solutions

The difference between both solutions is highlighted in Figure 4, in terms of the PDFs of the using PCE. It can be seen that, as compared to the deterministic solution, the robust solution presents lower mode value of the flutter speed, but a smaller dispersion.
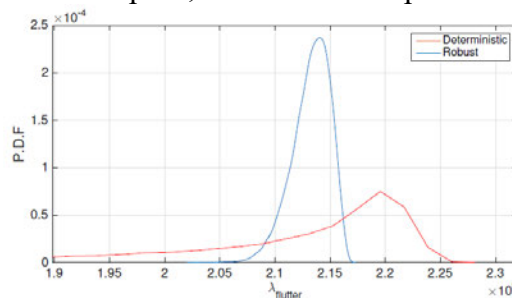
Figure 4. PDFs of the flutter velocity for deterministic and robust optimization solutions.

4

5   CONCLUSIONS

The influence of uncertainties affecting the tow angles of laminate composite panels on flutter speed of these later was assessed, both in terms of stochastic sensitivity analysis combine with Polynomial Chaos Expansion and robust optimization. The study was motivated by the need of dealing with imperfections introduced by the manufacturing process. The optimization results demonstrated that the deterministic optimization was capable of improving the flutter speed, but the optimal solution have shown to be quite sensitive to random perturbations in the design variables. On the other hand, robust solutions extracted from the set of solutions on the Pareto front demonstrated improvements in terms of the robustness with respect to those perturbations. The numerical strategy conceived have shown to be quite adequate in terms of computational burden.

6   ACKNOWLEDGMENTS

7   REFERENCES

[1]   E.H. Dowell. Nonlinear oscillations of a fluttering plate. *AIAA Journal*, 4(7):1267–1275, July 1966.

[2]   A. H. Akbarzadeh, M. Arian Nik, and D. Pasini. Vibration responses and suppression of variable stiffness laminates with optimally steered fibers and magnetostrictive layers. *Composites Part B: Engineering*, 91:315–326, 4 2016.

[3]   R. Jones. *Mechanics of composite materials*. CRC, 1998.

[4]   B. Bisplinghoff, H. Ashley and R. Halfman. *Aeroelasticity*. Dover, 1996.

VIBROACOUSTIC CONTROL OF DOUBLE-PANEL STRUCTURES USING VISCOELASTIC AND PIEZOELECTRIC MATERIALS - A FINITE ELEMENT REDUCED ORDER MODELING

W. Larbi, J.-F. Deü and R. Ohayon

Structural Mechanics and Coupled Systems Laboratory
Conservatoire National des Arts et Métiers (Cnam), 292 rue Saint-Martin, case 353,
75141 Paris Cedex 03, France
Email: (walid.larbi, jean-francois.deu, roger.ohayon)@cnam.fr

ABSTRACT

This work concerns the control of sound transmission through double laminated panels using passive piezoelectric shunt technique. More specifically, the system consists of two sandwich panels (each one composed of two elastic faces and a viscoelastic core) with an air gap in between. Furthermore, piezoelectric patches (connected to a resonant shunt circuit) are surface-mounted on the external faces of the structure in order to damp some specific resonance frequencies of the coupled system. Firstly, a finite element formulation of the fully coupled visco-electro-mechanical-acoustic system is presented. This formulation takes into account the frequency dependence of the viscoelastic material, the electro-mechanical coupling of the piezoelectric elements and the elastoacoustic interaction. A modal reduction approach is then proposed to solve the problem at a lower cost. To this end, the coupled system is solved by projecting the mechanical displacement and the pressure unknown on a truncated basis composed respectively of the first real short-circuit structural modes and the first acoustic modes with rigid boundaries conditions. A static correction is also introduced in order to take into account the effect of higher modes. Moreover, due to the fact that only two electrical variables per piezoelectric patch are used (the electric charge contained in the electrodes and the voltage between the electrodes), they are kept in the reduced system. Finally, numerical examples are analyzed to show the efficiency of the proposed reduced order model.

1   INTRODUCTION

Double-wall structures are widely used in noise control due to their superiority over single-leaf structures in providing better acoustic insulation. Typical examples include double glazed windows, fuselage of airplanes, panels of vehicles, etc.. By introducing a thin viscoelastic interlayer within the panels, a better acoustic insulation is obtained. In fact, sandwich structures with viscoelastic layer are commonly used in many applications for vibration damping and noise control. In such structures, the main energy loss mechanism is due to the transverse shear of the viscoelastic core. However, at low frequency, in particular around the mass-air-mass resonance of the double wall, the acoustic performance of this type of system is greatly deteriorated and the viscoelastic layer is not effective for treating the fall of the sound transmission loss. The aim of this work is to reduce the sound transmission at these resonance frequencies by a passive piezoelectric shunt technique through a full finite element modeling of the problem. In this technology, the elastic structure is equipped with piezoelectric patches that are connected to a passive electrical circuit, called a shunt. The piezoelectric patches transform mechanical energy of the vibrating structure into electrical energy, which is then dissipated by Joule heat in the shunt circuits.

The present work concerns the numerical modeling of noise and vibration reduction of double laminated walls with viscoelastic interlayers by using shunted piezoelectric elements. The objective is to propose efficient reduced order finite element model able to predict the shunt damping around the mass-air-mass resonance of the system.

2   FINITE ELEMENT FORMULATION

Consider the double-wall structure shown in Fig. 1. A prescribed force density $\mathbf{f}$ is applied to the external boundary Γ_t of the structural domain Ω_S. The acoustic enclosure is filled with a compressible and inviscid fluid occupying the domain Ω_F. The cavity walls are rigid except those in contact with the flexible wall structures noted Σ.
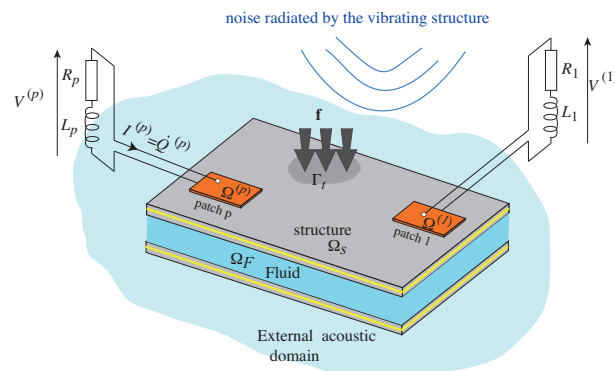
Figure 1. Double sandwich wall structure.

In order to achieve maximum vibration dissipation and acoustic radiation attenuation of selected modes, the passive piezoelectric shunt damping technique is used. Thus, a set of P piezoelectric patches are bounded on the structure surface and connected to resistive or resonant shunt circuits. In this technology, the piezoelectric patches converts a fraction of mechanical energy associated with the structure vibration into electrical energy, which is dissipated by heat through the resistor in the shunt circuits. Each piezoelectric patch has the shape of a plate with its upper and lower surfaces covered with very thin layer electrodes. Moreover, we denotes by $R^{(p)}$ and $L^{(p)}$ the resistance and the inductance of the resonant shunt circuit connected to the pth patch.

2

The general FE formulation of the electromechanical problem when the piezoelectric patches are RL shunted is [1]

$$
-\omega^2
\begin{bmatrix}
\mathbf{M}_u & \mathbf{0} & \mathbf{0} \\
\mathbf{0} & \mathbf{L} & \mathbf{0} \\
\mathbf{C}_{up}^T & \mathbf{0} & \mathbf{M}_p
\end{bmatrix}
\begin{bmatrix}
\mathbf{U} \\
\mathbf{Q} \\
\mathbf{P}
\end{bmatrix}
+ i\omega
\begin{bmatrix}
\mathbf{0} & \mathbf{0} & \mathbf{0} \\
\mathbf{0} & \mathbf{R} & \mathbf{0} \\
\mathbf{0} & \mathbf{0} & \mathbf{0}
\end{bmatrix}
\begin{bmatrix}
\mathbf{U} \\
\mathbf{Q} \\
\mathbf{P}
\end{bmatrix}
+
$$

$$
\begin{bmatrix}
\mathbf{K}_u + \mathbf{C}_{uV}\mathbf{K}_V^{-1}\mathbf{C}_{uV}^T & \mathbf{C}_{uV}\mathbf{K}_V^{-1} & -\mathbf{C}_{up} \\
\mathbf{K}_V^{-1}\mathbf{C}_{uV}^T & \mathbf{K}_V^{-1} & \mathbf{0} \\
\mathbf{0} & \mathbf{0} & \mathbf{K}_p
\end{bmatrix}
\begin{bmatrix}
\mathbf{U} \\
\mathbf{Q} \\
\mathbf{P}
\end{bmatrix}
=
\begin{bmatrix}
\mathbf{F} \\
\mathbf{0} \\
\mathbf{0}
\end{bmatrix}
\quad (1)
$$

where $\mathbf{U}$ is the column vector of nodal values of mechanical displacement; $\mathbf{M}_u$ and $\mathbf{K}_u$ are the mass and stiffness matrices of the structure (elastic structure and piezoelectric patches); $\mathbf{F}$ is the applied mechanical force vector, $\mathbf{P}$ is the column vector of nodal values of acoustic pressure; $\mathbf{M}_p$ and $\mathbf{K}_p$ are the mass and stiffness matrices of the fluid; $\mathbf{C}_{up}$ is the fluid-structure coupled matrix. Moreover, $\mathbf{Q}$ and $\mathbf{V}$ are the column vectors of electric charges and potential differences; $\mathbf{C}_{uV}$ is the electric mechanical coupled stiffness matrix; $\mathbf{K}_V$ is a diagonal matrix filled with the P capacitances of the piezoelectric patches; where $\mathbf{R}$ and $\mathbf{L}$ are the diagonal matrices filled with the electrical resistances and the electrical inductances of the shunt circuits.

3 VISCOELASTIC CORE

In order to provide better acoustic insulation, damped sandwich panels with a thin layer of viscoelastic core are used in this study (Fig. 1). In fact, when subjected to mechanical vibrations, the viscoelastic layer absorbs part of the vibratory energy in the form of heat. Another part of this energy is dissipated in the constrained core due to the shear motion.

In this work, a linear, homogeneous and isotropic viscoelastic core is used. This material is defined by a complex and frequency dependent shear modulus in the form [2]

$$
G^*(\omega) = G^{'}(\omega) + iG^{''}(\omega) \quad (2)
$$

where $G^{'}(\omega)$ is know as shear storage modulus, as it is related to storing energy in the volume and $G^{''}(\omega)$ is the shear loss modulus, which represents the energy dissipation effects.

4 REDUCED ORDER MODEL

The finite element model of Eq. (1) is applicable only to a model which does not imply a prohibitive number of degrees of freedom. To overcome these limitations, we developed a reduced-order formulation for computing the frequency response functions of the fully coupled visco-electro-mechanical-acoustic system. The proposed approach is based on a normal mode expansion and truncation of high-frequency modes. The chosen reduction concerns only the mechanical and acoustical variables $\mathbf{U}$ and $\mathbf{P}$. The electrical unknown field $\mathbf{Q}$ is not concerned by the reduction because the dimension of this vector corresponds to the number of piezo-patches and therefore is very small compared to the mechanical (i.e., displacement in the host structure and the piezo-patches) and acoustical finite element degrees-of-freedom. The mechanical displacement unknown is projected on a truncated basis composed by the first structural *in vacuo* modes with short-circuited patches while the acoustic pressure unknown is projected on a truncated basis composed by the first acoustic normal mode computed from the Helmholtz equation with rigid boundary conditions.

5   EXEMPLE

This example concerns the control of sound transmission through a double laminated glazing panels using shunted piezoelectric patches (Fig. 2-a). The system consists of two identical clamped laminated panels of glass separated by an air cavity. Each laminated glass is composed of two glass plates bonded together by a viscoelastic interlayer. Fig. 2-b presents the normal sound transmission loss of the laminated double wall with and without piezoelectric shunt. The response is calculated with a modal reduction approach using the first 20 in vacuo structural modes and the first 20 acoustic modes of the fluid in rigid cavity with static correction. It can be seen that the resonant magnitude of the second mode (the mass-air-mass resonance) has been significantly reduced. In fact, the strain energy contained in the piezoelectric material is converted into electrical energy and hence dissipated into heat using the RL shunt device.
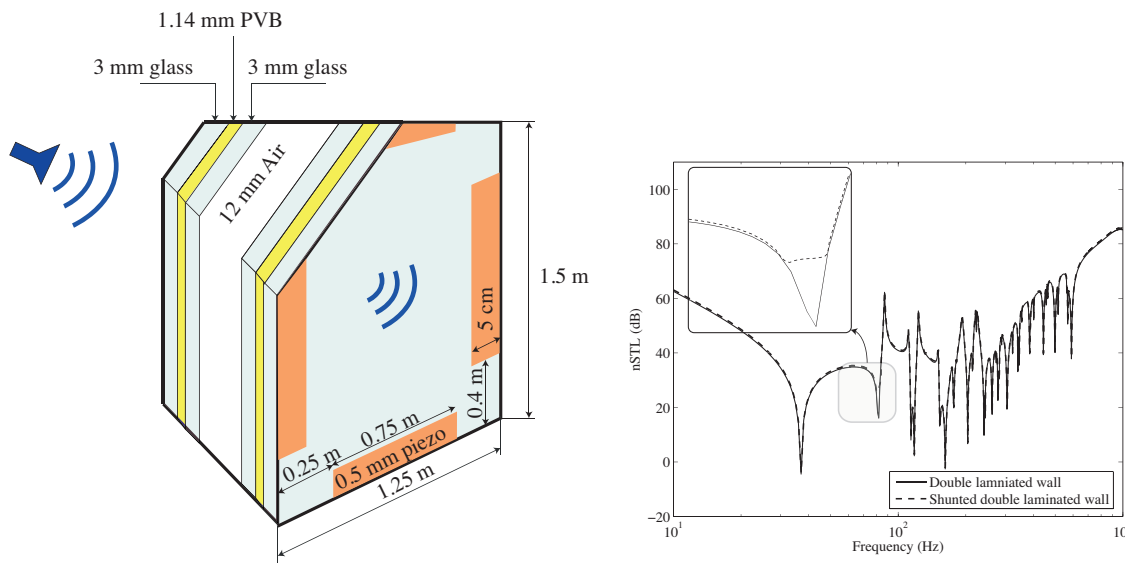
Figure 2:   (a) Double laminated glazing panels, (b) Normal sound transmission loss of laminated double panels: control of panel-air-panel resonance by shunted piezoelectric patches.

6   CONCLUSIONS

In this paper, a finite element formulation for sound transmission reduction through double wall sandwich panels with viscoelastic core and piezoelectric shunted patches is presented. A reduced-order model, based on a normal mode expansion, is then developed. The proposed methodology is applied to the control of the mass-air-mass resonance frequency of a double-glazing structure.

REFERENCES

[1] W. Larbi, J.-F. Deü, Ohayon, and R. Sampaio. Coupled fem/bem for control of noise radiation and sound transmission using piezoelectric shunt damping. *Applied Acoustics*, 86:146–153, 2014.

[2] R. Ohayon and C. Soize. Advanced computational vibroacoustics: Reduced-order models and uncertainty quantification. Cambridge University Press, 2014.

4

SIMULATION OF RACK-PINION GEARS IN STEERING SYSTEMS USING ELASTIC MULTIBODY MODELS

Christian Pfister[12*], Jens Pfister[2] and Peter Eberhard[1]

[1]Institute of Engineering and Computational Mechanics
University of Stuttgart, Pfaffenwaldring 9, 70569 Stuttgart, Germany
Email: christian.pfister@itm.uni-stuttgart.de, peter.eberhard@itm.uni-stuttgart.de

[2]Robert Bosch Automotive Steering GmbH
Richard Bullinger Str. 77, 73527 Schwäbisch Gmünd, Germany
Email: christian.pfister@bosch.com, jens.pfister@bosch.com

ABSTRACT

In this work the use of elastic multibody systems for noise, vibration, and harshness investigations in electric power steering systems is discussed. The gears in these systems can get highly stimulated in different driving situations and may produce undesired vibrations. Rigid multibody systems may represent the system dynamics very well, but elastic deformations in flexible systems are neglected with this method. Elastic multibody systems represent a good compromise between computation time and accuracy in the elastic deformations. This work presents an implementation of the software package Gear Train Module in the simulation environment at Bosch Automotive Steering. With this implementation it is possible to use elastic multibody systems for dynamic calculations of rack-pinion gears in automotive steering systems.

1   INTRODUCTION

Recently the automotive industry has seen a strong gain in the use of electric components. Also, in the field of steering systems hydraulic concepts have effectively been replaced by more efficient electric power steering (EPS) concepts. Instead of hydraulic pressure, the driver's steering input is supported by an auxiliary steering torque, generated by an electric servo drive. A summary of different EPS concepts can be found in [1]. The mostly used design in upper class cars is the EPS *axle parallel* (EPSapa) concept, where a belt driven ballnut gear transforms its rotary motion into a translative motion of the rack, see Figure 1. A great advantage of these systems is the low energy consumption. Additionally, they allow extra features like supporting lane departure warning systems, automatic parking assistance and even highly automated driving.
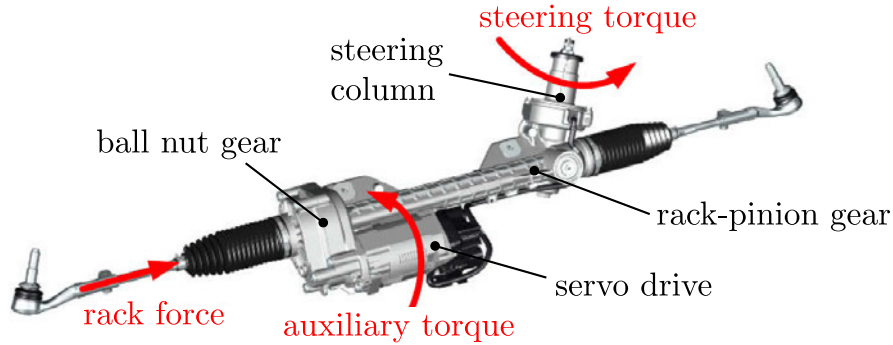
Figure 1: Acting forces on an electric power steering (EPSapa) [1].

However, one important challenge in developing EPS systems is the handling of arising vibrations from additional drive and gear components. Especially in gearing parts, different undesired phenomena may occur like toothing rattle or clunk. They may appear to the driver as audible noise or even as haptically sensible vibrations on the steering wheel and must be prevented to ensure a high driving comfort. Since these phenomena have a highly dynamic character, their identification requires efficient transient simulation approaches, like multibody systems (MBS). However, phenomena related to structural elasticity are often not represented correctly in rigid MBS. Also, finite element (FE) analyses are not appropriate for these tasks because despite offering very accurate results, they have the drawback of very big computation times. In such cases, elastic multibody systems (EMBS) offer a good compromise between fast computation and sufficient accuracy related to the elastic deformation. In [2] the use of EMBS on flexible gear wheels was shown.

This work discusses the use of the EMBS method to calculate accurate contact forces in the rack-pinion gear of an electric power steering. The software package *Gear Train Module* (GTM) [3] was used and extended to set up and simulate rack-pinion models.

2   ELASTIC MULTIBODY SYSTEMS WITH CONTACT

The concept of EMBS in the floating frame of reference formulation is described in detail in [4]. The equation of motion for a free body is

$$\boldsymbol{M}^i \underbrace{\begin{bmatrix} \dot{\boldsymbol{v}}^i \\ \dot{\boldsymbol{\omega}}^i \\ \ddot{\boldsymbol{q}}^i \end{bmatrix}}_{\dot{\boldsymbol{z}}^i_{II}} = -\boldsymbol{h}^i_e - \boldsymbol{h}^i_\omega - \boldsymbol{h}^i_p - \boldsymbol{h}^i_d, \tag{1}$$

2

where M^i is the symmetric mass matrix, containing mass, inertia and, coupling terms. The vector of generalized accelerations z_{II}^i holds the translational and rotational accelerations $\dot{v}^i$ and $\dot{\omega}^i$ of the rigid body motion and the elastic acceleration $\ddot{q}^i$ with $\dim(q^i) = n_i$. They are obtained via model order reduction from the original FE system with $\dim(\bar{q}^i) = N_i$ by $q^i \approx V \cdot \bar{q}^i$, containing the projection matrix $V \in \mathbb{R}^{N_i \times n_i}$. The force terms on the right hand side consist of inner forces h_e^i, volume forces h_ω^i, surface forces h_p^i, and discrete applied forces h_d^i.

There exist different approaches for the consideration of mechanical contact in MBS, see [5]. One detailed approach is the general 3-D node to surface contact search, where the FE meshes of the bodies are used for mutual intersection checks. In case of intersection, a penalty force is calculated based on the penetration depth. Benefits of this contact model are, that malpositioning of gears can be handled natively and elastic deformations of the bodies are respected by transforming the contact elements into the deformed configuration. However, because of the high computational effort of a node to surface contact search it is mandatory to execute a coarse collision detection upfront. In the special case of gear contact, based on the current tooth positions additionally a preselection of the contact sets can be done to limit the computational effort even further.

3   MODELING AND SIMULATION OF A RACK-PINION GEAR

The following shows the setup and results of an impact test, that was simulated in GTM with a rack-pinion model from [6]. The FE mesh of the model, with the components rack (red) and pinion (white), is illustrated in Figure 2. To classify the EMBS results, comparisons to corresponding rigid MBS and FE simulations are made.
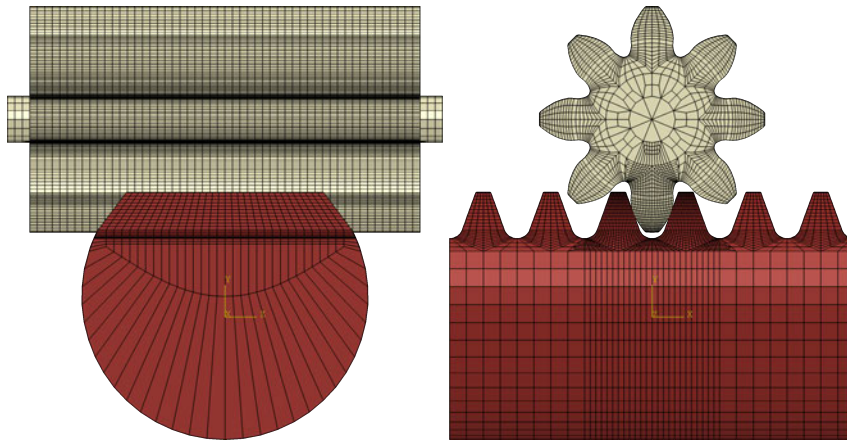
Figure 2: Rack-pinion gear test model [6].

For this test, the rack is fixed in all spatial directions, the pinion has a rotary degree of freedom around its main rotation axis with a starting angular velocity of 100 rad/s. The penalty contact stiffness is set to $3.5\mathrm{E}^7$ N/m. In [2] it was shown that modes up to 80 kHz are needed to provide an adequate result in the contact force. Both bodies were reduced by modal truncation to 200 elastic degrees of freedom.

The resulting cumulative contact forces and angular velocities of all investigated methods are shown in Figure 3. It can be seen, that the FE and EMBS results match very well. They contain significant oscillations due to elastic deformations during contact, while they are missing in the rigid model. The resulting simulation time for the EMBS method on an Intel Core i7 computer is shown in Table 1. It provides results 2.5 times slower than the rigid MBS, but is about 15 times faster then the FE simulation.

3
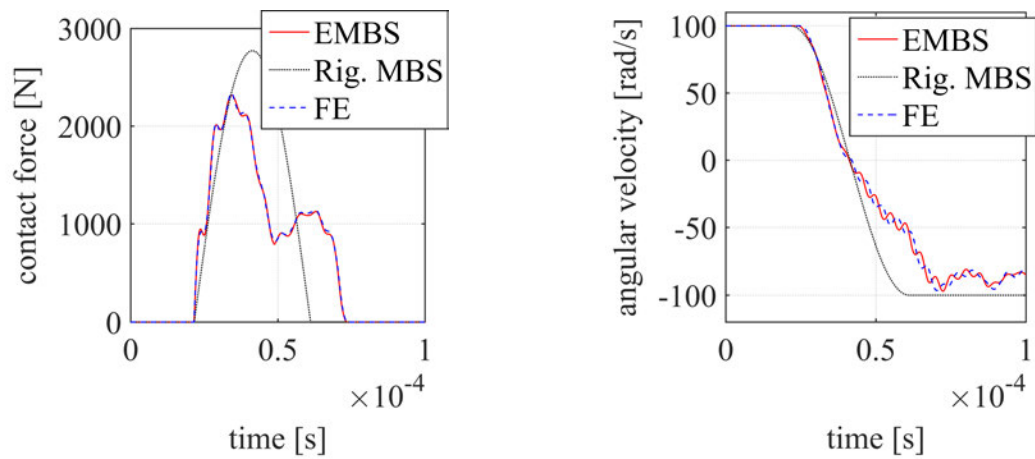
Figure 3: Cumulative contact forces and angular velocities in the different configurations.

Table 1: Comparison of simulation time (in seconds).

	EMBS	Rigid MBS	FE analysis
calculation time	210	80	3180

4   CONCLUSION

This work showed the benefit of using EMBS in gearing calculations within steering systems. With EMBS the elasticity of the gears can be considered in rack-pinion gearing calculations, enabling the identification of structural vibrations. Anyway, the computational effort is much smaller compared to a finite element analysis.

REFERENCES

[1] P. Pfeffer and M. Harrer. *Lenkungshandbuch (in German)*. ATZ/MTZ-Fachbuch. Springer, Wiesbaden, 2013.

[2] P. Ziegler. *Dynamische Simulation von Zahnradkontakten mit elastischen Modellen (in German)*. Dissertation, Schriften aus dem Institut für Technische und Numerische Mechanik der Universität Stuttgart, Band 23. Shaker Verlag, Aachen, 2012.

[3] P. Ziegler, D. Schurr, and C. Pfister. Software GTM. URL: `www.itm.uni-stuttgart.de/research/geartrain/introduction/intro_en.php`. Accessed: 2016-12-14.

[4] R. Schwertassek and O. Wallrapp. *Dynamik flexibler Mehrkörpersysteme (in German)*. Vieweg, Braunschweig, 1999.

[5] P. Wriggers. *Computational Contact Mechanics*. Springer, Wiesbaden, 2006.

[6] A. Wolfien. *Untersuchungen zum Beanspruchungsverhalten von Zahnstangengetrieben in PKW-Lenksystemen (in German)*. Private communications, 2016.

4

TIME DOMAIN FINITE ELEMENT ANALYSIS OF STRUCTURES WITH FRACTIONAL VISCOELASTIC DAMPING USING TIME-DIFFUSIVE SCHEME

J.F. Deü[1] , L. Rouleau[1*] and D. Matignon[2]

[1]Structural Mechanics and Coupled Systems Laboratory
Conservatoire national des arts et métiers (Cnam), 292 Rue Saint-Martin, F-75141 Paris cedex 03, France
Email: jean-francois.deu@cnam.fr, lucie.rouleau@cnam.fr

[2]Université de Toulouse,
ISAE-SUPAERO, 10 avenue Edouard Belin, B.P. 54032, F-31005, Toulouse cedex 4, France
Email: denis.matignon@isae.fr

ABSTRACT

This work aims at simulating the time response of a structure damped by viscoelastic materials. The structure is discretised by finite elements and a 4-parameter fractional derivative model is used to describe the frequency-dependency of the mechanical properties of the viscoelastic material. The proposed approach combines a classical Newmark time-integration scheme to solve the semi-discretised equation of motion with a diffusive representation of fractional derivatives. This approach is applied to a finite element model, and validated on a single degree-of-freedom system for which an analytical solution can be derived.

1 INTRODUCTION

The importance of fractional calculus for modeling viscoelastic material behavior has been recognized by the mechanical scientific community since the pioneering work of Bagley and Torvik [1]. The merits of using fractional differential operator lie in the fact that few parameters are needed to accurately describe the constitutive law of damping materials and the resulting model can be easily fitted to experimental data over a broad range of frequencies. While the use of such models is quite straightforward in the frequency domain, some difficulties arise from their application in the time-domain, due to the presence of fractional derivatives.

The resolution methods are classically either based on time discretization of the fractional dynamics (see e.g. [2]), or on diffusive representations (cf. [3]). For large scale systems, the first method proves memory consuming because it is necessary to store the whole displacement history of the system due to the non-local character of the fractional derivatives. The second method, based on diffusive realizations of fractional derivatives, is numerically more efficient because it has no hereditary behavior, thus avoiding the storage of the solution from all past time steps. The diffusive representation, coupled with a Newmark integration scheme, has already been developed and validated for a fractionally damped single-of-freedom system [4]. In [5], an extension of this approach to viscoelastic structures using FE modeling and a fractional derivative model has been presented but not tested. The purpose of this work is to implement the method described in [5] and to apply it to a structure with viscoelastic damping. The approach is validated on a single degree-of-freedom system for which an analytical solution can be derived.

2 FINITE ELEMENT VISCOELASTIC PROBLEM

We consider a structure composed of elastic and viscoelastic materials. A fractional derivative model is identified to described the frequency-dependency of the complex shear and the bulk moduli (resp. $\hat{G}$ and $\hat{K}$) of the viscoelastic material:

$$\hat{G}(\omega) = G_0 + \frac{(G_\infty - G_0)(i\omega\tau_G)^{\alpha_G}}{1 + (i\omega\tau_G)^{\alpha_G}} \quad \text{and} \quad \hat{K}(\omega) = K_0 + \frac{(K_\infty - K_0)(i\omega\tau_K)^{\alpha_K}}{1 + (i\omega\tau_K)^{\alpha_K}} \quad (1)$$

where G_0 and K_0 are relaxed moduli, G_∞ and K_∞ are unrelaxed moduli satisfying $G_\infty > G_0$ and $K_\infty > K_0$, $\tau_G > 0$ and $\tau_K > 0$ are relaxation times and α_G and α_K are fractional coefficients comprised bewteen 0 and 1. Figure 1 shows that the fractional derivative model enables a good representation of the frequency-dependency both the shear and the bulk moduli over a wide frequency range with few parameters.

The finite element discretization of the equation of motion leads to the following matrix system:

$$\left[\mathbb{K}_e + i\omega\hat{h}_G(\omega)\mathbb{K}_v^G + i\omega\hat{h}_K(\omega)\mathbb{K}_v^K - \omega^2\mathbb{M}\right]\hat{\mathbf{U}} = \hat{\mathbf{F}} \quad (2)$$

where $\mathbb{K}_e = \mathbb{K}_{ep} + G_0\left(\mathbb{K}_v^G\right)_0 + K_0\left(\mathbb{K}_v^K\right)_0$, $\mathbb{K}_v^G = (G_\infty - G_0)\left(\mathbb{K}_v^G\right)_0$, and $\mathbb{K}_v^K = (K_\infty - K_0)\left(\mathbb{K}_v^K\right)_0$. The matrix $\mathbb{K}_{ep}$ is the stiffness matrix associated to the volume of elastic part of the model, $\mathbb{M}$ is the mass matrix of the whole system, and the stiffness matrix associated to the volume of viscoelastic material (computed with unitary moduli), is separated into a spheric part $\left(\mathbb{K}_v^K\right)_0$ and a deviatoric part $\left(\mathbb{K}_v^G\right)_0$. According to Equation (1), the functions $\hat{h}_G(\omega)$ and $\hat{h}_K(\omega)$ are expressed as:

$$\hat{h}_G(\omega) = \frac{\tau_G^{\alpha_G}}{(i\omega)^{1-\alpha_G}[1 + (i\omega\tau_G)^{\alpha_G}]} \quad \text{and} \quad \hat{h}_K(\omega) = \frac{\tau_K^{\alpha_K}}{(i\omega)^{1-\alpha_K}[1 + (i\omega\tau_K)^{\alpha_K}]} \quad (3)$$
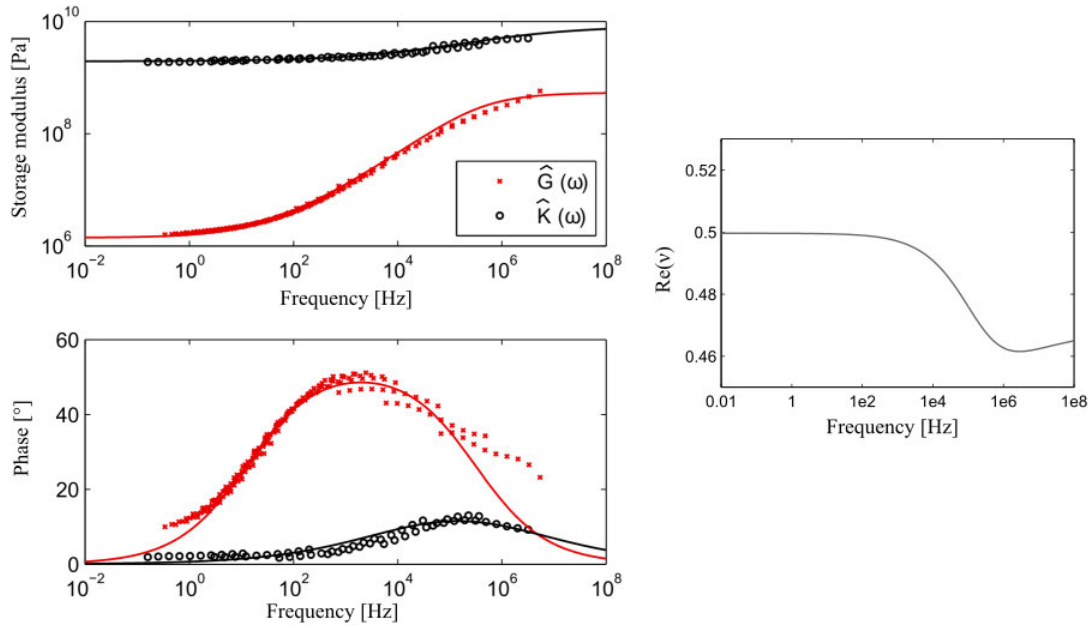
Figure 1: Master curves of the complex shear and bulk moduli of Deltane 350 (Paulstra®) measured (points) by DMA and fitted (lines) by a fractional derivative model (left). Real part of the complex Poisson ratio from identified models (right).

3   COUPLED NEWMARK-DIFFUSIVE SCHEME

Equation (2) can be rewritten in the time domain as follows:

$$\mathbb{M}\ddot{\mathbf{U}} + \left(h_G(t) \star \mathbb{K}_v^G + h_K(t) \star \mathbb{K}_v^K\right)\dot{\mathbf{U}} + \mathbb{K}_e\mathbf{U} = \mathbf{F}(t) \tag{4}$$

where the symbol $\star$ represents a convolution product.
Following e.g. [3, 5], letting $\mathbf{V} = \dot{\mathbf{U}}$, the functions $h_G(t)$ and $h_K(t)$ will be realized by a standard diffusive representation of the form:

$$\frac{\partial \boldsymbol{\varphi}(\xi,t)}{\partial t} = -\xi\boldsymbol{\varphi}(\xi,t) + \mathbf{V}(t), \quad \text{with } \boldsymbol{\varphi}(\xi,0) = \mathbf{0} \tag{5}$$

observed through the continuous superposition:

$$(h_j \star \mathbf{V})(t) = \int_0^\infty \mu^j(\xi)\boldsymbol{\varphi}(\xi,t)\mathrm{d}\xi \quad \text{with } j = G, K \tag{6}$$

This exact diffusive representation can be approximated as follows:

$$\int_0^\infty \mu^j(\xi)\boldsymbol{\varphi}(\xi,t)\mathrm{d}\xi \approx \sum_{n=1}^N \mu_n^j\boldsymbol{\varphi}(\xi_n,t) \quad \text{with } j = G, K \tag{7}$$

where N is the number of approximation nodes, ξ_n a sequence of angular frequencies in the frequency range of interest and μ_n^G and μ_n^K are the corresponding optimal weights computed by minimising the respective functions $\mathcal{C}_G(\boldsymbol{\mu}^G)$ and $\mathcal{C}_K(\boldsymbol{\mu}^K)$ defined as [4]:

$$\mathcal{C}_j(\boldsymbol{\mu}^j) = \sum_{l=1}^L \left|\sum_{n=1}^N \frac{\mu_n^j}{\mathrm{i}\omega_l + \xi_n} - \frac{1}{(\mathrm{i}\omega_l)^{1-\alpha_j}}\right|^2 \quad \text{with } j = G, K \tag{8}$$

3

where ω_l are angular frequencies and $L >> N$.

This diffusive representation is integrated into a Newmark integration scheme, by considering the functions $\varphi_n(\xi_n) := \varphi(\xi_n, t)$ as internal variables updated at each time steps. More details on the time integration scheme have been presented in [5].

4 ANALYTICAL SOLUTION FOR A SINGLE-DEGREE-OF-FREEDOM SYSTEM

The equation of motion for a single-degree-of-freedom system is:

$$\left(k_e + \frac{(i\omega\tau)^\alpha}{1 + (i\omega\tau)^\alpha} k_v - \omega^2 m \right) \hat{u} = \hat{f}, \tag{9}$$

and can be rewritten in the time domain as:

$$\left[m\tau^\alpha (D_t)^{2+\alpha} + m(D_t)^2 + (k_e + k_v)\tau_\alpha (D_t)^\alpha + k_e \right] u(t) = \left[1 + \tau^\alpha (D_t)^\alpha \right] f(t) \tag{10}$$

where $(D_t)^\beta$ represents the time derivative of order β (integer or fractional), and $\alpha = p/q$, with p and q integers satisfying $p/q \in [0, 1]$.

To analytically solve this equation, the exact solution is expressed in terms of fractional power series:

$$u(t) = \sum_{n=0}^{\infty} u_n t^{\frac{n}{q}} \tag{11}$$

where the coefficients u_n are calculated from initial conditions and recurrence relationships.

5 CONCLUSION

The coupled Newmark-diffusive scheme described in this paper will be used to compute the time response of a viscoelastically damped structure, modelled by 3D finite elements. Validation of the proposed approach will be carried out on the single-degree-of-freedom system, by comparing the analytical solution with that obtained by the proposed approach.

REFERENCES

[1] R. Bagley and P. Torvik. Fractional calculus – a different approach to the analysis of viscoelastically damped structures. *AIAA Journal*, 5(5):741–748, 1983.

[2] A.C. Galucio, J.-F. Deü, and R. Ohayon. Finite element formulation of viscoelastic sandwich beams using fractional derivative operators. *Computational Mechanics*, 33(4):282–291, 2004.

[3] D. Matignon. Stability properties for generalized fractional differential systems. in: ESAIM: Proceedings, pp. 145-158, 1998.

[4] J.-F. Deü and D. Matignon. Simulation of fractionally damped mechanical systems by means of a Newmark-diffusive scheme. *Computers and Mathematics with Applications*, 59:1745–1753, 2010.

[5] J.-F. Deü and D. Matignon. A numerical scheme of time-domain FE analysis of viscoelastic structures with fractional derivative contitutive equations. in: 4th International Conference on Computational Methods in Sturctural Dynamics and Earthquake Engineering, CompDyn'13, 2013.

4

A SPECTRAL BOUNDARY ELEMENT APPROACH TO REPRESENT SCATTERED WAVES IN UNBOUNDED ACOUSTIC REGIONS

F.J. Cruz-Muñoz[1], A. Romero[1], A. Tadeu[2] and P. Galvín[1]

[1]Escuela Técnica Superior de Ingeniería, Universidad de Sevilla
Camino de los Descubrimientos, 41092 Sevilla, SPAIN
Email: fracrumun@gmail.com, aro@us.es, pedrogalvin@us.es

[2]Department of Civil Engineering, University of Coimbra
Pólo II, Rua Luís Reis Santos, 3030-788 Coimbra, PORTUGAL
Email: tadeu@dec.uc.pt

ABSTRACT

This work presents a two-and-a-half (2.5D) spectral formulation based on the boundary element method (BEM) to study three dimensional (3D) wave propagation within acoustic regions. The BEM is used to analyse the acoustic field in unbounded regions with rigid cavities with arbitrary cross-section. The BEM is extended to its spectral formulation using Lagrange interpolant polynomials as element shape functions at the Legendre-Gauss-Lobatto (LGL) points. The proposed method is verified from a benchmark problem regarding the acoustic scattered wave in an unbounded medium by a rigid cavity. A h-p analysis is carried out to assess the accuracy of the method. The results show a high accuracy of the proposed method to represent this kind of problem.

1   INTRODUCTION

Time-harmonic wave propagation, such as fluid acoustics and solid scattering, is a common phenomenon that appears in many engineering fields. The propagation of acoustic waves triggered by static and moving pressure sources, the vibration assessment and the acoustic insulation involve fluid and solid interaction and must be considered rigorously. The finite element method (FEM) have been used is several works to predict the response in fluid-structure interaction problems. For the low frequency range, the conventional finite elements with linear shape represent accurately the fluid and solid scattering waves. However, at high frequencies, these shape functions do not provide reliable results due to so-called pollution effects [1, 2]: the accuracy of the numerical solution deteriorates with increasing non-dimensional wave number and it is not sufficient the commonly employed rules of n elements per wavelength [3]. High element resolutions are required in order to obtain results with reasonable accuracy.

The method proposed in this work regards with a two-and-a-half dimensional (2.5D) approach to represent scattered waves in fluid media. The proposed approach is useful for problems where the material and geometric properties are uniform along one direction, and the source exhibits 3D behaviour.

2   NUMERICAL MODEL

The 2.5D formulation computes the problem solution as the superposition of two-dimensional (2D) problems with a different longitudinal wavenumber, k_z, in the z direction. An inverse Fourier transform is used to compute the 3D solution:

$$a(\mathbf{x}, \omega) = \int_{-\infty}^{+\infty} \widehat{a}(\widehat{\mathbf{x}}, k_z, \omega) e^{-ik_z z} dk_z \tag{1}$$

where $a(\mathbf{x}, \omega)$ is an unknown variable (e.g., displacement or pressure), $\widehat{a}(\widehat{\mathbf{x}}, k_z, \omega)$ is its representation in the frequency-wavenumber domain, $\widehat{\mathbf{x}} = \mathbf{x}(x, y, 0)$, ω is the angular frequency, and $i = \sqrt{-1}$.

2.1   The 2.5D spectral boundary element formulation

The boundary element formulation presented in this work considers an arbitrary boundary submerged in an unbounded fluid medium. The integral representation of the pressure p^i for a point i located at the fluid subdomain $\Omega_{f\infty}$, with zero body forces and zero initial conditions may be written as [4]:

$$c^i p^i(\mathbf{x}^i, \omega) = \int_{\Gamma_f} p^{i*}(\mathbf{x}, \omega; \mathbf{x}^i) u^i(\mathbf{x}, \omega) d\Gamma - \int_{\Gamma_f} u^{i*}(\mathbf{x}, \omega; \mathbf{x}^i) p^i(\mathbf{x}, \omega) d\Gamma \tag{2}$$

where $u^i(\mathbf{x}, \omega)$ and $p^i(\mathbf{x}, \omega)$ are respectively the normal displacement to boundary Γ_f and the nodal pressure. $u^{i*}(\mathbf{x}, \omega; \mathbf{x}^i)$ and $p^{i*}(\mathbf{x}, \omega, \mathbf{x}^i)$ are respectively the fluid full-space fundamental solution for normal displacement and pressure at point $\mathbf{x}$ due to a point load at $\mathbf{x}^i$. The integral-free term c^i depends only on the boundary geometry at point i. The integration boundary Γ_f represents the boundary between the unbounded fluid medium ($\Omega_{f\infty}$) and the solid subdomain (Ω_s). The proposed spectral boundary element method for the 2.5D fluid element uses Legendre polynomials of order p as interpolation shape functions, where the local nodal coordinates ξ are found at the LGL integration points.

3   NUMERICAL VERIFICATION

The BEM model was verified with a benchmark problem. The model was implemented and validated by applying it to a fixed cylindrical circular cavity, submerged in a homogeneous unboundend fluid medium. The cavity is subjected to a harmonic point pressure load. The analytical solution to this problem can be found in Reference [5].

The cavity had a radius $r = 5$ m , located at the origin $(x, y) = (0, 0)$. The unbounded fluid medium properties were pressure wave velocity $\alpha = 1500$ m/s and density $\rho = 1000 \, \text{kg/m}^3$. The problem solution was computed for a dilatational point source placed at the fluid medium $\widehat{\mathbf{x}}_0 = (x_0, y_0) = (0, 15)$ 15 m away from the cavity centre. This loads emits a harmonic incident field $\widehat{p}_{inc}$ at a point $\widehat{\mathbf{x}}$ described by:

$$\widehat{p}_{inc} = (\widehat{\mathbf{x}}, \omega, k_z) = \frac{-iA}{2} H_0^{(2)}(k_\alpha \sqrt{(x - x_0)^2 + (y - y_0)^2}) \tag{3}$$

where A is the source amplitude, $H_0^{(2)}$ is the Hankel function of the second kind, and $k_\alpha = \sqrt{\alpha / \omega}$. In this problem, the longitudinal wavenumber was set to $k_z = 0$.

The problem solution was computed over a grid of 1376 receivers regularly spaced in a outer region defined by $-10\text{m} \leq x \leq 10\text{m}$ and $-10\text{m} \leq y \leq 10\text{m}$. Figure 1 shows the convergence curves for the scaled L_2 error ϵ_2. The curves show a monotonic convergence with the element order p. Finest meshes tend to a minimum error with a lower element order p.
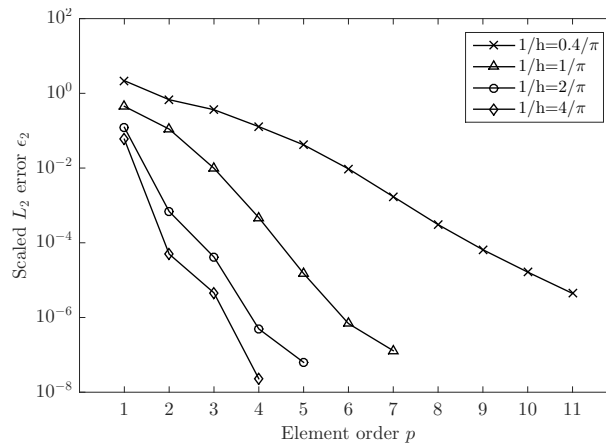
Figure 1: Convergence of scaled L_2 error ϵ_2 for different discretisations $1/h$ and element polynomial orders p.

4   CONCLUSIONS

This work has proposed a spectral based formulation based on the BEM to study acoustic wave propagation. This method looks at 3D problems whose materials and geometric properties remain homogeneous in one direction. A spectral 2.5D approach for fluid-acoustics media was developed to avoid the pollution effect at high frequencies in the problem solution. The model was verified with a benchmark problem with known analytical solution. The numerical result was in good agreement with the reference solution.

REFERENCES

[1] I. Babuka, F. Ihlenburg, E.T. Paik, and S.A. Sauter, *A generalized finite element method for solving the helmholtz equation in two dimensions with minimal pollution*, Computer Methods in Applied Mechanics and Engineering **128** (1995), no. 3-4, 325–359.

[2] F. Ihlenburg, I. Babuka, and S. Sauter, *Reliability of finite element methods for the numerical computation of waves*, Advances in Engineering Software **28** (1997), no. 7, 417–424.

[3] F. Ihlenburg, *The medium-frequency range in computational acoustics: Practical and numerical aspects*, Journal of Computational Acoustics **11** (2003), no. 2, 175–193.

[4] J. Domínguez, *Boundary elements in dynamics*, Computational Mechanics Publications and Elsevier Aplied Science, Southampton, 1993.

[5] A.J.B. Tadeu and L.M.C. Godinho, *Three-dimensional wave scattering by a fixed cylindrical inclusion submerged in a fluid medium*, Engineering Analysis with Boundary Elements **23** (1999), no. 9, 745–755.

4

EXTENSION OF THE VARIATIONAL THEORY OF COMPLEX RAYS FOR HETEROGENEOUS MEDIA

H. RIOU[1], H. LI[1] and P. LADEVEZE[1]

[1]LMT, ENS Cachan, CNRS, Université Paris-Saclay, F-94235, Cachan, FRANCE
Email: riou@lmt.ens-cachan.fr, hao-li@lmt.ens-cachan.fr, ladeveze@lmt.ens-cachan.fr

ABSTRACT

The Variational Theory of Complex Rays (VTCR) is a numerical technique that has been developed for the prediction of vibration problems in the medium frequency regime. It is a Trefftz Discontinuous Galerkin method which uses plane wave functions as shape functions. As such, one of its characteristics is the necessity for the shape functions to satisfy exactly the governing equation. For heterogeneous media, this is clearly a difficulty, as no such exact solution is known. In this paper, the VTCR is extended to bypass this difficulty, by creating a new base of shape functions.

[1] INTRODUCTION

Today, one way to efficiently solve the medium frequency problems is to adopt a Trefftz approach. By doing this, the user makes an analysis based on shape functions which satisfy exactly the governing equation, then containing a strong knowledge of the physical problem. These methods are, for example, the partition of unity method [1], the ultra weak variational method [2], the least square method [3], the plane wave discontinuous Galerkin method [4], the method of fundamental solutions [5] the discontinuous enrichment method [6], the wave based method [7]. The Variational Theory of Complex Rays (VTCR), which is the approach used in this paper, also belongs to this category of strategies. It has been introduced in [8]. All these techniques have shown a good efficiency for the resolution of vibration problems. However, they are mainly all limited to homogeneous media, i.e. to constant wave numbers.

In this paper, we propose a development of the VTCR which allows us to solve vibration problems with varying wave numbers. It is based on the definition of a new type of shape functions, composed of Airy functions, which satisfy a priori the dominant part of the governing equation.

[2] REFERENCE PROBLEM TO SOLVE

Let us consider a 2-D Helmholtz problem defined on Ω with the boundary $\partial\Omega=\partial_1\Omega\cup\partial_2\Omega$ where Dirichlet and Neumann can be prescribed. The reference problem to solve is: find $u\in H^1(\Omega)$ such that

$$(1-i\eta)\Delta u+k^2u=0 \text{ over } \Omega$$
$$u=u_d \text{ over } \partial_1\Omega$$
$$(1-i\eta)\partial_n u=g_d \text{ over } \partial_2\Omega$$

where η is the (positive) damping coefficient, k the wave number and ∂_n is the normal derivative. u_d and g_d are prescribed boundary conditions.

[3] VTCR FORMULATION OF THE REFERENCE PROBLEM

Let us suppose that Ω is partitioned in E subdomains: $\Omega=\cup_{e=1}^E \Omega_e$. We denote by $\Gamma_{e,e'}$ the common boundary between Ω_e and $\Omega_{e'}$, and by $\Gamma_{e,e}$ the common boundary between Ω_e and $\partial\Omega$. The VTCR strategy consists in finding the solution

$$u\in U=\left\{u/u_e\in U_e=\left\{u_e/(1-i\eta)u_E+k^2u_E=0 \text{ over } \Omega_e\right\}\right\}$$

such that

$$\text{Re}\left(-ik\left(\sum_e \int_{\Gamma_{e,e'}}\left(\frac{1}{2}\{q_u.n\}_{ee'}.\{\bar{v}\}_{ee'}-\frac{1}{2}[\bar{q}_v.n]_{ee'}.[u]_{ee'}\right)dS\right.\right.$$
$$\left.\left.-\sum_e \int_{\Gamma_{ee}\cap\partial_1\Omega}\bar{q}_v.n(u-u_d)dS+\sum_e \int_{\Gamma_{ee}\cap\partial_2\Omega}(q_u.n-g_d)\bar{v}dS\right)\right)$$
$$=0 \quad \forall v\in U$$

where $\{u\}_{ee'}=(u_e+u_{e'})_{\Gamma_{ee'}}$, $[u]_{ee'}=(u_e-u_{e'})_{\Gamma_{ee'}}$, $q_v=(1-i\eta)grad\, u$. The over bar represents the complex conjugated part of a number, and Re the real part. The existence and uniqueness of solution in this kind of variational formulation have been proved in [9]. An approximated solution can be found by satisfying this variational formulation in a subspace of U of finite dimension.

[4] DEFINITION OF SHAPE FUNCTIONS

As mentioned in the introduction, we consider here the case where the wave number varies. We suppose, then, that we can write $k^2=\alpha x+\beta y+\gamma$, α, β and γ being constant parameters in Ω_e. The shape function needs to satisfy $(1-i\eta)u+k^2u=0$. It can be shown that, in such a case, the shape function are described by Airy functions. Different description can be used when selecting Airy functions. We have decided to use this description: the shape functions are described by $\Psi(x,y)=F(\tilde{x})G(\tilde{y})$, where $F(\tilde{x})=Bi(-\tilde{x})+i\,Ai(-\tilde{y})$ and $G(\tilde{y})=Bi(-\tilde{y})+i\,Ai(-\tilde{x})$, where Ai and Bi are the Airy functions. The new space variables are defined by $\tilde{x}=\dfrac{k_m^2\cos^2\theta+\alpha(x-x_m)}{\alpha^{2/3}(1-i\eta)^{1/3}}$ and $\tilde{y}=\dfrac{k_m^2\sin^2\theta+\alpha(y-y_m)}{\beta^{2/3}(1-i\eta)^{1/3}}$. k_m^2 represents the

2

minimum value of k^2 on Ω_e and (x_m, y_m) is the coordinate which enables k^2 to take its minimum value k_m^2. θ represents the polar direction in the 2-D coordinates. Thanks to this way of doing, the selected shape functions satisfy the properties $F(\tilde{x}) \rightarrow \cos(k_1 x) + i \sin(k_1 x)$ when $\alpha \rightarrow 0$, and $G(\tilde{y}) \rightarrow \cos(k_2 y) + i \sin(k_2 xy)$ when $\beta \rightarrow 0$. Then, the shape functions tend toward propagative plane waves when the medium becomes homogeneous.

In order to have an approximated solution, one just needs to satisfy the variational formulation in a subspace U_N of U, of dimension N. The classical way to define such a subspace is to select only N direction θ_i, $\theta_i \in \{0 ; 2*\pi/N ; ... ;(N-1)\pi/N\}$, in the 2-D polar representation. By doing this, one naturally gets a matrix system to solve, where the matrix corresponds to the projection of the bilinear part of the variational formulation on $U_N \times U_N$, the second member its projection on U_N and the unknown vector the amplitudes of the N shape functions Ψ_i which approximate the exact solution.

[5] NUMERICAL ILLUSTRATION

We consider a simple geometry of square [0 m;1 m]×[0 m;1 m] for the domain Ω. In this domain, $\eta = 0.01$, α = 150 m^{-3}, β = 150 m^{-3} and γ = 1000 m. The selected boundary conditions are Dirichlet conditions such that the exact solution is $u_{ex} = \sum_{i=1}^{3} \Psi_i(x, y)$ with $\theta_1 = 10°$, $\theta_2 = 55°$ and $\theta_3 = 70°$. The relative error between the exact and the approximated solution is computed through $\sqrt{\int_\Omega |u - u_{ex}|^2 d\Omega / \int_\Omega |u_{ex}|^2 d\Omega}$. Three space decompositions are considered: either Ω is considered as one subdomain, or is cut in four parts, or in nine parts (see figure 1).
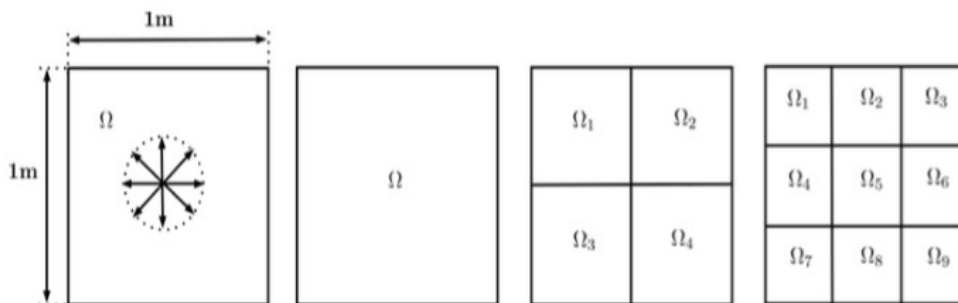
Figure 1. The considered decompositions for the selected example in Section 5.

As shown in figure 1 and explained in the last section, the approximated solutions are searched by using N shape functions regularly distributed in the 2-D polar coordinates, in each sub-domain of Ω. The convergence curve is represented in Figure 2.

As one can see, the strategy converges very fast toward the exact solution. Then, with the VTCR, few degrees of freedom are needed to get a good proximation of the solution of the reference problem. Moreover, one can see that the VTCR better works with large subdomains with many shape functions inside, than small subdomains with few shape functions inside. This behaviour has already been observed on the classic VTCR.

Figure 2. Convergence curves for the example considered in Section 5.

[6] CONCLUSION

In this works, we present how to use the VTCR for the resolution of heterogeneous media. The definition of a new type of shape function is done. This can be used on media where the wave number linearly varies thanks to the space. A numerical example shows that this works perfectly, and that it behaves like the classic VTCR. More complex media are the focus of our research.
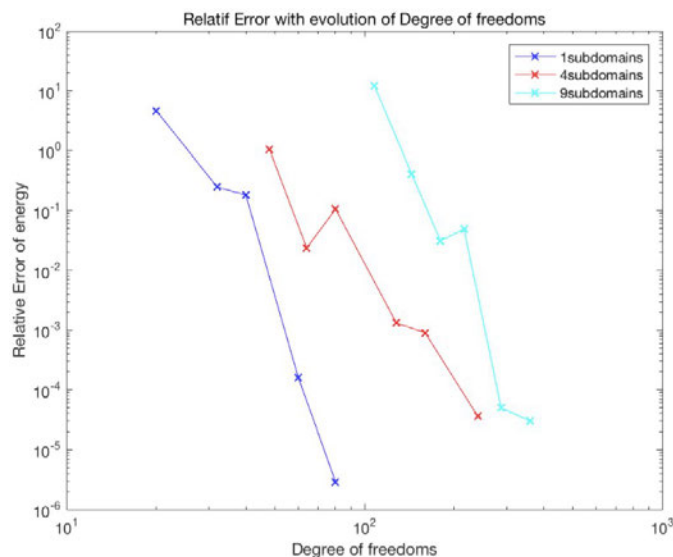
REFERENCES

[1] T. Strouboulis, R. Hidajat, Partition of unity method for Helmholtz equation: q-convergence for plane-wave and wave-band local bases, Appl. Math. 51 181-204, 2006.

[2] O. Cessenat, B. Despres, Application of an ultra weak variational formulation of elliptic PDEs to the two-dimensional Helmholtz prob- lem, SIAM J. Numer. Anal. 35 255-299, 1998.

[3] G. Gabard, P. Gamallo, T. Huttunen, A comparison of wave-based discontinuous Galerkin, ultra-weak and least-square methods for wave problems, Int. J. Num.Methods Eng. 85 380-402, 2011.

[4] C. J. Gittelson, R. Hiptmair, I. Perugia. Plane wave discontinuous Galerkin methods: analysis of the h-version, ESAIM: Mathematical Modeling and Numerical Analysis 43 297-331, 2009.

[5] A. Barnett, T. Betcke, Stability and convergence of the method of fundamental solutions for Helmholtz problems on analytic domains, J. Comput. Phys. 227 7003-7026, 2008.

[6] C. Farhat, I. Harari, L. Franca, The discontinuous enrichment method, Comput. Methods Appl. Mech. Eng. 190 6455-6479, 2001.

[7] W. Desmet, P. Sas, D. Vandepitte, An indirect Trefftz method for the steady-state dynamic analysis of coupled vibro-acoustic systems, Comput. Assisted Mech. Eng. Sci. 8 271-288, 2001.

[8] P. Ladevèze, A new computational approach for structure vibrations in the medium frequency range, C. R. Acad. Sci. Paris 332 849-856, 1996.

4

[9] P. Ladevèze, H. Riou. On Trefftz and weak Trefftz discontinnuous Galerkin approaches for medium-frequency acoustics, Computer Methods in Applied Mechanics and Engineering 278 729-743, 2014.

FAST 1D APPROACH OF SOLID ROCKET MOTOR THRUST/PRESSURE OSCILLATIONS AMPLIFICATION FACTOR

E. MAYEUR[1], J. POUCEL[1]

[1]AIRBUS SAFRAN LAUNCHERS
Rue de Touban, 33185, Le Haillan
Email: emmanuel.mayeur@airbusafran-launchers.com
julien.poucel@airbusafran-launchers.com

ABSTRACT

Under some conditions, Solid Rocket Motors (SRM) may exhibit internal Pressure Oscillations (PO) as a result of a coupling between aerothermal or combustion phenomena with the cavity longitudinal acoustic modes, and highly depend on the internal shape of the motor and the propellant formulation. The mechanical effects of pressure oscillations lead to SRM sinusoidal vibrations - Thrust Oscillations (TO) and acceleration - which could damage both the payload and the launcher (need of additional mechanical filtering devices in such case). Evaluation of TO/PO amplification factor is therefore mandatory in the early studies of a new SRM design. Tools using 3D FE-models have been developed but based on CAD-meshing and aren't appropriate for preliminary design project and sensitivity iterations. In this context andwith the cooperation of the Centre National d'EtudesSpatiales (CNES), a fast 1D purely geometrical approach has been developed, tested and confronted to the reference tools in order to evaluate the frequencies and shapes of the acoustic modes and the static TO/PO amplification factors. This paper describes the theoretical principles, the SRM modelling hypothesis and validation cases of the developed tool.

A FIXED POINT ALGORITHM AND MODEL REDUCTION IN JOINTED STRUCTURES SIMULATION

N. Peyret[1], G. Chevallier[2], A. Meurdefroid[1]

[1]Laboratoire Quartz
Supméca, 3, rue Fernand Hainaut, F-93400 Saint-Ouen, FRANCE
Email: nicolas.peyret@supmeca.fr, anthony.meurdefroid@supmeca.fr

[2]FEMTO-ST Institute Department of Applied Mechanics
Univ. Bourgogne Franche-Comté, 24, rue de l'épitaphe, F-25000 Besançon, France
gael.chevallier@femto-st.fr

ABSTRACT

The bolted joints have a strong impact on the damping and the stiffness of the structures. This impact remains difficult to predict because of the difference between the length scale of the real contact area and the wavelength of the vibration modes, and the uncertainties on the real geometry of the contact area. The method proposed in this paper is to divide the jointed structure into two parts : the linear part (L) and the non-linear one (NL) located around the joint. First, a linear analysis is performed on the global structure, neglecting dissipation inside the joint, to determine the normal modes of the structure. The normal modes subspace is normalized to the sti_ness matrix to associate to each eigenvectors the same strain energy. In the neighborhood of the bolted joint, eigenmodes are not orthogonal to each other's. Thus, it is possible to reduce the size of the subspace spanned by the local eigenmodes. Moreover, most of them do not dissipate energy. Thus, it is possible to select the only ones that inuence the joint behaviour. We introduce the Principal Joint Strain Basis (PJSB) which is the optimal Ritz basis deduced from the structure eigenmodes, and simplified thanks to the analysis of the dissipation potential of each eigenmode.

The dissipation potential is estimated by the energy coupling in the joint computed from the sensitivity of the eigenfrequency to the tightening configuration, i.e. when the surfaces of the interface are tied or when the tightening is very low. Then, we assume that a metamodel is able to represent the behaviour of the joints. In order to build it, we apply the PJSB as a loading on a finite element model of the joint and we post-process the results in order to use them in a reduce order model.

1   INTRODUCTION

The bolted joints strongly influence both the damping and the stiffness of the structures. Unfortunately, they remain difficult to predict, mainly because the physics involved occur with very different scales, i.e. the length scale of the real contact areas and the wavelength of the vibration modes. This make the classical finite element method difficult to use because in the contact areas, the mesh have to be fine whereas it can be coarse elsewhere. To overcome these difficulties, the purpose of this paper is to use a spatial decomposition of the domain in two subdomains that allows working with different spatial dicretizations on both subdomains. The subdomains are ΩS that includes all the structure parts and ΩJ that includes the joints. The first idea, detailed in section 2, is to solve alternatively the problems written on ΩS and ΩJ until the results on both become similar. This is strongly inspired of the LATIN method [6] but adapted to study periodic vibrations using Harmonic Balance Method (HBM) coupled with the Alternating Frequency Time (AFT) algorithm [2] or more recently [3]. The second idea of this work is to reduce the order of the model by using Ritz basis and meta-models spanning the subspace that contains the solutions.
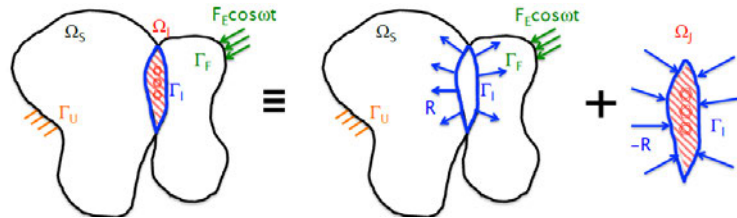

Figure 1. Typical schema for the study of jointed structures vibrations. Subdomain decomposition of the whole problem

2   DECOMPOSITION OF THE PROBLEM

This work focuses on dynamics of structural assemblies that involve parts that behave linearly and bolted joints that behave nonlinearly. Overall, the vibrations of the structure can be studied by solving the following problem:

$$\mathbf{M\ddot{U} + KU + F(U,\dot{U}) = F_E} \tag{1}$$

Where U is the displacement field, F_E is the excitation force and F is the non linear force induced by friction in the joints. M, K are the mass and the stiffness matrices. Equation 1 can be detailed by separating the Degrees of Freedom that belong to each subdomain Ω_S and Ω_J and to the interface Γ_I.

$$\begin{bmatrix} \mathbf{M_{LL}^S} & \mathbf{M_{LI}^S} & \mathbf{0} \\ \mathbf{M_{IL}^S} & \mathbf{M_{II}^S + M_{II}^J} & \mathbf{M_{IL}^J} \\ \mathbf{0} & \mathbf{M_{LI}^J} & \mathbf{M_{LL}^J} \end{bmatrix} \begin{bmatrix} \mathbf{\ddot{U}_L^S} \\ \mathbf{\ddot{U}_I} \\ \mathbf{\ddot{U}_L^J} \end{bmatrix} + \begin{bmatrix} \mathbf{K_{LL}^S} & \mathbf{K_{LI}^S} & \mathbf{0} \\ \mathbf{K_{IL}^S} & \mathbf{K_{II}^S + K_{II}^J} & \mathbf{K_{IL}^J} \\ \mathbf{0} & \mathbf{K_{LI}^J} & \mathbf{0} \end{bmatrix} \begin{bmatrix} \mathbf{U_L^S} \\ \mathbf{U_I} \\ \mathbf{U_L^J} \end{bmatrix} + \begin{bmatrix} \mathbf{0} \\ \mathbf{0} \\ \mathbf{F^J(U_L^J,\dot{U}_L^J)} \end{bmatrix} = \begin{bmatrix} \mathbf{F_E^S} \\ \mathbf{0} \\ \mathbf{0} \end{bmatrix} \tag{2}$$

In this work, we focus on harmonic excitation. For such kind of problem, the HBM is often used as it allows to compute steady-state periodic vibrations efficiently. Assuming steady-state vibrations and a periodic response, **U** can be written as:

$$\mathbf{U = U^0 + \sum_{h=1}^{H} \frac{U^h}{2} e^{jh\omega t} + \frac{U^{h*}}{2} e^{-jh\omega t}} \tag{3}$$

in a basis of exponential functions. Assuming the periodicity of the non-linear force, we can also expand it on a Fourier Basis

$$\mathbf{F(U,\dot{U}) = F^0 + \sum_{h=1}^{H} \frac{F^h}{2} e^{jh\omega t} + \frac{F^{h*}}{2} e^{-jh\omega t}} \tag{4}$$

Balancing, according to their harmonic order, each term of the obtained equation, we get:

$$\begin{cases} \left[-\omega^2 \mathbf{M} + \mathbf{K}\right] \mathbf{U}^1 + \mathbf{F}^1(\mathbf{U}^1...\mathbf{U}^H) = \mathbf{F_E} \\ ... \\ \left[-H^2\omega^2 \mathbf{M} + \mathbf{K}\right] \mathbf{U}^H + \mathbf{F}^H(\mathbf{U}^1...\mathbf{U}^H) = \mathbf{0} \end{cases} \tag{5}$$

This can be summarized in a more compact form:

$$[\Lambda]\hat{\mathbf{U}} + \hat{\mathbf{F}} = \hat{\mathbf{F}}_{\mathbf{E}} \tag{6}$$

Where Λ is the matrix of the complex impedances, $\hat{U}$ is the vector of unknowns that merges each harmonic order, $\hat{F}$ is the expansion of the nonlinear force on each harmonic order, $\hat{F}_E$ is the expansion of the excitation force. The Harmonic Balance Method is easy to use when $\mathbf{F}$ is mathematically regular. The problem is nonlinear but algebraic and it can be solve by a Newton-Raphson algorithm. When it is singular, the Alternating Frequency-Time (AFT) method can allow to solve the problem. The main idea of AFT is to evaluate the nonlinear force in the time-domain and to make the harmonic balance in the frequency domain. This allows to solve problems with contact and friction for which the nonlinear force is non regular. Nevertheless, unfortunately, AFT becomes too expensive to solve large scale problems due to the computation of the jacobean matrix $\mathbf{J}^{(k+1)}$ and the computation of the non-linear force $\mathbf{F}^{(k+1)}$. To overcome, this problem, the domain can be decomposed in two subdomains Ω_S and Ω_J, see Figure 1. This leads to two systems of equations that share an interaction force $\mathbf{R}$ and the displacement filed $\mathbf{U_I}$ on Γ_I. $\mathbf{R}$ and $\mathbf{U^I}$ allow to couple both systems.

$$\begin{bmatrix} \mathbf{M^S_{LL}} & \mathbf{M^S_{LI}} \\ \mathbf{M^S_{IL}} & \mathbf{M^S_{II}} \end{bmatrix} \begin{bmatrix} \ddot{\mathbf{U}}^S_L \\ \ddot{\mathbf{U}}_I \end{bmatrix} + \begin{bmatrix} \mathbf{K^S_{LL}} & \mathbf{K^S_{LI}} \\ \mathbf{K^S_{IL}} & \mathbf{K^S_{II}} \end{bmatrix} \begin{bmatrix} \mathbf{U}^S_L \\ \mathbf{U}_I \end{bmatrix} = \begin{bmatrix} \mathbf{F^S_E}\cos(\Omega t) \\ \mathbf{R} \end{bmatrix}$$

$$\begin{bmatrix} \mathbf{M^J_{II}} & \mathbf{M^J_{IL}} \\ \mathbf{M^J_{LI}} & \mathbf{M^J_{LL}} \end{bmatrix} \begin{bmatrix} \ddot{\mathbf{U}}_I \\ \ddot{\mathbf{U}}^J_L \end{bmatrix} + \begin{bmatrix} \mathbf{K^J_{II}} & \mathbf{K^J_{IL}} \\ \mathbf{K^J_{LI}} & \mathbf{0} \end{bmatrix} \begin{bmatrix} \mathbf{U}_I \\ \mathbf{U}^J_L \end{bmatrix} + \begin{bmatrix} \mathbf{0} \\ \mathbf{F}^J(\mathbf{U}^J_L, \dot{\mathbf{U}}^J_L) \end{bmatrix} = \begin{bmatrix} -\mathbf{R} \\ \mathbf{0} \end{bmatrix} \tag{7}$$

To solve this problem, we use a fixed point algorithm, that alternatively solve a linear problem in the frequency domain on Ω_S in order to get the kinematic field $\mathbf{U^S},\mathbf{U^I}$ when $\mathbf{R}$ and $\mathbf{F_E}$ are applied and a nonlinear quasi static problem in the time domain on Ω_J in order to get the kinematic field $\mathbf{U^J}$ and the reaction force $\mathbf{R}$ when $\mathbf{U^I}$ is applied. In order to make the problem easier to solve, one assume that the inertia terms are applied as a known field that comes from the previous increment, see [5] for more explanations.

3   MODEL REDUCTION

As seen before, the spatial decomposition of the problem associated with a fixed point algorithm and the Harmonic Bal- ance method allow to define a framework to compute the vibration levels of jointed structures under harmonic loadings. Nevertheless, on each subdomains, the problems involve a huge number of degrees of freedom. In order to compute the solution efficiently, one must use model order reduction techniques. Two reduction techniques are proposed here:

- the first one in order to reduce the number of DOFs, as many previous works [3], use the Craig-Bampton method to build a superelement of the linear part of the model;
- the second one, is the Principal Joint Strain Basis based on Dissipated Energy.

In a previous work, Festjens et al. [4] proposed the Principal Joint Strain Basis (PJSB) as a Model Order Reduction method for the joint domain. The idea is to find a very limited number of loadings $\mathbf{R}$ or boundary conditions $\mathbf{U_I}$ that span most the loadings induced by the vibration modes of the whole structure. If the PJSB exists, it allows to build meta-models for the behaviour of the structure. Such meta-models are often represented as mechanical charts, see [1].

To build the metamodels, a linear analysis is firstly performed on the global structure (full stick - interface tied) to determine the response function without any couplings. The basis Φ associated to the response function is normalized to stiffness matrix to give each eigenvectors the same strain energy. In order to reduce the joint model, one restrict the study to the joint:

$$\mathbf{U_I} = \Phi_\mathbf{I}\mathbf{Q} \tag{8}$$

with $\mathbf{U_I}$, the displacement field on the interface, and $\Phi_\mathbf{I}$, the truncated modal basis restricted to the interface area. In order to build detailed model of the joint, we introduce the Principal Joint Strain Basis Dissipated Energy (PJSBDE) as the optimal ritz basis to span the displacement field in the joint interface. To compute this basis, we build an energy indicator, The difference is obtained by observing two configurations of the joint - one which will totally sticking in the contact area, the other rather slippery in the interface (Eq. 9). It is therefore assumed that the strain energy difference is representative of the energy dissipation.

$$E_d = \Phi_\mathbf{I}^\mathbf{T} \left(\mathbf{K^J} - \tilde{\mathbf{K}}^\mathbf{J} \right) \Phi_\mathbf{I} \tag{9}$$

where E_d is the strain energy coupling matrix , $\Phi_\mathbf{I}$ the eigenmodes matrix, $\mathbf{K^J}$ is the stiffness matrix of the Ω_{NL} domain when the interface is tied, $\tilde{K}^J$ is the stiffness matrix of the ΩNL domain when the normal load is very low (bolt loosened). To compute the PJSBE, the idea is to simplify the basis $\Phi_\mathbf{I}$ since there must be redundancy between the eigenmodes as they have been considered locally. To achieve this goal, we extract the eigenvalues of the E_d . They are sorted and the eigenvector associated with the greatest one is kept as the boundary conditions $U_\mathbf{I}$. The meta model is built using these boundary conditions and making the associated generalized varying over the range of loading we want to study. The result is used to define the loadings we apply to a very detailed Non linear Finite Element model of the joint. The reaction forces, R, on the boundaries are extracted and used to solve the dynamic equation on Ω_L domain using Harmonic Balance Method

4   CONCLUSIONS

The theoretical frame proposed in this paper allows to simulate at a lower cost the dynamic behavior of the assembled structures. It is based on the use of methods of Ritz and meta - model. The latter are really interesting if several modes load the connection in the same way or if several connections are loaded in the same way.

REFERENCES

[1] A Caignot, P Ladeveze, D Néron, and J-F Durand. Virtual testing for the prediction of damping in joints. Engineering Computations, 27(5):621–644, 2010.

[2] TM Cameron and JH Griffin. An alternating frequency/time domain method for calculating the steady-state response of nonlinear dynamic systems. *Journal of applied mechanics*, 1989.

[3] M Claeys, JJ Sinou, JP Lambelin, and R Todeschini. Modal interactions due to friction in the nonlinear vibration response of the a harmony test structure: Experiments and simulations. Journal of Sound and Vibration, 376:131–148, 2016.

[4] H Festjens, G Chevallier, and JL Dion. Nonlinear model order reduction of jointed structures for dynamic analysis. Journal of Sound and Vibration, 333(7):2100–2113, 2014.

[5] Hugo Festjens, Gaël Chevallier, and Jean-luc Dion. A numerical tool for the design of assembled structures under dynamic loads. International Journal of Mechanical Sciences, 2013.

[6] Pierre Ladevèze, J-C Passieux, and David Néron. The latin multiscale computational method and the proper generalized decomposition. Computer Methods in Applied Mechanics and Engineering, 199(21):1287–1296, 2010.

CONTINUOUS DESCRIPTION FOR THE DYNAMIC BEHAVIOUR OF 1D FRAMED STRUCTURES

Xiangkun Sun[1], Changwei Zhou[2], Mohamed Ichchou[1*], Abdel-Malek Zine[3], Jean-Pierre Lainé[1], Stephane Hans[4] and Claude Boutin[4]

[1] Laboratoire de Tribologie et Dynamique des Systmes
Ecole centrale de Lyon, Lyon, France
Email: xiangkun.sun@doctorant.ec-lyon.fr, mohamed.ichchou@ec-lyon.fr,
jean-pierre.laine@ec-lyon.fr

[2] Laboratoire d'Acoustique de l'Universit du Maine
Universit du Maine, LE MANS, France
Email: changwei.zhou@gmail.com

[3] Institut Camille Jordan
Ecole centrale de Lyon, Lyon, France
Email: abdel-malek.zine@ec-lyon.fr

[4] Laboratoire de Tribologie et Dynamique des Systmes
Ecole Nationale des Travaux Publics de lEtat, Lyon, France
Email:stephane.hans@entpe.fr, claude.boutin@entpe.fr

ABSTRACT

This work deals with the longitudinal vibration and transverse vibration of a specific 1D periodic framed structure, whose unit cells are interconnected beams. The associated dynamic behaviour will be investigated by the numerical Condensed Wave Finite Element method (CWFE) and the analytical Homogenization method of Periodic Discrete Media (HPDM). Homogenized models are deduced by the HPDM, while the numerical results obtained by CWFE serve as the reference to validate these models. Dispersion curves are presented to evaluate the valid frequency range of these models.

1   INTRODUCTION

The framed materials are widely employed in various industries, such as aeronautics (lattice beams), civil engineering (buildings), materials science (mechanics of foam and glass wool) and biomechanics (vegetable tissue or bones). Numerous methods (numerical and analytical) aiming to find their dynamic behaviors have been developed. Among the numerical methods, the most widely used is the Wave Finite Element Method (WFEM). Based on Floquet-Bloch theorem, WFEM employs the conventional finite element models of the unit cell to deduce the dynamics of the whole structure [1, 2]. As for the analytical method, one frequently discussed approach is the homogenization theory. In order to find an appropriate analytical continuous description for the periodic structures, several homogenization approaches have been developed, such as material receptance method, asymptotic expansion method, and the homogenization of periodic discrete media (HPDM) [3–5].

In this work, both analytical HPDM and numerical CWFE are employed to study a periodic discrete framed structure. The principal objective of this work is to re-evaluate the validity of the HPDM using the wave characteristics identified by CWFE.

2   TECHNIQUES AND RESULTS

The studied structure is a 'ladder', which is formed by a large number of unbraced beams, Figure 1. These identical beam unit cells follow the Euler-Bernoulli theory, and they are linked by perfectly stiff and massless nodes.
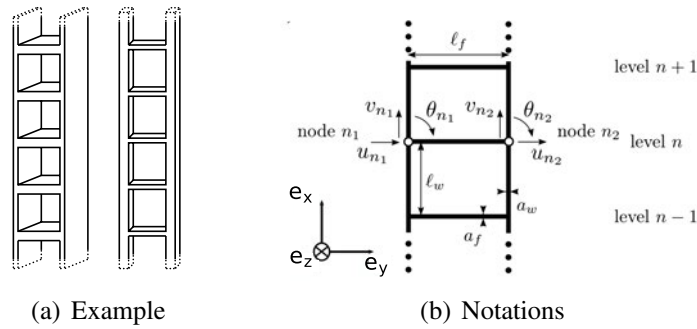

(a) Example   (b) Notations

Figure 1. Studied structures [5]

2.1   HPDM

The HPDM is composed of two parts: discretization and homogenization. As the studied structure is made of interconnected beams, the dynamic balance of the whole structure can be expressed in a discrete form using the element balance and nodal balance. Thus, the kinematic description of the structure can be described by the motions of the nodes. Then, the scale separation being satisfied, the dynamic variables of neighbouring nodes can be connected by Taylor's Series, and the discrete dynamic variables at each node can be considered as specific values of a continuous function. For more details, please refer to [3–5].

According to the HPDM, the homogenized models for the longitudinal vibration is:

$$\Lambda \omega^2 V + 2E_w A_w V'' = 0 \tag{1}$$

And the homogenized models for the transverse vibration is:

$$\frac{2E_w^2 I_w I}{K} U'''''' - (2E_w I_w + E_w I) U'''' - \frac{E_w I}{K} \Lambda \omega^2 U'' + \Lambda \omega^2 U = 0 \tag{2}$$

Where V is the mean longitudinal displacement, U is the mean transverse displacement, Λ is the linear mass of the cell, and $K^{-1} = K_w^{-1} + K_f^{-1}$ is the shear stiffness of the cell, with $K_w = 24E_wI_w/l_w^2$, $K_f = 12E_fI_f/(l_wl_f)$;

2.2   CWFEM

The CWFEM is a combination of WFEM and mode reduction technique. Here, the fixed interface component mode synthesis method, or the Craig-Bampton method, is chosen to reduce mode order and speed up the calculation. Then, the method begins with establishing the motion equation of the unit cell, where the mass and stiffness matrices $\mathbf{M}$ and $\mathbf{K}$ can be extracted from conventional FE packages. After the reduction, the physical DOFs are then reformulated to a reduced modal basis of modal DOFs. And the following process is the same as WFEM. More details are shown in [6].

2.3   Dispersion curves

Here is an example structure, whose characteristics are listed in Table 1. To ensure the convergence of the mesh, all the beams are discretized into 20 finite elements. Each unit cell contains 183 DOFs, among which 171 are internal DOFs. After the reduction, the first 20 fixed interface modes are conserved.

l_w (m)	l_f (m)	a_w (m)	a_f (m)	ρ (kg m^{-3})	E (GPa)	μ
3	3	0.1	0.1	7600	2e11	0.3

Table 1. Material Properties

By considering the propagative waves in positive-x direction, the dispersion relation obtained by CWFEM is given in Figure 2. And the associated wave shape is plotted in Figure 3. According to the wave shapes, the first wave corresponds to the transverse vibration and the second wave appears to be the longitudinal vibration. A third wave shows up at about 10Hz. This is an atypical gyration mode which can not be predicted by HPDM. Thus, the first two modes are investigated and the comparison of dispersion curves obtained by CWFEM and HPDM are illustrated in figure 4.
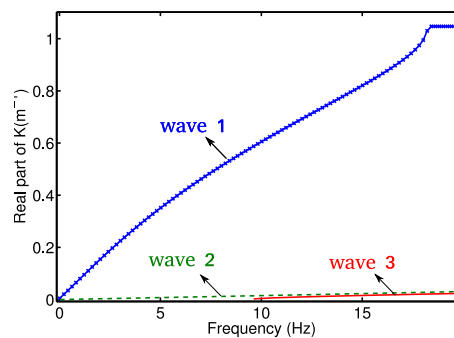

Figure 2. The dispersion relation from 0-20 Hz

3   CONCLUDING REMARKS

The wave propagation feature of the 1D framed structure is studied through the dispersion relation obtained by both HPDM and CWFEM. Good agreement between the two results is an
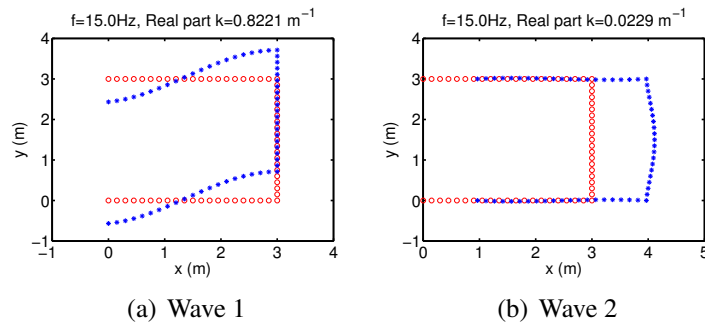
3

(a) Wave 1   (b) Wave 2

Figure 3. Wave shapes ($*$) Undeformed unit cell ($\circ$)
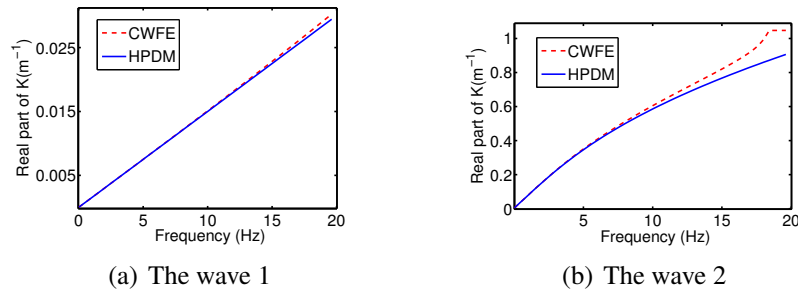

(a) The wave 1   (b) The wave 2

Figure 4. Dispersion relations by CWFEM and HPDM

evidence that the homogenized model achieves a reasonable accuracy. And the valid frequency range is limited in the first propagating zone.

REFERENCES

[1] Y Fan, M Collet, M Ichchou, L Li, O Bareille, and Z Dimitrijevic. Energy flow prediction in built-up structures through a hybrid finite element/wave and finite element approach. *Mechanical Systems and Signal Processing*, 66:137–158, 2016.

[2] C Droz, CW Zhou, M Ichchou, and JP Lainé. A hybrid wave-mode formulation for the vibro-acoustic analysis of 2d periodic structures. *Journal of Sound and Vibration*, 363:285–302, 2016.

[3] Claude Boutin and Stéphane Hans. Homogenisation of periodic discrete medium: Application to dynamics of framed structures. *Computers and Geotechnics*, 30(4):303–320, 2003.

[4] Stéphane Hans and Claude Boutin. Dynamics of discrete framed structures: A unified homogenized description. *Journal of Mechanics of Materials and Structures*, 3(9):1709–1739, 2008.

[5] Céline Chesnais, Claude Boutin, and Stéphane Hans. Effects of the local resonance on the dynamic behavior of periodic frame structures. In *EURODYN 2014-9th International Conference on Structural Dynamics*, pages pp–3447, 2014.

[6] CW Zhou, JP Lainé, M Ichchou, and AM Zine. Wave finite element method based on reduced model for one-dimensional periodic structures. *International Journal of Applied Mechanics*, 7(02):1550018, 2015.

4

AERODYNAMIC LOADING OF PERIODIC STRUCTURES

F. Errico[1], M. Ichchou[1], O. Bareille[1], S. De Rosa[2] and F. Franco[2]

[1] LTDS, Laboratoire de tribologie et dynamique des systems
Ecole Centrale de Lyon, Lyon, FRANCE
Email: fabrizio.errico@ec-lyon.fr ; mohamed.ichchou@ec-lyon.fr ; olivier.bareille@ec-lyon.fr

[2] Dipartimento di Ingegneria Industriale
University of Naples Federico II, Naples, ITALY
Email: sergio.derosa@unina.it ; francesco.franco@unina.it

ABSTRACT

The main aim of the present paper is to describe the issues and aspects related to the flow induced noise and vibrations, as well as the original features and the expected results of the ongoing research, mainly focused to a specific use of periodic structures for vibro-acoustic purposes. A literature review both on the flow excitation and on the induced response is reported. Some Early-stage research steps are then expressed to give a complete overview of the project.

Keywords: Flow-induced vibrations, radiated noise, TBL excitation, periodic structures, wave-base expansion, stochastic methods in structural dynamics

1 INTRODUCTION

Among the many noise and vibration sources, the aerodynamic load is surely one of the most relevant in engineering problems. This peculiar excitation source usually operates in a broadband frequency range, which widely increases the analysis issues when dealing with the forced response of a generic structure. It also concretizes in a spatially correlated stochastic load, as for the case of the Turbulent Boundary Layer (TBL) excitation, thus, deterministic approaches are not feasible and correlation functions are used instead.

Moreover, the need of investigating this peculiar field derives from its impact, in terms of radiated noise, on the acoustic comfort of transport means, such as airplanes. For example, the TBL, or the aerodynamic excitation in general, is the highest contributor to interior noise for an aircraft in cruise flight conditions. It affects even the structural dynamic behaviour of a submarine, despite its low speed. Launch vehicles, at lift-off or in flight ascent, are subject to a hard acoustic and aerodynamic environment, random by nature.

Depending on the frequency range of analysis different approaches are nowadays used, most of them limited by computational cost or invalidity outside specific operational borders.

On the other hand, increasing interest is tangible on periodic structures and their features, which enable, through the use of particular wave-bases, to easily compute the dispersion characteristics and the forced response of structures by analysing a single repetitive element. Many industrially relevant structures, even stiffened and curved, can, in fact, be considered as a periodic assemble of elementary cells.

Since these two fields seem to have been considered separately up to now, the ESR-2 doctorate has the target to bridge this gap enabling to efficiently evaluate the response of fluid-loaded periodic structures in a broadband operational field.

2 LITERATURE REVIEW

Over the past decades, many authors have investigated TBL both in terms of source characterization and application to dynamic and vibro-acoustic models, in order to simulate and calculate the radiated noise and the structural response. An overview, to set and clarify the problem background, is here reported. In any case the following assumptions will be given for granted:
1. TBL fully developed, stationary and homogeneous in space.
2. Weak coupling with the structural operator: pressure fields not influenced by structural vibrations.
3. Random processes are considered as ergodic.

2.1 TBL models

Even though many advances in computational fluid dynamics and in turbulence modelling, some semi-analytical models are still the most used. The Corcos model [1] and the Chase model [2] are among the references in this field. The first model, whose correlation function is here reported for clearness, describes the cross-spectra of the wall pressure fluctuations due to a TBL as a function of the sole distances between two different points, and as harmonically propagating only in the stream-wise direction. The coherence function is bi-dimensional and there is need to experimentally evaluate the stream/cross-wise correlation coefficients α .

$$X_{pp}\left(\xi_x,\xi_y,\omega\right)=S_p(\omega)\exp\left(-\alpha_x\left|\frac{\omega\xi_x}{U_c}\right|\right)\exp\left(-\alpha_y\left|\frac{\omega\xi_y}{U_c}\right|\right)\exp\left(\frac{i\omega\xi_x}{U_c}\right)$$

2.2 Structural Vibrations and Noise

The aerodynamic loading has the peculiarity of being a spatially correlated load. This increases the issues when evaluating the structural frequency response.

Taking into account the structural mode shapes, the power spectral density of the velocity of a structure, subject to random excitations, can be expressed using Green functions [3]. This leads to the need to evaluate the joint acceptance function (JAF), which is a costly integration of the product of the correlation function of the excitation and the structural steady modes. Ichchou et al. [4], for example, proposed an equivalent ROF excitation, with a wavenumber-space equivalence of the correlation function. This method allows an easier and cheaper evaluation of the JAF, in the medium-high frequency range, thus reducing the effort with respect to classic methodologies. On the other hand, the approach proposed by De Rosa et al. [5], making use of the modal aspects of the stochastic response, shows a simple and direct method to evaluate the vibratory field. Moreover, in [6], a methodology to reduce the computational cost of a full stochastic response is proposed. A pseudo deterministic modal excitation, based on the pseudo-excitation method (PEM), is simulated taking into account three different approximations, modulated for the three frequency ranges wherein the load matrix has different characteristics. Scaled models provided good accuracy in the medium high frequency range too, extending the applicability of a full model to higher frequencies [5].

Other methods proposed in literature make use of subsystem reductions, [7], to reduce the problem size in terms of degrees of freedom, nevertheless substituting the random load with deterministic point loads [8].

Different Approaches to couple a stochastic wall pressure field with deterministic vibro-acoustic models have been described by Matix et al., [9]. Among the techniques proposed the reciprocity method and the sampling of uncorrelated wall plane waves can be important inputs, even with deep modifications due to the limited applicability of these to very simple cases, in the framework of this EJD.

A SEA formulation using finite element and periodic structure theory has already been proposed by Cotoni et al., [11]. Even though its limited applicability to the cases of Born-von Karman boundaries, this gives a starting point of view for energy approaches to the problem.

2.3 Periodic Structure Theory

Examples of periodic structures can be found in every engineering field. If we think to a fuselage bay, a piezoelectric patch, honeycomb sandwich panels or a train rail we can always imagine the same structure as composed of periodic elementary cells assembled together. In this case the Bloch-Floquet theorem can be applied in order to relate the dynamic properties of the whole structure, as forces and displacements, to the ones of a single substructure, and the ones of a substructure to the ones of one single side or node [10]. A Bloch wave has the here reported form, with β a phase constant and ur a spatially periodic function.

$$\{\psi_r\} = e^{-i\beta r}\{u_r\}$$

The field on one point can be related to the field in any other point by a magnitude variation and phase shift. The entire problem of the forced response can be reformulated in a different base, which is the wave-base. A transformation is performed between the physical domain, where the system's behavior is described in terms of forces and displacement fields, and the wave domain, where the behavior is described in terms of waves travelling in the positive and negative directions, each with a specific amplitude depending on the excitation, boundary conditions and structure properties and geometries.
Directly excited and reflected wave amplitudes can be then computed using this wave-base and evaluated in the reference position to get the structural response.

3   FURTHER STEPS AND EXPECTED RESULTS

As said a broadband strategy to deal with the flow-induced vibrations is expected as final result. The main and most directly tangible issues that arise are to be addressed to the different work-bases of the PST and classic TBL vibro-acoustic models, in which a full description of the discretized structure is mandatory.
On the early stage phases, an analysis on where addressing the focus and efforts is needed. Both the load spectra and structural operator are characterized by peculiar features. Understanding on which aspect to operate is a key step for further developments.

A decomposition of the load cross-spectra might be a feasible approximation to make a first reduction of the size of the problem. Mathematical tools are already present for this purpose.

Deeper reduction can be achieved when and if the spatial description needed for the excitation can be related to the wave-base of the periodic structure. This latter achievement might be a breakthrough since we can make use of the developments on the deterministic response of any periodic structure, which can be calculated at very low computational cost within the wave-base expansion. About this, the present authors have already investigated and validated a WFE/FE approach, applied in the case of curved and stiffened structures, to get the structural frequency response for any point load.

The present authors are actually testing and validating a wave-based technique to get the stochastic response of a periodic structure.

Acknowledgements

REFERENCES

[1]   G.M. Corcos, *The structure of the turbulent pressure field in boundary-layer flows,* Journal of Fluid Mechanics 18 (1964) 353–379.

[2]   D.M. Chase, *Modelling the wavevector-frequency spectrum of turbulent boundary layer wall pressure*, Journal of Sound and Vibration 70 (1980) 29–67.

[3]   I. Elishakoff, *Probabilistic Methods in the Theory of Structures*, 2nd ed. Dover Publications, Mineola, NewYork, 1999.

[4]   M. Ichchou, B. Hiverniau, B. Troclet, *Equivalent 'rain on the roof' loads for random spatially correlated excitations in the mid-high frequency range*, Journal of Sound and Vibration 322 (2009) 926-940.

[5]   S. De Rosa, F.Franco, Exact and numerical responses of a plate under a turbulent boundary layer excitation, Journal of Fluids and Structures 24 (2008) 212-230.

[6]   S. De Rosa, F. Franco, E. Ciappi*, A simplified method for the analysis of the stochastic response in discrete coordinates*, Journal of Sound and Vibration 339 (2015) 359–375.

[7]   D. Chronopoulos, M. Ichchou, B. Troclet, O. Bareille, *Predicting the broadband vibroacoustic response of systems subject to aeroacoustic loads by a Krylov subspace reduction*, Applied Acoustics 74 (2013) 1394–1405

[8]   B. Troclet, B. Hiverniau, M.N. Ichchou, L. Jezequel, K. Kayvantash, T. Bekkour, J.B. Mouillet, A. Gallet, *FEM/SEA Hybrid Method for Predicting Mid and High Frequency Structure-Borne Transmission*, The Open Acoustics Journal, 2009, 2, 45-60

[9]   L. Maxit, M. Berton, C. Audoly, D. Juvè, *Discussion about different methods for introducing the turbulent boundary layer excitation in vibroacoustic models*, Flinovia- Flow Induced Noise and Vibration Issues and Aspects, Springer ed. 2015

[10]   D.J Mead, *Wave propagation in continuous periodic structures: research contributions from Southampton*, 1964-1995, Journal of Sound and Vibration 190 (1996) 496-525

[11]   V. Cotoni, R.S. Langley, P.J. Shorter, *A statistical energy analysis subsystem formulation using finite element and periodic structure theory,* Journal of Sound and Vibration 318 (2008) 1077-1108

MULTI-LAYER CORE TOPOLOGY SYSTEMS

N. Guenfoud[1,2], M. Ichchou[1*], O. Bareille[1], W. Desmet[2,3] and B. Pluymers[2,3]

[1]Laboratoire de Tribologie et Dynamique des Systèmes, Ecole Centrale de Lyon, Ecully, France
Email: mohamed.ichchou@ec-lyon.fr, olivier.bareille@ec-lyon.fr

[2]Department of Mechanical Engineering, KU Leuven, Leuven, Belgium
Email: bert.pluymers@kuleuven.be, wim.desmet@kuleuven.be

[3]Member of Flanders Make

ABSTRACT

The purpose of this paper is to describe the major issues regarding the topic ESR-4 and entitled "Multi-layer core topology systems" from the VIPER project (vibroacoustic of periodic media). The objective is to study multi-layer periodic structures to carry out an optimization of each periodic layer allowing to obtain better sound transmission properties. Transfer Matrix Method (TMM) mixed with Wave Finite Element Method (WFEM) is commonly used to model the Sound Transmission Loss (STL) and the Sound Absorption Coefficient (SAC) of periodic structures assuming an infinite plate without boundary conditions. In addition, this structure is designed using one type of periodicity. In the framework of multi-layer periodic structures, each layer has its own periodicity and different to each other, leading to a more complex problem as the extraction of the unit periodic cell. Several simple cases might be exploited to investigate the influence of the periodic layers layout.

*Keywords***:** *TMM-WFE / multi-layer periodic structure / Sound Transmission Loss / Sound Absorption Coefficient / Optimization*

1   INTRODUCTION

The problems related to the periodic structures sound properties are important in aerospace industry. Typically, this kind of structure is lighter whereas its stiffness is higher and lead, generally, to an unsatisfactory Sound Transmission Loss (STL) and Sound Absorption Coefficient (SAC). Modelling these structures is possible using the Transfer Matrix Method (TMM) mixed with Wave Finite Element Method (WFEM) and reduce significantly the computational cost. Nevertheless, the main assumptions define the structure as an infinite plate without boundary conditions. In addition, the topic ESR-4 for VIPER Project deals with muti-layer periodic structures which means that each layer has its own periodicity. Consequently, these periods as well as the possible phase differences between each layer involve extending the TMM to multi-layer periodic structures.

The first step is to consider simple cases with specifics periodicities at each layer to investigate the effect on the STL and the SAC. Secondly, an optimization should be performed to obtain the best configuration for the structure allowing to satisfy the industrial constraints for the STL and the SAC. This paper gives an overview of the literature which will lead to the achievement of the objectives and will explain in details the major issues of this topic.

2   LITERATURE REVIEW

2.1 TMM applied to periodic structures

The following picture (Figure 1) illustrate a multi-layer periodic structure:
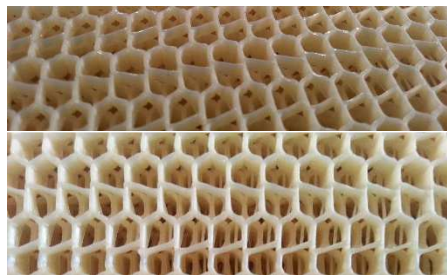

Figure 1. Multi-layer periodic structure.

Each layer is composed by a periodic structure as honeycomb or auxetic cores with a certain periodicity not supposed to be the same as each other. Moreover, the layers' depth could be different. Consequently, one periodic cell cannot be simply extracted from the whole structure to apply the TMM.

Recently, two close methods proposed by [1, 2] released to calculate the STL of a periodic structure manipulating the dynamic stiffness related to the periodic cell. These methods combine the use of the WFEM and the TMM and decrease considerably the computational cost. However, assumptions are required and lead sometimes to noticeable differences, especially at low frequencies since the boundary conditions have a strong effect.

2.2 Periodicity issues

Figure 2 shows 3 different periodicities of different core nature (honeycomb, auxetic and rectangular). A periodic structure with 3 layers is represented. The green figure is the minimal unit cell for the honeycomb layer, which is obviously inappropriate to extract one periodic cell through the depth of the whole structure. One of the issues is to deal with these different periodicities finding this unit cell to be able to model the structure using the methods described in [1, 2].
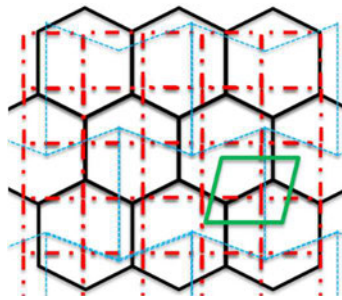
Figure 2. Different periodicities.

Furthermore, added to the periodicity, there is a possible phase difference as well as an angle of rotation between each layer. Those could lead to a more complex problem.

The first maintained approach will be a periodicity effect investigation modelling specifics cases. For instance, periodicities are multiple to each other allowing to model just one periodic cell containing all periodic layers but modifying the phase differences. It occurs that the previous exposed methods could be applied. In a first phase, the plate will be considered as laterally infinite, then, method as [3] is available to account for the finite size effects with a size correction factor.

A new challenge is proposed to extend the TMM to multi-layer periodic structures with boundary conditions and considering the problems previously listed and related to layers, to finally determine the STL and SAC of the structure with an accurate prediction. This model will integrate new types of parameters characterizing the periodicity, the phase difference or the topology of each layer. Then, the next step is the optimization of this structure.

2.3 Optimization

One of the main purpose is to manufacture a new structure with a better sound transmission efficiency characterized by the STL and SAC. Several papers were written trying to describe the effect of meso-scale parameters on the STL of periodic structures as [4]. It is noticed that the cell's geometry could alter the STL especially at the mid frequencies. The optimization will be based on the results of this article. The periodicity of each layer might be defined by several geometrical parameters as shown in Figure 3.
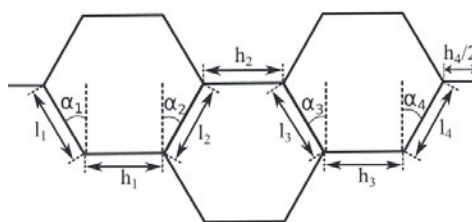

Figure 3. Geometrical parameters for honeycomb cores [4].

Other parameters should be required as the phase difference between two periodic layers, as well as parameters which would define the geometrical period of each periodic layer.

Performing an optimization needs to find out the inputs and outputs of the studied system. In this case, a multi-inputs/multi-output might be considered since the STL and the SAC are investigated. The developed algorithm will be able to identify the optimal geometrical parameters for each periodic layer. The optimization process depends on the frequency since the STL and SAC as well, and thus, will involve a wise choice for the frequency range of the study. Therefore, a relevant number of inputs will reduce the computational cost. For instance, thanks to [4], a conclusion is that the depth of each layer will have a significant effect on the STL but affecting the

3

stiffness-weight ratio of the layer. Consequently, this parameter might be constant for each layer to not influence the mechanical properties of the structure.

3   CONCLUSIONS

An overview of one topic of the Viper Project is proposed. A study is ongoing to model the sound transmission properties of multi-layer periodic structures which will serve to develop an optimization algorithm to manufacture a new optimal structure. The following major issues are exposed: boundary conditions, periodicity and the optimization. Nevertheless, an approach using specific cases at the beginning will lead to a better understanding of the periodicity effect and other parameters as the phase difference or the topology of each layer. The computation will be established according to the recent procedure described in papers [1, 2]. Finally, this topic will have an interest from an industrial point of view since it is useful at early stage of the manufacturing having all the optimal parameters of the structure.

ACKNOWLEDGEMENTS

REFERENCES

[1]   J.-L. Christen. Acoustic transmission through composite shells with noise treatment: Modelling and sensitivity. PhD Thesis, Ecole Centrale de Lyon, France, 2016.

[2]   A. Parinello and G.L. Ghiringhelli. Transfer Matrix representation for periodic planar media. *Journal of Sound and Vibration*, Elsevier, Milano, Italy, 2016.

[3]   S. Ghinet and N. Atalla. Sound transmission loss of insulating complex structures. *Canadian Acoustics*, vol. 29, no 3, Canada, 2001.

[4]   Z. Zergoune, M.N. Ichchou, O. Bareille, B. Harras, R. Benamar and B. Troclet. Assessments of shear core effects on sound transmission loss through sandwich panels using two-scale approach. *Computer and Structure*, 2016.

KIRIGAMI INSPIRED NATURAL FIBRE CELLULAR STRUCTURES FOR FUTURE VIBROACOUSTICS APPLICATIONS

[1]Simone Del Broccolo, [1]Rita Palumbo, [1]Marc-Antoine Campana, [1]Yousef Dobah, [1]Fabrizio Scarpa
[2]Morvan Ouisse, [3]Mohamed Ichchou,

[1] Advanced Composites Centre for Innovation and Science (ACCIS), University of Bristol
Queen's Building, University Walk, Bristol BS8 1TR, United Kingdom
Email: sd15134@bristol.ac.uk, rp16857@bristol.ac.uk, mc16271@bristol.ac.uk

[2]FEMTO-ST, Applied Mechanics Department, UMR-CNRS 6174
24 chemin de l'épitaphe, 25000 Besançon, France

[3]LTDS UMR-CNRS 5513, École Centrale de Lyon
36 avenue Guy de Collongue, 69134 Écully, France

ABSTRACT

The aerospace segment makes large use of cellular structures in sandwich panels, which are known to possess good stiffness while saving weight. Metallic cores are currently being replaced by different classes of composites, especially because of their poor vibration transmissibility. The inclusion of vibroacoustics constraints in the design process gives the opportunity to obtain multifunctional structures that still provide mechanical efficiency while introducing absorption, tunable vibration transmissibility or damping capabilities. In this work, natural fibre prepregs are turned into periodic panels using the ancient Japanese art technique of cutting and folding paper, known as Kirigami. Flax fibre with Polypropylene matrix was used to obtain a cellular structure with improved absorption properties and therefore, thermoforming was adopted due to its compatibility with Kirigami and thermoplasticity of the matrix. A dedicated mould and numerically controlled cutters as well as adhesive were adopted to complete the Kirigami procedure. Numerical simulations were carried out in order to identify the best performing candidates in terms of the properties mentioned above and through-the-thickness vibration transmissibility. Consequently, the selected configurations were manufactured and tested. This natural fibre composite cellular platform will be used for further improving the vibroacoustic properties of the manufactured cores by embedding periodic inclusions of various type and materials within the core, and by analysing different cell topologies.
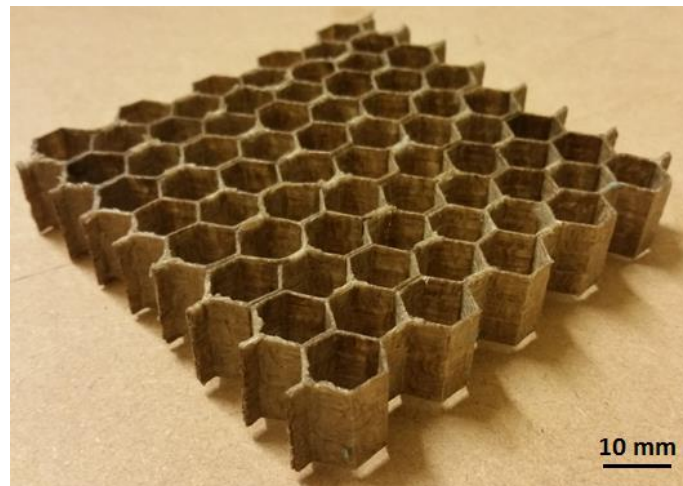
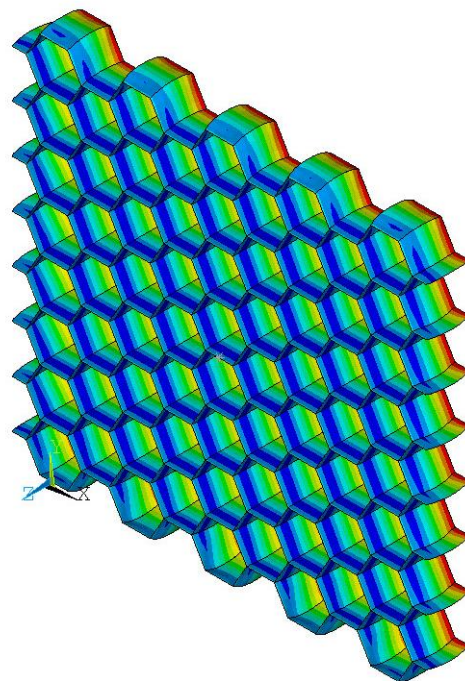Fig1. *Flax/PP Kirigami hexagonal core*

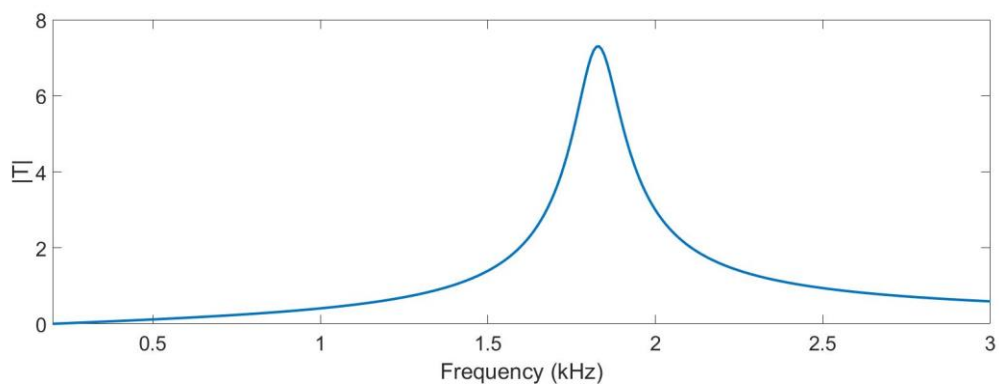Fig2. *Honeycomb deformed shape and relative displacements at f=1832 Hz.*

Fig3.Through-the-thickness *transmissibility analysis, 4% damping.*

2

A LITERATURE REVIEW FOR THE ANALYSIS OF VIBORACOUSTIC PROPERTIES OF PERIODIC INCLUSIONS IN POROUS MATERIALS

D. Magliacano[1], M. Ouisse[1], A. Khelif[1], S. De Rosa[2] and F. Franco[2]

[1] Univ. Bourgogne Franche-Comté, FEMTO-ST Institute, CNRS/UFC/ENSMM/UTBM, Besançon, FRANCE
Email: dario.magliacano@univ-fcomte.fr, morvan.ouisse@femto-st.fr, abdelkrim.khelif@univ-fcomte.fr

[2]Dipartimento di Ingegneria Industriale - Sezione Ingegneria Aerospaziale
Università degli Studi di Napoli "Federico II", Naples, ITALY
Email: sergio.derosa@unina.it, francesco.franco@unina.it

ABSTRACT

The design based on periodic elements is a powerful strategy for the achievement of lightweight sound packages and represents a convenient solution for manufacturing aspects. An interesting research target is the inclusion of vibroacoustic design rules at early stage of products development through the use of porous media with periodic inclusions, which exhibit proper dynamic filtering effects; this offers different applications in transportation (aeronautics, space, automotive, railway), energy and civil engineering sectors, where both weight and space, as well as vibroacoustic integrity and comfort, still remain as critical issues. This work is a literature review which mainly focuses on three aspects concerning periodic inclusions in porous materials: the concept of substitution of a fluid layer for a porous layer, the Transfer Matrix Method and the descriptions of two alternatives to multi-layering.

1 SUBSTITUTION OF A FLUID LAYER FOR A POROUS LAYER

1.1 Description of sound propagation in porous media

On a microscopic scale, sound propagation in porous materials is generally difficult to study because of the complicated geometries of the frames. Only the mean values of the quantities involved are of practical interest. The averages must be performed on a macroscopic scale, on a homogenization volume with sizes large enough to become meaningful. At the same time, these sizes must be much smaller than the acoustic wavelength. The description of sound propagation in porous material can be complicated by the fact that sound also excites and moves the frame of the material. If the frame is motionless, in a first step, the air inside the porous medium can be replaced at the macroscopic scale by an equivalent free fluid. This equivalent fluid has a complex effective density ρ and a complex bulk modulus K. The wave number k and the characteristic impedance Z_c of the equivalent fluid are also complex [1].

1.2 An empirical model provided by Delany and Bazley

The k and Z_c have been measured by Delany and Bazley (1970) for a large range of frequencies in many fibrous materials with almost unit porosity. According to these measurements, the quantities k and Z_c depend mainly on the angular frequency ω and on the flow resistivity σ of the material. Good fits for k and Z_c have been obtained:

$$Z_c = \rho_0 c_0 [1 + 0.057 X^{-0.754} - j0.087 X^{-0.732}]. \tag{1}$$

$$k = \frac{\omega}{c_0} [1 + 0.0978 X^{-0.700} - j0.189 X^{-0.595}]. \tag{2}$$

where ρ_0 and c_0 are the density of air and the speed of sound in air; X is a dimensionless parameter which is suggested to be valid within the range $0.01 < X < 1.00$.

These relations will not provide perfect predictions of acoustic behaviour of all the porous materials in every frequency ranges. Nevertheless, the laws of Delany and Bazley are widely used and can provide reasonable orders of magnitude for Z_c and k. With fibrous materials, which are anisotropic, the flow resistivity must be measured in the direction of propagation for waves travelling in either the normal or the planar direction. The case of oblique incidence is more complicated. It should be pointed out that after the work by Delany and Bazley, several authors suggested slightly different empirical expressions of k and Z_c for specific frequency ranges and for different materials [1].

1.3 Mesostructure based models

In the case of common porous materials, an analytical description of sound propagation that takes into account the complete geometry of the microstructure is not possible. This explains why the models of sound propagation in these materials are mostly phenomenological and provide a description only on a large scale [1]. In 1987, Johnson, Koplik and Dashen proposed a semi-phenomenological model to describe the complex density of an acoustical porous material with a motionless skeleton having arbitrary pore shapes; 4 parameters are involved in the calculation of this dynamic density: the open porosity ϕ, the static air flow resistivity σ, the high frequency limit of the tortuosity $\alpha\infty$ and the viscous characteristic length Λ. In 1991, Champoux and Allard introduced an expression for the dynamic bulk modulus for the same kind of porous material based on the previous work by Johnson et al.; 2 parameters are involved in the calculation of this dynamic bulk modulus: the open porosity ϕ and the thermal characteristic length Λ'. In Biot-Allard model, which includes the description of the skeleton movement, a material is characterized by a number of conventional mechanical parameters (density of the skeleton, Young's modulus of the skeleton in vacuum, Poisson's coefficient of the skeleton in vacuum, structural damping), as well as by

specific parameters called Biot parameters (porosity, resistivity, tortuosity, viscous characteristic length, thermal characteristic length).

2 MULTI-LAYERED SYSTEMS WITH POROUS MATERIALS MODELED USING THE TRANSFER MATRIX METHOD

The description of the acoustic field in a porous layer is complicated by the presence of the shear wave and the two longitudinal waves. In a layered medium with porous layers, elastic solid layers and fluid layers, a complete description can become very difficult. A matrix representation of sound propagation well consolidated in literature is described here. The stratified media are assumed laterally infinite. They can be of different nature: elastic solid, thin plate, fluid, rigid porous, limp porous and poroelastic. However, the different media are assumed to be homogeneous and isotropic. Figure 1 illustrates a plane acoustic wave impinging upon a material of thickness h, at an incidence angle θ. Various types of waves can propagate in the material, according to their nature. The x_1 component of the wave number for each wave, propagating in the finite medium, is equal to the x_1 component k_t of the incident wave in the free air:

$$k_t = k \sin \theta. \tag{3}$$

being k the wave number in free air. Sound propagation in the layer is represented by a transfer matrix $[T]$ such that

$$\boldsymbol{V}(M) = [T]\boldsymbol{V}(M'). \tag{4}$$

Where M and M' are set close to the forward and the backward face of the layer, respectively, and where the components of the vector $\boldsymbol{V(M)}$ are the variables which describe the acoustic field at a point M of the medium. The matrix $[T]$ depends on the thickness h and the physical properties of each medium [1].
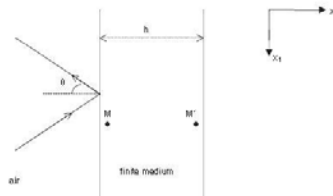

Figure 1. Plane wave impinging on a domain of thickness h.

3 ALTERNATIVES TO MULTI-LAYERING

Although porous materials are commonly used for vibroacoustic applications, they suffer from a lack of absorption at low frequencies compared to their efficiency at higher ones. This difficulty is usually overcome by multi-layering. However, while reducing the impedance mismatch at the air-material interface, the efficiency of such devices relies on the allowable thickness [2].

3.1 Embedding rigid inclusions

One way allowing to enhance the low frequency efficiency of sound packages consists in embedding periodic rigid inclusions in a porous layer [3]. If the radius of these periodic inclusions is comparable with the acoustic wavelength, then an increase of the absorption coefficient can be observed. In [3], the influence of the periodic inclusions on the absorption coefficient was explained by excitation of additional acoustic modes which dissipate acoustic energy. When the porous layer is backed by a flat rigid surface and when only one inclusion per unit cell grating is embedded, an additional trapped mode can be excited. This results in a quasi-total absorption peak at a frequency

below that of the usual quarter-wavelength resonance in the homogeneous layer case. Other interesting studies related to volume heterogeneities are in [4, 5-8].

3.2 Embedding Helmholtz resonators

The homogenization theory cannot be applied to cellular material made of large periodic unit-cell. In this case, a low frequency solution to improve the acoustic efficiency of passive open-cell porous materials is to embed Helmholtz resonators (HR) in the porous matrix. Doing so, at the Helmholtz resonance frequency, the transmission loss is greatly improved and the sound absorption of the host material is decreased if it is made of a highly sound absorbing material. One of the first works describing such structure is a patent filed in by Borchers et al. [6]. Much later, Sugie et al. [7] proposed a similar heterogeneous material made of a fibrous sound absorbers with resonant inclusions. More recently, the acoustic community had shown a keen interest in the equivalent material (also called effective material or metamaterial) presenting a negative bulk modulus at the HR resonance frequency [8]. In [9] the sound absorption efficiency is investigated in case of rigid backed acoustic foams with resonant split hollow cylinder inclusions. Under the assumption that the HR periodicity is much smaller than the acoustic wavelength, the resonant materials are usually modelled as homogenized equivalent material with modified bulk modulus to account for the presence of the resonant inclusion [8]. However, as already stated, cellular resonant material with large periodicity obviously prevents the use of the homogenization method. In this case, the orientation of the HR neck may have a strong influence on the sound absorption behaviour of the resonant material [9, 10].

REFERENCES

[1]   J. F. Allard and N. Atalla. *Propagation of Sound in Porous Media*. Wiley, 2009.

[2]   T. Weisser, J.-P. Groby, O. Dazel, F. Gaultier, E. Deckers, S. Futatsugi and L. Monteiro. Acoustic behavior of a rigidly backed poroelastic layer with periodic resonant inclusions by a multiple scattering approach. *Acoustical Society of America*. 617:629, 2016.

[3]   J.-P. Groby, E. Ogam, and A. Wirgin. Acoustic response of a periodic distribution of macroscopic inclusions within a rigid frame porous plate. *Waves Random Complex Media 18*. 409–433, 2008.

[4]   X. Olny and C. Boutin. Acoustic wave propagation in double porosity media. *Acoustical Society of America*. 73:89, 2003.

[5]   J.-P. Groby, A. Duclos, O. Dazel, L. Boeckx and W. Lauriks. Absorption of a rigid frame porous layer with periodic circular inclusions backed by a periodic grating. *Acoustical Society of America*. 3035:3046, 2011.

[6]   I. U. Borchers, S. T. Laemmlein, P. Bartels, A. Rausch, M. Faust, J. A. F. Coebergh and K. Koeble. Acoustic protection on payload fairings of expendable launch vehicles. 1997.

[7]   S. Sugie, J. Yoshimura and T. Iwase. Effect of inserting a Helmholtz resonator on sound insulation in a double-leaf partition cavity. *Acoustical Science and Technology*. 30(5):317-326, 2009.

[8]   N. Fang, D. Xi, J. Xu, M. Ambati, W. Srituravanich, C. Sun and X. Zhang. Ultrasonic meta-material with negative modulus. *Nature Materials*. 5:452–456, 2006.

[9]   C. Lagarrigue, J.-P. Groby, V. Tournat and O. Dazel. Absorption of sound by porous layers with embedded periodic arrays of resonant inclusions. 2013.

[10]   O. Doutres, N. Atalla and H. Osman. Modeling and experimental validation of cellular porous material with large resonant inclusions. *Inter-noise*, 2014.

FIRST LITERATURE REVIEW FOR THE ANALYSIS OF QUASI-PERIODICITY VARIABILITY EFFECTS AND MODELING STRATEGIES

S. Timorian[1], S. De Rosa[1], F. Franco[1], M. Ouisse[2] and N. Bouhaddi[2]

[1]PASTA-Lab / Laboratory for promoting experiences in Aeronautical Structures and Acoustics, Department of Industrial Engineering, University of Napoli "Federico II "
Via Claudio 21, 80125 Napoli, Italy
safiullah.timorian@gmail.com

[2]Univ. Bourgogne Franche-Comte, FEMTO-ST Institute, CNRS/UFC/ENSMM/UTBM, Department of Applied Mechanics, 25000
BESANCON, FRANCE

ABSTRACT

Quasi periodicity and variability effects on structures are spread in all the engineering branches. The inherent research works are carried out with both numerical and experimental activities. A more specific goal is the analysis of the influence of such effects on the vibroacoustic response. The modern tools for investigating the most significant impacts of imperfections and irregularities on the vibrational and acoustical response of a given structure are codes based on combination of wave and finite element, spectral finite elements, transfer matrix methods and the adoption of stochastic variables. In view of the foreseen work inside the VIPER project, this paper refers to the analysis of the most recent literature and possible initial strategy.

1   INTRODUCTION

"*Quasi-periodicity is the property of a system that displays irregular periodicity. Periodic behaviour is defined as recurring at regular <u>space and time</u> intervals. Quasi-periodic behaviour is a pattern of recurrence with a component of unpredictability that does not lend itself to precise measurements*": this simple definition is taken from Wikipedia.

It precisely points to the core of the problem. In fact, an increasing literature is appearing on methods for the analysis of a given system by replicating only its elemental cell in space directions and time scale, thus simulating conditions of perfect periodicity. How to simulate systems, if perfect periodic conditions are violated, is still to be analysed together with their influence.

This paper belongs to the VIPER project (http://viper.ec-lyon.fr.) which is fully centred on the vibroacoustic of periodic media. For the periodic structures, the definitions of the effect of quasi-periodicity is to be investigated in order to understand the physics, how this can be modelled and what are the effects of the final design. In fact, it will be important to analyse if and how the presence of imperfections or irregularities, on quasi-periodic bases, can have a significant impact on the vibro-acoustic responses of given components.

It is expected and already shown that the effects on micro-scale can influence the performance on macro-scale: the engineering design can receive important information if more light is shed in this link. Several effects are known in literature (the Anderson localization is one of the most famous) but some insights are now necessary in order

- to **improve the simulations** of these kind of problems;
- to **move to prototypes** which can demonstrate on experimental basis the achievement of increased vibroacoustic performances (structural damping and/or acoustic transmission loss).

2   LITERATURE REVIEW

Quasi periodic structures are scattered from those identical cells which has a periodic form in the assembly of a piece of element in the structures. The analysis could be done by the presence of imperfection or irregularity which have a significant impact on the vibrational and acoustic behaviour.

The difference between imperfection or irregularity in a quasi-periodic sequence has to be defined: the importance of this step should not be underestimated.

In [1], an enriched finite element method is presented to solve various wave propagations. However, the standard finite element method is not very effective for utilising the solution of the wave propagation problems [2]. The errors introduced in this method have been identified and analysed and they are due to the fact the wave propagation analysis is based on piecewise polynomial approximation: the accuracy of the numerical solution becomes rapidly worse with increasing wave number.

Ref. [3] and [4] are a good example of how the use of periodicity and the Wave and Finite Element can be real enhancements of the predictive quality.

An extension of WFEM is presented in [5]: the actual status of the wave and finite element method has been identified as a best approach for the vibroacoustic analysis over periodic structures. The numerical method has been carried out via Bloch's theorem and imposing periodicity conditions to a single cell which represents a repetitive part of the whole structure. The results show a promising agreement between Wave and Finite Element Method (WFEM) and Classical Finite Element Method (CFEM). Experimental testing and validating comparisons on stiffened cylinders are ongoing at Pasta-Lab.

It has to be remembered that the prototype under research and investigation is a structural component that has characteristics which periodically repeat in one or more directions. In general, a generic structure obtained as an assemble of identical elements, called *cells*, which can be considered as periodic structures. The modelling of a short section of the waveguide is expressed by supposing time harmonic motion, the equation of motion is implied by discrete coordinates, relating nodal degrees of freedom q and force f of the undamped section:

$$(K - \omega^2 M)q = f \tag{1}$$

where K and M are the stiffness and mass finite element matrices, [4-8]. The analysis of periodic systems is thus well undertaken through WFEM.

The analysis of transmission and diffusion at joints between waveguides as well as the damped periodical waveguides were investigated in several research works, [7-8].

In [9-11], the first models to take into account the irregularities are presented: they are very recent and represent useful investigations to guide the next required steps.

At the moment, the approach adopted in [3] seems the most promising for reproducing the forced response of periodic structures in presence of quasi-periodicity and variability effects. The flexibility of getting the K and M matrices from standard finite element codes and the definition of an external post-processing code appears as the most viable procedure even in view of the expected variations to be included for simulating the quasi-periodicity.

3   STRATEGY

The envisaged steps for facing a such complicated problem are the following:

```
A. definition of the quasi-periodicity;
B. analysis of the nature and sizes of the causes altering the perfect
   periodicity;
C. definition of the required
          1. mathematical,
          2. numerical and
          3. experimental tools.
```

They are all challenging. In Fig. 1 a sketch of the possible problems/configurations is reported: the perfect periodic system (a) can be altered to get a (b) quasi periodic system in terms of shapes, junctions, sizes, materials, manufacturing issues, etc.; what does *quasi* mean?

These effects could be evaluated adding each of them on a predictive environment: this will lead to development of a new class of codes expected to be based on a combination of wave and finite element, spectral finite element, transfer matrix methods and the adoption of stochastic variables, if needed. It has to be considered also the possibility to use non-deterministic (*possibilistic*) algebras as those associated to the fuzzy-logic or the interval algebra.

In literature, it is already shown that a sandwich panel, optimized versus the vibroacoustic performance, with added random properties of the core can exhibit stop-band characteristics in some frequency ranges. Therefore, the analysis of these quasi-periodicity effects is much closer to the engineering application than many others trying to simulate real structures with 3D models with huge computational costs.
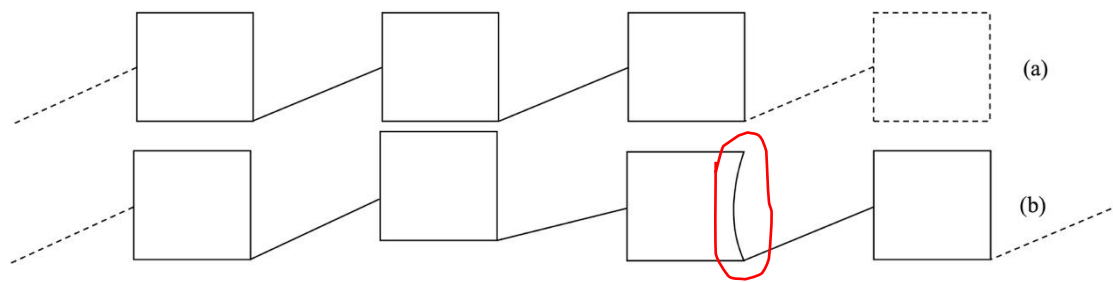
(a). Periodic System, (b). Quasi-Periodic System
Figure 1: Sketches of the periodic and *quasi*-periodic distribution of repeated cells.

ACKNOWLEDGEMENTS

REFERENCES

[1]   Seounghyun Ham and Klaus-Jürgen Bathe. "A finite element method enriched for wave propagation problems." *Computers & structures* 94 (2012): 1-12.

[2]   Harari I. A survey of finite element methods for time-harmonic acoustics. Comput Meth Appl 2006; 195:1594–607

[3]   V. Cotoni, R.S. Langley, P.J. Shorter, A statistical energy analysis subsystem formulation using finite element and periodic structure theory, Journal of Sound and Vibration 318 (2008) 1077–1108

[4]   E. Manconi and B. R. Mace, Modelling wave propagation in two dimensional structures using finite element analysis, Journal of Sound and Vibration, 318(4–5):884–902, 2008

[5]   F. Errico, Application of the Wave Finite Element Approach to the Structural Frequency Response, Master Thesis, University of Naples "Federico II", December 2016.

[6]   Moser F., Laurence J. J. and Qu J., "Modeling elastic wave propagation in waveguides with the finite element method." *Ndt & E International* 32.4 (1999): 225-234

[7]   J.-M. Mencik and M. N. Ichchou. Multi–mode propagation and diffusion in structures through finite elements. *European Journal of Mechanics - A / Solids*, 24(5):877–898, 2005

[8]   M. Collet, M. Ouisse, M. Ruzzene, M. Ichchou (2011) Floquet-bloch decomposition for the computation of dispersion of two-dimensional periodic, damped mechanical systems. International Journal of Solids and Structures, 48(20):2837–2848.

[9]   O. Doutres, M. Ouisse, N. Atalla and M. Ichchou: Impact of the irregular microgeometry of polyurethane foam on the macroscopic acoustic behavior predicted by a unit-cell model. Journal of the Acoustical Society of America, 2014.

[10]   M. Ouisse, M. Ichchou, S. Chedly, M. Collet (2012): On the sensitivity analysis of porous materials models. Journal of Sound and Vibration, Volume 331, Issue 24, Pages 5292-5308

[11]   G. Petrone, V. D'Alessandro, F. Franco, S. De Rosa (2014): Numerical and experimental investigations on the acoustic power radiated by Aluminum Foam Sandwich panels, Composite Structures 118.

A LITERATURE REVIEW FOR THE ANALYSIS OF STRUCTURED AND UNSTRUCTURED UNCERTAINTY EFFECTS ON VIBROACOUSTIC

R. P. Singh[1,2] , S. De Rosa[1] , F. Franco[1] ,M. Ichchou[2] and O. Bareille[2]

[1]PASTA-Lab / Laboratory for promoting experiences in Aeronautical Structures and Acoustics,
Department of Industrial Engineering, University of Napoli "Federico II "
Via Claudio 21, 80125 Napoli, Italy
ravipratap1428@gmail.com,{ sergio.derosa, francesco.franc}@unina.it

[2]VIAME / Vibroacoustics and Complex Media
École Centrale de Lyon
36 avenue Guy de Collongue - 69134 Écully, France
{mohamed.Ichchou, Olivier.Bareille}@ec-lyon.fr

ABSTRACT

A better knowledge of the structural response of periodic structures can be achieved through the classification of possible uncertainty, to be included in the predictive models. Nowadays, the wave finite element approach is used for the simulation of periodic structures to reduce the computational cost. On the contrary, it introduces ahigher complexity in the model formulation. Recently, the spectral approach has shown its relevance in the uncertainty analysis of structures.

This paper presents the literature on uncertainty effect on vibroacoustic of periodic media. The present work is an initial literature study on available analytical and numerical approaches for capturing the parametric and nonparametric uncertainties.
.

1. INTRODUCTION

The research community has been developing mathematical representation in the form of a mathematical model for a wide class of physical system to understand the process. Moreover, these models are being used to make the decision for design and manufacturing. It true that no mathematical model can be an ideal representation of physical system it is intended to capture because of the modeling assumption and limits of digital computing machines where numerical simulation performed. Although the digital computing is extending its wing in last decade, there are constraints of time and cost of computation. To the best of authors understanding, all derived model involve uncertainty and which are bound to come. The reason is how to model is represented, and how the physical system behaves in reality, there is always the issue of the goodness of fit.

The vibroacoustic performance and dynamics of the structure areimportant subjects in the area of aeronautic, transport, energy and space. To meet the regulatory compliance and user requirement, the designer accounts for variation in the input parameter at the design phase. For example, in the space industry designers consider the uncertainty in the system parameter to ensure that the during launch and orbital operation the vibration level are in a range that is acceptable. Which open plethora of opportunity for considering the effect of uncertainty with theaim to improve and develop the model for reliable and safe design. Keeping the view this paper summaries uncertainty quantification, uncertainty classification, modeling of uncertainty system and the most commonly used technique to analyses uncertainty in the low to high-frequency model prediction.

2. UNCERTAINTY QUANTIFICATION:

In general term the uncertainty quantification involves the five steps:
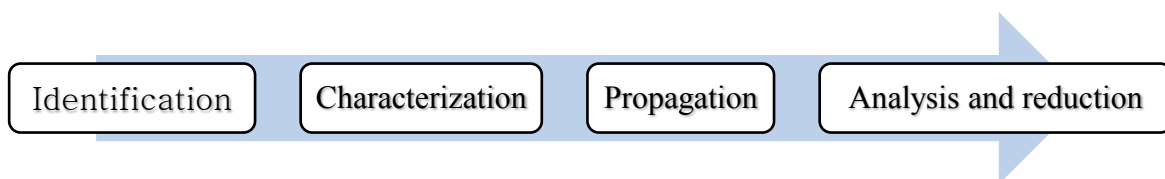
1. Identification: Finding the source and location of uncertainties in the system. In reality many sources of uncertainty such asuncertainties due to variabilities in the design parameter values, environmental condition, initial conditions, boundary conditions, imprecise and simplified physics, missing physics, model implementation, numerical errors and most importantly due to lack of unavailability of sufficient data
2. Characterization: Finding the form they are available. Mostly, the parametric uncertainty is characterized and defined in the form of probability distribution and intervals bound. Whereas nonparametric uncertainty so-called model uncertainties can have their form of uncertainties.
3. Propagation: Understanding how uncertainties are transmitting and spreading in the model and finding a relation between parameter uncertainties and response of the model.
4. Analysis and reduction: Establishing the relation between the uncertainty and its influence on the system response and reasoning of the same. Once it is done, what corrective measure can be taken to have the reliability of the original system.

3. MODELING OF UNCERTAINTY SYSTEM:

The uncertainty in structural response such as frequency response function, natural frequency, and mode shape are the result of propagation of uncertainty (may be parametrical or non-parametric). To capture the response with uncertainty in models and parameters, various

research group spread across the world using various approach to modeling the uncertainty. The basic uncertainty block of technique/tool available for uncertainty modeling in the structural dynamics[1-7] can be drawn (Figure 1).
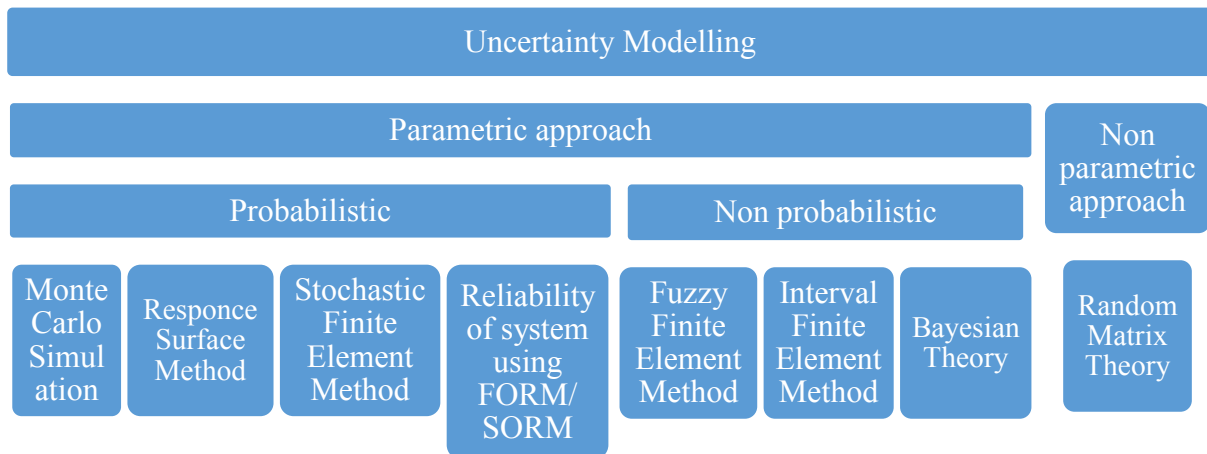

Figure 1. Uncertainty modeling approaches

4. VIBROACOUSTIC ANALYSIS WITH UNCERTAINTY

In thevibroacousticproblems, the interaction between a solid and fluid field in the form of vibration and sound happen respectively. The use of the numerical method for the numerical modeling and simulation varies, and itdepends on the frequency range of interest.

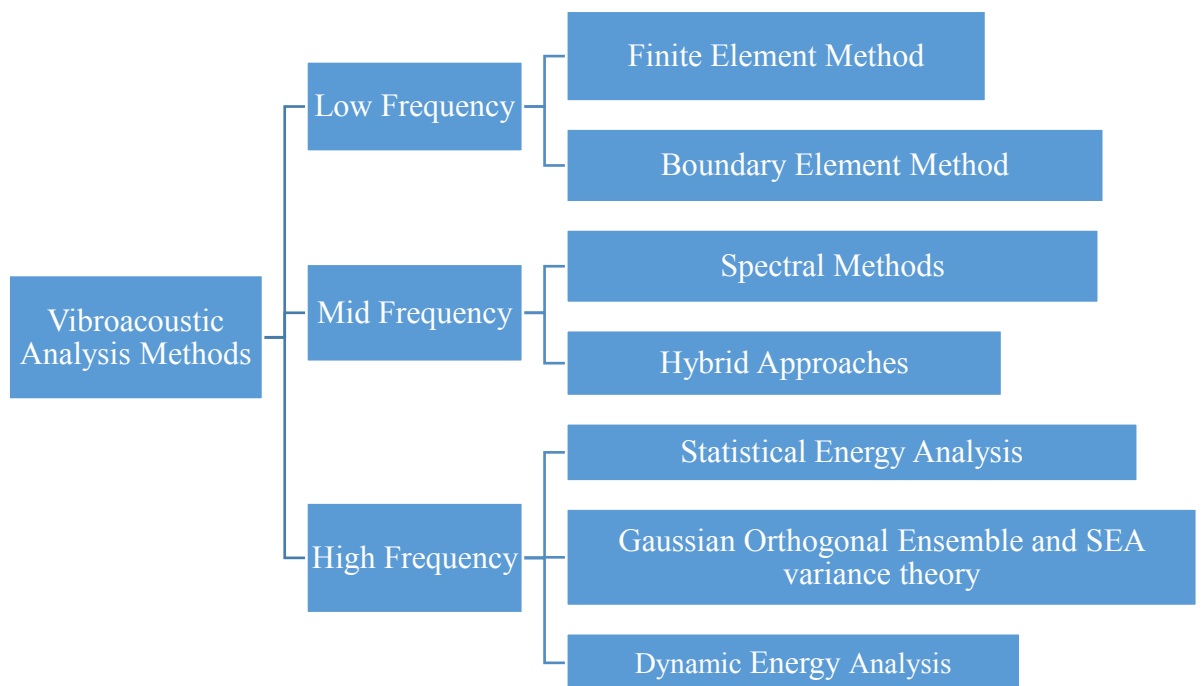Figure 2.Vibroacoustic analysis methods without uncertainty

A graphical representation is drawn (Figure 2) of the technique available for vibroacousticsimulation[8-11].When uncertainty introduced in the modeling and simulation of

3

vibroacoustic periodic media the low-frequency domain is unaffected (assumption), the high-frequency domain is modeled using statistical energy approach which can accommodate uncertainty. However mid frequency domain is in question. A tree is drawn (Figure 3) as based on available literature.
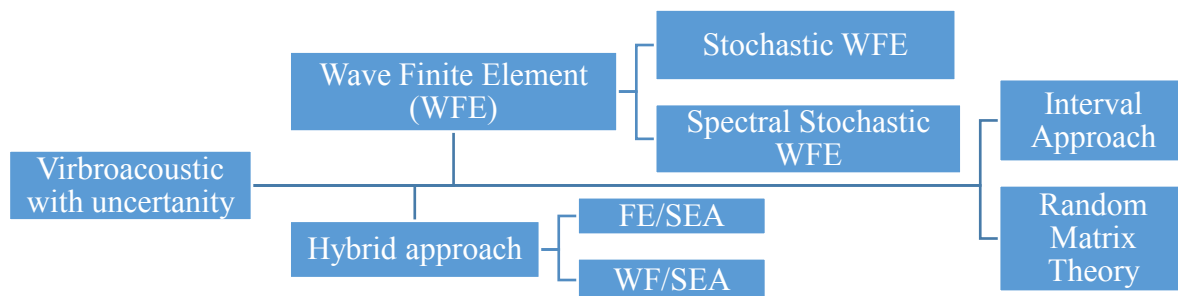

Figure 3.Vibroacousticanalysis methods with uncertainty

ACKNOWLEDGEMENTS

REFERENCES:

[1]   H. Zhang, R. L. Mullen, and R. L. Muhanna, "Interval Monte Carlo methods for structural reliability," *Struct. Saf.*, vol. 32, no. 3, pp. 183–190, 2010.
[2]   C. Majba, "A Review of Uncertainty Quantification of Estimation of Frequency Response Functions," University of Cincinnati, 2012.
[3]   G. Stefanou, "The stochastic finite element method: Past, present and future," *Comput. Methods Appl. Mech. Eng.*, vol. 198, no. 9–12, pp. 1031–1051, 2009.
[4]   C. Soize, "Random matrix theory and non-parametric model of random uncertainties in vibration analysis," *J. Sound Vib.*, vol. 263, no. 4, pp. 893–916, 2003.
[5]   L. Chen and S. S. Rao, "Fuzzy finite-element approach for the vibration analysis of imprecisely-defined systems," *Finite Elem. Anal. Des.*, vol. 27, no. 1, pp. 69–83, 1997.
[6]   S. Nannapaneni and S. Mahadevan, "Reliability analysis under epistemic uncertainty," *Reliab. Eng. Syst. Saf.*, vol. 155, pp. 9–20, 2016.
[7]   C. Soize, "A comprehensive overview of a non-parametric probabilistic approach of model uncertainties for predictive models in structural dynamics," *J. Sound Vib.*, vol. 288, no. 3, pp. 623–652, 2005.
[8]   B. R. Mace, K. Worden, and G. Manson, "Uncertainty in structural dynamics," *Journal of Sound and Vibration*, vol. 288, no. 3. pp. 423–429, 2005.
[9]   A. Cicirello and R. S. Langley, "Efficient parametric uncertainty analysis within the hybrid Finite Element/Statistical Energy Analysis method," *J. Sound Vib.*, vol. 333, no. 6, pp. 1698–1717, 2014.
[10]   M. N. Ichchou, F. Bouchoucha, M. A. Ben Souf, O. Dessombz, and M. Haddar, "Stochastic wave finite element for random periodic media through first-order perturbation," *Comput. Methods Appl. Mech. Eng.*, vol. 200, no. 41–44, pp. 2805–2813, 2011.
[11]   M. Xu, Z. Qiu, and X. Wang, "Uncertainty propagation in SEA for structural-acoustic

coupled systems with non-deterministic parameters," *J. Sound Vib.*, vol. 333, no. 17, pp. 3949–3965, 2014.

5

DESIGN AND EXPERIMENTAL VALIDATION OF A HIERARCHICAL AUXETIC RECTANGULAR PERFORATED METAMATERIAL

K. Billon[1*], M. Ouisse[1], F. Scarpa[2], E. Sadoulet-Reboul[1], M. Collet[3] and G. Chevallier[1]

[1]Univ. Bourgogne Franche-Comté
FEMTO-ST Institute CNRS/UFC/ENSMM/UTBM
Department of Applied Mechanics
24 chemin de l'Epitaphe, 25000 Besançon, France
Email: kevin.billon@femto-st.fr, morvan.ouisse@femto-st.fr,
emeline.sadoulet-reboul@univ-fcomte.fr, gael.chevallier@femto-st.fr

[2]Advanced Composites Centre for Innovation and Science (ACCIS)
University of Bristol
BS8 1TR Bristol, United Kingdom
Email: f.scarpa@bristol.ac.uk

[3]Laboratory of Tribology and Systems Dynamics (LTDS)
École Centrale de Lyon
36 avenue Guy de Collongue, 69134 Ecully, France
Email: manuel.collet@ec-lyon.fr

ABSTRACT

The understanding of wave propagation in a metamaterial with hierarchical, auxetic rectangular perforations is presented in this work. The metamaterial is a 2D structure with chaining horizontal and vertical perforations exhibing auxetic in-plane behaviour. Some numerical eigenvalue tools are used for the dispersion analysis of this structure. It is first observed that the total width of Band gaps increases with the hierarchy. In order to validate the design of the metamaterial, results issued from a full 3D model of a finite structure embedding an interface composed by a distributed set of the unit cells are presented. After this step, a comparison between the results obtained using the structure simulation and the experimental results are presented with critical analysis.

1   INTRODUCTION

A periodic medium is a material or a structural system that exhibits spatial periodicity. The study of periodic structures has a long history in the field of vibrations and acoustics [1]. This topic has interested researchers over the years, and a growing activity on this field is observed on the last years, with the objective of designing structures exhibiting properties that conventional ones cannot possess [2]. Dynamical behaviour analysis of plates with hierarchical, auxetic rectangular perforations are described in this paper.

2   GEOMETRY OF THE HIERARCHICAL PERFORATED AUXETIC LATTICE

Figure 1a shows the structural dimensions of the square lattice with rectangular perforations. The symmetry of the geometry in the $x - y$ plane allow to define the entire geometry of the unit cell using only 2 parameters: the void aspect ratio, $AR = a/b$ and the intercell spacing S [3].

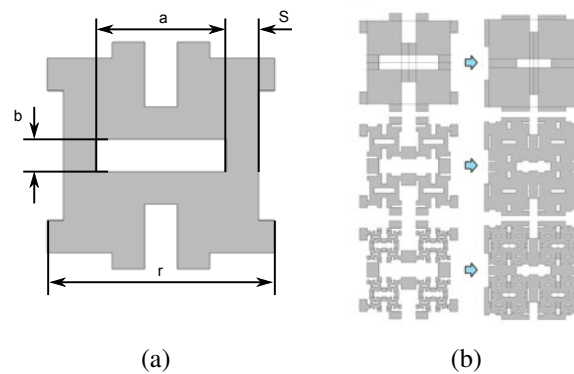(a)   (b)

Figure 1: a) Geometry parameters of the base unit cell. b) Hierarchical, auxetic rectangular perforations at Level 1, 2 and 3 with $AR = 4$ and from $S = 0.2$ to $S = 0.8$.

As a reference, the level 1 [3] is compared with the hierarchical levels 2 and 3. At level 1, 4 rigid squares are present in the unitcell. In each square, the reference structure is used by applying a scale ratio to obtain the level 2. Exactly the same at level 3, in this subunit. The parametric analysis is carried out with the aspect ratios (AR), the intercell spacing (S) and the level of hierarchy. Figure 1b shows how intercell spacing change in both levels of hierarchy. Voids are larger than a low parameter S and the porosity increases with the level of hierarchy.

3   DYNAMIC PROPERTIES

3.1   Dispersion analysis

Properties are calculated using the finite element model of the unit cell with Floquet-Bloch periodic conditions applied on the borders of the domain [4].

The results of the analysis correspond to dispersion diagrams which only provides information on the contour of the Brillouin zone allowing identification of the bandgaps. Hence, only specific directions are investigated.

Band gaps are observed at some specific values of AR and S (see figure 3).

These band gaps are called omnidirectional band gap because whatever the direction of the wave propagation, this wave can not propagate. In our case, a particular interest is given to omnidirectional band gaps. To compare the results of the eigenvalue analysis at different levels we have computed for each geometry configuration of the perforated composite plate
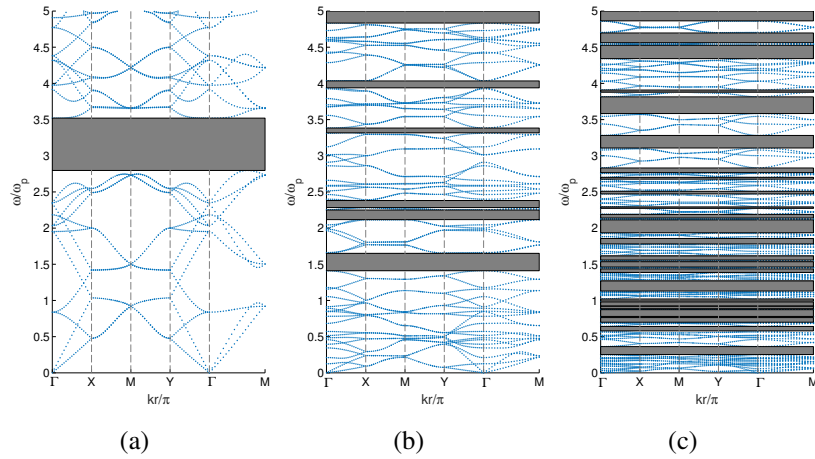
2

Figure 2: Dispersions in the k space for the lattice with $AR = 4$, $S = 0.3$ for a) Level 1, b) Level 2 and c) Level 3.

the equivalent volume fraction (ϕ) and computed by Finite Element the natural frequency of a rectangular plate (plane stress) with the same overall dimension of the lattice with Poisson's ratio equal to the one of the core material (ν_c), scaled density $\bar{\rho} = \phi\rho_c$ and equivalent Young's modulus $\bar{E} = E_c\phi^2$. The resulting fundamental frequency is denominated as ω_p. The modal density increase with the hierarchy, it is true whatever the value of the parameter S is. The reader is invited to refer to a previous article [5] for details.

3.2   Finite structure

The main goal of this section is to validate in a finite structure the phenomenon observed on an infinite structure. A finite element model is presented. This is followed by an experimental validation. The metamaterial ($68 \times 28 \times 0.4\ cm^3$) includes an interface composed by 4×4 unit cells ($7 \times 7 \times 0.4\ cm^3$) (figure 3a). The metamaterial is made in acrylic which properties properties are $E = 3.01\ GPa$, $\nu = 0.375$ and $\rho = 1190.25\ kg/m^3$ with a loss factor (η) equal to 4.2%.
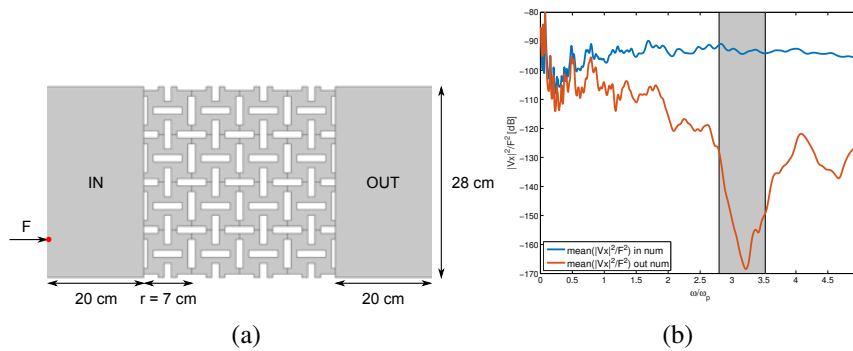

Figure 3: a) Finite structure with an interface composed by 16 unit cells for level 1. The point load is marked by a red dot. b) Numerical frequency responses for level 1. Average squared velocity amplitude $|Vx|^2$ for the input plate (IN) and the output plate (OUT) respectively in blue and red. The grey shape represent the bandgap predicted by the dispersion analysis.

Numerical frequency responses for level 1 are presented in figure 3b, squared velocity amplitudes $|Vx|^2$ are averaged for the input plate (IN) and the output plate (OUT). The bandgap

predicted by the dispersion analyse is represented by a grey shape. An output attenuation is well observed in the frequency range predicted by bandgap.

4   EXPERIMENTAL VALIDATION

The metamaterial is realised by laser cutting in a whole $4\ mm$ acrylic glass plate. This experimental validation is a real challenge. Boundary conditions need to respect the plane stress condition. Figure 4 illustrates the experimental facility with the metamateriel, its bracket, the vibrometer, the force sensor and the accelerometer. A shaker provides clean harmonic excitation up to $5\ kHz$.
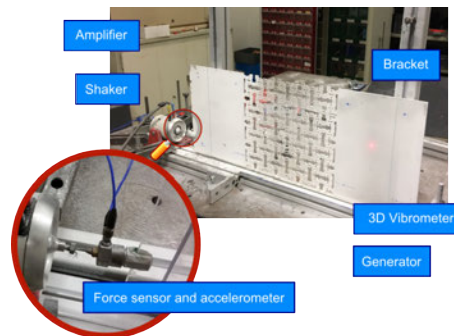

Figure 4: Experimental facility with the main equipment as the metamateriel and the vibrometer. A zoom is done on the excitation system, a shaker instrumented with force sensor cell and accelerometer.

5   CONCLUSION

This study shows the possibility of creating bandgaps by simple cutting in plane structures. The damping is important, an overall smoothing of the frequency response functions is observed and a very large attenuation between the input and the output of the network. The experimental setup was a real challenge. The results engage a critical analysis which highlight the strengths and weaknesses of this experiment.

REFERENCES

[1] M.I. Hussein, M.J. Leamy, and M. Ruzzene. Dynamics of phononic materials and structures: Historical origins, recent progress, and future outlook. *Applied Mechanics Reviews*, 66(4):040802, 2014.

[2] S. Shan, S.H. Kang, Z. Zhao, L. Fang, and K. Bertoldi. Design of planar isotropic negative poissons ratio structures. *Extreme Mechanics Letters*, 4:96–102, 2015.

[3] A. Slann, W. White, F. Scarpa, K. Boba, and I. Farrow. Cellular plates with auxetic rectangular perforations. *physica status solidi (b)*, 252(7):1533–1539, 2015.

[4] M. Collet, M. Ouisse, M. Ruzzene, and M.M. Ichchou. Floquet–bloch decomposition for the computation of dispersion of two-dimensional periodic, damped mechanical systems. *International Journal of Solids and Structures*, 48(20):2837–2848, 2011.

4

[5] K. Billon, I. Zampetakis, F. Scarpa, M. Ouisse, E. Sadoulet-Reboul, M. Collet, A. Perriman, and A. Hetherington. Mechanics and band gaps in hierarchical auxetic rectangular perforated composite metamaterials. *Composite Structures*, 160:1042–1050, 2017.

5

SPATIAL SPECTRA OF THE EIGENMODES OF RIBBED PLATES PROJECTED ON DISPERSION BRANCHES

G. Lefebvre[1] , X. Boutillon[1*] and M. Filoche[2]

[1]Laboratoire de Mécanique des solides
École polytechnique, 91128 Palaiseau Cedex, FRANCE
Email: lefebvre@lms.polytechnique.fr, boutillon@lms.polytechnique.fr

[2]Laboratoire de Physique de la matière condensée
École polytechnique, 91128 Palaiseau Cedex, FRANCE
Email: marcel.filoche@polytechnique.edu

ABSTRACT

A vast literature has been devoted to the transverse vibration and the sound radiation of ribbed plates over the last decades. The present study has been motivated by the analysis of the dynamical behaviour of piano soundboards. As a rough approximation, a piano soundboard can be considered as an orthotropic ribbed plate. Our purpose is to establish condensed descriptions for their dynamics. For low frequencies, regularly ribbed plates can be considered as homogeneous plates. It is usually considered that homogenization is valid only up to a frequency corresponding roughly to the confinement of one half wave-length between the (periodically spaced) ribs. Beyond that frequency, depending on the relative characteristic mobility of the ribs and that of the base plate, the ribs may constrain transverse waves to be guided between them. We focus here on the spatial spectrum of the normal modes of the ribbed plate (2D Fourier transforms of the modal shapes). It appears that most of the peaks of each spectrum can be seen as belonging to one of a few dispersion branches in an appropriate (ω, k)-plane. Interestingly, different peaks of a spectrum (of one given mode) usually "belong" to different dispersion branches. When valid, this description may prove an interesting intermediate step to derive approximations for the sound radiation of such plates.

1   INTRODUCTION

This study has been motivated by the analysis of the dynamics of piano soundboards, which are sophisticated ribbed plates[1]. We consider here a more simple system which consists in a thin rectangular plate represented in Fig. 1 (axes of the Oxy-frame of reference parallel to the sides of the rectangle, $L_x = 1.39\,\text{m}$, $L_y = 0.91\,\text{m}$, $h = 0.008\,\text{m}$). The regularly-spaced ribs are oriented in the OX-direction ($\theta = (Ox, OX) = 1.0065\,\text{rad}$), with inter-rib spacing $d = 0.13\,\text{m}$. Materials are orthotropic ($\rho = 392\,\text{kg m}^{-3}$, $E_X = 11.5 \times 10^9\,\text{Pa}$, $E_Y = 0.47 \times 10^9\,\text{Pa}$ for the main plate and for the ribs, corresponding to one quality of spruce). Note that the geometry does not correspond to the so-called *special orthotropy* configuration ($OX = Ox$) and that (incidentally, not necessarily) the ribs are in the direction of one orthotropy axis. Here, boundary conditions have been chosen as clamped all around the plate.

The plate has been modelled as a thin plate (Kirchhoff-Love theory) and treated by means of FreeFem++, a Finite-element software, yielding the normal modes.
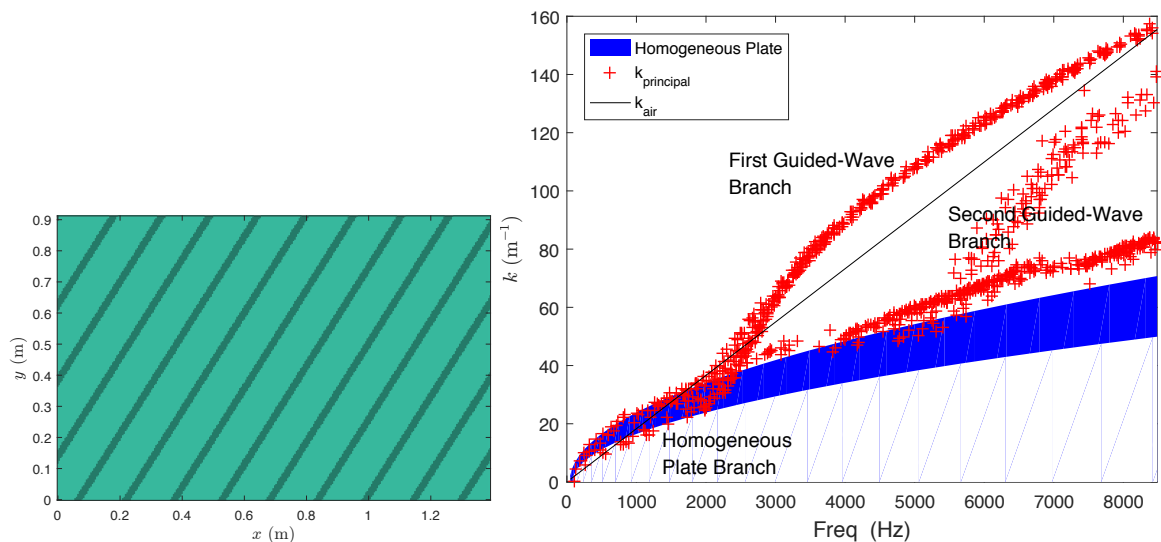
2   MODAL SPECTRA

Figure 1: Left: The ribbed plate. Right: largest peak of all the modes as a function of the corresponding eigenfrequency (the oblique thin lines are a graphic artefact)

Since no dissipation is included in the mechanical model, the eigenvectors are real. These modal shapes are represented with real numbers (positive or negative) and no phase (no information is lost). Given that choice, a 2D Fourier transform has been applied to all modal shapes, yielding modal spectra $S_m(k_x, k_y) \in \mathbb{R}$.

As a first step, we extract the dominant peak _principal_ from each spectrum. Its magnitude is represented in Fig. 1 as a function of the angular frequency of the corresponding normal mode. The figure displays three distinct branches which look like *dispersion branches*. However, one must keep in mind that data in this figure only represent a very partial view on the modes (limited to their principal wave-number).

Another view on all modes consists in adding all (spatial) spectral components in the (k_x, k_y)-plane. In such a representation, the eigenfrequencies are lost, as well as any form of visual clarity of the corresponding diagram (not represented). The interesting point is that clarity is retrieved when an appropriate ω-scaling is applied to the wave–number components k_x or k_y, as done in the next sections. The first scaling (Section 3) corresponds to a homogeneous-plate

dynamics whereas guided-wave regimes (not completely understood at this point) correspond to the first and second branches (Section 4).

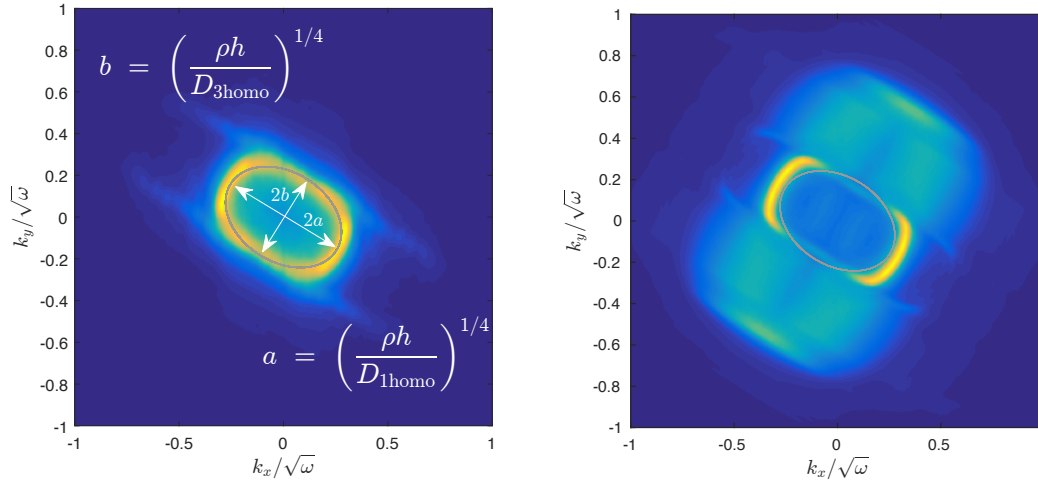## 3   HOMOGENEOUS-PLATE BRANCH

Figure 2: Dispersion maps. Left frame: scaling applied on modes with eigenfrequency below 2kHz. Right frame: same, on modes beyond 2kHz.

The dynamical equation ruling the transverse motion w of the non-homogeneous orthotropic thin plate is

$$\frac{\partial^2}{\partial X^2}\left(D_1\frac{\partial^2 w}{\partial X^2}\right)+\frac{\partial^2}{\partial X^2}\left(\frac{D_2}{2}\frac{\partial^2 w}{\partial Y^2}\right)+\frac{\partial^2}{\partial Y^2}\left(\frac{D_2}{2}\frac{\partial^2 w}{\partial X^2}\right)+\frac{\partial^2}{\partial Y^2}\left(D_3\frac{\partial^2 w}{\partial Y^2}\right)+\frac{\partial^2}{\partial X\partial Y}\left(D_4\frac{\partial^2 w}{\partial X\partial Y}\right)=\rho h(X,Y)\omega^2 w$$

(1)

where D_1 and D_3 on one hand, D_2 and D_4 on the other hand are of the form

$$D_{1,3}=\frac{E_{X,Y}h^3}{12(1-\nu_{XY}\nu_{YX})}\quad D_{2,4}=\frac{\nu_{YX}E_X h^3}{12(1-\nu_{XY}\nu_{YX})}+\frac{G_{XY}h^3}{6}\quad(\nu_{YX}E_X=\nu_{XY}E_Y)\quad(2)$$

The dynamical rigidities D are not constant over this non-homogeneous plate.

It is commonly accepted that homogenization theories can account for the dynamical behaviour of non-homogeneous plates at low frequencies only. Looking at Fig. 1, one can infer that more or less all modes below f_H (with $1.5 < f_H < 2$kHz) could be described as normal modes of a homogeneous plate. Applying homogenization to the ribbed plate considered here, as in studies reported in [1], yields $E_{XH} = 1.45 \times 10^9$ Pa, $E_{YH} = 5.51 \times 10^9$ Pa, $\rho = 227\,\mathrm{kg\,m^{-3}}$ and $d_H = 16.9\,\mathrm{mm}$ and the following dynamical equation for the equivalent homogeneous plate:

$$D_{1H}k_X^4 + (D_{2H} + D_{4H})k_X^2 k_Y^2 + D_{3H}k_Y^4 = \rho h_H \omega^2$$

(3)

in the reciprocal space (k_X, k_Y). By construction, the homogeneous equivalent plate has an *elliptic* orthotropy: $D_{2H} + D_{4H} = \sqrt{D_{1H}D_{3H}}$.

With $K = k/\sqrt{\omega}$ (generic notation), Eq. (3) becomes

$$\frac{D_1}{\rho h}K_X^4 + \frac{D_2 + D_4}{\rho h}K_X^2 K_Y^2 + \frac{D_3}{\rho h}K_Y^4 = 1$$

(4)

We represent the results of this rescaling on all the modal spectra in Fig. 2. By analogy with the "dispersion curve" terminology in the (ω, k)-plane, we call "dispersion map" this representation of the spectra of the normal modes.

3

Several features are quite remarkable here. (a) The left frame exhibits the expected homogeneous dynamical behaviour, but for *nearly all the spectral components* of the modes, not only the principal peaks. The figure is nearly elliptical and the expected quantities D_{1H} and D_{3H} are retrieved on the long and short axes respectively. (b) This homogeneous dynamics extends far beyond the upper frequency f_H beyond which the homogenization becomes invalid for describing the whole dynamics of the ribbed plate. This applies to *part of the spatial spectra*, as shown by the large blurry yellow zone, which does not follow this well-identified dynamics. (c) Above f_H, the elliptic homogenization is slightly altered.
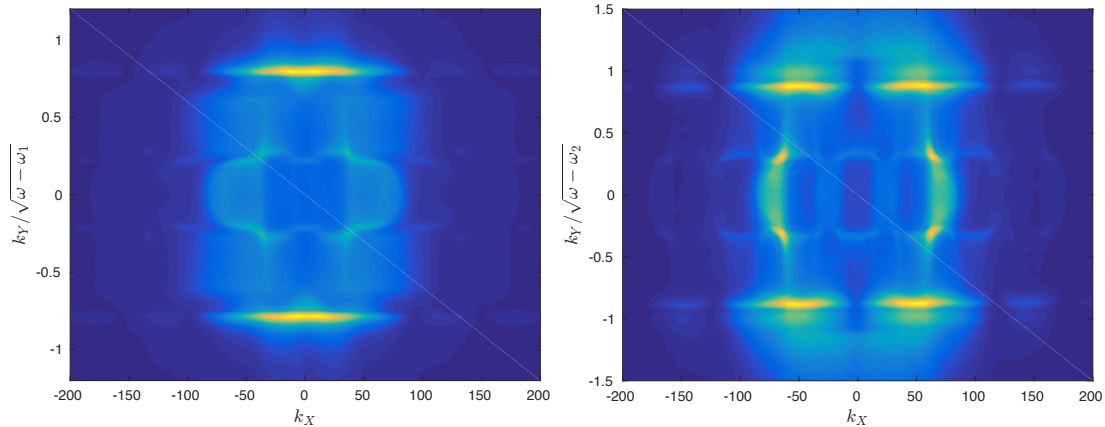
4   GUIDED-WAVE BRANCHES

Figure 3: Dispersion maps with scaling by $\sqrt{\omega - \omega_{1,2}}$ applied to k_Y, the k_X-axis remaining unchanged. Each scaling is suited to one guided-wave branch. Left: all modes with an eigenfrequency above ω_1. Right: all modes with an eigenfrequency above ω_2.

We observe in Fig. 1 that above a transition occurring around $\approx 1.5 - 2$kHz, the principal wavenumber of the two additional branches is essentially driven by its k_Y-component. A more detailed analysis reveals that the k_X-components of the first guided-wave branch are all in the $[0, \pi/d]$ interval (more or less uniformly distributed) whereas the k_X-components of the second guided-wave branch are more scattered in the $[3\pi/(2d), 3\pi/d]$ interval: modes start to exhibit a guided-wave behaviour. As opposed to the previous section, the scaling here is by $\sqrt{\omega - \omega_{1,2}}$. Hypothetically, the cut-off frequency $\omega_{1,2}$ corresponds, dynamically, to a low k_X, characteristic of the guided wave. An effective dynamical rigidity of the waveguide can be derived from Fig. 3. Surprisingly, its value appears to be less than that of the plate without ribs.

5   CONCLUDING REMARKS

Interestingly, the homogeneous and guided-wave regimes are not exclusive of each other. In fact, each mode tends to display some spectral components on each of the different branches (at least, above f_H).

REFERENCES

[1] Xavier Boutillon and Kerem Ege. Vibroacoustics of the piano soundboard: Reduced models, mobility synthesis, and acoustical radiation regime. *Journal of Sound and Vibration*, 332(18):4261–4279, 2013.

4

HYBRID WAVE BASED-FINITE ELEMENT UNIT CELL MODEL TO PREDICT REFLECTION, TRANSMISSION AND ABSORPTION COEFFICIENTS OF PERIODIC MATERIAL SYSTEMS

E. Deckers[1,2], S. Jonckheere[1,2], L. Van Belle[1,2*], C. Claeys[1,2] and W. Desmet[1,2]

[1]KU Leuven, Department of Mechanical Engineering
Celestijnenlaan 300B, box 2420, 3000 Leuven (Heverlee), BELGIUM
Email: elke.deckers@kuleuven.be, stijn.jonckheere@kuleuven.be,
lucas.vanbelle@kuleuven.be, claus.claeys@kuleuven.be, wim.desmet@kuleuven.be

[2]Member of Flanders Make

ABSTRACT

This paper presents a hybrid unit cell method to predict sound transmission and sound absorption properties of arbitrary two-dimensional periodic structures, combining the advantages of the Wave Based Method and the Finite Element Method. The planar periodic structure, represented by its unit cell, is modelled by the Finite Element Method and the acoustic pressure field in the semi-unbounded acoustic domains is represented using the Wave Based Method. The Finite Element Method allows to include geometrical details and any combination of governing physics in the unit cell. The Wave Based Method applies dedicated approximation functions that inherently satisfy the acoustic Helmholtz equation, the Sommerfeld radiation condition and the Bloch-Floquet periodicity conditions. The dynamic fields described within both frameworks are coupled using a direct coupling strategy. The method is validated for an infinite porous plate, modelled as an equivalent fluid, with periodic, rigid, circular inclusions and is shown to be a promising tool for the analysis of complex periodic structures.

1   INTRODUCTION

Lightweight designs are emerging to save material costs and to reduce the ecological footprint of industrial products. Due to their decreased mass and retained stiffness, however, noise and vibration isolation properties are impaired, with an impact on comfort and health. Periodically structured materials, such as resonant metamaterials and porous material with inclusions are promising lightweight concepts to obtain improved low-frequency STL or absorption in a dedicated frequency band.

The vibro-acoustic performance of periodic materials is classically predicted by calculating dispersion curves, describing the wave propagation throughout the infinite periodic medium, based on a representative unit cell (UC). By comparing these dispersion curves to the dispersion curves of air, the influence on the acoustic radiation can be predicted by assessing the occurrence of acoustic coincidence.

To predict actual levels for the acoustic transmission or absorption performance, numerical simulation techniques are applied. Recently, the Transfer Matrix Method has been extended with periodicity conditions [1]. This method is very effective, but breaks down when higher order acoustic Bloch-Floquet modes have to be accounted for. The Wave Based Method (WBM) [2] and the Multipole Method [3], allow the prediction of absorption, reflection and transmission coefficients, however, yet only apply to relatively simple geometries.

To analyse the vibro-acoustic response of periodic materials consisting of arbitrarily complex UCs, this paper proposes a hybrid Finite Element - Wave Based Method Unit Cell model as an extension of the WBM [2], also towards three-dimensional applications. The dynamic fields within the bounded UC are modelled with the Finite Element Method (FEM), allowing high geometrical flexibility and arbitrary subdomains. The acoustic pressure fields inside the semi-unbounded acoustic domains are modelled with the WBM. Its approximation functions are formulated to inherently fulfil the Helmholtz equation, the Bloch-Floquet periodicity boundary conditions and the Sommerfeld radiation condition, not relying on any artificial truncation or discretization of the domain, as would be required in a pure FEM setting. The dynamic field variables of both methods are coupled at the interface, using a direct coupling approach. The method is validated for numerous cases of which one is shown in this paper and proves to be a powerful tool.

2   NUMERICAL MODEL

2.1   Mathematical problem description

An infinite, 2D periodic structure is considered, with spatial period L_x and L_y in the xy-plane, coupled to one or two semi-unbounded acoustic domains, excited by an impinging acoustic plane wave with wave number $\mathbf{k_a}$, incident at elevation θ and azimuth ψ. The periodic structure may be built up of any combination of physical subdomains for vibro-acoustic analysis. Due to the geometrical periodicity and the plane wave excitation, the resulting dynamic fields have to be periodic in the x- and y-direction. By determining the dynamic field in a single reference UC and applying the Bloch-Floquet periodicity boundary conditions, the dynamic field $\zeta(x + ML_x, y + NL_y, z)$ in any point at a distance of M and N UCs from the reference UC can be obtained:

$$\zeta(x + ML_x, y + NL_y, z) = \zeta(x, y, z)e^{-\mathrm{j}(k_{ax}NL_x + k_{ay}ML_y)}, \ \forall \ M, N \in \mathbb{Z}, \tag{1}$$

where $k_{ax} = -k_a \sin\theta \cos\psi$ and $k_{ay} = -k_a \sin\theta \sin\psi$.

2.2   Hybrid Wave Based-Finite Element UC model

To analyse periodic structures of arbitrary complexity, the FEM and WBM are applied in a hybrid framework, combining best of both worlds for UC analysis. The FEM is used for the approximation of the dynamic fields within the unit cell of the periodic material as it allows high geometrical flexibility and any type of physics to be included. The WBM, on the other hand, can directly account for the semi-unbounded, periodic acoustic domain(s).

2.2.1   Finite Element Method

The FEM discretizes the considered UC of the periodic material into nodes and elements and approximates the field variables and the geometry by means of polynomial shape functions. The system of equations is obtained by approximating the governing differential equations, boundary and interface conditions via a weighted residual formulation, following a Galerkin approach. A summary of the governing equations of poro-elastic, acoustic, porous and elastic subdomains, their coupling conditions and possible boundary conditions can be found in [4].

2.2.2   Wave Based Method

The WBM, based on an indirect Trefftz approach, approximates the dynamic field variable(s) by a weighted sum of wave functions, that inherently fulfil the governing acoustic Helmholtz equation. The boundary conditions are approximated in a weak, integral sense. For this specific problem setting, to avoid integrations on infinite boundaries, semi-infinite, periodic wave functions are selected, analogous to [2] but in 3D, such that not only the acoustic Helmholtz equation is fulfilled, but also the Sommerfeld radiation condition and the Bloch-Floquet periodicity boundary conditions. All boundary conditions are thus fulfilled, except the coupling with the FE domain, which is discussed in section 2.2.3.

2.2.3   Hybrid coupling

The mutual interactions between the FE and WB dynamic field variables are directly introduced into the weighted residual formulations of both models. In [4], the hybrid coupling strategies and equations are presented for different kinds of physics in the FEM part and for acoustic WBM domains and are now applied using the semi-unbounded periodic wave functions. A hybrid system of equations is obtained, coupling the degrees of freedom from both models.

2.2.4   Solution and postprocessing

Bloch-Floquet boundary conditions are applied to the hybrid system of equations for each angle and wave number of interest. The resulting system of equations is solved for the unknown nodal degrees of freedom in the FE part and the wave function contribution factors in the WB part, following a three-step procedure [4] in order to benefit from efficient solvers for sparse and dense matrix systems. Similar to [2], the reflection, transmission and absorption coefficients of the periodic structure can be obtained from the wave function contribution factors.

3   NUMERICAL VERIFICATION

To validate the hybrid UC model presented above, it is applied to analyse an infinite porous material with periodically embedded rigid circular inclusions in a transmission context and its results are compared to a WBM prediction. The geometry and material properties considered are based on the transmission case presented in [2], extruding the geometry in the third direction,

3

such that a cubic UC with edge length $0.02m$ is obtained. The mesh and the obtained reflection and transmission coefficient are shown in Figure 1. The results obtained with the hybrid method (3D simulations) are in excellent agreement with the results obtained using the Wave Based Method (2D simulations), validating the procedure.
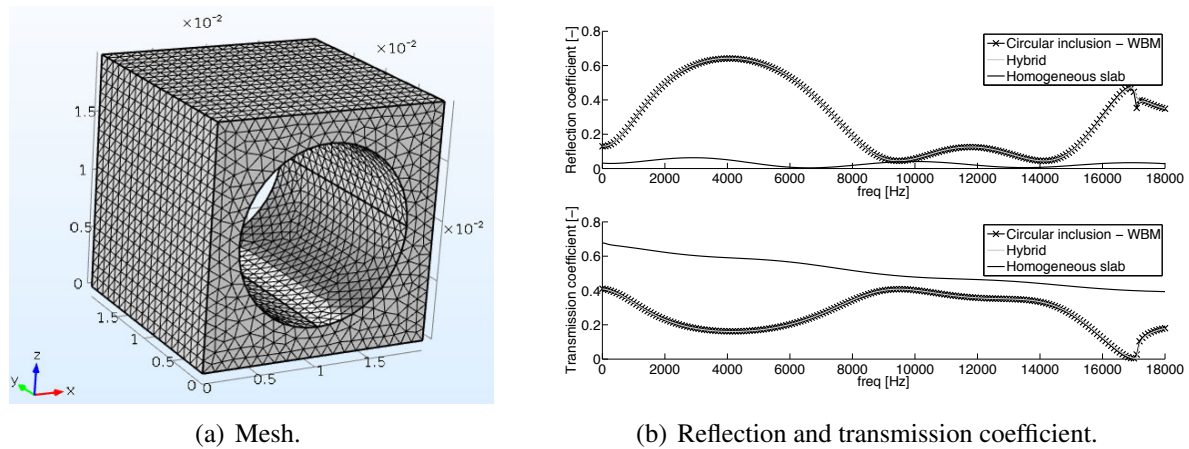

(a) Mesh.

(b) Reflection and transmission coefficient.

Figure 1: FE Mesh of the UC and obtained reflection and transmission coefficient under normal incidence with the hybrid method and the WBM.

4 CONCLUDING REMARKS

In this work a hybrid WB-FE UC method is presented to analyze the reflection, transmission and absorption coefficient of infinite, two-dimensional periodic structures of arbitrary complexity. The method is verified by numerous validation cases of which one is presented in this paper. A promising tool is obtained to support complex lightweight periodic structure design.

5 ACKNOWLEDGEMENTS

REFERENCES

[1] A. Parrinello and G.L. Ghiringhelli. Transfer matrix representation for periodic planar media. *Journal of Sound and Vibration*, 371:196 – 209, 2016.

[2] E. Deckers, C. Claeys, O. Atak, J.P. Groby, O. Dazel, and W. Desmet. A wave based method to predict the absorption, reflection and transmission coefficent of two-dimensional rigid frame porous structures with periodic inclusions. *Journal of Computational Physics*, 312:115–138, 2016.

[3] J.-P. Groby, A. Wirgin, and E. Ogam. Acoustic response of a periodic distribution of macroscopic inclusions within a rigid frame porous plate. *Waves in Random and Complex Media*, 18:409–433, 2008.

[4] S. Jonckheere. *Wave Based and Hybrid Methodologies for Vibro-acoustic Simulation with Complex Damping Treatments*. KU Leuven, PhD. thesis, 2015.

4

Chiral Lattice Hinge Metamaterial for multi-broadband vibroacoustics

[1]Wenjiao Zhang, [2]Dayi Zhang, [3]Robin Neville, [3]Fabrizio Scarpa, [4]Lifeng Wang,[5]Roderic Lakes

[1]School of Engineering, Northeast Agriculture University, No.59 Mucai Street, Harbin, 150030, China
email: zhangwenjiao2005@126.com
[2]School of Energy and Power Engineering, BUAA, Beijing, 100191, China
Email: dayi@buaa.edu.cn
[3]ACCIS, Queen's Building, University Walk, Bristol BS8 1TR, United Kingdom
Email: *f.scarpa@bristol.ac.uk, robin.neville@bristol.ac.uk*
[4]Department of Mechanical Engineering, State University of New York at Stony Brook, Stony Brook, New York 11794, USA
Email: lifeng.wang@stonybrook.edu
[5]Department of Engineering Physics, University of Wisconsin-Madison, 1500 Engineering Drive, Madison, WI 53706-1687
Email: lakes@engr.wisc.edu

ABSTRACT

We present a lattice metamaterialinspired to the topology of Peano curves and defined by patterns of slits that follow a rotational symmetry (chiral) configuration. The chiral pattern of the slits creates a series of hinges by that produce deformation mechanisms for the lattice due to bending of the ribs. The metamaterial has a marginal negative Poisson's ratio and an isotropic uniaxial stiffness. The chiral hinge lattice is almost one order of magnitude more compliant than other configurations with patterned slits and - contrary to other chiral Cosserat media - exhibits an in-plane shear stiffness closer to the one prescribed by classical elasticity for elastic isotropic continua. The planar topology of the lattice is conducive to highly tailored phononic behavior, with bandgaps depending upon the slit to rib length ratios. When undergoing bending the global deformation of the lattice induce partial stick-slip interactions in the compressed cells that enhance the global damping behavior. We present a series of experimental and FE simulations that show the mechanical and vibroacoustics behavior of these peculiar mechanical metamaterials.

Fig1. *Chiral lattice hinge plate and a unit cell with a rib/slit length ratio of 10*

ANALYTICAL AND NUMERICAL LOCAL SENSITIVITY ANALYSIS OF PERIODIC SPRING-MASS CHAINS

L.R.Cunha[1,2*], M.Ouisse[1] and D.A.Rade[3]

[1]Univ. Bourgogne Franche-Comté, FEMTO-ST Institute, CNRS/UFC/ENSMM/UTBM
Department of Applied Mechanics, 25000 Besançon, FRANCE
Email: leandro.rodrigues@femto-st.fr, morvan.ouisse@femto-st.fr

[2]School of Mechanical Engineering
UFU Federal University of Uberlandia, Uberlândia - MG, BRAZIL

[3]Division of Mechanical Engineering
ITA Aeronautics Institute of Technology, São José dos Campos - SP, BRAZIL
Email: rade@ita.br

ABSTRACT

Periodic structures can be used as mechanical filters in vibration control by creating destructive wave interferences to block the passage of propagating waves in certain frequency bands. Recently, researchers have been concentrating their effort to improve this phenomenon while creating more complex and adaptive structures. Nonetheless, there is still a lack of information about their behavior and parameters sensitivity to comprehend, for example, the effects of uncertainties. This study shows the use of analytical equations of spring-mass chains and their derivatives to compare the sensitivity of Bragg's and resonance bandgaps. The objective is to inspect the behavior and the influence of changing stiffness and inertia properties on the attenuation zones borders. The transfer matrix method is used and a general formulation is adopted to model the unit cells. The propagation constants obtained by solving eigenvalue problems and the frequency responses are used to analyze infinite and finite chains, respectively. Analytical partial derivatives and finite differences are used to calculate the local sensitivity. The bandgap borders are found to be highly sensitive to the distance from localized modes and anti-resonances. The results from the comparison between these two kinds of attenuation zones are presented.

1   INTRODUCTION

Periodic structures as chain of spring-mass systems have been studied since Newton's times [1]. More recent studies [2-3] present a complete outline about the past and recent works and the future of periodic structures. However, comparisons between the two known bandgaps types, Bragg's and resonance, are scarce. Based on these works, but with a different formulation, the present work investigates local sensitivity of bandgap borders by varying stiffness and inertia properties considering infinite and finite models. Analytical and semi-analytical solutions are used for infinite (IM) and finite (FM) models, respectively.

2   METHODOLOGY

The Figure 1.a) presents the general spring-mass cell. Bragg's (Figure 1.b) and resonance (Figure 1.c) bandgaps can be obtained by considering a combination of this general unit cell.
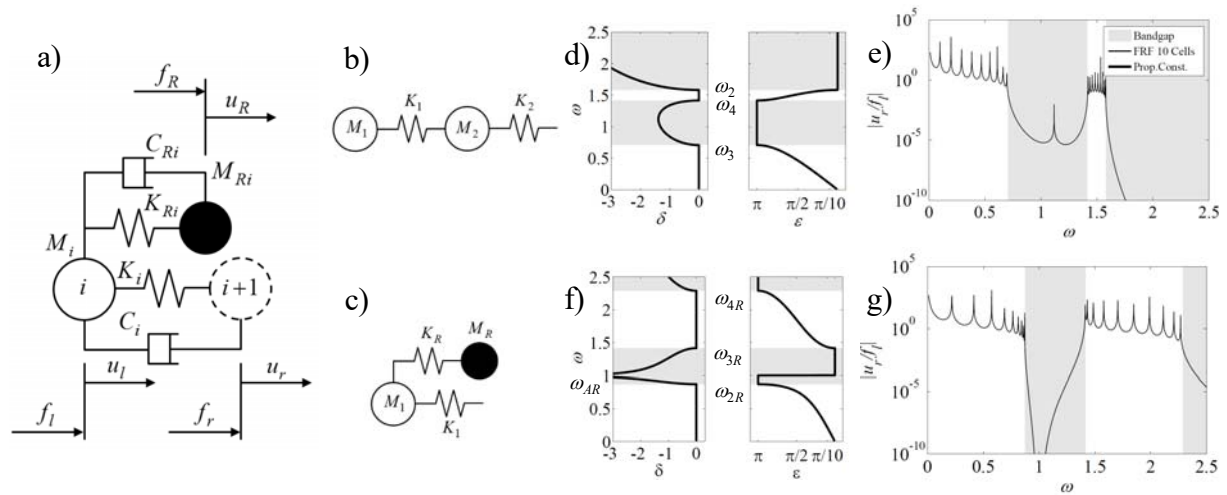

Figure 1. a) General spring-mass cell, b) Bragg's spring-mass cell , c) Resonance spring-mass cell and their corresponding propagation constants d) and f), frequency response functions e) and g).

The relation between displacements u and forces f to the left l and to the right r of the cell i is obtained by developing the equations of motion for these 2 degree-of-freedom systems. The transfer matrix method consists in characterizing the dynamics of each individual cell by its matrix $T^{(i)}$ and combining these matrices for the computation of the behavior of assembled structures. A finite periodic structure composed of n cells is hence described by Equations (1.a) and (1.b), showing the relation between left and right degrees-of-freedom.

$$\begin{Bmatrix} u_l^{(n)} \\ f_l^{(n)} \end{Bmatrix} = \prod_{i=1}^{n} \left[T_R^{(i)} \right] \begin{Bmatrix} u_r^{(i)} \\ f_r^{(i)} \end{Bmatrix} \qquad \text{with} \qquad (1.a)$$

$$\left[T_R^{(i)} \right] = \begin{bmatrix} \left(1 - \Omega_i^2\right) - \dfrac{K_R}{K_i} \left(\dfrac{\Omega_{Ri}^2}{1 - \Omega_{Ri}^2} \right) & -\dfrac{1}{K_i} \\ -K_i \Omega_i^2 - K_{Ri} \left(\dfrac{\Omega_{Ri}^2}{1 - \Omega_{Ri}^2} \right) & -1 \end{bmatrix}. \qquad (1.b)$$

The dimensionless frequencies are represented by $\Omega = \omega/\omega_0$ and $\Omega_R = \omega/\omega_{AR}$ with $\omega_0 = \sqrt{K/M}$ and $\omega_{AR} = \sqrt{K_R/M_R}$. The springs and masses of these models are represented by K and M with the subscript R standing for resonance. For the sake of simplicity, in analytical formulation, no damping is considered; it is important to mention that the definition of bandgaps

limits is lost for high damping levels. The analytical equation of the borders can be found by calculating the eigenvalues of the transfer matrix and imposing the condition of transition between real (δ) and imaginary (ε) propagation constants (Figures 1.d and 1.f). Using the same transfer matrix, but rearranging the DOF, the frequency response function (FRF) for one cell can also be found. For a finite structure, the multiplication of these matrices must be considered for each cell.

3   NUMERICAL EXAMPLE AND RESULTS

Table 1 shows the spring and mass values used for the numerical examples. For a Bragg's bandgap, the spring-mass cell 1 (SMC1) and 2 (SMC2) are used and for a resonance bandgap, the spring-mass cell 3 (SMC3) and 4 (SMC4) are used.

X	$K_1[N/m]$	$M_1[kg]$	$K_2[N/m]$	$M_2[kg]$	$K_R[N/m]$	$M_R[kg]$
SMC1 (a)	1	1	1	4	-	-
SMC2 (b)	0.5	1	1	2	-	-
SMC3 (c)	1	1	-	-	1	1
SMC4 (d)	1	2.5	-	-	1	1

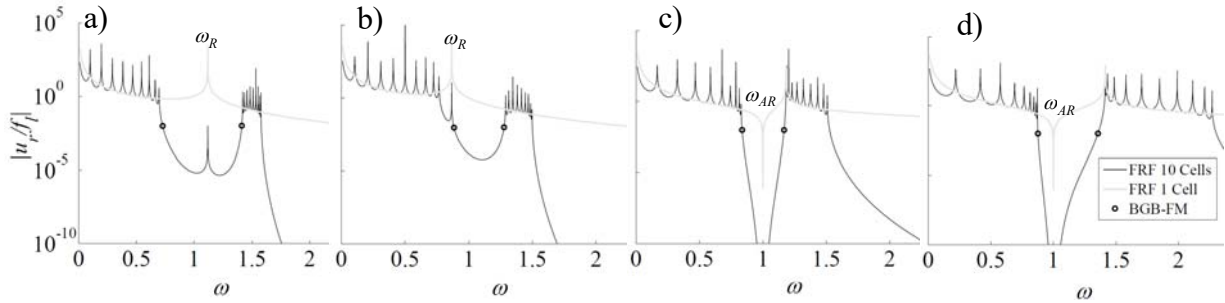Table 1. Spring and mass values for numerical examples.

Figure 2. Frequency responses for: a) SMC1, b) SMC2, c) SMC3 and d) SMC4.

The corresponding FRFs for a finite structure with 1 and 10 cells are shown in Figure 2. After calculating the propagation constants, the following equations defining the borders and the resonance inside the bandgap, can be found:

$$\omega_2 = \sqrt{\left(\frac{\omega_4}{2}\right) - \sqrt{\left(\frac{\omega_4}{2}\right)^2 - 4\frac{K_1 K_2}{M_1 M_2}}} \quad , \quad \omega_3 = \sqrt{\left(\frac{\omega_4}{2}\right) + \sqrt{\left(\frac{\omega_4}{2}\right)^2 - 4\frac{K_1 K_2}{M_1 M_2}}} \quad , \tag{2.a} \tag{2.b}$$

$$\omega_{2R} = \sqrt{\left(2\frac{K}{M} + \omega_{3R}\right) - \sqrt{\left(2\frac{K}{M} + \omega_{3R}\right)^2 - 4\frac{K_R K}{M_R M}}} \quad , \quad \omega_{4R} = \sqrt{\left(2\frac{K}{M} + \omega_{3R}\right) + \sqrt{\left(2\frac{K}{M} + \omega_{3R}\right)^2 - 4\frac{K_R K}{M_R M}}} \tag{3.a} \tag{3.b}$$

$$\text{with } \omega_4 = \sqrt{\frac{(K_1 + K_2)(M_1 + M_2)}{M_1 M_2}} \text{ and } \omega_{3R} = \sqrt{\frac{K_R (M_R + M)}{M_R M}} \quad . \tag{4.a} \tag{4.b}$$

$$\omega_R = \sqrt{\frac{K_1 (M_1 + M_2)}{M_1 M_2}} \tag{5.a}$$

These frequencies are represented in Figures 1.d, 1.f and 2. The derivative of these equations, in function of each parameter, gives local analytical sensitivity of bandgap borders for an infinite model (IM). For finite structures, a magnitude threshold equal to 10^{-2} is used to define the bandgap borders (BGB) using frequency response functions (FRF) as presented in Figure 2. In this case, finite differences are used to calculate de local sensitivity. The results are in Figure 3.
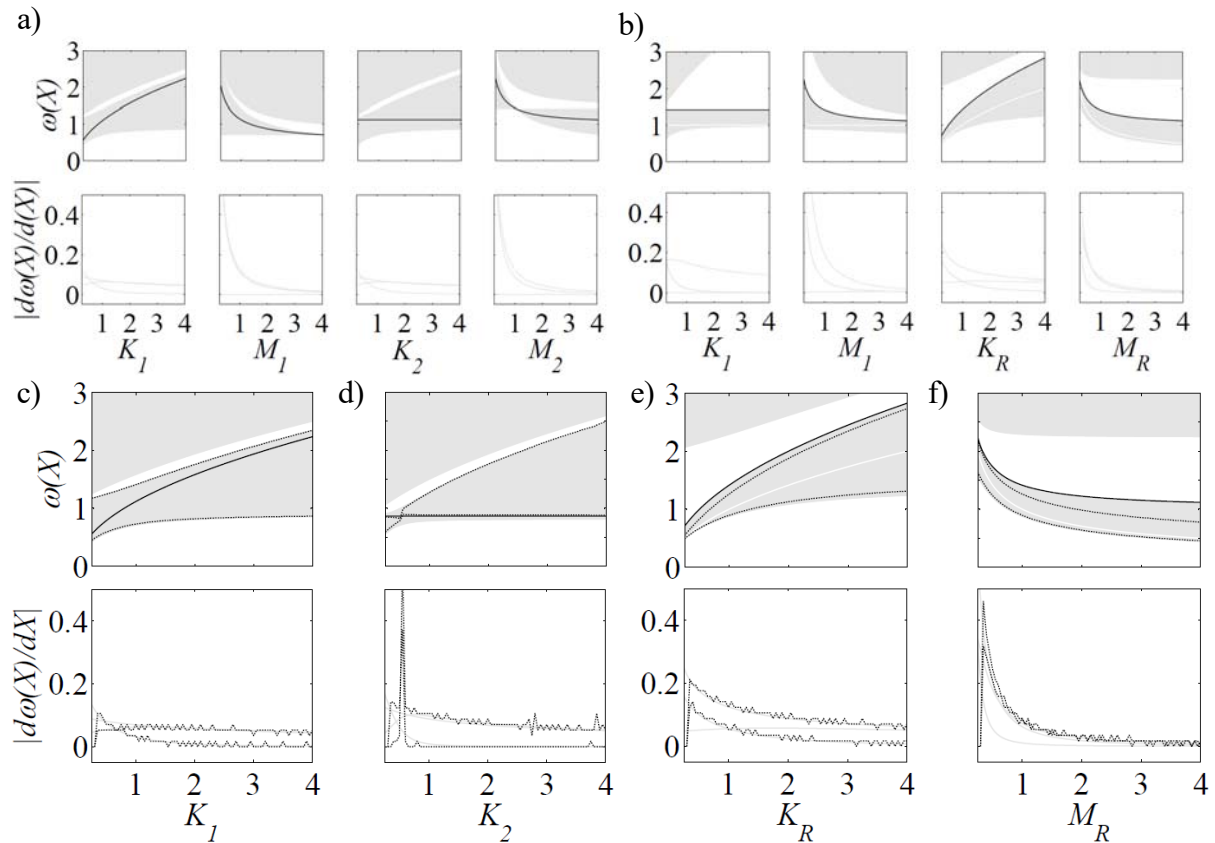
Figure 3. Varying spring and mass values and their analytical derivatives for a) SMC1 and b) SMC2, varying specified parameters for c) SMC1, d) SMC2, e) SMC3 and f) SMC4 with bandgap envelope for infinite model (▬), its borders analytical derivatives (──), finite model borders and their finite differences (┄┄┄), resonances (──) and anti-resonances (▬).

Figure 3.d shows that a resonance inside a bandgap can reduce the bandgap width depending on the number of cells for finite structures. Similarly, in Figures 3.e and 3.f, the anti-resonance does the same effect if it is located far from a bandgap border.

4   CONCLUSION

A simple transfer matrix model of a general spring-mass cell was used. The analytical solution for bandgap borders of Bragg's and resonance attenuation zones were presented. The local sensitive was found analytically by calculating the derivative and numerically by using finite differences. The behaviour for bandgap borders of Bragg's and resonance attenuation zones were compared. The resonances inside the bandgaps, also known as localized modes, and the anti-resonances can change the value for a bandgap border in a finite model.

REFERENCES

[1]   L. Brillouin. *Wave Propagation in Periodic Structures*. Dover, New York, 1946.

[2]   M. I. Hussein, M. J. Leamy, M. Ruzzene. Phononic Materials and Structures: Historical Origins, Recent Progress, and Future Outlook. *ASME*. v. 66, 2014.

[3]   S. S. Mester, H. Benaroya. Periodic and Near-Periodic Structures. *Shock and Vibration*. v. 2(1) p. 69-65, 1995.

Structural-acoustic optimization of 2-D Gradient Auxetic Sandwich Panels

Mohammad Sadegh Mazloomi[1], Mostafa Ranjbar[2], Luca Boldrin[3], Fabrizio Scarpa[3], Neriman Ozada[1]

[1] Department of Mechanical Engineering, Eastern Mediterranean University, TRNC via Mersin 10, Turkey
sadegh.mazloomi@emu.edu.tr, neriman.ozada@emu,edu,tr

[2] Department of Mechanical Engineering, TC Ankara Yildırım Beyazit University, Ankara, Turkey
mranjbar@ybu.edu.tr

[3] Advanced Composites Centre for Innovation and Science (ACCIS), University of Bristol, Bristol BS8 1TR, UK
luca.boldrin@bristol.ac.uk, f.scarpa@bristol.ac.uk

ABSTRACT

This paper investigates the vibroacoustic behavior of sandwich structures made of 2-dimensionally gradient auxetic hexagonal core. Homogenized finite element model has been used to determine the mechanical properties of the auxetic structures. Then this model is used to find the natural frequencies and radiated sound power level of sandwich panels made by the auxetic gradient cores. The radiated sound power level of the structure over the frequency range of 0–200 Hz is minimized by modifying the core geometry of the 2- dimensionally gradient auxetic sandwich panels. To do the optimization, Genetic algorithm method has been applied establishing an interactive link between MATLAB and ANSYS software. The results of this research present significant insights into the design of auxetic structures with respect to their vibroacoustical properties

Keywords: *auxetic; hexagonal; 2-D gradient; sandwich panel; vibroacoustic; genetic algorithm optimization*

1. INTRODUCTION

Honeycombs strcutures or hexagonal periodic cells have gained considerable attention in recent years as they possess outstanding out of plane mechanical properties [1]. Recently, a new types of honeycombs have been introduced which possess negative Poison's ratio [2]. In contrast to conventional materials, these materials called "auxetic", expand in all direction when subjected to uniaxial loading [3]. One of the iconic examples of auxetic materials is the hexagonal center-symmetric re-entrant configuration. They show an increase in the bending stiffness which can be useful in vibration[4]. Representative unit cells have been widely used to model mechanical properties of composite materials and sandwich structure [5]–[7]. Auxetic structure can also be considered as periodic repetition of the unit cell and their homogenized mechanical properties of the can be defined in terms of their geometrical parameters.

As the application of the auxetic materials are widespread they have been used in various areas of research. Auxetic cellular structures have been used to prototype morphing wings [8]. In another work, the wave propagation in sandwich panels having periodic auxetic core was investigated [9]. The above cited micro-structure configurations tessellate periodically in the plane. Therefore, the cellular structure is made of cells having same geometry in any part of the structure. However, this cellular structure can be produced with a gradient configuration in which the structure is made of a continuous distribution of unit cells with compatible geometry but a single variable parameter like the internal cell angle [10]. Several researches have investigated vibrational and acoustic behavior of sandwich structures with normal or gradient cellular core [4]. More recently, Ranjbar et al. [10], studied the effect of geometrical parameters of a 1-dimensionally gradient auxetic core on radiated sound power level of sandwich panel structures.

In this study the effect of geometrical parameters for a 2-dimensionally gradient auxetic honeycomb core on the radiated sound power level will be investigated. Furthermore, genetic algorithm (GA) optimization will be applied to minimize the radiated sound power level from the sandwich structure. To do so, an interactive link between MATLAB and ANSYS software has been established.

2. HOMOGENIZED MECHANICAL PROPERTIES OF AUXETIC CORE

An analytical model has been used to calculate the mechanical properties of auxetic hexagonal honeycombs. This models which have been previously used by Gibson and Ashby [11] and Lira et al [12] defines mechanical properties of hexagonal honeycombs based on three non-dimensional parameters $\alpha = \dfrac{h}{L}$, $\beta = \dfrac{t}{L}$, $\gamma = \dfrac{b}{L}$ and the angle θ. Figure 1.a., shows a representative unit cell of auxetic hexagonal honeycomb structure and its geometrical parameter. An orthotropic equivalent material have been used to model the mechanical properties of the honeycomb core plate. The compliance matrix [S] for an orthotropic material is defined, in which the engineering constants E_x, E_y, E_z, G_{xy} and G_{xz} can be found from Gibson and Ashby[11] or Lira et al [12]. Figure 1.b shows a 2-D gradient hexagonal cellular configuration. To generate the gradient core configuration, the unit cells with different internal angle θ have been assembled next to each other. The geometrical parameters of the original auxetic hexagonal unit cell have been shown in Table 1.

Table1. Geometrical parameters of auxetic hexagonal sandwich plate

h (mm)	l (mm)	t (mm)	b (mm)	θ (degree)
33.55	17.02	1	20	-30

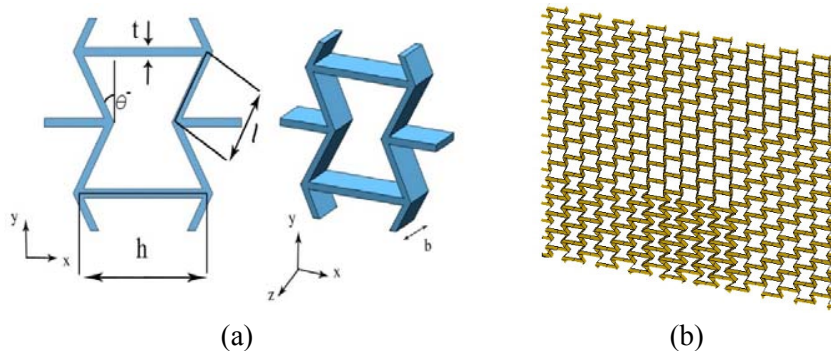(a)   (b)

Figure 1. a. A representative unit cell (RUC) of auxetic hexagonal honeycomb, b. 2-Dimensional hexagonal gradient core

3. FE MODELLING OF AUXETIC HEXAGONAL SANDWICH PANEL

The FE modeling for the auxetic hexagonal honeycomb sandwich panel with constant angle cell distribution has been performed using the ANSYS Rel. 14.0 commercial FE analysis package. The geometrical parameters of the auxetic hexagonal honeycomb core are listed in Table 1. The core is covered with two 960×996×2 mm skins plates. Both core and skins are made of ABS plastic with elastic properties listed in [12].

The homogenization of the sandwich panel is performed using shell elements to represent the skins, while the homogenized core of the auxetic hexagonal cells is represented by two solid element per gauge thickness. The mechanical properties of the skin are same as the mechanical properties of the ABS plastic and the mechanical properties of the homogenized core can be defined using the compliance matrix [S]. Figure 2.a. shows a full scale model of sandwich panel and Figure 2.b. demonstrates the homogenized single unit cell having a core and two skins. This homogenized unit cell is then reproduced along both x and y directions to make the sandwich panels with overall dimensions mentioned above.

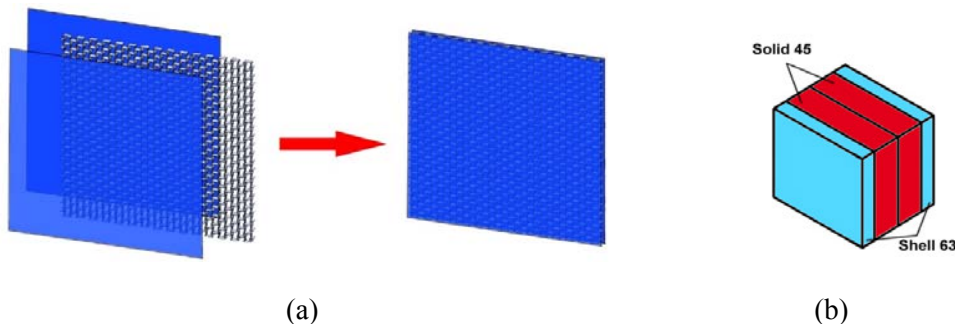(a)   (b)

Figure 2, a. Full scale demonstration of the sandwich panel with auxetic hexagonal core, b. Finite element model of a homogenized auxetic sandwich panel unit cell.

To compare the behavior of full scale FE model with detailed geometry of the core detailed model and the homogenized model, a modal analysis have been performed. Simply supported boundary condition (SSBC) is considered for the modal analysis. The natural frequencies of both models have been shown in Table 2. The first six mode shapes in both full scale detailed and homogenized model are alike. Moreover, the natural frequencies find by homogenized model are in good agreement with the ones calculated by the full scale detailed model.

To do the harmonic analysis a pressure loading has been applied on the sandwich panel in z direction with frequency range of 0-200 Hz. Figure 3 shows the applied pressure and the distribution of nine different homogenized auxetic hexagonal unit cells with different angles($\theta_1, \theta_2, \theta_3, \theta_4, \theta_5, \theta_6, \theta_7, \theta_8, \theta_9$). The main objective is to minimize the radiated noise from the

panel. To do so, the geometry of model in each region will be modified to reduce the radiated sound power level.

Table 2. Modal Analysis result of the auxetic honeycomb sandwich panel on the frequency range of 0 to 200 Hz for the homogenized and full scale FE models

	Model type	1	2	3	4	5	6
Frequency (Hz)	Homogenized FE	37.75	94.73	98.35	143.13	187.90	193.85
	Full Scale FE	34.80	83.84	87.31	133.17	160.88	170.90
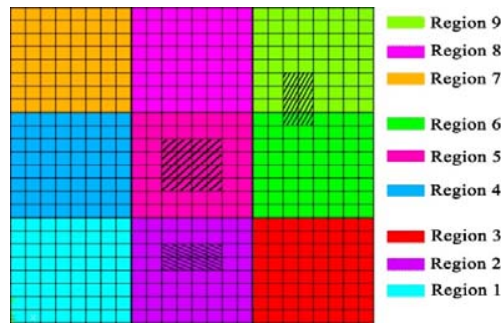
Figure 3. Applied pressure on the homogenized FE model

4. VIBRO-ACOUSTIC OPTIMIZATION OF THE SANDWICH PANEL

The minimization process of radiated sound power level over the frequency range of 0 to 200 Hz is discussed in this section. The objective function for the optimization process is the root mean square level of radiated sound power level (RMSL) of sandwich panel. The design variables of this optimization problem are the angles of unit cells in the different regions. The methodology to calculate RMSL can be find in [10].

The original design, is a non-gradient sandwich panel with core geometries given in Table1 and skin thickness of 2mm. At first, the effect of change in the core thickness on the RMSL of the sandwich panel with a constant cell angle of -30º is evaluated. Figure 4 shows the change of RMSL with variation of thickness. The increase in the thickness makes a reduction in RMSL. The optimum thickness of 30 mm is identified.
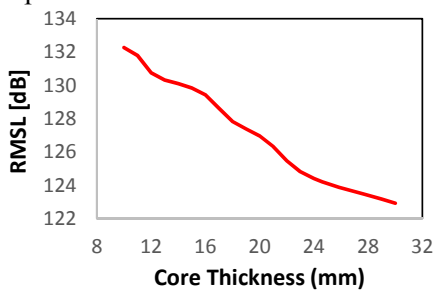

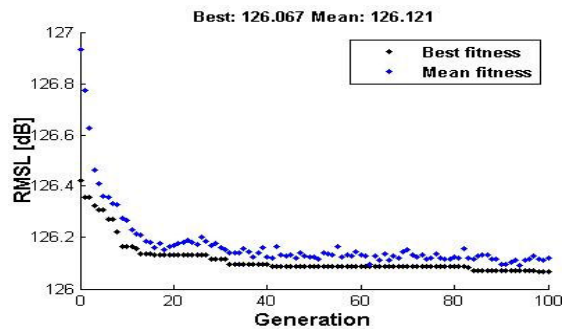Figure 4. Variation of RMSL with respect to the core thickness

Figure 5. Variation of RMSL versus generation as a result of GA optimization

Next, nine different regions with nine different angles have been considered to compose the gradient sandwich plate. A fixed original value of 20 mm is considered for the core thickness. To do the optimization process Genetic algorithm optimization toolbox in MATLAB has been used. In order to have a better exploration of the feasible region of this optimization problem which has nine design variables and population size of 50, the first generation of genetic algorithm, has been created by Latin hypercube sampling (LHS) method. The objective function of this problem, the root mean square of radiated sound power level, then is minimized over 100 generations. Figure 5 shows the variation of best and mean of the objective function in each

generation. After about 60 generation the objective function converges. The each function evaluation in this problem takes about 4.5 seconds and the total computation time was about 6 hrs and 15 minutes.Table 3 shows detailed geometry, optimization variables and total mass of the sandwich panel for the original design and after genetic algorithm optimization design with original thickness of 20 mm. As it is clear in Table 3 the genetic algorithm reduced root mean square of sound power level which is objective function of this problem to 126.07 dB and the mass of sandwich structure after GA optimization has increased about 3.2%.

Table 3. The optimization variables for the auxetic hexagonal sandwich panel

Design Set	θ_1	θ_2	θ_3	θ_4	θ_5	θ_6	θ_7	θ_8	θ_9	RMSL (dB)	Mass
Original Design	-30	-30	-30	-30	-30	-30	-30	-30	-30	126.95	5.635
GA Design	-48.84	-48.61	-45.83	-33.93	-49.32	-49.66	-10.36	-10.59	-10.78	126.07	5.815

Figure 6 illustrates the radiated sound power level over the frequency range of 0-200 Hz, for the original design and GA optimized design sets. The figure clears that the first natural frequency for the optimum designs is not substantially changed, while for the 2nd and 5th natural frequency shifted to a lower value and for the 4th and 6th natural frequency in moved to a higher value. The 6th natural frequency for the optimized design shifted to a 206.51 Hz. Figure 7 shows, the radiated sound power level over the frequency range of 0-200 Hz for the original design, design with original angles and optimum thickness and the design with optimum angles and optimum thickness. The figure depicts that for the optimum thickness designs, the first natural frequency is increased by 38 % for the optimum thickness and angles. Besides, all other five natural frequencies are shifted to a higher value. For the optimum thickness and angles design just the first four natural frequency remained in the range 0-200 Hz and the 5th and 6th natural frequencies are shifted to 248.42 Hz and 273.86 Hz respectively.
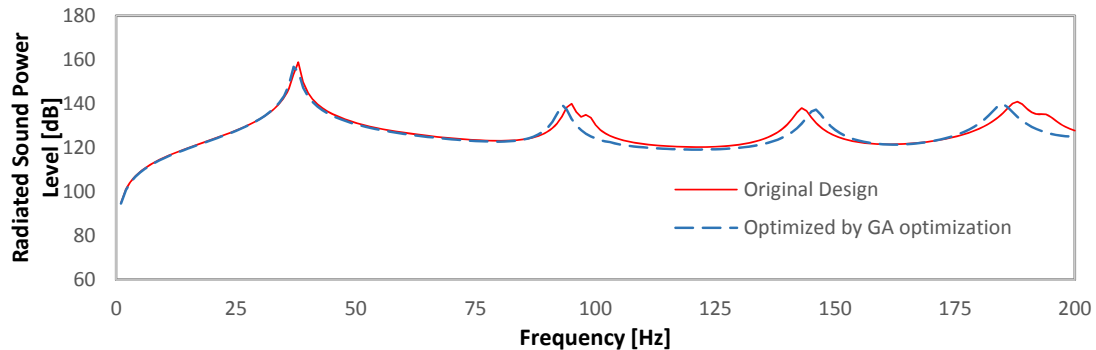

Figure 6. Effect of GA optimization methods on sound power level reduction
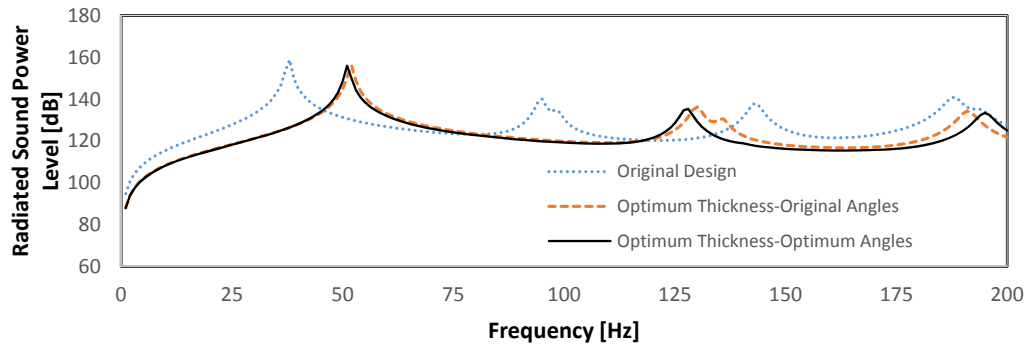

Figure 7. Sound power level reduction for the optimum thickness designs

5. CONCLUSION

This research has investigated the vibro-acoustic behavior of sandwich panels with 2-dimensionally gradient auxetic hexagonal honeycomb core. First, to determine the mechanical properties, the natural frequencies and the radiated sound power level of the hexagonal honeycomb sandwich panels made by the 2-D gradient auxetic cores, a homogenized finite element modeling approach has been implemented. The geometrical parameters of the core have effect on the radiated sound power level. The radiated noise level of the structure is significantly dependent to the location of the excitations. Therefore, it is recommended to use the gradient core geometries to cover the excitations areas.

For the optimization process an interactive link between MATLAB and ANSYS software was based. Genetic algorithm method has been used to optimize the root mean square of sound power level. The root mean square of radiated sound power level is reduced by about 1 dB. This reductions in RMSL is accompanied by an increase in total mass of the panel by 3.2 %. This designs behaves significantly better than the original design both in low and high frequency ranges. This feature could be considered for structures applications, in which weight reductions or control are paramount.

REFERENCES

[1]   A. Lorato *et al.*, "The transverse elastic properties of chiral honeycombs," *Compos. Sci. Technol.*, vol. 70, no. 7, pp. 1057–1063, 2010.

[2]   J. Huang, X. Gong, Q. Zhang, F. Scarpa, Y. Liu, and J. Leng, "In-plane mechanics of a novel zero Poisson's ratio honeycomb core," *Compos. Part B Eng.*, vol. 89, pp. 67–76, 2016.

[3]   R. Lakes, "Advances in negative Poisson's ratio materials," *Adv. Mater.*, vol. 5, no. 4, pp. 293–296, Apr. 1993.

[4]   F. SCARPA and G. TOMLINSON, "Theoretical Characteristics of the Vibration of Sandwich Plates With in-Plane Negative Poisson'S Ratio Values," *J. Sound Vib.*, vol. 230, no. 1, pp. 45–67, 2000.

[5]   M. M. Shokrieh and M. S. Mazloomi, "An analytical method for calculating stiffness of two-dimensional tri-axial braided composites," *Compos. Struct.*, vol. 92, no. 12, pp. 2901–2905, 2010.

[6]   M. M. Shokrieh and M. S. Mazloomi, "A new analytical model for calculation of stiffness of three-dimensional four-directional braided composites," *Compos. Struct.*, vol. 94, no. 3, pp. 1005–1015, 2012.

[7]   Y. J. Chen, F. Scarpa, Y. J. Liu, and J. S. Leng, "Elasticity of anti-tetrachiral anisotropic lattices," *Int. J. Solids Struct.*, vol. 50, no. 6, pp. 996–1004, 2013.

[8]   P. Bettini, A. Airoldi, G. Sala, L. Di Landro, M. Ruzzene, and A. Spadoni, "Composite chiral structures for morphing airfoils: Numerical analyses and development of a manufacturing process," *Compos. Part B Eng.*, vol. 41, no. 2, pp. 133–147, 2010.

[9]   M. Ruzzene, L. Mazzarella, P. Tsopelas, and F. Scarpa, "Wave Propagation in Sandwich Plates with Periodic Auxetic Core," *J. Intell. Mater. Syst. Struct.*, vol. 13, no. 9, pp. 587–597, 2002.

[10]   M. Ranjbar, L. Boldrin, F. Scarpa, S. Neild, and S. Patsias, "Vibroacoustic optimization of anti-tetrachiral and auxetic hexagonal sandwich panels with gradient geometry," *Smart Mater. Struct.*, vol. 25, no. 5, p. 54012, 2016.

[11]   L. J. Gibson and M. F. Ashby, *Cellular solids. Structure and properties*. 1997.

[12]   C. Lira, F. Scarpa, and R. Rajasekaran, "A Gradient Cellular Core for Aeroengine Fan Blades Based on Auxetic Configurations," *J. Intell. Mater. Syst. Struct.*, vol. 22, no. 9, pp. 907–917, 2011.

STUDY OF THE FIRST BRAGG BAND GAP FEATURES OF EULER CONTRASTED PERIODIC BEAMS

Adrien Pelat[1] , Thomas Gallot [2] and François Gautier[1]

[1]Laboratoire d'Acoustique de l'Universit du Maine
Universit du Maine, Avenue Olivier Messiaen, 72085 cedex 9 , Le Mans, FRANCE or address
Email: adrien.pelat@univ-lemans.fr , francois.gautier@univ-lemans.fr

[2]Instituto de Fisica de la Facultad de Ciencias,
Universidad de la Republica, Igua 4225, Montevideo, URUGUAY 11400
Email: tgallot@fisica.edu.uy

ABSTRACT

The vibration control of lightweight structures is nowadays a challenge of great industrial interest because of obvious ecological and economical reasons. Among the possible strategies, applying the concepts of metamaterials to the vibro-acoustics context seems to be promising. It can be done by designing the structures as a periodic distribution of a unit cell. The overall properties of such structures then result from a carefull design of the mechanical properties and possible resonances of the unit cell. This work deals with beams made of uniform material and with continuously graded flexural rigidity driven by variable thickness. The study focuses on the first Bragg band gap of such structures by means of both theoretical and experimental approaches. Particularly, explicit relations linking the properties contrast with the band gap width and central frequency are derived in an ideal case of a hollow beam without flanks for which a PWE model can be analytically solved. The theoretical results obtained in this ideal case succesfully match both the numerical results obtained from a PWE method and experimental measurements.

1 INTRODUCTION

From works of Brillouin on wave propagation in periodic media [1], meta-materials has been widely studied during the last decades in many fields of physics. The typical effects obtained with meta-materials can be exploited in three main categories of applications : wave filtering, wave collimation and cloaking.

When applied to the context of vibro-acoustics, the case of flexural waves is of particular interest when dealing with structure borne sound from shells or plates. Wave filtering effects can then be very usefull to get non resonant and so non radiating structures without added mass in given frequency bandwidths [2]. Then, providing general design rules of such meta-structures is of great interest and still an open question [3]. For example, no explicit link between band gap features and structure geometrical or material properties is well known.

As a preliminary work, the study of academic beams is often useful in order to apprehend the practical and more complicated case of plates. In this work, the aim is to study how the thickness contrast of a continuously varying periodic beam is driving the Bragg band gap central frequency and bandwidth.

After defining a general PWE formalism of Euler beams in section 2, the ideal case of a hollow rectangular beam is presented in section 3. Theoretical, numerical and experimental results are then compared and discussed in section 4.

2 PWE GENERAL FORMALISM FOR AN EULER-BERNOULLI BEAM

Under Euler-Bernoulli assumtions and considering harmonic motion ($e^{j\omega t}$), the free flexural displacement $w(x)$ in a beam of variable height $h(x)$ and constant width b satisfies to the equation of motion

$$-\rho h(x)\omega^2 w(x) + \frac{\partial^2}{\partial x^2}\left(D(x)\frac{\partial^2 w(x)}{\partial x^2}\right) = 0, \tag{1}$$

where $\rho h(x)$ is the surface mass with ρ the material volumic mass, $D(x) = \dfrac{Eh(x)^3}{12}$ is the surface flexural rigidity with $E = E_0(1+j\eta)$ the material complex young modulus in which E_0 is the elastic constant and η is the loss factor.

According to the plane wave expansion method, the solutions of equation (1) are sought as the following series

$$w(x) = \sum_{g_1} w_{g_1}(k)e^{jg_1 x}e^{jkx}, \tag{2}$$

with k a given flexural wavenumber, $g_1 = \dfrac{n_1 2\pi}{L}$ with n_1 an integer.

Considering the beam being a periodic distribution of a unit cell of size L, the mechanical properties can be expanded as the following Fourier series :

$$\rho h(x) = \sum_{g_2} \alpha_{g_2} e^{jg_2 x} \quad \text{and} \quad D(x) = \sum_{g_2} \delta_{g_2} e^{jg_2 x} \tag{3}$$

where $\alpha_\kappa = \dfrac{1}{L}\int_0^L \rho h(x)e^{-j\kappa x}dx$, $\delta_\kappa = \dfrac{1}{L}\int_0^L D(x)e^{-j\kappa x}dx$, and $g_2 = \dfrac{n_2 2\pi}{L}$ with n_2 an integer.

Truncating the Fourier series (3) with $n_2 \in [-N_2; N_2]$ and the plane wave expansion (2) with $n_1 \in [-N_1; N_1]$, the equation of motion (1) turns to a matrix equation

$$(P(k) - \omega^2 Q)\mathbf{W} = \mathbf{0}, \tag{4}$$

where $\mathbf{W}^t$ is a $[2N_1 + 1 \times 1]$ column vector, Q and P are $[2N_3 + 1 \times 2N_1 + 1]$ matrices with $N_3 = N_1 + N_2$ given by $Q_{n_3 n_1} = \alpha_{g_3 - g_1}$ and $P(k)_{n_3 n_1} = \delta_{g_3 - g_1}(k + g_1)^2(k + g_3)^2$.

3 ANALYTICAL DERIVATION OF THE FIRST BAND GAP WIDTH OF A HOLLOW RECTANGULAR BEAM

An ideal geometry sketched in figure 1 is now defined in order to simplify the matrices in equation (4) and then analytically solve the problem. The goal is to obtain an algebraic expression of the first Bragg band gap, defined as the difference between the two first eigenvalues at $k = \pi/L$.
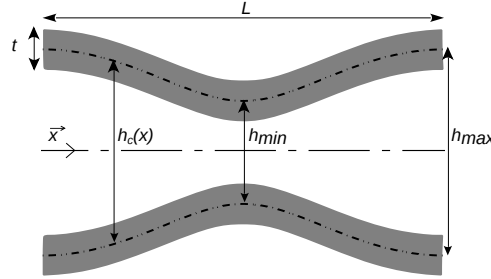

Figure 1: Profile view of the unit cell geomtry of the modeled rectangular hollow beam with no flanks. The constant width b is in the out-of-plane direction.

First, the beam cross-section is considered as a hollow rectangle where the lateral walls have been removed. The thickness t and width b of both top and bottom walls are constant while the cross-section height varies, as represented in figure 1.

Consequently, the surface mass $\rho h(x) = \rho 2t$ remains constant and so the property gradient is only carried by the varying surface flexural rigity $D(x) = \frac{Et}{2} h_c^2(x)$ whith $h_c(x)$ the central of both top and bottom wall.

Second, the spatial shape of beam unit cell profile is chosen as follows to make the flexural rigidity proportional to a cosine fonction :

$$h_c(x) = h_0 \sqrt{1 + C.cos\left(\frac{2\pi x}{L}\right)} \quad => \quad D(x) = \frac{Et}{2} h_0^2 \left[1 + C.cos\left(\frac{2\pi x}{L}\right)\right], \qquad (5)$$

where $h_0 = \sqrt{\frac{h_{max}^2 + h_{min}^2}{2}}$ is the equivalent central height for a uniform beam (same cross-section with constant height), and C is the so called contrast parameter defined as

$$C = \frac{h_{max}^2 - h_{min}^2}{h_{max}^2 + h_{min}^2}. \qquad (6)$$

with h_{max} and h_{min} the maximum and minimum central height, respectively.

From this ideal geometry, the Fourier series in equations (3) for the surface mass and flexural rigidity leave a single non zero term ($N_2 = 0$) and only three non zero terms ($N_2 = 1$), respectively. Finally, it can be shown that the matrix problem (4) can be rewritten as a classical eigenvalue problem with a tridiagonal matrix $M = P(k) - \omega^2 Q$ for which the determinant can be found from a recurence equation.

Assuming that the field plane wave expansion is truncated with $N_1 = 2$ (compromise between accuracy and convenience of analytical calculations) and after few algebra leading to cancel the matrix determinant, the gap relative bandwidth and central frequency are found to be only function of the thickness contrast C :

$$\frac{df}{f_0} \approx \frac{C}{2} \left(\frac{1 - C^2/2}{1 - 3C^2/4}\right)^{1/2} \quad ; \quad \frac{f_c}{f_0} \approx \left(\frac{1 - C^2/2}{1 - 3C^2/4}\right)^{-1/2}, \qquad (7)$$

whith $f_0 = \frac{\pi}{2L^2}\sqrt{\frac{Eh_0^2}{4\rho}}$.

3

4   RESULTS AND DISCUSSION

A thickness contrast variation is presented in figure 2. Figure 2(a) and 2(b) display the gap relative bandwidth and central frequency, respectively. Equations (7) corresponding to the ideal case of hollow beam with no flanks are plotted in dotted lines. The cases of the rectangular hollow beam (dashed lines) and fully filled rectangular beam (full line) are obtained from numerical resolution of equation (4).
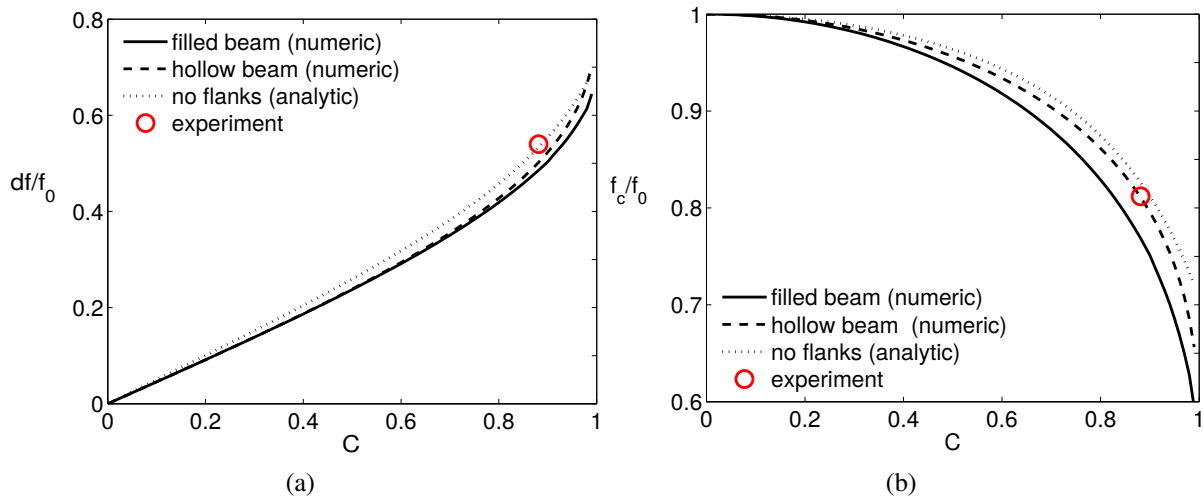

Figure 2: (a) First Bragg band gap bandwidth and (b) central frequency versus contrast parameter C shows no fundamental difference between cross-section geometries. Analytical results are in agreement with full PWE numerical solutions and an experimental results of an aluminium beam.

All results give same overall behavior : when the contrast increases, the gap is enlarged and shifted to low frequencies. The sligth discrepancies between the results make the no flanks assumption valid for giving a predictive analytical formula of the gap bandwidth of a fully filled contrasted real beam.

An experimental validation has also been performed with an aluminium beam. The beam geometry has been generated with a classical cutting machine. The relative gap width and position are in agreement with both analytical and numerical computation (red circle in Fig. 2).

This work demonstrates, in the case of flexural unidimensional wave, how the first frequency gap is fully characterized by a unique contrast parameter. Numerical simulation suggests that the influence of the cross-section geometry is weak. Finally, analytical expressions of gap bandwitdh and central frequency are derived and can be taken as benchmark for bandgap design.

REFERENCES

[1] Leon Brillouin. *Wave propagation in periodic structures: electric filters and crystal lattices*. Courier Corporation, 2003.

[2] DM Mead. Wave propagation in continuous periodic structures: research contributions from southampton, 1964–1995. *Journal of sound and vibration*, 190(3):495–524, 1996.

[3] Niels Olhoff, Bin Niu, and Gengdong Cheng. Optimum design of band-gap beam structures. *International Journal of Solids and Structures*, 49(22):3158 – 3169, 2012.

4

INDUSTRIAL APPLICATION OF PERIODIC STRUCTURES TO AIRCRAFT/LAUNCHERS

G. Tufano[1] , M. Ichchou[1] , O. Bareille[1] , A. Zine[1] , W. Desmet[2] and B. Pluymers[2]

[1]LTDS, Laboratoire de Tribologie et Dynamique des Systms
Ecole Centrale de Lyon, Ecully, FRANCE
Email: giovanni.tufano.91@gmail.com; mohamed.ichchou@ec-lyon.fr;
olivier.bareille@ec-lyon.fr; abdel-malek.zine@ec-lyon.fr

[2]PMA, Production Engineering, Machine Design and Automation
Katholieke Universiteit Leuven, Leuven, Belgium
Email: wim.desmet@kuleuven.be, bert.pluymers@kuleuven.be

ABSTRACT

The main aims of this paper are the description of the vibroacoustic response of a structure, in particular a periodic structure, subjected to an aerodynamic excitation, the modelling optimization and numerical models validation. A literature review on the response of simple structures, 1-D and 2-D, beams and panels, is reported. The state of the art in this research field and the work plan are presented to give a complete overview of the project and of the expected results.

1   INTRODUCTION

Composite materials are largely used in aerospace industry, mainly due to their advantage of being light and their ability to suit the particular demands of each structure type and manufacturer. On the other hand, these type of structure have poor acoustic performance, inducing high level of noise transmission within the payload or passenger compartment.

The prediction of the vibroacoustic behaviour of composite structures, with the knowledge of wave dispersion characteristics, is very important during the design process.
Depending on the nature of the material (isotropic or anisotropic, homogeneous or inhomogeneous), on the geometrical shape (beam, shell, panel with single or double curvature, cylinder, cone) and on frequency range there are different methods to determine the wave dispersion characteristics and to describe the structural dynamic response.

The vibrational modelling of coupled composite conical-cylindrical systems has been an area of sporadic scientific research. In literature we can find everything about one dimensional problems and some simple examples about two dimensional structures, like plane or curved panels. These problems are solved using different approaches, both numerical and experimental.

The scope of ESR-11 doctorate is to apply all these knowledge to conical and cylindrical composite structures, in presence both of axial and/or circumferential ribs, and viscoelastic patches, solving a fully three dimensional problem. In particular, the attention is focused on the *SYLDA* (from French acronym of *SY*stéme de *L*ancement *D*ouble d'*A*riane 5) structure of *Ariane 5* launcher, as reported in Figure 1a.
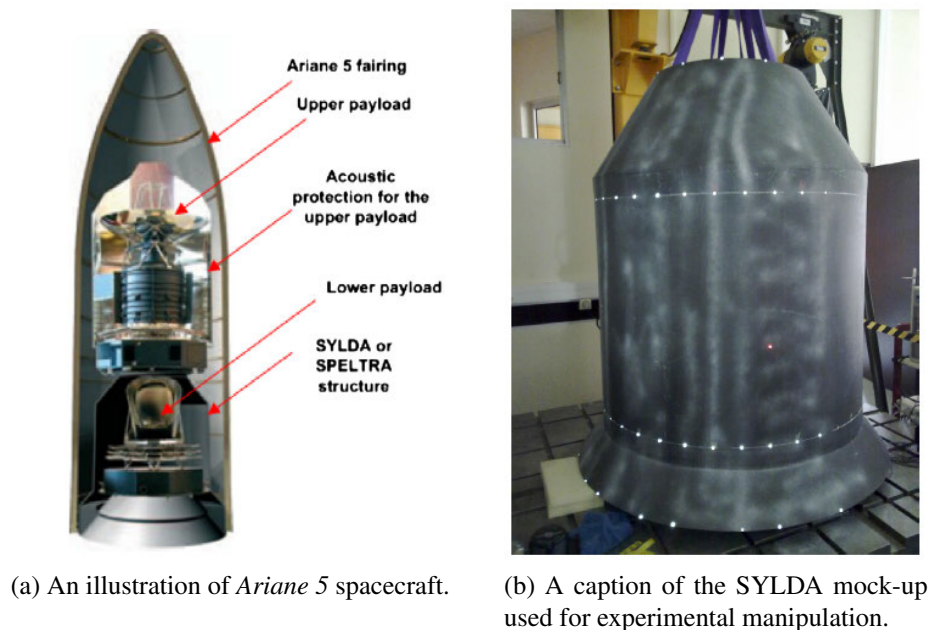

(a) An illustration of *Ariane 5* spacecraft.   (b) A caption of the SYLDA mock-up
                                                 used for experimental manipulation.

Figure 1: SYLDA component.

2   LITERATURE REVIEW

In the last thirty years many authors have investigated the vibroacoustic behaviour of a structure; in the first part, their attention was focused on one dimensional structures, of which we have

analytical solutions. After that, they studied two dimensional structures, plane or curved panels, made of metals or composite materials.

We can resume these works in the following manner:

- beam like structures;

- panel, both plane and curved;

- cylindrical and conical structures.

2.1 Beam like structures

When we have a one dimensional problem, in the Finite Element (FE) method we can consider it as a beam like structure. For these kind of problems there are some semi-analytical solutions to obtaining the dispersion curves [10]; other authors have predicted the energy flow using the Wave FE (WFE) method [5].

2.2 Panel, both plane and curved

In the last years this is a very intensive field of research. There are both numerical (using FE method of Statistical Energy Analysis (SEA)) and experimental solutions [2], [3], [7] and [8].

2.3 Cylindrical and conical structures

Cylindrical and conical structures are very complex, there are not analytical solutions; often experimental and numerical results are not published by the industries. In literature we can find some practical examples in [1], [9] and [10].

3 MAIN STEPS AND EXPECTED RESULTS

As said before, the main scope of this project is to apply all these knowledge to conical and cylindrical composite structures solving a fully three dimensional problem.

There are three main steps:

1. effects of lateral periodic ribs properties on the vibroacoustic response of the SYLDA under aerodynamic excitation. Modelling and optimization;

2. effects of circumferential ribs properties on the vibroacoustic response of the SYLDA under aerodynamic excitation. Modelling and optimization;

3. effects of periodic viscoelastic patches on the vibroacoustic response of the SYLDA under aerodynamic excitation. Modelling and optimization.

At the end, what we expect to obtain are some assessments of periodic design of the SYLDA component performance, the validation of numerical tools and optimization under realistic constraints. An intermediate result is how the energy flows inside the structure [5].

To do these we start from the simplest case, in order to validate the numerical and experimental tools, because of the poor results present in literature about conical and cylindrical structures, mainly in presence of ribs and stringers (too hard or impossible to solve analytically and experimental results covered by industrial intellectual properties).

After that, the starting point is the study made on the SYLDA component mock-up [1], which

3

consists only in the conical and cylindrical structure (Figure 1b), without ribs and stringers.

REFERENCES

[1] Chronopoulos, D., Ichchou, M., Troclet, B., Bareille, O., *Predicting the broadband response of a layered cone-cylinder-cone shell*, Composite Structures 107, pages 149-159, 2014.

[2] Chronopoulos, D., Ichchou, M., Troclet, B., Lainé, J., P., *A unified approach for the broadband vibroacoustic response of composite shells*, Composites: Part B 43, pages 1837-1846, 2012.

[3] Chronopoulos, D., Ichchou, M., Troclet, B., Bareille, O., *Modelling the response of composite panels by a dynamic stiffness approach*, Composite Structures 96, pages 111-120, 2013.

[4] Mencik, J., M., Ichchou, M., *Multi-mode propagation and diffusion in structures through finite elements*, European Journal of Mechanics A/Solids 24, pages 877-898, 2005.

[5] Fan, Y., Collet, M., Ichchou, M., Li, L., Bareille, O., Dimitrijevic, Z., *Energy flow prediction in built-up structures through a hybrid finite element/wave and finite element approach*, Mechanical Systems and Signal Processing 66-67, pages 137-158, 2016.

[6] Berthaut, J., Ichchou, M., Jezequel, L., *K-space identification of apparent structural behaviour*, Journal of Sound and Vibration 280, pages 1125-1131, 2005.

[7] Ichchou, M., Berthaut, J., Collet, M., *Multi-mode wave propagation in ribbed plates. Part I: wavenumber-space characteristics*, International Journal of Solids and Structures 45, pages 11791195, 2008.

[8] Ichchou, M., Berthaut, J., Collet, M., *Multi-mode wave propagation in ribbed plates. Part II: Predictions and comparisons*, International Journal of Solids and Structures 45, pages 11961216, 2008.

[9] Langley, R., S., *Wave motion and energy flow in cylindrical shells*, Journal of Sound and Vibration 169, pages 29-42, 1994.

[10] Zhou, W., J., Ichchou, M., Bareille, O., *Finite element techniques for calculations of wave modes in one-dimensional structural waveguides*, Structural control and Health monitoring 18, pages 737-751, 2011.

[11] Hiverniau, B., Ichchou, M., Bareille, O., Troclet, B., *Mid-high frequency vibrations of full-scale launch vehicles*, Journal of Aerospace Engineering 225, pages 449-463, 2011.

4

WAVE CONVERSION PROCESS IN LIGHTWEIGHT STRUCTURES: DIFFUSION THROUGH DEFECTS IN THE TRANSITION BANDWIDTH

Christophe Droz[1,2*] , Philip Becht[1,2], Bert Pluymers[1,2] and Wim Desmet[1,2]

[1]KU Leuven, Dept. of Mechanical Engineering,
Celestijnenlaan 300, box 2420, 3001 Leuven, BELGIUM
christophe.droz@kuleuven.be

[2]member of Flanders Make

ABSTRACT

Structural waveguides involving heterogeneous cross-sections or based on periodic patterns are often subjected to wave conversion phenomena. This paper is concerned with a specific type of conversion observed in sandwich structures called bending-to-shear conversion. It occurs in the "transition" bandwidth, where the flexural wave is partially localized in the core of the sandwich, hence mainly governed by its shear modulus. This conversion has consequences on the wave reflection characteristics through a defect's interface. The need for wave-based Structural Health Monitoring strategies providing sub-wavelength detection capabilities has been increasing with the development of advanced, often periodic lightweight components. It is therefore advantageous to predict and take into account conversion effects at the earliest design stage of SHM systems. This paper explores the consequences of such conversions on the reflection coefficient of flexural guided waves in lightweight structures. A Diffusion Matrix Method (DMM) is employed to estimate the diffusion of guided waves obtained using refined unit-cell FE models. Case-study is a composite sandwich waveguide with honeycomb core. Results show significant variations of the wave's sensitivity to small-scaled core defects and delaminations during the conversion process.

1   INTRODUCTION

Sandwich composites are widely use in aerospace and transportation industries. Their main advantage, apart from their exceptional strength-to-weight ratio, is their wide range of possible configurations. The variety of sandwich panels involving innovative core's geometries or skin laminates developed every year illustrates this growing interest in the design of structurally advanced lightweight components. Wave-based inspection techniques are usually exploiting Lamb waves for their ability to travel long distances with low attenuation and their predictable dispersion curves. Yet, wave conversions are commonly encountered in heterogeneous structures, especially at high frequencies. Literature is abundant with examples of wave conversion, steering or localisation effects appearing in sandwich structures. Recently, Putkis et al. [1] investigated the influence of various Lamb waves conversions in CFRP plates for practical NDE and SHM applications. Indeed, this phenomenon produces a modification of the strain energy distribution along the waveguide's cross-section, or in its unit-cell when the waveguide is based on a periodic pattern. For such structures, the Wave Finite Element Method (WFEM) is often used to perform broadband wave dispersion analyses and understand wave's physics in complex periodic waveguides.

The proposed study focuses on a phenomenon occurring in the so-called first transition bandwidth [2, 3], which is a specific type of wave conversion appearing in sandwich structures subjected to flexural vibrations. It usually occurs in the low- or medium-frequency range, where local resonances and Bragg scattering effects are not observed. This conversion can easily be determined from the dispersion curves, as the passage from a behavior where flexural wave is governed by the skins' stiffness to one governed by the core's transverse shear. The correlation between this conversion process and the sensitivity to localized defects can therefore be conducted using a spectral diffusion analysis based on a FEM description of the interface between the healthy and damaged waveguides.

2   DIFFUSION MATRIX METHOD

The waveguide is considered as a straight elastic structure made of N identical substructures of same length along the main direction x. The wave dispersion characteristics can be derived from Bloch's theorem, denoting λ the propagation constant relating the displacements $\mathbf{q_n}$, $\mathbf{q_{n+1}}$ between two cells, by solving the spectral problem:

$$\mathbf{S}(\lambda, \omega) = (\lambda \mathbf{D}_{LR} + (\mathbf{D}_{LL} + \mathbf{D}_{RR}) + \frac{1}{\lambda}\mathbf{D}_{RL})\mathbf{q_n} = \mathbf{0}, \tag{1}$$

where $\mathbf{D}_{ij}$ are the dynamic stiffness matrices related to the left and right degrees of freedom of the unit cell's governing equation. The displacement $\mathbf{q_n}$ of any substructure n can be written $\mathbf{q_n} = \mathbf{\Phi}\mathbf{Q}_n$ using the wave solutions of Eq.(1), where the incident 'inc' and reflected 'ref' wave amplitudes can be distinguished $\mathbf{Q}_n = \left[(\mathbf{Q}_n^{\text{inc}})^T, (\mathbf{Q}_n^{\text{ref}})^T\right]^T$ and the wave components are written:

$$\mathbf{\Phi} = \left[\begin{array}{cc} \mathbf{\Phi}_q^{\text{inc}} & \mathbf{\Phi}_q^{\text{ref}} \\ \mathbf{\Phi}_F^{\text{inc}} & \mathbf{\Phi}_F^{\text{ref}} \end{array} \right], \tag{2}$$

The coupling element describing the junction between the healthy (1) and damaged (2) waveguides is described using a classical FEM, as shown in Figure 1. The reflection coefficient is derived from the dynamic equation of the condensed coupling element $\mathbb{D}^c$, resulting in the following scattering problem:

$$\left(\begin{array}{c} \mathbf{Q}^{\text{ref}\,(1)} \\ \mathbf{Q}^{\text{ref}\,(2)} \end{array} \right) = \mathbb{C} \left(\begin{array}{c} \mathbf{Q}^{\text{inc}\,(1)} \\ \mathbf{Q}^{\text{inc}\,(2)} \end{array} \right) \tag{3}$$
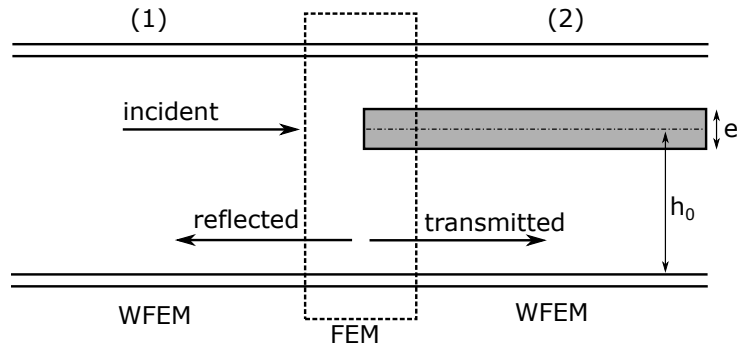
2

Figure 1. Description of the FEM/WFEM coupling problem for the diffusion analysis.

where $\mathbb{C}$ is the diffusion matrix written:

$$
\mathbb{C} = -\left[\mathbb{D}^c \begin{bmatrix} \boldsymbol{\Phi}_q^{\text{ref}(1)} & \mathbf{0} \\ \mathbf{0} & \boldsymbol{\Phi}_q^{\text{ref}(2)} \end{bmatrix} + \begin{bmatrix} \boldsymbol{\Phi}_F^{\text{ref}(1)} & \mathbf{0} \\ \mathbf{0} & \boldsymbol{\Phi}_F^{\text{ref}(2)} \end{bmatrix} \right]^{-1}
$$
$$
\times \left[\mathbb{D}^c \begin{bmatrix} \boldsymbol{\Phi}_q^{\text{inc}(1)} & \mathbf{0} \\ \mathbf{0} & \boldsymbol{\Phi}_q^{\text{inc}(2)} \end{bmatrix} + \begin{bmatrix} \boldsymbol{\Phi}_F^{\text{inc}(1)} & \mathbf{0} \\ \mathbf{0} & \boldsymbol{\Phi}_F^{\text{inc}(2)} \end{bmatrix} \right] \quad (4)
$$

The incident wave is a first-order flexural wavetype i with normalized amplitude along the positive x-direction in waveguide (1) and the coefficient considered in matrix $\mathbb{C}$ corresponds to the $i \to i$ reflection, while the converted wavetypes $i \to j \neq i$ are not taken into account. A recent discussion of the definition of the reflection and transmission coefficients provided by the DMM can be found in [4].

3   REFLECTION OF FLEXURAL WAVE DUE TO CORE DEFECTS

The sandwich structure involves composite skins of thickness $h_s = 0.5$ mm, density $\rho_s = 1451$ and tensile modulus $E_s = 45$ GPa while the core is an homogeneous honeycomb medium of thickness $h_c = 15$ mm, density $\rho_c = 35$ and equivalent shear modulus $G_c = 80$ MPa. Poisson ratio is $\nu = 0.35$ and the unit-cell dimensions are $d_x = d_y = 1$ mm. The defect is defined by a vertical location $z_0 = 8$ mm in the core, a thickness e. It is modelled as a reduced core's stiffness at the defect's location: $\tilde{G} = G/r$. The transition frequencies are defined as the local maximum and minimum of the group velocity. These frequencies are used to defined the bandwidth where shear motion is the predominant behaviour.

Different damage severities defined by the value of e are compared in Figure 2.a. It shows a clear increase of the reflection coefficient between the two transitions, while the maximal amplitude of the reflection increases as expected with the damage thickness. Noteworthy, for the largest defect, the maximum reflection is twice the value of the minimum reflection in the bandwidth $[2\omega_T, 6\omega_T]$. The influence of the damage severity, defined using the reduction coefficient r is shown in Figure 2.b, where reflection coefficients are normalized to their maximum in the transition bandwidth. A similar phenomena can be observed since the maximum reflection is shifted from the second transition to the first as the defect severity increases. Results also indicate the expected reduction of the reflection above the second transition, which corresponds to wave localization in the skins. Higher sensitivities will therefore be obtained for crack and other skin's damages.

4 CONCLUSIONS

A local increase of the flexural wave reflection coefficient was identified within the transition bandwidth, associated with a bending-to-shear conversion. This result was found for different types of sandwich configurations, and is consistent with other investigations describing a partial localisation of strain energy within the transition bandwidth. It is emphasized that higher frequencies will always yield increased sensitivity due to wavelength reduction, but are therefore subjected to significant spatial attenuation and may exhibit complex scattering effects due to the periodicity of the waveguide. It is also mentioned that reflection coefficients are used in this study, since the *transmission* cannot be defined as such between two different waveguides.
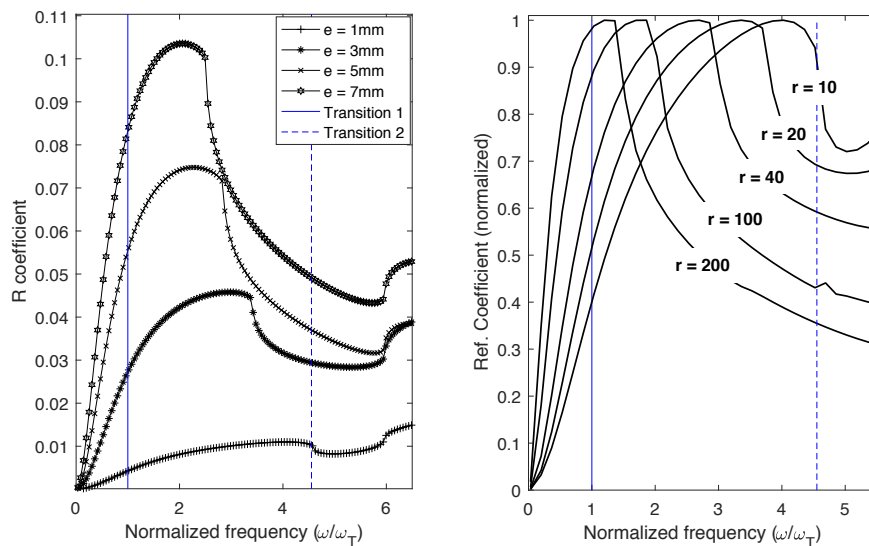
Figure 2: (a) Influence of the defect thickness on the reflection ($r = 10$). (b) Effect of the damage severity on the local maximum of the reflection ($e = 1\,\text{mm}$).

REFERENCES

[1] O. Putkis, R.P. Dalton, and A.J. Croxford. The anisotropic propagation of ultrasonic guided waves in composite materials and implications for practical applications. *Ultrasonics*, 65:390–399, 2016.

[2] O. Baho, Z. Zergoune, M. Ichchou, B. Harras, R. Benamar, B. Troclet, and O. Bareille. On global bendingshear core transition effects for the vibroacoustic of sandwich structures: Analytical and numerical investigations. *Compos. Struct.*, 154:453–463, 2016.

[3] C. Droz, Z. Zergoune, R. Boukadia, O. Bareille, and M.N. Ichchou. Vibro-acoustic optimisation of sandwich panels using the wave/finite element method. *Compos. Struct.*, 156:108–114, 2016.

[4] G. Mitrou, N. Ferguson, and J. Renno. Wave transmission through two-dimensional structures by the hybrid fe/wfe approach. *Journal of Sound and Vibration*, 389:484–501, 2017.

VIBRO-ACOUSTIC ENERGY FLOW ON A CAR FLOOR STRUCTURE USING DYNAMICAL ENERGY ANALYSIS

T. Hartmann[1], G. Xie[2] and G. Tanner[1*]

[1]School of Mathematical Sciences
University of Nottingham, UK
Email: timo.hartmann@nottingham.ac.uk, gregor.tanner@nottingham.ac.uk

[2]CDH AG, Germany
Email: gang.xie@cdh-ag.com

ABSTRACT

Dynamical Energy Analysis (DEA) in the form of Discrete Flow Mapping (DFM) is a fairly new mesh-based method for numerically modelling structure borne sound transmission in complex structures. A key feature is the possibility to work directly on existing finite element (FE) meshes avoiding time-consuming and costly re-modelling. Furthermore, DFM provides detailed spatial information about the vibrational energy distribution within a complex structure in the mid-to-high frequency range. In this work we will illustrate the method using a car floor structure which consists of a big panel and several rails connected by spot welds modeled in FE through Rigid Body Elements (RBE).

1 INTRODUCTION

Simulations of the vibro-acoustic properties of complex structures (such as cars, ships, air-planes, etc.) are routinely carried out in various design stages. For low frequencies, the established method of choice is the finite element method (FEM). But high frequency analysis using FEM requires extremely fine meshes of the body structure to capture the shorter wavelengths and is therefore computationally very costly. Furthermore the structural response at high frequencies is very sensitive to small variations in material properties, boundary conditions etc. This makes the output of a single FEM calculation less reliable and makes ensemble averages necessary furthermore enhancing computational cost. Therefore at high frequencies other numerical methods with better computational efficiency are preferable.

The Statistical Energy Analysis (SEA) [1] has been developed to deal with high frequency problems and leads to relatively small and simple models. However, SEA is based on a set of often hard to verify assumptions, which effectively require diffuse wave fields and quasi-equilibrium of wave energy within (weakly coupled and weakly damped) sub-systems.

One alternative to SEA is to instead consider the original vibrational wave problem in the high frequency limit, leading to a ray tracing model of the structural vibrations. The tracking of individual rays across multiple reflection is not computational feasible because of the proliferation of trajectories. Instead, a better approach is tracking densities of rays propagated by a transfer operator. This forms the basis of the Dynamical Energy Analysis (DEA) method introduced in [2]. DEA can be seen as an improvement over SEA where one lifts the diffusive field and the well separated subsystem assumption. One uses an energy density which depends both on position and momentum. DEA can work with relatively fine meshes where energy can flow freely between neighboring mesh cells. No remodeling as for SEA is necessary as DEA can use meshes created for a FE analysis. Also finer structural details than SEA can be resolved.

In this paper, we apply the DEA method to a caravan car floor structure. The floor structure consists of a floor panel, two longitudinal rails and six transverse rails, all built up from 2D plate elements, as illustrated in Fig. 1. The floor panel is connected to the rails through a number of spot-welds. First we discuss details of DEA itself and then we we present numerical results comparing DEA with FEM calculations.
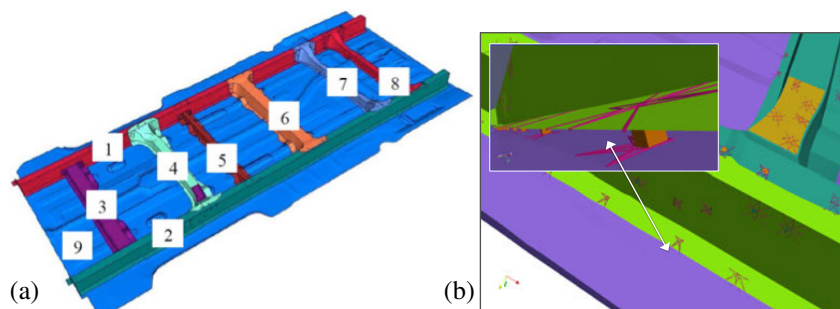

(a)   (b)

Figure 1: (a) car floor and (b) spotweld. The spotweld is modelled through RBEs (red) and a small solid element (yellow) in the middle.

2 DYNAMICAL ENERGY ANALYSIS / DISCRETE FLOW MAPPING

The implementation of DEA on meshes is called Discrete Flow Mapping (DFM). We will here briefly describe the idea behind DFM, for details see [3]. In DFM it is possible to compute vibro-acoustic energy densities in complex structures at high frequencies, including multi-modal propagation and curved surfaces. DFM is a mesh based technique where a transfer operator is used to describe the flow of energy through boundaries of subsystems of the structure; the energy flow is represented in terms of a density of rays ρ, that is, the energy flux through a given surface is given through the density of rays passing through the surface at point s with direction

2

p. Here, s parametrises the surface and p is the direction component tangential to the surface. In what follows, the surfaces is represented by the union of all boundaries of the mesh cells of the FE mesh describing the car floor. The density $\rho(s, p) = \rho(X_s)$, with phase space coordinate $X_s = (s, p)$, is transported from one boundary to the next boundary intersection via the boundary integral operator [3]

$$\mathcal{B}[\rho](X_s') := \int w(X_s')\delta(X_s' - \phi(X_s))\rho(X_s)\,\mathrm{d}X_s \qquad (1)$$

where $\phi(X_s)$ is the map determining where a ray starting on a boundary segment at point s with direction p_s passes through another boundary segment, and $w(X_s)$ is a factor containing damping and reflection/transmission coefficients (akin to the coupling loss factors in SEA). It also governs the mode conversion probabilities in the case of both in-plane and flexural waves, which are derived from wave scattering theory [4].

In a next step, the transfer operator (1) is discretised using a set of basis functions of the phase space. Once the matrix B has been constructed, the final energy density ρ on the boundary phase-space of each element is given in terms of the initial density ρ_0 by the solution of a linear system of the form

$$(\mathbf{1} - \mathbf{B})\rho = \rho_0. \qquad (2)$$

The integral in (1) can be adapted to incorporate further complexity and refinement in a DFM model. The vehicle floor in Fig. 1 contains spot welds fixing the stiff rails to the floor panel. This is modelled in the FE model with the connections shown in Fig. 1b, here in terms of a set of RBEs (red lines) together with solid element modelling extra mass and stiffness of the spot weld. The RBEs describe here constraint conditions and make it possible to transfer forces directly from one mesh to another. Such a set-up can not be used in a DFM treatment which is based on modelling energy flow through surfaces and mesh boundaries.

In order to avoid costly remodelling of the structure, in DFM we describe the energy transfer across spot weld by introducing coupling elements between edges connected to the spot welds both in the 'upper' and 'lower' sheet. Energy arriving at an edge connected to a spot weld is distributed uniformly (also in direction) among all neighbouring edges.

3   NUMERICAL RESULTS

In order to compare the different numerical approaches, first we have calculated the spatial kinetic energy distribution originating from a single (perpendicular) point excitation on the plain floor panel without rails (shown as component 9 in Fig. 1a). The DFM results are compared to one-third octave band frequency-averaged FEM results, with the band average at 2500 Hz. Note that the DFM calculation uses only the band average frequency. The calculation uses a hysteretic damping loss factor of $\eta = 0.04$.

The results are shown in Fig. 2a. The energy distribution predicted by FEM and DFM is very non-uniform and would not be well-captured by an SEA model. In contrast to SEA, DFM gives also the spatial distribution information, which is in close agreement with the FEM results. In particular, we see the directional dependence of the energy flow, which is predominantly in the horizontal direction as plotted. This is caused by several horizontally extended out-of-plane bulges. It is only in the lower right part of the panel, with negligible energy content, that deviations between the FEM and DFM predictions are visible. The results also show a good quantitative agreement. In particular, the total kinetic energy given by the DFM prediction is within 12% of the FEM prediction.

In a next step, we calculate the response of the full car floor model shown in Fig. 1a. This includes the coupling of the rails to the floor panel and between different rails via the spot-weld
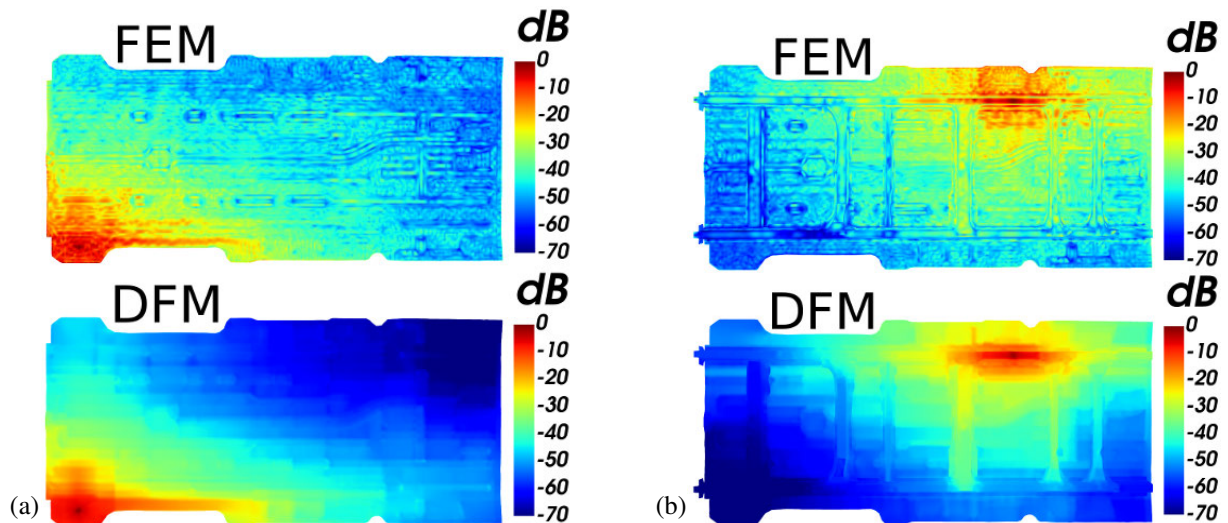
Figure 2: The kinetic energy distribution on a logarithmic color scale ((b) shifted by 5 dB relatively to (a)). The (frequency averaged) FEM results (upper panels) are compared to DEA results (lower panels). The left panels (a) show the bare floor panel, the right panels (b) show the full structure including rails.

models depicted in Fig. 1b. The point loading is now applied on top of a rail, but otherwise the scenario is equivalent to the previous calculation. The results are shown in Fig. 2b. The deviations between the FE result and the DEA result are within 18% when integrated over the total area of the car floor. A detailed analysis shows, that the energy is less pronounced in the DEA calculation compared to the FE calculation when moving away from the source. This suggest that the modelling of the coupling between different components is currently too weak in the DEA model, which calls for a more refined DEA modelling of the RBE connections.

4 CONCLUDING REMARKS

We have tested the DFM method for a car-floor structure at mid- and high- frequencies. The combination of the thin shell floor panel connected to a number of stiffer rails via spot welds poses challenges for a DFM calculations. We have developed a method for treating the coupling of different FE meshes via RBEs in a DFM simulation. The results compare well with (frequency-band averaged) FE calculations both for the floor panel alone and for the full car floor structure. Improvements of the coupling in the DEA set-up needs to be considered.

REFERENCES

[1] R.H. Lyon and R.G. DeJong. *Theory and Application of Statistical Energy Analysis*. Butterworth-Heinemann, Boston, 1995.

[2] G. Tanner. Dynamical energy analysis - determining wave energy distributions in vibro-acoustical structures in the high-frequency regime. *J. Sound Vib.*, 320:1023–1038, 2009.

[3] D.J. Chappell, G. Tanner, D. Löchel, and N. Søndergaard. Discrete flow mapping: transport of phase space densities on triangulated surfaces. *Proc. R. Soc. A*, 469:20130153, 2013.

[4] R.S. Langley and K.H. Heron. Elastic wave transmission through plate/beam junctions. *J. Sound Vib.*, 143:241–253, 1990.

4

MUSIC algorithm for vibro-acoustic defect detection

Philip Becht[1,2*], Elke Deckers[1,2], Claus Claeys[1,2], Bert Pluymers[1,2], Wim Desmet[1,2]

[1] KU Leuven,
Dept. of Mechanical Engineering, Celestijnenlaan 300, box 2420, 3001, Leuven, BELGIUM
Email: Philip.Becht@kuleuven.be

[2] member of Flanders Make

ABSTRACT

Defect detection based on the processing of ultrasonic signals using the MUSIC algorithm is a recent subject of research. This paper suggests to make use of the sub-wavelength detection accuracy that can be achieved with the MUSIC algorithm to lower the testing frequency. This allows the application of the detection strategy to periodic and heterogeneous materials, such as honeycomb structures, where defect detection at higher frequencies becomes difficult, due to the complex scattering behavior. Furthermore the sound radiated from the structure in the surrounding air can be picked up with microphones to replace structural sensors, with the consequence that coupling problems between structure and sensors, e.g. due to badly glued sensors, are avoided automatically and the time for setting up the measurement is reduced. In this paper, it is demonstrated using the example of an A3 Aluminum plate radiating in a half space that the detection accuracy of a vibro-acoustic test-setup (excitation: structural, sensor: microphone) is equal to that of a purely structural measurement (excitation: structural, sensor: structural).

1 INTRODUCTION

A commonly used method in the field of ultrasonic nondestructive testing (NDT) is defect detection based on ultrasonic waves. More recently, the combination of ultrasonic waves with the concept of time-reversal (TR) was introduced to NDT [1]. One sub-group of TR methods is the so called TR-MUSIC algorithm, where MUSIC stands for MUltiple SIgnal Classification. This technique proved to be very robust to measurement noise and reaches an imaging resolution that is significantly smaller than the wavelength [2, 3].

The latter feature allows to lower the testing frequency, while still being able to generate an accurate image of the defect location. This comes with the downside of a reduced interaction between incident wave and defect. On the other hand, e.g. in case of periodic structures characterized by the repetition of a unit cell (UC), ultrasonic waves can significantly scattered at the boundaries of the UC and therefore in these cases be problematic for defect detection of the entire structure. At lower frequencies, and thus larger wavelength, the scattering at the boundaries of the UC decreases, which is why waves in this frequency range, then can be employed to globally monitor the health status.

Furthermore, lowering the frequency enables to measure the radiation of structural vibrations in the surrounding air, which would not be possible at higher frequencies due to the stronger damping for a given distance of propagation. The advantage of employing microphones instead of structural sensors are versatile. E.g., one consequence is that no sensors need to be attached to the structure, which automatically avoids problems with the coupling. Furthermore, it avoids wave scattering at the sensors and saves time.

This paper provides a numerical study with the focus to determine the ability to use the radiation of structural vibrations in the surrounding air for the detection of a small defect (small as compared to the wavelength).

2 MUSIC IMAGING

The MUSIC algorithm is based on the idea to decompose the so called multi-static data matrix K in components belonging to a signal space and components belonging to a noise space. In a mechanical system the elements of K at one discrete frequency are

$$k_{m,n} = k_{D,m,n} - k_{l,m,n},$$ (1)

with $k_{\cdot,m,n}$ the transfer function from the n-th point of excitation to the m-th measurement point in the defected (subscript D) and the intact (subscript I) structure, respectively. The transfer path can be purely structural or vibro-acoustic.

The decomposition of K is done by means of a singular value decomposition

$$K = G_E V G_S^H,$$ (2)

where $G_E = [g_{E,1}, g_{E,2}, \dots, g_{E,N}]$ and $G_S = [g_{S,1}, g_{S,2}, \dots, g_{S,M}]$ are matrices containing the left and right hand side singular vectors, V is the matrix of the singular values and the superscript H denotes the complex conjugate transpose. G_E and G_S are $N \times N$ and $M \times M$ matrices, where N is the number of excitation points and M is the number of sensors. Throughout the paper quantities referring to the excitation are indicated with subscript E, those referring to sensors with subscript S.

V contains P singular values corresponding to the signal space and $\min(M, N) - P$ singular values corresponding to the noise space. According to this definition G_E can be split in a part corresponding to the signal space with singular vectors $g_{E,i \leq P}$ and a part corresponding to the noise space with singular vectors $g_{E,i > P}$. The choice of P is done as suggested in [4].

2

For the case of point scatterers under the Born approximation, P is equal to the number of scatterers. Following He and Yuan [3], for this case, due to the orthogonality of the singular values, the scalar product between $\boldsymbol{g}_{E,i \leq P}$ and a vector containing the transfer functions from the points of excitation to an arbitrary point x in the intact structure, $\boldsymbol{k}_{I,E}(x)$ is 0 only if x is not equal to the location of the defect x_i. Making use of the orthogonality between signal and noise space, this property can be used to calculate an image function, which peaks at all locations $x = x_i$

$$I(x) = \frac{1}{\sum\limits_{i=P+1}^{\min\{M,N\}} \left\langle \boldsymbol{g}_{E,i}, \boldsymbol{k}_{I,E}(x) \right\rangle}. \tag{3}$$

The theory can also be extended to scatterers with finite extent, with the outcome that $I(x)$ reaches its maximum at the location of the scatterers. The principle of imaging remains unchanged.

3   NUMERICAL ANLAYSIS

In this section the above described theory is applied to a simply supported A3 Aluminum plate ($E = 7 \cdot 10^{10}$ N/m^2, $\rho = 2700$ kg/m^3, $\nu = 0.3$, structural damping coefficient $= 5 \cdot 10^{-4}$) of 2mm thickness radiating in a half space filled with air. A square damage of 3mm x 3mm is assumed, which is modelled by removing one element. The plate is excited at 8000Hz, which results in a wavelength of 49mm. The mesh is composed of linear 2D elements with an edge length of 3mm.

3.1 Imaging based on structural vibration

At first the location of the defect is searched based on Equation (3) with randomly chosen 27 structural excitation points. The out-of-plane displacement of the plate is calculated at 27 arbitrarily chosen locations, which serve as virtual sensors. P is chosen as 9, following [4].
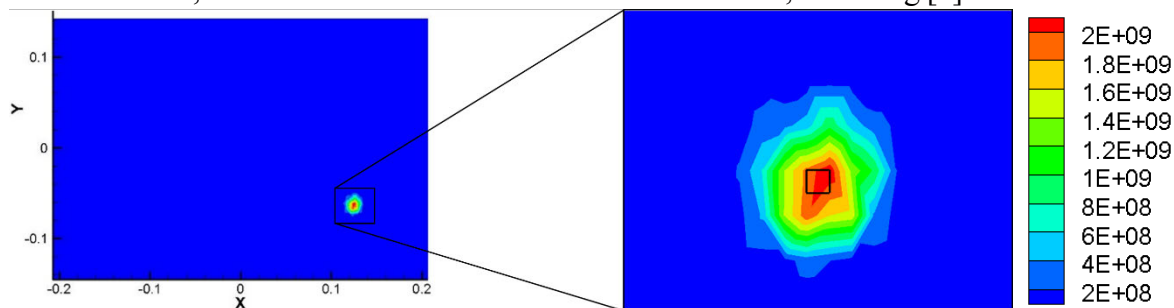

Figure 1. Purely structural imaging result ($I(x)$) of Equation 3 for the entire plate (left) and zoom to the defected region (right). Deleted element is indicated with black square in the right figure.

As can be seen from Figure 1, the maximum of the image index is shown at the top right corner of the defect. Furthermore it is evident that the region of the defect and its direct vicinity is clearly separated form the undefected regions of the plate. Assuming a possible defect in the region around the maximum, until the amplitude is lowered by a factor 10, gives a circle of roughly 20mm diameter, which proves that defects can be located with a sub-half-wavelength accuracy.

3.2 Imaging based on vibro-acoustic measurement

In this section the imaging is done based on the same equation with the same 27 structural excitation points already used in the previous section. As opposed to section 3.1, now only microphone measurements (pressure) are used for the imaging. The 27 (equal to the number of structural sensors in 3.1) microphones are located at randomly chosen points on a half-sphere with 620mm diameter and the center coinciding with the center of the plate. Also in this case P is chosen equal to 9.
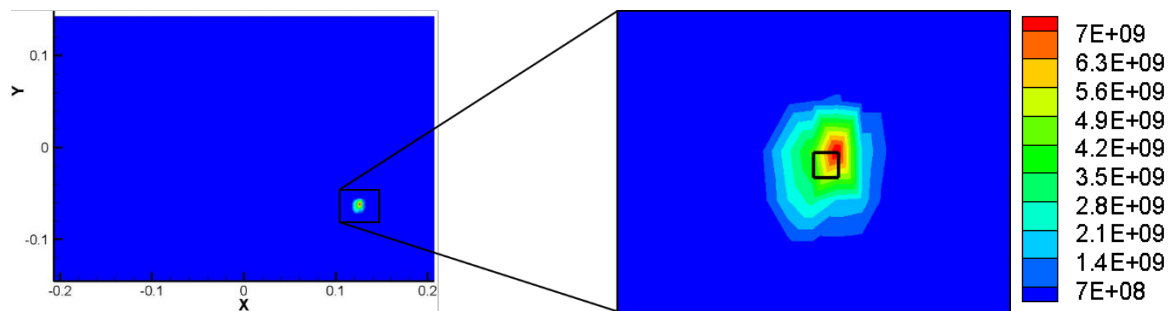
Figure 2. Vibro-acoustic imaging result ($I(x)$) of Equation 3 for the entire plate (left) and zoom to the defected region (right). Deleted element is indicated with black square in the right Figure.

As in Figure 1, also in the case of vibro-acoustic imaging (Figure 2), the maximum of the image index is located at the top right corner of the defect. Although the maximum in Figure 2 is more extreme than that in Figure 1, the area of a possible defect in the vibro-acoustic case is even smaller than it is in the purely structural case.

Further numerical simulations illustrate that the number of measurement and excitation points in both cases can be reduced to P+1 without a significant loss of detection accuracy. Also the stability of the algorithm at the presence of random measurement errors, which is reported in literature, can be observed, as will be shown at the conference presentation.

4   CONCLUDING REMARKS

As a numerical example, it is shown that the MUSIC algorithm can be used for the detection of a defect in a structure, while only microphone measurements are used. The comparison between a purely structural and a vibro-acoustic case suggests that the detection accuracy due to the vibro-acoustic measurement does not decrease. In both cases the location of a defect can be narrowed down to an area significantly smaller than the structural wavelength at the excitation frequency.

ACKNOWLEDGEMENTS

REFERENCES

[1]   H. Sohn, H. Park, W. Hyun, K. Law and C. Farrar. Damage detection in composite plates by using an enhanced time reversal method. *Journal of Aerospace Engineering*. 20(3):141-151, 2007.

[2]   H. Choi, Y. Ogawa, T. Nishimura and T. Ohgane. Time-reversal MUSIC imaging with time-domain gating technique. *IEICE transactions on communications*. 95(7):2377-2385, 2012.

[3]   J. He and F.-G. Yuan. Lamb wave-based subwavelength damage imaging using the DORT-MUSIC technique in metallic plates. Structural Health Monitoring. 15(1):65-80, 2016.

[4]   E. Marengo, F. Gruber and F. Simonetti. Time-reversal MUSIC imaging of extended targets. IEEE Transactions on image processing. 16(8):1967-1984, 2007.

4

HIGH-FREQUENCY STRUCTURE- AND AIR-BORNE SOUND TRANSMISSION FOR A TRACTOR MODEL USING DYNAMICAL ENERGY ANALYSIS

T. Hartmann[1], S. Morita[2] and G. Tanner[1]

[1]University of Nottingham
University Park, Nottingham NG7 2RD, UK
Email: timo.hartmann@nottingham.ac.uk, gregor.tanner@nottingham.ac.uk

[2]Yanmar Co, Ltd
2481, Umeghara, Maibara Shiga, 521-8511, Japan
Email: satoshi_morita@yanmar.com

ABSTRACT

Dynamical Energy Analysis (DEA) is a mesh-based high frequency method modelling structure borne sound for complex built-up structures. Vibro-acoustic simulations are done directly on finite element meshes circumventing re-modelling strategies. DEA provides detailed spatial information about the vibrational energy distribution within a complex structure in the mid-to-high frequency range. We will present here progress in the development of the DEA method towards handling complex FEM-meshes including Rigid Body Elements and sound radiation. The results for simulations are compared to measurements on a tractor model provided by Yanmar Co, Ltd both for structure borne vibrations and sound pressure levels (SPL) inside the cabin. For the latter, a combined DEA/SEA analysis has been developed. The simulation results compare favourably with measurement results both for vibration levels measured across the structure and SPLs inside the cabin.

1 INTRODUCTION

A major difficulty in modelling structure-borne sound lies in the complex geometry of the structures. The Finite Element Method (FEM) can describe geometric details with sufficient accuracy in the low frequency region, but requires extremely fine meshes at high frequencies to capture the shorter wavelengths. Statistical representations such as the *Statistical Energy Analysis* (SEA) [1] have been developed leading to relatively small and simple models in comparison with FEM. A range of methods have been proposed to extend the range of SEA such as the hybrid FEM/SEA method [2–4]. An alternative to SEA is ray-tracing in terms of integral equations leading to linear flow equations for the mean vibrational energy density; this forms the basis of the *Dynamical Energy Analysis* (DEA) method introduced in [5]. DEA includes SEA as special case via a low order representation of the transfer operator. Higher order implementations enrich the DEA model with information from the underlying ray dynamics, leading to a relaxation of SEA assumptions. In particular, DEA allows for more freedom in sub-structuring the total system and variations of the energy density across sub-structures can be modelled [6]. An efficient implementation of DEA on meshes has been presented in [6, 7]. Vibro-acoustic energy densities including multi-modal propagation and energy transport over curved surfaces is computed and coupling at material interfaces is described in terms of reflection/transmission matrices. Thus, DEA resolves the full geometrical complexity of the structure.

In this paper, we apply the DEA method to modelling a tractor model (cabin including windows and doors mounted on a chassis) as well as the SPL inside the cabin and compare with detailed measurements done across the structure. We focus here in particular on how to implement DEA in the presence of *Rigid Body Elements* (RBEs) or similar FE coupling methods. We will furthermore introduce a DEA/SEA method for determining the acoustical response inside the cabin.

2 THE TRACTOR MODEL AND THE SET-UP FOR VIBRO-ACOUSTIC MEASURE-MENTS

The tractor model under consideration has been provided by Yanmar Co, Ltd and is a stripped down version of a tractor of the EG400 series. The tractor body consists of a chassis frame and a cabin - the latter includes doors and windows - often referred to as a 'body-in-blue' (BiB). The chassis frame consists of the gear casing and a front frame. The cabin is mounted onto the chassis by four rubber mounts; the actual structure together with an FEM model is depicted in Fig. 1. In the FE model, the rubber mounts are treated as spring elements - so-called CELAS1 elements. Rubber material and glue (such as for describing the fixture of windows, doors and the roof) are modelled with rigid body elements (RBE), mostly of the RBE3 type. The coupling

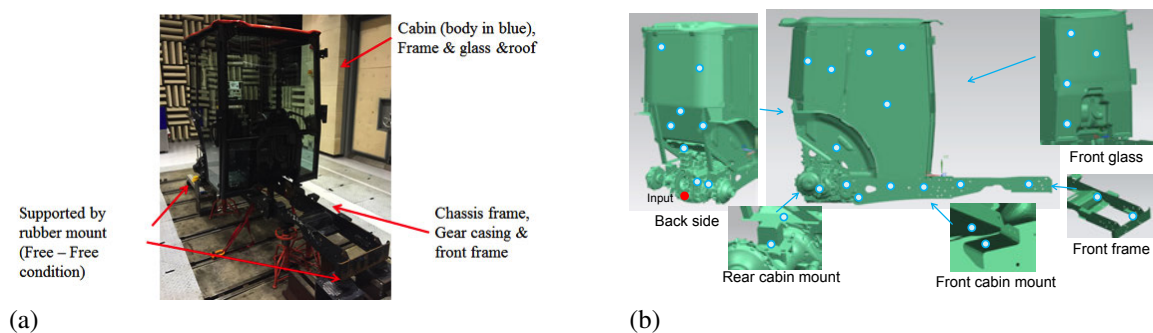(a)   (b)

Figure 1: (a) the tractor parts under consideration and (b) the corresponding FEM model of the tractor including the accelerometer positions across the structure (blue dots, 44 points in total).

2

elements provide a connection over which energy can be transferred. The chassis frame is supported by rubber mounts as free-free condition. The excitation is at the rear side of the gear casing. Excitation is applied using a modal shaker in a frequency range between 400Hz to 4000Hz. The sound pressure at the operator's ear location is measured with a microphone. In addition, the acceleration of the structure is measured at 29 points on the cabin and at 13 points on the chassis frame using an accelerometer. The acceleration on the upper and lower sides of each cabin mount are also measured giving valuable information about the coupling via the rubber mounts. Fig. 1b shows the location of the measurement points (blue dots).

3   DEA ON COMPLEX MESHES AND A DEA/SEA HYBRID TREATMENT

In the following we will focus on DEA on 2D meshes [7] and describe the modelling of connections between different meshes via RBE's such as used in the tractor model. DEA is a technique for determining the flow of (vibrational) energy through a structure in terms of a transfer operator defined on boundaries of subsystems of the structure, here the boundaries of the mesh elements. Mode conversion between in-plane and flexural waves at boundaries are included in the treatment, the reflection/transmission coefficients are obtained from wave scattering theory [8]. Shell effects leading to curved rays [9] are included by treating the meshed structure as a set of plate-like elements, see [6, 7] for details. Once the ray density ρ has been computed, the energy density at any location inside the structure may be obtained in a post-processing step as described below.

The FE model of the tractor structure shown in Fig. 1b is made up of different sub-meshes; these sub-meshes are connected via special FE elements, RBEs, at, for example, glass-metal interfaces, at the sidewall-roof interfaces or for connecting the doors to the cabin frame. We treat RBEs as DEA coupling elements directly. To describe the energy transfer across non-compatible meshes we introduce coupling between edges connected to the mesh cells next to the RBEs both in the 'upper' and 'lower' sheet connected by the RBE. Incoming ray-densities at one side of the RBE-interface are now mapped onto the other side of the interface via a probability density function in phase space (position on each edge and ray directions).

The sound pressure level (SPL) inside the cabin and in particular at the position of the driver's ear can be computed from the vibration levels obtained in the DEA computation. To do so, we identify the main panels of the cabin, determine the mean velocity v_i on each panel i with mass M_i from the DEA analysis and determine the input power P_i radiated off each plate

Figure 2: DEA results for the acceleration (given here in mm/s^2) at a frequency of 1000 Hz.
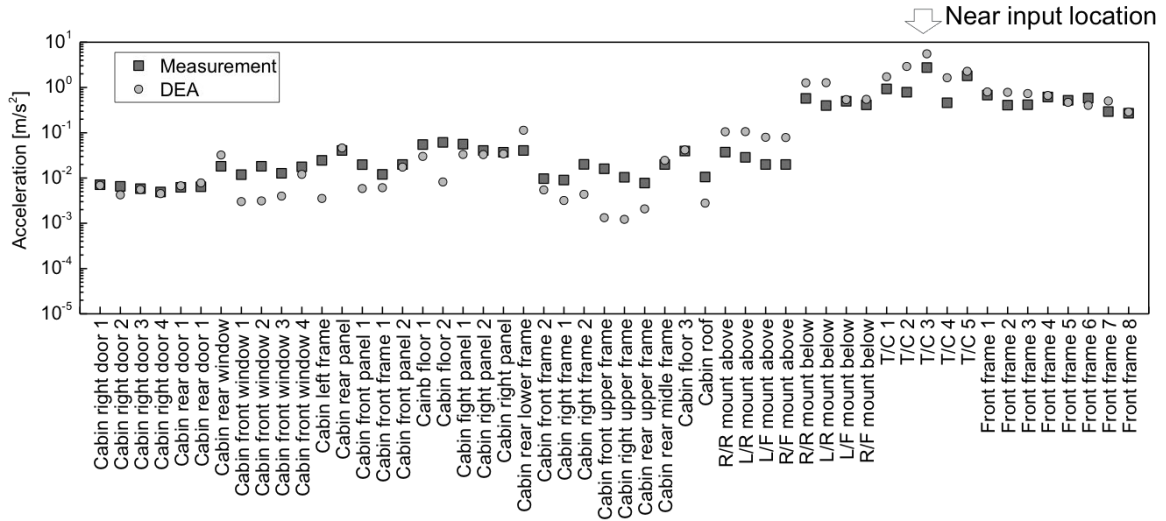
3

Figure 3: Comparison of Simulation and Measurement results at 1000 Hz.

using the relation

$$P_i = \omega(\eta_i + \eta_i^d)M_i < v_i^2 >, \quad \eta_i = \frac{Z_0 A_i \sigma_{rad}}{\omega M_i} \qquad (1)$$

Here, A_i is the area of plate i, η_i is the coupling loss factor between panel i and the interior volume and η_i^d is the loss factor due to dissipation in panel i. (We assume $\eta_i^d = 0.5\%$ and $\eta_V^d = 1.5\%$ for the interior volume). Furthermore Z_0 is the acoustic impedance and σ_{rad} is the radiation efficiency, here for rectangular plates in the approximation derived in [10]. The DEA result enters through the mean velocity $< v_i^2 >$ averaged over each of the panels.

4 RESULTS

We performed DEA calculations for the full structure shown in Fig. 1b in the frequency range 400 Hz – 10 kHz. The results are compared to experimental data obtained from measurements done by Yanmar for the input powers specified. In all calculations, a hysteretic damping level of 0.005 is assumed. The acceleration of surface points are measured in mm/s^2. Fig. 2 shows the outcome of the DEA calculation on the FEM mesh at 1000 Hz. Most of the vibrational energy remains near the source (rear end of the chassis) and in the chassis itself. The cabin shows less excitation which in addition decreases with the distance to the source. A point-by-point comparison with the measurement results can be found in Fig. 3. Overall, the simulation captures the energy distribution across the whole structure remarkably well despite the simplifying assumptions for the RBE coupling and the cabin mounts. We have also conducted SPL calculations at the driver's ear position following the approach sketched in Sec. 3. The results are summarised in Fig. 4. We note large variations in both the experimental data and the simulations, but the overall range (between 45 and 55 dB) is captured well by the simulation.

5 CONCLUSIONS

We demonstrate in this paper that the DEA method can compute structure borne sound across a complex structure – here a BiB substructure of a full tractor. The results presented in this paper emphasise the level of detail provided by the DEA method and its flexibility in handling RBE elements. Results over the full frequency range from 400 Hz to 4 kHz have been presented.
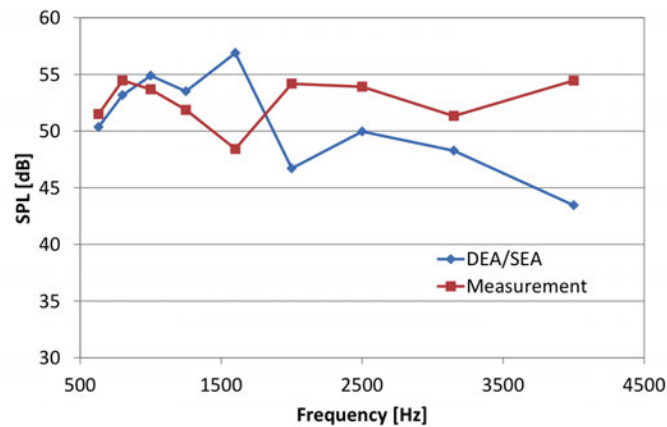
Figure 4: SPL at the driver's ear position: experiment (red); SEA/DEA simulations (blue).

ACKNOWLEDGEMENTS

REFERENCES

[1] R. H. Lyon, and R. G. DeJong, *Theory and Application of Statistical Energy Analysis*, Butterworth-Heinemann, Boston (1995).

[2] P. J. Shorter and R. S. Langley, *Vibro-acoustic analysis of complex systems*, J. Sound Vib., **288**, 669-699, 2005.

[3] V. Cotoni, P.J. Shorter, and R.S. Langley, *Numerical and experimental validation of a hybrid finite element-statistical energy analysis method*, J. Acoust. Soc. Am., **122**, 259-270, 2007.

[4] G. Xie, L. Dunne, A. Secgin and A. Zoghaib, *Mid-frequency modelling of a car floor structure with hybrid method and SEA*, International Symposium on the Computational Modelling and Analysis of Vehicle Body Noise and Vibration, 2012, Sussex, UK.

[5] G. Tanner, *Dynamical energy analysis – Determining wave energy distributions in vibro-acoustical structures in the high-frequency regime*, J. Sound Vib. **320**, 1023-1038, 2009.

[6] D. J. Chappell, D. Löchel, N. Søndergaard and G. Tanner, *Dynamical energy analysis on mesh grids: A new tool for describing the vibro-acoustic response of complex mechanical structures*, Wave Motion **51**, 589-597, 2014.

[7] D. J. Chappell, G. Tanner, D. Löchel and N. Søndergaard, *Discrete flow mapping: transport of phase space densities on triangulated surfaces*, Proc. R. Soc. A, **469**, 20130153, 2013.

[8] R. S. Langley and K. H. Heron, *Elastic wave transmission through plate/beam junctions*, J. Sound Vib. **143**, 241, 1990.

[9] A. N. Norris and D. A. Rebinsky, *Membrane and Flexural Waves on Thin Shells*, ASME J. Vib. Acoust. **116**, 457-467, 1994.

[10] G. Maidanik, *Response of Ribbed Panels to Reverberant Acoustic Fields*, J. Acoust. Soc. Am. **34**, 809-826, 1962.

5

SIMULATION OF FINITE-SIZED DYNAMIC SYSTEMS USING WAVE TRANSMISSION METHODS

Gerard Borello[1]

[1]InterAC
10 impasse Borde-Basse, 31240 L'Union, FRANCE
gerard.borello@interac.fr

ABSTRACT

For predicting machinery noise in operating conditions over the audio frequency range, statistical methods are required. The most popular is the Statistical Energy Analysis (SEA). Originally based on modal response of coupled oscillators, this method has become more a wave approach in diffuse field condition than a modal kind of analysis. This is due to basic assumption of weak coupling between subsystems that is still the drawback of SEA method. SEA parameters of a built-up system cannot directly be obtained from deterministic modal formulation and have to be inferred from measurement or numerical FEM modeling by inverse techniques. In SEA, all internal calculated parameters are wave-based parameters thanks to some a priori assumption on system behavior. These parameters are extracted from simple infinite or semi-infinite propagating wave models. As the system under analysis is bounded and generally weakly damped, it is necessary to tune infinite wave parameters to fit to finite systems. Series of examples are presented to illustrate the observed differences between finite and infinite systems and how to correct the infinite calculation to get realistic parameters for finite-sized systems.

1   INTRODUCTION

Acoustic transmission loss predictions are performed at low cost with the simplified Transfer Matrix Method (TMM). In TMM, layers are assumed isotropic and of infinite extent with finite small thickness in transverse direction. When gluing several layers on top of each other, the resulting system may be inserted within two semi-infinite acoustic volumes as shown in Figure 1. The sound transmission from a double-walled configuration may then be predicted by TMM representation by inserting an acoustic layer between two solid elastic layers. Sending an acoustic emitter wave impinging solid elastic layer 1, this wave will be partly reflected and partly transmitted through the different layers and will exit in the receiver fluid after some attenuation.

The infinite extent of layers may cause artefact in the noise transmission prediction as shown in next paragraph. Finite-sized corrections are then introduced to make the prediction more regular with better test fitted results.

2   MASS LAW SOUND TRANSMISSION USING INFINITE LAYER
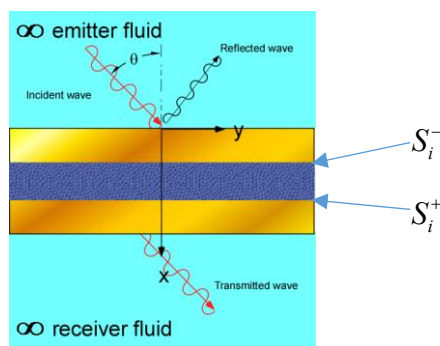
Figure 1. An acoustic sound package modelled as TMM.

For predicting this attenuation, the laws under which stress and displacement are transferred from one layer to another need to be given. These laws depend on layer type.

The simplest kind of layer is the pure inertial mass layer which oscillates without any residual stiffness. The mass layer is assumed uncompressible and is defined by ρ_s the mass density of the layer per m². The incident wave amplitude has constrained harmonic motion along y axis with acoustic potential defined as:

$$\varphi(x, y, \omega) = e^{-ik\cos\theta x} e^{-ik\sin\theta y} \tag{1}$$

from which pressure and velocity are derived:

$$p = i\omega\rho_0\varphi \qquad v = -\frac{\partial\varphi}{\partial x} \tag{2}$$

On emitter side, the wave is reflected while on receiver side the wave is simply transmitted. Emitter and receiver potentials are therefore given by:

$$\varphi_E = \left(e^{-ik\cos\theta x} + Re^{ik\cos\theta x}\right)e^{-ik\sin\theta y}; \qquad \varphi_R = Te^{-ik\cos\theta x}e^{-ik\sin\theta y} \tag{3}$$

with R and T resp. reflection and transmission wave amplitudes.
At each layer boundaries indexed by i, pressure and velocity are submitted to change, defining two state vectors both sides of the layer S_i^- and S_i^+ such as

$$S = \begin{bmatrix} v \\ -p \end{bmatrix} = \begin{bmatrix} v \\ \sigma \end{bmatrix} \tag{4}$$

where σ is the normal stress, opposite sign of the pressure.

Continuity of S at interface between two layers is also assumed: $S_i^+ = S_{i+1}^-$. Downward velocity, v^- and upward one, v^+ are then equal. The stress variation both sides of this layer is equal to the inertial force $\rho_s \dfrac{\partial v}{\partial x}$. It leads to the two following equations:

$$\left. \begin{array}{l} v^+ - v^- = 0 \\ \sigma^+ - \sigma^- - \rho_s \dfrac{\partial v}{\partial t} = 0 \end{array} \right\} \text{ and in matrix form } \begin{bmatrix} v^+ \\ \sigma^+ \end{bmatrix} = \begin{bmatrix} 1 & 0 \\ \rho_s \dfrac{\partial}{\partial t} & 1 \end{bmatrix} \begin{bmatrix} v^- \\ \sigma^- \end{bmatrix} = Z \begin{bmatrix} v^- \\ \sigma^- \end{bmatrix} \tag{5}$$

The Z-matrix is actually transferring the downward information contained in the state vector S^- to upward one S^+. Reversely $S^- = Z^- S^+$. In the case N layers are connected to each other's, if S_E is the source vector in the emitter fluid, with same state vector variables for each layer, the state vector in the receiver fluid is obtained as:

$$S_R = Z^{-1}{}_N Z^{-1}{}_{N-1} .. Z^{-1}{}_1 S_E \tag{6}$$

To fully solve this problem, S_E and S_R need to be expressed as function of R and T.

From (3), (4), (5) and (6), S_E and S_R are obtained:

$$S_E = ik \begin{bmatrix} \cos\theta & -\cos\theta \\ -\rho_f c_f & -\rho_f c_f \end{bmatrix} \begin{bmatrix} 1 \\ R \end{bmatrix} \qquad S_R = ik \begin{bmatrix} \cos\theta \\ -\rho_f c_f \end{bmatrix} T \tag{7}$$

Using (5) and (6) in frequency domain where $\dfrac{\partial}{\partial t} \to i\omega$, it comes:

$$\begin{bmatrix} \cos\theta \\ -\rho_f c_f \end{bmatrix} T = \begin{bmatrix} 1 & 0 \\ -i\omega\rho_s & 1 \end{bmatrix} \begin{bmatrix} \cos\theta & -\cos\theta \\ -\rho_f c_f & -\rho_f c_f \end{bmatrix} \begin{bmatrix} 1 \\ R \end{bmatrix} \tag{8}$$

We end up with two equations and two unknown's T and R of which solution is:

$$\left. \begin{array}{l} T = 1 - R \\ T - \dfrac{i\omega\rho_s \cos\theta}{\rho_f c_f} - 1 + R\left(\dfrac{i\omega\rho_s \cos\theta}{\rho_f c_f} - 1 \right) = 0 \end{array} \right\} \Rightarrow \left\{ \begin{array}{l} T = \dfrac{2}{2 - \dfrac{i\omega\rho_s \cos\theta}{\rho_f c_f}} \\ R = 1 - T \end{array} \right. \tag{9}$$

T expression is called the acoustic mass law predicting the sound transmission between two acoustic volumes containing same fluid and separated by a pure thin inertial layer.

It is remarkable to note that T is equal to 1 at grazing incidence $\theta = \dfrac{\pi}{2}$ independently from mass density value, which is not the result we intuitively expect. If the incident wave is parallel to the mass layer, there is a non-zero pressure on the related surface of the mass layer but its normal velocity will be zero and then the layer would not radiate any pressure in the receiver fluid. The radiated pressure should then be null. There is no contradiction if we come back to the definition of

3

T: *T* refers to the amplitude of the receiver wave which is parallel to the mass layer. The radiated intensity by the mass layer is given by the product of pressure time velocity which is expressed by:

$$I_{rad} = p_R v_R^*$$ (10)

From (7) it comes:

$$I_{rad} = k^2 \rho_f c_f |T|^2 \cos\theta$$ (11)

The normal radiated power is then effectively null when $\theta = \dfrac{\pi}{2}$ as $T = 1$.

The transmission loss coefficient is commonly expressed as the ratio of radiated power over incident power normal to the panel and using (2) for incident pressure and velocity, it gives:

$$\tau = \frac{I_{rad}}{I_{inc}} = \frac{k^2 \rho_f c_f |T|^2 \cos\theta}{\omega \rho_f k \cos\theta} = |T|^2$$ (12)

The definition of transmission coefficient is thus ill-suited for describing the effective noise transmission under grazing incidences when panel size is infinite. It leads to overestimate wave intensity originated from incidences near 90°. Due to constrained infinite motion in *y*-direction, the stress on receiver side has always to compensate the emitter-side stress under grazing incidence, leading to equal stress both sides at 90° incidence as no other force may exist in the layer to cancel out the emitter stress. This observation is also true for other kinds of layer (porous fluids or elastic plates) but mass layer is particularly affected by infinite assumption. This is known for a long time and empirical correction is used when dealing with random-incidence acoustic field [1]. The random-incidence transmission loss is calculated by averaging (12) over incidence and in the case of mass-law, the averaging is limited to angles not exceeding 78.5°. This empirical value provides an average transmission coefficient that fits better with experimental measurements.

To get more regular (i.e. more physical transmission loss prediction), we need to take into account the finite size of actual panels in deriving sound transmission loss expression.
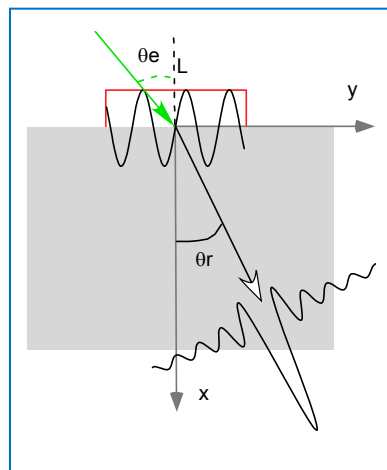
3   FINITE-SIZED SOUND TRANSMISSION LOSS

Figure 2. Convolution through aperture.

The junction interface is now considered with finite size L. As shown in Figure 2, a monochromatic emitter wave having wavenumber k_e and incidence θ_e, constrains the junction wavenumber in the in-plane direction y to follow the Descartes's law:

$$k_0 = k_e \sin\theta_e \tag{13}$$

In k_y-wavenumber space of the surface motion of the junction, the projected field of the incident wave is described by the distribution $\delta(k_y - k_0)$

The Spatial Fourier's Transform (SFT) of the velocity field $v(y)$ on junction is noted by $\tilde{v}(k_y)$ and from Parseval's theorem, the radiated power of the junction may be then expressed as:

$$P_{rad}^F(\omega,\theta_r) = \int p(y)v^*(y)dy = \frac{1}{2\pi}\int Z_{rad}\tilde{v}(k_y)\tilde{v}^*(k_y)dk_y \tag{14}$$

The junction aperture is introduced as a weighting window defined by the Heaviside function such as: $-L/2 \le x \le L/2$, $w = 1$ and $w = 0$ elsewhere.

The SFT of w is given by $\tilde{w}(k_y) = L\sin\left[\frac{L}{2}k_y\right]/\frac{L}{2}k_y = L\mathbf{sinc}(k_y)$.

Assuming Z_{rad} weakly dependent of k_y, the monochromatic wave radiated power gives:

$$P_{rad}^F(\omega,\theta_r) = Z_{rad}\left|V_\infty\right|^2 \int \delta(k_y - k_0)w^2(k_y)dk_y = P_{rad}^\infty \tilde{w}^2(k_y - k_0) \tag{15}$$

Intensity is thus expressed as:

$$I_{rad}^F(\omega,\theta_r) = I_{rad}^\infty \mathbf{sinc}^2(k_y - k_0) \tag{16}$$

The finite-sized transmission loss at a given incidence θ_e in the emitter is obtained from the infinite transmission loss under incidence α by the relationship:

$$\tau_{Finite}(\theta_e) = \frac{I_{n\_rad}^{finite}}{\rho_e c_e \cos\theta_e} = \frac{1}{\rho_e c_e \cos\theta_e}\frac{\displaystyle\int_0^{k_0} Z_f^\infty v^2 \cos(\alpha)\left|\mathbf{sinc}(k_0 - k_y)\right|^2 dk_y}{\displaystyle\int_0^{k_0}\left|\mathbf{sinc}(k_0 - k_y)\right|^2 dk_y} \tag{17}$$

Pushing the reference incident intensity under the integrand, gives the relationship between the infinite and finite transmission loss.

$$\tau_{Finite}(\theta_e) = \frac{\displaystyle\int_0^{k_0}\frac{Z_f^\infty v^2 \cos(\alpha)}{\rho_e c_e \cos\theta_e}\left|\mathbf{sinc}(k_0 - k_y)\right|^2 dk_y}{\displaystyle\int_0^{k_0}\left|\mathbf{sinc}(k_0 - k_y)\right|^2 dk_y} \approx \frac{\displaystyle\int_0^{\pi/2}\tau_\alpha^\infty \cos^2\alpha \left|\mathbf{sinc}(k_e \sin\theta_e - k_e \sin\alpha)\right|^2 d\alpha}{\displaystyle\int_0^{\pi/2}\cos(\alpha)\left|\mathbf{sinc}(k_0 - k_y)\right|^2 d\alpha} \tag{18}$$

The finite transmission loss is therefore obtained as a cosinus/sinc²-weighted average of the infinite transmission loss. This correction is called ***Convolution*** correction.

A more resource-demanding correction has been proposed in [3] and considers the finite window aperture (without the layer) as an additional transmission loss with specific radiation efficiency. A single specular wave impinging the aperture with $\theta_0 - incidence$ is carrying an incident intensity:

$$I_0 = \frac{p_0^2}{\rho_0 c_0} \cos \theta_0 \qquad (19)$$

When the layer is infinite, the radiated power is expressed as:

$$I_{rad}^{\infty} = \frac{p_r^2}{\rho_r c_r} \cos \theta_r \qquad (20)$$

The sound transmission loss coefficient in finite condition, τ_F, is written as function of infinite transmission coefficient, τ_{∞}:

$$\tau_F = \frac{I_r^F}{I_0} \frac{I_r^{\infty}}{I_r^{\infty}} = \tau_{\infty} \frac{I_r^F}{I_r^{\infty}} \qquad (21)$$

The insertion loss of the layer is assumed independent of the aperture.

The ratio $\dfrac{I_r^F}{I_r^{\infty}}$ is equal to the ratio of the intensity radiated by the velocity trace of the incident pressure to the intensity radiated by the infinite aperture. In next formulas emitter and receiver fluids are assumed of different nature.

$$I_r^F = \sigma_{rad} \rho_r c_r v_{n0}^2 = \sigma_{rad} \frac{\rho_r c_r p_0^2}{[\rho_0 c_0]^2} \cos^2 \theta_0 \text{ and } I_r^{\infty} = \frac{p_0^2}{\rho_0 c_0} \cos \theta_r \qquad (22)$$

$$\frac{I_r^F}{I_r^{\infty}} = \sigma_{rad} \frac{\rho_r c_r}{\rho_0 c_0} \frac{\cos^2 \theta_0}{\cos \theta_r} \qquad (23)$$

For identical fluids both sides of the aperture, the ratio of finite to infinite intensity becomes:

$$\frac{I_r^F}{I_r^{\infty}} = \sigma_{rad} \cos \theta_0 \qquad (24)$$
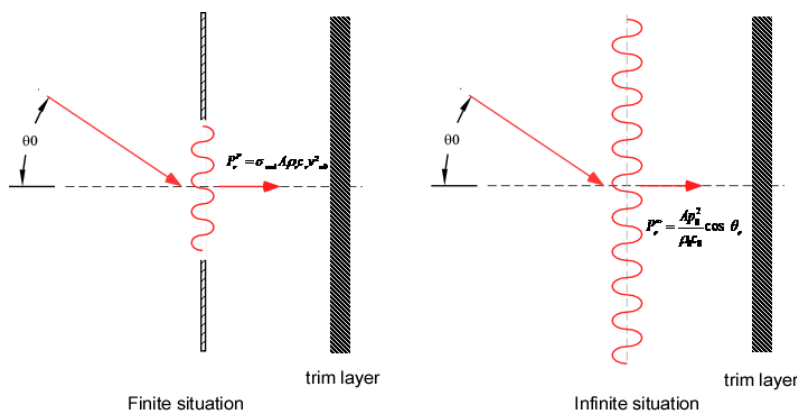
Figure 3. Radiation efficiency of the aperture.

Formula (24) proposes a cosinus/radiation efficiency weighting of the infinite transmission loss and requires to calculate the radiation efficiency of the aperture prior to apply the correction. This correction is called ***Sigmarad*** correction. Advanced demonstration of this correction may also be

6

found in [4]. Formula (14) may be modified using the normal velocity to the aperture, v_n. In that case, (14) becomes:

$$P_{rad}^F(\omega,\theta) = \frac{1}{2\pi} \int \frac{\rho_f c_f}{\cos\theta} \left| \tilde{v}_n(k_y) \right|^2 dk_y = \frac{k_0}{2\pi} \int \frac{\rho_f c_f}{\sqrt{k_y^2 - k_0^2}} \left| \tilde{v}_n(k_y) \right|^2 dk_y \tag{25}$$

The operator $1/\sqrt{k_y^2 - k_0^2}$ is proportional to the infinite radiation efficiency of the aperture and (14) may be then re-formulated as (22). The simple convolution correction does not operate on normal velocity and will imply some limitation in low frequency range as shown in next numerical examples.

4   NUMERICAL EXAMPLES

4.1 Mass layer transmission loss

The Transmission Loss in dB is computed as $TL = -10\log\left(\dfrac{I_t}{I_{inc}}\right)$ in SEA+ software [5]. SEA+ implements both **Convolution** and **Sigmarad** correction for transmission loss calculation using TMM. In that case graphed *TL's* are all random-incidence *TL* obtained by averaging discrete incident $TL(\theta)$ (over 0 to 90°). Fluid is standard air both sides.

TL is predicted for a 2.7 mm-thick mass layer with volume density 1000 kg/m³. The mass layer has then a density of 2.7 kg/m². The area is fixed to 1x1 m².

Predicted TL's are given in Figure 4 for three configurations: no correction, **Convolution** correction and **Sigmarad** correction. In Figure 4-left, spatial windowing increases the TL of 2 dB on average around 1000 Hz and below, larger correction factor is obtained with **Sigmarad** below 300 Hz (up to + 5 dB). In Figure 4 right, the opening is 5x5 m². The spatial windowing correction is found smaller as expected.

4.2 Dash panel firewall insulation

The firewall of a dash panel may incorporate many layers as shown hereafter in Figure 5 (left). In that particular case, the spatial window is about same effect than in previous case :+ 5 dB correction for **Sigmarad** correction in figure 5 (right).

4.3 Mass layer transmission loss in water

The calculation of transmission loss is performed by inserting between two SEA water cavities a 1x1 m² mass layer of mass density 390 kg/m². Figure 6 shows the effect of spatial windowing on TL leading to an increase of around 4 dB at low frequencies.

4.4   Spatial windowing of mechanical line junctions

The convolution correction is used also for correcting analytical calculation of line junctions SEA coupling loss factors (CLF) in [5]. This correction is applicable when two plates with a common edge are only physically connected on a fraction of this edge.

Figure 7 shows the predicted configuration. The Coupling Loss Factor (CLF) is first identified numerically by the Virtual SEA (VSEA) method [2], [6], applied to FEM model of the two coupled plates. This model takes into account the actual coupling geometry: the two plates are welded on 100 mm on a fraction of plate edges (1m length). VSEA model delivers the flexural CLF between the two plates in direction 1-2 and 2-1. Plate 1 is made of 1-mm steel and plate 2 of wood (10 mm-

OSB). Both systems are meshed with plate elements in Nastran and modal extraction is pushed up to 2000 Hz which corresponds to the frequency band of VSEA CLF identification.

Second, CLF is predicted from two coupled analytical plates of which transmission loss is computed from wave theory in SEA+. In the analytical model, plates are connected on a line of 100 mm. The edge length is declared equal to 1 m. Spatial windowing correction is successively activated and deactivated and resulting CLF's are compared with VSEA CLF. Results are given in Figure 8. We can see the effect is much more important than in previous acoustic cases. The spatial windowing analytical prediction is closer from VSEA CLF. Spatial windowing is thus a useful tool to improve the predictive quality of analytical mechanical transmission in SEA models.
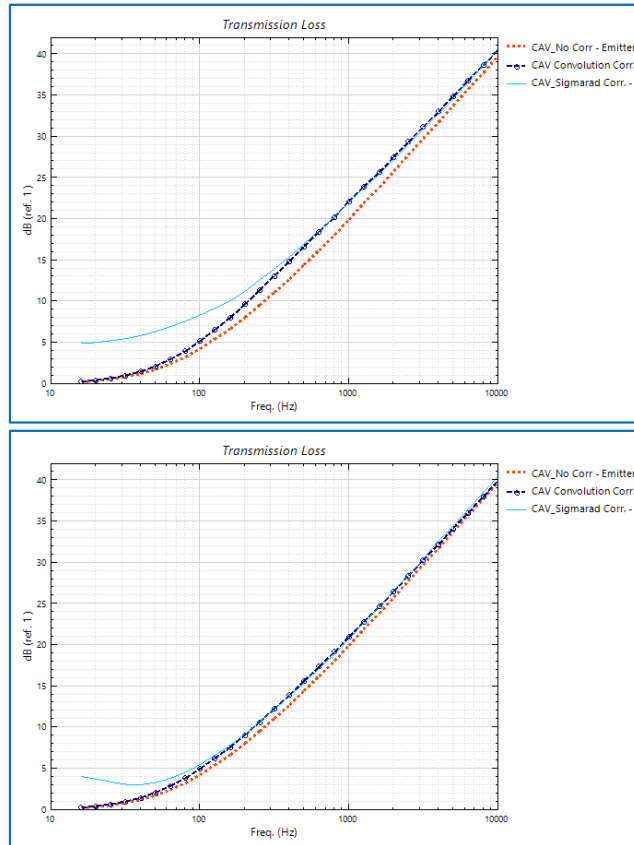
Figure 4. TL with spatial windowing for 2.7 kg/m² mass layer Area 1x1m² (left) & 5x5 m² (right).
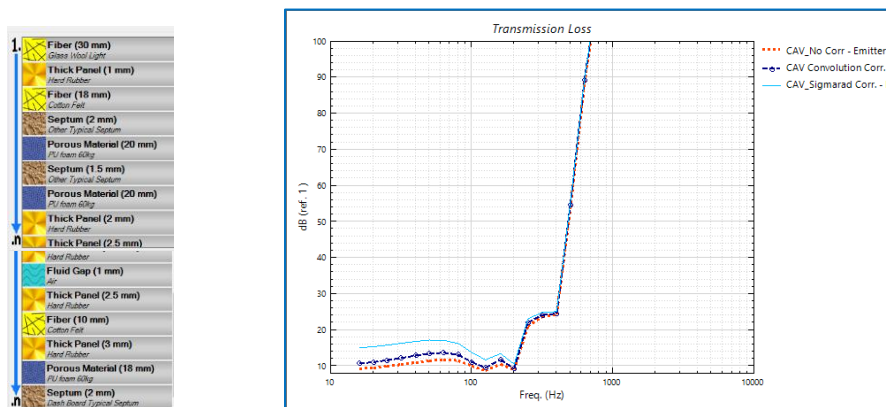
Figure 5. On right TL of dash panel (firewall) with and without spatial windowing (Area 1x1.5 m²) and on left dash panel layers.

8
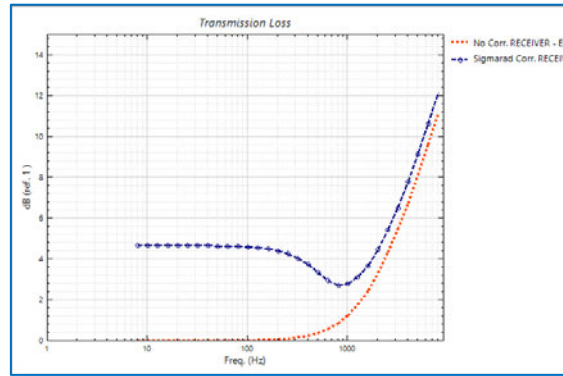
Figure 6. TL of mass layer 390 kg/m^2 between two sea water cavities (without spatial windowing and with **Sigmarad** correction).
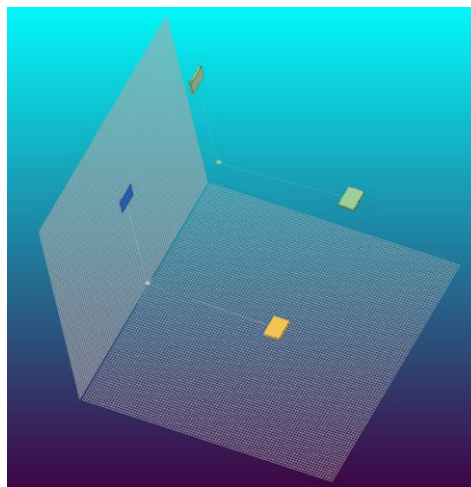
Figure 7. Spatial windowing correction of structural line-junction CLF (two square-1 m² plates connected at right angle on 100 mm along 1 m edge).
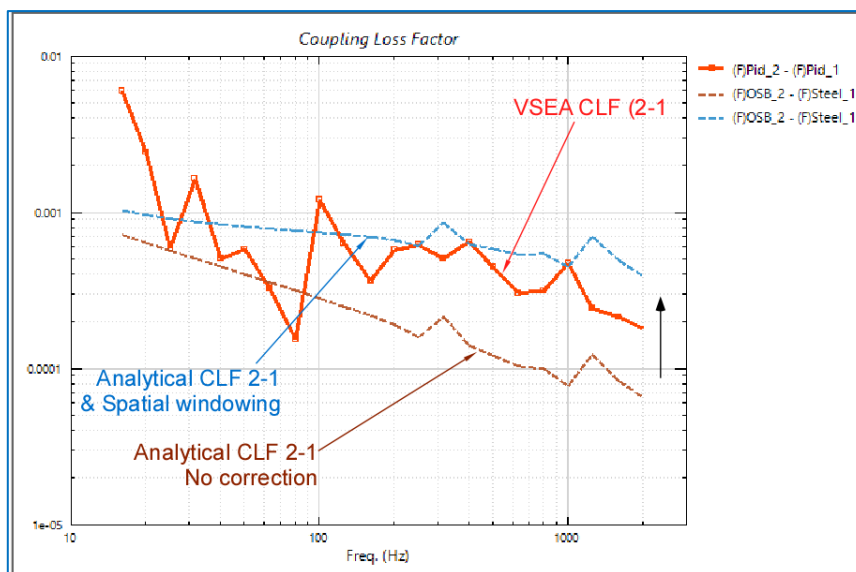
Figure 8. Spatial windowing correction of structural CLF compared to VSEA CLF.

5   CONCLUDING REMARKS

Spatial windowing technique is an efficient way to make analytical predictions closer to measured data. The amplitude of the correction depends on the physics of the model. We have seen an attenuation of the mass-driven sound transmission of around 4 to 5 dB in the low frequency regime for the acoustic coupling. For structural coupling, corrections vs. frequency are more broadband and may lead to increase of vibration transmission. They should be enabled when only a fraction of connected plate edge is allowed to transmit noise. More generally, the correction is valid when the aperture size of the junction is smaller than the container (plane or line) size. For dynamical systems with complex topology modelled using SEA, some care has then to be taken before to apply the relevant corrections.

REFERENCES

[1]   L. Beranek and L. Istvan, *Noise and Vibration Control Engineering: Principles and Applications*, Second Edition, Wiley.

[2]   Gagliardini L., Houillon L., Petrinelli L. and Borello G., "Virtual SEA: Mid-Frequency Structure-Borne Noise Modeling Based on Finite Element Analysis", 03NVC-94, SAE 2003.

[3]   Villot M., Guigou-Carter C. and Gagliardini L., Predicting the Acoustical Radiation of Finite Size Multi-Layered Structures by Applying Spatial Windowing on Infinite Structures, *Journal of Sound and Vibration*, 245(3), 433-455, 2001.

[4]   Allard J. F. and Atalla N., *Propagation of Sound in Porous Media*, Wiley, 2009.

[5]   Borello G., *SEA+ Advanced Theory* manual 2016, InterAC.

[6]   Borello G., *SEAVirt Theory* manual 2016, SEA+ software module, InterAC.

10

UNCERTAINTY QUANTIFICATION IN MID-FREQUENCY RANGE SIMULATIONS USING THE STATISTICAL MODAL ENERGY DISTRIBUTION ANALYSIS

E.Sadoulet-Reboul[1] , K. L. Van Buren[2], M.Ouisse[1], S.Cogan[1] and L.Maxit[3]

[1]Univ. Bourgogne Franche-Comté - FEMTO-ST Institute, CNRS/UFC/ENSMM/UTBM
Department of Applied Mechanics, 24 rue de l'épitaphe, 25000 Besançon
Email: Emeline.Sadoulet-Reboul@univ-fcomte.fr, Morvan.Ouisse@femto-st.fr,
Scott.Cogan@univ-fcomte.fr
[2]Los Alamos National Laboratory, Mail Stop F605
Los Alamos, New Mexico, 87544, United States
Email: klvan@lanl.gov
[3]Univ Lyon, INSA-Lyon
LVA EA677, F-69621, Villeurbanne, France
Email: Laurent.Maxit@insa-lyon.fr

ABSTRACT

The Statistical Modal Energy Analysis (SmEdA) is a variant of the Statistical Energy Analysis (SEA) developed to predict the high frequency behaviour of structures by dividing them into subsystems without requiring a modal energy equipartition. The method is based on the modal bases of uncoupled subsystems, and coupling loss factors are derived from Finite Element Analysis. Uncertainty Quantification can thus be applied in such a configuration at either the subsystem level, with respect to the physical input parameters (eg material properties and dimensions), or at the coupled model level with respect to the coupling factors or the modal data used to compute them. For UQ to be physically meaningful, it is necessary that uncertainty modeling at the coupled model level be representative of uncertainty at the subsystem level. A strategy based on sampling at the coupled model level using a covariance matrix computed at the subsystem level is proposed here. The methodology is formulated and applied to a four-subsystem structure. The UQ performed at the two levels is shown to be coherent but with reduced computational costs at the coupled model level allowing a higher number of UQ simulations.

1 INTRODUCTION

The prediction of high frequency noise and vibration levels requires the use of specific methods. One well-known approach is the Statistical Energy Analysis (SEA) that provides a statistical average of the vibratory or acoustical behavior of the structure of interest [1, 2]. The full system is divided into subsystems and energy flows between these subsystems are computed. The parameters and equations are obtained under certain hypotheses [3], one of which is the modal equipartition of energy in subsystems. To overcome this limitation, the SmEdA approach has been developed as a reformulation of SEA without requiring energy equipartition [4]. The modal energy equations lead to coupling coefficients derived from finite element simulations.

In an uncertain context the evaluation of the impact of different sources of uncertainty on the output quantifies of interest, called Uncertainty Quantification (UQ), is an important part of a global Quantification of Margins and Uncertainties (QMU). The effect of uncertainties in SEA models has been studied using many approaches such as the partial derivative analysis and the design of experiments on SEA factors [5], parametric methods on FE components and non-parametric studies on SEA elements in a hybrid FEM/SEA approach [6]. It thus appears that uncertainty quantification can be performed using either the input physical parameters or the coupled parameters involved in the energy equations and derived from the physical inputs [7]. UQ at the coupled model level is computationally more efficient but has no direct physical meaning. It is thus necessary to include information about how uncertainty is propagated from the subsystem level. A strategy based on the use at the coupled model level of a covariance matrix computed at the subsystem level is proposed here. The SmEdA equations are first recalled to introduce the coupled parameters, then the proposed methodologyis presented, and finally this methodology is applied to an academic model of four coupled plates.

2 SMEDA EQUATIONS

SmEdA relies on the equations of the SEA. The main difference between both approaches is that SmEdA not only describes the coupling between subsystems but also the coupling between the individual modes of the different subsystems. In this way the restrictive modal equipartition assumption is not required. The resulting formulation for a two-subsystems model can be written as follows,

$$\Pi_{inj}^{p} = \left(\omega_p \eta_p + \sum_{q=1}^{M_2} \omega_c \eta_{pq} \right) E_p - \sum_{q=1}^{M_2} \omega_c \eta_{pq} E_q, \ \forall p \in [1, ..., M_1], \tag{1}$$

$$\Pi_{inj}^{q} = -\sum_{p=1}^{M_1} \omega_c \eta_{pq} E_p + \left(\omega_q \eta_q + \sum_{p=1}^{M_1} \omega_c \eta_{pq} \right) E_q, \ \forall q \in [1, ..., M_2]. \tag{2}$$

where p and q are modes of subsystems 1 and 2, respectively, with corresponding natural frequencies, ω_p and ω_q, M_1 and M_2 are the number of modes for subsystems 1 and 2. The internal loss factors (ILF) η_p and η_q are computed for each mode, and the coupling loss factors (CLF) η_{pq} are derived for a pair of modes rather than for a subsystem pair. The subsystem energies are then determined as sums of the modal energies,

$$E_1 = \sum_{p=1}^{M_1} E_p, \quad E_2 = \sum_{q=1}^{M_2} E_q. \tag{3}$$

The method requires calculating the modes of each uncoupled subsystem, generally determined from a Finite Element (FE) analysis, and it can be considered as an approach for which uncertainty quantification can be performed at different levels: the first one, at the subsystem level,

where uncertainty is introduced in the input parameters (material, geometry), and the second one, at the coupled model level where uncertainty is introducing in the modal data.

3   METHODOLOGY

The figure 1 presents the flowchart of activities performed to quantify uncertainties at the subsystem and at the coupled model levels. Mesh refinement ensures the insensitivity of results to mesh discretization and a significant level of prediction uncertainty. Sampling is performed with the Monte Carlo (MC) method based on an assumed multivariate normal distribution. This sampling uses the mean and covariance matrix that define the distribution: the covariance matrix informs the sampling at the coupled model level using the results of sampling at the subsystem level. Effect screening is useful to limit uncertainty quantification to the most influential variables leading to significant computational savings.
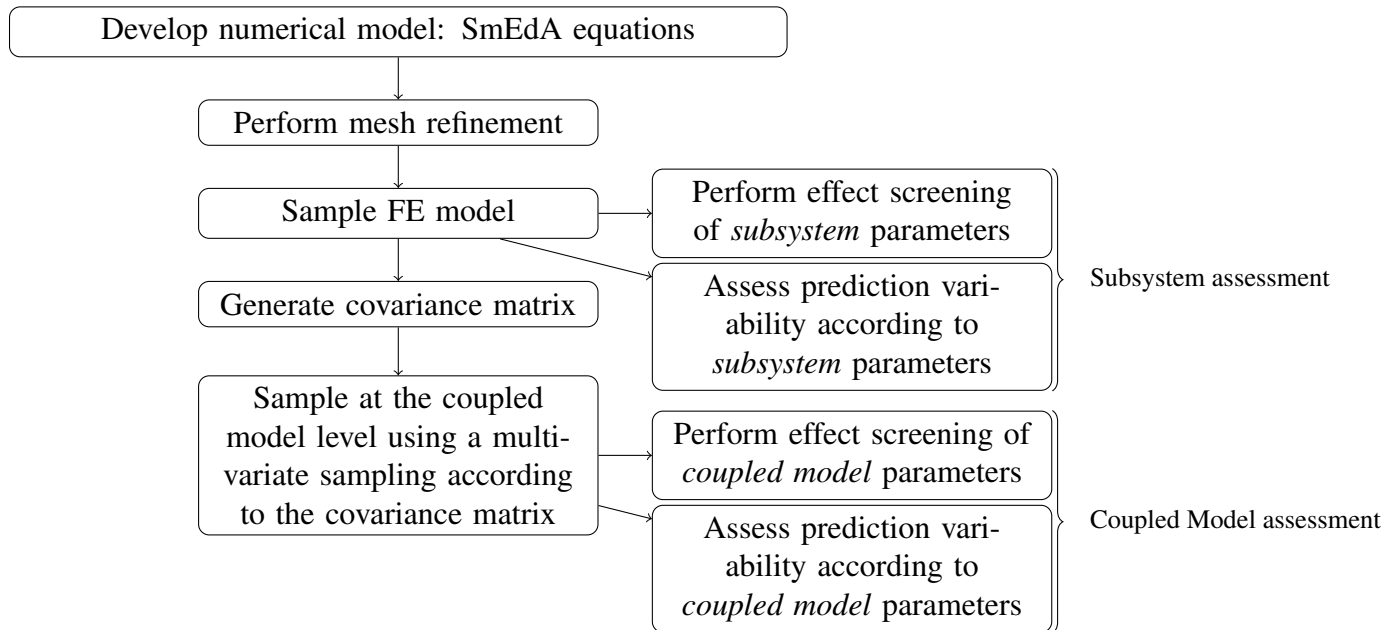
Figure 1: Uncertainty Quantification at the *subsystem* and at the *coupled model* levels.

4   CASE-STUDY APPLICATION

The methodology is applied to a four-subsystem model shown in figure 2. The plates are made of steel ($E = 210$ GPa, $\rho = 7800$ kg.m^3), with a constant damping ratio of 0.05 for all subsystems. Mesh refinement is performed both at the subsystem level and at the coupled system level to ensure less than 1% error on the natural frequencies up to 2 kHz, and the convergence of the number of modes and SmEdA energies. 5000 Monte Carlo samples are performed at the coupled model level and the vibratory energies thus obtained are compared to those resulting from 100 Monte Carlo samples performed at the subsystem level.
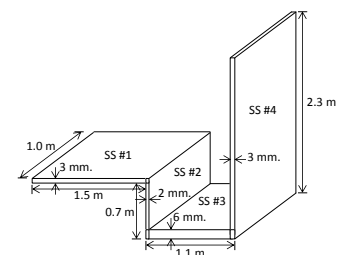
Figure 2: Four-subsystem model.

Figure 3 presents the vibratory energies obtained at the subsystem level (in red) and at the coupled level (in blue), and the global statistics for the Monte Carlo sampling : the diagonal plots show the comparison of the SmEdA histograms for each subsystem, the out-diagonal plots show the comparison of the output-output scatter plots for pairs of subsystems. The consistency in the obtained results demonstates that the use of coupled data such as the natural frequencies

3

constitute an adequate proxy to the use of the input parameters for uncertainty quantification, leading to a significant reduction in computational costs.
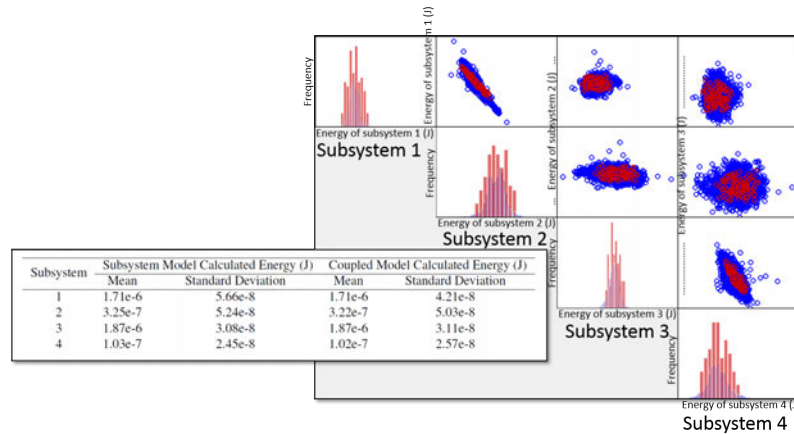

Subsystem	Subsystem Model Calculated Energy (J)		Coupled Model Calculated Energy (J)	
	Mean	Standard Deviation	Mean	Standard Deviation
1	1.71e-6	5.66e-8	1.71e-6	4.21e-8
2	3.25e-7	5.24e-8	3.22e-7	5.03e-8
3	1.87e-6	3.08e-8	1.87e-6	3.11e-8
4	1.03e-7	2.45e-8	1.02e-7	2.57e-8

Figure 3: Comparison of results obtained from MC sampling at the *subsystem* and *coupled model* levels.

5 CONCLUDING REMARKS

UQ at the subsystem level leads to results that are physically meaningful but computationally expensive, while UQ at the coupled model level is harder to interpret but computationally more efficient. The proposed approach uses a covariance matrix informed by minimal sampling at the subsystem level to propagate uncertainty at the coupled system level. The results are shown to be consistent and the reduction in computational burden allows to increase the range of predictions.

REFERENCES

[1] R.H. Lyon and G. Maidanik. Power flow between linearly coupled oscillators. *The Journal of the Acoustical Society of America*, 34(5):623 – 639, 1962.

[2] A. Le Bot. *Foundation of statistical energy analysis in vibroacoustics*. Oxford University Press, Oxford, United Kingdom ; New York, NY, first edition edition, 2015. OCLC: ocn919757793.

[3] T. Lafont, N. Totaro, and A. Le Bot. Review of statistical energy analysis hypotheses in vibroacoustics. *Proceedings of the Royal Society of London A: Mathematical, Physical and Engineering Sciences*, 470(2162):20130515, 2013.

[4] L. Maxit and J.L. Guyader. Extension of SEA model to subsystems with non-uniform modal energy distribution. *Journal of Sound and Vibration*, 265(2):337 – 358, 2003.

[5] A. Culla, W. D'Ambrogio, and A. Fregolent. Parametric approaches for uncertainty propagation in SEA. *Mechanical Systems and Signal Processing*, 25(1):193 – 204, 2011.

[6] A. Cicirello and R.S. Langley. The vibro-acoustic analysis of built-up systems using a hybrid method with parametric and non-parametric uncertainties. *Journal of Sound and Vibration*, 332(9):2165 – 2178, 2013.

[7] J.-L. Christen, M. N. Ichchou, B. Troclet, O. Bareille, and M. Ouisse. Global sensitivity analysis of analytical vibroacoustic transmission models. *Journal of Sound and Vibration*, 368:121 – 124, apr 2016.

4

A LAGRANGIAN BASED DAMAGE INDICATOR FOR USE ON COMPLEX STRUCTURES'

Y. Hui[1] , H. L. Kwa[1][2] O. Bareille[1*] and M. Ichchou[1]

[1]Ecole Centrale de Lyon
36 avenue Guy de Collongue, 69134 Ecully, France
Email: yi.hui@doctorant.ec-lyon.fr, hian-lee.kwa@master.ec-lyon.fr,
olivier.bareille@ec-lyon.fr, mohamed.ichchou@ec-lyon.fr

[2]University of Surrey
Guildford, United Kingdom

ABSTRACT

Structural health monitoring has attracted much attention in many engineering fields. The four-level damage identification process: existence, localisation, severity and prediction of damage evolution, can be partly realised if a suitable indicator is chosen. In this paper a new "Lagrangian" damage indicator for rib-reinforced plates is presented based on the structure's frequency response function (FRF). This has been developed from the concepts of strain energy and curvature allowing for the creation of a Lagrangian indicator field. Damages and singularities present in the structure are characterised by a localised drop in value of the Lagrangian in the field. In the post-processing of results, the plate is split into multiple segments and the mean Lagrangian is calculated for each segment. This process has made the damage more apparent and easier to identify. These results show that the developed damage indicator is effective in detecting damages in rib-reinforced plate structures.

1   INTRODUCTION

Plate-like structures are widely used in various engineering applications, ranging from their use in the aerospace industry to the mechanical industry. As such, it is important to monitor the damage condition of plates to avoid unpredicted structural failure which may have severe consequences. In the field of structural health monitoring (SHM), several techniques have been proposed to monitor damage on various structures. Doebling [1] performed a thorough review of damage identification techniques, focusing on the changes of dynamic response of the structure. These are more commonly known as vibration-based methods. A method based on a structure's mode curvature shape was first demonstrated by Pandey [2] who successfully applied it to both cantilever and simply supported beams. Based on this concept, Wu [3] proposed an indicator based on the change in uniform load surface (ULS) curvature for two-dimensional plate structures using the mode shapes of the first few modes of a damaged and undamaged structures. Another damage indicator proposed by Navabian [4] was based on a plate's mode shape curvature as well as its displacement and slope. Cornwell [5] has also shown that the mode strain energy before and after being damaged can be calculated from its curvature. An indicator using spectral strain energy proposed by Bayissa [6] has been proven to be effective in detecting damage in plates. This damage indicator uses the curvature power spectral density and moment power spectral density of the plate. Sampaio [7] chose to use a plate's frequency response function (FRF) to calculate its curvature.

In this paper a new Lagrangian damage indicator is introduced, based on the concepts mention above. This damage indicator was tested through the use of a $0.6m \times 0.0005m \times 0.0085m$ Akyplac$^®$ plate numerically modelled in ANSYS. The plate was then separated into 20 segments to calculate the mean damage indicator for each segment.

2   DAMAGE INDICATORS

It has been previously proven that the curvature can be an effective indicator for damage identification in structures [2, 7], which is calculated by using the finite central difference approximation. When taking into account the kinetic, strain and elastic energies of the plate, the Lagrange damage indicator can be written as:

$$\frac{1}{2}mv^2 - \frac{1}{2}D[(\frac{\partial^2 u}{\partial x^2})^2 + (\frac{\partial^2 u}{\partial y^2})^2 + 2(1-\nu)(\frac{\partial^2 u}{\partial x \partial y})^2 + 2\nu\frac{\partial^2 u}{\partial x^2}\frac{\partial^2 u}{\partial y^2}] \tag{1}$$

However, this paper focuses only on the kinetic variables - curvature and velocity. The effect of mass and flexural stiffness were neglected as these variables are difficult to measure when a plate is in service. Calculations of the damage indicator at the specific point of damage as well as the damaged segment showed that they increased when the poisson's ratio was increased from 0 to 0.5. However, this increase did not affect the average segment values significantly. Thus, the Poisson's Ratio was set as 0 for all performed calculations, ignoring the elastic energy term. The damage indicator used in this paper is therefore defined as:

$$ind = velocity^2 - (\frac{\partial^2 u}{\partial x^2})^2 - (\frac{\partial^2 u}{\partial y^2})^2 - 2(\frac{\partial^2 u}{\partial x \partial y})^2 \tag{2}$$

With the FRF of the structure, the distribution of the Lagrangian indicator field was obtained across the entire plate.

3   DAMAGE DETECTION ON NUMERICAL EXAMPLES

For the analyses, an Akyplac® twinwall polypropylene sheet was used. It is a lightweight durable corrugated plastic and is mostly used for packaging purposes. The model used for the dynamic analyses was a $0.6m \times 0.8m \times 0.01m$ plate, composed of a 0.75mm-thick upper and lower layer reinforced by 97 ribs with a thickness of 8.5mm. These ribs had the dimensions of $0.6m \times 0.0005m \times 0.0085m$ and were each separated by a 8.3mm gap. They were numbered sequentially from the bottom up and a distance of 1.6mm was between the first/last rib and its nearest edge. The SOLID185 elements in ANSYS were chosen for the modelling of both the layers and the ribs. Along the edges of plate, free boundary conditions were used and an excitation point was placed normally in the middle of plate.

Two types of damages were discussed: the damage in the ribs and the damage on the skin. It was found that the first Lagrangian-like indicator was more sensitive to the damage in the ribs. In the model used, there were 100mm-long damages in the 32th and 33th ribs with a distance of 100mm to the nearest edge. The presence and location of damage were able to be identified (Figure 1(a)) through a drops in the Lagrangian at the area of the damage. The lowest Lagrangian value was found to be -6.825 compared to the average plate Lagrangian value of -0.0587.

Numerical analyses on other damage cases were also performed. Figure 1(b) shows the indicator field with a 40mm-long damage in the 32th and 33th ribs where it can be seen that the zone with the reduced Lagrangian indicator has shortened. As such, this indicator is able to estimate the length of the damaged area, and hence, the severity of the damage. It should be noted that the Lagrangian value dropped to -49.171 at the damage zone compared to the plate average of -0.082. Another 100mm-long damage was created in the 23th and 24th ribs. The indicator field in Figure 1(c) shows the location and the length of damages. Furthermore, a study was performed with the two damages cases previously discussed and an additional 40mm-long damage in the 61th and 62th ribs (Figure 1(d)). From this, it has been shown that the indicator is able to identify multiple damaged areas on the same structure.
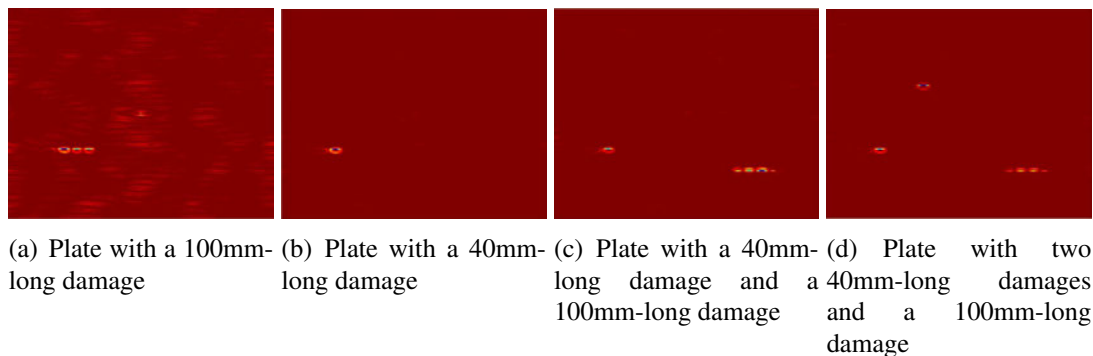

(a) Plate with a 100mm-long damage   (b) Plate with a 40mm-long damage   (c) Plate with a 40mm-long damage and a 100mm-long damage   (d) Plate with two 40mm-long damages and a 100mm-long damage

Figure 1. Lagrangian indicator field for different damage cases

4   RESULTS POST-PROCESSING

To make the results less susceptible to noise and other minor variations in the Lagrangian Indicator field, both the damaged and the undamaged plates were divided into 20 segments of $0.15m \times 0.16m$ each. The mean Lagrangian for each damaged segment was then calculated and the difference between it and its undamaged counterpart was found.

Two damage cases were used; the plate with a 100mm-long damage and the plate with a 40mm-long damage. Again, these damages have been characterised by a drop in the segment's

Lagrangian value. As can be seen in Figure 2, it is easier to identify the damage locations when it is compared to the original undamaged plate. The Lagrangian of the damaged segment also varied for the different damage cases. It was modelled to be at -0.4667 for the 40mm-long damage case and -0.1139 for the 100mm-long damage case.
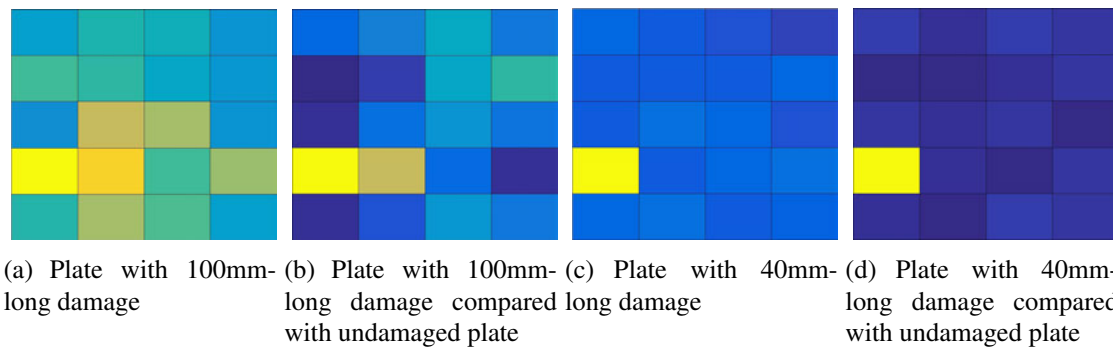

(a) Plate with 100mm-long damage

(b) Plate with 100mm-long damage compared with undamaged plate

(c) Plate with 40mm-long damage

(d) Plate with 40mm-long damage compared with undamaged plate

Figure 2. Damaged plates split into segments and compared to undamaged plate

5 CONCLUSION

In this paper, a Lagrangian damage indicator based on the kinetic energy and curvature of the plate has been proposed. This damage indicator has been proven to be effective in detecting and locating the presence of one or multiple damage cases.

For future work on the subject, the relationship between the damage severity and the change in Lagrangian should be further investigated. This will allow for a more accurate measurement of the extent of damage.

REFERENCES

[1] S. W. Doebling, C. R. Farrar and M. B. Prime, A summary review of vibration-based damage identification methods, *Shock and vibration digest* **30(2)**, 91-105 (1998).

[2] A. Pandey, M. Biswas and M. Samman, Damage detection from changes in curvature mode shapes, *Journal of Sound and Vibration* **145**, 321-332 (1991).

[3] D. Wu, S. Law, Damage localization in plate structures from uniform load surface curvature, *Journal of Sound and Vibration* **276**, 227-244 (2004).

[4] N. Navabian, M. Bozorgnasab, R. Taghipour and O. Yazdanpanah, Damage identification in plate-like structure using mode shape derivatives, *Archive of Applied Mechanics*, 1-12 (2015).

[5] P. Cornwell, S. Doebling and C. Farrar, Application of the strain energy damage detection method to plate-like structures, *Journal of Sound and Vibration* **224(2)**, 359-374 (1999).

[6] W. Beyissa, N. Rarito, Structural damage identification in plates using spectral strain energy analysis, *Journal of Sound and Vibration* **307**, 226-249 (2007).

[7] R. Sampaio, N. Maia and J. Silva, Damage detection using the frequency-response-function curvature method, *Journal of Sound and Vibration* **226(5)**, 1029-1042 (1999).

A DISCRETE MODEL FOR VIBRATION OF CRACKED BEAMS RESTING PARTIALLY ELASTIC FOUNDATIONS

A.KHNAIJAR[1], R.BENAMAR

[1]Laboratoire des Etudes et Recherches en Simulation, Instrumentation et Mesures (LERSIM)
Université Mohammed V – Ecole Mohammadia des Ingénieurs, Avenue Ibn Sina, BP 765, Rabat, Morocco.
E-mail addresses: khnaijar@gmail.com, rhali.benamar@gmail.com*

ABSTRACT

The present paper has introduced a discrete physical model to approach the problem of vibrations of cracked beams resting partially on elastic foundations. The model consisted on a beam made of several small bars, evenly spaced. The bending stiffness was modeled by spiral springs, the crack was also modeled as a spiral spring with a reduced stiffness, and the Winkler soil stiffness was modeled using linear vertical springs. Concentrated masses, presenting the inertia of the beam, were located at the bar ends. This model has the advantage of simplifying parametric studies, because of its discrete nature, allowing any modification in the mass and the stiffness matrixes. Therefore, an application for a simply supported beam resting partially on elastic foundations case is carried out.

Keywords: *Discrete; vibration; crack; foundation.*

1 INTRODUCTION

The vibration of cracked beam resting on elastic foundations wears a great interest for many engineering fields such as civil and mechanical engineering. Both continuous and discrete models have been established in order to approach this problem. However, the discrete models have the advantages of being more adaptable to computer programmes. A discrete method such as the Finite Element Method (FEM) is the first to address the problem numerically [1]. The Differential Quadrature Method (DQM) is also employed for the solution to similar engineering problems involving beam vibration and foundation [2]. Therefore, P. Malekzadeh and G. Karami [3] gather the advantages of both previous methods (DQM & FEM), to investigate the free vibration and buckling analysis of thick beams on two-parameter elastic foundations.

In this paper and based on previous works [4] a discrete model for the vibration of cracked beam resting partially on elastic foundations is established. A straight application of the theory is developed, where a cracked simply supported beam is resting partially on elastic foundations.

2 GENERAL FORMULATION

Based on the model introduced by A. Khnaijar and R. Benamar [4] for nonlinear vibrations of uncracked beams resting on elastic foundation, a new model is developed here by introducing a crack beam model. The present model consists on the N-degree-of-freedom discrete model shown in Fig. 2, with N masses $m_1,\ldots,m_N$, located at the ends of (N+1) rigid bars, connected by *(N+2-1)* spiral springs simulating the beam bending stiffness. The crack is modeled by *a* spiral spring simulating the crack reduced stiffness, estimated using the model presented in Fig. 1. The stiffness of the rth spring is denoted by C_r, for $r = 1$ to $(N+2-1)$), and the stiffness coefficient of the spiral spring, presenting the crack, is denoted by C^c. The bending moment M in the rth spiral spring connecting the bars *(r-1)* is given by: $M = -C_r\Delta\theta$; $\Delta\theta = \theta_r - \theta_{r-1}$ being the angle between the bars adjacent to the node r. The Winkler foundations are modeled using the longitudinal vertical spring distribution, with k^l_r presenting the stiffness coefficient of the rth linear spring, for $r = 1$ to N.
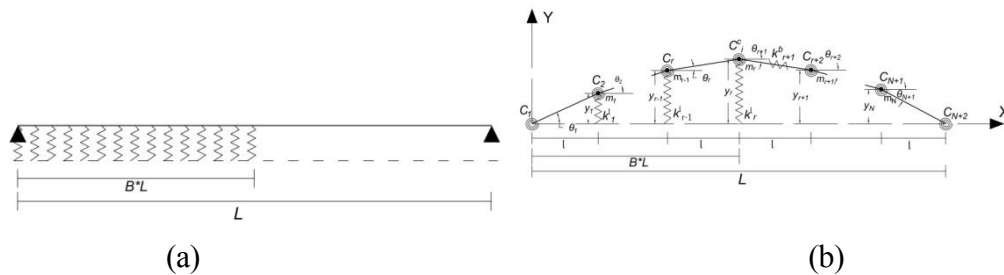
Figure 1. A partially supported continuous S-S beam.

The nondimensional formulation of the problem presented is essential to widen the validation basis of the results. To define the nondimensional parameters $m_{ij}, k^s_{ij}, k^l_{ij}$, let's put:

$$\frac{m_{ij}}{m^*_{ij}} = \frac{\overline{m_{ij}}}{m^*_{ij}} = \frac{\rho SL}{N+1} \; ; \; \frac{k^1_{ij}}{k^{1*}_{ij}} = \frac{\overline{k^1_{ij}}}{k^{1*}_{ij}} = \frac{EI(N+1)^3}{L^3} ; \frac{k^s_{ij}}{k^{s*}_{ij}} = \frac{\overline{k^s_{ij}}}{k^{s*}_{ij}} = \frac{EI(N+1)^3}{L^3} ; \text{for } i, j = 1,..,N \tag{1}$$

As the nondimensional formulation is established, the general expression for m^*_{ij}, k^{*s}_{ij} and k^{*l}_{ij} for the discrete model become as follows:

- The nondimensional Mass tensor $\left[\mathbf{M}^*\right]/m^*_{ij}$:

$$m^*_{ij} = \delta_{ij} \text{ for } i, j = 1,.., N \tag{2}$$

- The nondimensional Spiral springs tensor $\left[\mathbf{K}^{s*}\right]/k^{s*}_{ij}$

$$k^{*s}_{(r-2)r} = \left(\frac{I^x_r}{I}\right) \text{ for } r = 3,...,N \tag{3}$$

$$k^{*s}_{(r-1)r} = -\frac{2}{I}\left(I^x_r + I^x_{r+1}\right) \text{ for } r = 2,...,N \tag{4}$$

$$k^{*s}_{rr} = \frac{1}{I}\left(I^x_r + 4I^x_{r+1} + I^x_{r+2}\right) \text{ for } r = 1,...,N \tag{5}$$

and the other values of k^{*s}_{ij} are obtained by symmetry relations, or are equal to zero.

$$I^{cr}_i = \frac{bh^3(1-\xi)^3}{12} \text{ with } \xi = \left(\frac{a}{h}\right) \text{ and } I = \frac{bh^3}{12} \tag{6}$$

I_{cr} and I, for rectangular sections, are respectively being the inertial moment of the reduced beam, calculated by putting the neutral fiber of this section in the center of the reduced beam section and the inertial moment for uncracked section, and ξ refers to the dimensionless crack depth ratio.

- The nondimensional Winkler springs tensor $\left[\mathbf{K}^{*l}\right]/k^{*l}_{ij}$

$$k^{*l}_{ij} = \alpha\delta_{ij} \text{ for } i, j = 1,...,N \tag{7}$$

The Winkler stiffness coefficient is given by:

α and λ being the nondimensional parameter:

$$\alpha = \frac{kL^4}{EI(N+1)^4} = \frac{\lambda}{(N+1)^4} \text{ with } \lambda = \frac{kL^4}{EI} \tag{8}$$

3 APPLICATION: A PARTIALLY SUPPORTED BEAM WITH A SIMPLY SUPPORTED ENDS

A simply supported beam is assumed to be subjected to the effect of partial intermediate supports Fig. 1. Fig. 2 shows the cracked beam first two modes frequencies, for a simply supported beam, versus the crack position (c/l) and depth ($\xi=a/h$), with no elastic foundation ($B=0$). Fig. 3 shows the cracked beam first two modes frequency, for a simply supported beam, versus the crack position (c/l) and depth ($\xi=a/h$), the ratio of the supported span to the total span B chosen covers 50 percent of its span ($B=0.5$) and the soil stiffness $\lambda = \pi^4$. The shift in the curves for the case with elastic soil proves the effect of the soil stiffness and position on the beam frequencies.
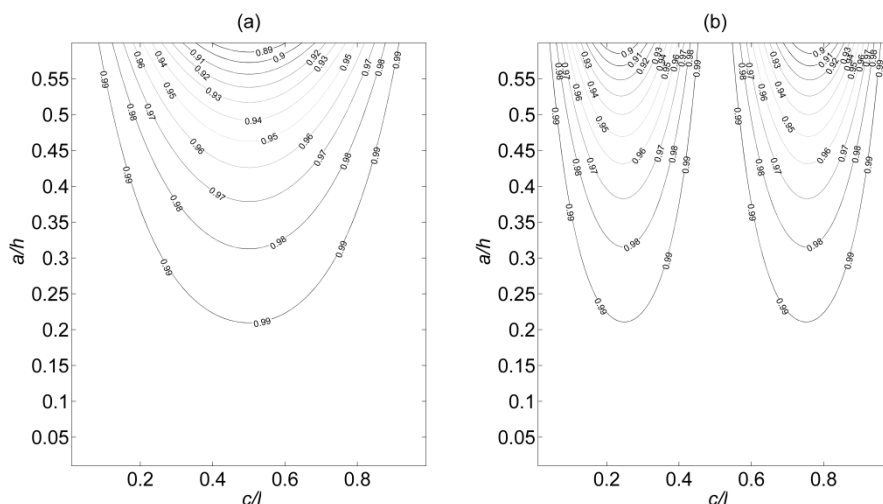
Figure 2. The cracked beam frequency, for a simply supported beam, versus the crack position (c/l) and depth ($\xi=a/h$) for the first 2 modes: $B=0$.
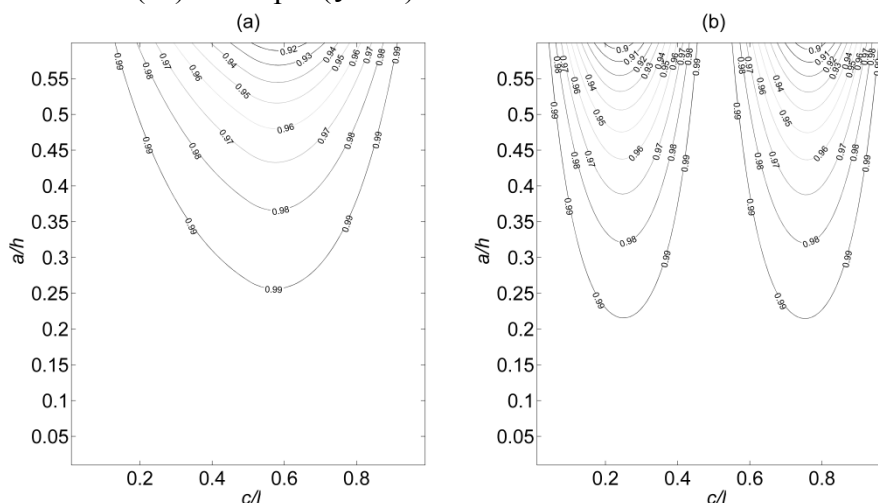
Figure 3. The cracked beam frequency, for a simply supported beam, versus the crack position (c/l) and depth ($\xi=a/h$) for the first 2 modes: $B=0.5$ and $\lambda = \pi^4$

4   CONCLUSION

A discrete model of cracked beam resting partially on elastic foundation was introduced in the present paper. An application was carried out for a simply supported beam, where a frequency curves versus crack magnitudes and locations were drawn for a partially supported cracked beam.

REFERENCES

[1]   T. Yokoyama, "Vibration analysis of Timoshenko beam-columns on two-parameter elastic foundations" Computers and Structures, 61:995–1007, 1996.

[2]   Chang-New Chen, "Vibration of prismatic beam on an elastic foundation by the differential quadrature element method", Computers and Structures, 77:1-9, 2000.

[3]   P. Malekzadeh and G. Karami, "A mixed differential quadrature and finite element free vibration and buckling analysis of thick beams on two-parameter elastic foundations", Applied Mathematical Modelling, 32:1381–1394,

[4]   A. Khnaijar and R. Benamar. A Discrete Model for Nonlinear Vibration of Beams Resting on Various Types of Elastic Foundations, Advances in Acoustics and Vibration, 2017.

STATISTICAL ENERGY ANALYSIS, ASSUMPTIONS AND VALIDITY

A. Le Bot[1] , N. Totaro[2] and T. Lafont[1,2]

[1]Laboratory of tribology and system dynamics
Ecole centrale de Lyon, Ecully, FRANCE
Email: alain.le-bot@ec-lyon.fr, thibault.lafont@cpe.fr

[2]Laboratory of vibration and acoustics
INSA de Lyon, Villeurbanne, FRANCE
Email: nicolas.totaro@insa-lyon.fr

ABSTRACT

This study outlines the question of validity of statistical energy analysis with regard to its assumptions. We discuss the necessity of four assumptions: rain-on-the-roof excitation, weak coupling, large number of modes and light damping. We show that when all of these assumptions are satisfied, statistical energy analysis provides a satisfactory result but when one of these assumptions is violated, statistical energy analysis prediction presents a discrepancy compared to a reference calculation. The discussion is illustrated with a simple example of coupled plates.

1   INTRODUCTION

Statistical energy analysis [1, 2] is a well-known theory of sound and vibration suited to the domain where the number of modes is so high that the usage of finite element method is not tractable. Statistical energy analysis is based on statistical physics concepts such as mean-free path, modal density and equipartition of energy. It is the counterpart of Sabine's theory of reverberation in room acoustics. Although it is commonly claimed that statistical energy analysis applies at high frequencies, it is more exact to say that statistical energy analysis is the theory of thermal equilibrium where sound and vibration are diffuse.

2   STATISTICAL ENERGY ANALYSIS

The principle of statistical energy analysis is quite simple. The main result is Lyon's law [3], or coupling power proportionality, which states that two subsystems in which the vibrational field (velocity field for structure or acoustical pressure for sound) is diffuse and lightly coupled exchange a vibrational power proportional to the difference of their modal energies. This reads

$$P_{ij} = \omega \eta_{ij} n_i \left(\frac{E_i}{n_i} - \frac{E_j}{n_j} \right) \tag{1}$$

where P_{ij} is the mean power between subsystems i and j, E_i the mean energy, n_i the modal density, ω the centre of the frequency band of analysis, and η_{ij} the coupling loss factor. If the two subsystems are coupled through a spring of stiffness K then the coupling loss factor is

$$\eta_{ij} = \frac{\pi K^2 n_j}{2\omega^3 M_i M_j} \tag{2}$$

where M_i is the total mass of subsystem i. If the two subsystems are two-dimensional (like plates) and are coupled through a line of length L whose mean transmission efficiency is noted T, then

$$\eta_{ij} = \frac{L c_{g_i} T}{\pi \omega S_i} \tag{3}$$

where c_{g_i} is the group speed of waves in subsystem i and S_i its area. In all cases, the coupling between subsystems must be conservative.

To derive this result, the minimal list of assumptions is

- Rain-on-the-roof excitation

- Light damping

- Large number of modes

- Weak coupling

When these conditions are satisfied, the vibrational field is diffuse in all subsystems or equivalently, equipartition of energy is reached. Each subsystem is therefore in the state of thermal equilibrium. The weak coupling limits the exchange of energy to a small level which does not disturb the diffuse field in the vicinity of coupling.

3   DIFFUSE FIELD

The first three conditions ensure that a diffuse field is established in all subsystems [4]. In Figure 1 is shown the relative standard deviation of repartition of energy in rectangular plates. The abscissa is the number of wavelengths per mean-free-path and the ordinate is the damping loss factor of the plate. We see that the domain of diffuse field for which the standard deviation is small is confined by two criteria. The frequency must be high (vertical line) and the attenuation of waves must be small (horizontal line tilted on the right).
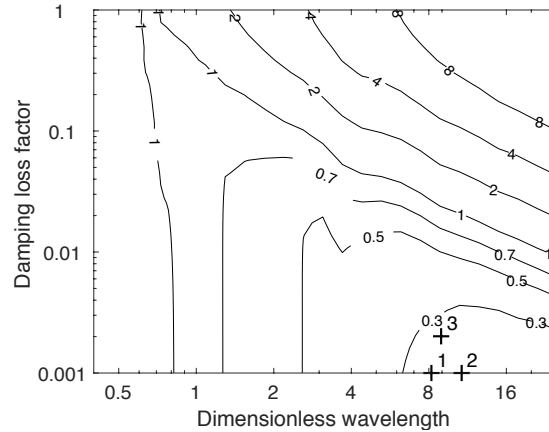
Figure 1: Relative standard deviation of repartition of energy in rectangular plate in the dimensionless wavelength - damping loss factor plane. The zone of diffuse field is confined to high frequencies and small damping.

4   EXAMPLES OF COUPLED PLATES

The first example is shown in Figure 2. The structure is made of six rectangular plates assembled by right angle couplings. Plate 1 is submitted to a random transverse force field (rain-on-the-roof). The response is observed in plate 6. Three calculations are performed: a reference calculation based on a closed form solution of the governing equations, a SEA calculation with Equations (1) and (3), and a geometrical acoustics prediction (see Reference [5]). We observe that when the damping is light ($\eta = 1\%$), the prediction of SEA is always correct. The four octave bands are located in the region of diffuse field of Figure 1. The error of SEA, compared with a reference calculation is negligible. But when the damping is strong ($\eta = 10\%$), significant errors of SEA appear. Note that geometrical acoustics prediction (ray) is still valid because the frequency remains high. This examples highlights that SEA requires two conditions in general: large number of modes (high frequency) and low damping.

The second example is shown in Figure 3. The system is made of three rectangular plates with random resonators and coupled through a spring of stiffness K. The coupling strength is controlled by varying K. A single point random force assumed to be white noise is applied to the top plate. Two calculations are performed: SEA by applying Equations (1) and (2) and a reference calculation by a semi-analytical method. We observe that the thermal conductivity $\beta_{\mathrm{SEA}} = \omega \eta_{ij} n_i$ predicted by SEA is correct compared to the ratio $\beta_{\mathrm{REF}} = P_{ij}/(E_i/n_i - E_j/n_j)$ computed by the reference calculation when the coupling is weak. But when the coupling strength increases, a large discrepancy is observed between SEA and reference. It may even arise that the flow of energy is reversed giving a negative value of β. This anti-thermodynamics flow of energy has been observed even for a population of nominally similar plates with different realisations of resonators as shown by the grey zones of Figure 3.
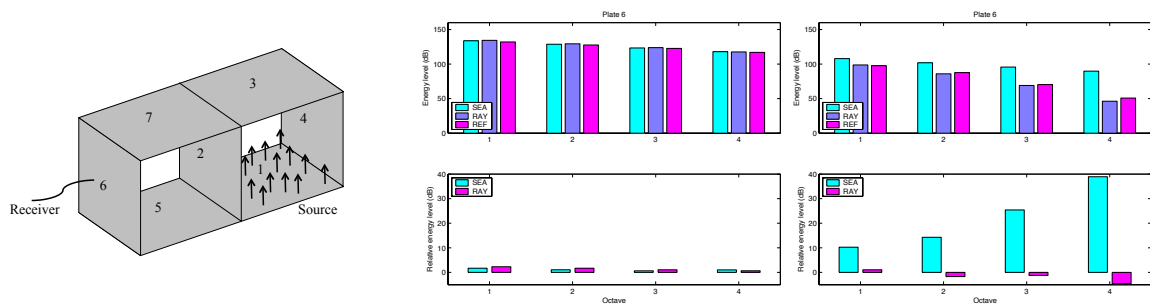
Figure 2: Six rectangular plates in bending vibration and results for $\eta = 1\%$ (middle) and $\eta = 10\%$ (right). The upper bar diagrams give the energy versus octave band by three methods: SEA, ray and reference calculation. The lower bar diagrams give the error of SEA and ray-tracing compared to reference.
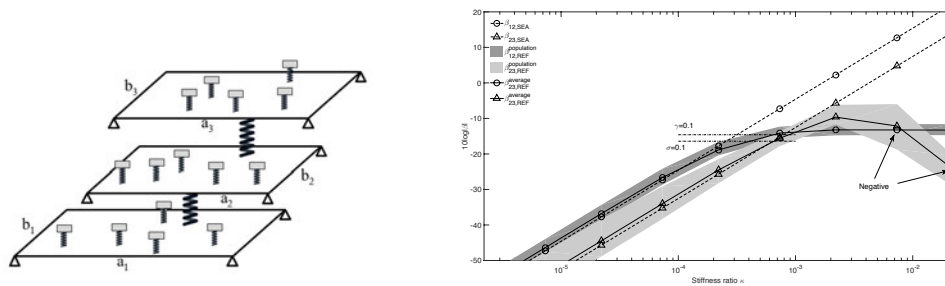

Figure 3. Three rectangular plates in bending vibration with random resonators.

5   CONCLUDING REMARKS

In this paper, we have shown that statistical energy analysis is based on several assumptions that are random excitation, light damping, large number of modes, and weak coupling. Although the first three conditions may be reduced to the single condition of diffuse field in all subsystems, the last one is an imperative requirement that cannot be relaxed in general.

REFERENCES

[1] Lyon RH, DeJong R. 1995 *Theory and Application of Statistical Energy Analysis* Butterworth-Heinemann, Boston MA.

[2] Le Bot A. 2015 *Foundation of Statistical Energy Analysis in Vibroacoustics.* Oxford University Press, Oxford.

[3] Lyon RH, Maidanik G. 1962 Power flow between linearly coupled oscillators *J. Acoust. Soc. Am.* **34**, 623–639.

[4] Lafont T, Totaro N, Le Bot A. 2014 Review of statistical energy analysis hypotheses in vibroacoustics. *Proc. R. Soc. A* **470**, 1471–2946.

[5] Le Bot A. 2007 Derivation of statistical energy analysis from radiative exchanges *J. Sound Vib.* **300**, 763–779.

STABILITY OF ROTATING MACHINE SUPPORTED BY ACTIVE MAGNETIC BEARINGS DURING BASE MOTION

C. Jarroux[1] , J. Mahfoud[1], R. Dufour[1], F. Legrand[1], B. Defoy[2] and T. Alban[2]

[1]Université de Lyon, INSA-Lyon, LaMCoS UMR5259, LaMCoS
18-20 rue des Sciences, Bât J. d'Alembert, 69621 Villeurbanne Cedex, France
Email: clement.jarroux@insa-lyon.fr

[2]GE Oil & Gas Thermodyn
480 allée G. Eiffel, BP 119, 71203 Le Creusot Cedex, France

ABSTRACT

The study is devoted to rotor supported by Active Magnetic Bearings (AMBs) and subjected to base motion. The machine casing is considered rigid and able to move with 3 translations and the 3 rotations. The objective is to assess the suitability of machine supported by AMBs to withstand base motions for applications such as compressors on FPSO (Floating production storage and offloading). Experiments were performed of an academic test rig. The controller was an augmented PID similar to that used in industrial applications. At this stage, only harmonic motion is considered. Two levels of severity were applied. The results obtained in this configuration demonstrated the stability of the rotor-AMB system.

1   INTRODUCTION

Turbomachines manage the fluid-structures energy transfer, they have to be able to withstand severe environmental conditions. Consequently, a major focus of the research engaged by industrial and academic laboratories concerns their reliability in any circumstances. Most of the rotating machinery can be considered as on-board machines. Aircraft engines, automotive turbochargers or compressors fixed on an oil offshore-platform are notable examples. The base motion generates complex rotor dynamics in particular in the case of base rotations yielding parametric instabilities. At certain rotating frequencies of the support, combined with the natural frequencies of the rotor, instability zones emerge and depend on the amplitude of the rotation angle [1, 2]. The dynamic behaviour of on-board rotating machines should then be carefully analysed to improve the reliability and to maintain a maximal operability of the machines. On the other hand, Active Magnetic Beatings (AMBs) are more and more utilized in industrial applications for their several advantages (no wear due to friction, no oil system, compact space requirement). They are inherently unstable, therefore a feedback control is needed and the PID is the most implemented controller. Different studies focused on the control of rotors subject to base motion using magnetic forces. The sinusoidal base motion of a non-rotating mass mounted on magnetic bearings was experimentally and numerically analysed by [3]. Three PID controllers were tested and non-linear responses were found in the less damped controller. In [4], the transient dynamic behaviour of a rotor supported by homopolar permanent magnet bias magnetic bearings subjected to vertical shock was simulated. Rotor-to-stator contact was found. The feedforward control loop is often used to control base motion in parallel with a feedback control loop. This method was employed by [5] to reduce the harmonic translation motion of the base considering a rigid rotor supported by non-linear AMBs. Three controllers were tested in [6] and the H_∞ controller has the greatest effect in reducing the rotor response due to unbalance and horizontal shock of the base. This work is a part of a research program aim at the development of turbomachines mounted on AMB. Previous work demonstrated the effectiveness of the developed control strategies to have a reliable behaviour under several operating conditions [7]. In this work, experimental investigations are presented, the aim is to assess the effectiveness of the developed augmented PID to maintain the rotor operating under severe events. Only experimental results are presented. The experimental conditions will be presented first, then the results will be discussed and finally conclusions and perspectives will be dressed.

2   EXPERIMENTAL CONDITIONS

The experiments were performed using an academic test rig (Figure 1). It is a commercial product manufactured by SKF® and was delivered with a dedicated PID controller. The test rig is equipped with two identical AMB called NDE (Non Drive End) and DE (Drive End) bearings. Each bearing has a maximum static capability of 280N. The action lines are positioned in the configuration load between axes. They are powered in differential driving mode with a bias current of 1A. Current are provided in the range of 0-3A using PWM amplifiers. Two displacement sensors (variable reluctance probes) are integrated in the housing of each bearing and are non-colocalised with actuators. The Input/Output panel gives access to the displacements measured and enables entering current settings for the amplifiers. Each AMB has one back-up bearing with a clearance radius of 0.1mm. The shaft is composed of three parts bolted together. A central part (diameter: 25mm; length 344mm) with a decentred disc 120mm in diameter and 25mm long placed at two-thirds of the central part length from the DE side, together with two shaft ends (50mm of main diameter). The stack of laminated steel sheets is shrunk on each of these two shafts. The total rotor length is 645mm. The rotor mass is 6.5kg. The rotor is driven by a 500W electric motor with a maximum speed of 12,600rpm. Power transmission is provided

by a flexible coupling. The operating speed range used in this work is 0 to 9,500rpm, which includes two first rigid modes. The speed of the rotor is monitored by using a speed sensor placed close to the motor.
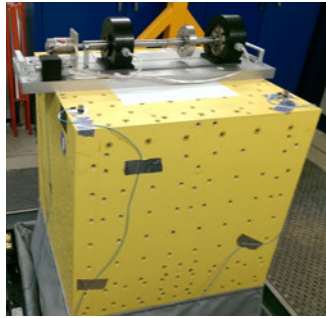

Figure 1. Experimental test rig.

The test rig was mounted on a shaker that has 6 real-time pilots able to reproduce various combinations of solicitations along the 3 axes (translations and rotations) with a maximum mass of 450 kg in a range [0-250] Hz. Sine, random, shock excitations or replication of signals previously recorded and with a maximum acceleration of 10g, $\pm$ 50 mm in translations and $\pm$ 4 degrees in rotation. The rotor at rest was subject during 5 seconds to two cases of excitation: 0.3g at 20 Hz, and 1.1g at 20 Hz. Only the last case led to contact between the rotor and the touch-down bearings (TDB). The characteristics of an augmented PID were determined as a function of the dynamic behaviour and the number of modes included in the operating conditions. Also, the stiffness was chosen low and the damping was concentrated around system natural frequencies (Figure 2).
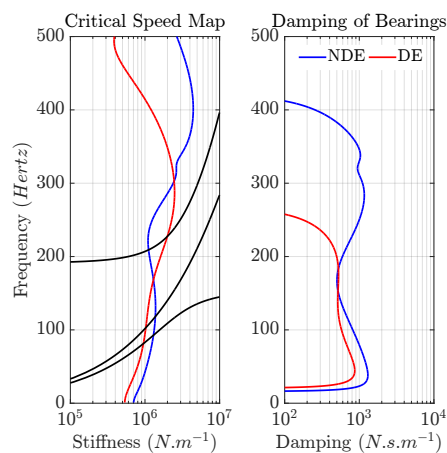
Figure 2. Controller damping and stiffness.

3   RESULTS

The displacements measured are presented in Figure 3. It can be noticed that the PID operated efficiently since the rotor was still controlled even after the contact with the TDB.

4   CONCLUDING REMARKS

The study was devoted to the assessment of the dynamic behaviour of a rotating machine under sever excitations. The aim was to check the ability of the developed control strategy to maintain

3
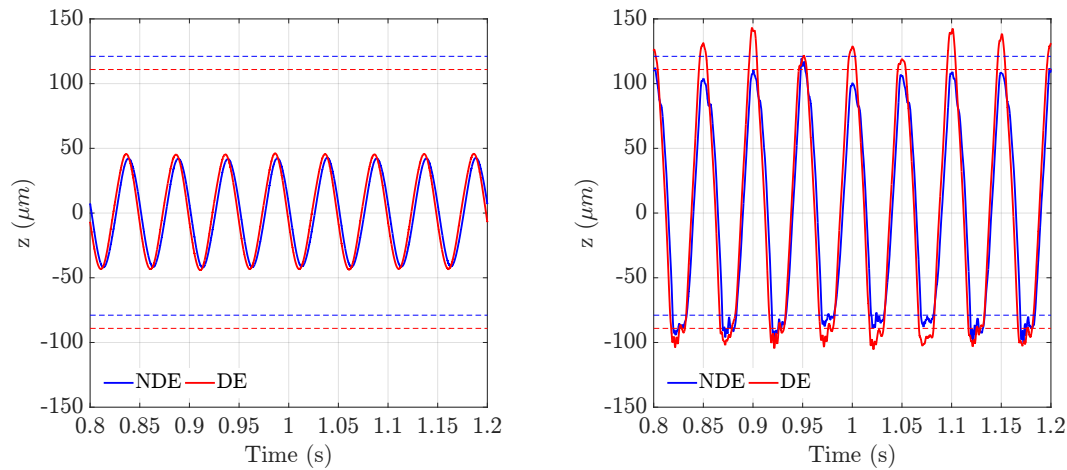
Figure 3. Displacement of the rotor subject to 0.3g (left) and to 1.1g (right).

the rotor in operation. In this paper only first results are presented, and it could be seen that the controller was able to maintain the rotor in operation.

5　ACKNOWLEDGMENTS

REFERENCES

[1] M. Dakel, S. Baguet, and R. Dufour. Steady-state dynamic behavior of an on-board rotor under combined base motions. *Journal of Vibration and Control*, 20(15):2254–2287, 2014.

[2] Q. Han and F. Chu. Parametric instability of flexible rotor-bearing system under time-periodic base angular motions. *Applied Mathematical Modelling*, 39(15):4511–4522, 2015.

[3] M. E. Kasarda, J. Clements, A. L. Wicks, C. D. Hall, and R. G. Kirk. Effect of sinusoidal base motion on a magnetic bearing. In *IEEE International Conference on Control Applications.*, pages 144–149, 2000.

[4] L. A. Hawkins. Shock analysis for a homopolar, permanent magnet bias magnetic bearing system. (78712):V004T14A040, 1997. 10.1115/97-GT-230.

[5] Steven Marx and C. Nataraj. Suppression of base excitation of rotors on magnetic bearings. *International Journal of Rotating Machinery*, 2007:10, 2007.

[6] M. O. T. Cole, P. S. Keogh, and C. R. Burrows. Vibration control of a flexible rotor/magnetic bearing system subject to direct forcing and base motion disturbances. *Proceedings of the Institution of Mechanical Engineers, Part C: Journal of Mechanical Engineering Science*, 212(7):535–546, 1998.

[7] B. Defoy, T. Alban, and J. Mahfoud. Energy cost assessment of a polar based controller applied to a flexible rotor supported by amb. *Mechanical Engineering Journal*, 2015.

4

THE INDUCED BY MESHING STIFFNESS VARIATION DYNAMICS OF PLANETARY GEARS USING AN ITERATIVE SPECTRAL METHOD.

J. Perret-Liaudet, Y. Xu, J. Neufond, and E. Rigaud

Laboratoire de Tribologie et Dynamique des Systèmes, UMR 5513
École centrale de Lyon, member of the Université de Lyon, F69134 Écully, FRANCE
Email: joel.perret-liaudet@ec-lyon.fr, emmanuel.rigaud@ec-lyon.fr

ABSTRACT

We investigate in this study the dynamic behavior of planetary gear systems induced by the time-varying mesh stiffnesses of the sun-planet and the ring-planet meshes. These internal excitations are of parametric kind and induce, under stationary conditions, multi-frequencial responses. These responses lead to parametric resonances when natural eigenmodes defined from the mean values stiffnesses are excited. In order to compute the planetary gear dynamic responses, a previously defined iterative spectral method is introduced and extended to this context, significantly saving computation times. By expanding the solution in the modal basis computed from the mean characteristics of the system, this method is derived in the frequency domain and directly provides the spectrum of the response.

As an example, a simple single stage planetary gears multi-degree-of-freedom modelling is built. Eigenmodes, dynamic transmission errors and dynamic mesh forces are computed and analyzed. Finally, comparisons with the Runge-Kutta time integration scheme is performed to demonstrate the method validity.

1   INTRODUCTION

Planetary gear systems form a reliable and efficient way to design compact power transmissions with high gear ratio. Consequently, these transmissions are very popular from wind turbines to home automation applications, or again automatic gearboxes, to only cite few cases. Concerning the NVH performance, their noise characteristics remain often unacceptable, especially in view of the more restrictive standards in the context of reduction in pollutant and greenhouse gas emissions. In particular, demand is now strong for reducing weight while respecting the vibroacoustic performance and reliability. In this context, it becomes of great importance to introduce advanced simulation tools applying right to the design stage. Whining noise of planetary gears is especially addressed in this study. This dominant noise results from the dynamic behaviour of the gears induced by the static transmission errors. These main excitation sources at each meshing result from the teeth deflection and manufacturing errors. In the context of dynamic modelling, they are introduced as displacement periodic excitations and internal parametric excitations (meshing stiffness fluctuations). Particularity of the planetary gears, these last induce couplings between the multiple meshings. Consequently, equations of motion projected into the modal base built from the time averaged mesh stiffness remains coupled. The principal aim of this study is to demonstrate the capability of a previously introduced iterative spectral method [1-2] to treat the special case of planetary gears. This method is devoted to compute the stationary dynamic responses of parametrically excited systems with time-varying characteristics, such as stiffness, subjected to stationary deterministic or stochastic external excitation. The case of standard cylindrical gears are well mastered with this method compared to experimental results [3-4].

2   DYNAMIC MODELLING

Consider a single stage planetary gear, we introduced a lumped dynamical multi-degree-of-freedom model similar to that introduced in [5]. This planetary gear is composed of 3 planets. By neglecting the centrigugal and Coriolis forces, the matrix equation of motion is given by

$$\mathbf{M}\ddot{\mathbf{x}} + \mathbf{C}\dot{\mathbf{x}} + \sum_{j=1}^{6} k_j(t)\mathbf{R}_j\mathbf{R}_j^t\mathbf{x} = \sum_{j=1}^{6} k_j(t)\mathbf{R}_j\mathbf{R}_j^t\mathbf{x}_s \qquad (1)$$

In this equation $\mathbf{M}$ and $\mathbf{C}$ are respectively the mass and damping matrices, $\mathbf{R}_j$ is a structural vector witch couples wheels through the j-th meshing process, $\mathbf{x}$ is the dynamic response co-ordinates vector, $\mathbf{x}_s$ is the static ones, and $k_j(t)$ is the time-varying meshing stiffness of the j-th mesh which represents the internal parametric excitation. Summation over 6 corresponds to the 3 sun-planet meshes and the 3 ring-planet meshes.

By considering the free undamped time-averaged system, we can defined a mean modal basis, which appears to be the pertinent basis for describing the parametric resonance phenomena. This modal basis is then deduced from the following eigenvalue problem

$$(\sum_{j=1}^{6} \overline{k_j}\mathbf{R}_j\mathbf{R}_j^t - \Omega^2\mathbf{M})\mathbf{V} = \mathbf{0} \qquad (2)$$

where $\overline{k_j}$ represents the mean time value of $k_j(t)$. As an example, a typical mode is shown in Figure 1. In practice, it is possible also to distinguish the nature of these modes by meshing storage energy computation.
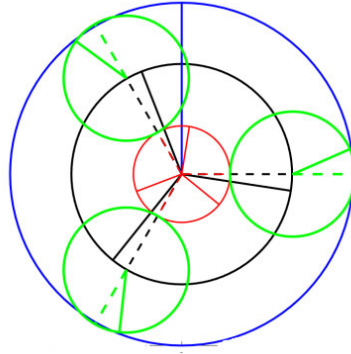
Figure 1. Typical mode with the modal motion of the planets and the sun.

3   COMPUTATIONAL PROCEDURE FOR THE STATIONARY RESPONSES

In order to simulate and compute the stationary coupled dynamic responses of the transmission model (which are multifrequential), we introduce the iterative spectral method. This method is based on the direct computation of the solutions in the spectral domain. To this end the matrix equation (1) is rewritten in the modal base as

$$diag[1]\ddot{\mathbf{q}} + diag[2\zeta_k\Omega_k]\dot{\mathbf{q}} + diag[\Omega_k{}^2]\mathbf{q} + \sum_{j=1}^6 g_j(t)\mathbf{r}_j\mathbf{r}_j^t\mathbf{q} = \sum_{j=1}^6 k_j(t)\mathbf{r}_j\mathbf{r}_j^t\mathbf{q}_s \quad (3)$$

or

$$diag[1]\ddot{\mathbf{q}} + diag[2\zeta_k\Omega_k]\dot{\mathbf{q}} + diag[\Omega_k{}^2]\mathbf{q} + \sum_{j=1}^6 g_j(t)\mathbf{r}_j E_j(t) = \sum_{j=1}^6 k_j(t)\mathbf{r}_j E_{(s)j}(t) \,(4)$$

In equations (3,4), $\mathbf{q} = \mathbf{V}\mathbf{x}$ is the modal co-ordinates vector, $\mathbf{r}_j = \mathbf{V}\mathbf{R}_j$ is the modal structural vector at the j-th mesh, Ω_k is the k-th natural frequency, ζ_k is the corresponding modal viscous damping, $g_j(t) = k_j(t) - \overline{k_j}$ is the fluctuating part of meshing stiffnesses, $E_j = \mathbf{r}_j^t\mathbf{q}$ is the dynamic transmission error and $E_{(s)j} = \mathbf{r}_j^t\mathbf{q}_s$, the static ones at the j-th mesh.

To solve equation (4), we introduced an iterative process directly achieved in the spectral domain. After several judicious transformations, the iterative process is written as follows

$$E_i(\omega)^{(p+1)} = E_i(\omega)^{(0)} - \sum_{j=1}^6 T_{ij}(\omega)[G_j(\omega) \otimes E_j(\omega)^{(p)}] \qquad (5)$$

with

$$T_{ij}(\omega) = \sum_{k=1}^N \mathbf{r}_{ik}\mathbf{r}_{jk}H_k(\omega) \qquad (6)$$

All the variables are expressed in the spectral domain by Fourier transform, the operator $\otimes$ denotes the convolution product, and $T_{ij}(\omega)$ is a function which only depends on the modal characteristics, in particular the classical frequency complex response functions $H_k(\omega)$.

4   RESULTS

After ensuring the method validity by comparisons with results obtained by Runge-Kutta time integration scheme, we have studied several test cases, including phase shifting effects between mesh stiffness fluctuations. As an example, we show in Figure 2 the evolution of the rms value of transmission errors versus the mesh frequency, obtained both by the Runge-Kutta method and our

Iterative Spectral method. We observe a very good agreement between methods. Further, one observes several dynamic amplifications that correspond to parametric resonances. These last can be easily interpreted by the knowledge of the spectral contents of responses and the mean modal characteristics of the geared system.
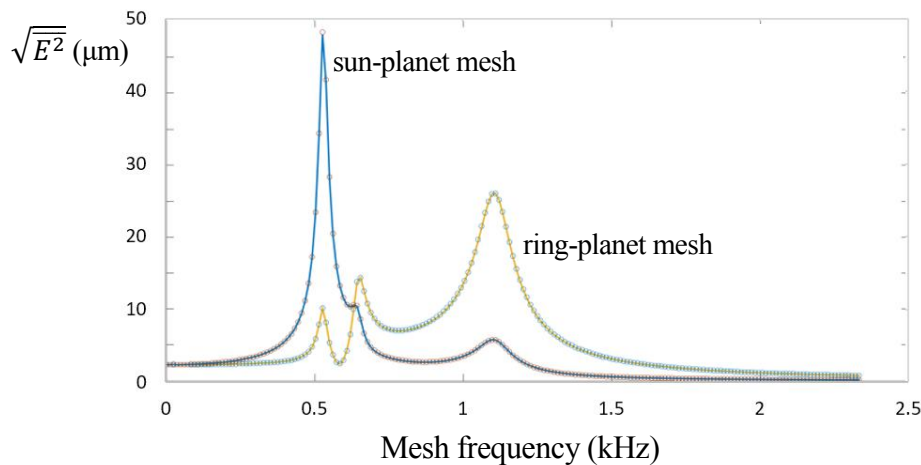

Figure 2. Rms values of Dynamic Transmission Errors versus the mesh frequency (continuous lines: Iterative Spectral Method; round marks: Runge Kutta Method).

Finally, results show that the main interest of the iterative spectral method is the very short computing time leading to very efficient simulation tools for predicting dynamic behaviour of planetary gear transmissions.

5   ACKNOWLEDGMENTS

REFERENCES

[1]   J. Perret-Liaudet, An original method for computing the response of a parametrically excited forced system. *Journal of sound and Vibration*. 196(2):165-177, 1996.

[2]   L. Bachelet, N. Driot, and J. Perret-Liaudet. A spectral method for describing the response of a parametrically excited system under external random excitation. *Journal of Computational and Nonlinear Dynamics*, *3*(1), 011008., 2008.

[3]   J. Perret-Liaudet, A. Carbonelli, E. Rigaud *et al*. Modeling of gearbox whining noise (No. 2014-01-2090). *SAE Technical Paper*, 2014.

[4]   A. Carbonelli, E. Rigaud, and J. Perret-Liaudet. Vibro-Acoustic Analysis of Geared Systems-Predicting and Controlling the Whining Noise. *Automotive NVH Technology*. Springer International Publishing, 63-79, 2016.

[5]   R. Parker. Analytical characterization of the unique properties of planetary gear free vibration. *Journal of Vibration and Acoustics, Trans. ASME* (121)3 :316-321, 1999.

EXTERNAL DISTURBANCE REJECTION FOR COMPRESSORS ON ACTIVE MAGNETIC BEARINGS

A. Bonfitto, N. Amati and A. Tonoli

Department of Mechanical and Aerospace Engineering – Mechatronics Laboratory
Politecnico di Torino, Turin, Italy
Email: angelo.bonfitto@polito.it, nicola.amati@polito.it, andrea.tonoli@polito.it

ABSTRACT

This paper presents the experimental results of a feedforward control strategy applied to a centrifugal compressor to reject disturbance coming from ground motion. The compressor is used for refrigeration tasks in public transport, it has a power of 30 kW with nominal speed of 51000 rpm and is levitated magnetically by means of cylindrical Active Magnetic Bearings (AMB). The proposed control strategy acts in combination with a classical decentralized control, it is implemented on a prototype of the compressor equipped with a substitute impeller without compression and is validated by means of acceleration tests simulating ground motion. The obtained results represents the basis for the future development of the proposed control strategy that will combined to an unbalance compensation action to minimize the effects of surge and stall of the compressor.

The paper illustrates the architecture of the machine, the control strategy and the experimental results conducted in laboratory environment and aiming to prove the validity of the proposed technique. According to the standards, the control is tested by shaking the system with an impulsive acceleration of the duration of 30ms and an amplitude of 5g. The obtained axial and radial displacement of the shaft are lower than 0.2mm.

1   INTRODUCTION

Compressors are widely adopted in several industrial processes like manufacturing, production lines and oil and gas industry. The main tasks requested to these machines are gas transportation and mixing, refrigeration and temperature control. In the last decades scientific research devoted many efforts to the development and the optimization of compressor technology aiming to improve reliability and performance. The current study is mainly focused on critical issues like stall and surge control and to the improvement of the efficiency of the machine. To this end, the adoption of active magnetic bearings (AMB) for the support of the compressor shaft witnessed a steady growth because of the intrinsic advantages of this technology: the absence of friction and fatigue issues, low maintenance allowing the installation in critical and harsh environments, the absence of contamination caused by lubricants and the possibility of tuning the suspension parameters by means of digital control [1][2].

When a compressor based on AMB is adopted for refrigeration tasks in mobile applications such as public transport, it is subjected to external disturbance coming from the ground that can generate heavy damage to the machine if the rotor comes in touch with the stator. It is important to find a control technique allowing the machine to work in safe condition without sacrificing the control devoted to the suspension of the shaft and permitting to minimize the clearance between the stator and the rotor to optimize the refrigeration efficiency [3][4]. In this paper a feedforward control acting in parallel to a classical decentralized control is adopted to reduce the axial and radial displacement of the shaft of a compressor with a nominal speed of 51000 rpm and a power of 30 kW used for refrigeration tasks in public transport. The proposed control technique is applied on a prototype of the compressor with an impeller mock up with the same inertial properties of the real one. The experimental validation is conducted with acceleration tests simulating ground motion. On the basis of this results, the strategy will be refined and used in combination with an unbalance compensation strategy to control surge and stall effects in real working conditions.

The architecture of the machine, the modelling and the control phases are exposed along with the experimental results conducted in laboratory environment aiming to prove the validity of the proposed technique. According to the standards, the control has been tested by shaking the system with an impulsive acceleration of the duration of 30ms and an amplitude of 5g. The reported experimental results show that maximum axial and radial displacement of the shaft are lower than 0.2mm.

2   ARCHITECTURE OF THE SYSTEM AND CONTROL DESIGN

The control strategy is tested on a prototype of the compressor supposed to be used for refrigeration and temperature control in public transport. Figure 1 reports the lateral cross section view of the machine. The shaft (17) is supported by means of cylindrical active magnetic bearings with two radial (4, 5, 12 and 13) and one axial actuator (11), the displacement is measured by five eddy current displacement sensors (1 and 3), an impeller mock up (14) is used in the place of the real one. An electronic control unit is responsible of the acquisition of displacement and current measurements and of the generation of the references for the power electronics adopted to drive the actuators.

The magnetic levitation is achieved with a standard decentralized control strategy based on two embedded control loops: the inner PI to control the current in the coils and the outer PID to control the position of the shaft. The rejection of the external disturbance is obtained by means of a feedforward control signal summed to the command of the external position controller as illustrated in Figure 2. The measured acceleration of the ground is filtered with an action that is equal to the inverse of the actuation dynamic.
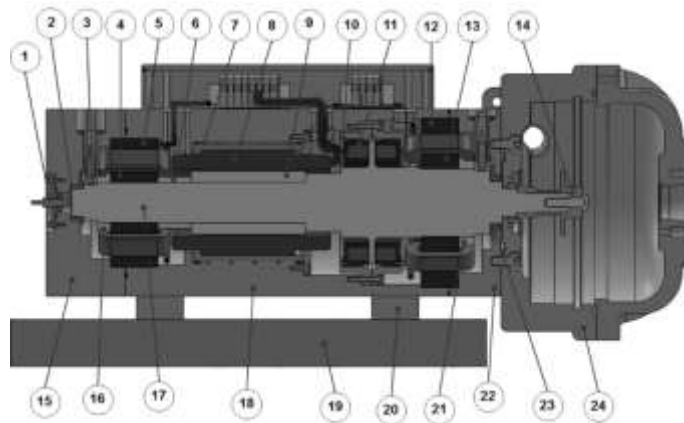
Figure 1. Lateral cross section view of the compressor. 1: Axial position sensor. 2: Lower landing bearing. 3: Radial position sensor. 5: Lower radial actuator, rotating part. 6: Lower radial actuator, static part. 7: Mechanical spacer. 8: Motor cooling system. 9: Electric motor, static part. 10: Electric motor, rotating part. 11: Axial bearing support. 12: Axial bearing. 13: Higher radial actuator, static part. 14: Higher radial actuator, rotating part. 15: Impeller mock-up. 16: Stator body, lower part. 17: Lower nut. 18: Shaft. 19: Stator body, central part. 20: Shaker slip table. 21: Compressor bracket (4 brackets in total). 22: Higher nut. 23: Stator body, higher part. 24: Higher landing bearing. 25: Volute.
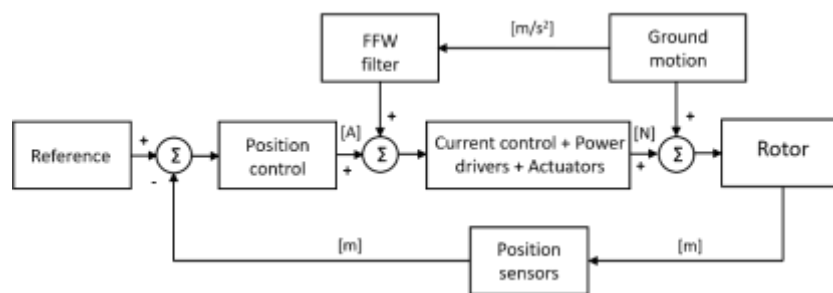
Figure 2. Control scheme.

3 EXPERIMENTAL RESULTS

The experimental tests are carried out to test the isolation from ground motion in operating conditions. The excitation is simulated by means of a shaker providing a profile of acceleration accordingly to the standards (Figure 3) where the peak A is equal to 5g and the duration in time is 30ms.
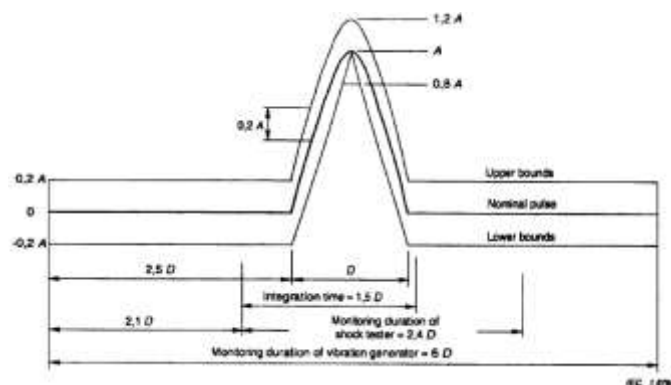
Figure 3. Acceleration profile.

3

Figure 4 shows the results obtained for the tests along axial (a) and radial direction at 0 rpm (b), 35000 rpm (c) and 51000 rpm (d). The maximum displacement is lower than 0.2 mm along both directions. The upper plots report the acceleration in g while lower plots show the displacement. Since acceleration of 5g when only PID control is running leads to the instability of the system, no plots are available when feedforward action is off.
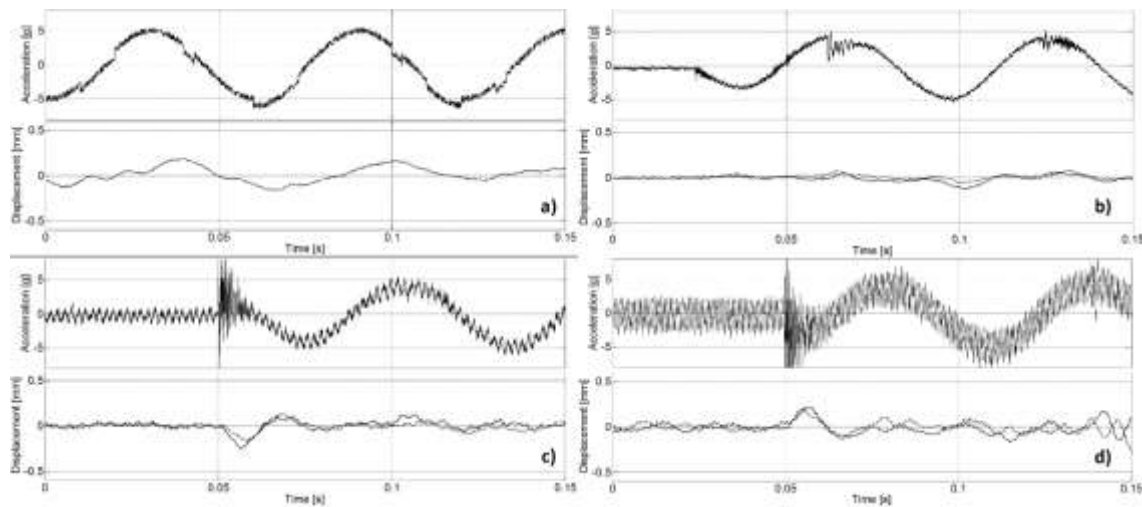
Figure 4. Experimental results. a) Axial direction at 51000 Rpm. b) Radial direction at 0 rpm. c) Radial direction at 35000 rpm. d) Radial direction at 51000 rpm. Solid line is x-axis and dashed line is y-axis in the lower plots of figures b), c) and d).

4   CONCLUDING REMARKS

A feedforward control technique has been presented to control ground motion on a compressor for refrigeration tasks in public transport. The control runs in parallel with a standard decentralized PID control devoted to magnetic suspension. The control architecture has been validated in the case of excitations coming from the ground when the machine is equipped with a substitute impeller without compression. Accelerations along longitudinal and transversal directions with a peak of 5g and a duration of 30ms have been provided with a shaker and the maximum recorded displacement are lower than 0.2mm. The obtained results represents the basis for the development of the control strategy that in the future will be used in combination with an unbalance compensation action to minimize the effects of surge and stall of the compressor in real working conditions.

REFERENCES

[1]   Bleuler, H., Cole, M., Keogh, P., Larsonneur, R., Maslen, E., Nordmann, R., Okada, Y., Schweitzer, G. and Traxler, A., Magnetic Bearings Theory, Design, and Application to Rotating Machinery, Springer, Berlin Heidelberg, (2009).

[2]   Chiba, A., Fukao, T., Ichikawa, O., Oshima, M., Takemoto, M. and Dorrell, D.G., Magnetic Bearings and Bearingless drives, Elsevier, Oxford, (2005).

[3]   Yoon S.Y, Lin Z, Allaire P.E, Control of surge in centrifugal compressors by active magnetic bearings – Theory and implementation, Springer, 2012

[4]   Cole m.O.T, Keogh P.S, Burrows C.R, Vibration control of a flexible rotor/magnetic bearing system subject to direct forcing and base motion disturbances. Proceedings of IME – Part C, 1998

4

THE DYNAMICS, STABILITY AND CONTROL OF ROTOR TOUCHDOWN IN ACTIVE MAGNETIC BEARING SYSTEMS

P.S. Keogh[1] and C. Lusty[1]

[1]Department of Mechanical Engineering
University of Bath, Bath, UK
Email: P.S.Keogh@bath.ac.uk, C.Lusty@bath.ac.uk

ABSTRACT

Power generation, gas compression, vacuum generation, and machining are example applications for spinning rotors. Higher power density is enabled by higher rotational speeds. Rotors levitated by active magnetic bearings (AMBs) allow such increase in speed because they have low torque resistance and the rotor dynamics are controllable. However, abnormal overload events or transient faults may give rise to a loss of functionality and cause a rotor to come into contact with emergency touchdown bearings (TDBs). The rotor may experience a number of responses ranging over bouncing and rubbing, which may result in excessive vibration at a level that may cause structural damage to the system. An understanding of the mechanisms that drive these persistent nonlinear contact dynamics is important if control strategies to restore contact-free rotor levitation are to be designed and implemented with confidence. This paper will explore the options that are available for AMBs and active TDBs.

1   INTRODUCTION

Contact-free operation of rotor/active magnetic bearing (AMB) systems is well known [1]. However, problems may arise when rotor/stator contact occurs and these are reviewed in [2] with respect to the rotor dynamic responses. In AMB-levitated rotor systems, rotor drop is a clearly defined problem. In the absence of AMB functionality, the TDB support characteristics are of importance in achieving a soft landing and acceptable rotor dynamic response during rundown [3]. However, contact induced rotor dynamics may also occur when the AMBs are still functional, hence active control options are also available. A typical layout in Figure 1 shows the AMB coils for the vertical axis, through which electrical currents (i_U, i_L) may be adjusted for levitation control of the rotor and to maintain clearance between the rotor and the AMB. Excessive external influences or faults conditions may cause the rotor to make contact with a touchdown bearing (TDB), which is in place to prevent excessive rotor dynamic excursions. When the rotor is in contact with the TDB, radial (normal) and tangential (friction) forces are introduced into the rotor dynamic behaviour. These forces may be large and may become persistent and undesirable [4, 5]. If control functionality is still available from an AMB or an active TDB, it may be possible to restore the rotor to a desirable contact-free state.
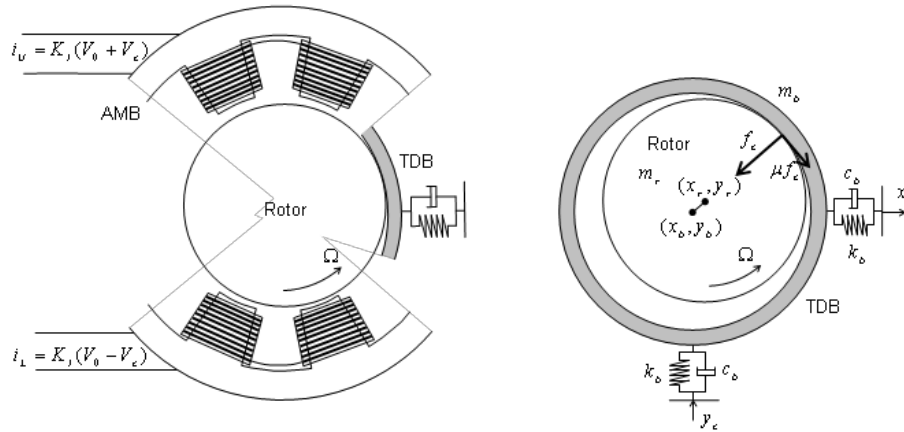
Figure 1. Spinning rotor within an AMB showing possible contact with a TDB.

2   PERSISTENT ROTOR CONTACT MODES

The linearized equation of motion of a rigid rotor (Figure 1) in an AMB having stiffness and damping properties is

$$\ddot{z} + 2\xi\omega_n\dot{z} + \omega_n^2 z = \frac{f_u}{m_r}e^{i\Omega t} - \frac{f_c}{m_r}(1+i\mu)\frac{z}{c_r},\tag{1}$$

where $z = x_r + iy_r$ is the inertial frame complex displacement, c_r is the radial clearance, μ is a Coulomb friction coefficient, and f_u is the unbalance. In an idealized representation, contacts may be represented by a series of delta function impulses. Between contacts ($f_c = 0$) analytical solutions may be sought that achieve repeatable bounce like motions before and after each contact (see Figure 2, left contact orbit B). Viewed in a synchronously rotating reference frame,

$$w = u_r + iv_r = ze^{-i\Omega t},\tag{2}$$

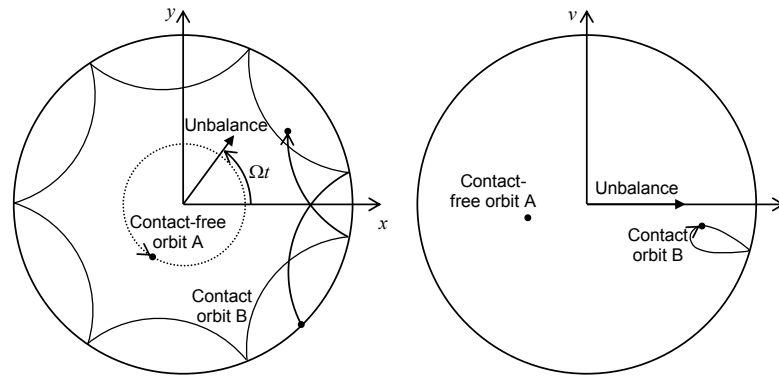orbit B has the loci shown in Figure 2 (right). Figure 2 also shows the completely contact-free

2

Figure 2. Bistable contact-free (A) and bouncing contact (B) motions in inertial (x, y) and synchronously rotating (u, v) frames of reference.

orbit A,

$$z = \frac{f_u}{m_r(\omega_n^2 - \Omega^2 + 2i\xi\omega_n\Omega)}e^{i\Omega t}, \quad w = \frac{f_u}{m_r(\omega_n^2 - \Omega^2 + 2i\xi\omega_n\Omega)}. \quad (3)$$

Figure 2 thus demonstrates an example of bistable responses driven by rotor unbalance. In orbit A, the rotor whirls in a circular contact-free condition within the clearance space of the AMB. In orbit B, a bouncing mode solution is also possible. In the left hand side diagram it is seen that the response of orbit B is lagging slightly behind the rotating unbalance vector, while the orbit A is almost in anti-phase with the unbalance vector. This effect is caused by the 'hard' boundary of the TDB, as represented by the delta function contacts. The phases of the orbits are seen more clearly in the rotating frame view of the right hand side diagram in which orbit A is represented by a single point and orbit B becomes a small loop on the TDB boundary.

Numerical simulations may also be undertaken in which the contact forces are represented in terms of Hertzian contact stresses and the TDB is resiliently mounted (Figure 1). These will be more representative of practical applications. Further, the TDB may be simulated in an active mode by imposing displacements (x_c, y_c) through the resilient mounts. Nonetheless, the idealized contact solutions may be used to guide understanding and decide upon appropriate control action.

Persistent contact is problematic since the contact force levels are typically large and in excess of the magnitude of the unbalance force vector. These may cause structural damage to the TDB and/or the rotor. Furthermore, frictional forces at a contact zone will be high, which will induce significant thermal inputs to the TDB and the rotor, resulting in thermal distortion and thermal bending, respectively.

3   OPTIONS TO RESTORE CONTACT-FREE LEVITATION

In this paper, two open-loop feedforward control actions are considered for AMBs and, if available, active TDBs. Their feedforward nature limits any problems that may arise from closed loop feedback.

3.1 Using AMB feedforward action

In this case, synchronous forces are applied through the AMBs to compensate for the unbalance that is driving the rotor dynamic contact. The compensating forces must have the appropriate amplitudes and phases so as to minimise the contact forces, preferably to zero. The control forces

may be applied in a ramped manner to reduce transient responses and achieve a smooth re-levitation of the rotor.

3.2 Using TDB feedforward action

In this case, synchronous control forces are applied to the TDBs in order that the contact forces between the rotor and the TDB may be influenced and minimised. Figure 3 shows an example of such control action that restores contact-free levitation.
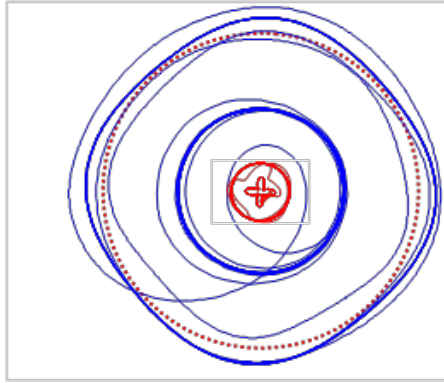

Figure 3. Active TDB motion (red) to induce a rotor out of a persistent rub contact mode (blue). Viewed in an inertial (x, y) frame of reference.

4   CONCLUDING REMARKS

This paper presents the options for restoring contact-free operation in AMB-levitated rotor systems. Without control, the contact rotor-dynamics may persist and become damaging for the components in the system. It is demonstrated that if functionality of the AMBs or active TDBs exists, appropriate control action may reduce contact forces to a level at which they become unsustainable and contact-free levitation follows.

REFERENCES

[1]   Magnetic Bearings: Theory, Design, and Application to Rotating Machinery, edited by Gerhard Schweitzer, Eric H. Maslen, Springer, ISBN 978-3-642-00496-4, 2009.

[2]   G. Jacquet-Richardet, M. Torkhani, P. Cartraud, F. Thouverez, T. Nouri Baranger, M. Herran, C. Gibert, S. Baguet, P. Almeida, L. Peletan, Rotor to Stator Contacts in Turbomachines. Review and Application. *Mechanical Systems and Signal Processing*, 40, 401-420, 2013.

[3]   C. Jarroux, R. Dufour, J. Mahfoud, B. Defoy, T. Alban and A. Delgado. On the Drop of a Rotor-AMB System onto Touch-Down Bearing. *VIRM 11 – Vibrations in Rotating Machinery*, University of Manchester, 671-682, 13-15 September 2016.

[4]   P.S. Keogh and M.O.T. Cole. Rotor Vibration with Auxiliary Bearing Contact in Magnetic Bearing Systems Part 1: Synchronous Dynamics, *Proc.I.Mech.E., Part C, Journal of Mechanical Engineering Science*, 217, 377-392, 2003.

[5]   S. Enemark and I.F. Santos. Nonlinear Dynamic Behaviour of a Rotor-Foundation System Coupled Through Passive Magnetic Bearings with Magnetic Anisotropy - Theory and Experiment. *Journal of Sound and Vibration*, 363, 407-427, 2016.

ON THE USE OF FLEXIBLY-MOUNTED, INTERNAL-STATOR MAGNETIC BEARINGS FOR VIBRATION CONTROL OF A FLEXIBLE ROTOR

C. Lusty[1] and P. Keogh[1]

[1]Department of Mechanical Engineering
University of Bath, UNITED KINGDOM
Email: C.Lusty@bath.ac.uk, P.S.Keogh@bath.ac.uk

ABSTRACT

Active magnetic bearings (AMBs) present a host of potential advantages over other bearing types in the design of rotor systems. An important category of such advantages is the ability to use the active nature of AMBs to influence the rotor-dynamics, and thus to control and reduce vibration exhibited by a rotor. The majority of work on this topic employs the same basic system geometry: the magnetic bearings are external to the rotor, and they tend to be large and rigidly mounted. In some situations it may be necessary or desirable to use a more compact arrangement, with AMBs mounted inside a hollow rotor, and mounted on a flexible structure. A system with such a topology is considered in this paper.

1   INTRODUCTION

The use of magnetic bearings for vibration control has been an active field of research for over half a century, and a number of authors have undertaken to summarise the progress in the field at various stages with significant review papers [1–3].

Throughout this period, however, the fundamental geometry of AMBs and of the overall rotor systems they are employed in has remained relatively stationary. From the use of magnetic bearings as active magnetic dampers (AMDs) [4–6] to the development of competent and efficient vibration controllers [7, 8], AMBs have tended to be large, externally and rigidly mounted components. However, in systems where space on the rotor surface or in its vicinity are limited, it may be advantageous to employ an alternate system geometry. In particular, the prospect of mounting magnetic bearings within a hollow-shaft rotor is substantially interesting. In many cases, such a geometry dictates that the structure supporting the AMB will be flexible, which complicates the system dynamics, as well as raising interesting new possibilities for vibration control.

2   TEST RIG

To allow an experimental investigation into the behaviour of a rotor system with flexibly-mounted, internal-stator magnetic bearings, a customised test rig has been constructed. A schematic showing the fundamental nature of the test rig is shown in Figure 1, while a photographic view of the finished test rig is shown in Figure 2.

The rotor is constructed with a variable cross-section, with large diameter, hollow ends, and a thin and solid centre. The thin section is present purely to lower the rotor's natural frequencies to allow supercritical speeds to be reasonably achievable in the laboratory. The magnetic bearings (marked "Active Coupling" in Figure 1) are mounted at the end of cantilever beams. In this example, the magnetic bearings are not used for levitation of the rotor, which is mounted at its ends on traditional passive bearings. Instead, the magnetic bearings are in place solely for the purpose of vibration control. In theory, however, the bearings could be used for a combination of both levitation and vibration control.
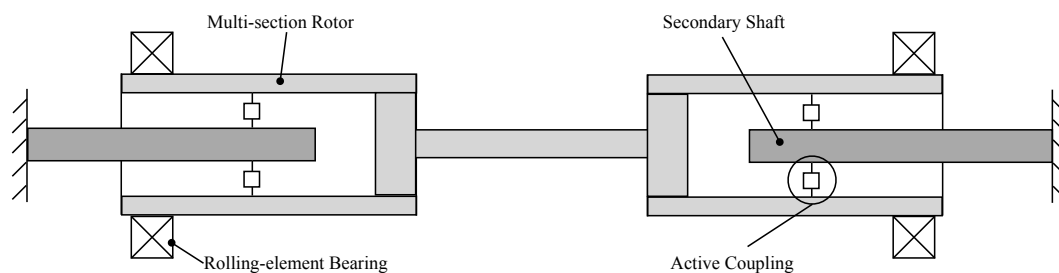
Figure 1: Schematic diagram illustrating layout of flexibly-mounted magnetic bearing test rig

3   CONTROL AND RESULTS

A key challenge is reducing the rotor vibration without exciting the magnetic bearing supports to vibrate excessively, and especially to avoid the combined vibration of rotor and magnetic bearing shaft causing contact between the rotor and the magnetic bearing to occur. From a system design point of view, it is therefore of great importance to ensure a substantial difference between the natural frequencies of the separate shafts.
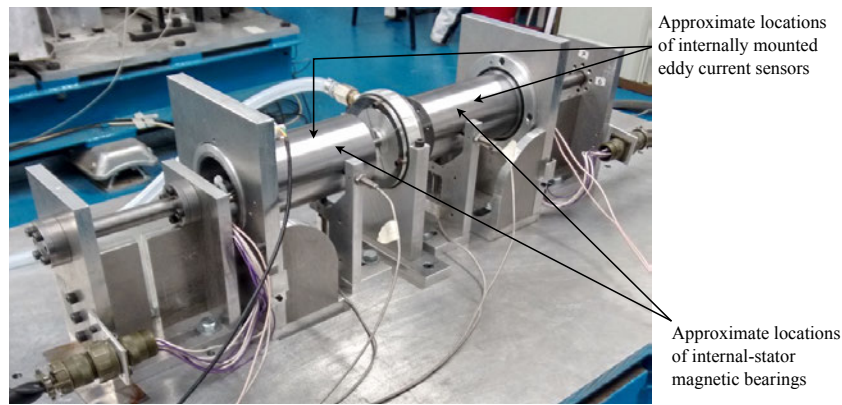
Figure 2: Photograph of flexibly-mounted magnetic bearing test rig

As the design under consideration uses the magnetic bearings purely for vibration reduction (and not for levitation), it is possible to only activate the bearings when excessive vibration behaviour is occurring in the rotor - for example when passing critical speeds.

In terms of particular control strategy, a variety of options are available. With carefully selected gains, a traditional PD controller can be employed to couple to rotor to the secondary shafts, thus altering the rotor behaviour. The controller may be devised, for example, to add stiffness to the rotor, thus shifting its natural frequencies, and therefore critical speeds. An interesting alternative to this may be not to use a closed loop controller at all, and instead just apply a bias current to all poles of the magnetic bearings, effectively reducing the rotor stiffness. An interesting study of such a techniques has been presented by Mahfoud and Der Hagopian [9].

A broader range of options are opened up by considering the use of model based controller for such a geometry. This allows the expression of specific goals; for instance, a controller could be designed to minimise the absolute vibration of the rotor as far as possible, while allowing the flexible magnetic bearing shaft to vibrate *provided* such motion will not cause a contact event. While more complex to design, such control schemes offer powerful capabilities to a system with flexibly mounted magnetic bearings.

By way of illustrating the capability of such a system topology for reducing vibration, some results from impulse testing on the rig in Figure 2 are shown in Figure 3. The impulses are measured by eddy current sensors (four in total) mounted adjacent to the magnetic bearings on the flexible support shafts. Thus they contain data relating both to the rotor (the target), and the shafts they are mounted on. The data presented is a Fourier transform of the time responses. The peaks around 45 Hz pertain to the rotor behaviour, while those around 120 Hz relate to the support shaft natural frequency. It is seen that the use of PD control in the bearings (3b) substantially reduces the vibration amplitudes compared to the uncontrolled system (3a), as well as increasing the frequencies at which they occur. These frequency increases are a result of the additional stiffness contributed by the magnetic bearings when operated under PD control. The extent of the frequency shift is governed by the value of the proportional gain. It is also possible to cause negative frequency shifts, achieved by using the magnetic bearings to add negative stiffness to the system, as done by Mahfoud and Der Hagopian [9].

4 CONCLUDING REMARKS

An atypical topology for a rotor system using magnetic bearings for vibration reduction has been presented, involving mounting internal-stator magnetic bearings within a hollow-shaft rotor. The AMBs are mounted on flexible beams. Options for using such a system for vibration control are considered, and example results illustrating the potential of such a topology are
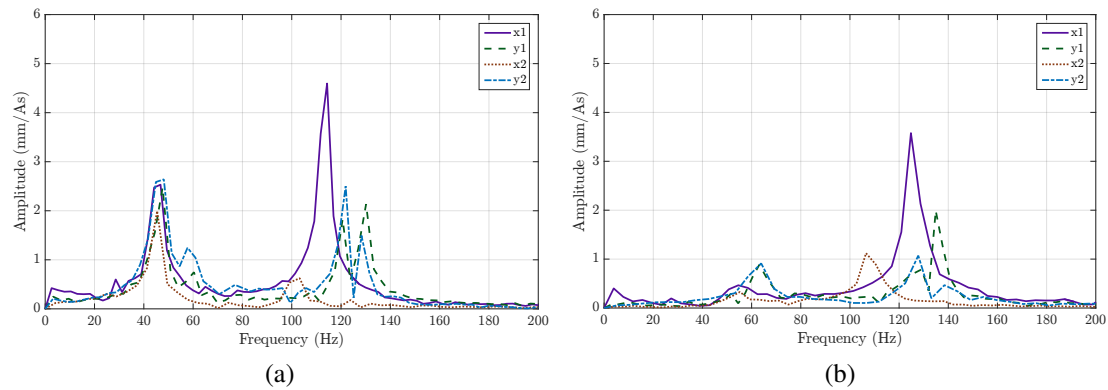
3

Figure 3: Fourier transforms of the impulse response of the rotor system comparing the behaviour without control (a) and with a PD controller (b)

included.

REFERENCES

[1] Michael K Swann. Magnetic bearings: Fifty years of progress. In *Magnetic Suspension Technology Workshop*, volume 1, pages 19–38, 1993.

[2] S Zhou and J Shi. Active balancing and vibration control of rotating machinery: a survey. *Shock and Vibration Digest*, 33(4):361–371, 2001.

[3] G Schweitzer. Applications and research topics for active magnetic bearings. In *IUTAM Symposium on Emerging Trends in Rotor Dynamics*, pages 263–273. Springer Netherlands, 2011.

[4] VM Gondhalekar, J Nikolajsen, and BV Jayawant. Electromagnetic control of flexible transmission shaft vibrations. In *Proceedings of the Institution of Electrical Engineers*, volume 126, pages 1008–1010. IET, 1979.

[5] MEF Kasarda, PE Allaire, RR Humphris, and LE Barrett. A magnetic damper for first-mode vibration reduction in multimass flexible rotors. *ASME Journal of Engineering for Gas Turbines and Power*, 112(4):463–469, 1990.

[6] MEF Kasarda, H Mendoza, RG Kirk, and A Wicks. Reduction of subsynchronous vibrations in a single-disk rotor using an active magnetic damper. *Mechanics Research Communications*, 31(6):689–695, 2004.

[7] H Bleuler and G Schweitzer. Dynamics of a magnetically suspended rotor with decentralized control. In *IASTED Applied Dynamics and Control Symposium, Copenhagen*, 1983.

[8] CR Burrows, MN Sahinkaya, and S Clements. Active vibration control of flexible rotors: an experimental and theoretical study. *Proceedings of the Royal Society of London. A. Mathematical and Physical Sciences*, 422(1862):123–146, 1989.

[9] Jarir Mahfoud and Johan Der Hagopian. Investigations on the critical speed suppressing by using electromagnetic actuators. *smarts structures and systems*, 9(4):303–311, 2012.

APPLICATION OF THE PARTITION OF UNITY FINITE ELEMENT METHOD TO EXTERIOR ACOUSTICS PROBLEMS

J.-D. Chazot[1] , B. Nennig[2] and E. Perrey-Debain[1]

[1]Laboratoire Roberval
Université de Technologie de Compiègne, UMR 7337, Sorbonne Universités, 60205
Compiègne, France
Email: jean-daniel.chazot@utc.fr

[2]Laboratoire Quartz EA 7393
Institut supérieur de mécanique (SUPMECA), 3 rue Fernand Hainaut, 93407 Saint-Ouen,
France

ABSTRACT

The Partition of Unity Finite Element Method (PUFEM) is dedicated in standard acoustics to high frequency problems or large dimensions problems. Its main feature is indeed to capture several wavelengths per element with a very high convergence rate. The modeling of acoustics waves in exterior unbounded domains seems therefore adapted for the PUFEM. However non reflecting boundary conditions are necessary to handle this task. Some analytical boundary conditions have already been tested with the PUFEM. Here we propose to extend the choice of possible non reflecting boundary conditions in the PUFEM with the Perfectly Matched Layers (PML).

1   FORMULATION

1.1   Non Reflecting Boundary Conditions (NRBC)

The following weak form of the Helmholtz equation is used in the finite element method applied to acoustics :

$$\int_{\Omega} (\nabla p \cdot \nabla \delta p - k^2 p \, \delta p) \, \mathrm{d}\Omega - \int_{\Gamma} \frac{\partial p}{\partial n} \, \delta p \, \mathrm{d}\Gamma = 0 \, . \tag{1}$$

It describes the behavior of the acoustic pressure p in a fluid domain Ω at an angular frequency ω with a wavenumber k. Here the exterior domain Ω is given with rigid boundaries Γ_r and non reflecting boundaries Γ_∞. To handle these last boundaries Laghrouche et al. [1] tested and compared some Non Reflecting Boundary Conditions (NRBC) such as Robin type boundary conditions, exact boundary conditions (DtN) and approximate NRBCs (Bayliss, Gunzburger and Turkel - Engquist and Majda - Feng). In the following we propose to extend the choice of possible NRBCs in the PUFEM with the Perfectly Matched Layers (PML). The idea behind the PML is to stretch the coordinates in the complex domain to get an absorbing domain. Along the x-axis for example, a plane wave $\exp(\mathrm{i}(kx - \omega t))$ becomes $\exp(\mathrm{i}(k\tilde{x} - \omega t))$ with $\tilde{x} = x + \mathrm{i}f(x)$. In the absorbing region of this PML the wave decays exponentially. By choosing also $\mathrm{d}f/\mathrm{d}x = \sigma_x(x)/\omega$, the attenuation rate becomes frequency independent. Note that the function $\sigma_x(x)$ cannot be a simple large constant since it would lead to numerical reflections at the end of the PML domain. However the larger the value of the integral $\int_{PML} \sigma_x(x)\mathrm{d}x$, the best. In order to achieve that goal, Bermúdez[2] tried unbounded functions such as $\int_{PML} \sigma_x(x)\mathrm{d}x = +\infty$ and concluded that the optimal absorbing function was $\sigma_x(x) = c \left(L_x - x \right)^{-1}$. In the following we keep this same function in both directions x and y.

In practice, the complex stretching of our original differential Equation (1) writes :

$$\int_{\Omega} (\frac{\gamma_y}{\gamma_x} \frac{\partial p}{\partial x} \frac{\partial \delta p}{\partial x}) \, \mathrm{d}x\mathrm{d}y + \int_{\Omega} (\frac{\gamma_x}{\gamma_y} \frac{\partial p}{\partial y} \frac{\partial \delta p}{\partial y}) \, \mathrm{d}x\mathrm{d}y - \int_{\Omega} (k^2 \gamma_x \gamma_y p \delta p) \, \mathrm{d}x\mathrm{d}y - \int_{\Gamma} \frac{\partial p}{\partial n} \, \delta p \, \mathrm{d}\Gamma = 0 \, , \tag{2}$$

with $\gamma_x(x) = 1 + \mathrm{i}\frac{\sigma_x(x)}{\omega}$ and $\gamma_y(y) = 1 + \mathrm{i}\frac{\sigma_y(y)}{\omega}$.

1.2   Partition of Unity Finite Element Method (PUFEM) in 2D

The key ingredient of the PUFEM relies on the enrichment of the conventional finite element approximation by including solutions of the homogeneous partial differential equation ([3, 4]). In this work, plane waves are chosen for the enrichment. In each sub-domain, the acoustic pressure is hence expanded as

$$p(\boldsymbol{r}) = \sum_{j=1}^{3} \sum_{q=1}^{Q_j^{(k)}} N_j^3(\xi, \eta) \exp \left(\mathrm{i}k\boldsymbol{d}^{(k)} \cdot (\boldsymbol{r} - \boldsymbol{r}_j^{(k)}) \right) A_{jq}^{(k)}, \tag{3}$$

where the plane waves amplitudes $A_{jq}^{(k)}$ are unknown coefficients and functions N_j^3 are the classical linear shape functions on triangular elements. Points $\boldsymbol{r}_j^{(k)}$ are the nodes associated with element $V^{(k)}$. The directions are chosen to be evenly distributed over the unit circle, that is

$$\boldsymbol{d}^{(k)} = (\cos(\theta_q), \sin(\theta_q)) \quad \text{where} \quad \theta_q = \frac{2\pi q}{Q_j^{(k)}}, \quad q = 1, \ldots, Q_j^{(k)}. \tag{4}$$

The number of plane waves attached to each node $j = 1, 2, 3$ depends on the frequency and the element size according to the following criteria [5] :

$$Q_j^{(k)} = \mathrm{round}[kh + C(kh)^{1/3}]. \tag{5}$$

2

Here, h is taken as largest element edge length connected to node j within the acoustic domain and the constant C is usually chosen to lie in the interval $C \in [2, 20]$. This coefficient can be adjusted depending on the configuration and the expected accuracy.

In the present work, the finite element geometries are defined using standard quadratic shape functions on triangular elements :

$$\boldsymbol{r}^{(k)}(\xi, \eta) = \sum_{j=1}^{6} N_j^6(\xi, \eta) \boldsymbol{r}_j^{(k)}, \tag{6}$$

as this description is integrated in most softwares (here the finite element mesh generator `Gmsh` is used). In Eq. (6) extra nodes $\boldsymbol{r}_j^{(k)}$ for $j = 4, 5, 6$ correspond to the mid-node of the edges.

2   RESULTS

Figure (1) presents the real part of the pressure radiated at 5000 Hz in a semi-infinite domain by a point source located at 5cm above an infinite plane. The acoustic domain spans over a 2 meters square while the added PML has a thickness of 0.5m. The result, obtained with an error $\mathcal{L}_2$ lower than 5% compared to analytical results, shows the good efficiency of the PML coupled to the PUFEM.
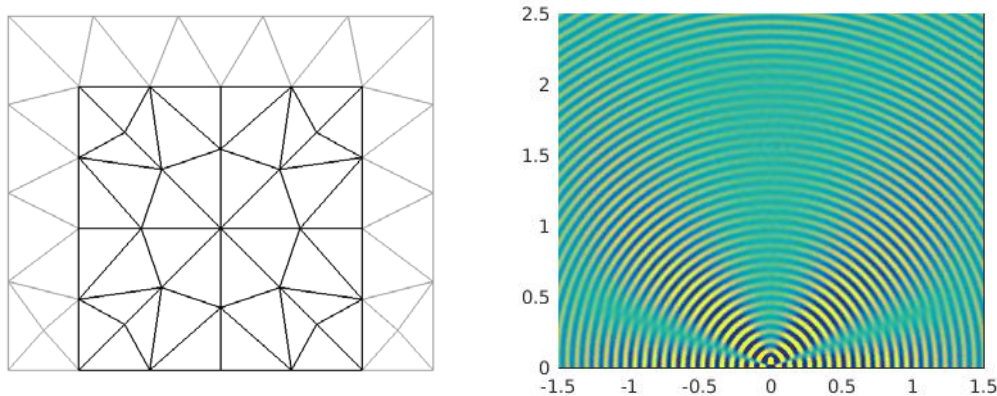
Figure 1: Point source radiating in a semi-infinite domain. From left to right : PUFEM mesh, real part of the pressure.

Figure (2) presents the real part of the pressure radiated at 1000 Hz in a semi-infinite domain by an imposed harmonic displacement over a circle. The acoustic domain spans over a disk of radius 5 with an included 0.5m thick PML. This result is an other illustration of the good efficiency of the PML coupled to the PUFEM.

3   CONCLUSION

In conclusion the stretching in the complex domain of the acoustic problem in order to create an absorbing layer called a PML works well with the PUFEM. It offers an other way to model non reflecting boundary conditions in the PUFEM, easy to implement in any configuration. The
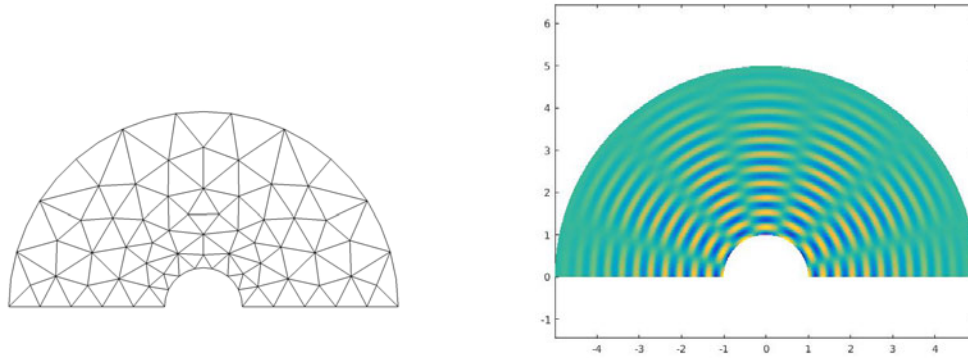
Figure 2. Imposed displacement - Radial PML for $R \in [2.5; 5]$.

PUFEM coupled with the PML offers hence an efficient tool to model the propagation and the scattering of acoustic waves at high frequency in exterior problems of large dimensions.

REFERENCES

[1] O. Laghrouche, A. El-Kacimi, and J. Trevelyan. A comparison of nrbcs for pufem in 2d helmholtz problems at high wave numbers. *Journal of Computational and Applied Mathematics*, 234:1670–1677, 2010.

[2] A. Bermúdez, L. Hervella-Nieto, A. Prieto, and R. Rodríguez. An optimal perfectly matched layer with unbounded absorbing function for time-harmonic acoustic scattering problems. *Journal of Computational Physics*, 223(2):469 – 488, 2007.

[3] JD Chazot, B Nennig, and E Perrey-Debain. Performances of the partition of unity finite element method for the analysis of two-dimensional interior sound field with absorbing materials. *Journal of Sound and Vibration*, 332(8):1918–1929, 2013.

[4] JD Chazot, E Perrey-Debain, and B Nennig. The partition of unity finite element method for the simulation of waves in air and poroelastic media. *Journal of the Acoustical Society of America*, 135(2):724–733, 2014.

[5] T. Huttunen, P. Gamallo, and R.J. Astley. Comparison of two wave element methods for the helmholtz problem. *Communications in Numerical Methods in Engineering*, 25:35–52, 2009.

4

PREDICTION OF ACOUSTIC AND SHOCK RESPONSES OF SPACECRAFTS OVER BROADBAND FREQUENCY RANGE

Gérard Borello[1]

[1]InterAC
10 impasse Borde-Basse, 31240 L'Union, FRANCE
gerard.borello@interac.fr

ABSTRACT

Spacecrafts are submitted to high levels of vibrations during the launcher flight. Broadband frequency loads are induced by three major environmental flight events: the lift-off with severe acoustic pressure from the jet, the transonic phase with turbulent pressure load associated to sonic shock waves and the separation of last stage followed by spacecraft separation from pyrozip devices. Long before the first technological flight of new launch vehicle, margins of safety against previous vibroacoustic environment are predicted from combinations of numerical models and tests leading to more robust diagnosis and better qualification process of spacecraft equipment vibrations. Several examples of applied methodology are reviewed and discussed.

1   INTRODUCTION

Launch vehicle loads are unsteady, random or transient with frequency spectra extending to 100 kHz for shocks and to 8 kHz for acoustic loads. The spacecraft so-called payload is protected during the atmospheric phase by the fairing, the launcher nose. The fairing itself has to bear the external loads from previous events and is carefully designed for this mission. As flight events are difficult to simulate on ground, spacecraft is submitted to specific environmental testing expected to envelope the actual flight loads. On-ground qualification tests generate safety margins to flight operating conditions. Margins of only 4 dB are taken in acoustic qualification tests of full payloads and are generally performed in large high-performance reverberant chambers to insure high degree of diffusion in the acoustic sound field. Equipment components are tested on shakers with appropriate vibration levels derived from a chain of calculation and tests on launch vehicle subparts.

For shock events, specific separation tests are performed between the spacecraft and its last-stage adaptor or the last stage itself. At component level, equipment is tested on shock machines based on load specifications written in term of Shock Response Spectrum (SRS). Transonic phase is generally qualified by acoustic test when proven by numerical simulation.

As testing environment differs from flight, evaluation of the actual effective safety margins may conveniently be estimated from numerical modeling. When confident, theoretical modeling is easier and cheaper to handle than full-scale tests. The confidence in calculated outputs is nevertheless a long term approach. First, knowledge has to be collected on the rocket environment for generating inputs to the calculation. Second, calculation methods have to be entirely controlled and approved. Selected calculation methods for acoustic environment at lift-off are mesh-based Boundary Element Method (BEM) for the low frequency range and Statistical Energy Analysis (SEA) for the high frequency range. For shock response simulation, time history simulation is required for predicting SRS outputs. Prediction methodology is nevertheless very similar: Finite-Element structural analysis for low frequency and SEA specific solver for managing fast transient events in high frequency range. For mid-frequency, methods may be hybridized in various ways.

In next paragraphs, highlight on applied methodologies is put through series of examples taken from the development program of Ariane European launch vehicle family.

2   VIBROACOUSTIC PREDICTIONS AT LIFT-OFF

2.1   Ariane Fairing and Internal Payload volume random responses

Figure 1 (left) shows the European launch vehicle Ariane 5. The fairing is the top external shell protecting the payload during the atmospheric part of the flight. The fairing is jettisoned as soon as the launcher leaves the earth atmosphere as shown in Figure 1 (right). During the atmospheric phase of the flight, two major events are dimensioning the payload random-vibration environment.

First, at lift-off, the rocket engines generate high Sound Pressure Level (SPL), increased by ground reflections and jet impact on launch table. For the fairing, this noise field is viewed as set of traveling acoustic waves exciting its structure and penetrating inside the payload volume inducing strong vibrations with frequency content up to 5 kHz. Around the launch vehicle, during a few seconds after ignition, acoustic pressure levels are rising between 180 dB near the engines down to 150 dB in the vicinity of the fairing and are quickly vanishing with altitude as soon as the vehicle is far enough from ground reflections. This fall is emphasized by the downward orientation of the directivity lobe of emission of the jet plume as its deflection decreases further and further from ground.

Second, when the launcher crosses the sound wall (transonic phase), the fairing is again strongly excited by shock wave attached to nozzle and by accompanying turbulence. To predict

these two major events in term of acoustic pressure level around payload, the source (i.e. the external wall pressure applied to the fairing) has to be known. These levels are determined all along the development program through series of ground testing and numerical simulations. Lift-off acoustic loads are experimentally determined using motorized-scaled model of rocket engine (1/20th scale for Ariane 4 and 5-cf. Figure 4) and measurements on launch facilities for first flights of the new rocket. Wind tunnel tests are performed for transonic loads.

They are followed by numerical simulations based on measured data as extrapolations are required for predicting full-scaled results. The spatial and time correlations of the acoustic field have also to be investigated as the sound field is unsteady with fast changing frequency content.

Figure 1. Left: Ariane 5 lift-off (Flight V209); right Fairing separation from Ariane 5 last stage when leaving earth atmosphere.

2.2 Prediction of Ariane 4 vibroacoustic environment

For predicting lift-off internal acoustic environment around the payload, the actual surrounding acoustic field may be idealized as an equivalent steady-state diffuse random noise. A diffuse sound acoustic field is made of traveling waves impacting the structure in all possible directions. Diffuse field is convenient as an input to vibroacoustic calculation for covering all possible ways an acoustic wave may enter the fairing volume. Assuming diffusion of acoustic and vibration fields at lift-off makes possible to predict responses using SEA energy-based method.

SEA prediction method was initiated by R. H. Lyon and G. Maidanik in 1962. It is typically applicable to the calculation of equipment responses of payload panels within a reverberant chamber or for estimating in-flight rocket vibrations. SEA assumes conservation of vibrational energy between the various parts of the rocket under dynamic loads. SEA is a valid method for the high frequencies because the power flow exchange relationships are assuming dynamic weak coupling between the "subsystems", a natural evolution of the coupling when frequency increases. Reversely SEA is losing accuracy and validity when applied in too low frequency domain. Because fairing loads are random with broadband frequency content, deterministic numerical simulations are at least difficult and in practice not possible for covering the required frequency range and SEA was at beginning of 80ths the only method able to deliver consistent predictions for this type of application.

The author joined the Ariane 4 European development program in 1984. The program was already well-advanced. Ariane 4 introduced series of innovations in term of design of the upper part (Figure 2-Left): a lighter structure with sandwich cross section made of two orthotropic carbon-fiber skins separated by an aluminum honeycomb sandwich. There were two separate payload

compartments (fairing on top and SPELDA below) for two-satellite launch and easier payload integration in launch pad facilities. Equipment bay was an external platform located below SPELDA. The Fairing was made by two half-shells attached by a clampband and jettisoned after atmospheric flight (Figures 1 and 2). Bending stiffness of the fairing in circumferential direction was three times lower than in axial direction. First breathing dynamic mode of half a shell was set at low enough frequency to avoid impacting payload after separation due to amplitude of breathing vibration motion.
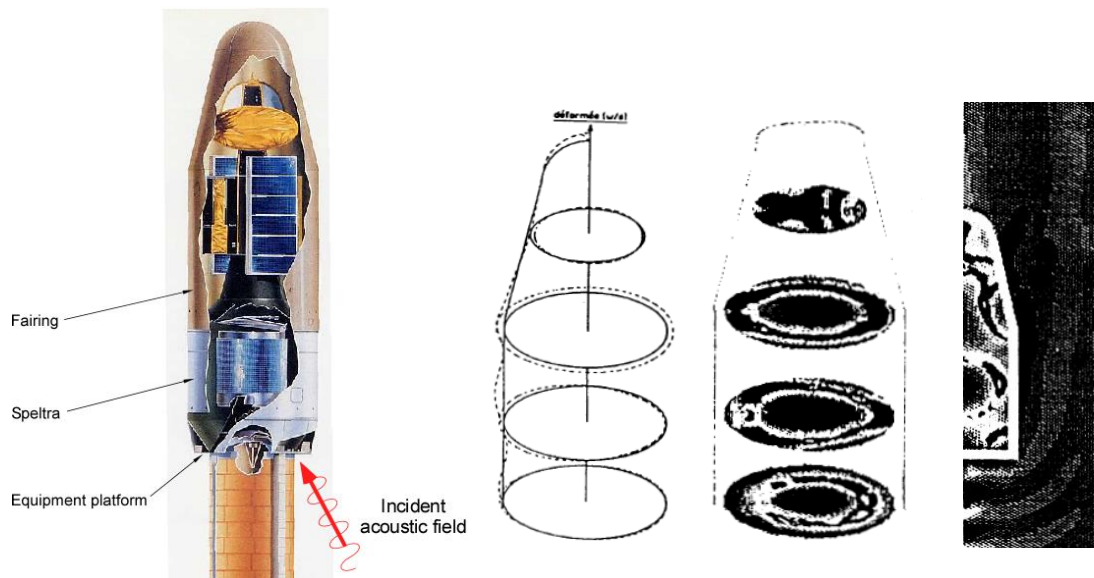
Figure 2. Left: Ariane 4 upper part. Right: First benchmark on fairing sound transmission using RAYON BEM software in 1985.

The new design, if mechanically very efficient, proved to deprecate the acoustic environment of the upper part. After scaled-model tests were performed, expected external SPL's were known around the upper part within some margin of safety. From this, first SEA predictions run by Aerospatiale, the Ariane 4 architect, were showing a general increase of the vibroacoustic environment compared to previous Ariane launchers. It showed a potential increase of launcher equipment random vibration levels of about 10 to 20 dB as well as noise increase around payloads, exceeding environmental specifications used to qualify launcher and payload components. Due to novelty of fairing construction, there was no available published references throughout the world to confirm the SEA diagnosis and get some trust in predicted numbers. Research studies were then engaged to understand the physical causes of this noise increase and for finding any possible counter measures if the diagnosis would be confirmed.

The origin of the noise increase was quickly identified and was due to the conjunction of several factors: solid propellant boosters, added to the first stage of Ariane 4, were generating noisier environment than previous Ariane versions. Maximum noise levels were lying in the range 200-500 Hz.

Unfortunately, the new sandwich fairing structure, stiffer and lighter than the classical Ariane 3 ribbed-aluminum structure, was showing acoustic critical frequencies just falling in this range. It led to very poor noise reduction in related frequency bands. As sketched in Figure 2 (Left), the equipment platform was also cantilevered with respect to the third stage, creating a corner in which impinging sound waves at lift-off from were badly scattered. This was generating an increase of about 10 dB of external pressure loading the equipment platform.

Emphasis was put on numerical acoustic prediction and engineering studies for :
- evaluating the various contributions to external noise level,
- mastering causes of uncertainty in the predictions
- improving the risk analysis knowledge.

There is a natural variability of the acoustic loads at lift-off due to the unsteady behavior of the engine noise, the type of boosters, the size of the payload inside the fairing. For qualifying equipment to random acoustic, a margin of + 4 dB is used for all frequency bands between the nominal expected level on launch pad and the specification which drives ground test level.

It was a very small margin in the currently faced situation. Predicting low and mid frequency content of internal fairing noise was investigated jointly with M.A. Hamdi [5][8][9][11][12], professor at UTC. He had developed during his thesis [2] a numerical kernel based on a new variational boundary element formulation (BEM) that was less subject to numerical drawback. His code called RAYON incorporated axisymmetrical formulation for coupling the lined-mesh structural FEM (Finite Element Method) model of the fairing with internal cavity. In place of solving the full 3D fairing-fluid cavity coupled problem, we could solve series of smaller 2D problems as CPU and memory was quite an issue in the eighties. 3D-dynamic behavior was retrieved by synthesizing series of 2D harmonics responses, for reaching higher frequency range. J. P Morand [16] and B. Chemoul from CNES provided the model of the orthotropic fairing structure. It was coupled with internal fairing volume and external sound field in RAYON by Hamdi & Co. Figure 2 (right) shows the first computation benchmark performed in 1985 with RAYON on a simplified model of the fairing. Original plots were in color and of better quality than current copy. It was the first time we could see at same time the motion of the structure and the wave patterns of exterior and interior sound pressure. This work was extended by developing a more industrial model of the Ariane 4 fairing/equipment bay for predicting the interior noise of the empty fairing surrounded by diffuse acoustic. This was a simulation of the acoustic fairing test inside reverberant chamber performed in the test facilities of Intespace company in Toulouse, cf. Figure 3 (right), after the delivery of the first fairing prototype by Contraves Corp., a Switzerland company.
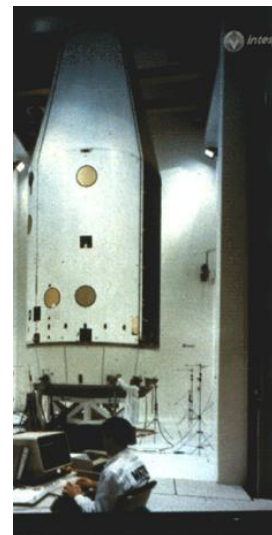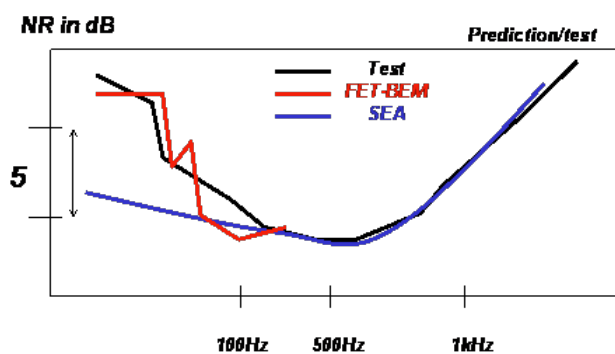
Figure 3. Combined BEM/SEA prediction (left) of the noise reduction of Ariane 4 fairing tested in reverberant chamber (right).

The author introduced the method of splitting the calculation of the random response into a set of deterministic BEM calculations under fixed grazing plane wave incidences in order to cover

5

all incidences seen in the test chamber and to quadratically sum-up incident-response to recover the random response. Under this source specification, model construction and calculations were undertaken by Hamdi & Co. In parallel, high frequency SEA prediction from Aerospatiale and CNES completed the frequency range of interest. Agreement between predicted and measured noise reduction was excellent over the whole frequency range as seen in Figure 3 (left). The prediction model was further improved in 1987 to simulate the environment of the first Ariane 4 flight [11], which was fired the same year.

The source model was built from a set of acoustic monopoles along the jet line of the Viking and booster engines of which power was estimated with the standard NASA jet model [14]. This source representation was entered as inputs in a Ray-tracing acoustic model of the ELA2 launch pad [7] and SPL outputs were correlated with measured data provided by the 1/20th motorized mockup of Ariane 4 (Figure 4). Main expected incidences on the fairing were then retained as inputs to new BEM model of Ariane 4 upper part. As this model was intended to be correlated with first flight data, payload presence under the fairing was simulated by their rigid body shapes. Figure 5 provides the resulting predicted/measured SPL at the two microphones position installed in the fairing and SPELDA volume of Ariane 4 V401.
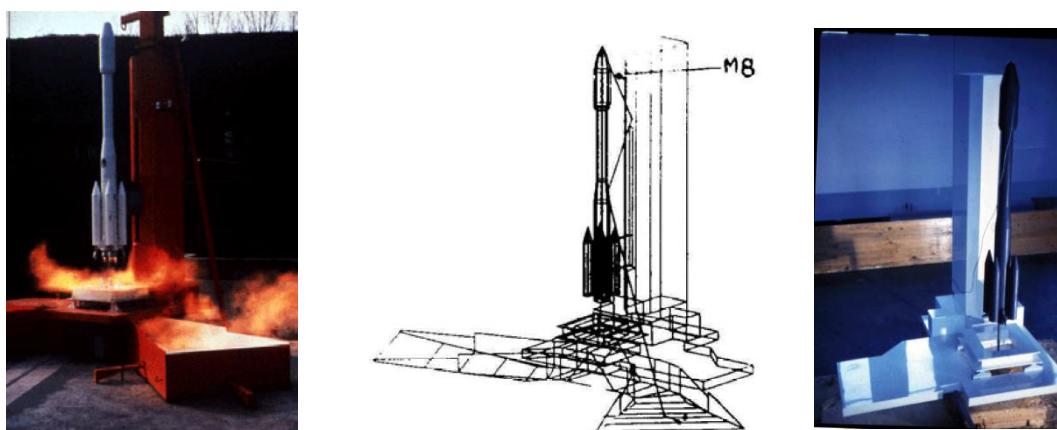
Figure 4 : On left, Motorized scaled-model acoustic test at Le Fauga (ONERA) and on right Ray-tracing acoustic model for jet radaited noise description with related scaled-acoustic model for measuring scattered field from ultrasonic sources (CSTB). M8 was the measured pressure reference on the launch pad to calibrate the source model.
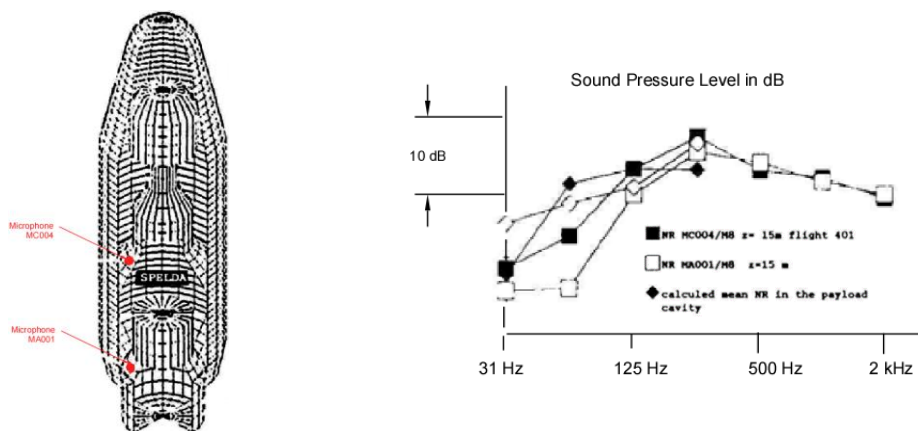
Figure 5. BEM/FEM coupled model and prediction against measured levels of flight acoustic levels in fairing and SPELDA compartments at the two in-flight microphone positions combining results of BEM/SEA models.

6

In parallel, the author investigated numerically the response of the equipment bay as the guidance platform was very sensitive to acoustic levels. Calculation was performed using FEM structural model of the equipment bay to which was applied estimated blocked random wall-pressure to simulate the acoustic loads [3]. Results from SEA modeling driven by Aerospatiale and FEM results were in good agreement up to 200 Hz, covering the equipment sensitivity range due to internal resonance of the guidance platform. These predictions were confirmed by joint work with ONERA supervised by R. Ohayon, [3][16], using a more sophisticated elastoacoustic model of the equipment bay coupled to internal cavity (including acoustic internal modes).

The critical aspect of acoustic vibrations at lift-off was thus confirmed before the first flight. After the first demonstration flight, June 15, 1988, criticality of vibroacoustic environment was verified. The guidance platform vibration was found at only -2dB from failure level observed in test and conformed to predicted values. Extrapolation of future second flight showed negative margins of safety due to a noisier booster configuration. A set of counter measures were immediately undertaken such as modifying the launch pad to minimize lift-off acoustics, over-qualifying some of the equipment and changing the guidance platform to another technology less sensitive to vibrations. Despite or because of this troubleshooting, Ariane 4 has been one of the safest launch vehicle with a long carrier.

2.3 Ariane 5 vibroacoustic environment improvement from design stage

On the new on-going Ariane 5 program starting in 1985, Project team was now well aware of acoustic problems arising as soon as these loads are underestimated in specifications.

Research was then performed for optimizing Ariane 5 noise environment, undertaking noise reduction solutions from design stage, acting on both for exterior noise and fairing interior comfort for payload passengers, [6][10][12].

Thanks to cooperation with ISVR and ESA, acoustic tests were performed on 1/5th scaled model of the fairing to investigate orthotropic effect on noise transmission. Pr. F. Fahy developed a specific theory for quickly predicting noise transmission for this type of system. The related software called PROXMODE was further used by Dornier company, responsible for the development of the SPELTRA structure of Ariane 5, located below the fairing and containing a third payload. From this work, Dornier developed a specific acoustic treatment to attenuate low frequencies in the fairing by means of Helmholtz's resonators spread on internal face of the fairing to increase internal absorption.

Fairing Bending stiffness was also tuned in the circumferential direction to gain a few dB. BEM/FEM modeling's were also more and more useful to calculate exotic noise reduction solutions like Helium purge of the internal fairing volume that in theory could reduce interior noise level from 10 dB as shown in Figure 6. SEA and dedicated analytical predictive models were complemented the frequency range [6] [12].
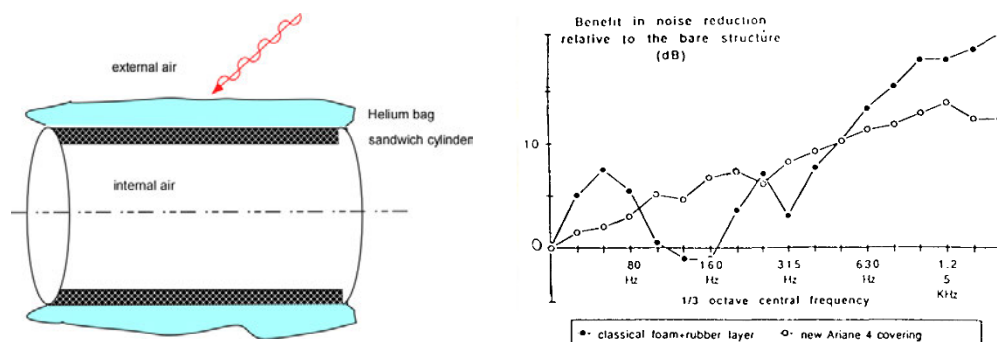

Figure 6. Helium bag to reducing noise inside fairing.

Nowadays BEM predictions are a standard method to design some of the equipment as large payload antennas. Capabilities of numerical BEM techniques have also improved in both model size and accuracy as shown in Figure 7.
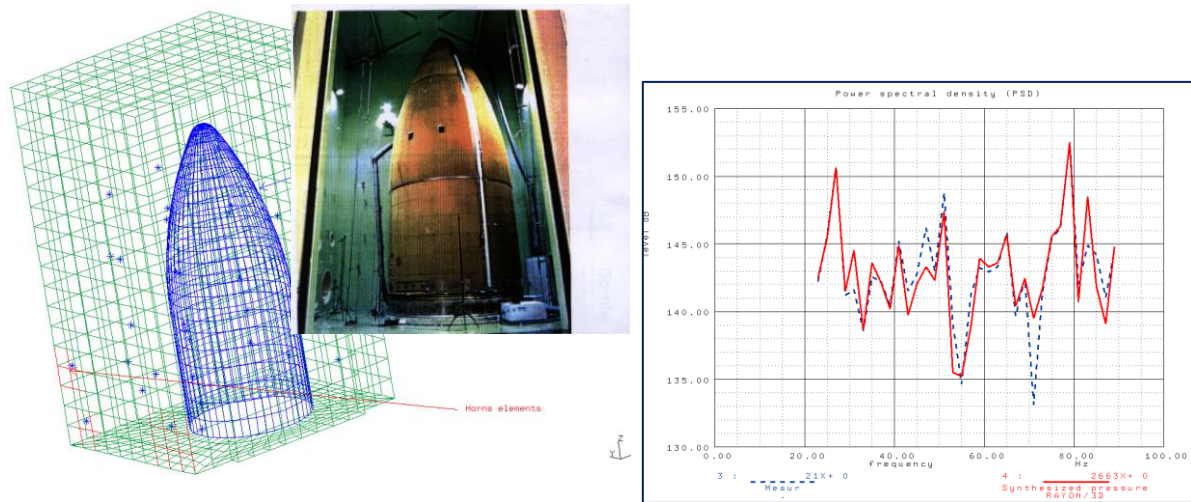

Figure 7 BEM analysis coupling FEM model of the Ariane 5 to both internal volume and to test acoustic chamber and correlation with test (Straco analysis for ESTEC).

3   ACOUSTIC QUALIFICATION OF THE ARIANE 5 VULCAIN ROCKET ENGINE

3.1   VULCAIN Engine vibroacoustic environment

Vulcain is the cryogenic engine of the central stage of Ariane 5 launch vehicle. Vulcain is surrounded by two solid propellant boosters (the EAP's) and is submitted to their acoustic noise at lift-off.

SPL levels generated by the boosters are around 10 dB higher than the self-noise of Vulcain. Noise is also maximum at lift-off in the high frequency range around 2000 Hz. Compared to previous Ariane generation of launch vehicle, this new environmental configuration needed to be understood and qualified . Specified SPL could not be reached in available reverberant rooms and even so, the engine would have been passive not allowing qualification of the equipment.

Analysis started by developing a theoretical SEA model of the engine to get broadband response prediction of acoustic vibrations of the engine. This analysis was completed by experimental SEA tests under instrumented-impact hammer to derive damping loss factors and coupling loss factors of the major subsystems: nozzle, turbo-pumps, gas generator and exhausts.

These data were injected in the SEA model at low frequencies to compensate lack of accuracy of analytical calculation in the related frequency domain.

The coupling with the acoustic field was computed analytically from radiation efficiency with the dedicated SEA EARTH software, used by the SNECMA and developed by the author. EARTH predictions up to 4000 Hz were satisfactorily validated against test of the engine in reverberant chamber (Figure 8), [18].
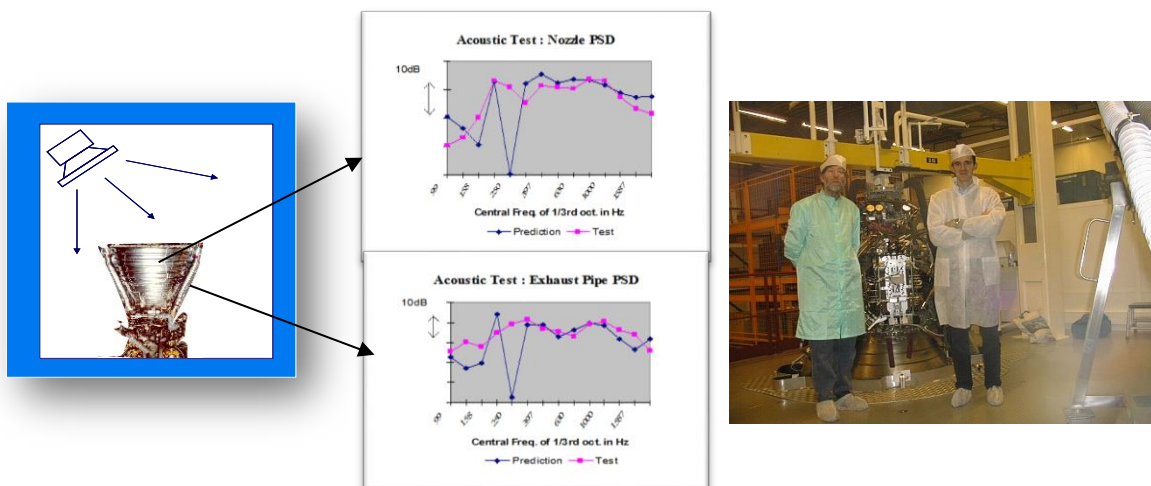
Figure 8. Test comparisons of VULCAIN SEA model Prediction of acoustic vibrations with SEA EARTH software.

3.2 VULCAIN Engine acoustic qualification process

Prior to undertake the Vulcain acoustic qualification process, a feasibility study started in 1993. Main idea was to concentrate the acoustic energy of the self-noise of the jet when fired in its test stand for increasing sound level on Vulcain nozzle. This increase of noise would simulate the noise of EAP's in the actual lift-off situation.

We had to prove enough energy could be trapped around the nozzle to reach the required qualification noise levels with the available radiated power by Vulcain. Radiated noise was predicted from [14].

The jet plume is split into slices along the flow line. Each slice has a global directivity diagram and a given spectrum of radiation efficiency computed from an experimental database of measurements on various kinds of engines. Abacuses of radiation of various engines contained in [14] were interpolated for covering the regime of cryogenic engines. Due to the scattering of sound wave on obstacles and to the presence of the jet guide, some corrections were necessary. As sketched in Figure 9, each slice of the plume is radiating in a given frequency band with given directivity. High frequencies are radiated by the nearest slices from the nozzle. Low frequencies are radiated by the furthest. The prediction of the sound pressure in the near field of Vulcain during a standard firing (Figure 10-left) was confirmed against measurement (Figure 9-right).
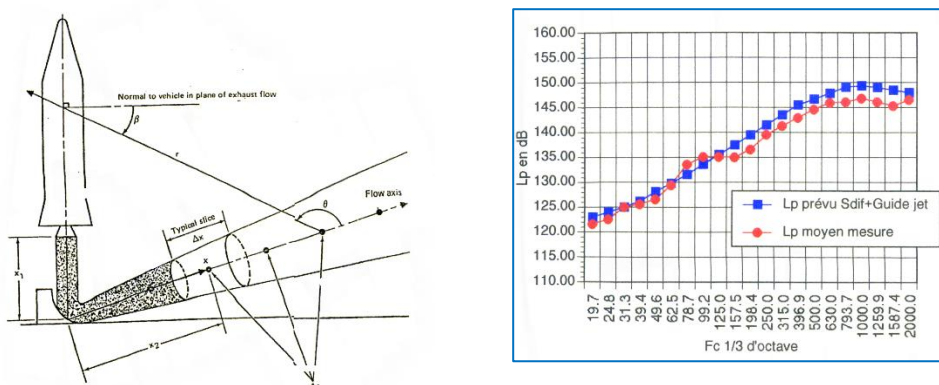
Figure 9. Prediction of Vulcain noise at test stand and related measured SPL.

9

From here, the first part of the jet was shown to be as appropriate source for delivering the required amount of diffuse SPL around the nozzle. A reflector structure was designed for confining the noise as shown in Figure 10-right.

Nevertheless, the reflector should have enough aperture for supporting the gas flow, enough stiffness for the resulting dynamic pressure and an optimized inclination for improving diffusivity and sound amplification. Its design was then performed thanks to 3D acoustic ray tracing model of the test stand to optimize its shape and its volume. There was also a risk of inducing local acoustic resonances in the fluid volume between reflector walls and nozzle.

Effect of the incidences on nozzle response was analyzed using EARTH software and the implemented reciprocal radiation integral that states the generalized applied acoustic force is reciprocal of its radiation efficiency in the direction of the incident wave.

Effect of depressurization due to jet aspiration was analyzed using a CFD model and the pressure outputs were used by EARTH SEA model to predict mean stress in the reflector panels.

Potential fluid resonances were analyzed using a BEM model with sources calculated from the jet model. The work was done in parallel by Acouphen company (ray-tracing optimization of the reflector structure), by Straco company and Pr. A. Hamdi for BEM risk analysis, by the Snecma (SEP division) for all CFD calculation, reflector construction and test realization and by the author for all SEA-based calculation, transducer calibration before the first qualification test and overall supervision of the study, [19].

The first qualification firing test lasted only 20 seconds and confirmed the prediction and the design choices as shown in Figure 11 (5 s past ignition) and Figure 12. The reflector was amplifying of about 8 to 10 dB the noise on the engine which was found acceptable despite achieved levels were 2dB below specification. The sound pressure measured during the lift-off of the 501 flight confirmed the correctness of the acoustic qualification process as shown in Figure 13.
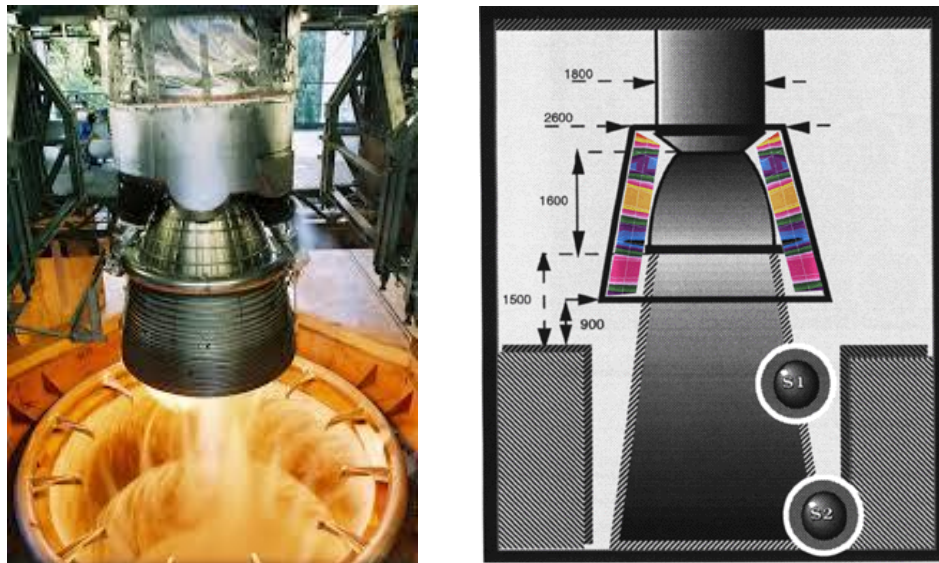
Figure 10. On left standard test stand configuration when firing the VULCAIN engine; on right acoustic qualification configuration with the acoustic reflector in position.
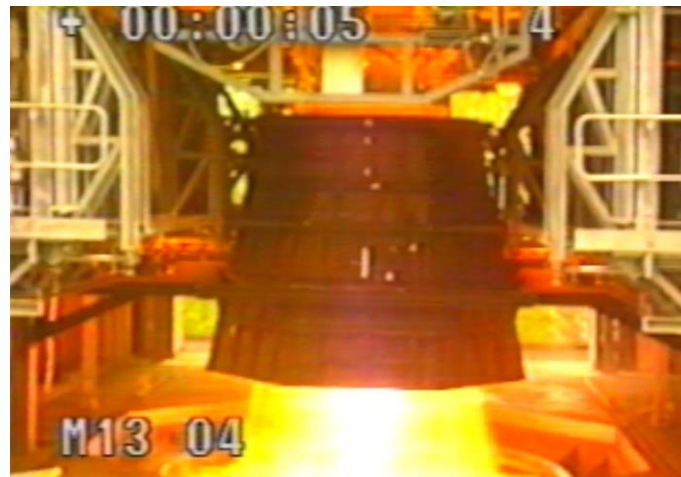
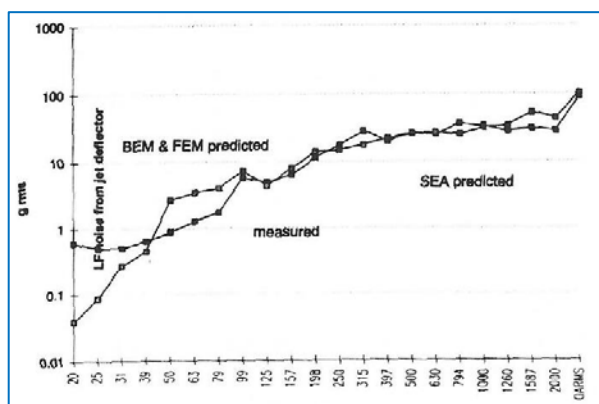Figure 11. Firing the engine with acoustic reflector in position.

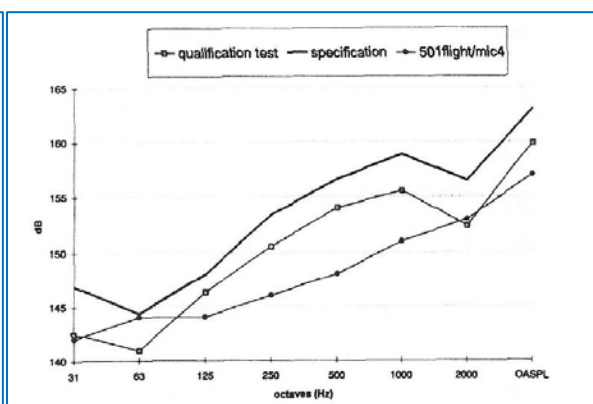| Figure 12. Reflector vibration: measured vs predicted.	Figure 13. Comparing qualification test and flight 501 measurement.

4   SHOCK RESPONSE PREDICTIONS

During the rocket flight, inter-stage separation is commonly performed by pyro-zip devices. Payload separation may also involve pyro-zip cut or explosive bolts for final in-orbit injection.

The cut is highly energetic and fast due to propagation of initial crack at 7000 m/s. It leads to very impulsive vibration signals near the separation line with very broad frequency band (above 100 kHz) and instantaneous levels of several thousands of g's and more.

Shocks are inducing failures on equipment such rupture of welds, malfunctioning electronics…

The severity of the shock is measured by the Shock Response Spectrum or SRS. The SRS of a signal $s(t)$ corresponds at a given frequency to the maximal response of a test oscillator with given Q-factor having this resonance frequency and excited at base by $s(t)$.

In general, the time history is required to perform SRS prediction in order to know the severity class in which the equipment is falling. Depending on equipment location on the launch vehicle, the specified SRS is different depending on distance to expected shock source. The payload has to be qualified to shocks and the resulting specified qualification SRS is an envelope of various shock events.

Pyrozip shock tests are known to be difficult to predict as the source itself is difficult to measure and calibrate. Specifying an SRS does not provide the deterministic signal to use in the

11

qualification test as the SRS transform is not reversible. Due to the high frequency content of shocks and the general variance in input description, a statistical approach appears as quite natural to predict response. Inside research program driven by the CNES, the author has demonstrated the validity of SEA method to predict fast transients generated by shocks. This may look like a paradox as SEA is predicting steady-state random vibration responses from forces and modal behavior.

This is only appearance. Near the source, the propagation is non-modal and response may be considered as constrained forced motion. The vibration level of the separation ring is considered as the effective source term. Away for the ring, frequency transfer functions on the various panels and equipment are close to SEA calculated transfers. Experimental work using shock sources shows SEA is given very good trends is term of transfer as soon as the force spectrum is known.

Nevertheless, SEA transfer has no phase. It is a real-valued transfer, not invertible for retrieving time domain response.

For this, a time history signal profile is allocated to the source: it may be a pre-defined simple-shaped force term like a triangle an impulse or half-sine pulse with given amplitude and duration. The force term is closely related to the separation process. Pyrozip cuts are delivering nearly perfect $\delta-$ Dirac's force profile but force has to be converted into injected power in the structure. For this a dedicated model to make this conversion is required.

For a fixed-position $\delta-$ Dirac, the conversion factor is known: $P_{in} = Y\left(x_i, f\right) F^2(x_i, f)$

where Y is the real part of the driving -point mobility at point x_i and F^2 is the square modulus of the autospectrum of applied force at x_i. In a pyrozip cut, the applied force moves along with the crack failure and this propagation speed has a strong influence on injected power in the structure. In a separation system using a clampband like in the Ariane 4 fairing, the clampband is first cut at both ends by explosive bolts creating a relaxation force moving at speed of sound in the clampband material, followed by internal potential energy liberation of the underlying compressed structure that was maintained by the clampband. Using Fourier's-based simple modeling of the injected power process due to propagating on edge of a continuous system leads to very good predictive model as shown in [24]. These models are also appropriate to predict measured responses near the source if force is scaled from tests. In example given in Figure 14, SEA-Shock method, as found in SEA+ software, is applied to the prediction of a pyrozip separation test of the Ariane 5 upper part. The time reconstruction is performed by the LMPR algorithm (Local Modal Phase Reconstruction) that develops the response in the receiver over its local analytical modes of vibration and scales it to expected real-value transfer function between the source and the receiver provided by the SEA model of the various coupled subsystems. The propagation force model for computing injected power was tested for the first time in this example study. Second similar example is given in Figure 15 and was part of benchmark test of SEA-Shock for the European Space Agency. Further details may be found in references [20] to [25], especially the application to shock responses of the payload. Recent developments implement shock prediction directly using specified SRS as the input to simplify the modeling work for launch vehicle passengers that do not know the underlying shock source at the origin of the specification.

5   CONCLUDING REMARKS

Various examples of usefulness of vibroacoustic calculation methods taken in the Ariane launch vehicle program have been presented in a way to put emphasis on the calculation scheme. The latter improves both risk analysis and engineering knowledge through easier interpretation of measured data and extrapolation to unmeasured configurations. BEM and SEA are complementary techniques

for covering the full spectral domain of investigated process. SEA method provides a very powerful insight into the random vibration behavior of such complex machines even for fast transient like separation shocks. This article is complemented by a bibliography related to the treated examples where readers will find related theoretical developments that are not presented here.
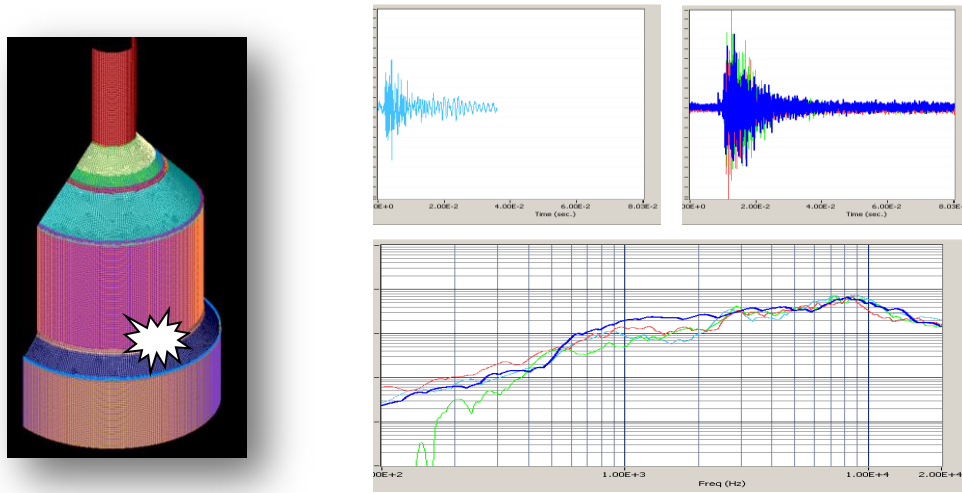

Figure 14. SEA-Shock prediction of Ariane 5 separation test of the upper part (top synthesized and measured time history on the payload, bottom SRS for predicted time signal (blue) compared to SRS from measurements.
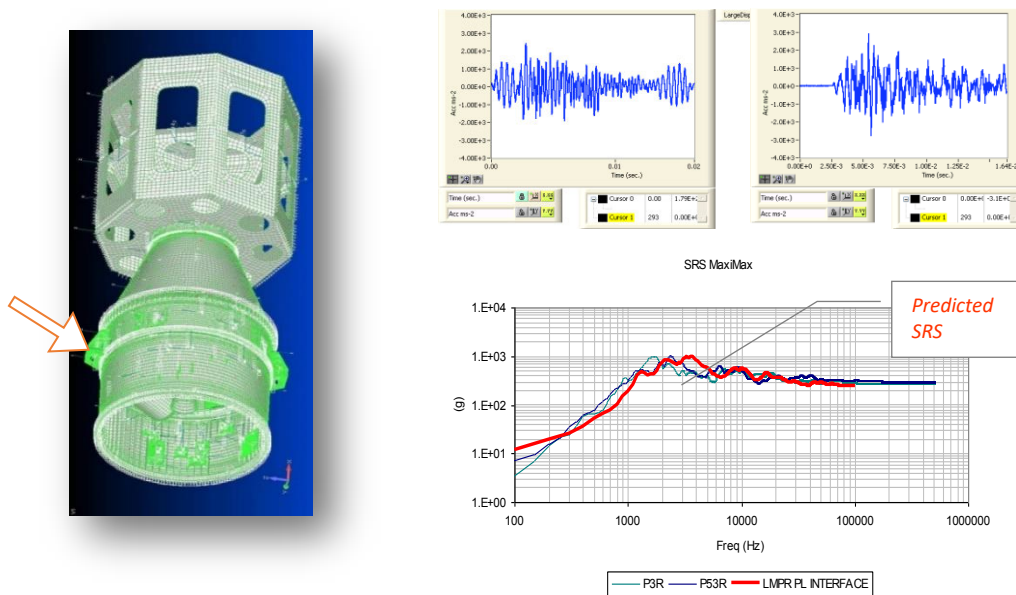
Figure 15. Prediction of Vega launch vehicle upper part: top left, predicted time history on payload interface and top right related measurement; bottom predicted vs measured SRS at same location.

REFERENCES

[1]   H. Morand and R. Ohayon. Variational Formulation for the Elastoacoustic Vibration Problem: Finite Element Results. 2ème Symposium International sur les méthodes d'éléments finis dans les problèmes d'écoulements, Rapallo 1976.

[2]   M. A. Hamdi. Formulation variationnelle par équations intégrales pour le calcul de champs acoustiques linéaires proches et lointains. Thèse UTC, 1982.

[3]   G. Borello. Réponses basses fréquences de structures axisymétriques en bruit diffus. Spacecraft Structures Conference. (ESA SP-238, April 1986), 1986.

[4]   G. Borello. Acoustic Intensity Techniques Applied to Parameter Identification of Noise under a Fairing through a SEA Mode. AIAA, Dynamic Specialists Conference, pp. 844-850, April 1987.

[5]   G. Borello. Numerical Methods for the Prediction of Internal Vibroacoustic Environment of Space Vehicle. Inter-Noise 1987.

[6]   G. Borello, A. Blaise, C. Lesueur, M. Gotteland and M. Barbe. Sound Transmission Studies of some Ariane Structures (Acoustic Optimization of Light-Weighted Aerospace Structures). Inter-Noise 1988.

[7]   Van Maercke, D. Kapus and E. Roland. Etude du champ acoustique au voisinage de la coiffe d'Ariane par une méthode d'acoustique géométrique. CSTB Grenoble, GA/87-637/JR/BEA pour CNES/DLA.

[8]   M. A. Hamdi. Recent Advances in Vibroacoustic Computation. Inter-Noise 1988.

[9]   J. Ben Mariem, L. Mebarek and A. Ounadjela. Vibroacoustic Analysis of Ariane 4 Launcher by a New Boundary Finite Element Method. Inter-Noise 1988.

[10]   G. Borello, N. Pinder and I. U. Borchers. Interior Noise Control of Spacecraft Launch Vehicles. IAF Congress, 1989.

[11]   G. Borello. Low Frequency Noise Prediction of Internal Acoustic Environment of a Launch Vehicle at Lift-off. Inter-Noise 1989.

[12]   G. Borello. Utilisation de l'hélium pour la protection acoustique des lanceurs. ASTE, 1990.

[13]   G. Borello, Payload Configuration Influence of the Ariane 4 Launcher on the Internal Acoustic Environment at Lift-off. Inter-Noise 1990.

[14]   Acoustic Loads Generated by the Propulsion System. NASA SP 8072. June 1971.

[15]   G. Borello. Identification of SEA Coupling Loss Factors on a Liquid Rocket Engine. Inter-Noise 1991.

[16]   H. J.-P. Morand and R. Ohayon. *Interactions fluides-structures*. Edition Masson 1992.

[17]   G. Borello. Vibrational Energy Prediction of the response of the Vulcain Rocket Engine using a Mixed FET/SEA Analysis. Inter-Noise 1992.

[18]   G. Borello, A.Kernilis, R. Gazave and P. Esparcieux. Ambiance Vibratoire des moteurs fusées. Colloque International Ambiance Acoustique et Vibratoire des Systèmes de Transport Spatial. 1994.

[19]   A. Kernilis, F. Desnot, G. Borello and J. M. Mondot. Acoustic Qualification of Ariane 5 Vulcain Engine. ECSSMMT (ESEA SP-428, February 1999), 1998.

14

[20]   G. Borello. Analysis of Wave Propagation in Pyrotechnical Shock Tests. 1er Colloque européen sur la Technologie des Lanceurs, Vibrations des Lanceurs, 1999.

[21]   E. Bodin, B. Brevard, P. Wagstaff and G. Borello. Pyrotechnic Shock Response Predictions Combining Statistical Energy Analysis and Local Random Phase Reconstruction. *The Journal of the Acoustical Society of America*. Vol. 112, iss. no.1, pp 156-163, July 2002.

[22]   G. Borello and V. Cipolla. Prediction of High Frequency Shock Response of a Satellite Using SEA. ECSSMMT 2002.

[23]   G. Borello. Analyse statistique énergétique SEA & Applications industrielles de la SEA. *Techniques de l'ingénieur*, R 6 215 & R 6 216, 2006 et mis à jour R 6215 V2, 2012.

[24]   G. Borello. J. Primus, R. Nguyen Van Lan and S. Kiryenko. Prediction of Payload Shock Response in the Mid and High Frequency Range. ECSSMMT, 2009.

[25]   G. Borello. Acoustic Response of Spacecraft Equipment and Shock Response from SEA Prediction. ECSSMMT, 2016.

AERO-ACOUSTIC EXPERIMENTAL IDENTIFICATION OF FEEDBACK MECHANISMS DUE TO HVAC COMPONENTS

JM.Ville[1*], S. Bennouna[2], N. Papaxanthos[1], E. Perrey-Debain[1] and S. Moreau[1]
[1]Laboratoire Roberval UMR CNRS 7337
Sorbonne Universités, Université de Technologie de Compiègne
CS 60319, 60203 Compiègne, France
Email: jean-michel.ville@utc.fr, emmanuel.perrey-debain@utc.fr

[2]Valeo Thermal Systems
8 rue Louis Lormand, 78320 La Verrière, France
Email: saad.bennouna@valeo.com

ABSTRACT

The Heating Ventilation and Air Conditioning (HVAC) system of a car has to provide air flow to ensure the passengers comfort regarding the temperature inside the vehicle cabin without damaging the acoustic environment. The acoustic sources are mainly produced by the blower and by the interaction between a low Mach number flow and the elements located in a duct. A research program CEVAS was conducted under the leadership of Valeo to develop a tool to design low noise car HVAC. The acoustic laboratory of the University of Technology of Compiègne (UTC) was in charge of the experimental and theoretical characterization of the aeroacoustics sources. With the experimental 2N-ports method, measurements of the scattering matrix and of the aero-acoustic power spectrum of the aero-acoustic sources are performed. The existence of fluid-resonant feedback mechanisms responsible for high level tones radiated sound power are identified and discussed for a butterfly flap and two diaphragms in tandem, the latter representing the association of HVAC elements.

WAVE FINITE ELEMENTS - FINITE ELEMENTS COUPLING TO COMPUTE THE DYNAMIC RESPONSE OF AN HETEROHENEOUS RAILWAY TRACK

T. Gras[1,2] , M-A. Hamdi[2] M. BenTahar[2] and Samir Assaf[1]

[1]Institut de Recherche Technologique Railenium
Technopôle Transalley, 180, rue Joseph-Louis Lagrange, 59300 FAMARS
Email: thibaut.gras@railenium.eu
Email: samir.assaf@railenium.eu

[2]Sorbonne universités, Université de technologie de Compiègne, CNRS UMR 7337 Roberval
Centre de recherche Royallieu - CS 60 319 - 60 203 Compiègne cedex FRANCE
Email: Mohamed-Ali.Hamdi@esi-group.com
Email : mabrouk.bentahar@utc.fr

ABSTRACT

Railway noise is a critical issue concerning environmental noise. At the wheel/rail contact point, both the wheel and the track are dynamically excited and vibrate together to emit the well-known rolling noise within a frequency range comprised between 100 Hz to 5000 Hz. The point receptance of the rail is an important quantity to accurately predict wheel-rail noise emission. The goal of this paper is to compute the dynamic behaviour of an heterogeneous railwaytrack using a biperiodicity method on a heterogeneous unit cell. A coupling between the Finite Element Method (FEM) and the Wave Finite Element Method (WFEM) is made to model all kinf of heterogeneities along the track. An example is applied by modelling the heterogeneities as elastic supports, an external force is applied inside the unit cell and the response gives good agreements with experimental results from litterature.

1 INTRODUCTION

Railway noise is a critical issue concerning environmental noise. At the wheel/rail contact point, both the wheel and the track are dynamically excited and vibrate together to emit the well-known rolling noise within a frequency range comprised between 100 Hz to 5000 Hz. The track is made of a rail supported by an elastomeric pad, a sleeper and a damp resilient ballast layer. The point receptance of the rail is an important quantity to accurately predict wheel-rail noise emission. The theory of periodicity developed by Mead [1] has been widely used to compute the response of heterogeneous infinite railwaytracks [2] i.e which are periodically supported. His theory allowed the use of finite elements [1, 3] to describe the dynamic behaviour of infinite periodic structures with arbitrary-shaped sections.

In this paper, the dynamic behaviour of an heterogeneous railwaytrack is computed using a biperiodicity method [1], through a coupling between the Finite Element Method (FEM) and the Wave Finite Element Method (WFEM) [4]. This coupling allows the use of all kinds of heterogeneities along the track. The principle of the WFEM is first recalled, then the forced response is computed inside a unit cell by using a biperiodicity method.

2 MODELLING APPROACH

2.1 The Wave Finite Element Method for periodic structures
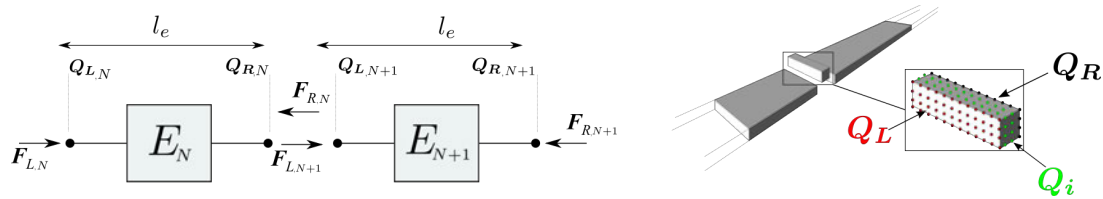
FIGURE 1. Displacements and forces applied on a unit cell of length l_e

The periodic structure is an infinite series of unit cells coupled with n_c degrees of freedom. The coupling coordinates are Q_L Q_R and the coupling forces F_L F_R. The dynamic stiffness matrix D, assembled with the finite element method, can be condensed [3] by expressing through a matrix inversion the internal coordinates Q_i in function of the coupling coordinates such as :

$$\begin{bmatrix} D_{LL} & D_{LR} \\ D_{RL} & D_{RR} \end{bmatrix} \begin{Bmatrix} Q_L \\ Q_R \end{Bmatrix} = \begin{Bmatrix} F_L \\ F_R \end{Bmatrix} \tag{1}$$

The use of the periodicity principle [3**?**] leads to a generalised eigenvalue problem which gives a set of $2n_c$ couples (Θ_j, Λ_j) for each frequency. Θ represents the waveshape basis splitted into waveshapes displacements Θ_q and waveshapes forces Θ_f. The eigenvalue Λ is associated with the propagation constant γ and the periodic lenght l_e of the unit cell such as [1, 3] :

$$\Lambda_j = e^{\gamma_j \, l_e} \quad \Theta_j = [\Theta_{q_j} \; \Theta_{f_j}]^T \tag{2}$$

The basis can be splitted into positive propagative direction if $|\Lambda_j| < 1$ associated with n_c $\Theta^+ = [\Theta_q^+ \; \Theta_f^+]^T$ and into negative propagative direction if $|\Lambda_j| > 1$ with n_c $\Theta^- = [\Theta_q^- \; \Theta_f^-]^T$. The forced response of a periodic structure can be written as a sum of these waves [3].

2.2 Computation of the forced response using a biperiodicity method

The periodicity theorem is applied on a $0.6m$ length cell (named *Unit Cell I*) which represents the distance between two elastic supports of a railway track. As reminded in the previous section, this cell needs to be condensed at its coupling interfaces. A biperiodicity method [1] is

2

used to condensate the homogeneous part (made of several slices of the rail named *Unit Slice*), it consists in expressing the condensed dynamic stiffness matrix of this part thanks to the wave-shape basis [3]. The heterogenous parts (which can contain the elastic supports) are modelled with two FEM parts and are coupled with the homogeneous part [4]. Unit cells I are associated
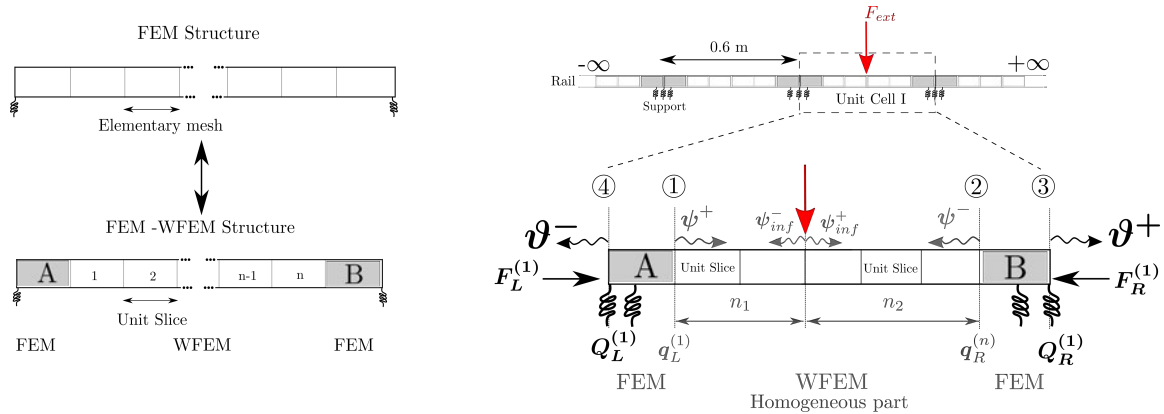

FIGURE 2. Waves inside and outside a discretized unit cell I made of a FEM-WFEM coupling

with the waveshapes $\boldsymbol{\Theta}$ of amplitudes $\boldsymbol{\vartheta}$, unit slices are associated with the waveshapes $\boldsymbol{\Phi}$ of amplitudes $\boldsymbol{\psi}$ and with the eigenvalue $\boldsymbol{\lambda}$ (such as $|\lambda| > 1$). The displacements and the forces inside the internal waveguide can be written as a sum of infinite waves $\boldsymbol{\psi}_{inf}$ i.e waves propagating in an infinite structure and of reflected waves $\boldsymbol{\psi}$ on the boundaries. The modal waveshape amplitude $\boldsymbol{\psi}_{inf}$ can be calculated as [1] :

$$\left\{\begin{matrix} \boldsymbol{\psi}_{inf}^{+} \\ \boldsymbol{\psi}_{inf}^{-} \end{matrix}\right\} = \begin{bmatrix} -\boldsymbol{\Phi_f}^{-} & -\boldsymbol{\Phi_f}^{+} \\ \boldsymbol{\Phi_q}^{-} & \boldsymbol{\Phi_q}^{+} \end{bmatrix}^{T} \left\{\begin{matrix} 0 \\ F_{ext} \end{matrix}\right\} \tag{3}$$

The numbers of unit slices on the left n_1 and on the right n_2 of the external force are such as $n_1 + n_2 = n$. The displacements $\boldsymbol{q}_L^{(k)}$ and the forces $\boldsymbol{f}_L^{(k)}$ of the unit slice k inside the homogeneous part and $\boldsymbol{Q}_L^{(1)}$ $\boldsymbol{F}_L^{(1)}$ those of the unit cell I interfaces can be written as :

$$\boldsymbol{q}_L^{(k)} = \quad \boldsymbol{\phi_q^+}\boldsymbol{\lambda}^{k-1}\boldsymbol{\psi}^+ \quad + \quad \boldsymbol{\phi_q^-}\boldsymbol{\lambda}^{n+1-k}\boldsymbol{\psi}^- + \quad \boldsymbol{\phi_q}^-\boldsymbol{\lambda}^{n_1+1-k}\boldsymbol{\psi}_{inf}^- \tag{4}$$

$$\boldsymbol{f}_L^{(k)} = \quad \boldsymbol{\phi_f^+}\boldsymbol{\lambda}^{k-1}\boldsymbol{\psi}^+ \quad + \quad \boldsymbol{\phi_f^-}\boldsymbol{\lambda}^{n+1-k}\boldsymbol{\psi}^- + \quad \boldsymbol{\phi_f}^-\boldsymbol{\lambda}^{n_1+1-k}\boldsymbol{\psi}_{inf}^- \tag{5}$$

$$\boldsymbol{Q}_L^{(1)} = \boldsymbol{\Theta_q^-}\boldsymbol{\vartheta}^- \quad \boldsymbol{F}_L^{(1)} = \boldsymbol{\Theta_f^-}\boldsymbol{\vartheta}^- \quad \boldsymbol{Q}_R^{(1)} = \boldsymbol{\Theta_q^+}\boldsymbol{\vartheta}^+ \quad \boldsymbol{F}_R^{(1)} = \boldsymbol{\Theta_f^+}\boldsymbol{\vartheta}^+ \tag{6}$$

The dynamic stiffness matrices of the A and B FEM parts are noted $\boldsymbol{D}_A$ $\boldsymbol{D}_B$, the dynamic equilibrium on the four interfaces (see Figure 2) gives after some rearrangements :

$$\left\{\begin{matrix} \boldsymbol{\psi}^+ \\ \boldsymbol{\psi}^- \\ \boldsymbol{\vartheta}^+ \\ \boldsymbol{\vartheta}^- \end{matrix}\right\} = \begin{bmatrix} \boldsymbol{I} & -\boldsymbol{R}^+\boldsymbol{\lambda}^n & \boldsymbol{0} & \boldsymbol{X}^{-1}\boldsymbol{D}_{A,RL}\boldsymbol{\Theta_q^-} \\ -\boldsymbol{R}^-\boldsymbol{\lambda}^n & \boldsymbol{I} & \boldsymbol{Y}^{-1}\boldsymbol{D}_{B,LR}\boldsymbol{\Theta_q^+} & \boldsymbol{0} \\ \boldsymbol{Z}^{-1}\boldsymbol{D}_{B,RL}\boldsymbol{\lambda}^n & \boldsymbol{Z}^{-1}\boldsymbol{D}_{B,RL} & \boldsymbol{I} & \boldsymbol{0} \\ \boldsymbol{W}^{-1}\boldsymbol{D}_{A,LR} & \boldsymbol{W}^{-1}\boldsymbol{D}_{A,LR}\boldsymbol{\lambda}^n & \boldsymbol{0} & \boldsymbol{I} \end{bmatrix}^{-1} \left\{\begin{matrix} \boldsymbol{R}^+\boldsymbol{\lambda}^{n_1}\boldsymbol{\psi}_{inf}^- \\ \boldsymbol{R}^-\boldsymbol{\lambda}^{n_2}\boldsymbol{\psi}_{inf}^+ \\ -\boldsymbol{Z}^{-1}\boldsymbol{D}_{B,RL}\boldsymbol{\lambda}^{n_2}\boldsymbol{\psi}_{inf}^+ \\ -\boldsymbol{W}^{-1}\boldsymbol{D}_{A,LR}\boldsymbol{\lambda}^{n_1}\boldsymbol{\psi}_{inf}^- \end{matrix}\right\} \tag{7}$$

$$\boldsymbol{W} = [\boldsymbol{D}_{A,LL}\,\boldsymbol{\Theta_q^-} - \boldsymbol{\Theta_f^-}] \qquad\qquad \boldsymbol{X} = [\boldsymbol{D}_{A,RR}\,\boldsymbol{\phi_q^+} + \boldsymbol{\phi_f^+}] \tag{8}$$

$$\boldsymbol{Y} = [\boldsymbol{D}_{B,LL}\,\boldsymbol{\phi_q^-} - \boldsymbol{\phi_f^-}] \qquad\qquad \boldsymbol{Z} = [\boldsymbol{D}_{B,RR}\,\boldsymbol{\Theta_q^+} + \boldsymbol{\Theta_f^+}]$$

$$\boldsymbol{R}^- = [\boldsymbol{D}_{B,LL}\,\boldsymbol{\phi_q^-} - \boldsymbol{\phi_f^-}]^{-1}[\boldsymbol{D}_{B,LL}\,\boldsymbol{\phi_q^+} - \boldsymbol{\phi_f^+}] \qquad \boldsymbol{R}^+ = [\boldsymbol{D}_{A,RR}\,\boldsymbol{\phi_q^+} + \boldsymbol{\phi_f^+}]^{-1}[\boldsymbol{D}_{A,RR}\,\boldsymbol{\phi_q^-} + \boldsymbol{\phi_f^-}] \tag{9}$$

The first two lines of Equation (7) are the coupling between the heterogenous parts and the homogenous one, the last two lines are the coupling between the heterogenous parts and the semi-infinite structures.

3

3   RESULTS

The method is applied on an heterogenous railway track periodically supported. The rail section is meshed with linear hexahedral elements, the 0.6m length cell is divided into 60 slices i.e a 1cm elementary mesh. Elastic support parameters are taken as given by L.Gry [5]. The Figure 3(a) represents the mobility of the track due to an external vertical force applied at the middle of the unit cell I. The simulation gives a good correspondance with experimental results from [5] and well reproduces the periodicity effects. The Figure 3(b) represents the receptance along an half-track at the pinned-pinned frequency (1090Hz) which appears when half the wavelength is equal to the distance between supports.
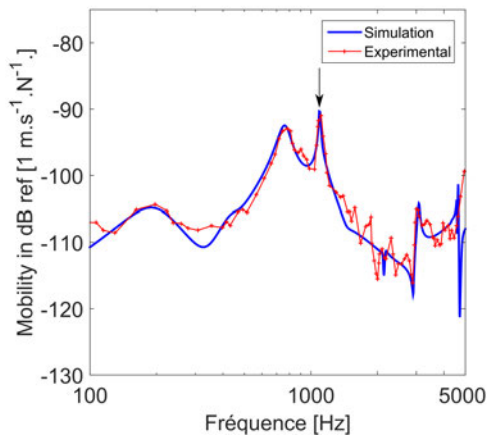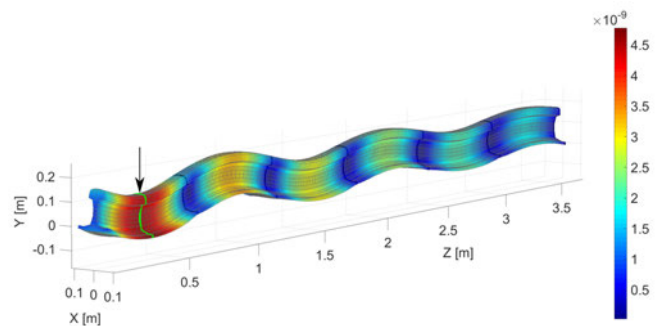
(a)   (b)

4   CONCLUSION

In this paper, a method to compute the response of a heterogeneous periodic structure due to an external force applied in a unit cell has been proposed. It uses a FEM-WFEM coupling to model all kinds of heterogeneities along the waveguide. The method has been applied on an heterogeneous railway track laid on elastic supports and gives good agreements with experimental results.

REFERENCES

[1] D.J. Mead. The forced vibration of one-dimensional multi-coupled periodic structures : An application to finite element analysis. *Journal of Sound and Vibration*, 319(1–2) :282 – 304, 2009.

[2] T. Gras, M.-A. Hamdi, and M. Ben Tahar. Finite element method - wave finite element method coupling to compute the forced response of an infinite periodically supported railway track. In *Proceedings of the Third International Conference on Railway Technology : Research, Development and Maintenance*, number Paper 181. Civil-Comp Press, 2016.

[3] D. Duhamel, B.R. Mace, and M.J. Brennan. Finite element analysis of the vibrations of waveguides and periodic structures. *Journal of Sound and Vibration*, 294(1–2) :205 – 220, 2006.

[4] J.-M. Mencik and D. Duhamel. A wave-based model reduction technique for the description of the dynamic behavior of periodic structures involving arbitrary-shaped substructures and large-sized finite element models. *Finite Elements in Analysis and Design*, 101 :1 – 14, 2015.

[5] L. Gry. Dynamic modelling of railway track based on wave propagation. *Journal of Sound and Vibration*, 195(3) :477 – 505, 1996.

4

Engine sources Identification using an Inverse BEM technique

C. Glandier[1], T. Vogt[2], J. Morkholt[2], A. Omrani[3] and M. A. Hamdi[3]

[1]Daimler AG, Sindelfingen GERMANY
Email: christian.c.glandier@daimler.com

[2] Innovations Group ,Brüel &Kjær A/S , Naerum, DENMARK

[3] STRACO SA, Compiègne, FRANCE

ABSTRACT

Acoustic equivalent source models play an important role in the automotive NVH design process. Such models represent the sound radiated by an engine e.g. with a set of point sources distributed over the engine's surface. These models can be used in combination with either measured or computed Noise Transfer Functions. This paper presents an investigation of engine noise radiation using a novel hybrid technique that allows the determination of surface equivalent sources. The method is based on the combination of up-to-date measurement techniques and a numerical Inverse Boundary Element Method (I-BEM). Starting from the measurement of the sound field surrounding a radiating object , the noise sources on the object's surface are identified using the I-BEM technique. This method is applied to a Mercedes-Benz A-class engine, in order to investigate its vibrational behaviour and predict the sound levels in the far field. Prior to the application to the real engine, the technique was tested on an engine mock-up equipped with six independently driven volume velocity sources. In this setup, the source positions as well as their volume velocities and time correlations are well known. The known source positions are well identified by the software. Good agreement is also obtained on farfield. microphones, both for the mockup and for the real running engine.

Lessons Learned from ARIANE 4 and ARIANE 5 Vibroacoustics Analysis

Bernard Troclet[1]

[1]AIRBUS SAFRAN LAUNCHERS, Les Mureaux, FRANCE
Email: bernard.troclet@airbusafran-launchers.com

ABSTRACT

The objective of this conference is to present the vibroacoustic approaches on Ariane launchers. Early in the design development of the Ariane 5 launcher, it was anticipated that the acoustic environment would be a severe case load. Consequently, very soon, noise reduction means have been investigated.

This conference will address:

- *The acoustic environment experienced by the launchers lift-off and during flight ascent and the work undertaken to reduce noise surrounding the ARIANE 5 launch vehicle and the noise inside the Fairing on the one hand. The reduced scale test to characterize the lift-off noise and to investigate potential noise reduction means, the Fairing full scale acoustic test are presented,*

- *And the methods used to estimate the vibroacoustic response of launch vehicles on the other hand.*

Finally, perspectives in the field will be presented.

Diffuse field loading of space structures - modeling and test

Bryce Gardner[1]

[1]ESI North America, Inc. San Diego, USA
Email: Bryce.Gardner@esi-group.com

ABSTRACT

This paper presents a comparison of different modeling approaches for honeycomb panel structures and a simplified satellite box. The problem at hand is the prediction of the response of these structures to a diffuse acoustic field. The structure is modeled with both a finite element method (FE) and a statistical energy analysis (SEA) approach. The surrounding acoustic fluid is modeled with boundary element analysis (BEM) and SEA. The following coupled models are considered: FE-BEM, Hybrid FE-SEA, and SEA. The predicted results are compared to experimental data. While all of the methods have their role, showing the comparing the methods across a broad frequency range provides insight into the strengths and weakness of the different methods.

Introduction

Noureddine Attala [*][†] [1]

[1] Department of Mechanical Engineering, Université de Sherbrooke – Sherbrooke, Quebec J1K 2R1,
Canada

[*]Speaker

[†]Corresponding author: noureddine.atalla@usherbrooke.ca

Video message for Prof. Mohamed Ali Hamdi

Claude Lesueur [*][†] [1]

[1] Département de Recherche en Ingénierie des Véhicules pour l'Environnement (LRMA-DRIVE) – ISAT – France

Video message for Prof. Mohamed Ali Hamdi

[*]Speaker
[†]Corresponding author:

The development of RAYON-PEM solver - Academic & Industrial Milestones

Marc Anciant & Lassen Mebarek[1]

[1]ESI-Group, 8 rue Clément Bayard, Bâtiment 3 – 2ème étage, 60200 COMPIEGNE, FRANCE
Email: marc.anciant@esi-group.com; lassen.mebarek@esi-group.com

ABSTRACT

This presentation gives an overview of the main stages which contribute to the development of the Porous Elastic Module (PEM) in the RAYON solver, dedicated to the simulation of the Porous Elastic Media based on a mixed displacement–pressure(U,p) Formulation to solve modified Biot's equations . This covers the academic aspects, such as the implementation of the (U,p) mixed formulation established in early of year 2000, using Mixed Finite Elements (MFE). Some basic academic and industrial applications have been solved and experimentally validated in cooperation with academic and industrial partners proofing the validity of the results obtained with RAYON-PEM Solver. During the last 15 years, many projects with major automotive and aerospace partners enabled to transform this RAYON-PEM module in a robust standalone simulation tool, also called Vehicle Trim Modeler (VTM), capable to compute the vibro-acoustic response of fully trimmed vehicles, but also the Transmission Loss (TL) of some vehicle components. More recently, the RAYON-PEM module has been integrated in two other ESI-Group products (VA-One and Visual-VPS). It is now worldwide distributed and can be considered as a reference tool in the domain of the vibro-acoustic simulation for low and medium frequencies..

Symmetric variational coupling of Boundary and Finite Element Methods for solving Vibro-Acoustic problems

Mohamed-Ali Hamdi [*][†] [1]

[1] Laboratoire Roberval UMR 7337 – Université de Technologie de Compiègne – CS 60319, 60203 Compiègne Cedex, France

Symmetric variational coupling of Boundary and Finite Element Methods for solving Vibro-Acoustic problems

[*]Speaker
[†]Corresponding author: mohamed-ali.hamdi@utc.fr

HOMOGENISATION AND DYNAMICS OF RANDOMLY IRREGULAR METAMATERIAL

Sondipon Adhikari[1]

[1] Aerospace Engineering, College of Engineering
Swansea University, UK
Email: s.adhikari@swansea.ac.uk

ABSTRACT

Metamaterials based on hexagonal periodic cells (honeycombs) have gained considerable attention in recent years. This can be an advanced material due to its capability of meeting high performance requirements in various critically desirable application-specific parameters [1]. These structural assemblies not only make an efficient use of material, but are also characterized by interesting dynamic and wave propagation properties. A semi-analytical formulation has been developed for wave propagation in irregular honeycombs. Spatial structural irregularity of hexagonal lattices has been considered. There are few scientific literatures available concerning analysis of wave propagation in regular honeycombs [2]. However, due to inevitable uncertainties associated with manufacturing and service conditions, honeycomb lattices may not be always perfectly regular. The effect of spatially random structural irregularity in wave velocities of such irregular honeycombs will be discussed. The nature of so called 'pass band' and 'stop bands' due to irregularities will be explained.

REFERENCES

[1]   Gibson L., Ashby M. F. (1999) Cellular Solids Structure and Properties. Cambridge University Press, Cambridge, UK.

[2]   Gonella S., Ruzzene M. (2008) Analysis of in-plane wave propagation in hexagonal and re-entrant lattices, Journal of Sound and Vibration 312 125–139

ON THE STABILITY LOSS OF LIMIT CYCLE OSCILLATIONS NEAR STRONG RESONANCES: SYNCHRONIZATION AND HETEROCLINIC BIFURCATION

B. W. Qin[1], K.W. Chung[2], A. Fahsi[3] and M. Belhaq[4]

[1]Dongguan University of Technology, P.R. China
[2]City University of Hong Kong, Hong Kong
[3]FST, University Hassan II- Casablanca, Morocco
[4]FSAC, University Hassan II-Casablanca, Morocco
Email: mbelhaq@yahoo.fr

ABSTRACT

In self-excited nonlinear oscillators subjected to harmonic forcing, frequency-locking can occur near strong resonances. This phenomenon results from synchronization between the frequency of the forcing and the frequency of the limit cycle oscillation leading to frequency-locked motions for which the response of the system follows the forcing frequency.

In the case of 1:4 resonance, which is considered as one of the unsolved problem in nonlinear dynamics [1], the limit cycle loses its stability at the synchronization via heteroclinic bifurcation. Usually, the transition between quasi-periodic and synchronized motions occurs via heteroclinic connections at two different frequencies causing hysteresis and bistability. Therefore, analytical approximation of heteroclinic bifurcations near the 1:4 resonance is of great importance since they determine the locations at which the frequency-locked motion takes place.

The existence of heteroclinic orbits in ordinary differential equations corresponds to the existence of coherent structures such as solitons and fronts in certain partial differential equations. For instance, they form the profiles of traveling wave solutions in reaction–diffusion problems and spatially localized post-buckling states in static dynamics. Also, heteroclinic orbits correspond to the onset of various types of synchronization in certain problems in physics and biology [2,3]. Therefore, one of the challenging problems is the analytical capture of the heteroclinic bifurcations location near the strong resonances [1]. To the best of our knowledge, rigorous analytical

expressions of heteroclinic bifurcation near these resonances have not been obtained, only numerical methods have been performed [4,5]. In this talk, recent analytical methods to capture approximation of such heteroclinic bifurcations in the problem of stability loss of limit cycle oscillations near the 1:4 resonance will be presented. The problem of 1:3 resonance will be also discussed.

REFERENCES

[1]   V.I. Arnold, Loss of stability of self-oscillation close to resonance and versal deformations of equivariant vector fields. Funkts. Anal. Priliozh. 303, 2–10 (1977)

[2]   K. Wiesenfeld, P. Colet, S.H. Strogatz, Frequency locking in Josephson arrays: connection with the Kuramoto model. Phys. Rev. E 57, 15631569 (1998)

[3]   P. Ashwin, O. Burylko, Y. Maistrenko, Bifurcation to heteroclinic cycles and sensitivity in three and four coupled phase oscillators. Phys. D 237, 454–466 (2008)

[4]   F.S. Berezovskaia, A.I. Khibnik, On the bifurcation of separatrices in the problem of stability loss of auto-oscillations near 1:4 resonance. J. Appl. Math. Mech. 44, 938–943 (1980)

[5]   B. Krauskopf, On the 1:4 resonance problem. Ph.D. Thesis, University of Groningen (1995)

MULTIBODY MODELING AND SIMULATION OF THE DYNAMICS OF RAILROAD VEHICLES AND TRACKS

José Luis Escalona

University of Sevilla, SPAIN
Email: escalona@us.es

ABSTRACT

Computational analysis of the dynamics of railroad vehicles is becoming an essential tool for this industry. Vehicle designers, rolling stock manufactures and railroad administrations benefit from the special modeling tools provided by the different railroad multibody softwares that are present in the market. Railroad dynamics is nowadays a sub-field of multibody dynamics that is characterized by the use of special algorithms for the treatment of the track geometry and the wheel-rail interaction. This presentation shows the theoretical foundations of these algorithms. Railroad vehicles have been traditionally designed using linearized equations that uncouple the longitudinal, lateral and vertical dynamics. Linear models can be used to find a first approximation of the response of the vehicle to the track geometric irregularities, the lateral stability or the curving behavior. Linear models are based on the kinematics of the conical wheels, linear creep wheel-rail forces and the vehicle is considered as a collection of rigid bodies connected by springs and dashpots. On the other hand, multibody models of the railroad vehicles and track take into account the complex wheel-rail contact geometry and their normal and tangential interaction forces. The railroad vehicle bodies are assumed to be connected by kinematic joints and the can be considered as deformable. These modeling capabilities provide a more detailed insight into the vehicle dynamics at the expense of much longer computational analysis. However, special techniques like the use of trajectory coordinates or contact lookup tables alleviate this problem without significant reduction in accuracy. This presentation shows the modelling keys for the real-time simulation of railway vehicles using multibody dynamics that can be used in on–board applications.

Author Index